GeoPlanet: Earth and Planetary Sciences

Paweł Rowiński
Andrea Marion *Editors*

Hydrodynamic and Mass Transport at Freshwater Aquatic Interfaces

34th International School of Hydraulics

Springer

GeoPlanet: Earth and Planetary Sciences

More information about this series at http://www.springer.com/series/8821

Paweł Rowiński · Andrea Marion
Editors

Hydrodynamic and Mass Transport at Freshwater Aquatic Interfaces

34th International School of Hydraulics

Springer

Editors
Paweł Rowiński
Polish Academy of Sciences
Institute of Geophysics
Warsaw
Poland

Andrea Marion
Department of Industrial Engineering
University of Padua
Padua
Italy

The GeoPlanet: Earth and Planetary Sciences Book Series is in part a continuation of Monographic Volumes of Publications of the Institute of Geophysics, Polish Academy of Sciences, the journal published since 1962 (http://pub.igf.edu.pl/index.php).

ISSN 2190-5193 ISSN 2190-5207 (electronic)
GeoPlanet: Earth and Planetary Sciences
ISBN 978-3-319-27749-3 ISBN 978-3-319-27750-9 (eBook)
DOI 10.1007/978-3-319-27750-9

Library of Congress Control Number: 2015957099

Printed on acid-free paper

This Springer imprint is published by SpringerNature
The registered company is Springer International Publishing AG Switzerland

The original version of the bookfrontmatter was revised: The editor's name was corrected throughout the book. The Erratum to the bookfrontmatter is available at 10.1007/978-3-319-27750-9_28

Series Editors

Managing Editor

Anna Dziembowska
Institute of Geophysics, Polish Academy of Sciences

Advisory Board

Preface

This book is the result of a collaborative effort between the Institute of Geophysics (IGF) of the Polish Academy of Sciences with its Center for Polar Studies KNOW and the European Initial Training Network Project HYTECH. The papers presented at the 34th International School of Hydraulics held at Żelechów Palace in Poland during May 11–14, 2015 constitute the basis for this volume. International School of Hydraulics is a biannual event run under the auspices of the International Association of Hydro Environment Engineering and Research IAHR and the Committee of Water Resources of the Polish Academy of Sciences. This year the School was devoted to hydrodynamic and mass transport at freshwater aquatic interfaces, but papers related to other problems from the broadly understood hydraulics were also accepted. Although not published in this volume we need to mention three invited lectures presented by renowned specialists in the field: Prof. Heidi Nepf from Massachusetts Institute of Technology, USA, talked about vegetation hydrodynamics at both the blade-scale and canopy-scale, Prof. Bernhard Statzner, former director of National Science Research Center (CNRS), France, talked about testing predictions of changes in the abundance and community structure of benthic invertebrates and fish after flow restoration in a large river (French Rhône), and Prof. Peter A. Davies from University of Dundee, UK, discussed the complex problem of waviness on density interfaces in stratified water bodies. The presence and advice of these eminent scientists created a fantastic scientific atmosphere during the meeting.

The International School of Hydraulics in its current form organized by the Institute of Geophysics was first held in 2006 and was initially conceived as a forum to bring together leaders in the field of broadly understood hydraulics and young scientists. The diversity of participants in this event allows for cross-fertilization between basic and experimental scientists as well as senior and more junior investigators. The School permits reflection on the current state of the field, unanswered but critical questions, and potential future directions for research.

This Conference Proceedings volume contains the written versions of most of the contributions presented during the School which took place at the Palace

Żelechów, situated in a historical building located some 90 km from Warsaw. The conference has been an excellent opportunity for participants coming from numerous countries from all over the world to present and discuss topics in their respective research areas.

Physical, biochemical, and ecological processes in natural water bodies have been the subject of intense research by different scientific disciplines in the past few decades. Environmental studies of natural water bodies are a relatively new area of research, spanning over no more than fifty years. As regards combined training in environmental sciences and engineering, the first undergraduate and graduate academic programs started in the US only in the 1980s. The dawning of environmental studies in the late twentieth century has seen developments often confined to individual classical areas of expertise, e.g., hydraulic engineering, water chemistry, and population ecology with only a few pioneering programs promoting interaction among specialities (e.g., the International Biological Program in the early 1960s). The development of a truly interdisciplinary approach to environmental studies, so as to address the modern concerns posed by climate change, appears one of the main challenges of the new century. In 2000, the European Commission made the sustainable use of water resources a priority (Water Framework Directive, WFD), setting a timetable for the achievement of adequate ecological standards. This timetable has been driving the work of environmental scientists and practitioners as well as environmental agencies and authorities throughout Europe over more than a decade. A call for the protection and sustainable use of water resources also came from the ICCP (Intergovernmental Panel on Climate Change, rep. 2007).

Natural water streams are characterized by heterogeneities in terms of transported matter, physical properties, biological species, and ecotones. Interfaces are the contact locations between two or more substances or phases, e.g., water and sediment. An inherent property of interfaces in natural water bodies is that they are sites of high gradients of quantities (e.g., fluid velocity, concentration, and temperature). This property induces significant, site-specific diffusive momentum, and mass fluxes at these physical interfaces. Understanding of transport mechanism is an essential step toward assessing the vulnerability of the natural environment to anthropogenic stresses. Typical stream interfaces at a micro scale are inorganic, microbial, and vegetated structures such as sediment grains, biofilms, and periphyton. At an intermediate (meso-) scale, comparable to the water depth, interfacial heterogeneities include sediment clusters, individual submerged and emergent plants, and shallow hyporheic zones. At larger scales heterogeneities include bedforms, bars, vegetation patches, and deep hyporheic zones. As the scale of consideration increases from micro- to meso- to macro-scale the analysis progressively changes from fundamental solutions applicable to well-defined conditions toward combined models where mutual interactions between transported matter and interfaces must be accounted for by adopting appropriate theoretical frameworks, statistical tools, and probabilistic methods.

The HYTECH—'Hydrodynamic Transport in Ecologically Critical Heterogeneous Interfaces'—project is an Initial Training Network funded within the Marie Skłodowska-Curie Actions in the 7th Framework Programme of the

European Commission. The project started in 2013 and will end in 2016. The HYTECH project provides training to doctoral and postdoctoral fellows to encourage innovation in the solution of environmental problems involving the transport of inorganic and organic matter, including solutes, colloids and sediments in river flows, and across the boundary interfaces. The HYTECH fellows originate from all continents, counting 8 fellows from Europe (Italy, Greece, Portugal, Latvia), 3 fellows from Asia (Iran), 2 fellows from Africa (Sudan), 1 fellow from America (Argentina), and 1 fellow from Oceania (New Zealand). Fellow supervision and network progress is assisted by the Expert Advisory Board comprising four eminent scholars: Profs. Peter Davies, Heidi Nepf, Gary Parker, and Bernhard Statzner. A number of institutions are involved in realizing the HYTECH project and they are listed below.

The *University of Padova* (*Italy*) is coordinating the HYTECH project and hosts one doctoral and one postdoctoral fellow. The two projects focus on modeling mass transport in wetlands looking at developing optimal design criteria and on the role of cohesive sediments in determining erosional resistance of bed deposits.

Gerstgraser Ingenieurbüro Für Renaturierung (gIR) is a German private company specialist in renaturalization projects. It contributes to HYTECH hosting a postdoctoral position devoted to the analysis of the implementation of the Water Framework Directive and the Flood Directive in different EU member states.

The *University of Aberdeen* (*UK*) participates in HYTECH hosting two doctoral fellows. They are developing innovative instrumentation for field observation of the hydrodynamics of vegetated streams and working on the development of new Double Averaging theoretical derivations of mass transport equations.

The *Centre National de La Recherche Scientifique* (*CNRS, France*) contributes to HYTECH through the Laboratory of Ecology LEHNA. They host a doctoral fellow conducting field research on the growth and feedback hydrodynamic processes of vegetated species in a French river.

The *Koninklijk Nederlands Instituut Voor Zeeonderzoek* (*NIOZ, NL*) participates in the project hosting one doctoral fellow focusing on geometrical patterns of aquatic vegetation and ecological engineering of aquatic landscapes.

GHT Photonics is an Italian private company specialized in hi-tech instrumentation for field survey and environmental monitoring. It hosts two postdoctoral fellows with the aim of developing a new instrument for river bed survey and new fiber-optics applications in fluid mechanics.

The *Technische Universitaet Braunschweig* (*D*) offers access to its large laboratory facilities to HYTECH fellows and hosts two doctoral fellows who concentrate on environmental-friendly engineering solutions to river restoration and on resistance models for vegetated channels.

The *Politecnico di Milano* (*Italy*) is involved in HYTECH through one doctoral position looking at Lagrangian observation of sediment particle dynamics.

The *University of Sheffield* (*UK*) hosts two doctoral fellows looking at experimental innovation for the observation of bedload and suspended sediment transport.

Water & Environmental technology (*WET Engineering, Italy*) is a private company specialized in hydropower and river tracer techniques. It hosts one doctoral fellow developing tracer tests methods and relevant modeling tools.

A series of institutions and private companies also support HYTECH as Associated Partners: Queen *Mary University of London*, *Leibniz Institute of Freshwater Ecology and Inland Fishery* (*Berlin*), *Centre for Ecology and Hydrology* (*Edinburgh*), *Norwegian University of Science and Technology, Umbria Region, SGI-Studio Galli* (*Padova*), *SELC* (*Venezia*).

It has been a great pleasure to edit the proceedings. We have considerably enjoyed working in cooperation with the International Scientific Committee to call for papers, review papers, and finalize papers to be included in the proceedings. Refereeing papers for an international conference such as International School of Hydraulics is a complex process that relies on the goodwill of those researchers involved in the field. A list of reviewers of papers is given below.

Paweł Rowiński
Andrea Marion

Acknowledgments

We would like to thank all the participants and speakers during the School for contributing to such a stimulating event. The School and this book would not be possible without financial support from the European Initial Training Network Project HYTECH, Institute of Geophysics statutory funds, *Centre for Polar Studies KNOW*—Leading National Research Center and the Committee of Water Resources of the Polish Academy of Sciences.

Enough thanks cannot be expressed to Monika Kalinowska, Web Master for ISH 2015, for dynamically building onto the online system that was introduced for ISH 2015. This facilitated the management of the reviewing process and uploading of papers and we anticipate that it will be a responsive system for future use. Whatever we asked, Monika would work out a way of tweaking the system to comply. She also took other duties, corresponded with the reviewers and authors of papers, and was also extremely helpful in organizing the meeting. A big help in that respect was also given by Magdalena Mrokowska and Matteo Tregnaghi. Also, thank you to Anna Zdunek and Anna Łukanowska who dealt with most of the logistics of the event. The ISH and proceedings are a credit to a large group of people and everyone should be proud of the outcome. A great help was given by young scientists and Ph.D. students, namely Joanna Doroszkiewicz, Emilia Karamuz, Anna Łoboda, Łukasz Przyborowski, and Agnieszka Rajwa-Kuligiewicz. We should also name Anna Dziembowska, responsible for the high quality of English of the papers that are in the volume.

We wish to thank and acknowledge the following reviewers, who have donated their time and expertise to assist in improving the quality of the submitted papers:

- Jochen Aberle, Norwegian University of Science and Technology, Norway,
- Francesco Ballio, Polytechnic University of Milan, Italy,
- Robert Bialik, Institute of Geophysics, Polish Academy of Sciences, Poland
- Monika Kalinowska, Institute of Geophysics, Polish Academy of Sciences, Poland
- Katinka Koll, Technical University Braunschweig, Germany
- Andrea Marion, University of Padova, Italy

- Wojciech Majewski, Institute of Meteorology and Water Management, Gdynia
- Marek Mitosek, Warsaw Technical University, Poland
- Magdalena Mrokowska, Institute of Geophysics, Polish Academy of Sciences, Poland
- Jarosław Napiórkowski, Institute of Geophysics, Polish Academy of Sciences, Poland
- Artur Radecki-Pawlik, Agricultural University of Cracow, Poland
- Paweł Rowiński, Institute of Geophysics, Polish Academy of Sciences, Poland
- Alexander Sukhodolov, Leibnitz Institute for Freshwater Ecology and Inland Fisheries, Germany
- Simon Tait, University of Sheffield, UK
- Steve Wallis, School of the Built Environment, Heriot-Watt University, United Kingdom
- Geraldene Wharton, Queen Mary University of London, UK
- Mattia Zaramella, WET Engineering, Italy

Contents

Time-Averaged Hydrodynamic Equations for Mobile-Bed Conditions

Konstantinos Papadopoulos, Vladimir Nikora, Stuart Cameron, Mark Stewart, Hamish Biggs and Christopher Gibbins

Abstract The objective of this paper is to expand the framework of the conventional Reynolds-Averaged Navier-Stokes equations for the study of mobile-boundary flows. The temporal averaging concept is discussed first, including relevant definitions and theorems. Time-averaged continuity, momentum, mass-transport and stress balance equations are then derived. These new equations contain additional terms that represent the mobile-boundary effects. Potential applications of the proposed equations include flow-biota interactions and sediment dynamics, among others.

1 Introduction

Environmental flows, aquatic or atmospheric, involve fluid motion and its interaction with fixed or mobile boundaries. Examples include rivers with vegetated or gravel beds, and atmospheric flows over terrestrial canopies. Recently, double-averaging (in time and space) has been implemented to cope with the spatial heterogeneities induced by the presence of boundary roughness where the traditional Reynolds averaging approach is inappropriate (e.g., Finnigan 2000; Nikora et al. 2007; Pedras and de Lemos 2000). However, conventional Reynolds averaging is also unsuitable for flows where the boundary is mobile, due to the discontinuity of hydrodynamic variables within the averaging interval. In a recent paper (Nikora et al. 2013), the double-averaging methodology has been refined by adapting an approach used in the study of multiphase systems (Gray and Lee 1977) to arrive at an advanced set of double-averaged conservation equations applicable to mobile-bed

K. Papadopoulos (✉) · V. Nikora · S. Cameron · M. Stewart · H. Biggs
School of Engineering, University of Aberdeen, Fraser Noble Building, King's College, Aberdeen AB24 3UE, UK
e-mail: kpapadopoulos@abdn.ac.uk

C. Gibbins
Northern Rivers Institute, School of Geosciences, University of Aberdeen, St Mary's Building, King's College, Aberdeen AB24 3UF, UK

P. Rowiński and A. Marion (eds.), *Hydrodynamic and Mass Transport at Freshwater Aquatic Interfaces*, GeoPlanet: Earth and Planetary Sciences,
DOI 10.1007/978-3-319-27750-9_1

flows. Following this direction, we first suggest a modification of the temporal averaging operation, including refined definitions and averaging theorems. Then, a new set of first- and second-order time-averaged conservation equations, suitable for the description of turbulent flows over mobile boundaries, is proposed. The new equations include terms responsible for bed mobility effects and, thus, can be used as a basis for physical analyses and numerical modelling of mobile-bed flows.

2 Theoretical Background

In the study of multiphase systems (e.g., Gray and Lee 1977), the use of a distribution function γ is introduced to cope with the spatial heterogeneity of the material within the averaging domain. In a similar way, a distribution function is used in our considerations and is set equal to unity when a point is in the fluid domain and zero otherwise. Two forms of the temporal average are defined: superficial and intrinsic. For an arbitrary variable $\theta(x_i, t)$, the superficial temporal average is defined over the interval T_o as:

$$\overline{\theta(x_i,t)}^{s} = \frac{1}{T_o}\int_{T_o} \theta(x_i, t+\tau)\gamma(x_i, t+\tau)d\tau \tag{1}$$

where x_i are the spatial coordinates and τ is the local time coordinate; superficial temporal averaging is denoted with an overbar with an index s. The intrinsic temporal average is defined as:

$$\overline{\theta(x_i,t)} = \frac{1}{T_f}\int_{T_o} \theta(x_i, t+\tau)\gamma(x_i, t+\tau)d\tau \tag{2}$$

where T_f is a part of T_o that contains the time instants at which the point x_i is occupied by fluid (Nikora et al. 2013); intrinsic temporal averaging is denoted with an overbar. At mobile boundary conditions, the averaging time interval T_o is set to be appropriately larger than the turbulent integral time scale and the time scale that characterises the variation of the moving boundary (e.g., Bendat and Piersol 2010; Monin and Yaglom 1971; Nikora et al. 2013). Superficial and intrinsic averages are linked through the relation:

$$\overline{\theta(x_i,t)}^{s} = \phi_T(x_i,t)\overline{\theta(x_i,t)} \tag{3}$$

where $\phi_T = T_f/T_o$ is the local time porosity (Nikora et al. 2013). Using the Reynolds decomposition, the local instantaneous variable θ can be separated into a mean and fluctuating part, i.e., $\theta(x_i,t) = \overline{\theta}(x_i) + \theta'(x_i,t)$. Due to the heterogeneities

previously noted, the Reynolds conditions (e.g., Nikora et al. 2007) are not completely satisfied; those valid for this case are summarised below:

$$\overline{f+g} = \bar{f} + \bar{g}, \quad \overline{af} = a\bar{f}, \quad \bar{a} = a, \quad \overline{\bar{f}g} = \bar{f}\,\bar{g} \tag{4}$$

where f and g are arbitrary variables and a is a constant. Using Eqs. (1) and (2), theorems that link the average partial derivatives with the derivatives of averaged quantities can be obtained. The averaging theorem for the superficial temporal average of the time derivative is:

$$\begin{aligned}\overline{\frac{\partial\theta}{\partial t}}^{s} &= \frac{1}{T_o}\int_{T_o}\frac{\partial\theta}{\partial t}\gamma dt = \frac{1}{T_o}\int_{T_o}\frac{\partial\theta\gamma}{\partial t}dt - \frac{1}{T_o}\int_{T_o}\theta\frac{\partial\gamma}{\partial t}dt \\ &= \frac{\partial}{\partial t}\left(\frac{1}{T_o}\int_{T_o}\theta\gamma dt\right) + \frac{1}{T_o}\int_{T_o}\theta w_i n_i \delta(x_i - x_{s_i})dt \\ &= \frac{\partial\bar{\theta}^{s}}{\partial t} + \frac{1}{T_o}\int_{T_o}\theta w_i n_i \delta(x_i - x_{s_i})dt\end{aligned} \tag{5}$$

where the relations (e.g., Gray and Lee 1977):

$$\frac{\partial\gamma}{\partial t} = -w_i\frac{\partial\gamma}{\partial x_i}, \frac{\partial\gamma}{\partial x_i} = n_i\delta(x_i - x_{s_i}) \tag{6}$$

are used and where the dependence on time and space coordinates is not shown for brevity. In Eq. (6), the ith velocity component of the moving boundary is denoted by w_i, n_i is the unit vector normal to the interfacial surface and directed into the fluid, δ is the three dimensional analogue of the Dirac delta function, and x_{si} is the position coordinate of the boundary. Correspondingly, the averaging theorem for the spatial derivative is:

$$\overline{\frac{\partial\theta}{\partial x_i}}^{s} = \frac{\partial\bar{\theta}^{s}}{\partial x_i} - \frac{1}{T_o}\int_{T_o}\theta n_i\delta(x_i - x_{s_i})dt \tag{7}$$

Employing Eq. (3), the theorems for the intrinsically averaged derivatives can be obtained from Eqs. (5) and (7) as:

$$\begin{aligned}\overline{\frac{\partial\theta}{\partial t}} &= \frac{1}{\phi_T}\frac{\partial\phi_T\bar{\theta}}{\partial t} + \frac{1}{T_f}\int_{T_o}\theta w_i n_i\delta(x_i - x_{s_i})dt \\ \overline{\frac{\partial\theta}{\partial x_i}} &= \frac{1}{\phi_T}\frac{\partial\phi_T\bar{\theta}}{\partial x_i} - \frac{1}{T_f}\int_{T_o}\theta n_i\delta(x_i - x_{s_i})dt\end{aligned} \tag{8}$$

3 Time-Averaged Hydrodynamic Equations

The derivation starts with the equations of mass (continuity) and momentum conservation for instantaneous variables:

$$\frac{\partial \rho}{\partial t} + \frac{\partial \rho u_j}{\partial x_j} = 0, \frac{\partial \rho u_i}{\partial t} + \frac{\partial \rho u_i u_j}{\partial x_j} = \rho g_i - \frac{\partial p}{\partial x_i} + \frac{\partial \tau_{ij}}{\partial x_j} \tag{9}$$

where ρ is fluid density, u_i is a velocity component in the ith direction, g_i is the gravity acceleration component, p is pressure, and τ_{ij} is the viscous stress component (note that repeated indices imply Einstein's summation convention). For the Newtonian incompressible fluid, the viscous stress term is given by $\tau_{ij} = \rho \nu \partial u_i / \partial x_j$, where ν is the coefficient of kinematic viscosity. The transport of a solute with a concentration c is described by the advection-diffusion equation as:

$$\frac{\partial c}{\partial t} + \frac{\partial u_j c}{\partial x_j} = \frac{\partial}{\partial x_j}\left(\chi_m \frac{\partial c}{\partial x_j}\right) + r \tag{10}$$

where χ_m is the coefficient of molecular diffusion, and r represents the homogeneous reaction rate (i.e., sink or source of c).

3.1 Time-Averaged Continuity, Momentum, and Mass Transport Equations

Employing the superficial averaging (1), the averaging theorems (5) and (7), the Reynolds decomposition, and the Reynolds conditions (4), the time-averaged continuity and momentum equations can be derived from Eq. (9) as:

$$\frac{\partial \phi_T}{\partial t} + \frac{\partial \phi_T \bar{u}_j}{\partial x_j} = 0 \tag{11}$$

$$\underbrace{\frac{\partial \phi_T \bar{u}_i}{\partial t}}_{\text{local acceleration}} + \underbrace{\frac{\partial \phi_T \bar{u}_i \bar{u}_j}{\partial x_j}}_{\text{convective acceleration}} = \underbrace{\phi_T g_i}_{\text{gravity term}} - \underbrace{\frac{1}{\rho}\frac{\partial \phi_T \bar{p}}{\partial x_i}}_{\text{pressure gradient}} - \underbrace{\frac{\partial \phi_T \overline{u_i' u_j'}}{\partial x_j}}_{\text{turbulent stress change}} + \underbrace{\frac{1}{\rho}\frac{\partial \phi_T \bar{\tau}_{ij}}{\partial x_j}}_{\text{viscous stress change}} + \underbrace{\frac{1}{\rho T_o}\int_{T_o}\left[p n_i \delta(x_i - x_{s_i}) - \tau_{ij} n_j \delta\left(x_j - x_{s_j}\right)\right] dt}_{\text{contribution from flow}-\text{boundary interactions}} \tag{12}$$

In deriving Eqs. (11) and (12), the no-slip boundary condition is used and the fluid density is assumed to be constant. The interpretation of most terms involved in Eqs. (11) and (12) is analogous to that of the conventional Reynolds-averaged continuity and momentum equations. The seventh term of Eq. (12) represents a contribution to the fluid momentum balance from the flow-boundary interactions. Similarly, the temporal average of the advection-diffusion equation is:

$$\underbrace{\frac{\partial \phi_T \bar{c}}{\partial t}}_{\substack{\text{local}\\ \text{change of } c}} + \underbrace{\frac{\partial \phi_T \bar{u}_j \bar{c}}{\partial x_j}}_{\substack{\text{spatial}\\ \text{change of } c}} = \underbrace{\frac{\partial}{\partial x_j}\left(\phi_T \chi_m \overline{\frac{\partial c}{\partial x_j}}\right)}_{\text{molecular diffusion transport}} - \underbrace{\frac{\partial \phi_T \overline{u_j' c'}}{\partial x_j}}_{\text{turbulent transport}} + \underbrace{\phi_T \bar{r}}_{\text{reaction rate}} - \underbrace{\frac{1}{T_o}\int_{T_o} \chi_m \frac{\partial c}{\partial x_j} n_j \delta\left(x_j - x_{s_j}\right) dt}_{\text{contribution from flow}-\text{boundary interactions}} \tag{13}$$

The last term of Eq. (13) represents a potential contribution to the transport of the solute mass due to the effect of the moving boundary.

3.2 Second-Order Balance Equations for Velocity Moments

To obtain the second-order hydrodynamic equations we employ an approach of Keller and Friedmann (Monin and Yaglom 1971). As a consequence of the Reynolds decomposition, the total average momentum flux (*I*) can be subdivided into mean field contribution (*II*) and turbulence field contribution (*III*), i.e.:

$$\underbrace{\phi_T \overline{u_i u_k}}_{I} = \underbrace{\phi_T \bar{u}_i \bar{u}_k}_{II} + \underbrace{\phi_T \overline{u_i' u_k'}}_{III}. \tag{14}$$

Assuming that the quantities *I* and *II* are given, the turbulent stress *III* can be determined by subtraction of *II* from *I*. The derivatives of the stress terms can be expanded following the product rule:

$$\begin{aligned} \frac{\partial u_i u_k}{\partial t} &= u_k \frac{\partial u_i}{\partial t} + u_i \frac{\partial u_k}{\partial t} \\ \frac{\partial \phi_T \bar{u}_i \bar{u}_k}{\partial t} &= \bar{u}_k \frac{\partial \phi_T \bar{u}_i}{\partial t} + \bar{u}_i \frac{\partial \phi_T \bar{u}_k}{\partial t} - \bar{u}_i \bar{u}_k \frac{\partial \phi_T}{\partial t} \end{aligned} \tag{15}$$

Substituting Eqs. (11) and (12) in the second relation of Eq. (15), the equation that describes the balance of $\phi_T \bar{u}_i \bar{u}_k$ can be produced:

$$\underbrace{\frac{\partial \phi_T \bar{u}_i \bar{u}_k}{\partial t}}_{\substack{\text{time rate}\\ \text{of change}}} + \underbrace{\frac{\partial \phi_T \bar{u}_i \bar{u}_k \bar{u}_j}{\partial x_j}}_{\text{mean convection}} = \underbrace{\phi_T(\bar{u}_k g_i + \bar{u}_i g_k)}_{\substack{\text{work rate of gravity:}\\ \text{energy supply to the mean flow}}} \underbrace{-\frac{1}{\rho}\frac{\partial \phi_T\left(\bar{u}_k \bar{p}\delta_{ij} + \bar{u}_i \bar{p}\delta_{kj}\right)}{\partial x_j}}_{\substack{\text{work rate of pressure:}\\ \text{pressure transport}}}$$

$$\underbrace{-\frac{\partial \phi_T\left(\bar{u}_k \overline{u_i' u_j'} + \bar{u}_i \overline{u_k' u_j'}\right)}{\partial x_j}}_{\substack{\text{work rate of turbulent stress:}\\ \text{turbulent transport}}} + \underbrace{\frac{1}{\rho}\frac{\partial \phi_T\left(\bar{u}_k \bar{\tau}_{ij} + \bar{u}_i \bar{\tau}_{kj}\right)}{\partial x_j}}_{\substack{\text{work rate of viscous stress:}\\ \text{viscous transport}}}$$

$$\underbrace{-\frac{\phi_T \bar{p}}{\rho}\left(\frac{\partial \bar{u}_k}{\partial x_i} + \frac{\partial \bar{u}_i}{\partial x_k}\right)}_{\substack{\text{work rate of } p \text{ against}\\ \text{mean strain rate}}} + \underbrace{\frac{\phi_T}{\rho}\left(\bar{\tau}_{ij}\frac{\partial \bar{u}_k}{\partial x_j} + \bar{\tau}_{kj}\frac{\partial \bar{u}_i}{\partial x_j}\right)}_{\substack{\text{work rate of } \tau \text{ against mean strain rate:}\\ \text{dissipation of kinetic energy}}}$$

$$\underbrace{+\ \phi_T\left(\overline{u_i' u_j'}\frac{\partial \bar{u}_k}{\partial x_j} + \overline{u_k' u_j'}\frac{\partial \bar{u}_i}{\partial x_j}\right)}_{\substack{\text{work rate of turbulent stress against mean}\\ \text{strain rate: turbulent energy production}}}$$

$$\underbrace{+\frac{1}{\rho T_o}\int_{T_o}\left(\bar{u}_k p\delta_{ij} + \bar{u}_i p\delta_{kj} - \bar{u}_k \tau_{ij} - \bar{u}_i \tau_{kj}\right)n_j \delta\left(x_j - x_{s_j}\right)dt}_{\text{contribution from flow}-\text{boundary interactions}}. \tag{16}$$

The last term in Eq. (16) is the consequence of the last term of Eq. (12) and is considered as a contribution to the mean stress balance exerted by the boundary motion. Substituting Eq. (9) into the first relation of Eq. (15) yields the balance of $u_i u_k$. By its averaging and then subtracting Eq. (16), one obtains the equation for the Reynolds stress:

$$\underbrace{\frac{\partial \phi_T \overline{u_i' u_k'}}{\partial t}}_{\substack{\text{time rate} \\ \text{of change}}} + \underbrace{\frac{\partial \phi_T \bar{u}_j \overline{u_i' u_k'}}{\partial x_j}}_{\text{mean convection}} = \underbrace{-\phi_T \left(\overline{u_i' u_j'} \frac{\partial \bar{u}_k}{\partial x_j} + \overline{u_k' u_j'} \frac{\partial \bar{u}_i}{\partial x_j} \right)}_{\text{production}}$$

$$\underbrace{-\frac{1}{\rho} \frac{\partial \phi_T \left(\overline{u_k' p'} \delta_{ij} + \overline{u_i' p'} \delta_{kj} \right)}{\partial x_j}}_{\text{pressure transport}} \underbrace{- \frac{\partial \phi_T \overline{u_i' u_k' u_j'}}{\partial x_j}}_{\text{turbulent transport}}$$

$$\underbrace{+\frac{1}{\rho} \frac{\partial \phi_T \left(\overline{u_k' \tau_{ij}'} + \overline{u_i' \tau_{kj}'} \right)}{\partial x_j}}_{\text{viscous transport}} \underbrace{+ \frac{\phi_T}{\rho} \overline{p' \left(\frac{\partial u_k'}{\partial x_i} + \frac{\partial u_i'}{\partial x_k} \right)}}_{\text{redistribution over space}}$$

$$\underbrace{-\frac{\phi_T}{\rho} \left(\overline{\tau_{ij}' \frac{\partial u_k'}{\partial x_j}} + \overline{\tau_{kj}' \frac{\partial u_i'}{\partial x_j}} \right)}_{\text{dissipation}}$$

$$\underbrace{+\frac{1}{\rho T_o} \int_{T_o} \left(u_k' p \delta_{ij} + u_i' p \delta_{kj} - u_k' \tau_{ij} - u_i' \tau_{kj} \right) n_j \delta \left(x_j - x_{s_j} \right) dt}_{\text{contribution due to flow} - \text{boundary interaction}} \tag{17}$$

Compared to the conventional Reynolds stress equation (e.g., Hanjalic and Launder 1972; Monin and Yaglom 1971), here the effect of the porosity function and the ninth term are included. In the reasoning followed in Eqs. (12) and (16), the ninth term of Eq. (17) is considered as an external contribution to the Reynolds stress balance, caused by the boundary motion.

4 Discussion

The suggested equations are developed for the study of flows over mobile boundaries, implying the existence of temporal heterogeneities. These heterogeneities result in the discontinuities of a hydrodynamic variable within the time averaging domain. This difficulty is surpassed with the use of the distribution function, which in turn leads to the appearance of the local time porosity and additional time integrals in the equations. These additional terms constitute the main difference between the proposed equations and the conventional Reynolds-Averaged hydrodynamic equations for flows over fixed boundaries. For the case in which the boundaries are fixed, we have $\phi_T \equiv 1$ and therefore operations of temporal averaging and differentiation commute (the distribution function is constant; i.e. $\partial \gamma / \partial x_i = 0$). Thus, for the fixed-bed conditions, Eqs. (11), (12),

(16) and (17) coincide with the conventional Reynolds-averaged continuity, momentum, mass transport and stress balance equations. Theorems for temporal averaging have also been proposed in Ishii and Hibiki (2006), in order to introduce interfacial terms in the conservation equations for a two-phase mixture. Material discontinuities and temporal heterogeneities are also reported there. However, the authors' definition of the temporal average follows the conventional one, while discontinuity is considered for the integration domain, when the relation between $\overline{\partial\theta/\partial s}$ and $\partial\bar{\theta}/\partial s$ (s is the domain of differentiation) is needed (Ishii and Hibiki 2006).

Applications of the proposed equations include the study of the interactions between aquatic flow and submerged vegetation or the study of sediment dynamics.

5 Conclusions

In the preceding sections, a method of temporal averaging was discussed, based on the concepts reported in Gray and Lee (1977) and Nikora et al. (2013). This method is followed for the development of equations for momentum, mass and stress transport for mobile-bed flows. The effect of a moving boundary is introduced through the local porosity function and interfacial terms. The suggested equations are intended to assist in studies involving the interaction of fluid flow with in-stream moving objects. The time-averaged transport equations alone may not be sufficient for the numerical investigation of such cases. However, complemented with spatial averaging as a second step, they may be used in the development of the theoretical framework that is needed for the experimental and numerical study of mobile-boundary flows.

Acknowledgements This study is a part of the research project "Hydrodynamic Transport in Ecologically Critical Heterogeneous interfaces" (HYTECH), the support of which, under the European Union's Seventh Framework Programme (Marie Curie FP7-PEOPLE-2012-ITN, European Commission grant agreement with number 316546), is gratefully acknowledged by the authors.

References

Bendat J, Piersol A (2010) Random data, analysis and measurement process. Wiley, New Jersey

Finnigan J (2000) Turbulence in plant canopies. Annu Rev Fluid Mech 32(1):519–571. doi:10.1146/annurev.fluid.32.1.519

Gray W, Lee P (1977) On the theorems for local volume averaging of multiphase systems. Int J Multiph Flow 3(4):333–340. doi:10.1016/0301-9322(77)90013-1

Hanjalic K, Launder B (1972) A Reynolds stress model of turbulence and its application to thin shear flows. J Fluid Mech 52(4):609–638. doi:10.1017/S002211207200268X

Ishii M, Hibiki T (2006) Thermo-fluid dynamics of two phase flow. Springer, New York

Monin A, Yaglom A (1971) Statistical fluid mechanics: mechanics of turbulence, vols I and II. M.I.T. Press, Cambridge

Nikora V, McEwan I, McLean S, Coleman S, Pokrajac D, Walters R (2007) Double-averaging concept for rough-bed open-channel and overland flows: theoretical background. J Hydraul Eng 133(8):873–883. doi:10.1061/(ASCE)0733-9429(2007)133:8(873)

Nikora V, Ballio F, Coleman S, Pokrajac D (2013) Spatially averaged flows over mobile rough beds: definitions, averaging theorems and conservation equations. J Hydraul Eng 139(8): 803–811. doi:10.1061/(ASCE)HY.1943-7900.0000738

Pedras M, de Lemos M (2000) On the definition of turbulent kinetic energy for flow in porous media. Int Commun Heat Mass Transf 27(2):211–220. doi:10.1016/S0735-1933(00)00102-0

Potential Application of Mesh-Free SPH Method in Turbulent River Flows

Ehsan Kazemi, Simon Tait, Songdong Shao and Andrew Nichols

Abstract A comprehensive review has been completed on the simulation of turbulent flow over rough beds using mesh-free particle models. Based on the outcomes of this review, an improved Smoothed Particle Hydrodynamics (SPH) method has been developed for open channel flows over a rough bed, in which a mixing length model is used for modeling the 2D turbulence and a drag force equation is proposed for treating the boundary shear. The proposed model was applied to simulate a depth-limited open channel flow over a rough bed surface. The results of the velocity profile and shear stress distribution show a good agreement with the experimental data and existing analytical solutions. This work reveals that in order to correctly model turbulent open channel flow over a rough bed, the treatment of both flow turbulence and bed roughness effect is equally important.

1 Introduction

Turbulence behavior in natural river flow is one of the most important issues in river engineering as it can generate a significant effect on the flow structure and plays a key role in the transport of sediments, especially fine suspended particles. Since river flows are usually turbulent and the river beds are often composed of sands, gravels, ripples, or dunes, the study of turbulent flow over rough bed channels has been an important topic in the last decades. However, the flow behavior near the bed and the effect of rough elements on the flow velocity and turbulence characteristics are not fully understood yet.

The main effect of bed roughness is on the vertical distribution of flow velocity and turbulence near the bed, which then affects the whole flow structure. As the roughness characteristics and bed geometry vary from one river channel to another,

E. Kazemi · S. Tait · S. Shao (✉) · A. Nichols
Department of Civil and Structural Engineering, University of Sheffield,
Sheffield S1 3JD, UK
e-mail: s.shao@sheffield.ac.uk

P. Rowiński and A. Marion (eds.), *Hydrodynamic and Mass Transport at Freshwater Aquatic Interfaces*, GeoPlanet: Earth and Planetary Sciences,
DOI 10.1007/978-3-319-27750-9_2

the effects of roughness on the flow are different and should be treated differently in various theoretical and numerical studies. However, most of models for sand grain bed roughness have assumed a standard organized roughness pattern and so related the roughness effect with an equivalent roughness height. The classical scheme based on experimental data of Nikuradse (1933), Clauser (1954), Rotta (1962) and Perry et al. (1969) revealed that the flow velocity profile in a semi-logarithmic scale has the same slope (von-Karman constant, κ) for both the smooth and rough walls, but with a vertical shift in the mean velocity for the case of a rough wall. A number of research studies have been carried out to find a relationship between the shift in velocity and the physical roughness size and also to find the effective location of the wall, i.e. where the flow mean velocity is zero. Based on the experiments for uniform sand grain roughness, Nikuradse (1933) found that the shift is a function of the equivalent roughness height $k_s^+ = k_s u^*/\nu$ only, where k_s is the diameter of the sand grain, u^* is the boundary shear velocity and ν is the kinematic viscosity. However, the data analysis made by Clauser (1954) has shown that the shift is also related to the pattern and shape of the roughness. Generally speaking, the effect of bed roughness on the velocity field and flow turbulence has not been precisely addressed because of the complex nature of this problem. On the other hand, numerous experimental and numerical studies have been carried out to understand the complicated process of turbulent channel flows and their interactions with the bed. With regard to the treatment of rough bed surfaces, Table 1 summarizes some existing numerical models as well as an assessment of their strengths and weaknesses.

Table 1 Summary of numerical models treating shear boundary layer near rough wall

Boundary treatment method	Turbulence model	Characteristics	Examples
Wall function model	k-ε model	Suitable for smooth and small-scale boundary roughness, but not efficient for large-scale one as the velocity distribution is not logarithmic near rough wall	Hsu et al. (1998), Nicholas and Smith (1999), Zeng and Li (2012)
Modified turbulence model	Mixing length model	Simple but applicable only for shear flows where the distribution of the mixing length is known	van Driest (1956), Rotta (1962), Granville (1985, 1988), Krogstad (1991)
Drag-force model	Any turbulence model	Suitable for rough boundaries with large discrete roughness elements, also reflects the effects of rough wall based on shape and geometry of the roughness element	Christoph and Pletcher (1983), Taylor et al. (1985), Wiberg and Smith (1991), Miyake et al. (1999), Cui et al. (2003), Rameshwaran et al. (2011), Zeng and Li (2012)

2 Mesh-Free Particle Models for Open Channel Flow

In recent years, mesh-free particle modelling approaches, such as SPH, have been investigated for their potential in simulating open channel flows, but their potential has not been fully explored for the turbulent channel flows over rough wall boundaries. There are two main reasons for this, firstly the lack of adequate turbulence models which can be used to close with the Lagrangian SPH equations, and secondly the difficulty in modelling the flow structure near wall boundaries, especially when the wall is composed of rough elements. In the following section, established turbulence and rough bed models used in existing particle based methods are reviewed.

2.1 Turbulence Modelling in Particle Methods

Turbulence modelling in particle methods is very challenging as all well-known turbulence models have been originally developed and tested for the mesh-based methods. However, there have been some attempts in recent years to apply different turbulence models in particle methods. One of the earliest and successful works was made by Gotoh et al. (2001) who applied a sub-particle scale (SPS) turbulence model in their Moving Particle Semi-implicit (MPS) method for simulating a turbulent jet. The key idea of this approach is that large scale turbulent eddies are resolved by the spatially averaged Navier-Stokes (N-S) equations and small scale eddies are calculated through the SPS formulation which relates the Reynolds stress to the mean flow strain rate according to the Boussinesq approximation. Later on, Violeau et al. (2002) proposed two approaches in modelling the flow turbulence in SPH. One was based on the eddy viscosity assumption and another was based on the Generalized Langevin Model (GLM). They tested these two turbulence models by solving the Lagrangian form of N-S equations for a turbulent Poiseuille flow in a pipe. Violeau and Issa (2007) also developed turbulence models to be used with SPH for some complex free surface flows. They developed a k-ε model as well as an explicit algebraic Reynolds stress model (EARSM) and they even used a 3D Large Eddy Simulation (LES) model to simulate the collapse of a water column. The authors stated that, despite its simplicity, the LES-SPS model needs more computational costs in comparison with the traditional RANS turbulence closures. Lopez et al. (2010) developed a SPH model for the hydraulic jumps with different Froude numbers (Fr). They achieved a good result for the cases with low Froude number by using the standard SPH formulations without any turbulence closure, but a variable artificial viscosity formulation had to be used to achieve good accuracy for flows with $Fr > 5$. In addition, some researchers have applied Smagorinsky-based SPS models in turbulence modelling for the particle methods, including but not limited to Sahebari et al. (2011), Chern and Syamsuri (2013) and Fu and Jin (2013), where the Smagorinsky constant of 0.12–0.15 was taken in their models. In a recent study,

De Padova et al. (2013) used a mixing length model for 3D hydraulic jumps in a large channel. The turbulence model was first validated by simulating a 2D uniform open channel flow over a wall with roughness size $k_s = 0.02H$, where H is the water depth. Then it was used to simulate hydraulic jumps and the model result of free surface profiles was compared with that computed by a k-ε model.

2.2 Rough Bed Boundary Treatment in Particle Methods

In addition to the inclusion of turbulence model, the treatment of bed boundary is also very important in modelling open channel flows. However, in most of the developed particle models, the effect of bed roughness is not taken into consideration. Shakibaeinia and Jin (2011), Sahebari et al. (2011), Federico et al. (2012) and De Padova et al. (2013) have not explicitly included any treatment of the channel bed in their models. On the other hand, this issue has been tentatively addressed in some other mesh-free SPH and MPS models. Violeau et al. (2002) and Violeau and Issa (2007) applied a wall function approach to their turbulence models to impose the logarithmic velocity distribution near the wall. Lopez et al. (2010) applied a Lennard-Jones repulsive force on the bed to prevent the particles from penetrating into the wall and this produced a "numerical" resistance arising from the roughness effect. Chern and Syamsuri (2013) used bottom boundaries for the smooth, triangular, trapezoidal and sinusoidal beds defined by lines of particles to simulate the effect of corrugated bed on the hydraulic jump characteristics. They used a repulsive force similar to Lopez et al. (2010) in that the wall particles exert a force on the fluid particles to represent the resistance of the rough bed. Fu and Jin (2013) accounted for the bed roughness in their MPS model by setting several layers of ghost particles beyond the bed boundary and assigning an artificial velocity to these imaginary particles in the opposite direction of the flow. The model presented a simple method to reflect the effect of bottom roughness on the flow by imposing a numerical adjustment of velocity at the bed, which was not based on an actual physical mechanism.

As reviewed, in most of mesh-free particle models developed for open channel flows, bed roughness effect is not explicitly accounted for. Since the bed is the main source of turbulence production, there should be some treatments in the numerical modelling for the flow over rough surfaces. The roughness reduces velocity near the bed to produce a velocity gradient, and this effect can be transferred to the upper layers of the flow by the turbulent shear stress. According to the summary presented in Table 1, the drag force method coupled with a suitable turbulence model has been shown to be an appropriate way of modelling the roughness effect in grid-based methods (Taylor et al. 1985; Wiberg and Smith 1991; Zeng and Li 2012), which can be also applied in mesh-free particle methods. Ideally, the production of near-wall velocity gradient can be modelled by an appropriate drag force model and the transportation of shear to upper layers can be modelled by a suitable turbulence model.

Thus, the aim of the present study is to investigate the feasibility of mesh-free particle methods (e.g. SPH) and propose effective solutions for the simulation of turbulent open channel flows over a rough bed surface. We suggest applying a drag force equation to account for the effect of bed roughness based on the selection of drag force models as found in the literature, and coupling it with a suitable mixing length model to address the flow turbulence effect. The mixing length approach is preferred because of its simplicity and effectiveness in modelling shear flows.

3 SPH Model and Its Application

In this application study, a numerical model is developed by the authors based on the SPH method to solve the 2D Lagrangian form of conservation equations of mass and momentum to simulate a depth-limited turbulent open channel flow over a fully rough bed consisting of regular spheres. This model is developed to ultimately provide a mesh free based modelling capability to simulate the flow over and within rough, potentially mobile porous boundaries. The development is part of the EU funded HYTECH project that is focusing on the physical processes at important aquatic boundaries (Marion et al. 2014). The solved equations of the current version of the model are defined as

$$\frac{D\rho}{Dt} = -\rho \nabla \cdot \mathbf{u} \tag{1}$$

$$\frac{D\mathbf{u}}{Dt} = -\frac{1}{\rho}\nabla P + \mathbf{g} + v_0 \nabla^2 \mathbf{u} + \frac{1}{\rho}\nabla \cdot \boldsymbol{\tau} + \frac{1}{\rho}\boldsymbol{\tau}_d \tag{2}$$

where t (s) is time, ρ (kg/m^3) is density, $\mathbf{u}$ (m/s) is velocity, P (Pa) is pressure, $\mathbf{g}$ (m/s^2) is gravitational acceleration, v_0 (m^2/s) is kinematic viscosity of water, $\boldsymbol{\tau}$ (Pa) is the turbulent shear stress tensor and $\boldsymbol{\tau}_d$ (Pa/m) is the drag-induced shear stress. The fourth term on the right hand side of the momentum equation can be modelled by using different turbulence closure models. In a 2D uniform open channel flow, by considering x and z as horizontal and vertical coordinates, respectively, $\nabla \cdot \boldsymbol{\tau}$ can be simply substituted by $\partial \tau_{xz}/\partial z$, where τ_{xz} is the xz component of the shear stress tensor, since other stress components are much smaller and can thus be ignored. According to the mixing length theory, the following equation can be solved for the turbulent shear stress

$$\frac{\tau_{xz}}{\rho} = l_m^2 \left|\frac{\partial u}{\partial z}\right| \left(\frac{\partial u}{\partial z}\right) \tag{3}$$

where u (m/s) is the velocity component in x direction and l_m (m) is the mixing length which is calculated by Nezu and Rodi's formula (1986).

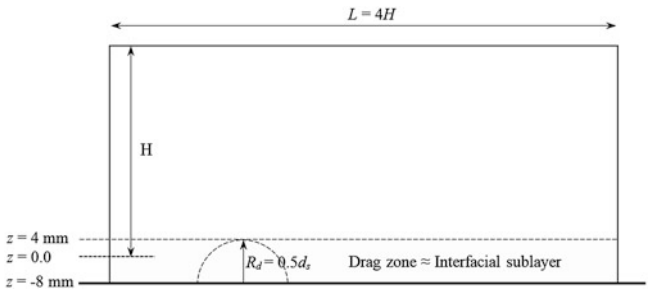

Fig. 1 A schematic view of the computational domain and drag zone

The fifth term on the right hand side of the momentum equation is the drag stress term added to account for the effect of rough bed boundary. This term is calculated only for the particles which are located in a drag zone (see Fig. 1), where the drag-induced shear stress $\boldsymbol{\tau}_d$ is calculated by the following equation

$$\boldsymbol{\tau}_d = \frac{\mathbf{F}_d}{A_\tau} \tag{4}$$

where $\mathbf{F}_d$ (N) is the drag force exerted on fluid particle from the bed, which is assumed to be equal to and in the opposite direction of the force from the fluid particle to the bed, and A_τ (m^2) is the bed-parallel planar area affected by the fluid particle which is equal to $d_s d_p$ (where d_s is the bed grain diameter and d_p is the SPH particle spacing). The drag force $\mathbf{F}_d$ is calculated by

$$\mathbf{F}_d = -\frac{1}{2} C_d \rho A_d \mathbf{u}|\mathbf{u}| \tag{5}$$

where C_d is the drag coefficient and A_d (m) is the cross-sectional area that is equal to the particle spacing d_p.

As mentioned before, the SPH method is used to discretize the governing equations. SPH is a Lagrangian particle approach that was developed by Gingold and Monaghan (1977) and Lucy (1977) initially for the astrophysical problems. Then it was used widely for simulating the fluid flows. In the SPH approximation, a variable like "A" is estimated at the location of particle "a" according to the values at neighboring particles "b" by the following equation

$$A(\mathbf{r}_a) = \sum_b m_b \frac{A(\mathbf{r}_b)}{\rho_b} W(\mathbf{r}_a - \mathbf{r}_b, h) \tag{6}$$

where $\mathbf{r}$ is the particle position, h is the smoothing length, m_b and ρ_b are respectively the mass and density of neighboring particles, and $W(\mathbf{r}_a - \mathbf{r}_b, h)$ is the weighting or kernel function that is specified by a cubic spline function in the

present work (refer to Monaghan and Lattanzio 1985). The derivative of $A(\mathbf{r}_a)$ in x_j direction can be approximated as follows

$$\frac{\partial A(\mathbf{r}_a)}{\partial x_j} = \sum_b m_b \frac{A(\mathbf{r}_b)}{\rho_b} \frac{\partial W(\mathbf{r}_a - \mathbf{r}_b, h)}{\partial x_j} \tag{7}$$

According to the SPH formulations, the governing Eqs. (1) and (2) are discretized as below, respectively, to calculate the density and velocity of particles

$$\frac{D\rho_a}{Dt} = \rho_a \sum_b \frac{m_b}{\rho_b} \mathbf{u}_{ab} \cdot \nabla_a W_{ab} \tag{8}$$

$$\begin{aligned} \frac{d\mathbf{u}_a}{dt} = & -\sum_b m_b \left(\frac{P_a}{\rho_a^2} + \frac{P_b}{\rho_b^2} \right) \nabla_a W_{ab} + \mathbf{g} \\ & + \sum_b m_b \frac{4v_0}{(\rho_a + \rho_b)} \frac{\mathbf{r}_{ab} \cdot \nabla_a W_{ab}}{|\mathbf{r}_{ab}|^2 + \eta^2} \mathbf{u}_{ab} \\ & + \sum_b m_b \left(\frac{\boldsymbol{\tau}_a}{\rho_a^2} + \frac{\boldsymbol{\tau}_b}{\rho_b^2} \right) \cdot \nabla_a W_{ab} + \frac{1}{\rho_a} (\boldsymbol{\tau}_d)_a \end{aligned} \tag{9}$$

where $\mathbf{u}_{ab} = \mathbf{u}_a - \mathbf{u}_b$, $\mathbf{r}_{ab} = \mathbf{r}_a - \mathbf{r}_b$, $\nabla_a W_{ab}$ is the gradient of the kernel function between particles "a" and "b" with respect to the position of particle "a", and η is a small number introduced to avoid a zero denominator during computations and is set to 0.1 h. In the present model, the following equation is used to relate the pressure explicitly with the fluid density as

$$P = c_0^2(\rho - \rho_0) \tag{10}$$

where ρ_0 is the reference density and c_0 is the speed of sound. In SPH, it is assumed that the flow is slightly compressible so the speed of sound is chosen to be much smaller than the physical one to ensure the fluid compressibility being less than 1 %. ρ_0 and c_0 are thus taken as 1000 kg/m^2 and 16 m/s, respectively, in the present study. To solve the equations in time, a predictor-corrector marching scheme is applied (refer to Monaghan 1989).

To assess the capability of the proposed SPH model, a test case of open channel flow over a rough bed is simulated and the model results are validated by comparing with experimental data. In the experimental tests, a steady uniform flow with water depth H = 50 mm was established in a 0.459 m wide and 12 m long laboratory flume with a gradient of S_0 = 0.004 (Nichols 2013). The bed was composed of hexagonally packed spheres with a diameter d_s = 24 mm. Two-dimensional Particle Image Velocimetry (PIV) was used to measure the time-dependent flow field beneath the water surface, in a vertical plane along the centerline of the flume at a position of 8.4 m from the flume inlet. Two calibrated CCD cameras, with an image area of 1600 × 600 pixels, were focused on the laser

sheet, and were synchronized with the laser pulses. The overlapping field of view of these two cameras covered an area of approximately 247 × 89 mm. Neutrally buoyant PIV seeding particles were added to the flow and a pair of particle images separated by a time delay of 1 ms was captured on each camera. This was repeated at a fixed frequency of 26.9 Hz for a duration of 5 min.

Each image pair from the two PIV cameras was divided into interrogation areas with a physical area of around 4.9 × 4.9 mm, with a 50 % overlap so that the spatial resolution of the measurements was around 2.5 mm. A two dimensional cross-correlation technique determined the velocity vector for each interrogation area by comparing the images captured in the frame pairs. Vector maps then underwent range validation and moving average validation to correct any spurious data points, with fewer than 5 % of vectors being replaced. Finally, the vector maps from the two PIV cameras were combined to form a time series of vector maps which would enable comparison with the SPH data.

Since the bed elements have a diameter d_s = 24 mm, half of d_s is taken as the effective roughness height (R_d) in the model. The drag stress term is calculated only for the particles located within a distance less than $R_d = d_s/2$ from the bed. A sketch view of the computational domain is shown in Fig. 1. There are different values of drag coefficient C_d as addressed in the literature for spheres. This coefficient is set equal to 0.5 in the present study for universality at high Reynolds Numbers. The initial SPH particle spacing is 2 mm. As shown in Fig. 1, the zero datum in the model is set 4 mm below the top of the sphere for consistency with the experimental data, and the bed level which is $d_s/2$ below the top of the sphere is hence located at $z = -8$ mm. The relevant computational parameters are summarized in Table 2.

Figure 2a shows the comparison between time-averaged computed and measured streamwise velocity profiles. It can be seen that there is good agreement with the experimental data in terms of magnitude and slope of the velocity profile. According to Fig. 2b, the SPH model can also accurately predict the shear stress close to the analytical solutions ($\tau = \rho g H S_0(1 - z/H)$). Meanwhile, Fig. 2c shows the vertical distribution of the drag stress term ($\boldsymbol{\tau}_d/\rho$). As shown in Fig. 2b, the maximum turbulent shear stress occurs at the top of the bed grain. This is because the velocity gradient is a maximum at this interface due to the drag force effect. The simulation results have revealed that the mixing length model coupled with the drag force equation worked well in estimating the roughness effect on the flow. The drag force produced an extra shear stress near the bed and the mixing length model transported the resulting effect through the water depth.

Figure 3 shows the distribution of mixing length calculated by Nezu and Rodi formula (1986). According to this, l_m increases from zero at the reference datum below the top of the bed grain with a slope $\kappa = 0.41$ (according to Prandtl's theory) and then decreases to zero at the free surface. According to Nezu and Rodi (1986),

Table 2 Computational parameters

H (mm)	S_0	d_s (mm)	C_d	R_d (mm)	d_p (mm)
50	0.004	24	0.5	12	2

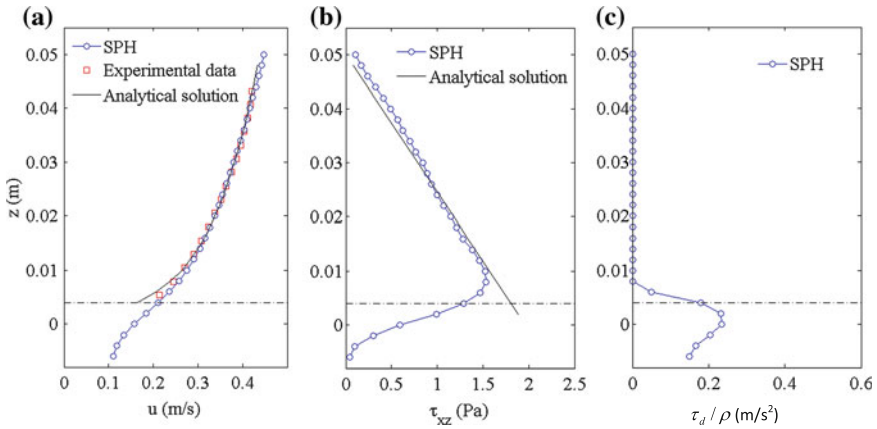

Fig. 2 Results of the model: **a** streamwise velocity; **b** turbulent shear stress; **c** drag-induced stress term. The *dash-dotted line* shows top level of the bed particles

this decrease is due to the fact that the water surface restricts the size of turbulence eddies and hence reduces the turbulent length scale. In this study, the zero-reference of the mixing length profile is set at $z = -3.5$ mm, i.e. 4.5 mm above the bed level (See Fig. 3) and below this level l_m is assumed to be zero. However, in some other studies, the distribution of mixing length in the interfacial sub-layer is assumed in a different way (For instance see Zeng and Li 2012). In the present work, the zero-reference of the mixing length has been found by using numerical trials so as to achieve the best fit of mean velocity profile to the measured data.

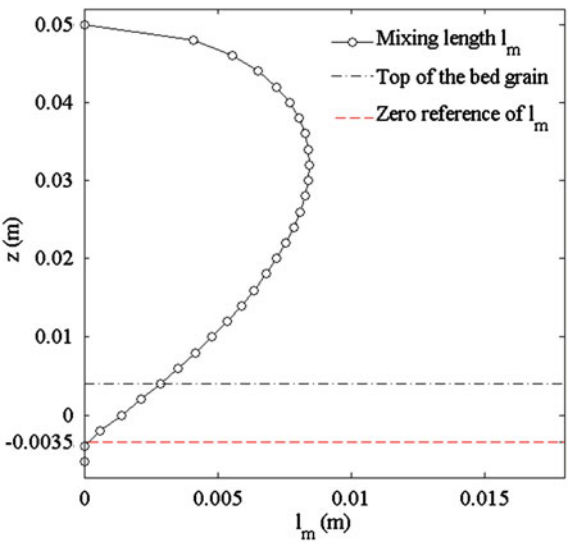

Fig. 3 Vertical distribution of the calculated mixing length

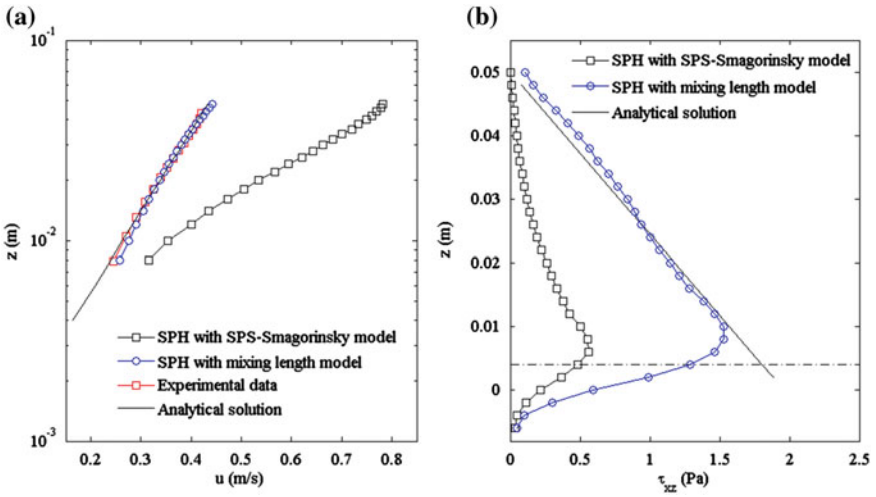

Fig. 4 Comparison of results between the mixing length model and the SPS-Smagorinsky model with $C_s = 0.15$. **a** Semi-logarithmic streamwise velocity; **b** Turbulent shear stress. The *dash-dotted line* shows top level of the bed grain

To further investigate the importance of the turbulence model, the calculations have been repeated by applying the SPS model (Gotoh et al. 2001) with the Smagorinsky constant $C_s = 0.15$ and a filter size (Δ) equal to the SPH particle spacing d_p. Here, the product of $C_s\Delta$ should be equivalent to the mixing length l_m, but it remains constant with a value of 0.0003. Comparing this value with the mixing length value obtained in the previous simulation, as shown in Fig. 3, the turbulent shear stress will be expected to be underestimated. This is demonstrated in Fig. 4b, where the turbulent shear stress calculated by the SPS-Smagorinsky model is compared with the analytical solution and the shear stress calculated by the mixing length model. Figure 4a also presents a comparison between the SPS-Smagorinsky model, SPH-mixing length model, experimental data and the analytical solution in terms of time-averaged streamwise velocity. Due to the underestimation of the turbulent shear stress, the velocity profile is not correctly reproduced by the SPS-Smagorinsky model. Thus, it can be noticed that the SPS model with $C_s = 0.15$ is unable to predict the correct mechanism of momentum transfer in 2D uniform turbulent channel flow over a rough bed. Nonetheless, this model might be successfully applied to non-uniform or 3D open channel flows, where the shear strains are significant in the two other directions (see Violeau and Issa 2007).

4 Conclusions

In this paper, a comprehensive review has been completed on turbulence models and shear boundary layer treatment used in existing particle models in order to find potential applicability of the SPH method in modelling open channel flows over rough bed boundaries. Accordingly, the mixing length model has been suggested for turbulence modelling and the drag-induced shear stress has been proposed to be included in the N-S equations to account for the roughness effect. A numerical model has been developed based on the SPH method coupled with the proposed approaches and finally a test case of turbulent open channel flow over a fully rough channel bed has been solved by the developed model. The numerical results were compared to experimental data and analytical solutions where a good agreement was observed in terms of flow velocity and shear stress. This indicated that the drag force model successfully reproduced the mechanism of velocity reduction in the shear boundary layer and the mixing length model correctly transferred this effect to the upper flow. It has also been shown that the SPS-Smagorinsky model with $C_s = 0.15$ was unable to reproduce the correct turbulent shear stress in uniform open channel flows over rough beds. Hence, for modelling such flows, the SPS-Smagorinsky model could be adopted but with a mixing length approach to determine the eddy viscosity, instead of using the fixed Smagorinsky constant.

Acknowledgements This work was supported by the Research Executive Agency, through the 7th Framework Programme of the European Union, Support for Training and Career Development of Researchers (Marie Curie—FP7-PEOPLE-2012-ITN), which funded the Initial Training Network (ITN) HYTECH 'Hydrodynamic Transport in Ecologically Critical Heterogeneous Interfaces', N.316546.

References

Chern M, Syamsuri S (2013) Effect of corrugated bed on hydraulic jump characteristic using SPH method. J Hydraul Eng 139(2):221–232

Christoph GH, Pletcher RH (1983) Prediction of rough-wall skin friction and heat transfer. AIAA J 21:509–515

Clauser FH (1954) Turbulent boundary layers in adverse pressure gradients. J Aeronaut Sci 21:91–108

Cui J, Patel VC, Lin CL (2003) Prediction of turbulent flow over rough surfaces using a force field in large eddy simulation. J Fluids Eng Trans ASME 125:2–9

De Padova D, Mossa M, Sibilla S, Torti E (2013) 3D SPH modelling of hydraulic jump in a very large channel. J Hydraul Res 51(2):158–173

Federico I, Marrone S, Colagrossi A, Aristodemo F, Antuono M (2012) Simulating 2D open-channel flows through an SPH model. Eur J Mech B/Fluids 34:35–46

Fu L, Jin YC (2013) A mesh-free method boundary condition technique in open channel flow simulation. J Hydraul Res 51(2):174–185

Gingold RA, Monaghan JJ (1977) Smoothed particle hydrodynamics: theory and application to non-spherical stars. Mon Not R Astron Soc 181:375–398

Gotoh H, Shibahara T, Sakai T (2001) Sub-particle-scale turbulence model for the MPS method—Lagrangian flow model for hydraulic engineering. Comput Fluid Dyn J 9(4):339–347
Granville PS (1985) Mixing-length formulations for turbulent boundary layers over arbitrary rough surfaces. J Ship Res 29(4):223–233
Granville PS (1988) Eddy viscosities and mixing lengths for turbulent boundary layers on flat plates, smooth or rough. J Ship Res 32:229–237
Hsu CC, Wu FS, Lee WJ (1998) Flow at 90 degrees equal-width open-channel junction. J Hydraul Eng ASCE 124:186–191
Krogstad PA (1991) Modification of the van driest damping function to include the effects of surface roughness. AIAA J 29:888–894
Lopez D, Marivela R, Garrote L (2010) Smoothed particle hydrodynamics model applied to hydraulic structures: a hydraulic jump test case. J Hydraul Res 48:142–158
Lucy LB (1977) Numerical approach to testing the fission hypothesis. Astron J 82(12):1013–1024
Marion A, Nikora V, Puijalon S, Bouma T, Koll K, Ballio F, Tait S, Zaramella M, Sukhodolov A, O'Hare M, Wharton G, Aberle J, Tregnaghi M, Davies P, Nepf H, Parker G, Statzner B (2014) Aquatic interfaces: a hydrodynamic and ecological perspective. J Hydraul Res 52(6):744–758. doi:10.1080/00221686.2014.968887
Miyake Y, Tsujimoto K, Agata Y (1999) A DNS of a turbulent flow in a rough-wall channel using roughness elements model. JSME Int J 43(2):233–242
Monaghan JJ (1989) On the problem of penetration in particle methods. J Comput Phys 82(1):1–15
Monaghan JJ, Lattanzio JC (1985) A refined method for astrophysical problems. Astron Astrophys 149:135–143
Nezu I, Rodi W (1986) Open-channel flow measurements with a Laser Doppler anemometer. J Hydraul Eng ASCE 112(5):335–355
Nicholas AP, Smith GHS (1999) Numerical simulation of three-dimensional flow hydraulics in a braided channel. Hydrol Process 13:913–929
Nichols A (2013) Free surface dynamics in shallow turbulent flows. Ph.D thesis, School of Engineering, University of Bradford, UK
Nikuradse J (1933) Laws of flow in rough pipes. VDI Forschungsheft 361. English translation: NACA TM 1292, 1950
Perry AE, Schofield WH, Joubert PN (1969) Rough wall turbulent boundary layers. J Fluid Mech 37(2):383–413
Rameshwaran P, Naden PS, Lawless M (2011) Flow modelling in gravel-bed rivers: rethinking the bottom boundary condition. Earth Surf Proc Land 36:1350–1366
Rotta J (1962) Turbulent Boundary layers in incompressible flow. Prog Aerosp Sci, Oxford, UK, 2:73–82
Sahebari AJ, Jin YC, Shakibaeinia A (2011) Flow over sills by the MPS mesh-free particle method. J Hydraul Res 49(5):649–656
Shakibaeinia A, Jin YC (2011) MPS-based mesh-free particle method for modeling open-channel flows. J Hydraul Eng 137:1375–1385
Taylor RP, Colemau HW, Hodge BK (1985) Prediction of turbulent rough-wall skin friction using a discrete element approach. ASME J Fluids Eng 107:251–257
van Driest ER (1956) On turbulent flow near a wall. J Aeronaut Sci 23:1007–1011
Violeau D, Issa R (2007) Numerical modelling of complex turbulent free-surface flows with the SPH method: an overview. Int J Numer Meth Fluids 53(2):277–304
Violeau D, Piccon S, Chabard JP (2002) Two attempts of turbulence modelling in smoothed particle hydrodynamics. Proceedings of the 8th symposium on flow modelling and turbulence measurements. Advances in Fluid Modelling and Turbulence Measurements. World Scientific: Singapore, 339–346
Wiberg PL, Smith JD (1991) Velocity distribution and bed roughness in high-gradient streams. Water Resour Res 27:825–838
Zeng C, Li CW (2012) Modeling flows over gravel beds by a drag force method and a modified S-A turbulence closure. Adv Water Resour 46:84–95

Interaction Between Storm Water Conduit Flow and Overland Flow for Numerical Modelling of Urban Area Inundation

Jakub Hakiel and Michał Szydłowski

Abstract Nowadays we can observe increasing frequency of inundations in cities. This makes accurate predicting of inundations more important than ever. Numerical modeling of this issue requires complex approach with simultaneous calculations of pipe flow and surface flow. In this paper, after a short review of known methods used for solving pipe and surface flow, we will try to answer the question if presented methods would be sufficiently accurate for inundation modeling. We will also investigate if known formulas used for modeling interaction between pipe and surface flow describe the issue well and if they can be developed in any direction. There will be presented comparison between results of calculations and experiments built on test stand made for this purpose in Gdańsk University of Technology. The results could be treated as a starting point for further recognition of the phenomenon.

1 Introduction

Nowadays we can observe increasing frequency of inundations in cities. This is connected with rapid development of urban areas and consequently a growth of impervious area. This, in combination with more frequent extreme weather events, is causing a great increase in runoff. At the same time, it is impossible to redesign and rebuild rain water sewage systems in most cities, which results in more frequent surcharge. In this situation accurate predicting of inundations is more important than ever.

Numerical modeling of this issue requires complex approach with simultaneous calculations of pipe flow and surface flow. These are well known topics and there

J. Hakiel (✉) · M. Szydłowski
Gdańsk University of Technology, G. Narutowicza 11/12, 80-233 Gdańsk, Poland
e-mail: jakub.hakiel@pg.gda.pl

M. Szydłowski
e-mail: mszyd@pg.gda.pl

P. Rowiński and A. Marion (eds.), *Hydrodynamic and Mass Transport at Freshwater Aquatic Interfaces*, GeoPlanet: Earth and Planetary Sciences,
DOI 10.1007/978-3-319-27750-9_3

are numerous methods that correctly describe such flows, such as the Saint-Venant equations which can be used to calculate one-dimensional flow (Szymkiewicz 2010) or shallow water equations (Tan 1992) for two-dimensional overland water flow. Problematic part of modeling inundations is an interaction between surface and sewage flow. In this paper we will try to answer the question if the proposed methods would be accurate enough for modeling this issue.

2 Model of Storm Water Pipe Flow

The free surface flow in sewer pipes can be described using the Saint-Venant equations, which are generally valid for gradually varied flows. During high surface water runoff from urban areas, various local phenomena such as hydraulic jumps can occur in sewers, thus a special form of one-dimentional flow model equations has to be used. To correctly reproduce the steep water surface fronts, the conservative form of flow equations should be used in modeling (Cunge et al. 1980). The form of Eqs. (1) and (2) was chosen due to physical nature of the solution which it guarantees (i.e. discontinuity in the form of a hydraulic jump). For the case of prismatic channel, such as a pipe with no lateral inflow or outflow, the Saint-Venant system, written in the conservative form (Szymkiewicz 2010), can be presented as

$$\frac{\partial \mathbf{U}}{\partial t} + \frac{\partial \mathbf{F}}{\partial x} = \mathbf{S} \tag{1}$$

where the vectors **U**, **F** and **S** are given as:

$$\mathbf{U} = \begin{pmatrix} A \\ Q \end{pmatrix}, \mathbf{F} = \begin{pmatrix} Q \\ Q^2/A + I \end{pmatrix}, \mathbf{S} = \begin{pmatrix} 0 \\ gA\left(S_o - S_f\right) \end{pmatrix} \tag{2}$$

where x represents distance along the sewer conduit, t represents time, A is the cross-sectional wetted area, Q is the flow discharge and g is the gravitational acceleration. $I = pA/\rho$, where p is a pressure at the centroid of A, and ρ is the constant fluid density. For the hydrostatic pressure distribution, the term I can be defined as $I = gAh_c$, where h_c is the distance between the free surface and centroid of flow cross-sectional area. S_0 and S_f are the bottom and friction slopes, respectively. The friction slope can be defined by Manning formula.

In order to simulate the water flow under pressurized conditions, the 'Preissmann slot' concept can be applied. The idea of a hypothetical slot at the top of the pipe was presented by Cunge et al. (1980) and it was implemented for numerical modeling of storm sewers, for example by Capart et al. (1997). It was also investigated by Szydłowski and Machalińska-Murawska (2012).

The Preissmann slot idea makes the simulation of transient flow possible without the need to separately track the pressurization front, but such a solution has some disadvantages, such as inability to simulate full pipe subatmospheric flow.

The Saint-Venant Eqs. (1) and (2) are a system of partial differential equations and their solution for the given initial and boundary conditions is composed of functions $A(x, t)$ and $Q(x, t)$. In order to solve the model equations, a numerical method must be applied. In this paper we propose using an improved McCormack scheme (Tseng 2003) of finite differences method (FDM) to approximate the model equations. The improvement of the scheme is based on the theory of total variation diminishing schemes that are capable of capturing sharp discontinuities without generating the spurious oscillations. The scheme is of second-order accuracy both in time and space in non-critical sections, but it switches the accuracy to the first-order at extreme points where the oscillations occur. This technique was previously described by Garcia-Navarro et al. (1992) and it was originally proposed for solving one-dimensional open-channel flow equations. The same scheme was also used by Szydłowski and Machalińska-Murawska (2012) to simulate the transient flow in storm sewers pipe and the results were examined against the arbitrary data. Finally the storm water pipe flow model was verified by Szydłowski (2014) using the laboratory experiments carried out in a single pipe for the transient and trans critical flow conditions.

3 Model of Overland Water Flow

The model which is the most widely used to simulate the flood propagation on the surface of the inundation areas is a system of two-dimensional Shallow Water Equations (SWE) (Tan 1992). The SWE model can be presented in conservative form:

$$\frac{\partial \mathbf{U}}{\partial t} + \frac{\partial \mathbf{E}}{\partial x} + \frac{\partial \mathbf{G}}{\partial y} + \mathbf{S} = 0, \tag{3}$$

where:

$$\mathbf{U} = \begin{pmatrix} h \\ uh \\ vh \end{pmatrix}, \quad \mathbf{S} = \begin{pmatrix} 0 \\ -gh\left(S_{ox} - S_{fx}\right) \\ -gh\left(S_{oy} - S_{fy}\right) \end{pmatrix} \tag{4a, b}$$

and

$$\mathbf{E} = \begin{pmatrix} uh \\ u^2h + 0.5gh^2 \\ uvh \end{pmatrix}, \quad \mathbf{G} = \begin{pmatrix} vh \\ uvh \\ v^2h + 0.5gh^2 \end{pmatrix} \tag{4c, d}$$

In the above system, h represents the water depth, u and v are the horizontal components of the velocity, S_{ox} and S_{oy} denote the bed slope terms, S_{fx} and S_{fy} are

the hydraulic slopes defined using Manning formula, and g is the acceleration due to gravity. Equation (4a–d) can be written in the vector form as:

$$\frac{\partial \mathbf{U}}{\partial t} + \nabla \mathbf{F} + \mathbf{S} = 0, \tag{5}$$

where $\mathbf{F}$ is the vector of mass and momentum fluxes. In order to integrate the SWE in space we propose to use the finite volume method (LeVeque 2002). After integration in space, Eq. (5) can be rewritten for one triangular finite volume (i) as:

$$\frac{\partial \mathbf{U}_i}{\partial t} \Delta A_i + \sum_{r=1}^{3} (\mathbf{F}_r \mathbf{n}_r) \Delta L_r + \sum_{r=1}^{3} \mathbf{S}_r \Delta A_r = 0, \tag{6}$$

where $\mathbf{F}$ is the numerical flux, $\mathbf{n}$ is the normal vector and ΔL is the cell-interface length. Symbols $\mathbf{S}$ and ΔA represent the components of source terms and area of cell i assigned to rth cell-interface, respectively. The surface water flow model described above was applied for simulations of many types of inundations in natural river valleys and built–up areas (Szydłowski 2007; Gutry-Korycka et al. 2006) as well as for modelling the rapidly varied flow in open channels with bridge pillars constrictions and transcritical flow in artificial canals with satisfactory results (Szydłowski 2011).

4 Application of Quasi Coupled Models

One approach for solving complex models of pipe flow and overland flow is the quasi coupled model. Such approach was compared with the measurements carried out at the hydraulic laboratory of the Gdansk University of Technology. Hydraulic test stand was prepared to carry out the experiment of urban area inundation. A measuring station, 6.75 m long and 3.5 m wide, was built in concrete, steel and wood (see Figs. 1 and 2). To simulate real situation of city flooding, two ways of water supplying were provided: the one through a pipe mounted underneath the platform simulating stormwater sewage and the other through a breach in embankment wall simulating overland inflow.

In order to simulate street flow, the area of surface water flow was restricted to 50 cm wide trough. The pipe was connected to the surface through five manholes. The water was supplied only from pipe mounted underneath the platform. During the experiment, the breach was permanently closed, and the water level in supply tank was set at 41 cm depth. The flow in pipe was set as constant. At some moment the valve located at the pipe outflow was suddenly closed, resulting in complete filling of pipe, flow pressurization, and further the outflow from manholes. The water level on some surface points (A3, A4, A7) was measured with hydrostatic probes.

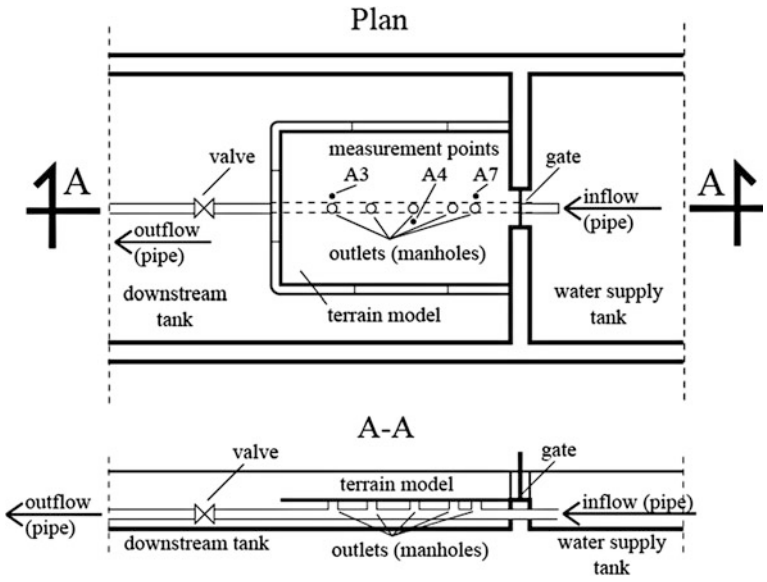

Fig. 1 Scheme of urban area inundation laboratory stand

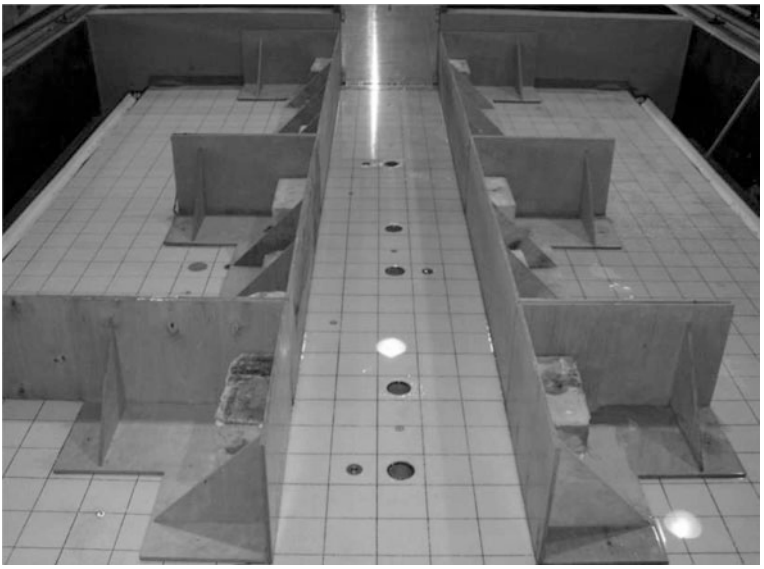

Fig. 2 Photograph of urban area inundation laboratory stand

In order to numerically simulate street inundation, at first, the calculations of storm water conduit flow were made separately. In the model, the pipe was made from PVC with diameter of 0.045 m and Manning's coefficient n = 0.009 $s/m^{1/3}$.

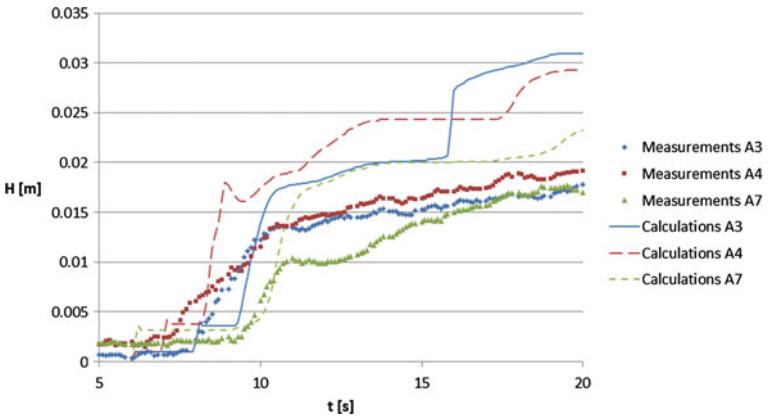

Fig. 3 Comparison of measurements and calculations for urban area inundation experiment

The spatial step was set as $\Delta x = 0.02$ m and time step as $\Delta t = 0.002$ s, which ensured the stability. The second part of calculations was to simulate surface flow. The inundation area was replaced with numerical grid consisting of 4522 cells. Near the manholes, the grid was concentrated.

As a starting point of calculations, measured constant pipe flow and hydrostatic state equal to a lack of water on the surface were taken. The rest of simulation, after time for stabilization, was performed under unsteady flow conditions. Closing of the valve and filling of the pipe were simulated and, as a result, the piezometric pressure evolution was first calculated. Then, as a second step, the pressure was used in surface flow model as water level over the manholes. Such approach forms the inner boundary condition at manholes location points. The result of simulation was the water depth across the area during the simulation.

The results of calculations were compared with measurements from experiment in Fig. 3. Lines *calculations A3, A4* and *A7* present results of numerical modeling, whereas dots *measurement A3, A4* and *A7* show measurements from the experiment.

As we can see in Fig. 3, the discrepancy between compared data is significant. However, it can be concluded that the results are qualitatively similar. The differences are results of restrictions of measurement (no information about water depth at manholes), possible inaccuracy of hydraulic model (small leaks between model elements) and unsatisfactory laboratory equipment precision. Moreover, the simulation was made using split models of flow in pipe and on the surface, which excludes the achievement of reliable results. Such unsatisfying results suggest that the research of flow integration method is absolutely essential for city inundation modeling.

5 Model of Interaction Between Pipe and Surface Flow

Because of imperfections of quasi coupled models described in this paper, there is a need for more accurate approach to problem. The solution can be a direct model of interaction between pipe and surface flow. Such a model should describe inflow and outflow of manholes with physical formulas and would let us model inundation comprehensively taking into account both situations of surface flow with properly working drainage system (inflow into the sewage), surcharge in stormwater system (outflow from sewage) and mixed situation.

One of such techniques, as presented by Chen et al. (2007), can be linkage between difference in water level in sewage and on the surface with the flow rate between them. Water elevations would be taken from surface flow model and sewage flow model. The formula chosen would differ according to situation. Neglecting the dynamics of surface flow, we can distinguish three main hydraulic qualifications:

- free weir linkage
- submerged weir linkage
- orifice linkage

The first one would be adopted for situations where crest elevation is between surface water level and sewage water depth (see Fig. 4) and would be described by the formula

$$Q = sign[h_{mh} - h_{2d}]c_w w\sqrt{2g}(h_U - z_{crest})^{3/2}, \tag{7}$$

where Q is the discharge of interaction [m^3/s], h_{mh}, h_{2d} and z_{crest} are, respectively, water depth at manhole (in sewage), water level on surface and crest elevation, c_w is the weir discharge coefficient, w is the weir crest width and h_U is the upstream water depth which means $h_U = \max\{h_{mh}, h_{2d}\}$.

The submerged weir linkage would be described with formula (8) and would be adopted for situations where the water level both in the sewage and on the surface are above the crest (see Fig. 5) and upstream water depth above the crest ($h_U - z_{crest}$) is less than A_{mh}/w, where A_{mh} is the hole area (in this case manhole area).

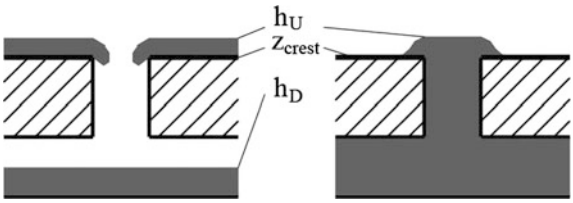

Fig. 4 Scheme of conditions for usage of free weir linkage formula

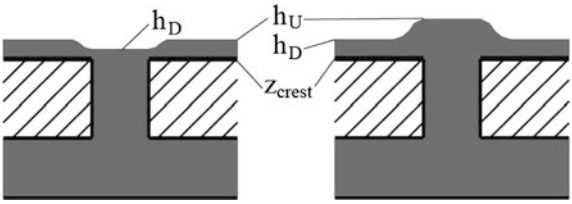

Fig. 5 Scheme of conditions for usage of submerged weir and orifice linkage formulas

$$Q = sign[h_{mh} - h_{2d}]c_w w\sqrt{2g}(h_U - z_{crest})(h_U - h_D)^{1/2}, \tag{8}$$

where h_D is the downstream water level, which means $h_D = \min\{h_{mh}, h_{2d}\}$.

The orifice linkage case describes the situation when water levels both in the sewage and on the surface are above the crest (see Fig. 5) but upstream water depth above the crest ($h_U - z_{crest}$) is more than A_{mh}/w and is defined by the formula

$$Q = sign[h_{mh} - h_{2d}]c_o A_{mh}\sqrt{2g}(h_U - h_D)^{1/2}, \tag{9}$$

where c_o is the orifice discharge coefficient.

The approach presented above can give us more detailed information about interaction between surface and sewage flow than quasi coupled model and it can be relatively easily applied into numerical model of dual drainage system. However, the question arises if such, still relatively simple approach, devoid of surface flow dynamics elements, can be used to describe complex case of bidirectional flow interaction. In general, the manholes inflow and outflow discharge depends also on surface slope and velocity, which has been neglected in formulas (7)–(9), so formally these equations are not valid for all flow scenarios. In order to answer how important this problem is for real flow cases we have started experimental investigation in hydraulic laboratory.

6 Laboratory Experiment of Flow Interaction

At the hydraulic laboratory of the Gdansk University of Technology, an experiment to determine if formulas (7)–(9) can be successfully used in inundation models was carried out. For that purpose, a new test stand was build (see Figs. 6 and 7).

The main part of the stand is made of wooden channel and PVC pipe fixed under its bottom. The two parts are connected at some point with tee joint which was simulating the manhole in sewage systems. Such construction is used to simulate overland and rain water sewage flow and its interaction at the connection point (manhole). The channel has a length of 5.5 m and a width of 0.4 m. All experiments are conducted in steady flow conditions with inflow only from surface or pipe at a time. On the stand there is provided a volumetric measurement of outflow separately from surface and from sewage pipe and a measurement of water levels along the channel. The specification of test stand can be seen in Fig. 7.

Fig. 6 Photograph of laboratory stand for surface and sewage flow interaction experiments

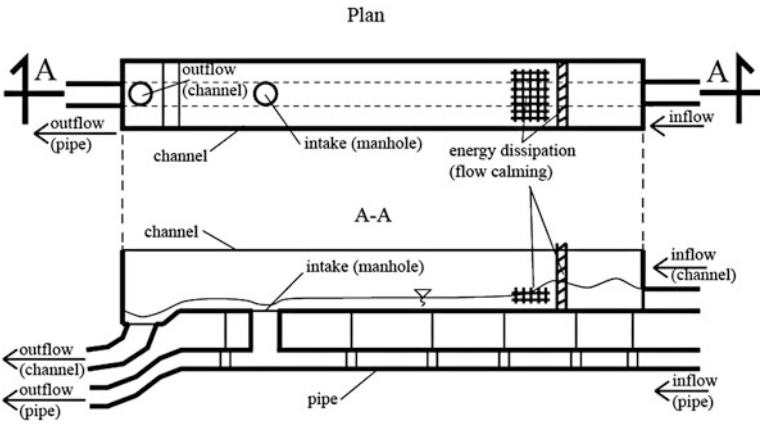

Fig. 7 Scheme of laboratory stand for surface and sewage flow interaction experiments

The first stage of research consists of three series of tests (see Table 1).

The first test was carried out in order to preliminarily check the accuracy of formulas (7)–(9). For 6 different flow rates, the full set of parameters was measured (flow rates, water levels). The results were compared with calculations made with formula for non-submerged weir which is equivalent to the situation during the test. In Fig. 8 the results of first experiment and calculation are presented.

Two other series of measurement were conducted to determine if the flow rate taken over by the manhole from surface is dependent on the velocity which is dependent on the surface slope. The results, which were different flow rates for

Table 1 Conditions under which the tests were carried out

Test number	Slope tilt (%)	Conditions
1	0.3	Steady flow, water supply from surface, without water level rising
2	1.3	Same as test 1
3	2.2	Same as test 1

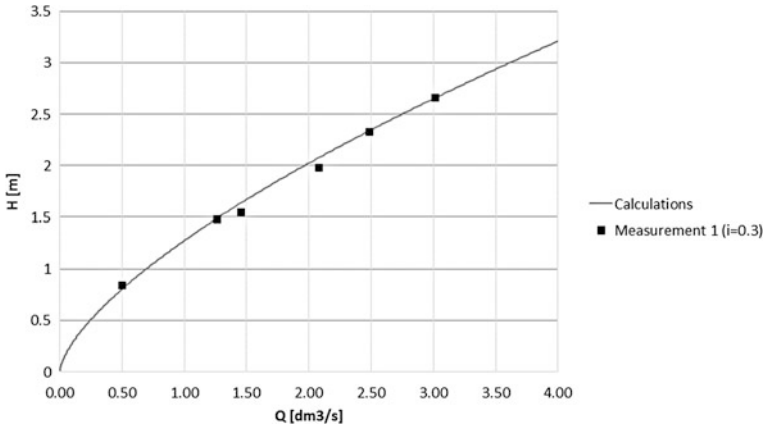

Fig. 8 Results of test 1 compared with calculations

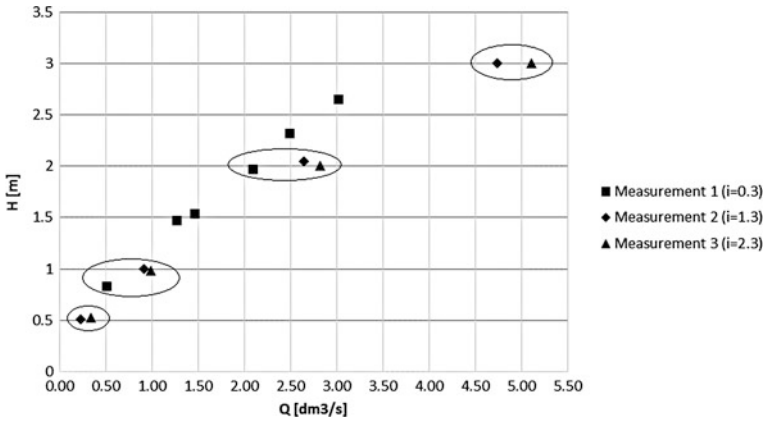

Fig. 9 Comparison of test results

fixed water depth depending on the set surface slope, were compared. This comparison is presented in Fig. 9. Results of measurements that were made for similar water depth with different surface slope are encircled. From them we can see that, according to slope, the flow taken by manhole differs.

The results of tests are only first step to properly verify the analyzed formulas, but they can suggest direction of future research. From Fig. 8 it can be seen that formula (7) can quite well describe the phenomenon of inflow into manhole. The measurements are close to results of calculations with weir coefficient taken for broad weir with sharp edges (c_w = 0.51). This can give us the impression that the formula can be used in this particular situation. What makes the situation more difficult are results of later tests. The measurements from experiment two and three show us that for different surface slope flow rates significantly differ. This is an important observation, because formulas (7)–(9) do not consider velocity or slope tilt value in any way.

7 Conclusions

Concluding, according to growing risk of inundations it is essential to develop effective ways of predicting such events. The two elements of the process, namely models of storm water pipe and overland flow, are well recognized and with the present state of knowledge can be successfully used in such tasks. The problematic part is the interaction between them. The simple quasi coupled model seems to be inaccurate and not useful in inundation predictions. This results in the need for another way of representing such cases.

The technique presented in this paper, based on weir and orifice formulas, can be used to calculate discharge of interaction between surface and sewage flow. Such approach takes into account more parameters than quasi coupled models. The interaction depends on water levels and characteristics of manhole, which makes it applicable to more cases.

From tests we can draw only basic conclusions considering that it is only the beginning of experiment. The results which were compared with calculations can give us some information about usefulness of the described formulas. What we can see is that the measured flow rate is dependent on slope value which means it is also dependent on velocity. These parameters are not included in the calculations by any formulas described in this paper Eqs. (7)–(9). Inundation modeling involves doing calculations for highly urbanized areas where we have plenty of steep terrain. This allows us to suspect that formulas must be developed to include this parameter.

After short series of experiments it can be found that formulas (7)–(9) presented in the paper are quite good for calculating inflow rate from surface to sewage, for specific velocities of surface water flow. These makes them useful for inundation modeling if the problem of slope consideration can be solved.

Acknowledgments Authors express gratitude to Regional Fund for Environmental Protection and Water Management in Gdańsk for research project No. RX-09/01/2014.

References

Capart H, Sillen X, Zech Y (1997) Numerical and experimental water transients in sewer pipes. J Hydraul Res 35(5):659–672

Chen A, Djordjević S, Leandro J, Savić D (2007) The urban inundation model with biderctional flow interaction between 2D overland surface and 1D sewer networks. Novatech 2007, GRAIE, Lyon, France

Cunge JA, Holly FM, Verwey A (1980) Practical aspects of computational river hydraulics. Pitman Publ. Ltd, London

Garcia-Navarro P, Alcrudo F, Saviron JM (1992) 1-D open-channel flow simulation using TVD-McCormack scheme. J Hydraul Eng 118(10):1359–1372

GutryKorycka M, Magnuszewski A, Suchożebrski J, Jaworski W, Marcinkowski M and Szydłowski M (2006) Numerical estimation of flood zones in the Vistula River valley, Warsaw, Poland. In: Climate Variability and Change—Hydrological Impacts, IAHS Publ, 308: 191–195

LeVeque R J (2002) Finite volume method for hyperbolic problems. Cambridge University Press, New York

Szydłowski M (2007) Mathematical modeling of flood waves in urban areas, Monographs of Gdańsk University of Technology, Gdańsk, vol 86

Szydłowski M (2011) Numerical simulation of open channel flow between bridge piers. TASK Q, Gdańsk, 15: 3–4

Szydłowski M, Machalińska-Murawska J (2012) Numerical simulation of transient flow in storm sewers using standard and improved McCormack scheme. Task Q 16(1):53–74

Szydłowski M (2014) Experimental verification of storm sewer transient flow simulation. Arch Hydro-Eng Env Mech 61(3–4):205–215

Szymkiewicz R (2010) Numerical modeling in open channel hydraulics. Springer, London

Tan W (1992) Shallow water hydrodynamics. Elsevier, Amsterdam

Tseng MH (2003) The improved surface gradient method for flows simulation in variable bed topography channel using TVD-MacCormack scheme. Int J Numer Meth Fluids 43:71–91

Modeling of Ice Passage Through Reservoirs System on the Vistula River

Tomasz Kolerski

Abstract A numerical model was used to assess ice passage through proposed reservoir on the lower Vistula River. Model results were compared with observation on the Vistula River, but because the dam is not constructed yet, the direct comparison was not possible. The study focused on ice movement and accumulation in the reservoir for variety of low flow condition with and without wind effect. Bridge's piers in the upper part of the reservoir were found to be one of the most important parameters affecting ice passage at the proposed dam. The other parameter which hampers or may even lead to stopping ice movement is western wind. The study took place within the framework of exclusive analysis for selecting the final location of a new dam which is critical for ensuring permanent safety of the Włocławek dam. Based on the performed study, the Przypust and Siarzewo variants accomplished the required goals to the largest extent at acceptable risk of ice stoppage and accumulation. Icebreaker operation is required during the ice sluicing operation in the new reservoir.

1 Introduction

In the mid of the last century, a new project was developed by the Water Management Committee established at the Polish Academy of Sciences which included the system of power dams on the entire length of the Vistula River (Granatowicz 2013; Majewski 2013). In a lower reach of the river, construction of a cascade of eight low head dams with run-of-river reservoirs was proposed by the Central Office of Hydraulic Engineering Studies and Designs 'Hydroproject' in Gdańsk. The first dam of the Lower Vistula Cascade was built in Włocławek (km 674 + 750) in 1970, but due to economic and political problems, construction of the

T. Kolerski (✉)
Gdańsk University of Technology, Department of Civil and Environmental Engineering, Narutowicza 11/12, 80-233 Gdańsk, Poland
e-mail: tomasz.kolerski@wilis.pg.gda.pl

P. Rowiński and A. Marion (eds.), *Hydrodynamic and Mass Transport at Freshwater Aquatic Interfaces*, GeoPlanet: Earth and Planetary Sciences,
DOI 10.1007/978-3-319-27750-9_4

other projects was abandoned. For more than 40 years Włocławek has been functioning as the only one dam without a downstream hydraulic support provided for in the design. Currently, the situation of the Włocławek facility is critical due to extensive downstream bed erosion and decline of tailwater level. If the degradation process will not be stopped the entire power dam will be breached in next few years, causing severe disaster. A construction of the new dam downstream is now considered to increase the Włocławek tailwater and provide permanent safety. A number of locations for a new dam were considered and the final four were proposed after the comprehensive studies of exclusive analysis (Fig. 1). The studies included but were

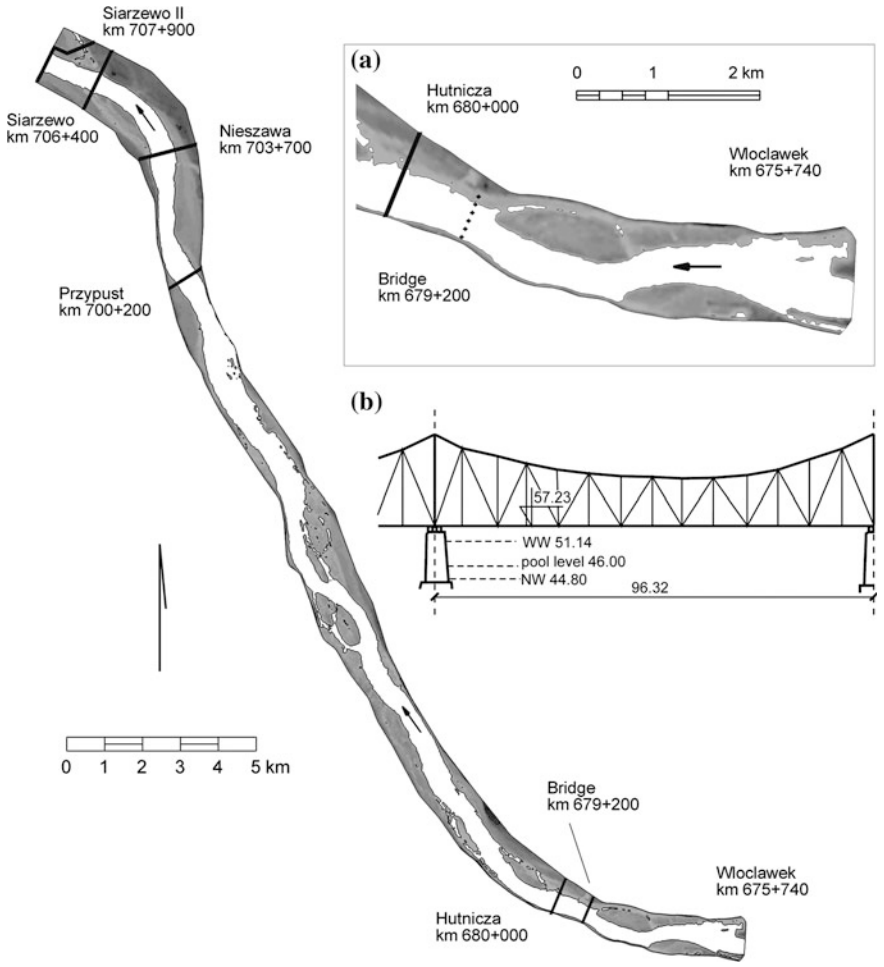

Fig. 1 Vistula River section downstream of the Włocławek Dam with potentially possible locational variants of the new dam; Hutnicza Dam detail with bridge piers location (**a**); Typical section of the Rydz Śmigły Bridge in km 679 + 200 (**b**)

not limited to the new project safety related to ice phenomena on the Vistula River (Kolerski 2013). Final locations for the new dam are considered within the river section located about 30 km downstream of the existing dam and they are as follows: Przypust (km 700 + 200), Nieszawa (km 703 + 700), Siarzewo (km 706 + 400) and Siarzewo II (km 707 + 900). Below, the results of the mathematical modeling of ice passage through the system of reservoirs and the new project effect on ice sluicing in various meteorological and hydrodynamic conditions are presented.

Meteorological conditions in a majority of winter seasons in Poland are suitable to cause freezing of surface waters. Ice interferes with power production, water intakes and navigation on many of the major rivers in Poland. For minimalizing ice related problems on inland waters, quick formation of smooth ice cover on the entire river reach at the beginning of the winter season is desirable (Bajkiewicz and Olifirowicz 2014; Kolerski 2015). During the spring time ice breakup is expected, which generally is not causing any problems if ice deteriorates in an event of thermal meltdown. Difficulties arise if, due to rapid change of water level, a dynamical breakup occurs, which, if not properly managed, may lead to ice accumulation and jams in the river. Authorities responsible for managing the two main Polish rivers, Vistula and Odra, know about the potential hazard related to winter ice jams and put every effort to decrease flood risk caused by ice jams. The most effective way to keep rivers safe is a use of icebreakers, which are specially designed ships that are strengthened to prevent damage of the hulls and have larger propulsion (Ashton 1986). Their uses include keeping harbors clean of ice, breaking up ice jams and initiating breakup in the rivers. Currently, on lower section of the Vistula River, icebreakers operate on the river outlet to the Gdańsk Bay and on the Włocławek reservoir.

The possibility of new dam construction in the lower section of the Vistula River is hampered due to arbitrarily introduced environment and species protection program Natura 2000. The program provides restrictive provisions within the areas included as Natura 2000 sites; however, investments are possible if they are complying with conditions described in Article 34 of the Environmental Protection Law (Environmental Protection Law (2004). Therefore, in addition to locations in the vicinity of Nieszawa–Ciechocinek region, a location for new dam was considered in a city of Włocławek (Hutnicza Dam in km 680 + 000; Fig. 1a). This dam, with approximately 2 m head, will stabilize the tailwater for the Włocławek Dam as an effect of the reservoir being 5 km long. The project is not economically reasonable and is considered only because it does not affect the Natura 2000 sites. In the paper, the ice sluicing through this site will be also presented.

2 Input Data

The bathymetry data were provided by Ove Arup & Partners International Ltd and were with spatial accuracy of 5 × 5 m for 5 km river reach (Hutnicza reservoir) and 20 × 20 m for the 30 km river section from Włocławek Dam down to Siarzewo II

site. All data were in Polish Cartographic System 1992 (Poland CS92), horizontal coordinates system and in Kronstadt 86 (HKron86) vertical system. Finite element meshes were prepared for each reservoir based on the river bathymetry data. Land boundaries for model domains were set to not include too many dry areas; however, the model can handle dry nodes problem by using minimum depth approach. In the river reach between Włocławek Dam and a new dam there is one bridge, which is located about 4.5 km downstream of the existing dam (km 679 + 200). It is a truss bridge on the local road 2044C (Rydz Smigły Bridge). The bridge's deck is supported by 6 elongated caisson piers with semi-circular ends which are located in a main channel, 96.32 m apart from each other. Low chord of the bridge's deck is horizontal and has elevation of 57.23 m, which will produce more than 10 m vertical clearance for normal and low flow conditions after the new reservoir is constructed (Fig. 1b). In a model, the bridge was included in a form of six islands of a shape of the bridge piers. In calculations, the island is interpreted as a vertical land boundary and is impermeable for water and ice.

Based on the hydrologic data provided by Ove Arup & Partners International Ltd, the average flow for cross-sections where new dams are proposed varies between 909 and 914 $m^3 s^{-1}$. Historical observations indicated that the majority of ice related problems in the analyzed river section occurred during the flow lower than the average (Grześ 1991). The reason for this is that if the ice sluicing was proceeded during the low water discharge, the ice run was slowed and it could be easily stopped by opposite wind. Also, low water depth is favorable for ice grounding in shallow areas which could lead to severe ice jams. Therefore, to include the worst case scenario, numerical simulations for ice dynamics were made for two low flow scenarios: 300 and 600 $m^3 s^{-1}$. All scenarios were run for one day (24 h) of ice sluicing from Włocławek Dam with constant ice and water discharge as well the pool level at the new dam.

Spillway gates operation in Włocławek Dam is regulated according to the water discharge at upstream. Each spillway section has a width of 20 m and can discharge maximum amount of 105 $m^3 s^{-1}$. Therefore, for analyzed cases, opening of 3 and 6 spans was simulated for discharges of 300 and 600 $m^3 s^{-1}$, accordingly. For all the proposed dams, spillways will have 15 spans with a width of 25 m each. The operation of the new dam gates is not established yet, thus selection of spillway's spans for opening is based on ice load calculations. In the checking procedure, ice run without sluicing was simulated for average water discharge. In such case, ice piled up in a front of the proposed dam, causing load on the spillway gates. The reading of the highest load indicated which spillway span should be opened for sluicing ice. An example for ice load distribution in time for the Siarzewo Dam (km 706 + 400), is presented in Fig. 2. Based on the results from that case, spillway's spans no. 8, 9 and 10 should be open for 300 $m^3 s^{-1}$ discharge and sections no. 7–12 for 600 $m^3 s^{-1}$flow.

According to the ice sluicing practice on Włocławek reservoir (RZGW 2009), the ice passage may be hampered or even completely stopped due to the wind blowing from the opposite direction to the flow. The Vistula River in its lower reach flows from the east, then in km 685 the river turns towards the north and in the vicinity of

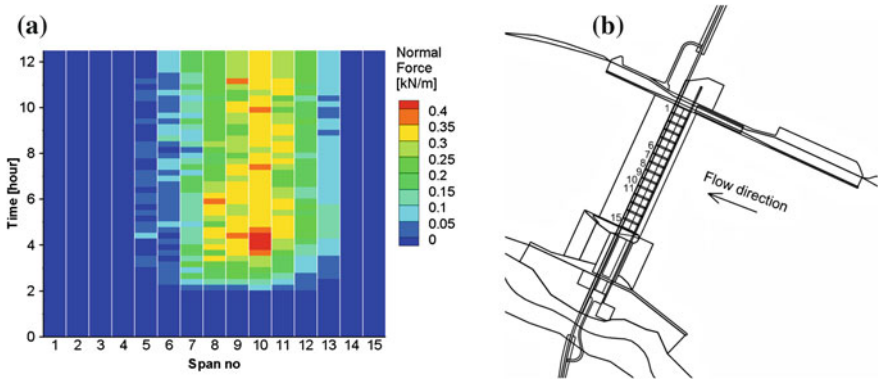

Fig. 2 Distribution of ice load in time along the spillway spans (**a**); Plan view of the proposed Siarzewo Dam with arrangement of the spillway's spans (**b**)

Nieszawa city it bends right and flows toward the north-west direction (Fig. 1). Dominant wind directions in Nieszawa—Ciechocinek region are west and south-west. This shows possible problems with ice sluicing caused by opposite wind, which may be especially troublesome for river section lying on the east-west line. The icebreaking guide (RZGW 2009), informs that during the western wind of 5 m s^{-1} velocity, ice cannot be sluiced through the Włocławek dam. Also strong side winds which are perpendicular to the flow direction (northern or southern) cause problems during the ice passage operation. In sensitivity analysis, no wind condition was assumed, as well as cases with the western wind of speed of 2 and 5 m s^{-1}.

3 Governing Equation

DynaRICE is a two dimensional, depth average hydro- and ice-dynamic model which allows to simulate super- and subcritical flow in rivers, reservoirs and other inland water bodies (Kolerski et al. 2013; Lu et al. 1999; Shen and Liu 2003). The model calculates hydrodynamics and ice dynamics simultaneously and the mutual interactions between these two modules are transferred every coupling time step. Depth averaged shallow water equations containing ice action on the flow can be presented in conservative form as (Shen 2010):

$$\frac{\partial H}{\partial t} + \frac{\partial (q_{tx})}{\partial x} + \frac{\partial (q_{ty})}{\partial y} = \frac{\partial}{\partial t}(Nt_i'), \tag{1}$$

$$\frac{\partial q_{tx}}{\partial t} + \frac{\partial}{\partial x}\left(\frac{q_{tx}^2}{H_t}\right) + \frac{\partial}{\partial y}\left(\frac{q_{tx}q_{ty}}{H_t}\right) = \frac{1}{\rho}(\tau_{sx} - \tau_{bx}) + \frac{1}{\rho}\left(\frac{\partial T_{xx}}{\partial x} + \frac{\partial T_{yx}}{\partial y}\right) - gH_t\frac{\partial \eta}{\partial x}, \tag{2}$$

$$\frac{\partial q_{ty}}{\partial t}+\frac{\partial}{\partial x}\left(\frac{q_{tx}q_{ty}}{H_t}\right)+\frac{\partial}{\partial y}\left(\frac{q_{ty}^2}{H_t}\right)=\frac{1}{\rho}(\tau_{sy}-\tau_{by})+\frac{1}{\rho}\left(\frac{\partial T_{xy}}{\partial x}+\frac{\partial T_{yy}}{\partial y}\right)-gH_t\frac{\partial \eta}{\partial y}. \tag{3}$$

In the above equations, H = total water depth; $\vec{q}_t$ = unit-width total water discharge; $\vec{q}_t=\vec{q}_u+\vec{q}_l$; $\vec{q}_u$ = unit-width water discharge in the surface ice layer; $\vec{q}_l$ = unit-width water discharge beneath the ice layer; q_{tx} and q_{ty} = components of total unit-width water discharge; t_i' = submerged ice layer thickness; N = ice concentration; x and y = independent variable of space; t = independent time variable; $T_{xx}=\varepsilon_{xy}\left(\frac{\partial q_{tx}}{\partial y}+\frac{\partial q_{ty}}{\partial x}\right)$; ε_{xy} = generalized eddy viscosity coefficients; τ_s and τ_b = shear stresses at ice-water interface and the river bed; H_t = equivalent water depth for the total water discharge $\vec{q}_t$; η = water surface elevation above the reference level ρ = density of water; and g = gravitational acceleration. The Manning's resistance coefficient for the underside of the ice increases linearly with ice jam thickness and this parameter is adjusted during model calibration. Because no data for ice calibration in the analyzed river reach were available, the calibrated ice parameters from Włocławek reservoir (Kolerski 2011) and the Vistula River estuary (Kolerski 2014) were used for these simulations. The bed roughness parameters were provided by the Ove Arup & Partners International Ltd and the Manning's coefficients were in the range of 0.032–0.038. Finite element Petrov-Galerkin concept was used to solve the system of hydrodynamic equation with simple robust approach for treating the dry-and-wet bed problem (Kolerski 2015).

The ice dynamic equation in the model which considers all external and internal forces, including water drag $\vec{F}_w$, wind drag $\vec{F}_a$, gravity force computed due to water slope $\vec{G}$ and internal resistance of ice $\vec{R}$, is written as (Shen et al. 2000):

$$(M_i)_k\left(\frac{D\vec{V}_i}{Dt}\right)_k=\left(\vec{R}\right)_k+\left(\vec{F}_a\right)_k+\left(\vec{F}_w\right)_k+\left(\vec{G}\right)_k \tag{4}$$

The above equation is second Newtonian law concept in which $\left(D\vec{V}_i/Dt\right)_k$= acceleration of ice parcel k; M_i = ice mass per unit area; and $\vec{V}_i$ = ice velocity. The internal ice resistance is governed by the material behavior of the ice and described by viscous-elastic and elastic-plastic constitutive law. The internal friction angle for ice was not calibrated and a value of 46°, which is default for river ice, was applied (Shen 2010). A meshless Lagrangian discrete-parcel method (DPM) based on the Smoothed Particle Hydrodynamics (SPH) is used to simulate the ice dynamics. This method uses Lagrangian parcels to represent the ice mass in the ice run and jam.

Thermal calculations for static border ice were needed to estimate ice cover range in a new reservoir. Total heat transfer at the water surface is computed by calculating the components of short and long wave radiation, evaporative and conductive heat fluxes. Linear formula for heat loss at the water surface was applied, because the rough estimation of the border ice zone was only needed.

Linear approximations of the heat transfer, at the air-water interface, depends on the difference between air and water temperature and short wave radiation component, which is independent of the air temperature (Liu and Shen 2005):

$$\varphi_{wa}^{*} = -\varphi_{Rw} + \alpha' + \beta'(T_w - T_a), \tag{5}$$

where φ_{wa}^{*} = net rate of heat loss at the water surface; T_a = air temperature; T_w = water temperature; α', β' are constants depending on the weather parameters; φ_{Rw} = the net short wave radiation penetrating through the water surface, which has to be computed separately making use of geographical latitude and cloud cover condition.

Based on Matousek (1984), the conditions in which the static ice cover is formed must satisfy all of the following criteria: (a) surface water temperature is below the threshold value, (b) ice buoyancy force exceeds vertical turbulence (c) depth-averaged water velocity is below the critical velocity. All the threshold values were estimated based on the literature reviews (Bijeljanin and Clark 2010; Hammar et al. 2002; Liu and Shen 2005; Shen 2008). Static border ice zones were determined for all potentially possible reservoir variants.

4 Simulation Results

Sensitivity analysis on ice passage through a new dam was performed with varying model parameters based on low flow conditions. These parameters were the wind speed and water discharge at the Włocławek dam. For each potentially possible locational variant of the new dam, a total of six cases with different combinations of flow (300 and 600 $m^3\ s^{-1}$) and wind condition (no wind, western wind with velocity of 2 and 5 $m\ s^{-1}$) were simulated to determine the range of the effects the ice would have on the reservoir operation in the winter season.

The first step, before the ice dynamic simulations, was to determine border ice zones in new reservoirs. Thermodynamic calculations were performed for average flow conditions (Q = 900 $m^3\ s^{-1}$), air temperature T_a = −10 °C, and water temperature at upstream (tailwater of the Włocławek dam) T_w = 0.01 °C. Because threshold parameters for static border ice were not calibrated, a comparison between calculated (Fig. 3) and observed static border ice zones was made based on the aerial photo of the proposed location of the Hutnicza reservoir, downstream of Włocławek Dam (Fig. 4). Due to increase of the head on the new dam, the simulated conditions were not identical with observed; however, the general similarity of the static ice cover zones can be observed. The ice free channel along the entire reservoir is close to open water area on the aerial photograph or the dynamic ice cover which is observed upstream of the bridge. In the direct vicinity of the Włocławek Dam, the difference in static border ice zones is caused by not including water released from the power plant (south from the spillway). After setting up the

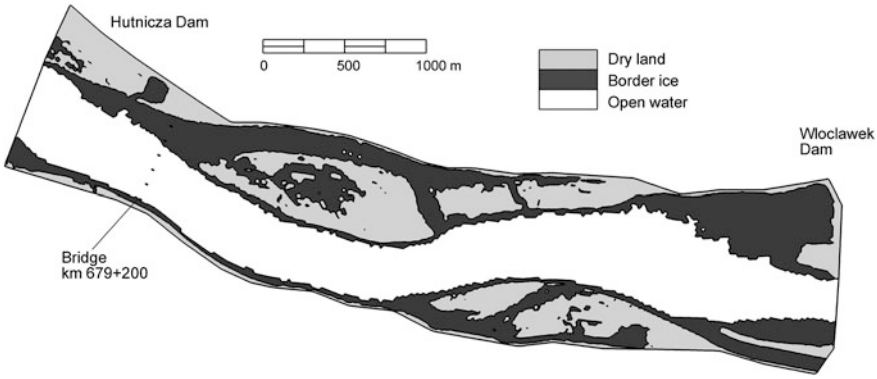

Fig. 3 Simulated border ice zones in the Hutnicza reservoir for average discharge $Q = 900\ m^3\ s^{-1}$

Fig. 4 Aerial photo of the ice forms downstream of Włocławek Dam on January 16, 1985 (courtesy of Prof. M. Grześ)

thermodynamic model parameters based on the Hutnicza case, the same calculations were applied to the rest of the proposed reservoirs.

Hydrodynamic simulations were performed to assess the effect of new dam location on ice run during the breakup. Ice sluicing through the Włocławek Dam is complicated and its operation is complex, which may lead to severe problems if not properly undertaken. Detail instructions and good practice in ice sluicing and ice-breaking operation on Włocławek reservoir are collected in yearly released guide (RZGW 2009). Usually ice sluicing through the Włocławek spillway is performed during the water discharge in a range 600–1500 $m^3\ s^{-1}$ (personal communication with power dam staff) and when the wind speed does not exceed a limit of 2 $m\ s^{-1}$. It is expected that similar procedure will be applied to the new reservoir. The low flow conditions are not favorable for ice sluicing because the contraction of the flow at the spillway (only 3 spans are open) may lead to accumulation of ice in the forebay of the dam. Also during the low flow condition, the drag force from the

water is significantly reduced due to low water velocity. In such case, even small wind blowing from opposite direction will cause stoppage of the ice run. In addition, in deep section of the reservoir, as a result of small water discharge, a horizontal pool level is observed. Therefore, gravitational force cannot set the ice floes to motion and its stoppage is highly probable. Low flow conditions together with the western wind were selected as the worst case scenario, which was confirmed by the simulation results.

In all simulated cases it was noticed that the bridge cross-section is critical for ice run during the breakup. The six piers located on the deep section of the river cause narrowing of the flow area and cause increased ice concentration and decrease of its speed. Ice floes are not stopped by the existence of the bridge, but the process of slowing down its movement affects the fluency of ice motion in an upstream section of the reservoir. This could be confirmed by aerial photo shown in Fig. 4 where dynamic ice cover formed from juxtaposed ice floes is visible on the river section upstream of the bridge. Because the bridge is located only 4 km downstream of the existing dam, its effect quickly reaches the Włocławek spillway. In some simulated cases the effect is visible in a form of slowly moving ice with increased thickness ranging from 0.9 to 1.86 m. This ice accumulation is not significant in comparison to average depth of the proposed reservoirs, but because it is located in a close distance from the spillway stilling basin, it is a serious obstacle for further ice passage. The thickest ice accumulation was observed for Hutnicza Dam case with wind blowing in opposite direction to the flow. For the other reservoirs, bridge piers also limited ice outflow to downstream section, but because of the much larger size of reservoir the effect was not critical for ice passage operation.

For the Hutnicza reservoir, ice can be sluiced without significant problems for no wind conditions. For low flow condition (discharge of 300 $m^3\ s^{-1}$) it was possible to sluice about $1 \times 10^6\ m^3$ of ice per day (ice discharge of about 12 $m^3\ s^{-1}$). The route of ice movement was consistent with designed waterway, where some dredging is planned. The amount of ice in the Hutnicza reservoir oscillated slightly around the value of 500,000 m^3, which means that the ice passed the spillway without stoppage (ice inflow equals to the outflow). If the wind effect is included in the simulations, the situation in the Hutnicza reservoir is similar, because less ice is entering the reservoir form the Włocławek spillway. For higher water discharge (600 $m^3\ s^{-1}$), ice inflow to the reservoir increased to 20 $m^3\ s^{-1}$. It caused that not all ice was sluicing through the new dam, and its volume in the reservoir enlarged in time. Due to the small retention availability of the Hutnicza reservoir, limitation of ice inflow could be performed to eliminate the potentially dangerous situation. This action extended the duration of the ice passage process to about 14 days, if no wind occured. For simulation with western wind, the bridge has significant impact on ice run, causing ice piling up in about 1 km long upstream section of the reservoir with up to 1.85 m thickness (Fig. 5).

All the other locations for the new dam are planned to be built on 8 km long reach of the Vistula River, in the vicinity of the Nieszawa-Ciechocinek region. For these variants pool levels had the same elevation of 46 m (HKron86); therefore, the

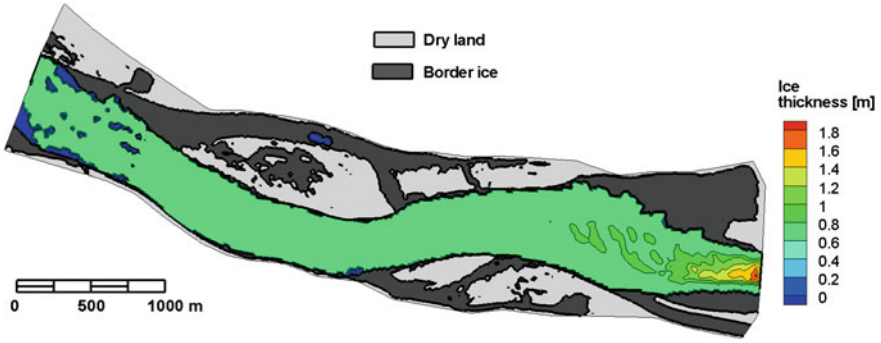

Fig. 5 Ice thickness distribution in the Hutnicza Reservoir (discharge of 600 m^3 s^{-1}, wind velocity of 5 m s^{-1})

farther the dam location, the higher the designed head will be produced. The Vistula River valley is relatively compact in the section where Przypust variant is proposed, and for the other three locations the river has extensive floodplains on both sides. After the new dam is constructed in Przypust location, the river width will increase from about 600 m at normal water depth to 900 m for designed pool level. For all the other locations, damming the river will cause inundation in more areas which will lead to widening the channel up to 3 times in comparison to the current river width. In consequence of a dam construction in the Nieszawa or Siarzewo location, the reservoir in a close upstream vicinity of the dam will have a compound cross-section profile with deep main channel and shallow flood plains. The logical expectation of flooding shallow areas is the formation of static border ice, which was confirmed by thermodynamic calculations. However, if cover is not formed or will be broken, in these areas ice can accumulate, causing grounded ice jam which is specifically dangerous during the breakup time. Western wind could enhance the process, especially for the Nieszawa case, where 700 m long and 2 m deep shoal will be produced on the left bank of reservoir due to the damming. The problem could be solved by stationary ice boom whose purpose is to stabilize the ice cover during the freeze up and, in conjunction with the icebreakers, to make the ice sheet less resistant to movement under the influence of water current. The most effective location of the protective piers need to be evaluated by numerical calculation, but typically the length of the structure is presumed to extend about five times the distance from the shore to the structure.

Based on the simulation results, ice sluicing through the proposed dams proceeds without significant impediments if calculation without wind impact is performed. The differences in ice movement in each considered variant were due to morphometric parameters of river channels, such as sinuosity of the river's current. The larger the distance of the next dam from Włocławek, the more variable is the morphology of the foreseen reservoir, contributing to possible ice stoppage. Numerical simulation of the ice dynamics with western wind showed that the most advantageous situation can be achieved for Przypust reservoir. For that variant, ice

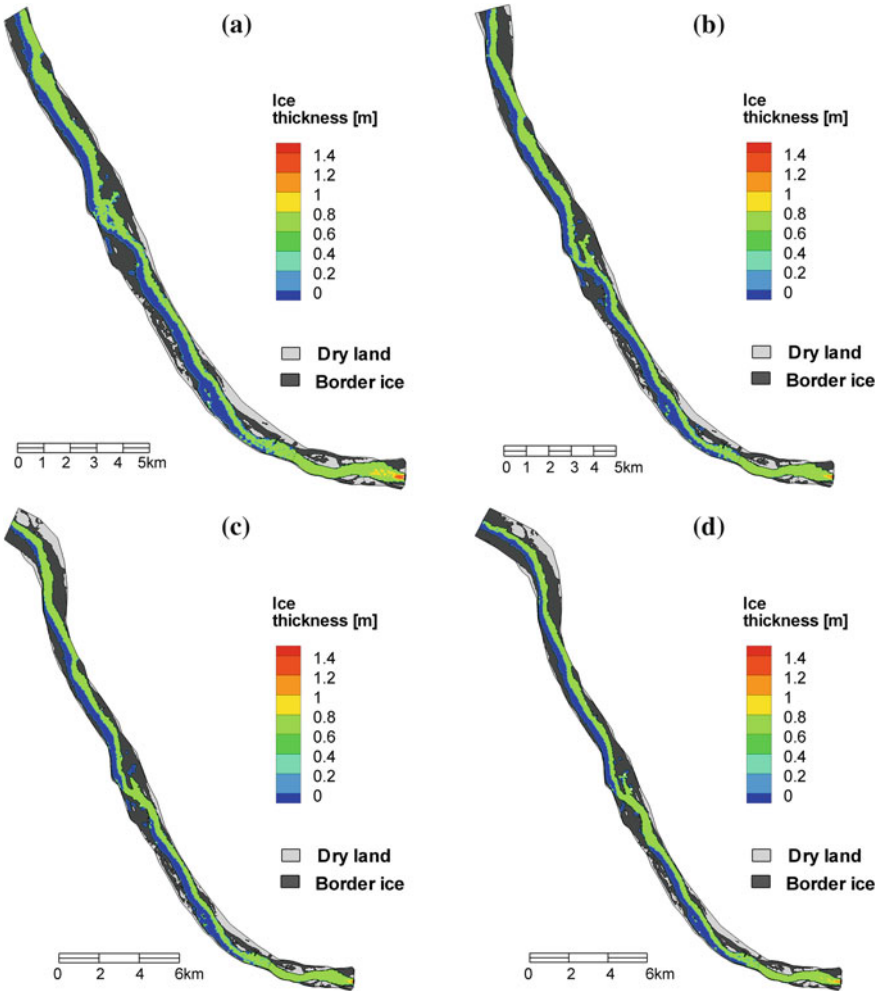

Fig. 6 Ice thickness distribution for water discharge of 600 $m^3 s^{-1}$ and wind velocity of 5 $m s^{-1}$ for variants Przypust (**a**); Nieszawa (**b**); Siarzewo (**c**) and Siarzewo II (**d**)

sluicing through the spillway was still possible even though the high western wind was simulated (Fig. 6a). The reason for that situation is the reservoir layout on the south-north direction, which is favorable for ice movement. The Nieszawa case was similar but the side wind caused ice to be pushed towards the left bank, and was stopped in the large area of shallow water (Fig. 6b). Fixed ice control structure, in a form of protective piers, needs to be considered to direct ice from dam forebay into the spillway's section. Both dam locations in the vicinity of Siarzewo village are planned to be on the river reach oriented towards north-west direction. However, the dam in km 706 + 400 caused relatively smooth ice transport even for the high

western wind (Fig. 6c). The ice movement in this dam forebay was contributed by water current which was still directing north because it is within the close distance from the river bend. For the Siarzewo II location in km 707 + 900, which is about three kilometers downstream of the bend, water flows towards north-west and the wind caused complete stoppage of the ice sluicing (Fig. 6d). Because of economic reason, the higher the design head the greater the contribution from the new dam; therefore, from the two selected dam variants, Siarzewo and Przypust, the first one is more desirable.

5 Conclusions

Numerical simulations were carried out for the four locations which were recommended based on exclusive analysis. In addition, the Hutnicza location was included in the paper which is the only variant that allows the maintenance of the Natura 2000 ecological sites in an untouched state. The mathematical model was applied to current river bathymetry, and sensitivity study including low flow conditions and western wind was performed. The goal of the study was to find the optimal location of the new dam, allowing for the provision of relevant icebreaking conditions.

Based on the simulations results it was found that ice passage through the new reservoir is generally possible for any dam location and does not cause significant jam risk for no wind condition. The only exception is the Hutnicza reservoir where some ice accumulation is observed as an effect of bridge piers interaction. The accumulation is not significant and could be released by redirecting the ice flow to the other spillway sections. However, for the Hutnicza reservoir the major problem is the small size, so that the ice retention possibility is limited. In any exceptional situation, such as spillway gates damage or freezing, it is impossible to continue ice sluicing from the Włocławek dam.

Sensitivity study indicates that ice sluicing during the unfavorable western wind conditions could proceed only for dam locations at Przypust and Siarzewo. Also the risk of occurring ice jams was reduced due to construction of the new dam in both above-mentioned locations. Including other criteria, such as environmental impact or economic aspect of power production, the Siarzewo variant is the best location for the new dam downstream of the Włocławek dam.

References

Ashton GD (1986) River and Lake Ice engineering. Water Resources Publications, Littleton, CO, USA

Bajkiewicz S, Olifirowicz J (2014) Influence of the Wkra River ice phenomena on its energy resources. Acta Sci Pol, Formatio Circumiectus 13 (4): 15–24 (in polish)

Bijeljanin M, Clark S (2010) Development of a numerical model for predicting ice conditions on the upper nelson river, 20th IAHR international symposium on Ice. Lahti, Finland
Environmental Protection Law (April 16th 2004) J Laws 2004.92.880, as amended (in Polish)
Granatowicz J (2013) The next dam on the Vistula River below Włocławek. Acta Energetica 3 (16):99–105
Grześ M (1991) Ice-Jam and floods on the Lower Vistula. Mechanisms and Conditions, Institute of Geography and Spatial Organization, PAS, Warszawa
Hammar L, Shen HT, Evers K-U, Kolerski T, Yuan Y, Sobczak L (2002) A laboratory study of freeze-up ice runs in river channels. 16th IAHR international symposium on Ice. Dunedin, NZ 3:22–29
Kolerski T (2011) Numerical modeling of Ice jam formation in the Włocławek reservoir. Task Quarterly 15(3–4):283–295
Kolerski T (2013) Ensuring public safety in the area of Włocławek Dam with the use of water energy as well as improvement in the potential of water ecosystems and ecosystems dependent on waters; Report no VS-29-A000-HR-001-0A, Modeling of the ice processes assessment due to new dam below Włocławek, prepared by Ove Arup & Partners International Ltd, on behalf of ENERGA SA (in polish)
Kolerski T (2014) Modeling of ice phenomena in the mouth of the Vistula River. Acta Geophys 62 (4):893–914
Kolerski T (2015) Ice cover progression due to flow regulation at the Włocławek Dam, Acta Sci Pol, Formatio Circumiectus, 14(1): 229–240 (in Polish)
Kolerski T, Shen HT, Kioka S (2013) A numerical model study on Ice boom in a Coastal Lake. J Coastal Res 29(6a):177–186
Liu L, Shen HT (2003) A two-dimensional characteristic upwind finite element method for transitional open channel flow, Rep 03–04, Department of Civil and Environmental Engineering, Clarkson University, Potsdam, USA
Liu L, Shen HT (2005) CRISSP2D Version 1.0 Programmer's Manual. CEE Report 05–19, Clarkson University, Potsdam, New York, USA
Lu S, Shen HT, Crissman RD (1999) Numerical study of ice dynamics in upper Niagara River. J Cold Reg Eng 13(2):78–102
Majewski W (2013) The development of hydro power in Poland. The most important hydro engineering facilities. Acta Energet 3(16):45–53
Malenchak J, Doering J, Shen, HT, Morris M (2008) Numerical simulation of Ice conditions on the Nelson River. 19th IAHR international symposium on Ice. Vancouver, British Columbia, Canada, 251–262
Matousek V (1984) Types of Ice Run and Conditions for their Formation. IAHR symposium on Ice, Hamburg, Germany, pp 315–328
RZGW (2009) Instruction of icebreaking and ice sluicing thorough Włocławek Dam, version XI, Włocławek, (in Polish)
Shen HT (2010) Mathematical modeling of river ice processes. Cold Reg Sci Technol 62(1):3–13
Shen HT, Liu L (2003) Shokotsu River ice jam formation. Cold Reg Sci Technol 37(1):35–49
Shen HT, Su J, Liu L (2000) SPH simulation of River Ice dynamics. J Comput Phys 165(2): 752–770

Development of a Laboratory System and 2D Routing Analysis to Determine Solute Mixing Within Aquatic Vegetation

Patrick West, James Hart, Ian Guymer and Virginia Stovin

Abstract A laser induced fluorometry (LIF) system was developed to quantify mixing within spatially variable aquatic vegetation. A comparison is made between intrusive fluorometry techniques and the application of LIF, to quantify mixing in real vegetation in the laboratory setting. LIF provides greater spatial resolution when compared to point fluorometry. Furthermore, LIF is non-intrusive. A two-dimensional routing procedure is used to calculate the longitudinal and transverse velocities and mixing coefficients from a single pulse injection of tracer within a vegetation patch.

1 Introduction

Diffuse, or non-point source, contamination is the most significant contributor to surface water pollution within the UK and Europe (National Audit Office and Environment Agency 2010). Pond and wetland environments are becoming an increasingly favoured method of providing appropriate pre-treatment before contaminated water enters major watercourses (Kadlec and Wallace 2009; Serra et al. 2004). As well as offering ecological habitat and amenity to local residents, wetland treatment systems present an integrated approach to sustainable water resource

P. West (✉) · J. Hart · I. Guymer
School of Engineering, Univeristy of Warwick, Coventry CV4 7AL, UK
e-mail: p.west@warwick.ac.uk

J. Hart
e-mail: j.hart@warwick.ac.uk

I. Guymer
e-mail: i.guymer@warwick.ac.uk

V. Stovin
Department of Civil and Structural Engineering, The University of Sheffield, Mappin Street, Sheffield S1 3JD, UK
e-mail: v.stovin@sheffield.ac.uk

P. Rowiński and A. Marion (eds.), *Hydrodynamic and Mass Transport at Freshwater Aquatic Interfaces*, GeoPlanet: Earth and Planetary Sciences,
DOI 10.1007/978-3-319-27750-9_5

Fig. 1 Tracer study used for flow visualization in a treatment pond. Image courtesy of Hart et al. (2014)

management. The presence of vegetation in these systems acts as a habitat for organisms (Taylor et al. 1995) and bio-chemical degradation of contaminants (Edgar 1990; Kadlec and Knight 1996; Dixon and Florian 1993; Nixon 1980). Moreover, vegetation affects the local hydrodynamics and thus the installation's detention characteristics (Nepf 1999; Nepf et al. 2007; Burba et al. 1999).

The prevalence of controlled laboratory studies (White and Nepf 2007; Ghisalberti and Nepf 2002, 2005; Nepf et al. 2007; Boxall and Guymer 2007) has helped to understand the influence of hydrodynamics and channel porosity on detention times and dispersion. Laboratory studies have also proved essential when verifying, often empirical, modelling techniques (Serra et al. 2004; Ghisalberti and Nepf 2005). From previous laboratory studies there is a paucity of information on the influence of plant species, age and geometry on solute mixing.

Pond systems generally comprise borders and patches of emergent vegetation (e.g. Fig. 1). The lateral heterogeneity in drag caused by these patches influences the velocity field creating a complex, multi-dimensional system (Ghisalberti and Nepf 2002, 2004; Nepf et al. 2007; Nepf and Vivoni 2002; Murphy et al. 2007; White and Nepf 2007; Rominger and Nepf 2011). Figure 1 shows an example of a field trace study in a large treatment pond (Hart et al. 2014). The fluorescent dye highlights the spatially variable flow fields around borders and patches of vegetation.

This paper describes the development of a laboratory method and analysis technique as part of a 3 year EPSRC funded grant projects 'Residence Times in Vegetated Stormwater Ponds EP/K024442/1 and EP/K025589/1'. The project aims are to derive an understanding of how the hydraulic residence time of a stormwater pond is affected by the type and spatial distribution of vegetation. The project has 3 core objectives: to produce a CFD model that can predict how vegetation density and spatial distribution affect the pond's flow field, mixing characteristics and residence time distribution; to collect detailed laboratory data to parameterise the CFD model, and to validate the model against a range of field tests on real stormwater ponds.

Tests were conducted in fully-width artificial vegetation as a controlled case for the development of the technique—with the view to its later application in shear layer systems. The development and calibration of a bespoke laser induced florescence (LIF) system will be described, and compared to the point fluorometry technique. In addition, a 2D routing procedure based on the Advection Dispersion Equation is evaluated to obtain the longitudinal and transverse dispersion coefficients and respective velocities from pulse injection tests within vegetation patches.

1.1 Background

The trace study in Fig. 1, showing the spatially heterogeneous flows common to ponds, exemplifies the motivation to conduct this research. Tracer dye studies are a common tool for elucidating the hydrodynamic properties of a system (Lightbody and Nepf 2006a; Shucksmith et al. 2011; Kashefipour and Falconer 2002; Deng et al. 2001). Mixing in ponds is a complex phenomenon for two reasons. Firstly, the spatial heterogeneity in the flow field, pond geometry and dispersion can make modelling and experimentation difficult. Secondly, the prevalence of low velocities (<0.1 m/s) also presents a number of experimental difficulties. If we wish to predict the retention characteristics of ponds with live vegetation then a more robust method for quantifying mixing in aquatic vegetatation needs to be developed.

Reynolds number in pond and wetland environments is very low (Nepf 1999; Serra et al. 2004; Nepf et al. 1997). Nepf et al. (1997) and Serra et al. (2004) recorded stem Reynolds number in the field at $Re < 200$ and $5 < Re < 20$, respectively. Stem Reynolds number is used as the preferred length scaling in vegetated flow

$$Re_s = \frac{Ud}{v} \tag{1}$$

where the preferred length scale is d, the stem diameter, U is the mean stream-wise velocity and ν is the kinematic viscosity of water. It follows that flow in these environments can be fully laminar or transitional from laminar to turbulent (Tamura et al. 1980; Nepf et al. 1997).

In general, the degree of mixing in a system can be described using a dispersion coefficient ($m^2\ s^{-1}$). Historically this has been calculated by observing the temporal or spatial rate of change of variance in the concentration distribution of a tracer (Fishcer 1968). Here, the term *mixing* is used to describe the cumulative effects of all processes that cause a contaminant to spread or dilute. As such, the term mixing aggregates diffusion, shear dispersion, turbulent diffusion and mechanical diffusion into one parameter. The dispersion coefficient, D, is proportional to the spatial rate of change in variance of the concentration distribution. In the x-direction,

$$D_x = \frac{u}{2}\frac{d\sigma_x^2}{dx} \tag{2}$$

where σ_x^2 is the variance in the tracer cloud at position x.

The dispersion coefficient and travel time in a particular direction can be optimized by performing a routing procedure from the tracer's temporal concentration distribution (TCD) (Boxall 2000; Boxall and Guymer 2007). The downstream TCD is fitted by routing the measured upstream profile until the fit between measurement and prediction is maximized. This process used a Gaussian transfer function. It follows that, if a two-dimensional distribution can be obtained, a two-dimensional routing procedure can optimize the longitudinal dispersion and transverse mixing coefficients and their respective velocities (u and v).

A low Reynolds number does not readily permit assumptions and simplifications—such as rapid cross-sectional mixing and a Gaussian transfer function. Research presented here indicates that, under typical flow velocities in ponds, cross-sectional mixing does not occur for a number of metres from the source. This has implications for the experimental techniques and is described below.

Figure 2 is a schematic of the phenomena shown in Fig. 1. A velocity shear is caused by the drag discontinuity between the free-flow and the vegetation elements (Nepf and Vivoni 2002; Ghisalberti and Nepf 2002). The discontinuity in drag leads to the generation of shear layer vortices. White and Nepf (2007) show that the penetration of shear-generated vortices along an emergent vegetation interface is inversely proportional to the vegetation density. Unlike free shear layers, the vortex growth is arrested when the potential gradient balances with the vegetation drag (Ghisalberti and Nepf 2004).

Take the region beyond the extent of the shear layer vortices depicted in Fig. 2. In the fully vegetated emergent region transverse and/or vertical shear effects are negligible; when compared to stem wake generated turbulence. Turbulence is therefore found at the scale of the vegetation elements (Lightbody and Nepf 2006). Thus, a local stem Reynolds number is a preferred method of quantifying turbulence (Serra et al. 2004; White and Nepf 2007; Ghisalberti and Nepf 2005). Using this preferred scaling, Lightbody and Nepf (2006) show that the lateral dispersion in

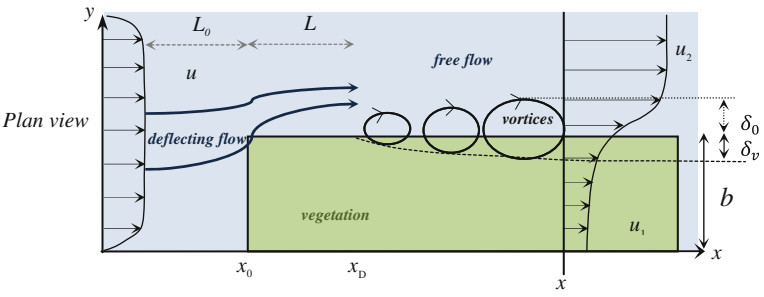

Fig. 2 Vegetated shear layer

emergent cylinders is dependent on the mean streamwise velocity and the diameter, d, of each element; empirically

$$D_y = 0.17ud \tag{3}$$

Accurate measurement of transverse mixing in real vegetation is lacking. Further, a number of studies have shown that observational error increases in such low velocity environments (Nepf 1999; Boxall and Guymer 2003, 2007). Detailed research is lacking for the quantification of mixing processes in and around the partially vegetated/open channel boundary, its bulk effect on wetland retention times and to predict parameters for CFD applications.

1.2 Research Aims

We wish to quantify the mass transport in real vegetated shear layers. Imperative to the observation and quantification of these processes is the successful development of a precise tracer detection system. Mixing in spatially uniform emergent vegetation (fully vegetated) is here used as a test case to develop a measurement process. Rhodamine 6G dye injections are made to observe the spatial and temporal spread of concentration in an array of emergent artificial cylinders and two measurement techniques are compared.

2 Experimental Methods

2.1 Point Probe Fluorometry

Two Rhodamine tracer studies were conducted in a recirculating flat flume at the University of Warwick, UK. The first experiment assessed the feasibility of using point flurometers for measuring spatially variable concentration distributions. Point source pulses of dye were generated in a partially vegetated array of emergent plastic cylinders (Fig. 3). The artificial vegetation was 7 m long with the leading edge 12 m downstream of the inlet to the 24 m long flume. 0.20 m high, 0.004 m diameter plastic straws were arranged in a staggered array spanning 0.3 m of the 0.99 m wide flume.

Dye injections were made 2.8 m downstream of the vegetation leading edge. Ultrasound velocity measurements indicated that this was the location of fully developed flow. A point copper pipe delivered dye to the channel mid-depth and was fed by a constant head tank positioned directly above. Software controlled injections were made via a solenoid valve to enable instantaneous release—providing accuracy in both time of injection and in the mass of tracer. Four discharges (3.0, 5.0, 6.4, 8.4 l/s) were investigated as they produced typical in-vegetation

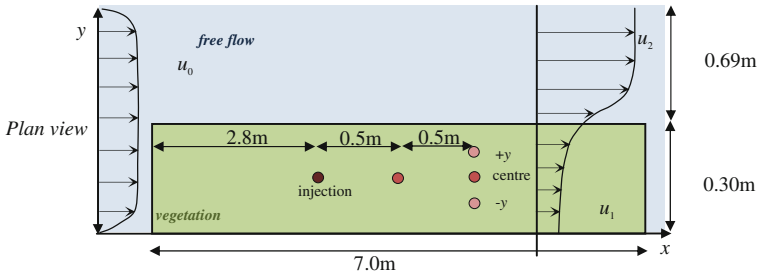

Fig. 3 Fluorometer measurement system. Deviated downstream sites are 0.04 m either side of the centerline

velocities found in ponds, i.e. $u_{1max} \approx 10$ cm s^{-1}. In all test cases the mean travel time between longitudinal profiles is used to compute a mean flow velocity.

Tracer pulses were input for 20 s. Concentration was measured at 0.5 m and 1.0 m downstream using *Cyclops* fluorometers—positioned in line and at the same depth as the injection point. Temporal and spatial constraints within the laboratory procedure meant that the downstream concentration profiles needed to be recorded in relative close proximity to the injection point. Further, the low turbulent environment, due to the slow velocities, leads to poor mixing within the trace profile. It was therefore necessary to take up to twenty repeat trials for each test condition. Concentration was measured at 1 Hz to provide adequate temporal resolution. Each pulse was delayed to allow sufficient time for the previous trace to be completely advected through the test section.

The locations of the two downstream fluorometers are shown in Fig. 3. Each test, using the point source injection method, was repeated for these deviated downstream fluorometer locations to observe the lateral spread in concentration distribution. Displacements of $y = 4$ cm (y+) and $y = -4$ cm (y−), relative to the injection position, were chosen.

2.2 Laser Induced Fluorometry

The second experiment evaluates Laser Induced Fluorometry (LIF) in its application to record over multiple locations in space—in this case a transverse line. The LIF system was developed to observe spatially variable mixing in the partially vegetated system described in Fig. 3. In this preliminary experiment, LIF was evaluated in the simplified fully vegetated scenario. LIF relies on the same principles employed using the point fluorometer probes. A laser is directed perpendicularly through the flow at the channel mid-depth. As the Rhodamine 6G trace passes through the laser beam the dye absorbs some of the incident light and re-emits it—known as fluorescence. The principle mechanisms of LIF are shown in Fig. 4 indicating the passage of dye through the laser beam. A photo-detector is

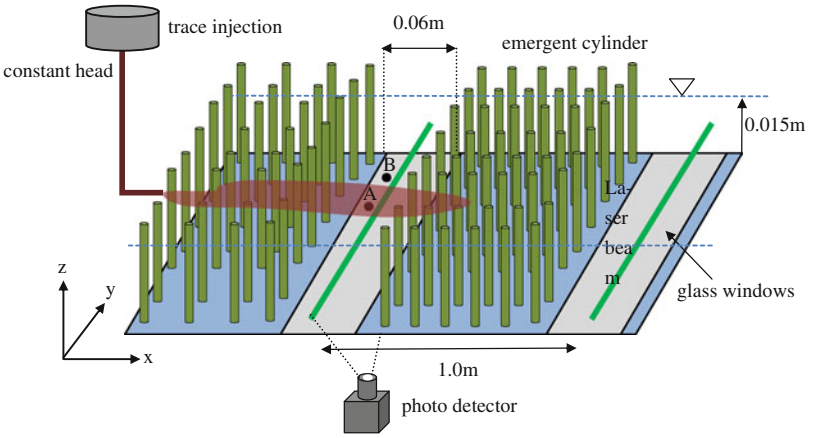

Fig. 4 Schematic diagram of emergent, full-cross-sectional vegetation with LIF windows. Note that the cylinder diameter and density are not to scale

mounted directly beneath the flow and a wide-angle lens chosen to image the entire beam. Dye concentration is directly proportional to fluorescence intensity and therefore camera pixel intensity. The same laboratory flume depicted in Fig. 3 is also used for this experiment.

Laser attenuation through ~ 1 m of water is significant and laser power was observed to reduce by up to 50 %. Further, the laser's attenuation is a function of the local dye concentration. Consider the scenario where intensity is compared from points *A* to *B* (Fig. 4). A weak intensity (and therefore concentration) recorded at *B* could be as a result of two phenomena. Firstly, a comparatively weak concentration is recorded as there is less dye at *B* than *A*. Secondly, the laser beam is attenuated through dye on its propagation to *B* and is weaker, resulting in lower fluorescence. Thus, a simple calibration using the Beer-Lambert Law relating the exponential decay in laser intensity to an attenuation coefficient could not be used.

LIF calibration is conducted by recording the change in laser attenuation coefficient as a function of initial laser power. In short, this method considers the power entering a cell and that leaving. If the concentration of the first cell is known, then the concentration of subsequent cells can be determined in a step-by-step effect.

The two LIF windows are shown in Fig. 4. The first window was located 1 m downstream of the dye injection point and the second was positioned 1 m downstream from that. A 200 mW green laser (λ = 532 nm) was mounted such that it pointed through the flow at a mid-depth of 0.075 m. A small 0.06 m transverse gap within the array was made to accommodate the laser beam and Ultrasound Velocity Profiling (UVP) equipment. Glass windows in the side and bottom of the flume were sealed. A grey-scale camera was mounted underneath each glass window and focused onto the location of the laser beam. The camera shutter-speed was set to maximize the full range of the 8-bit setting for the desired range in trace concentration. Camera images were cropped before saving—to facilitate smooth computer

operation—to 20 × 1280 pixels (0.015 m × 0.99 m). Spatial resolution was therefore roughly every millimetre and the resolution in concentration, set by the chosen range in concentration, was 0.2 ppb (per pixel intensity). The entire channel system was covered in black-coated wooden paneling to reduce the impact of background ambient light. Discharge was set such that the mean, stream-wise flow velocity, u, within the vegetation was O (1 cm s^{-1}). Four discharges were investigated (1.0, 1.8, 2.4, 3.6 l/s); flow depth was maintained at approximately 0.15 m and was measured using a Vernier accurate to 100 μm.

Rhodamine 6G was injected from a point source using a copper pipe connected to a constant head tank. Pulse injections, of 10 s duration, were made to observe mixing both longitudinally and transversely. Ten repeat pulse injections were made to acquire an average distribution. Camera images were recorded at 5 Hz providing ample temporal resolution. Velocity was recorded at 50 Hz for 3 min using a *Nortek Vectrino* UVP at ten transverse locations. The channel mean velocity was then calculated from the average of the temporal mean values from ten transverse locations. In spatially homogeneous vegetation this is deemed appropriate.

3 Results

3.1 Point Probe Fluorometry

The average longitudinal concentration profile measured with the *Cyclops* fluorometers, for the 6.4 l/s discharge, injection is shown in Fig. 5a. The corresponding tests for the lateral deviation in downstream fluorometer location both positively and negatively are given in Fig. 5b, c, respectively. Profiles were averaged at a fixed time relative to the automated injection time for all 20 repeat injections.

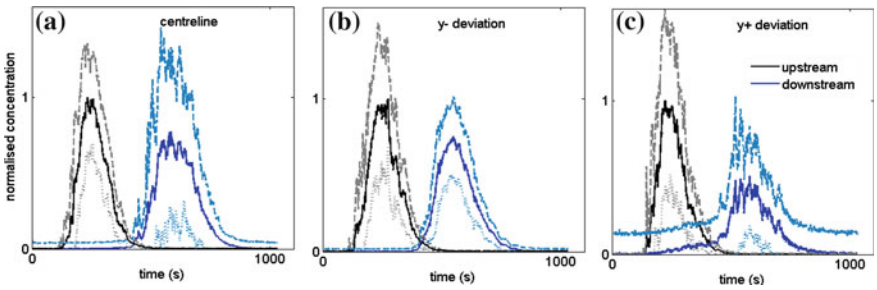

Fig. 5 Longitudinal concentration profiles for the vegetation pulse point injection are given for **a** centreline detection and **b** $y-$, **c** $y+$ downstream deviation. Plus or minus 1 standard deviation is shown with the *dashed* and *dotted lines*. Each profile is the average of 20 repeat tests

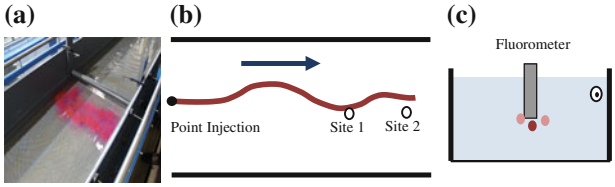

Fig. 6 **a** An example of poor mixing and tracer "clouding". **b** Stream-tube meander around the fluorometer. **c** Positioning error and difficulties using single-point detection probes

Figure 5 shows an increase in the downstream profile peak concentration when the downstream fluorometer is translated negatively in the y direction i.e. further from the effect of the shear layer (Fig. 5b). Conversely, downstream profile concentration reduces when the fluorometer is translated positively in the y direction (Fig. 5c). The progression in mass-loss at the downstream site from 5b to 5a to 5c gives the illusion that the trace is transported deeper within the vegetation; whereas the increased mixing due to shear layer turbulence diffuses the trace closer to the interface thus reducing the concentration more rapidly.

The point detection results in Fig. 5 were obtained from three independent tests to minimise flow disruption by the physical presence of multiple probes. The difference in concentration distribution between the three downstream profiles (e.g. for the centerline, positive y and negative y) indicates that the flow field in the test was not spatially homogeneous. Thus, point source detection is inappropriate in such a system. Poor initial mixing does not lead to a cross-sectionally, well-mixed tracer (Fig. 6a); resulting in noisy data. Secondly, the physical obstruction of the fluorometers was seen to direct the flow around the device (Fig. 6b). This was particularly noticeable in the point source injection tests. The small-scale tracer plume was observed to travel around the flurometer. Figure 6b shows how the plume meander from site 1–2 could result in a mass imbalance between the two profiles as site 2 may detect only the edge of the plume.

Thirdly, the small spread in tracer plume, particularly in the lower velocities, is comparable in diameter to the fluorometer probes (0.003 m). This makes the correct positioning of equipment challenging (Fig. 6c). Further, the combination of stream-tube meandering and comparably small plume diameter can lead to the collection of unrepresentative data. It is expected that the transverse mixing and longitudinal dispersion coefficients will be functions of lateral distance across the flow—with mixing peaking in the turbulent shear layer (Ghisalberti and Nepf 2005). Spatially extensive detection sites across the flow are therefore required to observe and quantify mixing in vegetated shear flows. However, given the local effect on flow and tracer propagation positioning a number of in situ fluorometers across the flow would obstruct the flow and result in secondary circulations at a comparable scale to that of the vegetation elements. Therefore point detection is not suitable for quantifying mixing in spatially variable flow fields.

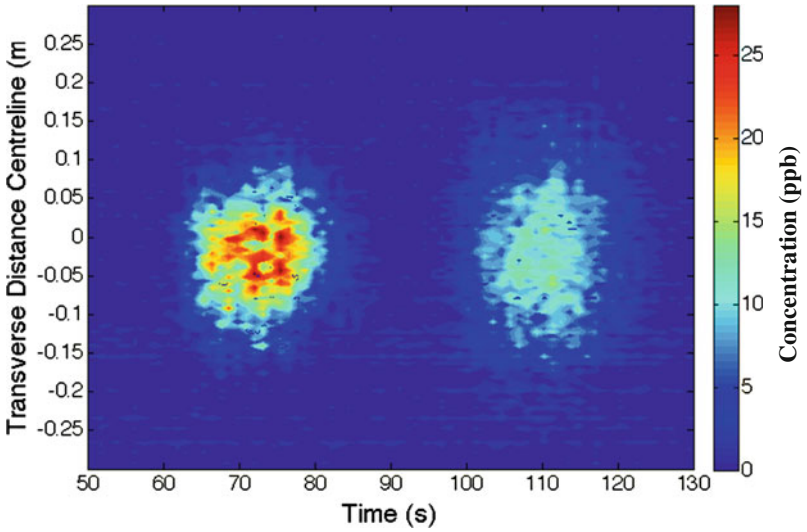

Fig. 7 Contour plots of concentration measured using the LIF system for 1.8 l/s emergent vegetation

3.2 LIF

An example of a two-dimensional (y, t) concentration distribution for a single pulse injection is given in Fig. 7. Upstream and downstream distributions are plotted on the same figure for time from injection against transverse location. The colour in Fig. 7 denotes concentration in ppb. Employing LIF to produce the 2D distribution is very successful. The use of a camera detection system provides high spatial resolution of up to 1280 pixels. The plot has been calibrated taking into account the dependence of laser attenuation on trace concentration as described in the preceding section. The frequent image rate (5 Hz) provides insightful imaging of the trace evolution; showing detailed turbulent structures.

A two-dimensional routing procedure was undertaken to analyse the concentration distributions given in Fig. 7. The upstream distribution is broken into discretized elements of concentration. The advection and dispersion of these elements is then modelled as Gaussian using the ADE. By varying the input values of longitudinal dispersion coefficient, transverse mixing coefficient and mean, stream-wise and transverse velocity, a prediction of the downstream distribution is optimized such that the error between prediction and measurement is minimized. Optimization in this manner is applied to the full two-dimensional array of data. This differs from many previous optimized routing techniques that have generally been applied to one-dimensional data (e.g. $C = f(t)$).

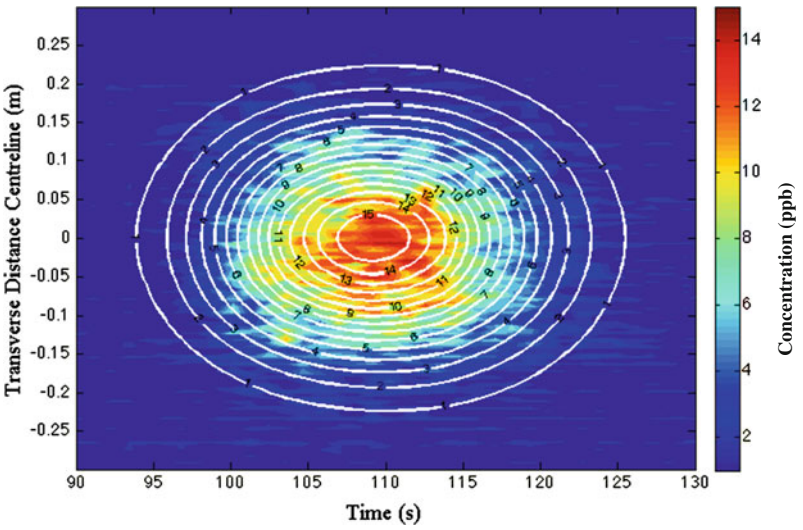

Fig. 8 2D routing prediction overlaid onto the downstream measured 2D concentration distribution

An example routing optimization is shown in Fig. 8. The downstream measured profile is compared to the prediction (solid white lines in Fig. 8) made by routing the upstream measurement to that downstream.

4 Discussion

The optimization procedure assumes a spatially constant value of longitudinal dispersion and transverse mixing coefficient as well as mean longitudinal and transverse velocities. This is assumed to be a valid assumption for the present spatially homogeneous, fully vegetated test case. Figure 8 shows a successful fit between routed prediction and downstream observation. The approximate spread of the trace, in both y and t, is predicted. Further, the prediction is made from only one pulse measurement; predictions made using the average distribution of all 10× repeats will provide a stronger fit. The 2D routing procedure is successful. Table 1 presents the optimized parameters from the 2D routing procedure. The average, depth mean velocity for each discharge case is compared to that predicted from profile travel time using the routing procedure. The measured and predicted velocities are comparable. However, velocity predicted based on the profile travel time over-predicts that measured using UVP. Note that the UVP measurements are the transverse average, depth-mean velocity. Calculating velocity from the mean travel time is more representative of the speed that the tracer experiences. Longitudinal Dispersion Coefficient and Transverse Mixing Coefficient are given

Table 1 Measured UVP velocities and mean optimized parameters for 10× repeats from the two-dimensional LIF

Q (l/s)	u measured (m/s)	u travel time (m/s)	D_x (m^2/s) × 10^{-5} (%)	D_y (m^2/s) × 10^{-5} (%)	Fit (R^2)	D_y (m^2/s) × 10^{-5} Predict Eq. 3
1.8	0.010	0.013 ± 0.00015	8.66 ± 16.7	2.42 ± 7.4	0.90 ± 0.01	0.88
2.4	0.013	0.017 ± 0.00016	17.0 ± 51.3	2.97 ± 18.7	0.84 ± 0.02	1.12
3.6	0.020	0.026 ± 0.00007	19.0 ± 11.1	4.22 ± 2.5	0.91 ± 0.02	1.77

for the three discharges. Longitudinal dispersion becomes more dominant at the higher velocity. The optimized Transverse Mixing Coefficients are compared to prediction made using Eq. 2 (Lightbody and Nepf 2006). Predicted values are of the same order of magnitude as the measurements although consistently lower in each case. It is not yet known what the under-prediction is attributed to.

5 Conclusion

Dye tracer studies were conducted in artificial vegetation to develop an accurate fluorometry detection system. In spatially heterogeneous vegetated wetlands, the mixing properties vary with location within the flow. It is therefore a necessity that any fluorometry detection has the ability to record at a range of channel locations. Employing a number of point detection fluorometers is inappropriate; resulting in unwanted flow deviation and poor spatial resolution.

A two dimensional Laser Induced Fluorometry system was developed and tested on a spatially homogeneous array of emergent cylinders. LIF provides greater spatial resolution and being non-intrusive yields more reliable data. Finally, a two-dimensional routing procedure provides estimates of the mean longitudinal and transverse velocities and the longitudinal dispersion and transverse mixing coefficients by routing the upstream and downstream, two dimensional concentration distributions.

References

Boxall JB (2000) Dispersion of solutes in sinuous open channel flows. PhD thesis, University of Sheffield, UK

Boxall JB, Guymer I (2003) Analysis and prediction of transverse mixing coefficients in natural channels. J Hydraul Eng-ASCE 129(2):129–139

Boxall JB, Guymer I (2007) Longitudinal mixing in meandering channels: new experimental data set and verification of a predictive technique. Water Res 41:341–354

Burba GG, Verma SB, Kim J (1999) Energy fluxes of an open water area in mid-latitude Prairie wetland. Bound Layer Metrol 91:495–504

Deng ZQ, Singh VP, Bengtsson L (2001) Longitudinal dispersion coefficient in straight rivers. J Hydraul Eng-ASCE 127(11):919–927
Dixon K, Florian J (1993) Modeling mobility and effects of contaminants in wetlands. Environ Toxicol Chem 12:2281–2292
Edgar GJ (1990) The influence of plant structure on the species richness, biomass and secondary production of macrofaunal assemblages associated with Western Austrailian seagrass beds, J. Exp Mar Biol Ecol 137:215–240
Fishcer BH (1968) Dispersion Predictions in natural streams, J Saint Eng Div, ASCE 94(5):927–943.
Ghisalberti M, Nepf HM (2002) Mixing layer and coherent structures in vegetated aquatic flow. J Geophys Res 107(C2):1–11
Ghisalberti M, Nepf HM (2004) The limited growth of vegetated shear layers. Water Resour Res 40(7)
Ghisalberti M, Nepf HM (2005) Mass transport in vegetated shear flows. Environ Fluid Mech 5 (6):527–551
Hart JR, Tiev V, Stovin VR, Lacoursiere JO, Guymer I (2014) The effects of vegetation on the hydraulic residence time of stormwater ponds. In: Proceedings of the 19th IAHR-APD congress 2014, Hanoi, Vietnam
Kadlec RH, Knight RL (1996) Treatment wetlands. Lewis Publishers, Boca Raton, FL
Kadlec RH, Wallace SD (2009) Treatment wetlands, 2nd edn. CRC Press
Kashefipour SM, Falconer RA (2002) Longitudinal dispersion coefficients in natural channels. Water Res 36(7):1854–1868
Lightbody AF, Nepf HM (2006) Prediction of near-field shear dispersion in an emergent canopy with heterogeneous morphology. Environ Fluid Mech 6:477–488
Murphy E, Ghisalberti M, Nepf H (2007) Model and laboratory study of dispersion in flows with submerged vegetation. Water Resour Res 43
National Audit Office and Environment Agency (2010) Tackling diffuse water pollution in England (Online)
Nepf HM, Sullivan JA, Zavistoski RA (1997) A model for diffusion within emergent plant canopy. Limnol Oceanogr 42(8):85–95
Nepf HM (1999) Drag, turbulence, and diffusion in flow through emergent vegetation. Water Resour Res 35(3):479–489
Nepf HM, Ghisalberti M, White B, Murphy E (2007) Retention time and dispersion associated with submerged aquatic canopies. Water Resour Res 43(5):1–10
Nepf HM, Vivoni ER (2002) Flow structure in depth-limited, vegetated flow. J Geophys Res 105 (C12):319–327
Nixon S (1980) Between coastal marsh and coastal waters—a review of twenty years of speculation and research on the role of salt marshes in estuarine productivity and water chemistry. Estuarine and Wetland processes, pp 438–525
Rominger JT, Nepf HM (2011) Flow adjustment and interior flow associated with a rectangular porous obstruction. J Fluid Mechanics 680:636–659
Serra T, Fernando HJS, Rodriguez RV (2004) Effects of emergent vegetation on lateral diffusion in wetlands. Water Res 38:139–147
Shucksmith JD, Boxall JB, Guymer I (2011) Determining longitudinal dispersion coefficients for submerged vegetated flow. Water Resour Res 47(10):503–516
Tamura H, Kiya M, Arie M (1980) Vortex shedding from circular cylinder in moderate-Reynolds number shear flows. J Fluid Mech 141:721–735
Taylor DS, Nixon S, Granger S, Buckley B (1995) Nutrient limitation and the eutrophication of coastal lagoons. Mar Ecol Prog Ser 127:235–244
White BL, Nepf HM (2007) A vortex based model of velocity and shear stress in a partially vegetated shallow channel. Water Resour Res 44

Feasibility of the Porous Zone Approach to Modelling Vegetation in CFD

Fred Sonnenwald, Virginia Stovin and Ian Guymer

Abstract Vegetation within stormwater ponds varies seasonly and its presence affects the flow field, which in turn affects the pond's Residence Time Distribution and its effectiveness at pollutant removal. Vegetated flows are complex and, as a result, few suitable tools exist for evaluating realistic stormwater pond designs. Recent research has suggested using a porous zone to represent vegetation within a CFD model, and this paper investigates the feasibility of this approach using ANSYS Fluent. One of the main benefits of using a porous zone is the ability to derive the relevant parameters from the known physical characteristics of stem diameter and porosity using the Ergun equation. A sensitivity analysis on the viscous resistance factor $1/\alpha$ and the inertial resistance factor C_2 has been undertaken by comparing model results to data collected from an experimental vegetated channel. Best fit values of C_2 were obtained for a range of flow conditions including emergent and submerged vegetation. Results show the CFD model to be insensitive to $1/\alpha$ but very sensitive to values of C_2. For submerged vegetation, values of C_2 derived from the Ergun equation are under-predictions of best-fit C_2 values as only the turbulence due to the shear layer is represented. The porous zone approach does not take into account turbulence generated from stem wakes such that no meaningful predictions for emergent vegetation were obtained. C_2 values calculated using a force balance show better agreement with best-fit C_2 values than those derived from the Ergun equation. Manually fixing values of k and ε within the porous zone of the model shows initial promise as a means of taking stem wakes into account.

F. Sonnenwald (✉) · V. Stovin
Department of Civil and Structural Engineering, The University of Sheffield,
Mappin Street, Sheffield S1 3JD, UK
e-mail: f.sonnenwald@sheffield.ac.uk

V. Stovin
e-mail: v.stovin@sheffield.ac.uk

I. Guymer
School of Engineering, University of Warwick, Coventry CV4 7AL, UK
e-mail: i.guymer@warwick.ac.uk

P. Rowiński and A. Marion (eds.), *Hydrodynamic and Mass Transport at Freshwater Aquatic Interfaces*, GeoPlanet: Earth and Planetary Sciences,
DOI 10.1007/978-3-319-27750-9_6

1 Introduction

Stormwater, the run-off from rainfall events, typically carries pollutants that negatively affect the environment. Engineered devices, commonly referred to as SuDS, or Sustainable Drainage Systems, are introduced to detain flows and help remove pollutants, protecting receiving waters. As they are engineered devices, they are designed and implemented with specific goals in mind. However, as semi-natural systems they are complex and in many cases robust tools to assess both their design and performance do not exist.

Stormwater treatment ponds, for example, contain both open water and vegetation in highly asymmetric configurations. Pond performance is typically assumed to depend on the nominal residence time, V/Q, where Q is discharge and V is pond volume (Persson 2000). A Residence Time Distribution (RTD) (Levenspiel 1972), describing the range of times water takes to travel through the pond, can be experimentally determined after construction and better reflects pond performance. An RTD closer to "plug flow", where all water remains in the pond for a similar time (i.e. the nominal residence time), is considered ideal for treatment (Holland et al. 2004).

Natural vegetation, which may vary by season and year, affects the flow field and makes assessing pond performance complex. The nominal residence time does not take vegetation into account and it is impractical to experimentally determine the RTD of every pond repeatedly as the vegetation grows or dies off. A more robust modelling approach capable of assessing pond performance that includes vegetation would therefore be of benefit.

1.1 Modelling Vegetation

Modelling the impacts of vegetation on flow (and thereby mixing) is necessary to robustly estimate residence times. This is a problem not only in stormwater ponds, but also in channels (Souliotis and Prinos 2011; Patil and Singh 2011), wetlands (Kjellin et al. 2007; Huang et al. 2008), and coastal areas (Lightbody and Nepf 2006). There are several parallel tracks of investigation being undertaken to understand and quantify the impacts of vegetation on flow, from the very theoretical (Nepf 1999) drag to more practical engineering approaches (Kadlec 1990).

Most approaches to modelling vegetation consist of estimating a co-efficient of drag, C_D, obtained through experimental and/or theoretical means, e.g. Jadhav and Buchberger (1995), Nepf (1999), Tanino and Nepf (2008). More empirical approaches use Manning's n, e.g. Hoffmann (2004) Wu and He (2009). King et al. (2012) propose a new $k-\varepsilon$ turbulence model for inclusion in a Computational Fluid Dynamics (CFD) model that takes the effects of vegetation into account. Alternatively, Stoesser et al. (2010) directly simulate flow through vegetation stems using Large Eddy Simulation.

1.2 CFD Modelling of Ponds

CFD has become established as a common tool for pond design and evaluation, e.g. Shilton (2000), Peterson et al. (2000), Persson (2005), Shilton et al. (2008), Khan et al. (2012), Alvarado et al. (2013). These studies have typically focused on pond shape or configuration, but have not taken into account the presence of vegetation.

Saggiori (2010), Tsavdaris et al. (2013, 2014) and Li (2014) have modelled vegetated ponds using the commercial CFD code ANSYS Fluent (ANSYS Inc. 2012) by treating vegetated areas as a "Porous Zone". A CFD model solves a discretised form of the Navier-Stokes equations, which balance forces acting on a volume of water. Equation 1 shows the balance of forces acting in the x-direction, assuming a 2-D problem and excluding turbulence (Fluent Inc. 1998), where ρ is density, u is velocity in the x-direction, v is velocity in the y-direction, p is pressure, and τ is shear stress in the subscripted directions.

$$\frac{\partial \rho uu}{\partial x} + \frac{\partial \rho vu}{\partial y} = -\frac{\partial p}{\partial x} + \frac{\partial \tau_{xx}}{\partial x} + \frac{\partial \tau_{xy}}{\partial y} + F_x \tag{1}$$

$$F_x = -\left(\frac{\mu}{\alpha}u + C_2\left(\frac{1}{2}\rho u|u|\right)\right) \tag{2}$$

The effects of the porous zone are included as part of the additional source term F_x, shown in Eq. 2, where μ is the fluid viscosity, $1/\alpha$ is a viscous resistance coefficient (based on Darcy's law), and C_2 is an inertial resistance coefficient. ANSYS suggests that the $1/\alpha$ and C_2 parameters may be calculated using Eqs. 3 and 4 respectively, which are derived from the Ergun equation (Ergun 1952), where d is stem diameter and ϕ is porosity. This paper further investigates the porous zone approach to modelling vegetation in CFD.

$$\alpha = \frac{d^2}{150}\frac{\phi^3}{(1-\phi)^2} \tag{3}$$

$$C_2 = \frac{3.5}{d}\frac{(1-\phi)}{\phi^3} \tag{4}$$

2 Methodology

A preliminary 2D investigation of the porous zone approach to modelling vegetation in CFD has been carried out in 2 stages using ANSYS Fluent 14.5 (the double precision solver). The first stage consists of evaluating the sensitivity of the porous zone parameters ($1/\alpha$ and C_2). The second stage consists of fitting these parameters to different experimental conditions.

Table 1 Outline of measurement sets, Ergun equation derived C_2 values, best fit C_2 values at 29 l s^{-1} flow rate, and C_2 values derived from a force balance

Measurement set	1	2	3	4	5	6	7	8
Age (weeks)	2	5	7	10	16	20	24	26
d (m)	0.010	0.015	0.020	0.030	0.040	0.045	0.050	0.055
ϕ	0.998	0.996	0.992	0.982	0.969	0.960	0.951	0.941
Ergun C_2 (m^{-1})	0.69	1.04	1.41	2.17	3.03	3.49	4.00	4.54
Best fit C_2 (m^{-1})	40.00	3.79	6.84	6.84	6.84	6.84	6.84	6.84
Force C_2 (m^{-1})	5.01	6.10	6.23	6.49	6.27	5.58	7.50	9.18

Experimental data collected by Shucksmith et al. (2010) has been used for validation of the CFD model. They investigated longitudinal dispersion in a vegetated channel, emergent or submerged depending on flow rate. *Carex*, a common aquatic plant, was grown for a period of 26 weeks in a channel 14.48 × 0.6 m. 8 measurement sets (outlined in Table 1) were collected over this period as the vegetation grew, each consisting of vertical velocity profiles (at 5.6 m into the vegetation) and 5 repeat solute transport traces at 5 flow rates ranging between 9.19 and 29.42 l s^{-1}. These flow rates correspond to mean velocities of 0.099–0.264 m s^{-1} and stem Reynolds numbers of 1490–7083. The solute was injected onto the surface at the start of the vegetation and the traces were recorded at 3 locations within and above the vegetation at 7.36, 9.80, and 12.24 m downstream using fluorometers.

The CFD model geometry used is a simplified 2D representation of the channel centreline. 15 m of open water was added before the vegetation for flow establishment, the vegetation was changed to a 14.5 m length, and 0.5 m free water was added after the vegetation. The vegetation itself was modelled as a porous zone, with the $1/\alpha$ and C_2 parameters applied in the x-direction only. Boundary conditions were specified as a velocity-inlet, a pressure-outlet, a symmetry boundary (fixed-lid approximation) at the surface, and a channel bed roughness height of 7e-4 m (representative of gravel).

A mesh independence study showed that a rectangular mesh with a cell size of 14.625 mm was a good balance of mesh independence, number of cells, and the log-law boundary layer treatment requirement of $30 < y^+ < 300$. According to the results of a discretisation settings and turbulence model sensitivity study, second order spatial discretisation, the PRESTO! pressure discretisation formulation (an interpolation scheme to calculate pressure on cell faces), the Standard Wall Functions (a log-law viscous sub-layer approximation), and the Realisable $k - \varepsilon$ turbulence model have been used. The inlet and outlet turbulence boundary conditions have been specified as a turbulent intensity of 5 % and a turbulent length scale equivalent to the water depth. All models were run for sufficient iterations for their residuals to stabilise, indicating model convergence. The SIMPLE pressure-velocity coupling was used (an uncoupled solver).

Particle tracking was used to generate solute trace data comparable to the experimental dye injections. This approach has previously compared favourably with experimental results, e.g. Stovin et al. (2008). 40,000 neutrally buoyant particles were injected just below the surface at the start of the vegetation and tracked using the Discrete Random Walk Model until leaving the outlet. As the particles crossed the three monitoring planes, the times at which they crossed and whether they crossed in the vegetation or water was recorded.

2.1 Sensitivity of $1/\alpha$ and C_2

A sensitivity analysis was carried out to explore the impact of the porous zone parameters $1/\alpha$ and C_2 on the modelled solute transport in the vegetated channel. Logarithmically spaced values were used: $1/\alpha$ = 0.60, 3.11, 16.10, 83.40, 431.80, 2236.60, 11584.20, and 60000 m^{-2}; and C_2 = 0.20, 0.54, 1.44, 3.86, 10.34, 27.79, 74.55, and 200 m^{-1}. The 64 combinations of these values are representative of d from 1 to 50 mm and ϕ from 0.900 to 0.999. The CFD model was configured to represent measurement set 3 with a 28.66 l s^{-1} flow rate, for a flow depth of 0.234 m, a vegetation depth of 0.160 m, and a mean velocity of 0.204 m s^{-1}. Measured values of $d = 0.02$ m and $\phi = 0.992$, give $1/\alpha = 24.6$ m^{-2} and $C_2 =$ 1.41 m^{-1}.

To compare the CFD solute traces with the experimental data, the latter has been pre-processed to subtract background concentration using a linear approximation based on the first and last 5 s of data. As the laboratory calibration data could not be found, the experimental traces were scaled according to the mass-balance of their CFD counterparts, assuming 100 % conservation of mass. The start times of the experimental data were unavailable and so were approximated based on the CFD results.

2.2 Porous Zone Parameter Fitting

Best fit porous zone model parameters for the experimental results have been generated. CFD models for all 8 vegetation measurement sets at all 5 flow rates (covering emergent and submerged vegetation) have been created. Results to be discussed show that the porous zone model in the scenarios examined is primarily sensitive to values of C_2 and so $1/\alpha$ has been fixed at a value of 1. Based on those same results, the range of values of C_2 was modified so that 10 values of C_2 = 0.20, 0.36, 0.65, 1.17, 2.11, 3.79, 6.84, 12.32, 22.20, 40.00 m^{-1} have been used. For each configuration, the solute traces generated using particle tracking have been compared to their corresponding experimental solute traces. This comparison was carried out using the R^2 correlation measure (Eq. 5, Nash and Sutcliffe 1970) after

aligning the centroids of the traces. The value of C_2 with the highest R^2 is assumed to best represent the experimental data as R^2 values close to 1.0 indicate a better fit, while values below 0 indicate no fit.

$$R^2 = 1 - \frac{\sum_{i=1}^{N} (C_i - \hat{C}_i)^2}{\sum_{i=1}^{N} (C_i - \bar{C}_i)^2} \tag{5}$$

3 Results and Discussion

8 values of $1/\alpha$ and 8 values of C_2 were used in 64 combinations to evaluate CFD model sensitivity to the porous zone parameters. A subset of these is presented in Fig. 1, which shows CFD model particle tracking solute traces recorded in the open water above the vegetation compared to the experimental results. The traces are significantly less sensitive to the $1/\alpha$ parameter than to C_2. Considering Eq. 2, the viscous ($1/\alpha$) term is several orders of magnitude lower than the inertial (C_2) term for most combinations of $1/\alpha$ and C_2. However, as velocity approaches zero, the viscous term becomes more significant. Therefore, the insensitivity of the model to $1/\alpha$ may need to be revisited at lower velocities.

The model predictions are very sensitive to the C_2 parameter. Visual inspection suggests that $C_2 = 3.86\ \mathrm{m}^{-1}$ produces a much better fit to experimental data than $C_2 = 1.44\ \mathrm{m}^{-1}$ (comparable to the value of $1.41\ \mathrm{m}^{-1}$ derived from the Ergun equation for this experimental configuration). Even small errors in estimating d or ϕ can therefore significantly influence the model. Given the inherent variability in

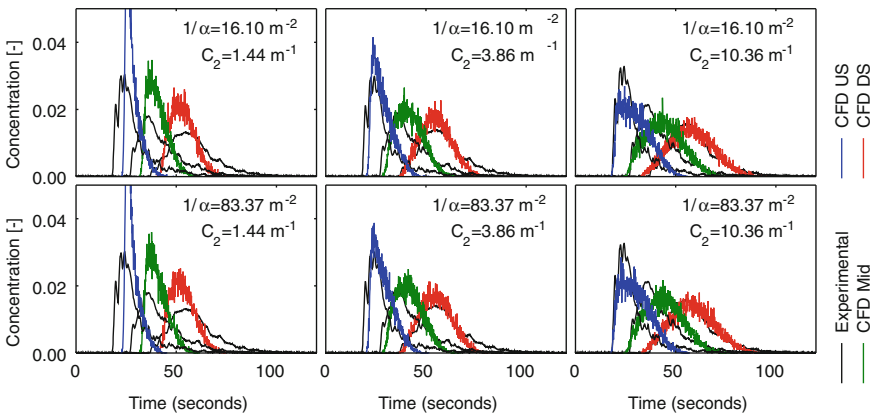

Fig. 1 Particle tracking solute traces recorded at 7.36 (*US*), 9.80 (*Mid*) and 12.24 m (*DS*) within the open water above the vegetation compared to experimental solute traces, showing variation in the CFD model with $1/\alpha$ and C_2 (measurement set 3 at 28.66 l s^{-1})

measuring vegetation, this suggests that using the Ergun equation to estimate $1/\alpha$ and C_2 may not be robust.

Equation 6 is the standard stem drag formula, where a is frontal area. It is similar to the inertial loss term of Eq. 2. This, combined with the sensitivity analysis presented above, suggests that the viscous loss term can be ignored, while maintaining the relevant model physics. This assumption allows the second stage of investigation to focus solely on C_2.

$$F_x = -\left(\frac{1}{2} C_D a \rho u^2\right) \tag{6}$$

3.1 The Porous Zone Problem

A CFD model has been created with constant $1/\alpha = 1\ \mathrm{m}^{-2}$ for each combination of 8 measurement sets, 5 flow rates, and 10 values of C_2, giving 400 models in total. Not all of these models ran as expected. Figure 2 shows an example of poor model prediction, where the CFD generated solute traces indicate plug flow. This is clearly not the case in the experimental results. The unexpected plug flow traces occur in all cases when the vegetation is emergent or only just submerged—only the fully submerged cases produce reasonable results. In all cases the velocity profiles match the experimental data. However, it is evident that turbulence, which influences the particle tracking (i.e. mixing), is not being properly modelled within the vegetation.

Turbulence around vegetation can be thought of as being primarily generated by two mechanisms. When vegetation is submerged, water travels slower in the vegetation than the water above it due to resistance and as a result of this differential in velocity a shear layer forms, expressed as an asymptote in a velocity profile. This shear layer generates turbulence. Within the vegetation, the mean flow velocity is fairly uniform due to the drag of the stems acting on the water passing them. Although there is no velocity differential and no shear layer, turbulence is still generated as a result of the wake effect of water passing the stems.

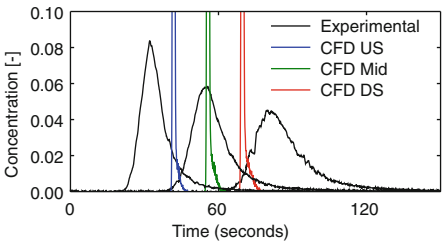

Fig. 2 Emergent vegetation particle tracking solute traces recorded at 7.36 (*US*), 9.80 (*Mid*) and 12.24 m (*DS*) compared to experimental solute traces for $C_2 = 1.71$ (measurement set 3 at 10.19 l s^{-1})

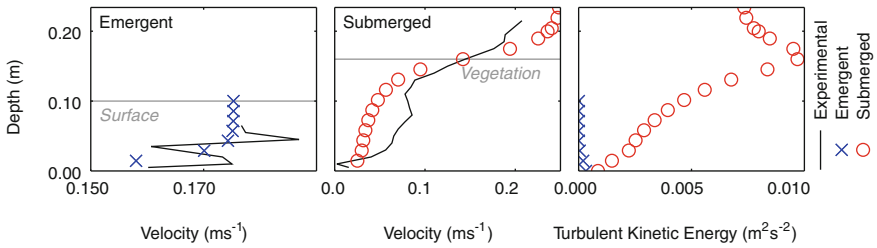

Fig. 3 Velocity and turbulent kinetic energy for emergent vegetation and submerged vegetation (measurement set 3 at 10.19 and 28.66 l s^{-1} respectively)

When representing submerged vegetation via a porous zone, the flow is slowed in the porous zone and a shear layer forms at the porous zone/open water interface as a result of the velocity differential. However, nothing within the CFD model generates the within-vegetation wake effect, i.e. there is no source of turbulence within the porous zone. As such no mixing can take place when the vegetation is emergent, as observed. It is clear that the default porous media approach to vegetation modelling is inappropriate for reproducing mixing effects. Despite this, the CFD model appears to function well in the submerged vegetation cases when there is a sufficient depth of water above the vegetation for the shear layer to fully form, suggesting the mixing caused by a shear layer dominates.

Figure 3 compares velocity and turbulent kinetic energy profiles for emergent and submerged vegetation, clearly showing the lack of turbulence within the emergent vegetation model. The experimental velocity profiles have been scaled according to the ratio of their area-weighted average to the mean velocity (Saggiori 2010) to account for an experimental mass-balance error believed to be due to the existence of a preferential flow path around the vegetation at the side of the channel. This preferential path is also may account for some of the differences between the CFD generated and the experimental solute traces.

3.2 *Best Fit Values of C_2 for Submerged Vegetation*

As previously mentioned, the predicted solute traces for the submerged cases closely match the experimental data. Figure 4 shows a subset of the submerged vegetation particle tracking data within the vegetation for measurement set 6 at 28.74 l s^{-1} flow. Visual inspection indicates that the best fit C_2 value is in the range of 6.84–12.32 for this experimental trial. Figure 5 shows the range of best fit C_2 values determined by R^2 value at the maximum flow rate (25.22–29.42 l s^{-1}) for each dye injection trial at each measuring point. There is some variation within each measurement set, although for sets 3–8 the median values are consistently 6.84. The higher values for measurement set 1 may correspond to stiffer vegetation, causing increased mixing.

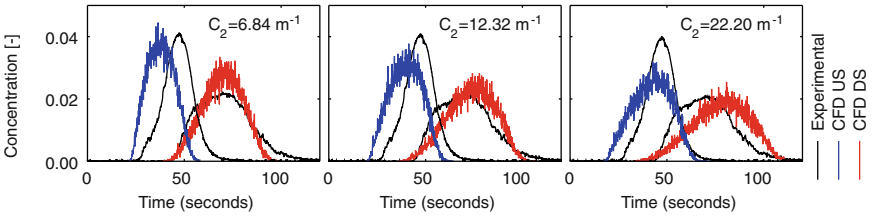

Fig. 4 Particle tracking solute traces recorded at 7.36 (*US*) and 12.24 m (*DS*) within the the vegetation compared to experimental solute traces, showing variation in the CFD model with C_2 (measurement set 6 at 28.74 l s^{-1})

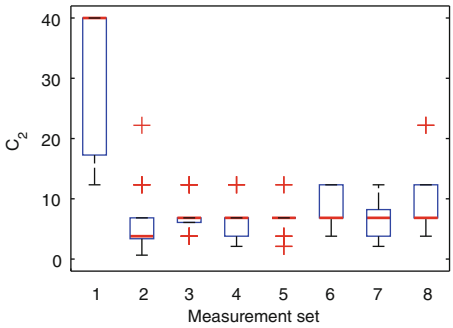

Fig. 5 A box plot comparing best fit C_2 values at the 29 l s^{-1} flow rate across measurement set for each possible R^2 comparison between CFD and experimental solute traces, where the thick line is the median, the box shows the 25th–75th percentile, the whiskers $\pm 2.7\sigma$, and the pluses values that fall outside the range of the whiskers

Table 1 shows the C_2 values for each measurement set derived from Eq. 4. The calculated values consistently under-estimate the best-fit values. This may be in part due to the latter compensating for the lack of stem eddy mixing by artificially increasing the shear layer mixing. In turn the flow field will be affected, under-estimating flow in the vegetation and over-estimating it in the canopy, as seen in Fig. 3. The under-estimate also potentially indicates the Ergun equation is unsuitable for this application.

Tsavdaris et al. (2013) used the porous zone approach to model the hydraulic effects of vegetation in a channel, but noted that it could not be used to predict turbulence. Without taking into account the turbulent effects of the vegetation stems, no CFD model utilising a porous zone will produce an accurate description of the treatment capability of a pond (e.g. an accurate RTD). Despite this, Tsavdaris et al. (2014) used the porous zone approach to evaluate various pond designs, including those with emergent vegetation. They note increased turbulence around vegetation, which is the result of a porous zone interface, but their models do not account for turbulence within the vegetation. Their conclusions on large scale

hydraulics do not appear to be directly affected by this, but their discussion implies a level of functionality of porous zone modelling that is not the case.

3.3 The Porous Zone Solution?

Two problems have been identified with using porous zones. The first problem is the potential unreliability in estimating C_2. The second is the lack of turbulence generation within the porous zone to represent stem wake effects within vegetation. It is possible that relationship between C_2 and C_D could be developed (Zinke 2010; King et al. 2012). Equation 7 provides an estimate of C_2 by balancing of gravity forces and drag forces, where g is the acceleration due to gravity, S is channel slope, and h is flow depth. Table 1 shows C_2 values derived with this equation, which provide reasonable agreement with the best fit values.

$$C_2 = \frac{2gS}{u^2 h} \tag{7}$$

It is possible to simulate additional turbulence within the vegetation. ANSYS Fluent allows the k and ε values of a porous zone to be manually set. Assuming that the vegetation is uniform and that the velocity distribution over the depth of the vegetation is uniform (two assumptions made for the application of the porous zone), the mixing effects of the stem wakes could be reproduced by choosing the correct k and ε values. Figure 6 shows CFD generated solute traces corresponding to $k = 0.005$ and $\varepsilon = 0.0003$ for the same experimental configuration as Fig. 2, and shows more reasonable agreement with the experimental solute traces. These initial results are promising, but there are questions to be answered and potential limitations.

k and ε are complex parameters and suitable values should ideally be derived from the physical characteristics of the vegetation. The new $k - \varepsilon$ model proposed by King et al. (2012) for vegetation may offer insight into how k and ε values may

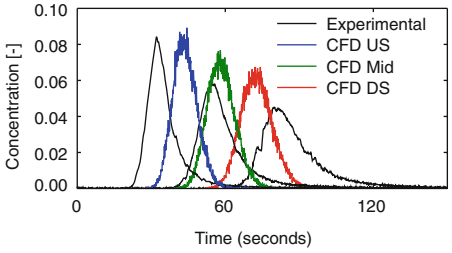

Fig. 6 Particle tracking solute traces recorded at 7.36 (*US*), 9.80 (*Mid*) and 12.24 m (*DS*) within the vegetation compared to experimental solute traces for $C_2 = 1.71$ with fixed $k = 0.005$ and $\varepsilon = 0.0003$ (measurement set 3 at 10.19 l s^{-1}, emergent vegetation)

be determined empirically. Their results suggest this may be possible down to Reynolds number as low as 36. However, further work is required to implement and evaluate this approach.

4 Conclusions

This study showed CFD models of vegetation using a porous zone were insensitive to $1/\alpha$, but very sensitive to C_2. The porous zone approach could not reproduce solute transport data with emergent vegetation. This is attributed to the lack of a source of turbulence within the CFD model equivalent to that generated by stem wakes. As such, the default approach to modelling vegetation with a porous zone is inappropriate for reproducing mixing effects.

Best fit C_2 values for submerged vegetation show that C_2 values derived from the Ergun equation are under-estimates, and therefore the Ergun equation may not be an appropriate means of estimating porous zone parameters. The higher best fit values may be compensating for the missing mixing effects of the vegetation stems. Better estimates of C_2 may possibly be obtained by treating it similarly to a drag coefficient, i.e. C_D, and using a force balance to estimate it from experimental data. Values obtained using this approach show better agreement with the best fit values, although such an approach still fails to represent the within-vegetation generation of turbulence.

To better represent vegetation, the porous zone can be configured with fixed k and ε values, simulating the additional turbulence caused by stem wakes. This shows promising initial results and it may be possible to estimate suitable values based on vegetation characteristics. Therefore, although at present care must be taken when using the porous zone approach to modelling vegetation in CFD as it only reproduces the flow field, it may be feasible to use it to accurately represent the effects of vegetation on mixing in the future.

Acknowledgments This research was funded by EPSRC grants EP/K024442/1 and EP/K025589/1. The authors are grateful to Dr. James Shucksmith for access to the experimental data used in this research.

References

Alvarado A, Vesvikar M, Cisneros JF, Maere T, Goethals P, Nopens I (2013) CFD study to determine the optimal configuration of aerators in a full-scale waste stabilization pond. Water Res 47(13):4528–4537

ANSYS Inc (2012) ANSYS Fluent 14.5. Cecil Township, PA

Ergun S (1952) Fluid flow through packed columns. Chem Eng Prog 48:89–94

Hoffmann MR (2004) Application of a simple space-time averaged porous media model to flow in densely vegetated channels. J Porous Media 7(3)

Holland JF, Martin JF, Granata T, Bouchard V, Quigley M, Brown L (2004) Effects of wetland depth and flow rate on residence time distribution characteristics. Ecol Eng 23(3):189–203
Huang YH, Saiers JE, Harvey JW, Noe GB, Mylon S (2008) Advection, dispersion, and filtration of fine particles within emergent vegetation of the florida everglades. Water Resour Res 44(4)
Fluent Inc (1998) FLUENT 5 user's guide, vol I. Lebanon, NH
Jadhav RS, Buchberger SG (1995) Effects of vegetation on flow through free water surface wetlands. Ecol Eng 5(4):481–496
Kadlec RH (1990) Overland flow in wetlands: vegetation resistance. J Hydraul Eng 116(5):691–706
Khan S, Melville BW, Shamseldin AY, Fischer C (2012) Investigation of flow patterns in storm water retention ponds using CFD. J Environ Eng 139(1):61–69
King A, Tinoco R, Cowen E (2012) A k–ε turbulencemodel based on the scales of vertical shear and stem wakes valid for emergent and submerged vegetated flows. J Fluid Mech 701:1–39
Kjellin J, Wörman A, Johansson H, Lindahl A (2007) Controlling factors for water residence time and flow patterns in Ekeby treatment wetland Sweden. Adv Water Resour 30(4):838–850
Levenspiel O (1972) Chemical reaction engineering. Wiley
Li Q (2014) Effects of vegetation on pond residence time distributions using CFD modelling Master's thesis, University of Sheffield
Lightbody AF, Nepf HM (2006) Prediction of velocity profiles and longitudinal dispersion in emergent salt marsh vegetation. Limnol Oceanogr 51(1):218–228
Nash JE, Sutcliffe JV (1970) River flow forecasting through conceptual models part I – A discussion of principles. J Hydrol 10(3):282–290
Nepf H (1999) Drag, turbulence, and diffusion in flow through emergent vegetation. Water Resour Res 35(2):479–489
Patil S, Singh V (2011) Dispersion model for varying vertical shear in vegetated channels. J Hydraul Eng 137(10):1293–1297
Persson J (2000) The hydraulic performance of ponds of various layouts. Urban Water 2(3):243–250
Persson J (2005) The use of design elements in wetlands. Nord Hydrol 36(2):113–120
Peterson EL, Harris JA, Wadhwa LC (2000) CFD modelling pond dynamic processes. Aquacult Eng 23(1):61–93
Saggiori S (2010) CFD modelling of solute transport in vegetated flow. Master's thesis, University of Sheffield
Shilton A (2000) Potential application of computational fluid dynamics to pond design. Water Sci Technol 42(10):327–334
Shilton A, Kreegher S, Grigg N (2008) Comparison of computation fluid dynamics simulation against tracer data from a scale model and full-sized waste stabilization pond. J Environ Eng 134(10):845–850
Shucksmith J, Boxall J, Guymer I (2010) Effects of emergent and submerged natural vegetation on longitudinal mixing in open channel flow. Water Resour Res 46(4)
Souliotis D, Prinos P (2011) Effect of a vegetation patch on turbulent channel flow. J Hydraul Res 49(2):157–167
Stoesser T, Kim S, Diplas P (2010) Turbulent flow through idealized emergent vegetation. J Hydraul Eng 136(12):1003–1017
Stovin VR, Grimm JP, Lau STD (2008) Solute transport modeling for urban drainage structures. J Environ Eng 134(8):640–650
Tanino Y, Nepf HM (2008) Lateral dispersion in random cylinder arrays at high reynolds number. J Fluid Mech 600:339–371
Tsavdaris A, Mitchell S, Williams B (2013) Use of CFD to model emergent vegetation in detention ponds. ARPN J Eng Appl Sci 8(7):495–503

Tsavdaris A, Mitchell S, Williams JB (2014) Computational fluid dynamics modelling of different detention pond configurations in the interest of sustainable flow regimes and gravity sedimentation potential. Water Environ J

Wu W, He Z (2009) Effects of vegetation on flow conveyance and sediment transport capacity. Int J Sedim Res 24(3):247–259

Zinke P (2010) Flow resistance parameters for natural emergent vegetation derived from a porous media model. In: Proceedings of RiverFlow 2010

A Comparison of Three Solute Transport Models Using Mountain Stream Tracer Experiments

J. Russell Manson, Steve G. Wallis, Benoit O.L. Demars, John D. Mick, Gisli M. Gíslason, Jon S. Ólafsson and Nikolai Friberg

Abstract Stream ecology may be influenced by the temporary trapping of solutes in geomorphologic structures, which is usually quantified by fitting the Transient Storage Model to tracer data. This paper explores the relationships between the parameters of this model and those of two simpler models, namely the Advection-Dispersion Model and the Aggregated Dead Zone model. It is motivated by the possibility of obtaining more reliable transient storage parameter values by correlating them with the parameters of the other models instead of evaluating them directly. Results were obtained by fitting all three models to a set of tracer data from mountain streams, predominantly in Iceland. Some strong correlations were found between some of the parameters of the transient storage model and the advection-dispersion model, but no strong correlations were found between the parameters of the transient storage model and the aggregated dead zone model. For all three models, combinations of the optimized parameters correctly described the bulk movement of the solute cloud, giving confidence in the optimized parameters.

J.R. Manson (✉)
Richard Stockton College, Atlantic, NJ, USA
e-mail: Russell.Manson@stockton.edu

S.G. Wallis
Heriot-Watt University, Edinburgh, UK

B.O.L. Demars
James Hutton Institute, Aberdeen, UK

J.D. Mick
General Dynamics Information Technology, Panama, NJ, USA

G.M. Gíslason
University of Iceland, Reykjavik, Iceland

J.S. Ólafsson
Inst. of Freshwater Fisheries, Reykjavik, Iceland

N. Friberg
Norwegian Institute for Water Research, Oslo, Norway

P. Rowiński and A. Marion (eds.), *Hydrodynamic and Mass Transport at Freshwater Aquatic Interfaces*, GeoPlanet: Earth and Planetary Sciences,
DOI 10.1007/978-3-319-27750-9_7

1 Introduction

In this paper we compare three models of solute transport for mountain streams. We examine the models' effectiveness at describing the transport of a tracer through many stream reaches and, by fitting them to tracer data, elucidate meaningful parameters that describe the streams physically. The work is part of a larger study investigating the effect of temperature and water transient storage on stream metabolism and nutrient cycling (Friberg et al. 2009; Woodward et al. 2010; Demars et al.2011a, b; Gudmundsdottir et al. 2011; Manson et al. 2011; Rasmussen et al. 2011; O'Gorman et al. 2012; Hannesdottir et al. 2013). Information from 66 tracer experiments executed in several geothermal areas in Iceland (Hengill, Hveragerdi, Hveravellir, Kerlingarfjöll, Torfajökull and Vonarskard) was combined into a single data-set. Four additional experiments from similar geothermal and climatic sites in Kamchatka, Russia, were also used (O'Gorman et al. 2014).

In much previous work the so-called Transient Storage Model (e.g. Bencala and Walters 1983) has been fitted to tracer data in order to evaluate the parameters that quantify the transient storage process. Although good fits to the data are often achieved, questions have been raised over how well the parameters can be identified (e.g. Wagner and Harvey 1997; Wagener et al. 2002; Worman and Wachniew 2007). Here we are motivated by the possibility of obtaining the parameters from correlations with the parameters of alternative models. Hence we seek to explore relationships between the parameters of the Transient Storage Model, the Advection Dispersion Model and the Aggregated Dead Zone Model.

2 Solute Transport Models

This section provides background information on the three models used, namely the Advection-Dispersion Model, the Transient Storage Model and the Aggregated Dead Zone Model.

2.1 The Advection-Dispersion Model (ADM)

In the ADM, advection refers to the movement of a solute caused by the longitudinal velocity of flow and dispersion refers to the longitudinal spreading of solute that takes place simultaneously with the advection. The advection is characterised by the cross-sectional average longitudinal flow velocity. In reality, solute is carried faster than the average velocity in the deeper parts of a river cross-section and is carried slower than the average velocity in the shallower parts of a river cross-section. The longitudinal spreading is caused by the interaction between this cross-sectional variation in longitudinal advection and mechanisms causing

cross-sectional mixing, which also vary throughout the cross-section. In the model, turbulent diffusion and secondary currents are responsible for the cross-sectional mixing. The overall spreading effect is quantified by the dispersion coefficient and the process is often termed shear flow dispersion. Once a solute cloud has been evolving for long enough in a steady, longitudinally uniform, turbulent flow field Taylor (1954) showed that the ADM applies to the cross-sectional average concentration of a conservative solute and that the magnitude of the dispersion coefficient is controlled by the details of the velocity and mixing fields. His model (originally derived for flows in pipes) is described by the following equation:

$$\frac{\partial c(x,t)}{\partial t} + U_{AD}\frac{\partial c(x,t)}{\partial x} = D_{AD}\frac{\partial^2 c(x,t)}{\partial x^2} \tag{1}$$

where c is the cross-sectional average solute concentration, U_{AD} is the cross-sectional average longitudinal flow velocity, D_{AD} is the dispersion coefficient, t is time and x is the longitudinal co-ordinate direction.

Fischer (1967) showed that since rivers have large aspects ratios the transverse variations in longitudinal velocity and cross-sectional mixing are much more important than the corresponding vertical variations. Consequently much use is made of vertically averaged flow and mixing parameters when dispersion coefficients in rivers are estimated from flow and mixing parameters, see e.g. Rutherford (1994); Wallis and Manson (2004). An advantage of the ADM is access to easily applied analytical solutions of Eq. (1). On the other hand these solutions do not always fit observations well.

2.2 The Transient Storage Model (TSM)

The TSM is an extended version of the ADM, and its origins can be traced back over about 50 years. The earliest need to modify the ADM stemmed from work in pipes and channels which suggested that the storage and slow release of solute by laminar boundary layers might explain some discrepancies between observations and model predictions (Taylor 1954; Elder 1959). In rivers a similar mechanism was attributed to dead zones which were originally associated with "pools and stagnant areas, or both, cause by debris or unevenness of the banks or bottom" (Thackston and Krenkel 1967). Further evidence from rivers, see e.g. Nordin and Sabol (1974) and Day (1975), suggested that observed concentration-time profiles were not predicted well by the ADM. More recently, several other geomorphologic features, such as pool-riffle structures (e.g. Bencala and Walters 1983) and interactions between a river channel and the surrounding hyporheic zone (e.g. Elliott and Brooks 1997) have been added to dead zones, and the term transient storage is now often used to describe the effects of a range of storage phenomena on solute transport in rivers (Worman 2000; Wallis et al. 2013).

The TSM is described by two equations, one representing solute transport in the main river channel, including advection, dispersion and the effect of the storage zones, and the other representing a dynamic mass balance of solute in the storage zones themselves. In these equations a first-order exchange mechanism is used to describe the transport of solute between the main channel and the storage zones (and back again) and the solute is assumed to behave conservatively. Several slightly different formulations of the equations have appeared in the literature since their first appearance (Thackston and Krenkel 1967), see e.g. Bencala and Walters (1983), Rutherford (1994), Worman (2000), Deng et al. (2010), Bottacin-Busolin et al. (2011) and Wallis et al. (2013). These reflect various issues such as the choice of geometric variables used, the inclusion of lateral inflow, the interpretation of the transient storage process(es) and the presence of variable time scales over which the transient storage takes place. The model equations used in this work, assuming steady and longitudinally uniform flow, are:

$$\frac{\partial c(x,t)}{\partial t} + U_{TS}\frac{\partial c(x,t)}{\partial x} = D_{TS}\frac{\partial^2 c(x,t)}{\partial x^2} + k_1(s(x,t) - c(x,t)) \tag{2}$$

$$\frac{\partial s(x,t)}{\partial t} = -k_2(s(x,t) - c(x,t)) \tag{3}$$

where U_{TS} is the cross-sectional average flow velocity in the main channel, D_{TS} is the dispersion coefficient in the main channel, k_1 and k_2 are model parameters (see below), s is the solute concentration in the storage zones and the other symbols are as previously defined. Note that the velocity and dispersion appearing in Eq. (3) are not necessarily the same as the corresponding parameters appearing in Eq. (1).

The model parameters introduced above are defined as:

$$k_1 = \alpha \tag{4}$$

$$k_2 = k_1\frac{A}{A_S} \tag{5}$$

where α is the exchange rate between the main channel and the storage zones, A is the cross-sectional area of the main channel and A_S is the cross-sectional area of the storage zones. The model is often successful in fitting observations, but the interpretation of the transient storage parameters is not straightforward, particularly when different combinations of parameter values yield very similar outputs.

2.3 The Aggregated Dead Zone Model (ADZM)

Similarly to the origins of the TSM, the ADZM was developed because of reported deficiencies of the ADM. In a radical departure from previous work, it was postulated (Beer and Young 1983) that the dispersion occurring in dead zones

dominated the shear flow dispersion. Hence a model could be constructed on the basis of transient storage only. Or more pragmatically, the effects of all dispersive mechanisms in a river reach could be amalgamated and represented by a single effective dead zone. A further radical approach was to formulate the model only in the time domain (by spatial integration of the physical processes). This had several consequences, e.g. a much simpler mass balance equation than either the ADM or TSM and access to powerful model calibration techniques via time-series analysis (Young 1984).

The model resembles simple hydrologic models for flood propagation in rivers, many of which are based on the concept of storage routing (Young and Wallis 1985; Shaw et al. 2011). Importantly, however, the ADZM includes an explicit time delay to cater for the purely advective transport processes. The transport of a conservative solute in steady flow is described by the following equation:

$$\frac{\partial y(t)}{\partial t} = \frac{1}{V}\left[Q_u u(t-\tau) - Q_y y(t)\right] \tag{6}$$

where y(t) and u(t-τ) are the cross-sectional average solute concentrations at the downstream and upstream ends of a river reach, respectively, τ is the time delay, V is the volume of the aggregated dead zone and Q_y and Q_u are, respectively, the flow rates at the downstream and upstream ends of the reach. In practical terms: τ is the minimum reach travel time (time interval between the first arrival of solute at the two ends of the reach); T_{ADZ} (V/Q_y) is the time solute spends in the aggregated dead zone; and the sum of τ and T_{ADZ} is the ADZ travel time. Wallis (1994) showed that ADZ travel time is theoretically equal to the time interval between the centroids of temporal solute concentration profiles at the two ends of a reach.

Several studies have shown that the ADZM is able to reproduce solute transport in rivers very satisfactorily (Wallis et al. 1989; Green et al. 1994; Lees et al. 2000). However, the fact that the model's parameters are not related to the traditional concepts of advection and dispersion may be considered a disadvantage (Rutherford 1994). On the other hand, both the time delay and the residence time for a reach have been found to vary with flow rate in a physically realistic way, both decreasing as flow rate increases (Wallis et al. 1989; Green et al. 1994).

3 Data Collection

For each experiment, YSI-600xlm multiparameter sondes (YSI, Yellow Spring, USA) were placed at two longitudinal stations (typically about 60 m apart) in the study stream and set to record conductivity at a fixed time interval (typically around 2–10 s). Pre-weighed NaCl was fully dissolved in a small amount (typically 2 L) of stream water and then immediately released into the stream at some distance upstream of the upper station. Generally the initial mixing zone was sufficiently long (typically about 10–20 m) for complete cross-sectional mixing to take place

before the upper station. In the shortest reaches, additional deflectors and pools were created upstream of the upper station to increase mixing. Any naturally occurring background conductivity signal was subtracted from the observations prior to the modelling. The flow rates at the stations were evaluated via dilution gauging, and the upstream and downstream temporal conductivity profiles were analysed to elucidate stream transport parameters, as described below. The median (range) stream characteristics were: width 0.9 (0.2–3.6) m, depth 6 (1–23) cm, velocity 15 (1–52) cm s^{-1}, reach length 36 (13–107) m and flow rate 7 (0.2–70) L s^{-1}.

4 Application of Models

Equation (1) and equation system (2/3) were solved using a finite volume approach in space, evaluating the advection term explicitly in time and evaluating the dispersion and transient storage terms implicitly in time. The DISCUS method (Wallis et al. 1998; Manson and Wallis 1999; Manson and Wallis 2000; Manson et al. 2001) was used for the advective terms in Eqs. (1) and (2) and the Crank-Nicolson method (Press et al. 1992) was used for the dispersion terms in Eqs. (1) and (2) and for the transient storage term in Eq. (2). The rationale behind these choices is that both methods are individually well-suited, being unconditionally stable and robust, for those particular terms, respectively. Equations (3) and (6) were solved using the Crank-Nicolson method.

The models were fitted to the observations by parameter optimization, minimising the sum of squared residuals, SSR, by a modified Levenberg-Marquardt algorithm (Press et al. 1992). A Python script was used to undertake the minimisation by calling C code implementations of the three models. Python and C were linked using the BOOST library. Only main channel concentration was used for the fitting because concentrations in the storage zones were not measured. A normalised fitting parameter (NRMSE) was defined for comparing the performance of the models to different data sets, defined by:

$$NRMSE = \frac{1}{\max(C_{OBS})}\left(\frac{SSR}{N}\right)^{0.5} \tag{7}$$

where N is the number of data points and C_{OBS} refers to the observed concentration profile. To aid the identification of the best model for any individual data set, allowing for a penalty for using more parameters than were justified, the Akaike Information Criterion (AIC) was calculated (assuming the Gaussian case) using:

$$AIC = 2k + N\ \ln\left(\frac{SSR}{N}\right) \tag{8}$$

where k is the number of estimated parameters, including the residual error term (Burnham and Anderson 2002). The best model has the smallest AIC. For the TSM α and A_s/A were evaluated from the optimized values of k_1 and k_2 using Eqs. (4) and (5). The effect of lateral inflow was included in the ADM and TSM by adding the term -qc(x,t)/A to the right-hand sides of Eqs. (1) and (2). The lateral inflow rate, q, was known from the upstream and downstream flow rates and A was estimated from the flow rates and the centroid velocity (see Sect. 5).

5 Results and Discussion

All three models were successfully optimized to the great majority of the 70 sets of tracer data. A few cases failed (5 with the ADM, 9 with the TSM, 5 with the ADZM) either due to inherent problems with the data or due to convergence problems during optimization. Results are presented in various ways below. Figure 1 shows the goodness of fit of the successfully optimized models to all the data. The mean goodness of fit for each model across all the data is also shown.

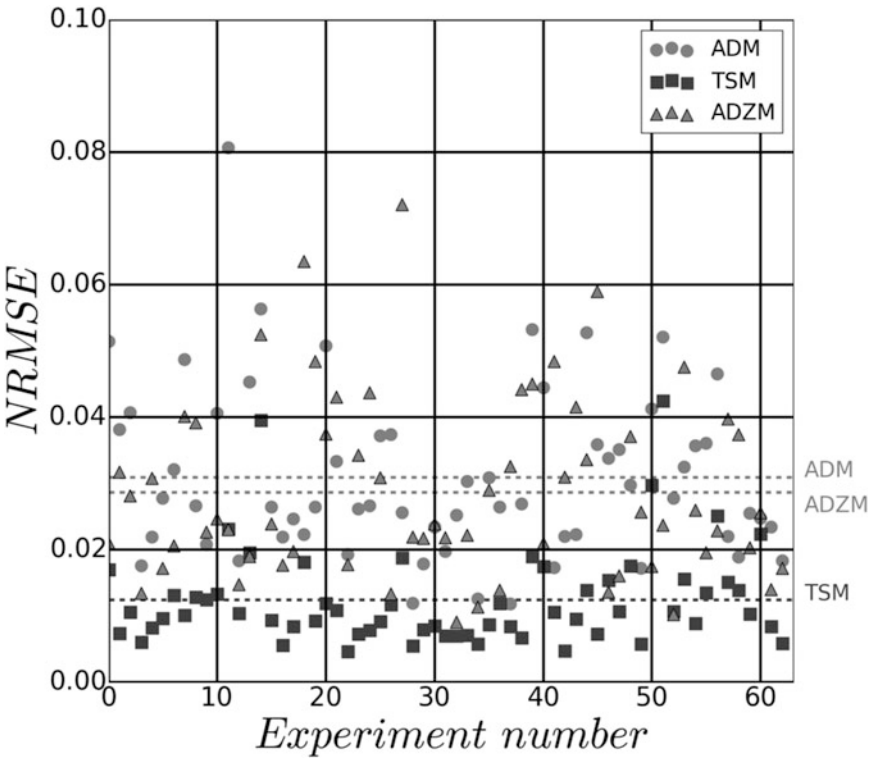

Fig. 1 Comparison of goodness of fit

Although there is a lot of scatter, it is clear that the TSM tends to fit the data best (mean NRMSE of ~ 0.01). The ADE and ADZ models achieve a similar average goodness of fit to each other (mean NRMSEs of ~ 0.03), which is significantly larger than the mean value for the TSM. This is expected because, with 4 parameters, the TSM has a greater ability to represent the finer detail of the solute transport processes than either of the two 2-parameter models. However, it is important to guard against the possibility of over-fitting. Hence values of the AIC were also considered. These showed that in nearly all cases the order of model preference was TSM, ADZM and ADM. In a few cases, corresponding with little transient storage activity, the ADM was preferred to the other two models.

Figure 2 shows correlations between logarithms of the parameters of the TSM and the ADM. Arbitrarily assuming that a correlation coefficient (absolute

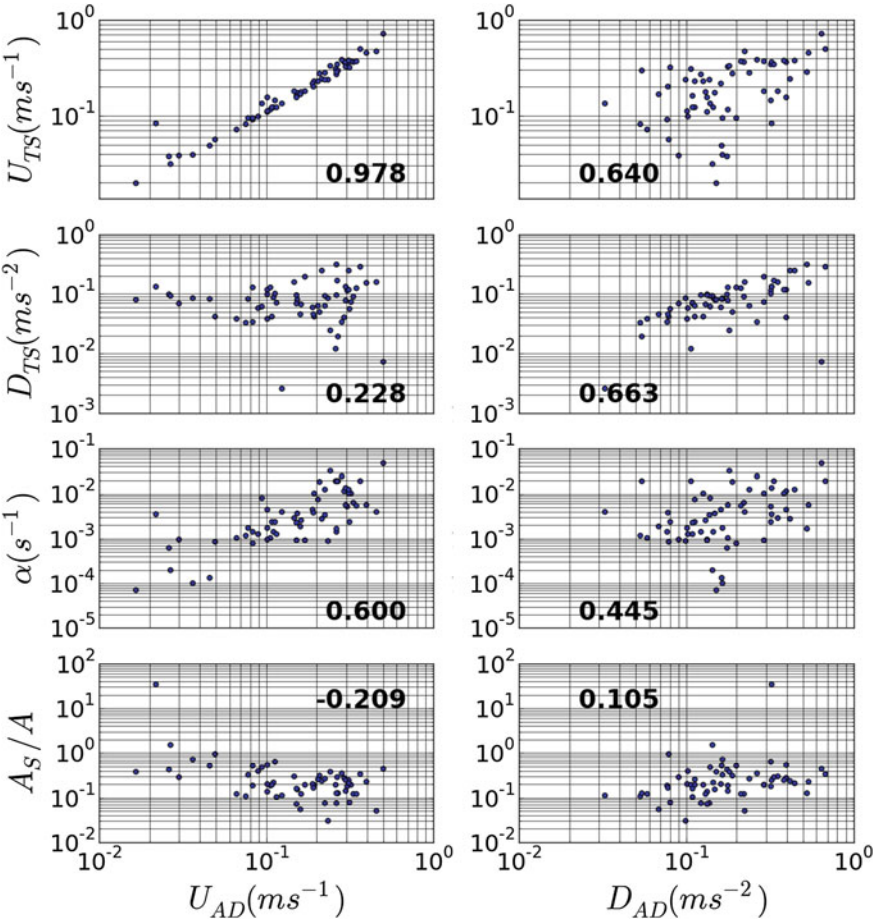

Fig. 2 Comparison of TSM and ADM parameters (with correlation coefficients)

value) > ~ 0.6 indicates a strong correlation, relationships exist between U_{TS} and U_{AD}, α and U_{AD}, U_{TS} and D_{AD}, and D_{TS} and D_{AD}. The correlations between the two velocities and the two dispersion coefficients are expected. In general $U_{TS} > U_{AD}$ because in the ADM the retardation of longitudinal tracer transport due to transient storage can only be accounted for by U_{AD}. Similarly, in general $D_{TS} < D_{AD}$ because in the ADM dispersion caused by transient storage can only be accounted for by D_{AD}. The range of velocity values (0.02–0.5 ms^{-1}) is a consequence of the different slope, roughness and flow rate of the streams, and the range of the dispersion coefficients (0.03–0.7 m^2s^{-1}) is typical for the stream size (Heron 2015).

The correlation between α and U_{AD} is consistent with the idea that the boundary layer across which solute exchange takes place decreases as velocity increases.

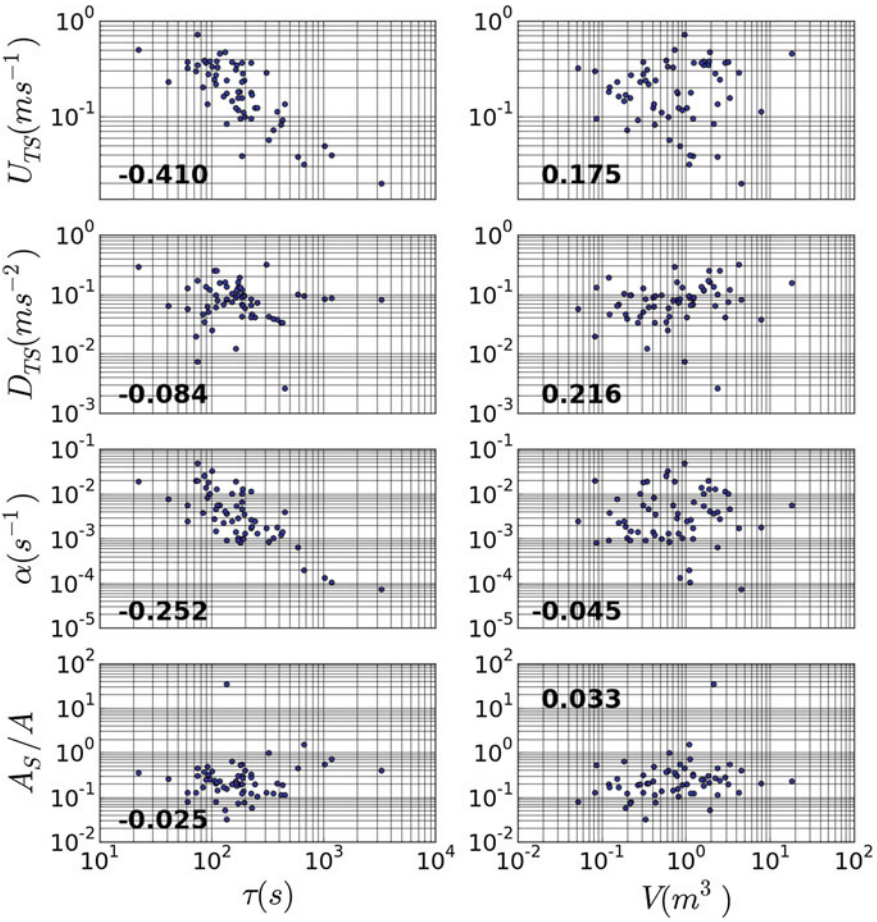

Fig. 3 Comparison of TSM and ADZM parameters (with correlation coefficients)

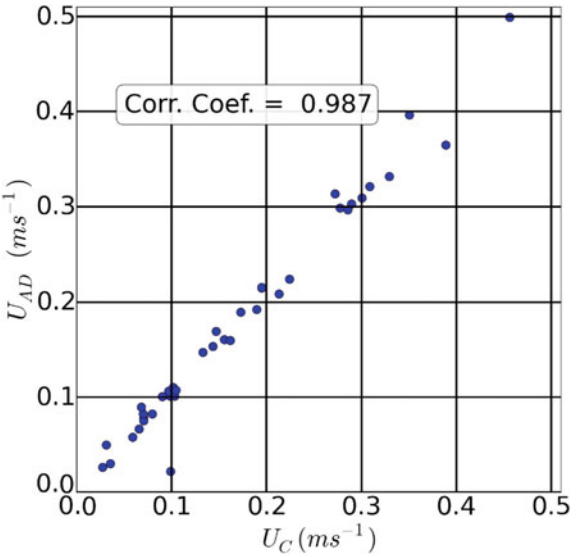

Fig. 4 ADM velocity vs centroid velocity

Although it is interesting that there appears to be a relationship between U_{TS} and D_{AD}, it is of little practical value since U_{TS} is more strongly correlated with U_{AD}. Values of α and A_s/A are typical of those found in previous applications of the TSM to mountain streams, see e.g. D'Angelo et al. (1993) and Gooseff et al. (2003).

Using the same criterion as above for identifying strong correlations, Fig. 3 suggests there are no relationships between the logarithms of the parameters of the TSM and the ADZM. Interestingly, however, two of the largest correlation coefficients are between U_{TS} and τ and α and τ. Since we might expect time delay to be correlated with velocity, these are consistent with the relationships identified from Fig. 2. Finally, it is worth reporting that the range of values of the ratio of residence time to reach mean travel time ($T_{ADZ}/(\tau + T_{ADZ})$), known as the dispersive fraction, (0.1–0.6) is consistent with previous work (Wallis et al. 1989; Green et al. 1994; Guymer 2002).

Figures 4, 5 and 6 compare various advective transport parameters against the movement of the centre of mass of the solute cloud. The latter was evaluated from the centroids of the upstream and downstream temporal tracer concentration profiles, giving estimates of centroid travel time, t_C, and centroid velocity, U_C. Both of these are independent of the ADM, TSM and ADZM. Figure 4 suggests a one-to-one relationship between U_{AD} and U_C, indicating that the ADM correctly describes the bulk transport of the solute cloud. Figure 5 shows a modified TSM velocity plotted against U_C. The modification reduces U_{TS} by an amount that reflects the effect of the transient storage (Czernuszenko and Rowinski 1997; Worman 1998; Lees et al. 2000). The figure suggests that the combination of the optimized TSM parameters correctly describes the bulk transport of the solute cloud. Figure 6 shows the ADZ travel time plotted against t_C. Again the

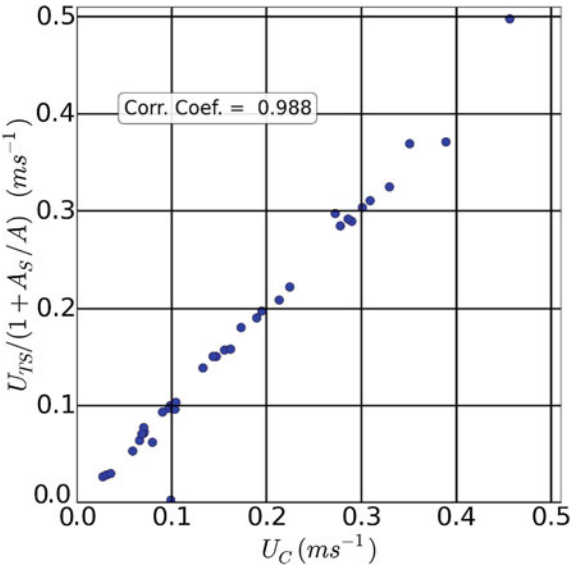

Fig. 5 Modified TSM velocity vs centroid velocity

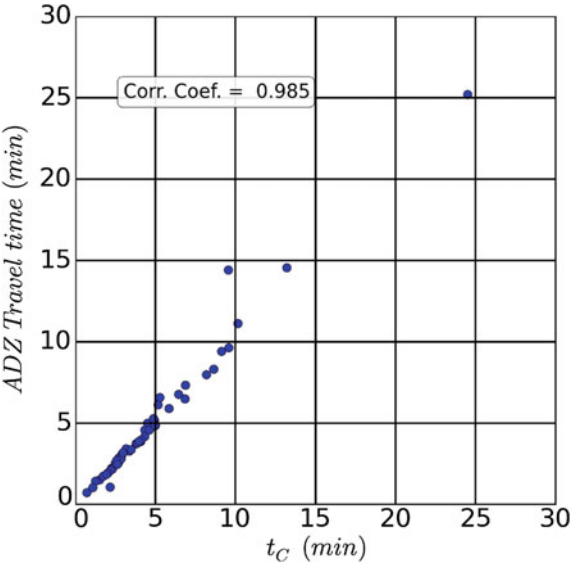

Fig. 6 ADZ travel time vs centroid travel time

combination of the optimized parameters correctly describes the bulk transport of the solute cloud. Overall, the good agreement between these velocities and travel times suggests that the optimized parameter values are robust.

6 Conclusions

Three solute transport models were optimized to a large number of sets of tracer data collected in similar mountain streams. The TSM consistently fitted the tracer data better than either the ADM or the ADZM: the ADZM performed a little better than the ADM. Apparently useful correlations were found between the logarithms of some of the parameters of the TSM and the ADM, but no useful correlations were found between the parameters of the TSM and the ADZM. For all three models, combinations of the optimized parameters correctly described the bulk movement of the solute cloud, giving confidence in the optimized parameters.

References

Beer T, Young PC (1983) Longitudinal dispersion in natural streams. J Env Eng Am Soc Civ Eng 109:1049–1067

Bencala KE, Walters RA (1983) Simulation of solute transport in a mountain pool-and-rifle stream: a transient storage model. Water Resour Res 19:718–724

Bottacin-Busolin A, Marion A, Musner T, Tregnaghi M, Zaramella M (2011) Evidence of distinct contaminant transport patterns in rivers using tracer tests and a multiple domain retention model. Adv Water Resour 34:737–746

Burnham KP, Anderson DR (2002) Model selection and multimodel inference: a practical information-theoretic approach, 2nd edn. Springer

Czernuszenko W, Rowinski PM (1997) Properties of the dead-zone model of longitudinal dispersion in rivers. J Hydraul Res 35:491–504

D'Angelo DJ, Webster JR, Gregory SV, Meyer JL (1993) Transient storage in Appalachian and Cascade mountain streams as related to hydraulic characteristics. J N Am Benthol Soc 12:223–235

Day TJ (1975) Longitudinal dispersion in natural channels. Water Resour Res 11:909–918

Demars BOL, Manson JR, Olafsson JS, Gislason GM, Friberg N (2011a) Stream hydraulics and temperature determine the metabolism of geothermal Icelandic streams. Knowl Manag Aquat Ecosyst 402:05

Demars BOL, Manson JR, Olafsson JS, Gislason GM, Gudmundsdottir R et al (2011b) Temperature and the metabolic balance of streams. Freshwater Biol 56:1106–1121

Deng Z-Q, Jung H-S, Ghimire B (2010) Effect of channel size on solute residence time distributions in rivers. Adv Water Resour 33:1118–1127

Elder JW (1959) The dispersion of marked fluid in turbulent shear flow. J Fluid Mech 5:544–560

Elliott AH, Brooks NH (1997) Transfer of nonsorbing solutes to a streambed with bedforms: theory. Water Resour Res 33:123–136

Fischer HB (1967) The mechanics of dispersion in natural streams. J Hydraul Div Proc Am Soc Civ Eng 93:187–216

Friberg N, Dybkjaer JB, Olafsson JS, Gislason GM, Larsen SE, Lauridsen TL (2009) Relationships between structure and function in streams contrasting in temperature. Freshwater Biol 54:2051–2068

Gooseff MN, Wondzell SM, Haggerty R, Anderson J (2003) Comparing transient storage modeling and residence time distribution (RTD) analysis in geomorphically varied reaches in the Lookout Creek basin, Oregon, USA. Adv Water Resour 26:925–937

Green HM, Beven KJ, Buckley K, Young PC (1994) Pollution prediction with uncertainty. In: Beven K, Chatwin P, Millbank J (eds) Mixing and Transport in the Environment. Wiley, pp 113–137

Gudmundsdottir R, Olafsson JS, Palsson S, Gislason GM, Moss B (2011) How will increased temperature and nutrient enrichment affect primary producers in sub-Arctic streams? Freshwater Biol 56:2045–2058

Guymer I (2002) A national database of travel time, dispersion and methodologies for the protection of river abstractions. Research and Development Technical Report P346, Environmental Agency of England and Wales

Hannesdottir ER, Gislason GM, Olafsson JS, Olafsson OP, O'Gorman EJ (2013) Increased stream productivity with warming supports higher trophic levels. In: Woodward G, O'Gorman EJ (eds) Advances in Ecological Research: Global Change in Multispecies Systems, Pt 3. Academic Press, pp 285–342

Heron AJ (2015) Pollutant transport in rivers: estimating dispersion coefficients from tracer experiments. MPhil Thesis, Heriot-Watt University

Lees MJ, Camacho LA, Chapra S (2000) On the relationship of transient storage and aggregated dead zone models of longitudinal solute transport in streams. Water Resour Res 36:213–224

Manson JR, Wallis SG (1999) A conservative semi-Lagrangian algorithm for solute transport in steady non-uniform flows in rivers. J Env Eng Proc Am Soc Civ Eng 125:486–489

Manson JR, Wallis SG (2000) A conservative semi-Lagrangian fate and transport model for fluvial systems: Part 1 – Theoretical development. Water Res 34:3769–3777

Manson JR, Wallis SG, Hope D (2001) A conservative semi-Lagrangian transport model for rivers with transient storage zones. Water Resour Res 37:3321–3330

Manson JR, Demars BOL, Wallis SG (2011) Integrated experimental and computational hydraulic science in a unique natural laboratory. In: Rowinski P (ed) Experimental and computational solutions of hydraulic problems. Springer, pp 123–131

Nordin CF, Sabol GV (1974) Empirical data on longitudinal dispersion in rivers. US GS Water Resources Investigations 20–74

O'Gorman EJ, Pichler DE, Adams G, Benstead JP, Cohen H, Craig N et al (2012) Impacts of warming on the structure and functioning of aquatic communities: individual to ecosystem level responses. Adv Ecol Res 47:81–176

O'Gorman EJ, Benstead JP, Cross WF, Friberg N, Hood JM, Johnson PW et al (2014) Climate change and geothermal ecosystems: natural laboratories, sentinel systems, and future refugia. Glob Change Biol 20:3291–3299

Press, W.H., Teukolsky, S.A., Vetterling,W.T., and Flannery,B.P. (1992) Numerical recipes in C: the art of scientific computing, 2nd edn. Cambridge University Press

Rasmussen JJ, Baattrup-Pedersen A, Riis T, Friberg N (2011) Stream ecosystem properties and processes along a temperature gradient. Aquat Ecol 45:231–242

Rutherford JC (1994) River Mixing. Wiley

Shaw EM, Beven KJ, Chappell NA, Lamb R (2011) Hydrology in Practice, 4th edn. Spon Press

Taylor GI (1954) The dispersion of matter in turbulent flow through a pipe. Proc R Soc Lond A 233:446–468

Thackston EL, Krenkel PA (1967) Longitudinal mixing in natural streams. J Sanit Eng Div Proc Am Soc Civ Eng 93:67–90

Wagener T, Camacho LA, Wheater HS (2002) Dynamic identifiability analysis of the transient storage model for solute transport in rivers. J Hydroinform 4:199–211

Wagner BJ, Harvey JW (1997) Experimental design for estimating parameters of rate-limited mass transfer: analysis of stream tracer studies. Water Resour Res 33:1731–1741

Wallis SG (1994) Simulation of solute transport in open channel flow. In: Beven K, Chatwin P, Millbank J (eds) Mixing and Transport in the Environment. Wiley, pp 89–111

Wallis SG, Manson JR (2004) Methods for predicting dispersion coefficients in rivers. Proc Inst Civ Eng Water Man 157:131–141

Wallis SG, Young PC, Beven KJ (1989) Experimental investigation of the aggregated dead zone model for longitudinal solute transport in stream channels. Proc Inst Civ Eng 87(2):1–22

Wallis SG, Manson JR, Filippi L (1998) A conservative semi-Lagrangian algorithm for one-dimensional advection-diffusion. Commun Numer Meth Eng 14:671–679

Wallis SG, Osuch M, Manson JR, Romanowicz R, Demars BOL (2013) On the estimation of solute transport parameters for rivers. In: Rowinski P (ed) Experimental and Computational Solutions of Hydraulic Problems. Springer, pp 415–425

Woodward G, Dybkjaer JB, Olafsson JS, Gislason GM, Hannesdottir ER, Friberg N (2010) Sentinel systems on the razor's edge: effects of warming on Arctic geothermal stream ecosystems. Global Change Biol 16:1979–1991

Worman A (1998) Analytical solution and timescale for transport of reacting solutes in rivers and streams. Water Resour Res 34:2703–2716

Worman A (2000) Comparison of models for transient storage of solutes in small streams. Water Resour Res 36:455–468

Worman A, Wachniew P (2007) Reach scale and evaluation methods as limitations for transient storage properties in streams and rivers. Water Resour Res 43:W10405. doi:10.1029/2006WR005808

Young PC (1984) Recursive estimation and time series analysis: an introduction. Springer Verlag

Young PC, Wallis SG (1985) Recursive estimation: A unified approach to the identification, estimation and forecasting of hydrological systems. Appl Math Comp 17:299–334

Vegetation and Flow Rate Impact on In-stream Longitudinal Dispersion and Retention Processes

Jevgenijs Savickis, Mattia Zaramella, Andrea Bottacin-Busolin, Gunnar Nützmann and Andrea Marion

Abstract This paper is an attempt to explain influence of vegetation and flow rate in natural stream (Epre, Germany) on mixing and transport processes. For this purpose, we conducted two tracer tests in Germany using rhodamine WT (RWT) as a fluorescence dye. Both tests were performed under different vegetation and flow rate conditions. The STIR (Solute Transport In Rivers) code was used for calibration of dispersion coefficients, exchange rates and residence times. We used the STIR model to separate short—and long—time retention. Our tracer test results confirm previous findings and also reveal a correlation between storage zone exchanges rate and reach lengths, strong influence of vegetation and flow rate on transport and mixing parameters, and the significance of the equipment on storage domain characterisation.

J. Savickis (✉) · M. Zaramella
Water and Environmental Technologies (WET) Srl,
viale Brigata C. Battisti 32, 31033 Castelfranco Vento, Italy
e-mail: jevgenijs.savickis@inbox.com

M. Zaramella
e-mail: mattia.zaramella@gmail.com

A. Bottacin-Busolin
School of Mechanical, Aerospace and Civil Engineering
University of Manchester, Manchester M13 9PL, UK
e-mail: andrea.bottacinbusolin@manchester.ac.uk

G. Nützmann
Department of Ecohydrology, Institute of Freshwater Ecology and Inland Fisheries (IGB), Müggelseedamm 310, 12587 Berlin, Germany
e-mail: nuetzmann@igb-berlin.de

A. Marion
Department of Industrial Engineering, University of Padua,
via F. Marzolo 9, 35131 Padua, Italy
e-mail: andrea.marion@unipd.it

P. Rowiński and A. Marion (eds.), *Hydrodynamic and Mass Transport at Freshwater Aquatic Interfaces*, GeoPlanet: Earth and Planetary Sciences,
DOI 10.1007/978-3-319-27750-9_8

1 Introduction

Transport and mixing of mass are extremely important processes in fluvial ecosystems. Understanding these processes is important in order to prevent contamination, preserve biodiversity and environmental quality. Depending on hydrodynamics, transport and mixing processes in aquatic system can be described by advection, diffusion and dispersion parameters. Precise evaluation of these parameters is a complex task and becomes even more challenging in case of flow through vegetation. It is well known that vegetation has remarkable impacts on a flow field by creating strong velocity gradients in both vertical and transverse profiles (Nepf 2012; Nikora et al. 2013), therefore altering mass transport and mixing processes in the water column (Murphy et al. 2007; Nepf et al. 1997). Furthermore, vegetation acts as a temporary storage zone by creating low recirculation or stagnant water pools, where solutes can be temporarily stored. Depending on the residence time, transient storage processes can be distinguished between short (vegetated zones and side pockets) and long (hyporheic zone) timescale processes.

When a solute is injected in a river, mass is advected and dispersed in the main flow channel as a consequence of the average flow velocity, turbulent diffusion and velocity gradients, and can be occasionally trapped in a storage zone where the solute is temporarily retained. After some time, the mass trapped in the storage zone is released back to the main channel producing a positive skewness of the solute breakthrough curves (BTC) (Nordin et al. 1980). This temporary mass retention increases the overall in-stream residence time and as a consequence also increases the contact time with aquatic interfaces, e.g. sediments and biota (Marion et al. 2014).

Since Taylor (1954) derived a one-dimensional (1D) advection-dispersion equation (ADE), more complex mathematical expressions were developed trying to explain transport and mixing processes in rivers accounting for storage zone phenomena. The most widely accepted model is the Transient Storage Model (TSM) formulated by Bencala and Walters (1983), in which the exchange between main channel and storage domain is represented as a first-order mass transfer. It has been shown that the TSM does not provide a good approximation for long timescale pumping processes (Marion et al. 2003).

Haggerty et al. (2000) presented an advection-dispersion-mass-transfer equation (ADMTE), where mass attenuation within a storage domain is solved through a convolution of the storage zone residence time distribution (RTD) with the in-stream solute concentration. The use of a single RTD is suitable for the evaluation of the total transient storage parameters, but is not applicable for separate short and long timescale storage zones analysis. This coupling can cause an over/under estimation of storage zone parameters depending on the permeability of stream boundaries (riverbed and banks), and the parameterization of a longitudinal dispersion coefficient becomes arguable.

Solute transport in rivers (STIR) is a one-dimensional model that provides a more detailed picture of retention processes as it can be used to quantitatively separate short-term and long-term retention processes (Marion et al. 2008). Under the assumption of Fickian, the STIR model reduces to an advection-dispersion mass-transfer model. Because an objective of this work is to examine the influence of vegetation, as a short timescale storage zone, on the longitudinal dispersion coefficient and transient storage parameters, the STIR code is applied here to field collected data. For this work, we conducted tracer tests in Germany using RWT as a tracer dye. The tests were performed on the Erpe (Neuenhagener Mühlenfließ) stream under different vegetation conditions.

2 STIR model

The STIR model is a general residence time distribution model that uses a multiple storage zone approach for parameterization of storage parameters.

Under the assumption of Fickian dispersion in the main channel, and that the exchange between the main channel and the storage zone is a Poisson process, the variation of concentration $C_w(x,t)$ in the main channel is described by the following advection-dispersion multi-rate-mass-transfer equation

$$\frac{\partial C_w(x,t)}{\partial t} + U\frac{\partial C_w(x,t)}{\partial x} = D_w\frac{\partial^2 C_w(x,t)}{\partial x^2} - \alpha\left(C_w(x,t) - \int_0^t C_w(x,t-\tau)\varphi(\tau)d\tau\right), \quad (1)$$

where $C_w(x,t)$ is the solute concentration in the surface water [M L^{-3}], D_w is the longitudinal dispersion coefficient [M^2 T^{-1}], α is the flow rate into the storage zone per unit surficial volume [T^{-1}], and $\varphi(\tau)$ is the probability density function (pdf) of the residence time distribution in the storage zone [T^{-1}]. Equation (1) is a special case of the STIR model. In this study, the residence time distribution in the storage zones for a single trapping event is parameterized as follows:

$$\alpha_i = \frac{q_b}{d} \quad (2a)$$

$$\alpha = \alpha_1 + \alpha_2 \quad (2b)$$

$$\varphi_i = \frac{1}{T_i}e^{-\frac{t}{T_i}} \quad (3a)$$

$$\varphi(t) = \frac{1}{\alpha}(\alpha_1\varphi_1(t) + \alpha_2\varphi_2(t)), \quad (3b)$$

where q_b is the average flow rate into the storage zone per unit surficial cross-section area [L T^{-1}] and d is the flow depth [L], α_i, φ_i (τ) and T_i $(i = 1, 2)$ correspond to the exchange rate [T^{-1}], pdf of the residence time distribution [T^{-1}] and retention timescale of the storage zone [T]. For parameters calibration, we applied exponential residence time distribution functions (Eq. 3a) to both short and long timescale storage zones. Calibration of the longitudinal dispersion coefficient and the storage domain parameters is accomplished by minimizing the root mean square error (Bottacin-Busolin et al. 2011). For the fitting procedure optimization, a linear scale is used to fit the bulk data of the BTC and log-scale to fit the tail.

3 Study site and methods

3.1 Study site

Two tracer tests were performed in Germany on the Erpe stream stretch, between Mönchsheimer Weg and L339 urban roads (Fig. 1). The stream catchment basin is affected by anthropogenic actions and resulting pollutants released into the stream which is one of Müggelspree tributaries.

From the L339 road bridge upstream (approx. 600 m), the stream has several bends with minimal bank erosion. In general, the study stretch is nearly uniform width with fine sediment bed. At the injection point, an upper layer of sediments is mainly homogenous fine sand. From the injection point downstream the fine sand

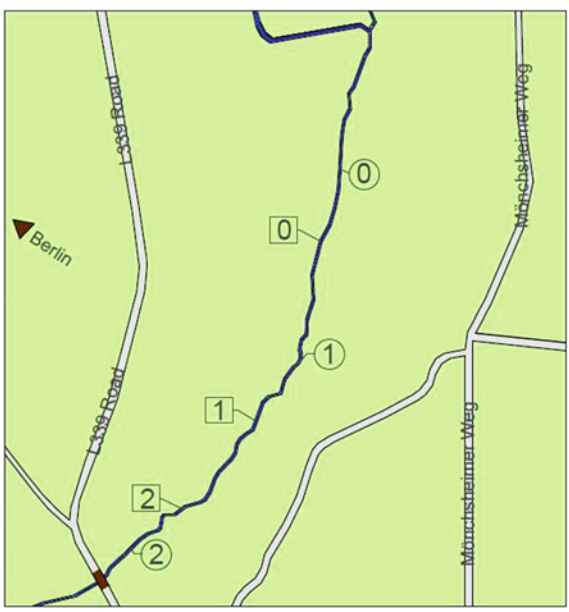

Fig. 1 The injection positions are indicated with zeros and fluorometer stations are numbers from 1 to 2 (in *square*s 2013 test and in *circles* 2014 test)

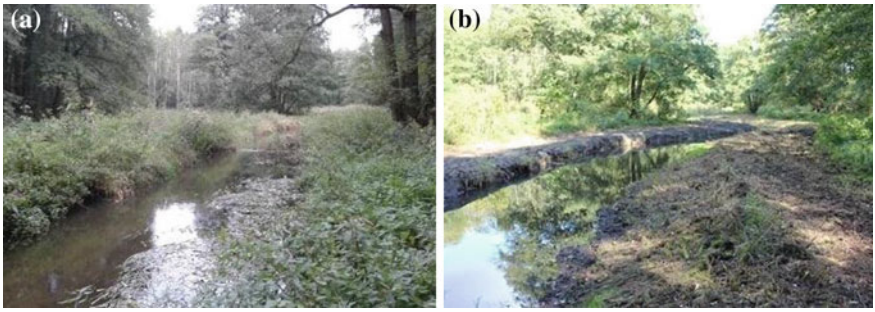

Fig. 2 Erpe stream during tests (**a**) in 2013 and (**b**) 2014

gradual substituted with loose finest grained sediments (organic material); hence at the last stations (Fig. 1) the streambed is completely covered with an organic material.

At time of the first test, in September 2013, along the study stretch there were debris, thick riparian and some submerged vegetation (Fig. 2a).

In September 2014, local authorities cleaned the stream banks and main flow channel from vegetation and debris (Fig. 2b). Minor local changes of the stream banks were noted after removal works, which could not significant impact test results, therefore conditions were reasonably preserved for our analysis.

3.2 Methods

Tracer tests were carried out in September 2013 and in September 2014 using RWT as a fluorescent dye. In both tests a continuous (step) injection of a dye solution was performed using a constant flow rate peristaltic pump.

In the experiments performed in September 2013, the tracer concentration was measured using two submersible fluorometer types: SCUFA and YSI 6920. The fluorometers were installed in the middle of the channel, at a depth of 10 cm, from the water surface to the detection optics. All fluorometers were equipped with turbidity probes and the data from them was simultaneously recorded with concentration readings. Then, when necessary, the concentration readings were adjusted with monitored turbidity. The injection and station locations are shown in Fig. 1 and detail of reaches are reported in Table 1.

Table 1 Measured quantities: reach lengths and flow rates

Test	Reach 0–1 (m)	Reach 0–2 (m)	Flow rate (m^3s^{-1})
Sep. 2013	325.0	520.8	0.19
Sep. 2014	210.0	716.0	0.08

During the last tracer test, in September 2014, we used two GGUN-FL fluorometers. To avoid pressure build-up effect, on turbidity and concentration readings, we kept fluorometers on the stream bank. The fluorometers were connected to constant flow rate immersible pumps (*Geo-Duplo-Plus*). At each station, an individual pump was positioned in the mid-channel, and supplied water via a flexible PVC hose to a fluorometer inlet. Then, water from an outlet was discharged back to the main channel downstream through a second PVC hose. The fluorometer stations and injection point are illustrated in Fig. 1 and details are reported in Table 1.

4 Results and discussion

In September 2013, the flow rate was 1.4 times larger than in 2014 (Table 1). Therefore, the initial objective of this work, defining influence of vegetation on dispersion and storage domain parameters in natural stream, cannot be directly achieved due to the combined change of flow rate and vegetation condition. The obtained data sets can be used anyway to assess influence of both hydrodynamic and vegetation condition changes on parameters of interest. Based on Shucksmith et al. (2011) work, decrease of flow rate and vegetation should lower dispersion coefficient. Clearly, decrease of flow rate will reduce hydraulic radius and exchange rate between main flow channel and storage domain. Moreover, decrease of exchange rate will reflect on residence time within storage domain.

In STIR, breakthrough curves were simulated using injection data (time and concentration) as upper boundary conditions, which were then fitted to observed data (Fig. 3). The graphs in Fig. 3 are plotted in semi-log scale and using normalized time $t^* = t/t_{ad}$, where t_{ad} is the advection time, and normalized concentration $C^* = C(x, t)/C_{max}$, where C_{max} is the peak concentration.

Comparing test results obtained in 2013 and 2014, dispersion coefficient and flow cross-sectional area dropped in 2014 by 78 and 70 %, respectively (Table 2). Similarly, the short timescale exchange rates α_1 decreased by 32 %, from 9.97×10^{-4} to 6.74×10^{-4}. However, variation of long timescale exchange rates α_2 is not strongly influenced by flow rate or vegetation conditions but apparently depends on reach length.

Exchange rate and storage zone residence time are inversely related but the result of short reaches (0–1) proposes some overlapping. In 2014, the exchange rate α_1 decreased by 32 %, whereas residence time T_1 increased by 9 % (145–159 s). Meanwhile, the residence time T_1 of long reach (0–2) increased more significantly, by 66 % (160–266 s).

Comparison of results suggests dependence of residence time T_1 on distance. At some point, the flow rate effect becomes dominant over vegetation; hence, the long reach (716 m) demonstrated significantly higher residence time T_1. Residence time T_2 has almost doubled in 2014 (Table 2) despite negligible increase of α_2 exchange rates. Moreover, there is no evidence in results of reach length or exchange rate dependency.

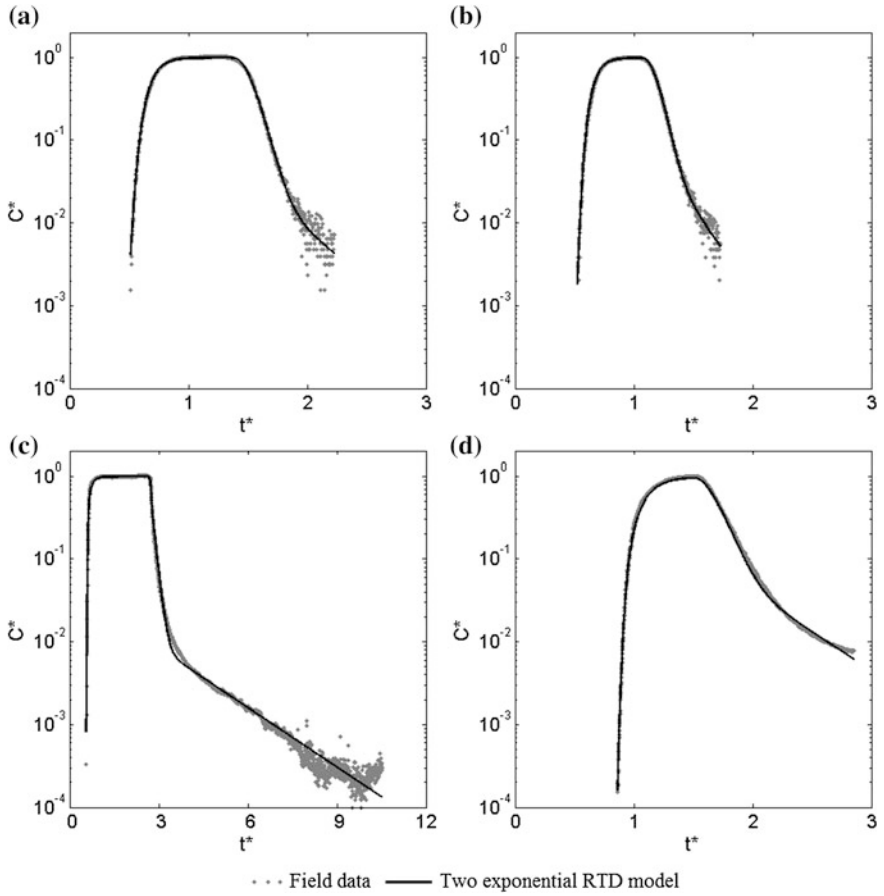

Fig. 3 Figures **a** and **b** represent 2013 test BTCs of reaches 0–1 and 0–2, respectively, but **c** and **d** illustrate 2014 test BTCs of reaches 0–1 and 0–2, accordingly

Table 2 Parameters of STIR model with two exponential RTDs

Reach	Test Sep. 2013		Test Sep. 2014	
	0–1	0–2	0–1	0–2
A (m^2)	1.39	1.35	0.42	0.62
D (m^2s^{-1})	0.142	0.105	0.031	0.037
α_1 ($\times 10^{-4}$ s^{-1})	9.97	9.08	6.69	6.74
α_2 ($\times 10^{-4}$ s^{-1})	0.12	0.17	0.13	0.18
T_1 (s)	145	160	159	266
T_2 (s)	1212	1111	2792	2161

We hypothesise that this behaviour of residence time T_2 is linked to equipment capabilities and in-stream velocity decrease. Detection limits of SCUFA and YSI 6920 fluorometers are higher by order of magnitude than of GGUN-FL, 10^{-3} and 10^{-4} ppb, respectively (Fig. 3a, c). For that reason, the GGUN-FL fluorometers recorded longer tails which enabled to extend characterisation of residence time within the long timescale storage zones.

5 Conclusions

Our experimental results confirmed the previous laboratory findings that increase of flow rate and vegetation enhances dispersion in water column. For the conditions analysed in this study, an increase of flow rate from 80 to 190 L s^{-1} combined with naturally developed vegetation resulted in a 78 %—increase in the dispersion coefficient.

However, not all results matched our expectations. The average residence time associated with short timescale storage zones was found to be dependent on reach length. In the experiment performed in 2014, the residence time T_1 for the short reach (0–1) is almost the same as that found in 2013 for the same reach. As the results suggest, the vegetation removal effect is prevalent over short distances and enables to compensate flow rate decrease, thus keeping residence time unaffected.

In this paper, we want to emphasize the importance of equipment sensitivity. The analysis of long timescale storage zones requires fluorometers with adequate detection capabilities, because these zones generate long-tailed breakthrough curves. During this experimental work, we used different fluorometers, and a comparison of results revealed that an accurate long timescale storage zones analysis requires fluorometers with sensitivity of 10^{-4} ppb or lower. In general, the residence time concept is very attractive due to its understandable mathematical formulation, which allows defining meaningful storage domain parameters and realistically model mass transport and mixing processes in natural streams.

Acknowledgments This work was supported by the Research Executive Agency, through the Seventh Framework Programme of the European Union, Support for Training and Career Development of Researchers (Marie Curie-FP7-PEOPLE-2012-ITN), which funded Initial Training Network (ITN) HYTECH 'Hydrodynamic Transport in Ecologically Critical Heterogeneous Interfaces', No. 316546. We thank Jörg Lewandowski, Christine Sturm, Annika Lüdeking, Rose Stefes and Viktor Baranov for valuable assistance during field works.

References

Bencala KE, Walters RA (1983) Simulation of solute transport in a mountain pool-and-riffle stream: A transient storage model. Water Resour Res 19(3):718–724

Bottacin-Busolin A, Marion A, Tommaso Musner, Tregnaghi M, Zaramella M (2011) Evidence of distinct contaminant transport patterns in rivers using tracer test and a multiple domain retention model. Adv Water Res 34(6):737–746. doi:10.1016/j.advwatres.2011.03.005

Haggerty R, McKenna SA, Meigs LC (2000) On the late-time behavior of tracer test breakthrough curve. Water Resour Res 36(12):3467–3479. doi:10.1029/2000WR900214

Marion A, Nikora V, Puijalon S, Bouma T, Koll K, Ballio F, Tait S, Zaramella M, Sukhodolov A, O'Hare M, Wharton G, Aberle J, Tregnaghi M, Davies P, Nepf H, Parker G, Statzner B (2014) Aquatic interfaces: a hydrodynamic and ecological perspective. J Hydraul Res 52(6):744–758. doi:10.1080/00221686.2014.968887

Marion A, Zaramella M, Bottacin-Busolin A (2008) Solute transport in rivers with multiple storage zones: the STIR model. Water Resour Res 44(10):W10406. doi:10.1029/2008WR007037

Marion A, Zaramella M, Packman AI (2003) Parameter estimation of the transient storage model for stream-subsurface exchange. J Environ Eng 129(5):456–463. doi:10.1061/ (ASCE) 0733-9372(2003)129:5(456)

Murphy E, Ghisalberti M, Nepf H (2007) Model and laboratory study of dispersion in flows with submerged vegetation. Water Resour Res 43(5):W05438. doi:10.1029/2006WR005229

Nepf HM (2012) Flow and transport in regions with aquatic vegetation. Ann Rev Fluid Mech 44 (1):123–142

Nepf HM, Zavistoski M, Zavistoski RA (1997) The effect of vegetation on longitudinal dispersion. Estuar Cost Shelf Sci 44(6):675–684

Nikora N, Nikora V, O'Donoghue T (2013) Velocity profiles in vegetated open-channel flows: combined effects of multiple mechanisms. J Hydraul Eng 139(10):1021–1032. doi:10.1061/ (ASCE)HY.1943-7900.0000779

Nordin CF, Troutman JM, Troutman BM (1980) Longitudinal dispersion in rivers: the persistence of skewness in observed data. Water Resour Res 16(1):123–128

Shucksmith JD, Boxall JB, Guymer I (2011) Determining longitudinal dispersion coefficients for submerged vegetated flow. Water Resour Res 47(10):W10516. doi:10.1029/2011WR010547

Taylor GI (1954) The dispersion of matter in turbulent flow through a pipe. Proc R Soc London Ser A 223:446–468

Effects of Vegetation Density and Wetland Aspect Ratio Variation on Hydraulic Efficiency of Wetlands

Nima Sabokrouhiyeh, Andrea Bottacin-Busolin, Heidi Nepf and Andrea Marion

Abstract Hydraulic efficiency of wetlands, evaluated through retention time and mixing levels, was investigated as a function of wetland shape and vegetation density using a two-dimensional numerical model. The numerical model was applied to four different aspect ratios of a rectangular wetland (i.e. 1:1 to 1:4) with 1-ha area and vegetation density varying from 20 to 1500 stems/m^2. The results, modeled velocity field and the simulated transport of a continuously injected tracer, were used to develop Residence Time Distribution graphs (RTDs). Analysis of RTDs showed that the efficiency measure related to retention time, e, and the measure of mixing, λ_p, improved for denser vegetation before reaching to a constant value. It was also observed that narrow rectangular-shaped wetlands (higher aspect ratio) have better efficiency than square wetlands. The results from the study provide a quantitative understanding of hydraulic efficiency in connection with wetland vegetation and shape which may help engineers to design more efficient and cost-effective water systems.

N. Sabokrouhiyeh (✉) · A. Marion
Department of Industrial Engineering, University of Padua, via F. Marzolo 9, 35131 Padova, Italy
e-mail: nima.sabokrouhiyeh@unipd.it

A. Marion
e-mail: andrea.marion@unipd.it

A. Bottacin-Busolin
School of Mechanical Aerospace and Civil Engineering, University of Manchester, Manchester M13 9PL, UK
e-mail: andreabottacin@gmail.com

H. Nepf
Department of Civil and Environmental Engineering, Massachusetts Institute of Technology, Cambridge, MA 02139, USA
e-mail: hmnepf@mit.edu

P. Rowiński and A. Marion (eds.), *Hydrodynamic and Mass Transport at Freshwater Aquatic Interfaces*, GeoPlanet: Earth and Planetary Sciences,
DOI 10.1007/978-3-319-27750-9_9

1 Introduction

Constructed wetlands (CWs) are frequently used to recondition nutrient contamination (Jadhav and Buchberger 1995), wastewater effluent (Torrens et al. 2009), and storm water (Somes et al. 1999). The effectiveness of constructed wetlands in reducing different forms of contaminants is well documented (Tilley and Brown 1998). For example, Hsueh et al. (2014) reported that a subtropical constructed wetland with retention time of 3.7 days had concentration removal efficiency (CRE) of approximately 85 % in both cold and warm seasons. A wetland with 14-day residence time was able to remove 90 % of total phosphorous (TP) (Rushton et al. 1995). Reinelt and Horner (1995) found that the removal of the TP load to a wetland was 86 % for a nonurban wetland (1.5 ha) under groundwater inputs contribution. The same study estimated that mean annual removal percentages (over the 2-year study period) for total suspended solids (TSS), zinc, and fecal coliforms (FC) were 56, 23, and 29 %, respectively. In recent decades there has been an increasing interest in the construction and restoration of wetlands (Marion et al. 2014). An understanding of flow structure and mass transport is fundamental to CWs proper design and operation. Insufficient consideration to the hydraulics of wetlands has caused poor performance in wetlands pollutant removal potential (Kadlec and Wallace 2008). Many of the wetland problems can be minimized or avoided by applying proper engineering design criteria (Marion et al. 2014).

Hydraulic efficiency of a wetland needs to fulfill two main requirements: (1) to facilitate an optimal level of residence time (Werner and Kadlec 1996) and (2) to provide enough level of mixing and re-circulation (Holland et al. 2004; Persson et al. 1999). Hydraulic retention time is a key factor in the design of CWs, as it describes the average amount of time a plug of flow spends in a wetland system. The degree of biological and chemical functions necessary for pollutant removal is directly dependent on the time pollutants stay in wetland system. A higher retention time provides a longer time for reactions to take place in a basin, which consequently increases wetland efficiency. The residence time related efficiency may be estimated by dimensionless retention time, $e = t_m/t_n$, where t_m = observed mean residence time, and t_n = nominal residence time ($=V/Q$, where V is the volume of the wetland and Q is the input discharge rate) (Thackston et al. 1987). The ideal residence time would be achieved when the ratio approaches unity ($t_m = t_n$), which implies that the entire active circulation pattern within the wetland includes the full wetland volume, such that the full volume actively contributes in treatment processes. Deviations from the nominal retention time are caused by dead zones where the flow velocities are so small that the region is effectively excluded from the main circulation pattern within the wetland. This reduces the effective volume of wetland, and thus the effective residence time. The second design criterion that influences wetland performance is the ability of a wetland to distribute its flow uniformly throughout its volume and is defined based on departures from plug flow associated with dispersion processes. Dispersion arises from inlet and outlet effects, vegetation distribution patterns, bottom topography, wind effects and shear stresses from sides.

Dispersion makes some parcels of water exit before and after the nominal resistance time (t_n). The heterogeneity affects treatment efficiency adversely and should be controlled. Both efficiency factors are determinable and calculable, with a considerable degree of confidence (Persson et al. 1999).

Vegetation is an essential component of wetland systems and its properties influence wetland efficiency (Jenkins and Greenway 2005). The most important effects of vegetation on CWs are (1) the uptake of nutrient pollution and oxygen release from roots, (2) the contribution of additional hydrodynamic drag that impacts the wetland hydraulics. Several studies have investigated the effects of vegetation type and density on CWs hydraulics. Jenkins and Greenway (2005) applied a numerical model to study the effects of emergent fringing and banded vegetation on the hydraulic characteristics of constructed wetlands. The results proved that inappropriate layout of wetland vegetation results in poor performance of a wetland system. Musner et al. (2014) used a two-dimensional depth-averaged model to study the residence time distribution of a tracer under different vegetation patterns in a channelized wetland and reported that increasing vegetation densities produce an increasingly pronounced bimodality of the RTDs reflecting a separation between flow traversing the channels and flow traversing the vegetated regions.

Considering the importance of vegetation in wetland design, there is a need to further investigate the significance of different vegetation densities on wetland hydraulics. This paper introduces a two-dimensional numerical model to study the wetland hydrodynamics and mass transport patterns. The model is used to study the interaction between the vegetation density, wetland shape and the hydraulic efficiency of a constructed surface water wetland system. The aim of study is to provide a quantitative understanding of hydraulic efficiency in connection with wetland vegetation and wetland shape. Such an understanding might help engineers to design more efficient and cost-effective water systems.

2 Theoretical Background

2.1 Two-Dimensional Numerical Wetland Model

A 2-dimensional numerical model of a wetland was established to simulate velocity field and the transport of a dissolved tracer under steady conditions. The hydrodynamic model solves the shallow-water equations and a solute transport model solves advection diffusion equations.

2.1.1 Hydrodynamic Model

Under the assumption of hydrostatic pressure, stationary flow, and negligible wind and Coriolis forces, the depth-averaged velocity field and water depth can be described by the following equations (Wu 2007).

$$\frac{\partial(hU_x)}{\partial x} + \frac{\partial(hU_y)}{\partial y} = 0 \tag{1}$$

$$\frac{\partial(hU_x^2)}{\partial x} + \frac{\partial(hU_xU_y)}{\partial y} = -gh\frac{\partial(z_s)}{\partial x} - \frac{\tau_{bx}}{\rho} - \frac{\tau_{vx}}{\rho} \tag{2}$$

$$\frac{\partial(hU_xU_y)}{\partial x} + \frac{\partial(hU_y^2)}{\partial y} = -gh\frac{\partial(z_s)}{\partial y} - \frac{\tau_{by}}{\rho} - \frac{\tau_{vy}}{\rho} \tag{3}$$

Here, U_x and U_y are the velocity components along x and y directions; h is the water depth; z_s is the water surface elevation; ρ is the water density; τ_{bx} and τ_{by} are the bed shear stresses in x and y directions; and τ_{vx} and τ_{vy} represents vegetation drag for x and y directions.

The bed shear stresses can be determined by Eqs. (4) and (5) (Kadlec and Wallace 2008; Werner and Kadlec 1996).

$$\tau_{bx} = \rho C_b U_x \sqrt{U_x^2 + U_y^2} \tag{4}$$

$$\tau_{by} = \rho C_b U_y \sqrt{U_x^2 + U_y^2} \tag{5}$$

The corresponding bed-drag coefficient (C_b) is defined by Eq. (6):

$$C_b = \frac{3\mu}{h\rho\sqrt{U_x^2 + U_y^2}} + \frac{M^2 g}{h^{\frac{1}{3}}} = \frac{3}{Re_b} + \frac{M^2 g}{h^{\frac{1}{3}}} \tag{6}$$

where μ is the water dynamic viscosity; and M is the Manning friction coefficient. Bed drag coefficient consists of two different terms of laminar and turbulent flow. Under laminar and transitional flow ($Re \leq 500$), the first term of the equation dominates, whereas the turbulent term characterized by Manning equation becomes important for larger Reynolds numbers ($Re \geq 1250$) (Kadlec and Wallace 2008). Experimental results confirm that for vegetated systems with vegetation volume fraction higher than 0.01 the bed shear stresses become negligible compared to vegetation shear stresses (Nepf 1999).

Vegetation drag is modeled using the following expressions for the drag exerted by the stems, as described by Kadlec and Wallace (2008):

$$\tau_{vx} = \rho C_D a l \frac{U_x}{2} \sqrt{U_x^2 + U_y^2} \tag{7}$$

$$\tau_{vy} = \rho C_D a l \frac{U_y}{2} \sqrt{U_x^2 + U_y^2} \tag{8}$$

where C_D is the vegetation-drag coefficient (dimensionless), and l is the stem length (assumed equal to water depth). If the plants are modeled as cylinders, the vegetation density parameter (a) can be defined as:

$$a = n_s d \tag{9}$$

where n_s is the number of vegetation stems per unit area ($1/m^2$), and d is the cylinder diameter of vegetation (m). From Eq. 9 a non-dimensional vegetation volume fraction is defined by $VF = ad = n_s d^2$, which represents the fractional volume of the flow domain occupied by plants (Nepf 1999; Stoesser et al. 2010; Tanino and Nepf 2008).

2.1.2 Solute Transport Model

Solute transport of a passive tracer through a wetland is simulated with a depth-averaged solute transport model,

$$\frac{\partial(h\mathrm{C})}{\partial t} + \frac{\partial(hU_xC)}{\partial x} + \frac{\partial(hU_yC)}{\partial y} = \frac{\partial}{\partial x}\left(hE_{xx}\frac{\partial C}{\partial x} + hE_{xy}\frac{\partial C}{\partial y}\right) + \frac{\partial}{\partial y}\left(hE_{yx}\frac{\partial C}{\partial x} + hE_{yy}\frac{\partial C}{\partial y}\right) \tag{10}$$

where C is the depth-averaged solute concentration, whereas the coefficients E_{ij}, account for both turbulent diffusion and shear dispersion due to vertical velocity gradients.

2.2 Residence Time Distribution

Hydraulic tracer tests are used in wetlands to evaluate the hydraulic efficiency (Bodin et al. 2012; Holland et al. 2004; Koskiaho 2003). After a release of tracer mass at the wetland inflow, the concentration recorded versus time at the wetland outflow reveals the residence time distribution (RTD). Hydraulic RTDs provide a measure of both the mean retention time and the degrees of dispersion. Thackston et al. (1987) defined the concept of hydraulic efficiency as a function of the RTD's

centroid position. Any reduction in wetland retention time is associated with a shift of the centroid towards the origin, i.e. a reduction in mean residence time. Such inefficiency is explained by the presence of stagnant zones. A difference between the observed retention time (t_m) and the nominal retention time ($t_n = V/Q$) indicates that not all of the wetland volume (V) is utilized in the detention of the tracer. Mixing levels (i.e. dispersion) within a wetland are quantified by the variance of the RTD. Under pure plug flow conditions, the RTD appears as a spike at the nominal retention time (t_n) with zero variance. The pure plug flow provides the same retention time for all tracer parcels. In this study we use the method of moments to describe the RTD and quantify the wetland efficiency parameters of mean hydraulic residence time (t_m) and RTD variance (Thackston et al. 1987). We examine how these parameters vary with changes in vegetation density and wetland aspect ratio. A non-reactive continuous tracer is introduced at the system inlet, and the outlet concentration is measured as a function of time, $C_{out}(t)$, from which the RTD can be found. The residence time distribution function, represented by $E(t)$, is:

$$E(t) = \frac{Q_{out}(t)C_{out}(t)}{\int_0^\infty Q_{out}(t)C_{out}(t)dt} \tag{11}$$

where $Q_{out}(t)$ is the outlet tracer concentration, and dt is the difference in sampling time. The first moment of the RTD represents the mean residence time, t_m, which is the average time that tracer particles remain in the wetland (Werner and Kadlec 1996),

$$t_m = \int_0^\infty tE(t)dt \tag{12}$$

In theory, $t_m = 1$ for a normalized RTD of a conservative tracer happens in an ideal system with no dead zones. The variance (σ^2), i.e. the second moment, is:

$$\sigma^2 = \int_0^\infty (t - t_m)^2 E(t)dt \tag{13}$$

The second moment of the RTD accounts for the spread of the tracer over time. A large variance indicates that there is a large variation in the times spent by individual parcels of water within the wetland. This variation can be caused by the presence of different flow paths, e.g. short circuiting flow paths, recirculation zones, or by a high level of turbulent mixing. On the other hand, the variance is equal to zero for ideal plug flow. A wetland can also be modeled by a number of continuously stirred tank reactors (CSTRs). Assuming a single CSTR, water is uniformly and instantly mixed in a wetland, and therefore the wetland behaves similar to one CSTR and represents a distribution of a hydraulic residence time in the form of an exponential decay curve. The number of CSTRs is a key factor in wetland modeling; many small tanks or a few large tanks may simulate a wetland. The first suggests a system with a low degree of mixing and flow path variance, which

results in a small RTD variance. The second suggests a high degree of mixing and flow path variance, which causes a high RTD variance. According to Fogler (1992), the number of CSTRs in series can be determined from the inverse of the dimensionless variance (σ_θ):

$$N = (\sigma_\theta)^{-2} = \left(\frac{\sigma}{t_n}\right)^{-2} \tag{14}$$

Thakston et al. (1987) introduced another index, the dimensionless retention time, as the ratio of the mean detention period (t_m) over nominal residence time (t_n) representing the effective volume of a wetland system.

$$e = \left(\frac{t_m}{t_n}\right) = \left(\frac{V_{effective}}{V_{total}}\right) \tag{15}$$

Low values of the ratio indicate the presence of dead zones and/or dispersion, allowing the tracer to traverse the wetland in a time shorter than t_n.

Persson et al. (1999) also defined a hydraulic efficiency index, λ_p, incorporating both effects of retention time and dispersion.

$$\lambda_p = e\left(1 - \frac{1}{N}\right) \tag{16}$$

A high value of the index suggests decreased level of dispersion and consequently a better wetland performance.

3 Model Application

The numerical model study was undertaken to simulate velocity fields and tracer transport patterns for a free water surface (FWS) wetland system (Fig. 1). In this study, four different wetland configurations (aspect ratios 1:1, 1:2, 1:3, 1:4) each with the area of 1 ha and 0.5 m depth and variable vegetation densities were simulated. The boundary conditions were defined for the Eqs. (1)–(3), by the inflow at the inlet, 0.83 L/s, and the water depth at the outlet, 0.5 m, producing a nominal hydraulic retention time of t_n = 7 days. In all the studied cases, the flow was modeled for a constant discharge rate through an inlet of 10 m width and an outlet with 10 m width and 0.5 m height, under atmospheric pressure. Both the inflow and outflow were centrally located. These design values were chosen according to the values described by (Persson et al. 1999; Thackston et al. 1987).

For the solute transport equation, the boundary conditions were given by a constant tracer injection at the inlet, C = 1 kg/m^3, an open boundary condition at the outlet, and the no-flux condition on the remaining part of the flow boundary. The equations were solved via a finite element method using COMSOL Multiphysics®

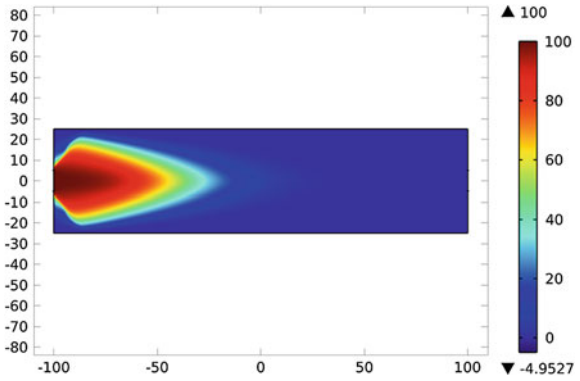

Fig. 1 Simulations for a uniformly vegetated wetland (aspect ratio 1:4), tracer concentration distribution-After elapsed time = 1.2 days

with quadratic shape functions. The computational grid was made of approximately 150,000 triangular elements, with higher spatial resolution near the inlet and the outlet, and a maximum element size of 2 m.

A numerical tracer study was performed to generate RTDs for all configurations. Response to the tracer injection was simulated for rectangular wetlands of vegetation densities 20–1500 stems/m^2. The vegetation shear stresses were determined by the Eqs. (7) and (8) by assuming that all of the vegetation had a diameter of D = 10 mm, which is typical for a constructed FWS wetland. Marsh grasses are relatively sparse; the vegetation volume fraction is in the range of VF = 0.001–0.15 associated with the stem diameter of d = 1–12 mm (Jadhav and Buchberger 1995; Lightbody and Nepf 2006; Valiela et al. 1978). In contrast, in constructed wetlands aquatic vegetation conditions may be designed quite dense with diameters of 8–15 mm (Serra et al. 2004). The wetland Manning coefficient for bottom friction was 0.035 s/m$^{1/3}$.

4 Results and discussion

4.1 Vegetation Effects

The outlet tracer concentration variation and corresponding RTDs simulated by the numerical model grouped for different vegetation densities are illustrated in Fig. 2. The summary of wetland hydraulic efficiency indexes is given in Table 1. Similar positively skewed RTDs with elongated tails to the right were observed for different vegetation densities. However, the data points showed a tendency to be closer to the centroid, as the vegetation density increased. Moreover, there was also an increase in the mean retention time with increasing stem density.

The numerical simulations returned different values of the variance of the RTDs (Fig. 2), which revealed that wetlands of dissimilar vegetation density experience different hydraulic performances. Generally, an increase in vegetation density

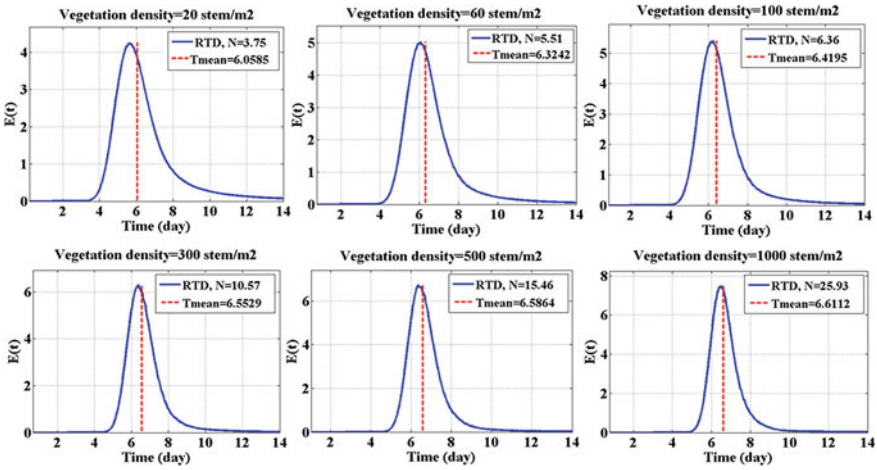

Fig. 2 Normalized residence time distributions, E(t) (10^{-6}), for six different vegetation densities

Table 1 Estimated statistic-hydraulic parameters of a wetland (aspect ratio 1:4): Mean residence time (t_m), the variance of RTD (σ), number of continuously stirred tank reactors, CSTRs, (N), dimensionless retention time (e), Persson hydraulic index (λ_p)

Vegetation density (stems/m^2)	t_m-day	σ-day	N	e	λ_p
20	6.0558	3.13	3.75	0.86	0.63
60	6.3242	2.69	5.52	0.90	0.74
100	6.4195	2.55	6.36	0.92	0.77
180	6.5034	2.31	7.91	0.93	0.81
260	6.5419	2.10	9.68	0.93	0.84
340	6.5651	1.92	11.68	0.94	0.86
420	6.5778	1.79	13.46	0.94	0.87
500	6.5864	1.68	15.46	0.94	0.88
700	6.6006	1.48	19.77	0.94	0.89
800	6.6048	1.40	22.20	0.94	0.90
1000	6.6112	1.30	25.93	0.94	0.91
1500	6.6162	1.41	33.67	0.95	0.92

produced an increase of mean retention time and variance before reaching an approximately constant value of efficiency (Table 1).

In response to a vegetation density boost from 20 to 260 stems/m^2, the efficiency measure related to retention time, e, and measure of mixing, λ_p, improved by, respectively, 7 and 20 %, whereas each of the hydraulic efficiency parameters exhibited smaller changes due to vegetation density increase for densities higher than 260 stems/m^2 (i.e. $e \approx 1\,\%$ and $\lambda_p \approx 8\,\%$). Above the threshold vegetation density, in this case 260 stems/m^2, changes in wetland performance were not

significant and suggested negligible improvement in efficiency factors. As already mentioned, the number of CSTRs in series, N, can be used as a measure of mixing, and to quantify the heterogeneity of mixed tracers. In this manner, the sparse vegetation density of 20 stems/m^2 can be compared to a series of $N = 3.75$ and the more dense vegetation pattern of 260 stems/m^2 compares to a series of $N = 9.86$. The higher numbers of CSTRs were achievable by increasing the vegetation density (i.e. $N = 25.93$ for $a = 1000$ stems/m^2); however, such a change for very dense vegetation covers did not necessarily improve the mixing efficiency factor (Table 1).

More dense vegetation coverage is associated with higher variances of RTDs and larger number of continuously stirred tank reactors (N) (Table 1). This indicates that better efficiencies are most likely related to the high coverage of emergent vegetation in wetlands. However, it was observed that the factors λ_p and e remained almost constant and increasing vegetation density did not significantly improve the efficiencies above a certain value of density. From a design and management point of view, determining this vegetation density threshold is necessary for a cost effective wetland design.

4.2 Aspect Ratio Effects

The impact of aspect ratio on wetland efficiencies was investigated by analyzing four different wetland configurations of 1-ha area with aspect ratios of 1:1, 1:2, 1:3 and 1:4. It was observed that an evolving wetland shape from a square to a narrow rectangle (i.e. $L/W \geq 1$) led to a better hydraulic performance. As it can be seen from Fig. 3b, Persson hydraulic index (λ_p) for a rectangular-shaped wetland with aspect ratio of 1:4 was approximately 25 % larger than a square wetland of same area and same vegetation density. The dimensionless retention time, e, experienced a moderate increase of approximately 5 % for the same cases.

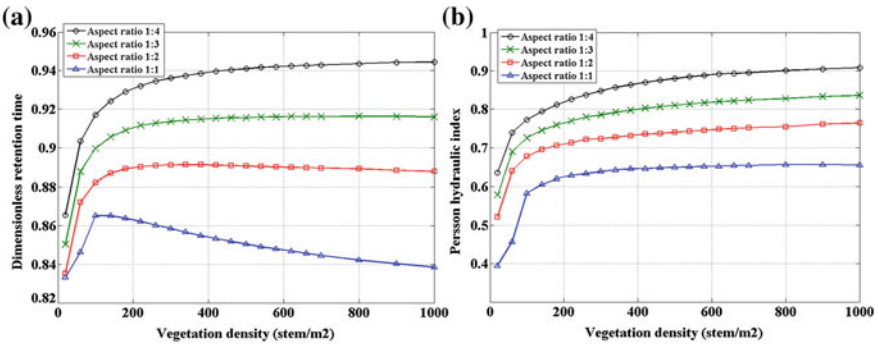

Fig. 3 Rectangle-shape wetlands efficiency parameters variation for different aspect ratios: (**a**) dimensionless retention time (e), (**b**) Persson hydraulic index (λ_p)

According to Persson et al. (1999), wetlands with $\lambda_p \leq 0.50$ are wetlands with ineffective hydraulic conditions. Thakston et al. (1987) has also categorized wetlands as those with a moderate amount of dead zones ($0.5 \leq e \leq 0.75$), and others with large dead areas values below ($e \leq 0.5$). Considering the above mentioned evaluation criteria, it can be seen from Fig. 3 that low hydraulic performance can result from a poor geometric design and/or sparse vegetation coverage. However, the better efficiencies are achievable by considering proper geometric design criteria and sufficient vegetation densities.

These results confirmed the observations by Jadhav and Buchberger (1995) who found that a wetland might exhibit static or dynamic behavior. Under static conditions, the wetland behaves like a pond in which displacement effects caused by submerged plant mass invariably decrease detention times. Under dynamic conditions, stem drag induced by aquatic plants predominates and wetland detention times increase with vegetation density. As can be seen from Fig. 3a, a square-shaped wetland (i.e. aspect ratio 1:1) behaved statically where the detention time fell after reaching a maximum for vegetation density of 200 stems/m^2. Unlike the square-shape wetland, rectangle wetlands showed a proper dynamic behavior. In summary, it can be concluded that narrow rectangle-shape wetlands (i.e. $L/W \geq 1$) are more likely to show a dynamic behavior than a square wetland (1:1).

5 Conclusions

- Vegetation density variation and aspect ratio changes affect the hydraulic residence time distribution. This means that these factors should be carefully taken into account for wetland design and management.
- It was observed that the efficiency measure related to retention time, e, and the measure of mixing, λ_p, improved before reaching a maximum in response to vegetation density increase. The wetland exhibited negligible hydraulic efficiency improvement due to vegetation growth after reaching the threshold value. It can be concluded that vegetation density higher than a certain level might not be necessarily useful.
- More dense vegetation density gives rise to a slightly elevated retention times in wetlands, whereas it considerably improves mixing efficiency of a wetland.
- Results showed that as the vegetation density increases, square wetlands experience a decrease of retention time after an initial increase for sparse vegetation covers.
- The study confirmed some of the results obtained by Persson et al. (1999) who observed that narrow rectangular wetlands (i.e. $L/W \geq 1$) have a better hydraulic performance than square wetlands. In this paper, the analysis was extended by considering variable vegetation density.
- Results showed that low coverage of emergent vegetation in combination with aspect ratio causes more dispersion and larger dead zones and consequently

leads to poor hydraulic efficiency. The resulting performance was quantified in this study.
- The analysis of the hydraulic efficiency presented in this work can be complemented by the analysis of the concentration reduction efficiency, by inclusion of an appropriate uptake function in the solute transport model. This is left for future work.
- More study is needed to investigate the impact of more complex geometric wetland shapes and heterogeneous vegetation patterns on wetland performance.

Acknowledgments This work was supported by the Research Executive Agency, through the Seventh Framework Programme of the European Union, Support for Training and Career Development of Researchers (Marie Curie-FP7-PEOPLE-2012-ITN), which funded Initial Training Network (ITN) HYTECH 'Hydrodynamic Transport in Ecologically Critical Heterogeneous Interfaces', N. 316546.

References

Bodin H, Mietto A, Ehde PM, Persson J, Weisner SEB (2012) Tracer behaviour and analysis of hydraulics in experimental free water surface wetlands. Ecol Eng 49:201–211. doi:10.1016/j.ecoleng.2012.07.009

Fogler HS (1992) Elements of chemical reaction engineering. Prentice-Hall, Englewood cliffs

Holland JF, Martin JF, Granata T, Bouchard V, Quigley M, Brown L (2004) Effects of wetland depth and flow rate on residence time distribution characteristics. Ecol Eng 23:189–203. doi:10.1016/j.ecoleng.2004.09.003

Hsueh M-L, Yang L, Hsieh L-Y, Lin H-J (2014) Nitrogen removal along the treatment cells of a free-water surface constructed wetland in subtropical Taiwan. Ecol Eng 73:579–587. doi:10.1016/j.ecoleng.2014.09.100

Jadhav RS, Buchberger SG (1995) Effects of vegetation on flow through free water surface wetlands. Ecol Eng 5:481–496. doi:10.1016/0925-8574(95)00039-9

Jenkins GA, Greenway M (2005) The hydraulic efficiency of fringing versus banded vegetation in constructed wetlands. Ecol Eng 25:61–72. doi:10.1016/j.ecoleng.2005.03.001

Kadlec R, Wallace S (2008) Treatment wetlands, 2nd edn. CRC Press, Boca raton

Koskiaho J (2003) Flow velocity retardation and sediment retention in two constructed wetland-ponds. Ecol Eng 19:325–337

Lightbody AF, Nepf HM (2006) Prediction of velocity profiles and longitudinal dispersion in salt marsh vegetation. Limnol Oceanogr 51:218–228. doi:10.4319/lo.2006.51.1.0218

Marion A, Nikora V, Puijalon S, Bouma T, Koll K, Ballio F, Tait S, Zaramella M, Sukhodolov A, Hare O, Wharton G, Aberle J, Tregnaghi M, Davies P, Parker G, Statzner B (2014) Aquatic interfaces: a hydrodynamic and ecological perspective. J Hydraul Res 52:744–758. doi:10.1080/00221686.2014.968887

Musner T, Bottacin-Busolin A, Zaramella M, Marion A (2014) A contaminant transport model for wetlands accounting for distinct residence time bimodality. J Hydrol 515:237–246. doi:10.1016/j.jhydrol.2014.04.043

Nepf HM (1999) Drag, turbulence, and diffusion in flow through emergent vegetation. Water Resour Res 35:479–489. doi:10.1029/1998WR900069

Persson J, Somes N, Wong T (1999) Hydraulics efficiency of constructed wetlands and ponds. Water Sci Technol 40:291–300. doi:10.1016/S0273-1223(99)00448-5

Reinelt LE, Horner RR (1995) Pollutant removal from stormwater runoff by palustrine wetlands based on comprehensive budgets. Ecol Eng 4:77–97. doi:10.1016/0925-8574(94)00002-M
Rushton B, Miller C, Hull C (1995) Residence time as a pollutant removal mechanism in stormwater detention ponds
Serra T, Fernando HJS, Rodríguez RV (2004) Effects of emergent vegetation on lateral diffusion in wetlands. Water Res 38:139–147. doi:10.1016/j.watres.2003.09.009
Somes NLG, Bishop WA, Wong THF (1999) Numerical simulation of wetland hydrodynamics. Environ Int 25:773–779. doi:10.1016/S0160-4120(99)00058-6
Stoesser T, Asce M, Kim SJ, Diplas P (2010) Turbulent flow through idealized emergent vegetation. J Hydraul Eng 136:1003–1017
Tanino Y, Nepf HM (2008) Laboratory investigation of mean drag in a random array of rigid, emergent cylinders. J Hydraul Eng 134:34–41
Thackston EL, Shields FD, Schroeder PR (1987) Residence time distributions of shallow basins. J Environ Eng 113:1319–1332. doi:10.1061/(ASCE)0733-9372(1987)113:6(1319)
Tilley DR, Brown MT (1998) Wetland networks for stormwater management in subtropical urban watersheds. Ecol Eng 10:131–158. doi:10.1016/S0925-8574(98)00010-X
Torrens A, Molle P, Boutin C, Salgot M (2009) Impact of design and operation variables on the performance of vertical-flow constructed wetlands and intermittent sand filters treating pond effluent. Water Res 43:1851–1858. doi:10.1016/j.watres.2009.01.023
Valiela I, Teal JM, Deuser WG (1978) The nature of growth forms in the salt marsh grass spartina alterniflora. Am Nat 112:461. doi:10.1086/283290
Werner TM, Kadlec RH (1996) Application of residence time distributions to stormwater treatment systems. Ecol Eng 7:213–234. doi:10.1016/0925-8574(96)00013-4
Wu W (2007) Computational river dynamics. CRC Press

Experimental Investigations on the Oxygen Transfer Efficiency at Low-Head Hydraulic Structures

Agnieszka Rajwa-Kuligiewicz, Robert J. Bialik and Paweł Rowiński

Abstract The aim of this work was to examine the oxygen transfer efficiency at two hydraulic structures located on the Narew and Wilga rivers in order to assess their impact on downstream oxygen conditions. This has been done through the continuous 'in situ' measurements of dissolved oxygen concentrations over 24-h periods of time above and below the considered structures. Simultaneous measurements have been taken in the river channel downstream of these structures. Gas transfer efficiencies and deficit ratios have been calculated according to the available formulae reported in the literature. The obtained transfer characteristics were compared with the results of shorter measurements carried out at the same structures, but under different oxygen deficits. Moreover, a brief discussion on the measurement techniques, gas transfer uncertainties and temperature correction factor is given.

1 Introduction

Hydraulic structures are important elements of water management playing a substantial role in flood protection, energy production, irrigation, transport and water supply. From the ecological point of view, these structures sustain high water quality and, thus, are also important in river restoration practices. The majority of experimental works on aeration characteristics of hydraulic structures have shown a considerable potential for the addition of dissolved oxygen (e.g., Gameson 1957;

A. Rajwa-Kuligiewicz (✉) · R.J. Bialik · P. Rowiński
Institute of Geophysics, Polish Academy of Sciences—Centre for Polar Studies KNOW (Leading National Research Centre), Księcia Janusza 64, 01-452 Warsaw, Poland
e-mail: arajwa@igf.edu.pl

R.J. Bialik
e-mail: rbialik@igf.edu.pl

P. Rowiński
e-mail: pawelr@igf.edu.pl

P. Rowiński and A. Marion (eds.), *Hydrodynamic and Mass Transport at Freshwater Aquatic Interfaces*, GeoPlanet: Earth and Planetary Sciences,
DOI 10.1007/978-3-319-27750-9_10

Butts and Evans 1978; Wilhelms et al. 1992; Chanson 1995; Gulliver et al. 1998), which is accomplished through the higher level of turbulence, energy dissipation and air bubble entrainment.

While other studies (e.g., Chanson 1994; Chanson and Toombes 2000; Witt and Gulliver 2012; Wüthrich and Chanson 2014) have focused on the aeration potential of these structures, developing transfer coefficients and formulae relating them to flow regimes and structure characteristics, this work concentrates on the behaviour of DO concentration on the particular structure and assesses the impact of this structure on downstream oxygen conditions. The aim of this study was to gather and quantify gas transfer characteristics of hydraulic structures under a small oxygen deficit. In this work we focused basically on small- and medium-sized hydraulic structures such as weirs and water steps.

2 Aeration Process

Hydraulic structures are places of high transfer of volatile gases such as oxygen, which can be expressed mathematically as

$$\frac{dC}{dt} = K_L a(C_s - C) \tag{1}$$

where K_L represents the reaeration coefficient, which is a constant independent of bubble size and flow (Kawase and Moo-Young 1992). K_L is multiplied by 'a' being a specific surface area (m^{-1}) or the interfacial surface area per unit volume of air and water. This parameter varies greatly depending on flow turbulence, air entrainment rate and interactions between both of them. However, it is still impossible to accurately estimate this area due to the dual interactions between interfacial properties and turbulence characteristics. Thus, the overall coefficient $K_L a$ is usually considered collectively.

According to the first equation, the transfer of oxygen at the air-water interface is primarily driven by the negative gradient of gas concentration known as the oxygen deficit, being the difference between saturation concentration (C_s) and oxygen concentration in water (C). Hydraulic structures usually increase oxygen saturation and minimize oxygen deficit. As a result, at both sides of the particular structure two different deficits can be observed.

Due to the short residence time of water at hydraulic structures, all sources and losses of oxygen can be neglected. Therefore, based on the upstream (C_{US}) and downstream (C_{DS}) concentrations of dissolved oxygen and their saturation concentration (C_s), the deficit ratio can be calculated according to the Gameson (1957) formula:

$$r = \frac{C_s - C_{US}}{C_s - C_{DS}} = exp\left[\int_{up}^{down} K_L a dt\right] \tag{2}$$

Finally, assuming that K_L remains constant over a hydraulic structure and C_s is constant with respect to time, the gas transfer efficiency ratio can be calculated by integrating Eq. 1 (Gameson 1957) which yields:

$$E = \frac{C_{DS} - C_{US}}{C_S - C_{US}} = 1 - \frac{1}{r} \tag{3}$$

Generally, the gas transfer efficiency ratio (E) is the capability of water to absorb oxygen from the air. However, it does not relate to the reverse process. The values of efficiency ratio (E) range from 0 to 1. For instance, the value of 1 means that all of upstream deficit was satisfied by the oxygen transfer and the downstream concentration is at saturation. When E equalled 0, no oxygen transfer was observed. Due to the fact that oxygen solubility is primarily dependent on water temperature, the aeration efficiency should be corrected by the temperature factor. So far, several temperature corrections have been developed, among them that proposed by Gulliver et al. (1990), which basically has a good precision in the temperature range from 0 to 40 °C:

$$E_{20} = 1 - (1 - E)^{\frac{1}{f}}; \quad f = 1 + \alpha(T - 20) + \beta(T - 20)^2 \tag{4}$$

where parameters $\alpha = 0.02103$, $\beta = 8.261 \times 10^{-5}$, E is the aeration efficiency at the water temperature of measurement and E_{20} is the aeration efficiency at 20 °C. Finally, the cumulative uncertainty analysis associated with E, to the 95 % confidence interval can be performed following Gulliver and Rindels' (1993) formula:

$$U_E = \frac{\left(W_{C_{DS}}^2 + (W_{C_{US}}(1 - E))^2 + (B_C E)^2 + (B_{Cs} E)^2\right)^{\frac{1}{2}}}{C_s - C_{US}} \tag{5}$$

where U_E represents total uncertainty in E, Wc_{US} and Wc_{DS} are the precision uncertainties in C_{US} and C_{DS}, respectively, B_C denotes bias uncertainty in the measurement of C_{US} and $C_{DS,}$ and B_{Cs} is the bias uncertainty in Cs.

3 Study Sites

Measurements have been conducted on two typical overflow structures. In such structures the undisturbed coherent jet carries small amounts of air into the tail basin. Basic hydraulic characteristics of rivers during the time of measurements are summarized in Table 1.

Table 1 Hydraulic characteristics of rivers behind the hydraulic structures

River	B (m)	H (m)	T (°C)	Q (m^3s^{-1})	U (ms^{-1})	Re	Fr
Wilga	9.5	0.5	5.5	1.16	0.25	12×10^4	0.17
Narew	15.0	2.5	13.0	5.32	0.17	51×10^4	0.05

B—width of the river, *H*—longitudinal mean flow depth, *Q*—discharge at the structure during the day of measurement, $Re = UH/v$—Reynolds number, $Fr = U(Hg)^{-0.5}$—Froude number

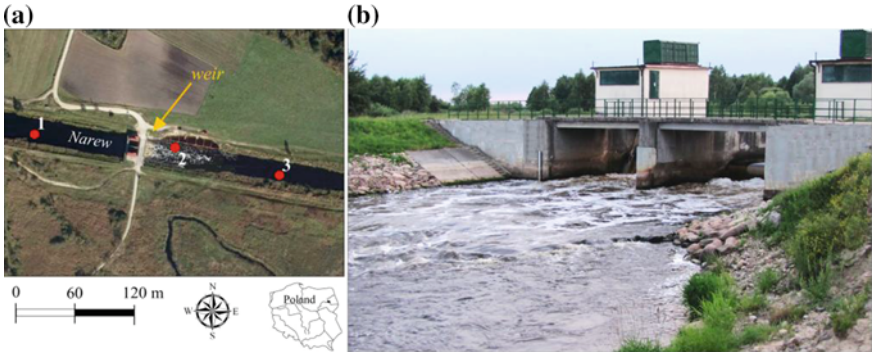

Fig. 1 Study site location (the Narew river)

The first structure was a rectangular weir located on the Narew river in Rzędziany village being the closing part of the Narew National Park (Fig. 1). The weir was built in order to maintain the fluvial system of the anastomosing river and provide optimal irrigation of marshes. Simultaneously, this weir is a part of the water trail from Rzędziany to Wizna villages with other five structures. The weir in Rzędziany is a typical overflow structure with a single plough-shaped divider. The weir is broad crested and has a free overfall with an unventilated, adhering jet (Fig. 1b).

The second structure discussed in this work was a small water step in a regulated channel of the Wilga river situated about 50 km south of Warsaw (Fig. 2). The channel is located in the outlet part of the river. It is about 3.5 km long broad-crested sloping channel ended with a small water step of trapezoidal shape, which is followed by an armoured dissipation basin (approx. 50 m^2).

The discharge, bathymetry and velocity field in cross-sections (Fig. 3a, b) before the structures were obtained using an acoustic Doppler current profiler (ADCP RiverSurveyor S5, manufactured by SonTek) equipped with an echo-sounding system, working at the frequency of 1 MHz and accuracy of 1 % of measuring values. Figure 3a shows a window of the weir with blank cells in the middle of cross section representing a pillar dividing the weir into two parts. Moreover, the areas of stagnant water before the concrete walls are visible at the edges of the profile. Figure 3b shows the cross-sectional profile of the channel before the water step with a visible area of increased velocities.

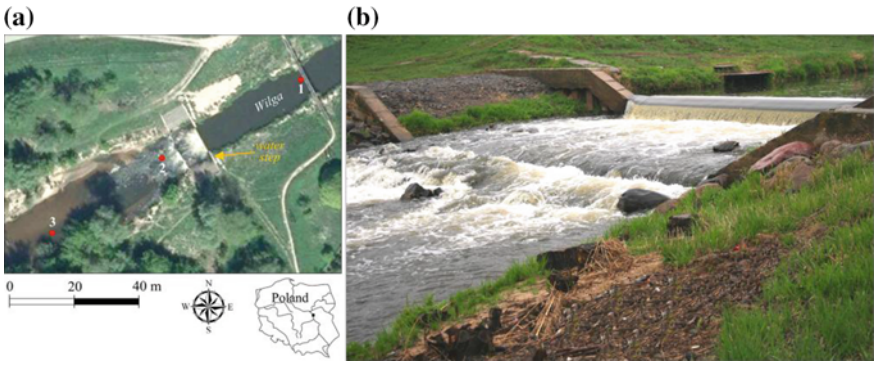

Fig. 2 Study site location (the Wilga river)

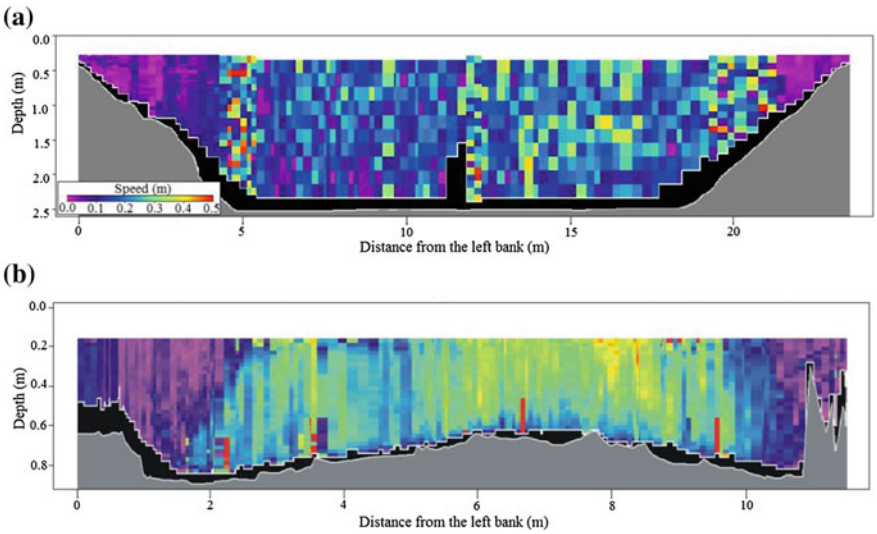

Fig. 3 Flow structure and bathymetry before the weir (**a**) and water step (**b**)

4 Instrumentation and Study Design

Field measurements were conducted between May and November 2014. In the present study, dissolved oxygen (in mg dm^3 and % of saturation), water temperature and air pressure were measured continuously over 2 days at 1-min time intervals using three DO meters manufactured by YSI, Yellow Springs. Two of them were equipped with optical sensors, and one was galvanic. The accuracy of these instruments was 0.1 and 0.2 mg dm^3 of a measured value for optical and galvanic sensors, respectively. All instruments were calibrated prior to deployment at 100 % water saturated air and several measurements were taken simultaneously at one spot

with all sensors to ensure that recordings are within acceptable measurement error margins. Once we ensured the recordings were correct, sensors were placed at a medium depth approximately in the middle of the river channel: the first of them was installed behind the structure, the second one directly below the structure near the plunge pool and the last one was placed at a certain distance from the structure (see Figs. 1 and 2). The location of sensors was intentional as they should demonstrate three stages involved in the oxygen transfer process. The first stage (1st station upstream) refers to molecular diffusion resulting from concentration gradients (initial oxygen deficit), which initially controls the oxygen transfer into the water. The second step (2nd station downstream) refers to the transport of oxygen through the liquid interface film by the turbulent mixing. Herein, the interface film is broken and the absorption of oxygen is controlled by the surface renewal rate. The rate of renewal of the film determines the frequency at which liquid with an oxygen concentration replaces that from the interface with an oxygen concentration at saturation (C_s). The last stage (3rd station downstream) refers to the transfer of oxygen to the bulk of the liquid by diffusion and convection. In contrast to the first two stages, where the hydrodynamics of water play a substantial role, the last stage is essentialy dependent on water quality parameters such as initial DO deficit, water temperature or pH.

For the purpose of this study, recordings from a 24-h period of time were selected from the whole dataset. During this period the weather was stable and the flow was nearly stationary. These measurements provided further a means by which transfer efficiences were calculated.

5 Results

During the measurements the oxygen deficit was positive, ranging from 0.1 to 2.0 mg dm^3, meaning the under-saturation of water with dissolved oxygen. Figures 4 and 5 show diurnal curves of DO concentration obtained from DO meters placed at three different locations upstream and downstream of the structures. It is clearly visible that both structures substantially increased the oxygen content. However, these differences are much more pronounced in terms of saturation values. Moreover, small diurnal fluctuations of DO resulting from the day-night cycle are visible not only before the structure but also for other two locations downstream. Finally, it is noteworthy that considered structures increase oxygen concentration only locally, but have little effect on the overall oxygenation of rivers.

The fluctuations in the oxygen transfer efficiency ratio for weir and water step corrected for the temperature factor are presented in Fig. 6a, b. The application of the temperature correction factor arises from the fact that the aeration efficiency is primarily dependent on water temperature (Gulliver et al. 1990; Gameson 1957; Demars and Manson 2013). However, as noticed by Markofsky and Kobus (1978), the aeration efficiency for laboratory models and small streams such as the Wilga

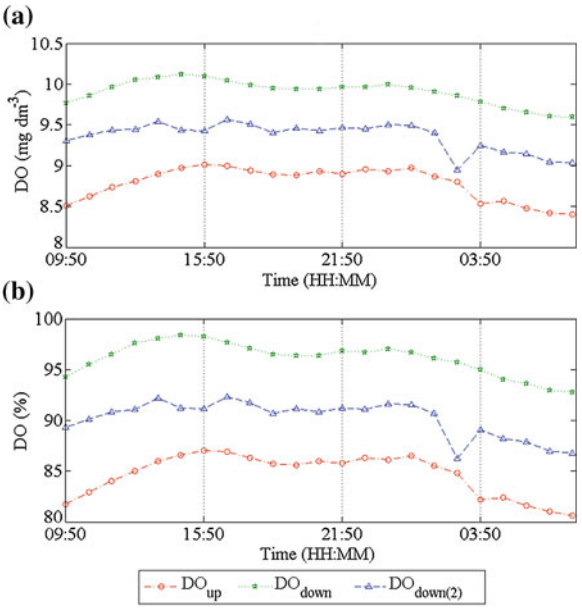

Fig. 4 Dissolved oxygen curves: **a** DO concentration, **b** DO saturation (weir on the Narew river)

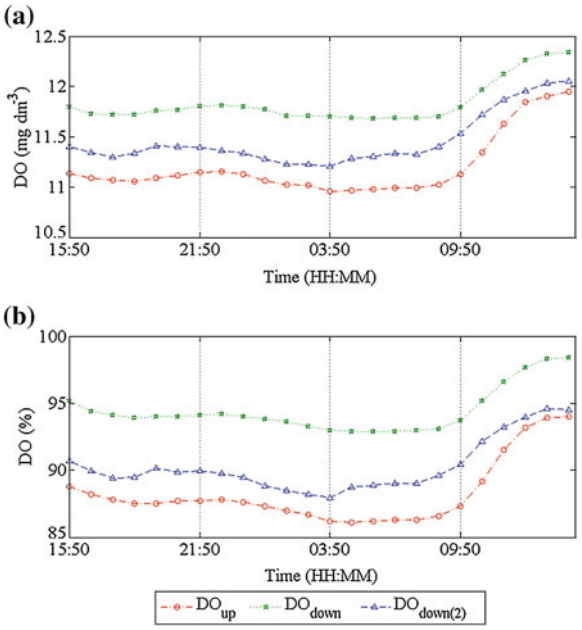

Fig. 5 Dissolved oxygen curves: **a** DO concentration, **b** saturation (water step on the Wilga river)

river ($Re < 5 \times 10^5$) is not only the function of water temperature but also the function of Reynolds and Froude numbers, whereas for the highly turbulent jets like in the Narew river ($Re > 5 \times 10^5$), it just depends on the Froude number.

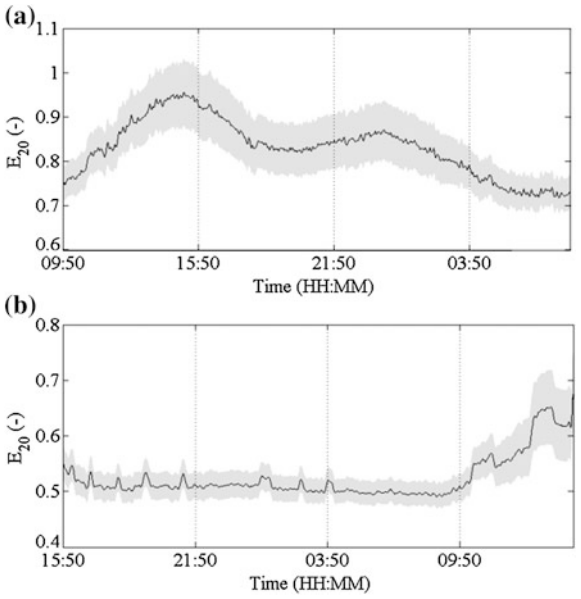

Fig. 6 Gas transfer efficiency fluctuations over time (*black line*) with uncertainty (*grey area*): **a** weir on the Narew river, **b** water step on the Wilga river

The gas transfer efficiency obtained directly from oxygen concentration values is an important measure when it comes to the prediction of rivers' oxygenation downstream of the structure. More importantly, because all of the predictive equations developed for oxygen transfer at hydraulic structures are conceptual and based on empirical relationships (Gulliver et al. 1998). It is also noteworthy, that the calculated transfer efficiency of oxygen can be easily transferred to other gases and vice versa through the indexing method developed by Gulliver et al. (1990).

It is visible (Fig. 6) that under the same river discharge and head loss of the structure, the transfer efficiency of the weir varies from 0.72 to 0.97, whereas for the water step it ranges from 0.48 to 0.68. The results indicated that the oxygen transfer efficiency was strongly affected by the flow regime. Due to the different mechanisms of air entrainment in the nappe, transition and skimming flow regimes, the aeration efficiency observed at these structures differ from each other. The efficiency of the gas transfer at the water step results from smaller discharge, low tail-water depth and the presence of the armoured basin behind the construction, which increases the specific surface area and enhances free-surface aeration. This process might exert a major control on gas transfer at the water step.

On the contrary, higher head loss and tailwater depth seem to be crucial for the gas transfer at the weir. Apparently, high tailwater depth is more effective than shallow tailwater in the armoured basin, in terms of aeration. As reported by Avery and Novak (1978) the transfer efficiency reaches the highest level when the tailwater depth equals 0.6 times the drop height. This can be explained by the fact that in deep tailwater, a greater amount of air is carried underwater and remains underwater for a relatively long time. According to Unsal (2010), the oxygen mass

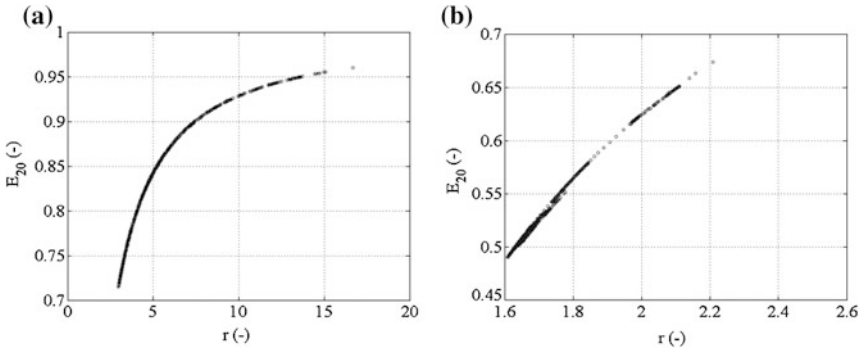

Fig. 7 Scatter plots of E_{20} versus deficit ratio: **a** weir, **b** water step

transfer is directly affected by the residence time of entrained air bubbles. Moreover, as pointed by Gulliver et al. (1997), a higher discharge increases effective bubble depth, as long as it becomes limited by the depth of dissipation basin. However, in such cases, the free-surface aeration can be substantially reduced (Chanson 1995). On the whole, the weir has significantly higher gas transfer efficiency than the water step resulting from the flow regime on that structure. Noticeably, the flow regime strongly affects the oxygen transfer.

Finally, it is worth adding that under a high deficit ratio a higher transfer efficiency is observed (Fig. 7a, b). The results have shown that the deficit ratio for the weir was higher than for the water step. Assuming that the equilibrium concentration is at atmospheric pressure and the oxygen deficit is relatively small, the transfer efficiency is a function of an initial oxygen deficit (Fig. 8a, b). However, this observation is really rare as usually the transfer efficiency is directly proportional to the initial oxygen deficit.

Our results show an ambiguous region on the variable plot. Apparently, it can be explained by the insufficient oxygen deficit upstream of the structure. Thus,

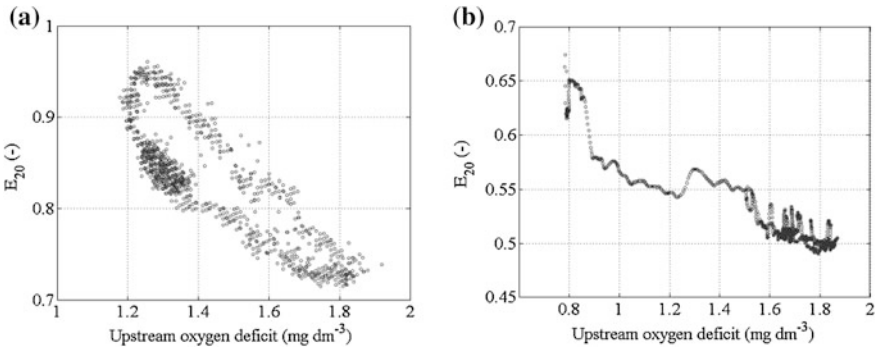

Fig. 8 Scatter plots of E_{20} versus upstream oxygen deficit: **a** weir, **b** water step

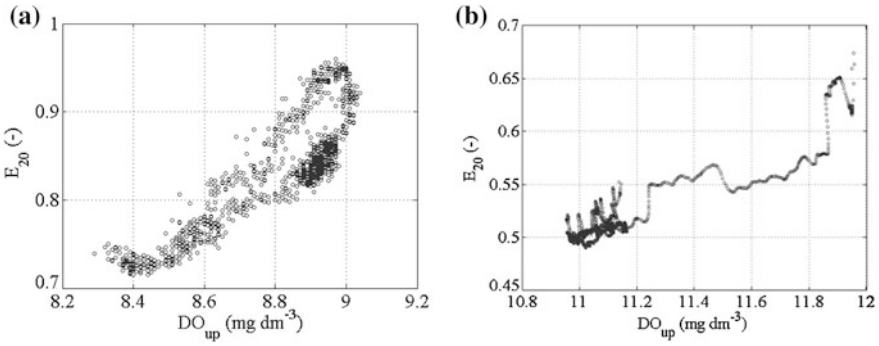

Fig. 9 Scatter plots of E_{20} versus upstream DO concentration: **a** weir, **b** water step

paradoxically, the gas transfer efficiency appeared to be a function of the upstream DO concentration (Fig. 9). According to Gulliver and Wilhelms (1992) an upstream oxygen deficit greater than 2.5 mg dm^{-3} is usually required for accuracy in the measurement of oxygen-transfer efficiency, otherwise tracer methods should be applied.

In order to evaluate DO variance distribution in the frequency domain, the DO fluctuations were analysed using the power spectral density (PSD). The results of spectral analysis of DO time curves have shown that at higher frequencies the noise greatly affects the shape of the estimated spectra (Fig. 10). In the PSD of the downstream DO concentration (Fig. 10a) two slopes can be distinguished. In the low-frequency range, the DO spectra for the weir (DO_{down}) show a sharp decay resembling power function behaviour. Noticeably, the decaying range of the PSD of the downstream oxygen concentration (Fig. 10a) can be roughly approximated by a −5/3 slope. Apparently, the DO fluctuations experienced downstream of the weir can be related to the surrounding flow structures, i.e., turbulent vortices.

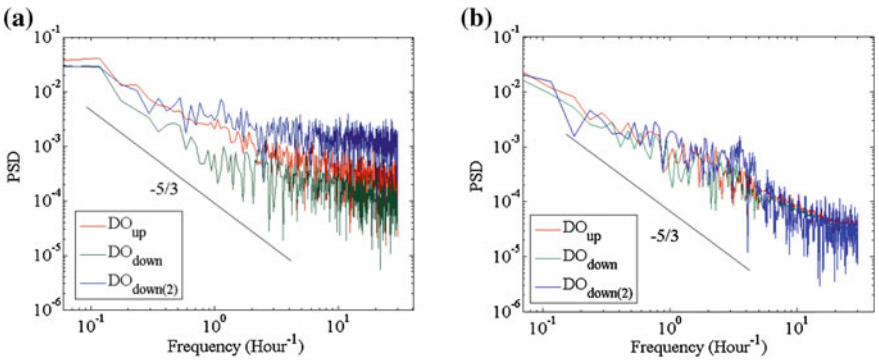

Fig. 10 Power spectral density of DO time curves: **a** weir, **b** water step

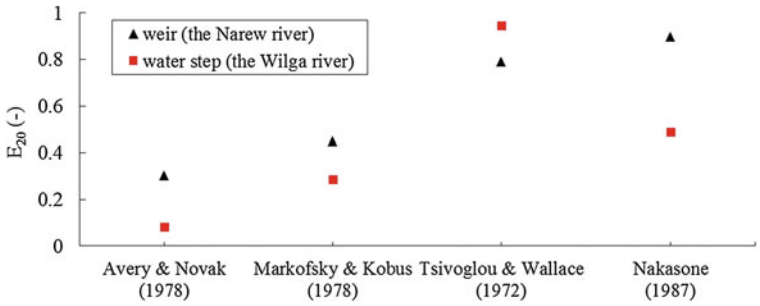

Fig. 11 Aeration efficiencies derived from predictive equations

Finally, the aeration efficiencies of weir and water step calculated according to the chosen predictive equations (Avery and Novak 1978; Markofsky and Kobus 1978; Tsivoglou and Wallace 1972; Nakasone 1987) are displayed in Fig. 11. In contrast to the Gameson formula (1957), which takes into account oxygen concentrations upstream and downstream of the particular structure, these equations incorporate only hydraulic properties of the jet and flow regime, such as head loss, minimum velocity required to entrain air, critical water depth, Froude and Reynolds number of the jet. The results show a relatively high discrepancy between those methods, indicating that the applicability of existing formulae is rather limited and strongly dependent upon detailed estimations of parameters of the jet.

6 Discussion

On the basis of data collected at the experimental structures, aeration characteristics have been assessed. Paradoxically, due to the low initial oxygen deficit upstream of the structure, transfer efficiency was a function of the upstream DO concentration (Gulliver et al. 1997). Since no other data are available for these structures, it is suggested that the values obtained from this study can be accepted as being valid only for these structures. Moreover, the calculated efficiency ratio should be verified in order to predict oxygen concentration downstream of the structure.

Although in the literature there is evidence to suggest that maximum aeration depends on the height of the structure, our results, however, suggest that the efficiency of structure might vary substantially under the constant height. This can be explained by the fact that the inflowing water exhibits the daily changes of DO resulting from the diurnal cycle of biological processes such as photosynthesis and respiration. However, this effect can solely be observed basing on continuous in situ measurements. From this point of view, field measurements provide the most accurate way to quantify the gas transfer characteristics of hydraulic structures.

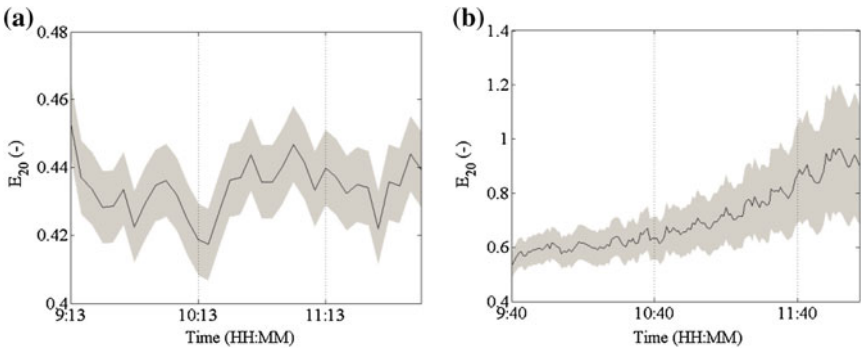

Fig. 12 Gas transfer efficiency fluctuations over time (*black line*) with uncertainty (*grey area*): **a** weir on the Narew river, **b** water step on the Wilga river

For comparative purposes, the results of gas transfer obtained at the same structures, under different oxygen deficit, are presented in Fig. 12a, b. In the first case (Fig. 12a) the discharge was 3 times higher, ~ 16.8 m^3 s^{-1}, and the initial oxygen deficit upstream of the weir remained nearly constant, ~ 4 mg dm^{-3}. In the second case (Fig. 12b) the discharge was ~ 1.2 m^3 s^{-1}, and the initial oxygen deficit upstream of the water step ranged from 0.4 to 1 mg dm^{-3}. It is visible that, under a smaller initial oxygen deficit and similar discharge, the water step exhibited higher aeration efficiency than the weir. However, the result is burdened with a high degree of uncertainty.

7 Conclusions

Transfer efficiencies of the considered hydraulic structures can be calculated with a fair degree of accuracy. The results revealed that weir was more efficient at transferring dissolved oxygen than the water step. As expected, the weir produced more turbulence increasing the transfer efficiency. The results indicated that hydraulic structures such as water steps and weirs elevate DO concentrations downstream and attenuate daily variations of DO resulting from the changes of water temperature and biological activity. Moreover, our findings have shown that the transfer efficiency ratio varies within each day depending on the oxygen deficit of the inflowing water. Thus it has been suggested that these variations should be taken into account when predicting downstream oxygen concentration.

Acknowledgments Funding for this research was provided in part by the Institute of Geophysics of the Polish Academy of Sciences through the project for Young Scientists No. 500-10-16 and by the Ministry of Sciences and Higher Education within statutory activities No. 3841/E-41/S/2015. Agnieszka Rajwa-Kuligiewicz gratefully acknowledges the financial support from the Interdyscyplinary Polar Studies.

References

Avery ST, Novak P (1978) Oxygen transfer at hydraulic structures. J Hydr Div 104(11):1521–1540
Butts TA, Evans RL (1978) Effects of channel dams on dissolved oxygen concentrations in Northeastern Illinois streams. Circular 132, Illinois State Water Survey, Urbana, IL
Demars BOL, Manson JR (2013) Temperature dependence of stream aeration coefficients and the effect of water turbulence: a critical review. Water Res 47:1–15
Chanson H (1994) Hydraulics of skimming flows over stepped channel and spillways. J Hydraul Res 32(3):445–460
Chanson H (1995) Predicting oxygen content downstream of weirs, spillways and waterways. Proc Instn Civ Engrs Wat Marit Energy 112:20–30
Chanson H, Toombes L (2000) Discussion of stream reaeration in nonuniform flow: macroroughness enhancement. J Hydraul Eng 126(3):222–224
Gameson ALH (1957) Weirs and the aeration of rivers. J Inst Water Eng 11(6):477–490
Gulliver JS, Rindels AJ (1993) Measurement of air-water oxygen transfer at hydraulic structures. J Hydraul Eng 119(3):327–349
Gulliver JS, Wilhelms SC (1992) Discussion of 'Aeration at Ohio river basin navigation dams', by SF Railsback, JM Bownds, MJ Sak, MM Stevens and GH Taylor. J Environ Eng 108 (3):444–446
Gulliver JS, Thene JR, Rindels AJ (1990) Indexing gas transfer in self-aerated flows. J Environ Eng 116(3):503–523
Gulliver JS, Hibbs DE, McDonald JP (1997) Measurement of effective saturation concentration for gas transfer. J Hydraul Eng 123:86–97
Gulliver JS, Wilhelms SC, Parkhill KL (1998) Predictive capabilities in oxygen transfer at hydraulic structures. J Hydraul Eng 124(7):664–671
Kawase Y, Moo-Young M (1992) Correlations for liquid-phase mass transfer coefficients in bubble column reactors with Newtonian and non-Newtonian fluids. Can J Chem Eng 70(1):48–54
Markofsky M, Kobus H (1978) Unified presentation of weir aeration data. J Hydr Div 104:562–568
Nakasone H (1987) Study of aeration at weirs and cascades. J Environ Eng 113(1):64–81
Tsivoglou EC, Wallace JR (1972) Characterization of stream reaeration capacity. EPA-R3-72-012, US EPA, Washington, DC
Unsal M (2010) Modeling of penetration depth of air bubbles entrained by sharp crested weirs using ANFIS. Int J Phys Sci 5(5):507–517
Wilhelms SC, Gulliver JS, Parkhill K (1992) Reaeration at low-head hydraulic structures. W-93-2, US Army Engineer Waterways Experiment Station, Vicksburg, MS
Witt AM, Gulliver JS (2012) Predicting oxygen transfer efficiency at low-head gated sill structures. J Hydraul Res 50(5):521–531
Wüthrich D, Chanson H (2014) Hydraulics, air entrainment, and energy dissipation on a Gabion stepped weir. J Hydraul Eng 140(9):04014046

Effect of Aquatic Plant Patches on Flow and Sediment Characteristics: The Case of *Callitriche platycarpa* and *Elodea nuttallii*

Sofia Licci, Cécile Delolme, Pierre Marmonier, Marc Philippe, Loreta Cornacchia, Vanessa Gardette, Tjeerd Bouma and Sara Puijalon

Abstract In lotic ecosystems, submerged aquatic vegetation has important effects on hydrodynamic and sediment processes. These effects depend on plant morphology and patch structure. This study aimed to test the effect of 2 aquatic plant species on flow and sediment characteristics. For this purpose we measured under natural conditions 3D velocity profiles and sediment characteristics along the main axis of one patch of each species. The 2 species presented contrasting effects on velocity, turbulence profiles and sediment characteristics: one species had significant effects on hydrodynamics and accumulation of fine sediment also further downstream of the patch, whereas the second one accumulated very fine sediment mainly in the upstream half of the patch. These results emphasize the role of plant morphology on hydrodynamics and sediment physic-chemical characteristics.

1 Introduction

In freshwater lotic environments, interfaces between biota and sediment or flow are recognised as important regions where many critical biophysical processes occur, as recently reviewed by Marion et al. (2014). Particularly, complex and fundamental physical and biogeochemical processes occur at the plants-water-sediment interfaces (Carpenter and Lodge 1986). For instance, rooted submerged plants reduce velocity and increase sedimentation inside plant patches, and some species are able

S. Licci (✉) · C. Delolme · P. Marmonier · V. Gardette · S. Puijalon
UMR 5023 LEHNA, CNRS, Université Lyon 1, ENTPE, Villeurbanne, France
e-mail: sofia.licci@univ-lyon1.fr

M. Philippe
UMR 5276, CNRS, Université Lyon 1, Villeurbanne, France

L. Cornacchia · T. Bouma
Royal Netherlands Institute for Sea Research (NIOZ-Yerseke), Yerseke, The Netherlands

P. Rowiński and A. Marion (eds.), *Hydrodynamic and Mass Transport at Freshwater Aquatic Interfaces*, GeoPlanet: Earth and Planetary Sciences,
DOI 10.1007/978-3-319-27750-9_11

to oxygenate the substrate, influencing the microbial activity and hence the biogeochemical processes in the sediment. Submerged plants also induce important modification of flow conditions, acting as ecosystem engineers (*sensu* Jones et al. 1994) and increasing structural complexity and heterogeneity of lotic ecosystems. Plant patches behave as porous walls: on the one hand, they form an obstacle deviating the flow above and towards the sides of the canopy, locally increasing the velocity, whereas, on the other hand, the flow going through the patch shows a reduced velocity (Sand-Jensen and Mebus 1996; Sand-Jensen and Pedersen 2008, Vandenbruwaene et al. 2011). Consequently, the near-bed velocity, shear stress (James et al. 2004) as well as turbulence are significantly reduced inside the patches.

The changes in hydrodynamic conditions due to flow-plant interactions have indirect cascading effects on sediment dynamics: potential of resuspension and erosion are reduced, favouring sedimentation and reducing water turbidity (Hendriks et al. 2009; Sand-Jensen 1998; Schulz et al. 2003). Submerged plants also induce direct trapping of suspended particles and transported in bed-load through collisions with stem and leaf surfaces (Hendriks et al. 2008; Pluntke and Kozerski 2003). As a consequence, sediment accumulates inside the vegetation patches, with an increased proportion of fine particles compared to non-vegetated areas (Sand-Jensen 1998; Schoelynck et al. 2013).

The effect of aquatic plants on flow and sediment deposition depends on plant morphology and patch structure. For instance, species with dense canopies, as *Callitriche cophocarpa* Sendtn. and *Elodea canadensis* Michx., induce a high reduction of flow velocity inside their patches, increasing sediment retention (Sand-Jensen 1998; Sand-Jensen and Mebus 1996). On the contrary, species with open canopy, as *Sparganium emersum* Rehmann, have less impact on flow and sediment dynamics (Sand-Jensen 1998; Sand-Jensen and Mebus 1996). Plant flexibility also influences the interactions: reconfiguration of flexible plants minimizes the surface area in contact with water, reducing the resistance to flow (Miler et al. 2012; O'Hare et al. 2007; Sand-Jensen 2003). At the plant level, the leaf area index (*i.e.* the ratio of leaf surface area to the ground area covered by the plant canopy) is an example of morphological traits that have been demonstrated to have a significant effect on the amount of fine sediment accumulated in submerged patches (Petticrew and Kalff 1992). However, only a few studies (Sand-Jensen 1998) have investigated simultaneously the effect of different plant morphologies on both flow and sediment characteristics (e.g. grain size, organic matter content, nutrient content …). Sand-Jensen (1998) has analysed the effect of vegetation patches only on the streamwise component of velocity, although the flow can also impacted on the lateral and vertical components.

The objective of the present study was to evaluate the effects of 2 submerged plant species having contrasting morphologies on different directional components of flow velocity and sediment characteristics. For this purpose, we carried out an in situ investigation of natural patches, combining 3D velocity, sediment grain size distribution and organic matter content measurements. An interdisciplinary

approach was applied for this study, as it is recognised fundamental to fully understand plants-water-sediment interactions (Marion et al. 2014). These complex interactions were then addressed and presented in an ecological perspective.

2 Materials and Methods

2.1 Study Sites and Plant Species

The study was conducted in two drainage channels of the Upper Rhône River (France), near the localities of Brégnier-Cordon (45° 38' 43''N, 5° 36' 29''E) and Peyrieu (45° 40' 46''N, 5° 42' 3''E). Drainage artificial channels were selected because they present uniform structure (cross-section, water depth) with long straight sections and natural colonization by submerged aquatic vegetation. The 2 channels presented similar length (2.1 and 2.8 km for Brégnier-Cordon and Peyrieu channels, respectively), width (6.0–8.0 m) and depth (0.6–0.7 m). These channels are fed by Rhône river seepage and hillslope aquifers. Cover by aquatic vegetation ranges from 30 to 90 % depending on season and channel section. The most abundant submerged species are *Callitriche platycarpa* Kütz., *Berula erecta* (Huds.) Coville, *Myriophyllum spicatum* L. and *Groenlandia densa* (L.) Fourr. in the site of Brégnier-Cordon, and *Veronica anagallis-aquatica* L. and *Elodea nuttallii* (Planch.) St.-John in the site of Peyrieu.

We selected two species with contrasting morphology and patch architectural structure: *Callitriche platycarpa* and *Elodea nuttallii*. *C. platycarpa* has thin, flexible and highly branched stems that can be 10–200 cm long (Tison and de Foucault 2014) and is heterophyllous: submerged leaves are opposite (*i.e.* two leaves per node), linear to narrowly oblanceolate and emergent ones are rhomboidal to obovate. At shoot apex, leaves get densely packed at the apex other forming a rosette. Plants of *C. platycarpa* tend to be organized in elliptic patches as flow pushes downstream the long stems generating an overhanging canopy. Patches are dense as stems get entangled, with most of the biomass concentrated in the upper part of the canopy. *E. nuttallii* has relatively rigid stems, 10–50 cm up to 150 cm long (Tison and de Foucault 2014), with few or no ramifications. Stems present three-leaved whorls densely packed and distributed almost uniformly along all their length. Patches of *E. nuttallii* are dense and compact with an elongated shape in direction of the flow and do not present an overhanging canopy.

2.2 Field Sampling

During summer 2014, one patch of *C. platycarpa* was sampled in Brégnier-Cordon and one patch of *E. nuttallii* in Peyrieu. These patches were selected because they

presented similar lengths (respectively 1.6 and 1.3 m) and were located as far as possible from the channel banks and from other patches to avoid hydrodynamical interferences.

For each patch, coupled measurements of hydrodynamics and sediment collection were carried out at five sampling points all along its central axis (2 outside and 3 inside plant patch). The 2 sampling points outside the patch were located approximately 1 m upstream from its leading edge (U) and 1 m downstream its rear edge (D). The 3 sampling points inside the patch were located at 10, 50, and 90 % of the canopy length. For each position, the velocity profile was measured and a core of sediment was collected (5 cm in diameter and 10 cm deep).

2.3 Velocity Profiles

Velocity vertical profiles were measured using a 3D Acoustic Doppler Velocimeter (ADV) (FlowTracker Handheld-ADV, SonTek). Vertical profiles consisted in depth steps of less than 12 cm, reduced to 1–4 cm near plants-water-sediment interfaces. For technical reasons, measurements closest to the sediment (near-bed) were taken at 4 cm above the channel bed. Velocity was recorded over 100 s at 1 Hz. For each component of velocity (streamwise, u; spanwise, v; vertical, w), mean velocity profiles $(\overline{u}, \overline{v}, \overline{w})$ were obtained and the turbulence intensity was quantified as the velocity variation around the mean (standard deviation). Standard deviation was then divided by the mean velocity to calculate the relative turbulence intensity.

2.4 Sediment Characterisation

The collected sediment cores were stored at 4 °C until measurements. To perform grain size analyses, sediments were wet sieved with distilled water at 1.6 mm and then dried at 70 °C for 48 h, to allow sample conservation until analyses were completed. Grain size analyses of sediment were carried out in aqueous phase by laser diffractometry, using a Malvern Mastersizer 2000 G (diameter range: 0.01–2000 μm). The analytical model used is based on the Frauhofer theory and considers particles equal to spheres. Prior to the measurements, sediments were exposed to a treatment of ultrasound for 2 min to destroy the aggregated particles developed during the drying process, necessary for the preservation of the samples. The results of the analysis were displayed as grain size distributions curves. The mode of the curve indicates the most abundant grain size in volumic percentage present in the sample. The curves were then transformed in cumulative curves and the percentile values $d_{0.1}$, $d_{0.3}$, $d_{0.5}$ were calculated (maximum diameter corresponding to 10, 30 and 50 % of particle volume). The 3 values were correlated and only the percentile value $d_{0.3}$ was kept for analyses.

Finally, organic matter content was measured by weight loss after ignition at 550 °C for 2 h.

All the measurements were triplicated for each sample.

For each species, comparisons of sediment parameters relative to different positions were tested by one-way ANOVA, followed by a post hoc Tukey HSD correction. Linear regressions were performed to test the correlation between flow (near-bed velocities and relative turbulence intensities) and sediment parameters (grain size and organic matter content).

3 Results

3.1 Velocity Profiles

Both species presented a different pattern of canopy height: the canopy height was relatively constant all over the patch length for *E. nuttallii*, whereas for *C. platycarpa* the canopy height gradually increased from the upstream to the downstream part of the patch (Fig. 1). For both species, velocity profiles upstream plant patch (U position) presented a steep decrease in streamwise velocity ($\overline{u}$) near the flow-sediment interface (Fig. 1). The profiles were more linear than logarithmic. For both species, the profiles downstream the patches (D position) were very similar to the upstream ones, except regarding the higher variability observed for *C. platycarpa.* For both species, $\overline{u}$ decreased immediately above the canopy, reaching approximately 0 within the canopy.

Profiles of mean spanwise velocity ($\overline{v}$) showed little variation for *E. nuttallii*, with values ranging between 0 and 0.01 m s^{-1}. For *C. platycarpa,* $\overline{v}$ increased above the canopy at the 50 and 90 % sampling points, due to flow deviation. At the D position, the velocity profile was more similar to the 90 % profile than to the U one but with a much higher variability.

For *E. nuttallii*, the $\overline{w}$ slightly increased above the canopy at the 10 % position, due to upwelling, whereas at the 90 % position $\overline{w}$ became negative, due to downwelling. For *C. platycarpa*, $\overline{w}$ profiles were similar along its axis and presented mainly negative values, except a slight increase just above the canopy, at the 90 % position. At the D position, the velocity profile was very similar to the 90 % profile but with a higher variability.

For each direction and species, relative turbulence intensity increases at the flow-canopy and flow-sediment interfaces (Fig. 2). In the streamwise direction, relative turbulence intensity was higher for *E. nuttallii* than for *C. platycarpa*. The highest relative turbulence intensity was observed in the streamwise direction for *E. nuttallii*, and in the spanwise direction, above the canopy, for C. *platycarpa.*

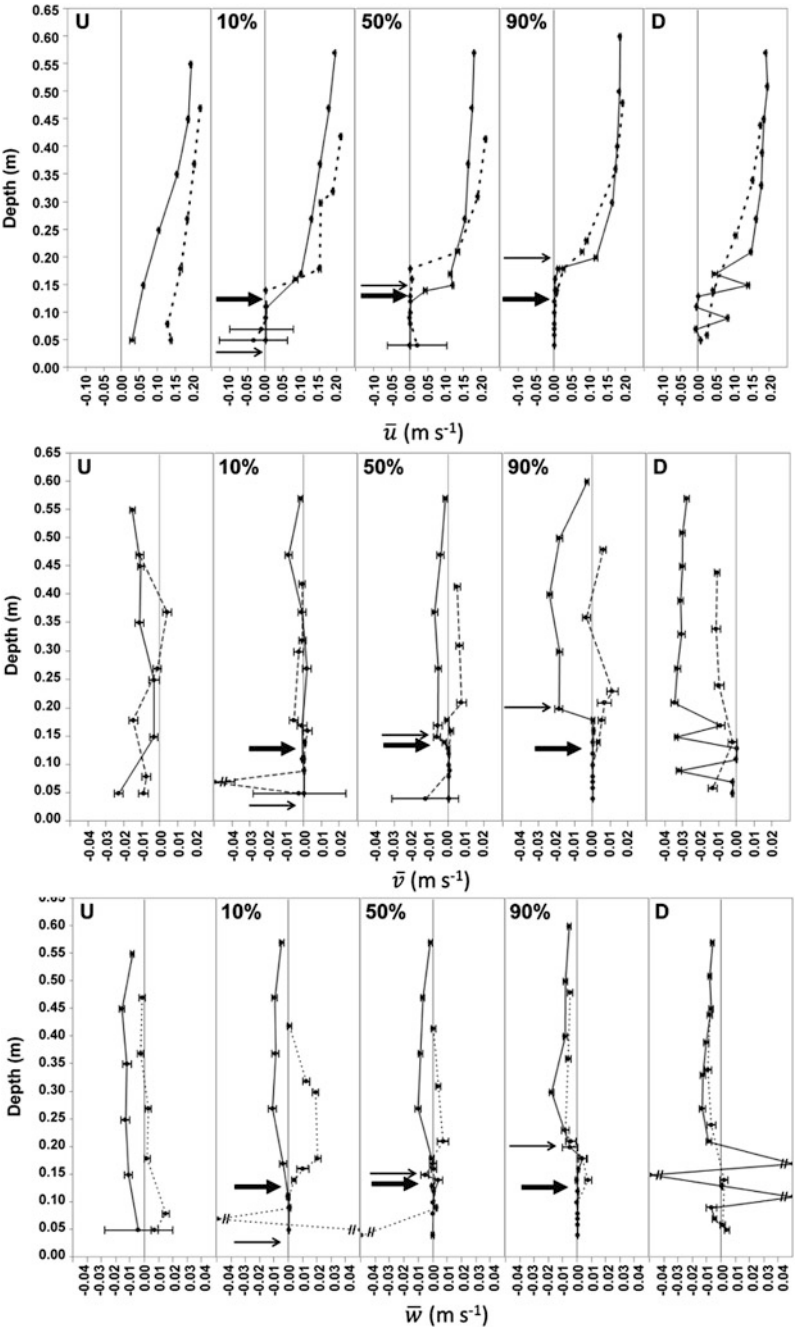
U
10%
50%
90%
D
Depth (m)
$\bar{u}$ (m s^{-1})
$\bar{v}$ (m s^{-1})
$\bar{w}$ (m s^{-1})

◀ **Fig. 1** Mean vertical profiles of the three components of velocity $(\overline{u}, \overline{v}, \overline{w})$ for *E. nuttallii* (*dashed line*) and *C. platycarpa* (*solid line*), in the positions upstream (*U*), inside the patch at 10, 50 and 90 % of its length and downstream (*D*). The *thick* and *thin arrows* indicate the height of the patch for *E. nuttallii* and *C. platycarpa,* respectively

3.2 Sediment Characterisation

The grain size distribution curves were overall different for each species (Fig. 3). For *E. nuttallii*, two main modes were observed in each sampling position: a main mode around 350 µm and a secondary one around 60 µm. The sediment in the D position was the coarsest with a very homogeneous particle size around 450 µm. For *C. platycarpa*, the sediments texture was distributed around one main mode. The upstream sediment was the coarsest (main mode around 350 µm), whereas the sediment collected in the others positions were enriched in fine particles leading to an increase of particles with a silty texture (20–100 µm).

The two species presented different patterns of accumulation of fine sediment. For *E. nuttallii*, it decreased from the upstream position to a minimum at the 50 % position and then increased to a maximum reached at the D position (Fig. 4). For *C. platycarpa,* the $d_{0.3}$ was significantly higher at the U position than at all other positions.

No positive relationship was found between near-bed velocity $(\overline{u}, \overline{v}, \overline{w})$ and $d_{0.1}$ and $d_{0.3}$ for both species, whereas a positive linear relation was found between near-bed vertical relative turbulent intensity and $d_{0.3}$ (*E. nuttallii* $r^2 = 0.82$, $p < 0.05$; *C. platycarpa* $r^2 = 0.77$, $p = 0.05$).

The organic matter content ranged between 0.97 and 6.18 % of dry mass for *E. nuttallii*, and between 1.33 and 2.78 % for *C. platycarpa* (Fig. 5). For *E. nuttallii*, the organic matter content was maximal at the 50 % position and minimal at the D one. For *C. platycarpa*, the organic matter content was generally significantly higher within (10, 50 or 90 %) and downstream the patch. Organic matter tended to be inversely related to $d_{0.3}$ for both species (linear regression, $r^2 = 0.89$, $p = 0.01$, for *C. platycarpa* and $r^2 = 0.78$, $p = 0.06$, for *E. nuttallii*).

4 Discussion

In accordance with our expectations, the present results demonstrated that the two species had different effects on hydrodynamics, probably due to their differences in morphology and patch structure. *E. nuttallii* had a uniform canopy height and relatively rigid stems and deviated the flow towards the surface at the beginning of the patch, and then towards the streambed at the end of the patch. The upstream flow conditions were mainly restored downstream the patch. Relative turbulence intensity was higher inside the canopy and especially at the sediment-flow and canopy-flow interfaces. On the contrary, *C. platycarpa* had gradually increasing

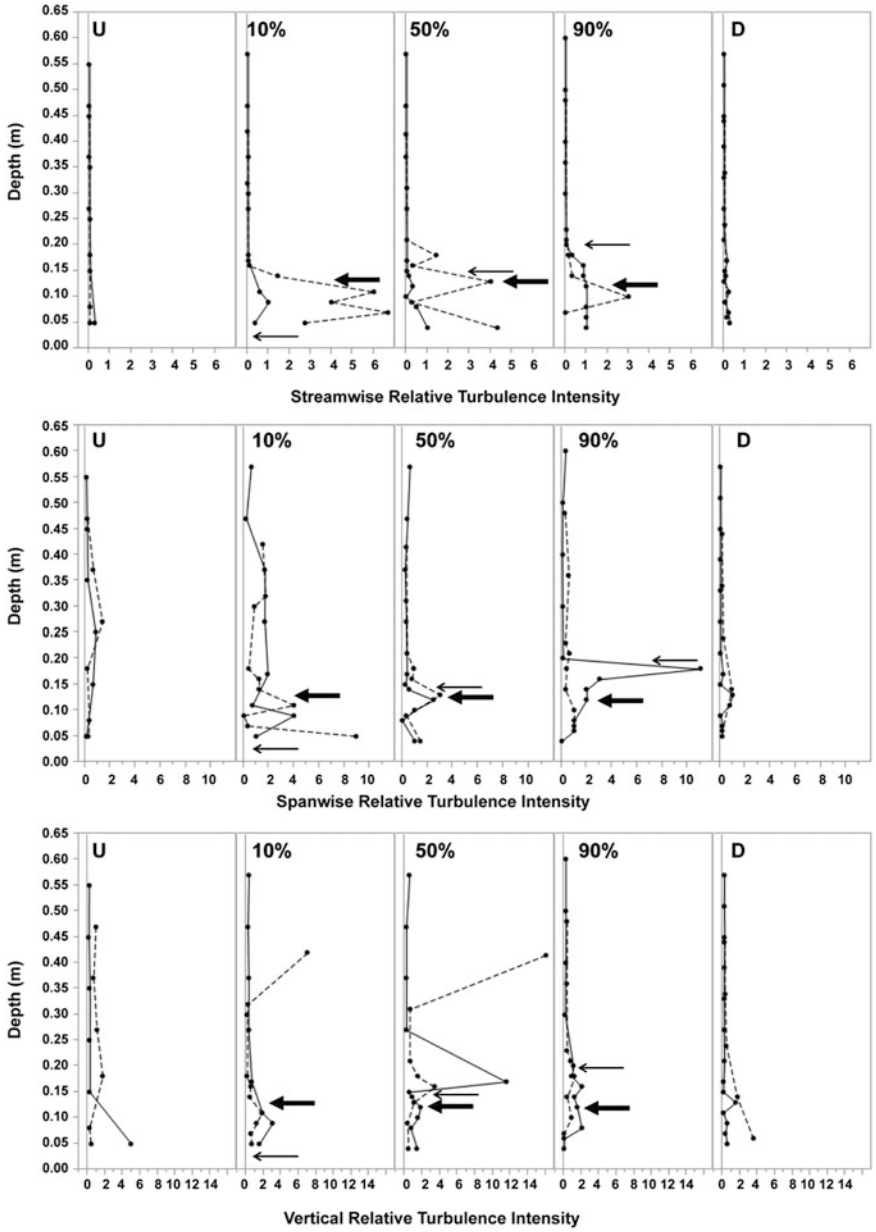

Fig. 2 Relative Turbulence Intensity of the three components of velocity $(\overline{u}, \overline{v}, \overline{w})$ for *E. nuttallii* (*dashed line*) and *C. platycarpa* (*solid line*). The *thick* and *thin arrows* indicate the height of the canopy for *E. nuttallii* and *C. platycarpa,* respectively. Positions are described in the legend of Fig. 1

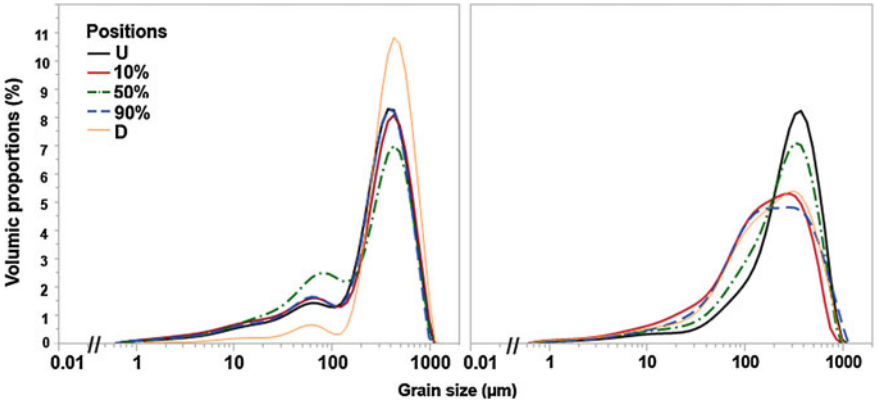

Fig. 3 Mean grain size distributions of sediment in different positions along the main axis of the patch of: (**a**) *E. nuttallii* and (**b**) *C. platycarpa.* Positions are explained in the legend of Fig. 1

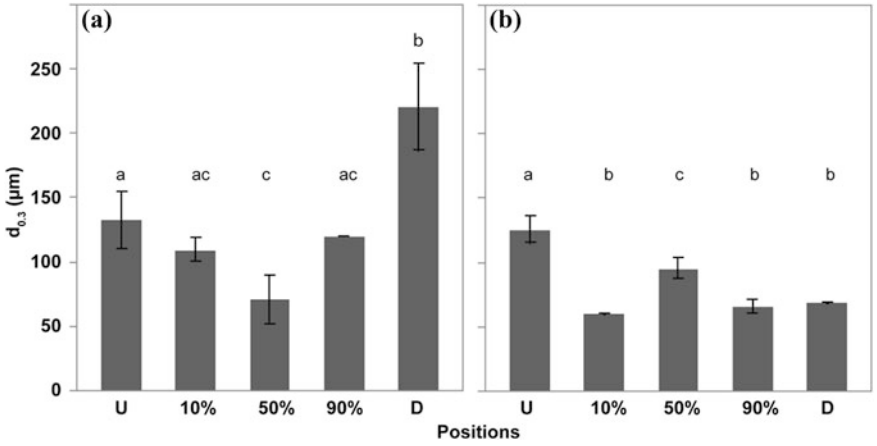

Fig. 4 Mean value of $d_{0.3}$ in sediment collected in different positions along the main axis of the patches of: (**a**) *Elodea nuttallii* and (**b**) *Callitriche platycarpa.* The positions are described in the legend of Fig. 1. *Bars* with different letters are significantly different (one way ANOVA, followed by post hoc Tukey's HSD correction, $p < 0.05$)

biomass and canopy height from upstream to downstream. When the flow encountered the dense canopy, the flow was deviated on patch side, creating high spanwise relative turbulence at the canopy-flow interface. The effects of the patch of this species on hydrodynamics were also observed further downstream the patch. Similar effects of *C. platycarpa* on hydrodynamics were previously reported in literature (Schoelynck et al. 2012, 2013).

As expected, both species also induced contrasting effects on sediment characteristics. The effects observed for the patch of *C. platycarpa* were consistent with its

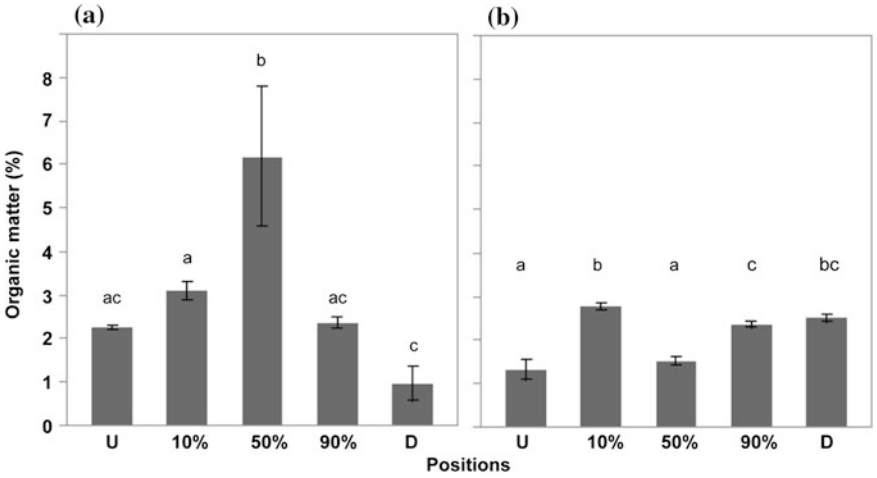

Fig. 5 Mean value of organic matter content (%) in sediment collected in different positions along the main axis of the patches of: (**a**) *Elodea nuttallii* and (**b**) *Callitriche platycarpa.* The positions are described in the legend of Fig. 1. *Bars* with different letters are significantly different (one way ANOVA, followed by post hoc Tukey's HSD correction, $p < 0.05$)

effect on hydrodynamics: $d_{0.3}$ revealed that very fine sand and coarse silt were trapped not only within the patch, but deposited also downstream the patch, consistently with previous results (Schoelynck et al. 2013). On the contrary, the patch of *E. nuttallii* trapped most of the sediment in the upstream half of the patch and the finest sediment in the middle part of the patch. No fine sediment was accumulated in the downstream half of the patch, possibly because the trapping was high enough to deplete the suspended sediment that moved inside the patch. Similar patterns were observed for species *E. canadensis*, morphologically similar to *E. nuttallii* (Sand-Jensen 1998).

The two species influenced also the accumulation of organic matter inside and downstream the patch, showing contrasting patterns. The negative relation observed between the $d_{0.3}$ and the organic matter seemed to indicate that the finer sediments were enriched in organic matter. Moreover, the two species showed a significant difference in the amount of organic matter percentage accumulated within and downstream the patch. *E. nuttallii* and *C. platycarpa* thus had contrasted action on organic matter content in sediment. High concentration of organic matter in anaerobic conditions can lead to the accumulation of soluble organic compounds and other substances that are potentially toxic for plants (Barko and Smart 1983). Therefore, differences in organic matter could have consequences for the growth of both species, especially in the downstream part of the patch, where patch usually tends to develop. For *E. nuttallii*, the sediment downstream patches had a low organic matter content, possibly without limitation for plant growth. For *C. platycarpa,* instead, the sediment downstream the patch presented a similar value than within the patch and higher than upstream, potentially limiting plants growth.

Contrary to previous studies, no positive relationship was found between near-bed velocity and $d_{0.1}$ and $d_{0.3}$ for both species (Sand-Jensen 1998). This lack of correlation could be due to the too low number of sampling points in our study. However a positive correlation was found between near-bed vertical relative turbulent intensity and $d_{0.3}$, underlining the importance of the vertical component of turbulence in the processes of deposition (and resuspension) of fine sediment particles.

Our results emphasize the role of morphological and structural factors in the effects of submerged vegetation on flow and sediment processes. For instance *E. nuttallii* has relatively rigid stems and almost a uniform height all over the patch length. On the contrary *C. platycarpa* has flexible stems and most of the biomass located in the upper part of the canopy: the upstream part of the canopy, with less biomass, is more subject to flow pressure and is then compressed near the sediment bed, whereas further downstream plants gradually increment their biomass acquiring buoyancy and then increasing the patch height. This morphological and structural difference influences the relative depth of submergence (H/h, flow depth to canopy height ratio; Nepf 2012). The patch of *E. nuttallii,* with a uniform height, had a constant relative depth of submergence, corresponding to shallow submerged ($H/h < 5$). On the contrary, the patch of *C. platycarpa* presented a varying relative depth of submergence along the length ranging from deeply submerged ($H/h > 10$) to shallow submerged ($H/h < 5$) or even to emergent ($H/h = 1$) when the patches reach the surface. As differences in relative depth of submergence correspond to different flow and turbulence structures (Nepf 2012), they could explain the contrasting effects on both hydrodynamics and sediment composition (*i.e.* mass transport) for the two species. As other morphological and structural properties of vegetation have an effect on hydrodynamics and sediment composition (*e.g.* stem/leaf length, leaf surface, flexibility, patch size …), further in situ studies with combined measurements of several morphologies, hydrodynamics and sediment composition are necessary to understand the relative effect of these characteristics on flow and sediment dynamics.

This study showed how morphology and patch structure substantially controlled the effects of vegetation on flow and sediment dynamics, not only inside the patch but also downstream the patch. The presence of different species in lotic ecosystems as streams may contribute to the hydrodynamical and geomorphological heterogeneity of these systems.

Acknowledgments This work was supported by the Research Executive Agency, through the 7th Framework Programme of the European Union, Support for Training and Career Development of Researchers (Marie Curie—FP7-PEOPLE-2012-ITN), which funded the Initial Training Network (ITN) HYTECH 'Hydrodynamic Transport in Ecologically Critical Heterogeneous Interfaces', No. 316546. We thank Félix Vallier and Thérèse Bastide for field and technical assistance and the CNR (Compagnie Nationale du Rhône) for access to field sites. This study was carried out under the aegis of the Rhône Basin Long-Term Environmental Research (ZABR, Zone Atelier Bassin du Rhône).

References

Barko J, Smart R (1983) Effects of organic matter additions to sediment on the growth of aquatic plants. J Ecol 161–175

Carpenter SR, Lodge DM (1986) Effects of submersed macrophytes on ecosystem processes. Aquat Bot 26:341–370

Hendriks IE, Sintes T, Bouma TJ, Duarte CM (2008) Experimental assessment and modeling evaluation of the effects of the seagrass Posidonia oceanica on flow and particle trapping. Mar Ecol Prog Ser 356:163–173

Hendriks IE, Bouma TJ, Morris EP, Duarte CM (2009) Effects of seagrasses and algae of the Caulerpa family on hydrodynamics and particle-trapping rates. Mar Biol 157:473–481

James WF, Barko JW, Butler MG (2004) Shear stress and sediment resuspension in relation to submersed macrophyte biomass. Hydrobiologia 515:181–191

Jones CG, Lawton JH, Shachak M (1994) Organisms as ecosystem engineers. Oikos 373–386

Marion A, Nikora V, Puijalon S et al (2014) Aquatic interfaces: a hydrodynamic and ecological perspective. J Hydraul Res 52:744–758

Miler O, Albayrak I, Nikora V, O'Hare M (2012) Biomechanical properties of aquatic plants and their effects on plant–flow interactions in streams and rivers. Aquat Sci 74:31–44

Nepf HM (2012) Flow and transport in regions with aquatic vegetation. Annu Rev Fluid Mech 44:123–142

O'Hare MT, Hutchinson KA, Clarke RT (2007) The drag and reconfiguration experienced by five macrophytes from a lowland river. Aquat Bot 86:253–259

Petticrew EL, Kalff J (1992) Water flow and clay retention in submerged macrophyte beds. Can J Fish Aquat Sci 49:2483–2489

Pluntke T, Kozerski HP (2003) Particle trapping on leaves and on the bottom in simulated submerged plant stands. Hydrobiologia 506:575–581

Sand-Jensen K (1998) Influence of submerged macrophytes on sediment composition and near-bed flow in lowland streams. Freshw Biol 39:663–679

Sand-Jensen K (2003) Drag and reconfiguration of freshwater macrophytes. Freshw Biol 48:271–283

Sand-Jensen K, Mebus JR (1996) Fine-scale patterns of water velocity within macrophyte patches in streams. Oikos 169–180

Sand-Jensen KAJ, Pedersen ML (2008) Streamlining of plant patches in streams. Freshw Biol 53:714–726

Schoelynck J, de Groote T, Bal K, Vandenbruwaene W, Meire P, Temmerman S (2012) Self-organised patchiness and scale-dependent bio-geomorphic feedbacks in aquatic river vegetation. Ecography 35:760–768

Schoelynck J, Meire D, Bal K et al (2013) Submerged macrophytes avoiding a negative feedback in reaction to hydrodynamic stress. Limnologica Ecol Manage Inland Waters 43:371–380

Schulz M, Kozerski HP, Pluntke T, Rinke K (2003) The influence of macrophytes on sedimentation and nutrient retention in the lower River Spree (Germany). Water Res 37:569–578

Tison J-M, de Foucault B (2014) Flora Gallica - Flore de France. Biotope Editions 1195

Vandenbruwaene W, Temmerman S, Bouma TJ et al. (2011) Flow interaction with dynamic vegetation patches: Implications for biogeomorphic evolution of a tidal landscape. J Geophys Res 116

Flow Velocity and Morphology of a Submerged Patch of the Aquatic Species *Veronica anagallis-aquatica* L.

Loreta Cornacchia, Sofia Licci, Johan van de Koppel, Daphne van der Wal, Geraldene Wharton, Sara Puijalon and Tjeerd J. Bouma

Abstract The interaction between macrophytes and hydrodynamic conditions is an important feature in many aquatic ecosystems. Submerged macrophytes can form monospecific patches that interact with the flow and alter current velocity; within the same vegetation patch, plants are exposed to different levels of hydrodynamic stress. Due to the high morphological variability of aquatic plants, we expect different architectural and morphological traits to emerge for individuals located at different positions within the same patch. In this study, we have measured the flow velocity around a patch of *Veronica anagallis-aquatica* in submerged conditions and measured the morphological traits of individuals along a gradient of exposure to flow velocity within the patch. Results show that the more exposed individuals present smaller sizes than the sheltered ones, lower relative allocation to stems, higher allocation to roots and reduced water content in roots and stems. The knowledge obtained helps to clarify the role of morphological adaptations to flow stress in the context of plant-flow interactions.

1 Introduction

At the interface between sediments and flowing water, aquatic macrophytes are key organisms in stream ecosystems (Carpenter and Lodge 1986). They play a strong role in modifying flow conditions and sedimentation patterns: particularly, they are

L. Cornacchia (✉) · J. van de Koppel · D. van der Wal · T.J. Bouma
Royal Netherlands Institute for Sea Research (NIOZ-Yerseke), Yerseke, The Netherlands
e-mail: loreta.cornacchia@nioz.nl

S. Licci · S. Puijalon
Université de Lyon, UMR 5023 "Ecologie des hydrosystèmes naturels et anthropisés", Université Lyon 1 CNRS, ENTPE, 69622 Villeurbanne Cedex, France
e-mail: sofia.licci@univ-lyon1.fr

G. Wharton
Department of Geography, Queen Mary, University of London, London, UK

P. Rowiński and A. Marion (eds.), *Hydrodynamic and Mass Transport at Freshwater Aquatic Interfaces*, GeoPlanet: Earth and Planetary Sciences,
DOI 10.1007/978-3-319-27750-9_12

able to stabilize sediment and provide sheltered habitats with lower flow velocity (Sand-Jensen 1998).

Submerged macrophytes in streams may form monospecific patches that interact with the flowing water (Sand-Jensen 1998). The most important consequence of this interaction is a sharp decline in flow velocity at the surface of the plant patches. The ability of different macrophyte species to alter flow velocity is directly linked to their morphological traits (Sand-Jensen and Mebus 1996; Peralta et al. 2008). The plants' presence and morphology also influence turbulence inside the canopies, which is maintained high enough to ensure the exchange of solutes between the plant and the water (Sand-Jensen and Pedersen 1999; Morris et al. 2008; Bal et al. 2013).

While flow velocity is slowed down inside the macrophyte patches, the individuals in the upstream part of the patch are always under the influence of the high velocity (Sand-Jensen and Mebus 1996). Flow acceleration as typically occurring just next to vegetation patches (van Wesenbeeck et al. 2008; Schoelynck et al. 2012), also leads to an increased hydrodynamic stress for the plants located along the sides.

If, on the one hand, the aggregation into patches can reduce the drag acting on individual plants, light penetration in the canopy will decrease with increasing plant density (Nikora 2010; Bal et al. 2011). Shading by neighboring individuals may also be enhanced by the bending and streamlining of plants in the flow. The interplay between stress reduction and light interception can lead to the emergence of different conditions within a single patch. As a consequence, this different exposure to currents and to light could determine changes in the architectural and morphological traits of the individuals within the same patch. Indeed, aquatic plants present a high morphological variability when growing in contrasting habitats: when exposed to mechanical stress, such as current or wave action, many plant species display architectural and morphological adjustments known as phenotypic plasticity (Santamaría 2002; Puijalon and Bornette 2006; La Nafie et al. 2012). Such changes also affect the allocation of biomass towards anchorage or photosynthetic organs (Peralta et al. 2006).

The submerged species *Veronica anagallis-aquatica* L. (Scrophulariaceae) is an amphibious macropyhte (Schulthorpe 1967), with the ability to grow in both air and water. This species can present morphological adaptations under different flow regimes, with an emergent form in low flow and a submerged form in faster flow (Boeger and Poulson 2003). Morphological, anatomical and physiological adaptations allow this species to live under contrasting conditions and to withstand the stress imposed by water flow. Thus, we expect that its phenotypic plasticity can also lead to the emergence of morphological variations inside a single vegetation patch due to the contrasting light and current conditions.

In this study, we investigated the interactive effect between vegetation and hydrodynamics. That is, we study the effect of a vegetation patch on local hydrodynamic conditions, and vice versa, the influence of water velocity on the

morphology and biomass allocation of the plants in the different locations inside the patch. Such interdisciplinary approach towards studying biophysical interfaces, combining ecological with hydraulic principles, is essential to increase current knowledge about water-biota interactions in aquatic systems at the patch scale (Marion et al. 2014).

2 Materials and Methods

2.1 Study Site

The study site is represented by an artificial drainage channel located along the Upper Rhône River (France), near Peyrieu (45.6765° N, 5.6773° E). The channel is uniform in terms of width and water depth, with relatively straight banks (Fig. 1). The channel is 2.8 km long, 4.70 m wide, with a maximum depth of 0.7 m. The maximum flow velocities are around 0.3 m s^{-1}, with a discharge of 0.24 m^3 s^{-1} in June. The channel is fed by Rhône river seepage and hillslope aquifers. The aquatic vegetation in the sampled reach is dominated by *Veronica anagallis-aquatica,* growing in submerged monospecific patches. All measurements and plant sampling were performed in June 2014.

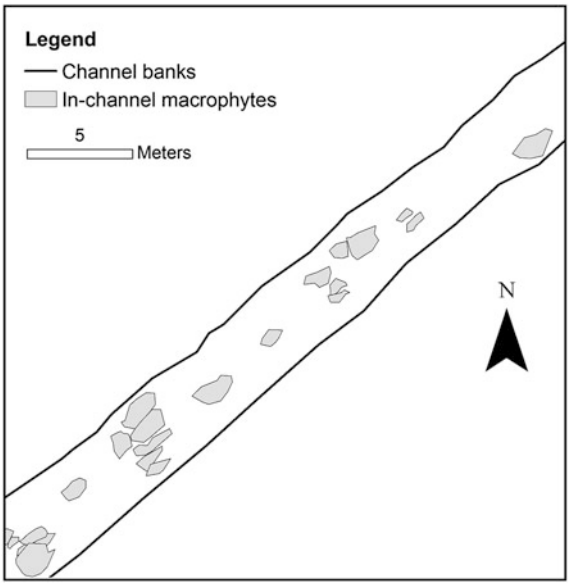

Fig. 1 Planform representation of the study site near Peyrieu (France), showing the distribution of in-stream macrophyte patches

2.2 Hydrodynamic Measurements

We selected a representative submerged patch of *V. anagallis-aquatica* which was 1.70 m long and 1.40 m wide. Hydrodynamic measurements around the patch were carried out using a StreamPro acoustic Doppler current profiler (ADCP) manufactured by Teledyne RD Instruments. The ADCP probe is mounted on a floating boat which is towed across the river section. Since the ADCP probe is submerged in the river, it is not possible to measure the top 0.16 m of the water. Due to the potential for sidelobe contamination, it is not possible to measure all the way to the bottom (RD Instruments 2006). Thus, the bottom 6 % of the water depth between the transducers and the river bed is excluded from the measurements.

Hydrodynamic measurements were performed in three transects located along the length of the patch. For each transect, we slowly pulled the ADCP across the river section and performed five replicated measurements. Transect *i* was located ≈40 cm upstream of the patch, Transect *ii* was halfway in the length of the patch (0.9 m inside the vegetation), Transect *iii* was located ≈40 cm downstream of the patch. Within the transects, vertical velocity profiles were selected at specific locations to investigate the effects of the vegetation patch on hydrodynamics: Profile *i* was located upstream, along the patch centerline; Profile *ii* was halfway in the length of the patch and on its side, at 40 cm from the patch edge; Profile *iii* was located downstream along the patch centerline (Fig. 2). Vertical velocity profiles were measured at 6 cm depth intervals.

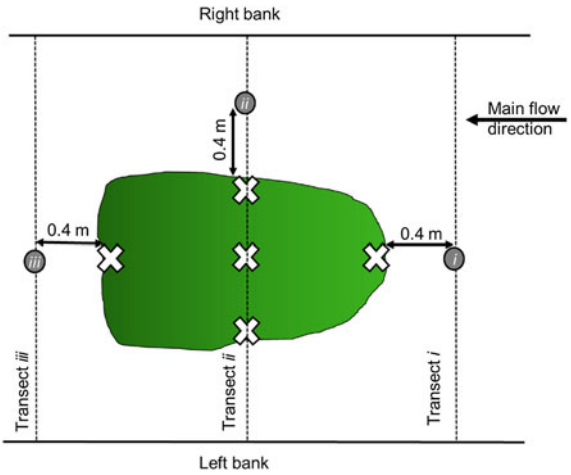

Fig. 2 Schematic overview of the hydrodynamic transects and plant sampling locations around the patch of *V. anagallis-aquatica*. The locations of the ADCP transects (*dotted lines*) and locations where plants were sampled (*cross symbols*) are indicated. *Grey circles* represent the location within the transects of the three vertical profiles plotted in Fig. 3. The average flow velocity in the water column was additionally measured for all the positions where plants were sampled

Additionally, we measured the average velocity for the positions where plants were sampled (see locations in Fig. 2 and section '*Plant sampling*'), in order to obtain a representative measure of the flow velocity encountered by the plants. The velocity in these positions was measured down from the water surface at 60 % of the total flow depth, to have an estimate of average flow velocity in the water column (Dingman 1984).

2.3 Plant Sampling and Morphometry

For 5 positions inside the patch (upstream, downstream, and halfway in the length of the patch on the left side, middle and right side), we collected 5 plant individuals. Plants were kept for no more than 48 h before measurements were made.

We measured the following traits on each plant:

- Plant size: plant height (cm) and plant mass (g). Plant height was measured as the maximum length of the shoot. For measuring the mass, plants were divided into roots, leaves, stems and flowers (if present), and the different parts were weighed to obtain fresh and dry mass (measured after drying for 72 h at 60 °C).
- Number and length of ramifications, maximum root length, stem diameter, root diameter.
- Water content in root, stem and leaf tissues: the density of the tissues was measured as water content in the organs (1—dry mass/fresh mass). Low water content of organs reveals denser tissues, which can provide higher resistance to breakage (Usherwood et al. 1997; Puijalon and Bornette 2006).

All statistical analyses were performed in R 3.1.2. A one-way ANOVA, followed by a post hoc Tukey HSD test, were performed to compare sample groups. Regressions were performed using standard least square regressions.

3 Results

3.1 Flow Velocity Around the Vegetation Patch

Vertical profiles measured upstream the plant patch showed a decline in flow velocities with depth (Fig. 3, Profile *i*). The presence of vegetation modified the profiles leading to flow deflection and acceleration in the unvegetated zone located on the side of the patch, at 40 cm from the patch edge (Fig. 3, Profile *ii*). The stand of *V. anagallis-aquatica* also led to a decline in flow velocities downstream of the vegetation patch (Fig. 3, Profile *iii*), compared to the upstream location. The vegetation caused a reduction in velocity that leads to an area of very low flow behind the patch.

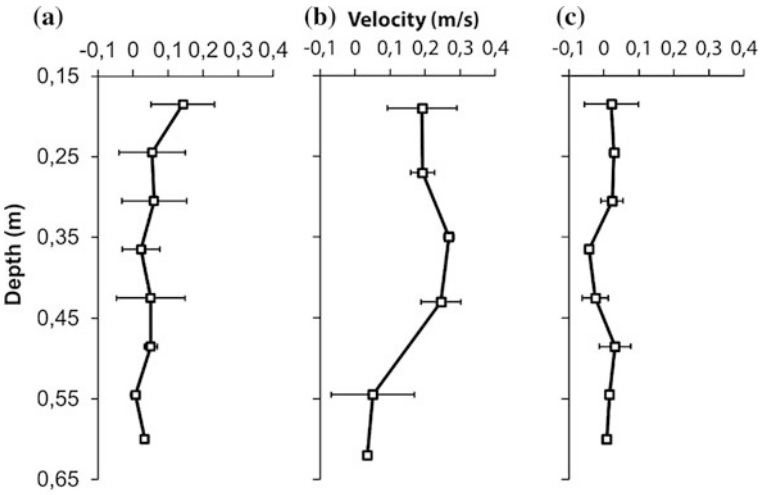

Fig. 3 Flow velocity profiles located upstream (*i*), adjacent (*ii*), and downstream (*iii*) of the *Veronica anagallis-aquatica* patch

3.2 Variations of Morphological Plant Traits

The height of the individual plants, as an indicator of their size, significantly decreased with increasing flow velocity encountered by plants (R^2 = 0.7682, p = 0.02, Fig. 4). Height was significantly lower in the upstream position than in the middle, downstream and right edge locations (Tukey's HSD p = 0.001, p = 0.02, and p = 0.045, respectively). The size of plants located upstream and on the left edge of the patch did not significantly differ (Tukey's HSD p = 0.06).

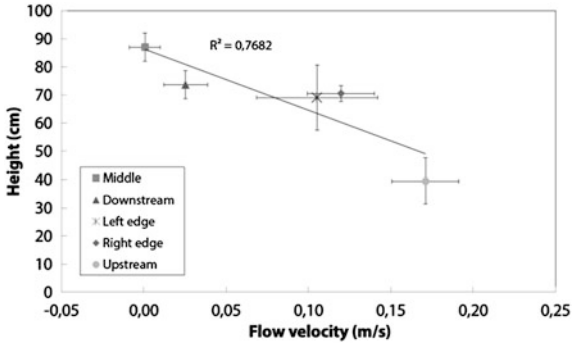

Fig. 4 Average plant height for the individuals sampled in different locations inside the patch (n = 5 per position), along the gradient of increasing flow velocity. The average velocity for each location was measured in the positions where plants were sampled. *Error bars* represent standard error of the mean

Table 1 Statistical comparisons of (A) growth and (B) architectural traits for the plant individuals sampled in the five locations inside the macrophyte patch

Plant trait	F_{df}	*P-value*	Direction
(A) Growth and production			
Height of mother ramet	$F_{4,\ 20} = 5.821$	**	high vel. < low vel.
Root dry mass	$F_{4,\ 20} = 0.646$	ns	–
Leaves dry mass	$F_{4,\ 20} = 0.553$	ns	–
Stems dry mass	$F_{4,\ 20} = 0.843$	ns	–
Flowers dry mass	$F_{4,\ 20} = 1.509$	ns	–
Total dry mass	$F_{4,\ 20} = 0.431$	ns	–
(B) Architecture and morphology			
No. of ramifications	$F_{4,\ 20} = 1.954$	ns	–
Maximum root length	$F_{4,\ 20} = 2.233$	ns	–
Ramification length	$F_{4,\ 20} = 2.768$	ns	–
Stem diameter	$F_{4,\ 20} = 0.583$	ns	–
Root diameter	$F_{4,\ 20} = 0.732$	ns	–
Allocation to roots	$F_{4,\ 20} = 2.870$	*	high vel. > low vel.
Allocation to leaves	$F_{4,\ 20} = 0.272$	ns	–
Allocation to stems	$F_{4,\ 20} = 10.78$	***	high vel. < low vel.
Total water content	$F_{4,\ 20} = 10.58$	***	high vel. < low vel.
Water content of roots	$F_{4,\ 20} = 3.996$	*	high vel. < low vel.
Water content of leaves	$F_{4,\ 20} = 0.704$	ns	–
Water content of stems	$F_{4,\ 20} = 2.854$	*	high vel. < low vel.

The statistical test carried out was one-way ANOVA between the different positions. For this test, F_{df} values are indicated. For all tests, significance levels and direction of the variation along the gradient of flow velocity, if significant, are given. Asterisks indicate significant differences: ***$P < 0.001$; **$P < 0.01$; *$P < 0.05$; *ns* not significant

Total plant dry mass was not significantly different between the five positions inside the patch ($F_{4,\ 20} = 0.431$, p = 0.78, Table 1).

Dry mass allocation to stems, relative to total dry mass, was significantly lower in the upstream position than in all the others (Tukey's HSD $p \leq 0.007$ for all pairwise comparisons, Fig. 5). Relative dry mass allocation to roots was higher in the upstream location than on the left edge of the patch (Tukey's HSD p = 0.05), while allocation to leaves showed no significant differences ($F_{4,\ 20} = 0.272$, p = 0.893, Fig. 5).

Total water content was significantly lower in the upstream plants than in all the others (Tukey's HSD $p \leq 0.001$ for all pairwise comparisons, Fig. 6). The analysis of water content for each plant organ revealed that differences in water content were found in roots and stems ($F_{4,\ 20} = 3.996$, p = 0.015 and $F_{4,\ 20} = 2.854$, p = 0.05) while no significant differences were found in leaves ($F_{4,\ 20} = 0.332$, p = 0.853, Table 1).

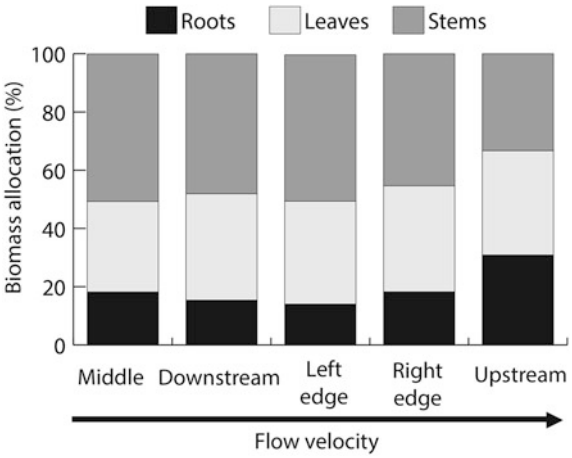

Fig. 5 Average biomass allocation between roots, shoots and leaves of the plants along the gradient of increasing flow velocity inside the macrophyte patch (n = 5 per position)

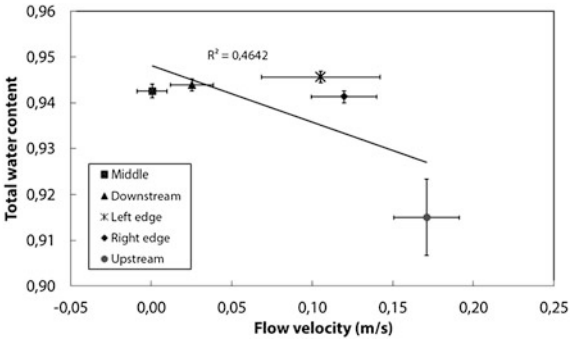

Fig. 6 Average total water content for the individuals along the gradient of increasing flow velocity inside the macrophyte patch (n = 5 individuals per position). *Error bars* represent standard error of the mean

4 Discussion

4.1 Flow Patterns Around the Macrophyte Patch

The velocity patterns around the macrophyte patch show that this species, forming a relatively closed canopy, can strongly reduce the flow within the stand and increase it along its sides. Flow velocities in the transect located next to the patch are in average 20 % higher than the upstream, vegetation-free transect. The flow velocity is also much higher in the profile adjacent to the patch than in the initial upstream profile. This value of stream velocity acceleration is comparable with results

obtained in previous studies with patch mimics (Schoelynck et al. 2012) and in situ measurements of aquatic macrophytes (Schoelynck et al. 2013). In these studies, such an increase in water velocity was found to create a negative feedback for the plants, limiting their growth in terms of lateral spread, which may be mediated by erosional processes (van Wesenbeeck et al. 2008; Bouma et al. 2009).

The height of the plants relative to water depth can determine partly the effect of the macrophytes on flow velocity. Within the dense canopy of this species, the plants in the middle and downstream part are able to occupy the whole water column, causing a decrease in flow velocities just downstream. Behind the patch, an area is created of very low or even negative stream velocity, as a result of turbulent flow (Sand-Jensen 1998; Schoelynck et al. 2012). It may be speculated that such low-flow area facilitates patch expansion.

4.2 Morphological Variations in Relation to Hydrodynamics

The reduced size of *V. anagallis-aquatica* individuals located in the upstream position is a commonly observed response to mechanical stress (Puijalon and Bornette 2006), since the upstream plants are constantly exposed to the highest flow velocities.

Even though the aggregation into patches leads to individuals being exposed to a range of hydrodynamic conditions, plant dry mass is comparable between the different positions along the stress gradient. Although no significant differences were found, total plant dry mass was higher in the most sheltered, middle position than in the upstream and left side of the patch. The apparent trend is in the expected direction, but it may be necessary to increase the power of the statistical tests with higher replication number for each sampling position.

A higher allocation of biomass in the roots at the highest flow velocity suggests that the upstream plants have higher anchorage strength compared to the other locations in the patch (Puijalon et al. 2005). This response is similar as observed in other plants exposed to strong hydrodynamics (e.g. Peralta et al. 2006).

A higher allocation to stems in the positions farther away in the canopy may be due to an increased vertical growth enabling plants to reduce self-shading from the upstream individuals that bend in the flow. At the same time, the proportion of biomass allocated to leaves remains the same, but leaves themselves are located towards the upper portion of the stem. A similar self-shading mechanism has been described in seagrass canopies exposed to tidal currents, where leaves bend in the direction of the flow and rest on top of each other (Fonseca et al. 1982; Zimmerman 2003), thus limiting light availability in the canopy. Understanding the trade-offs between hydrodynamics and light capture is not only important for understanding the patch morphometry, but also for understanding the spreading of aquatic plant species in a river basin (Bal et al. 2011).

The reduced water content of plant organs at the highest flow velocity reveals that the plants located in the upstream part of the patch have the highest tissue density (Usherwood et al. 1997; Puijalon and Bornette 2006). The production of high-density tissues is likely to modify the biomechanical properties of the plants by increasing their mechanical resistance. The plants located along the edges of the patch are exposed to friction drag from the flow accelerating next to the canopy, but are also sheltered from frontal drag by individuals located upstream. Frontal drag is typically much higher than friction drag, so that plants in the upstream part of the patch will experience the highest drag forces. These patterns in drag forces may explain the comparable tissue density in all the positions in the patch, except for the upstream plants, which are constantly exposed to the water flow, and therefore require stronger tissues to withstand high frontal drag forces.

5 Conclusions

We can conclude that the patchy distribution of *Veronica anagallis-aquatica* in freshwater streams can reduce hydrodynamic stress inside the patches, leading to morphological differences in terms of plant height, biomass allocation and tissue density.

Although the observed morphological adaptations are mostly displayed in response to mechanical stress, the results also suggest that such morphological plasticity may help aquatic plants to grow inside patches and cope with limited light penetration inside the canopy (for instance, the higher biomass allocation to stems for the plants within the patch may be related to their increased vertical growth reducing shading by neighboring individuals).

This study helps to clarify the influence of vegetation patches on the incoming flow in streams, and how morphological adaptations within the same species can influence the resistance to flow stress and the ability to grow aggregated into patches.

Acknowledgments This work was supported by the Research Executive Agency, through the Seventh Framework Programme of the European Union, Support for Training and Career Development of Researchers (Marie Curie—FP7-PEOPLE-2012-ITN), which funded the Initial Training Network (ITN) HYTECH 'Hydrodynamic Transport in Ecologically Critical Heterogeneous Interfaces', N. 316546. We thank Youssouf Sy for assistance during field measurements and Vanessa Gardette (CNRS—Université Lyon 1) for her help in the laboratory. We are also grateful to the CNR (Compagnie Nationale du Rhône) for their interest in the experiment and authorization to work on the study sites.

References

Bal KD, Bouma TJ, Buis K, Struyf E, Jonas S, Backx H, Meire P (2011) Trade-off between drag reduction and light interception of macrophytes: comparing five aquatic plants with contrasting morphology. Funct Ecol 25:1197–1205. doi:10.1111/j.1365-2435.2011.01909.x

Bal KD, Brion N, Woulé-Ebongué V, Schoelynck J, Jooste A, Barrón C, Dehairs F, Meire P, Bouma TJ (2013) Influence of hydraulics on the uptake of ammonium by two freshwater plants. Freshw Biol 58:2452–2463

Boeger MRT, Poulson ME (2003) Morphological adaptations and photosynthetic rates of amphibious Veronica anagallis-aquatica L. (Scrophulariaceae) under different flow regimes. Aquat Bot 75:123–135

Bouma T, Friedrichs M, Van Wesenbeeck B, Temmerman S, Graf G, Herman P (2009) Density-dependent linkage of scale-dependent feedbacks: a flume study on the intertidal macrophyte Spartina anglica. Oikos 118:260–268

Carpenter SR, Lodge DM (1986) Effects of submersed macrophytes on ecosystem processes. Aquat Bot 26:341–370

Dingman SL (1984) Fluvial hydrology. In: Freeman WH (ed). New York

Fonseca M, Fisher J, Zieman J, Thayer G (1982) Influence of the seagrass, *Zostera marina* L., on current flow. Estuar Coast Shelf Sci 15:351–364

La Nafie YA, De Los Santos CB, Brun FG, Van Katwijk MM, Bouma TJ (2012) Waves and high nutrient loads jointly decrease survival and separately affect morphological and biomechanical properties in the seagrass Zostera noltii. Limnol Oceanogr 57:1664

Marion A, Nikora V, Puijalon S, Bouma T, Koll K, Ballio F, Tait S, Zaramella M, Sukhodolov A, O'Hare M, Wharton G, Aberle J, Tregnaghi M, Davies P, Nepf H, Parker G, Statzner B (2014) Aquatic interfaces: a hydrodynamic and ecological perspective. J Hydraul Res 52(6):744–758. doi:10.1080/00221686.2014.968887

Morris EP, Peralta G, Brun FG, Van Duren LA, Bouma TJ, Perez-Llorens JL (2008) Interaction between hydrodynamics and seagrass canopy structure: spatially explicit effects on ammonium uptake rates. Limnol Oceanogr 53:1531–1539

Nikora V (2010) Hydrodynamics of aquatic ecosystems: an interface between ecology, biomechanics and environmental fluid mechanics. River Res Appl 26:367–384. doi:10.1002/rra.1291

Peralta G, van Duren LA, Morris EP, Bouma TJ (2008) Consequences of shoot density and stiffness for ecosystem engineering by benthic macrophytes in flow dominated areas: a hydrodynamic flume study. Mar Ecol Prog Ser 368:103–115. doi:10.3354/meps07574

Peralta P, Brun FG, Pérez-Lloréns J, Bouma TJ (2006) Direct effects of current velocity on the growth, morphometry and architecture of seagrasses: a case study on Zostera noltii. Mar Ecol Prog Ser 327

Puijalon S, Bornette G (2006) Phenotypic plasticity and mechanical stress: biomass partitioning and clonal growth of an aquatic plant species. Amer J Bot 93:1090–1099. doi:10.3732/ajb.93.8.1090

Puijalon S, Bornette G, Sagnes P (2005) Adaptations to increasing hydraulic stress: morphology, hydrodynamics and fitness of two higher aquatic plant species. J Exp Bot 56:777–786

RD Instruments (2006) StreamPro ADCP Operation Manual. P. N 95B–6003-00. RD Instruments, Poway, CA

Sand-Jensen K, Mebus JR (1996) Fine-scale patterns of water velocity within macrophyte patches in streams. Oikos 169–180

Sand-Jensen K, Pedersen O (1999) Velocity gradients and turbulence around macrophyte stands in streams. Freshw Biol 42:315–328. doi:10.1046/j.1365-2427.1999.444495.x

Sand-Jensen K (1998) Influence of submerged macrophytes on sediment composition and near-bed flow in lowland streams. Freshw Biol 39:663–679

Santamaría L (2002) Why are most aquatic plants widely distributed? Dispersal, clonal growth and small-scale heterogeneity in a stressful environment. Acta Oecol 23:137–154. doi:http://dx.doi.org/10.1016/S1146-609X(02)01146-3

Schoelynck J, De Groote T, Bal K, Vandenbruwaene W, Meire P, Temmerman S (2012) Self-organised patchiness and scale-dependent bio-geomorphic feedbacks in aquatic river vegetation. Ecography 35:760–768

Schoelynck J, Meire D, Bal K, Buis K, Troch P, Bouma T, Meire P, Temmerman S (2013) Submerged macrophytes avoiding a negative feedback in reaction to hydrodynamic stress. Limnol—Ecol Manag Inland Waters 43:371–380. doi:http://dx.doi.org/10.1016/j.limno.2013.05.003

Schulthorpe C (1967) The biology of aquatic vascular plants. London

Usherwood J, Ennos A, Ball D (1997) Mechanical and anatomical adaptations in terrestrial and aquatic buttercups to their respective environments. J Exp Bot 48:1469–1475

van Wesenbeeck BK, Van De Koppel J, MJ Herman P, J Bouma T (2008) Does scale-dependent feedback explain spatial complexity in salt-marsh ecosystems? Oikos 117:152–159

Zimmerman RC (2003) A biooptical model of irradiance distribution and photosynthesis in seagrass canopies. Limnol Oceanogr 48:568–585

The Influence of Rating Curve Uncertainty on Flow Conditions in the River Vistula in Warsaw

Emilia Karamuz, Marzena Osuch and Renata J. Romanowicz

Abstract The flow forecasting system for the middle reach of the River Vistula consists of a distributed flow routing model and rainfall-runoff modules. The MIKE 11 flow routing model, applied in the study, requires specification of a number of input variables, including roughness coefficients, initial conditions, river geometry and boundary conditions. All listed variables introduce errors into the system that have an impact on the uncertainty of flow predictions. This work focuses on the estimation of uncertainty of flow predictions resulting from inaccuracy of boundary conditions and parametric uncertainty. In particular, we are interested in the influence of a stage-discharge relationship (rating curve) uncertainty applied as the downstream boundary condition. The influence of parameter and rating curve (RC) uncertainty on model predictions is studied using the Generalised Likelihood Uncertainty Estimation GLUE framework. We parameterised downstream RC using a power law. The RC parameters were optimised together with the model roughness coefficients. The optimal parameter values were subsequently used as mean values of a priori distribution within the GLUE approach to derive the flow routing model prediction uncertainty. The results were superior to those without RC uncertainty taken into account only in Warsaw Port Praski gauging station. The proposed methodology was applied to the Middle Vistula reach between Zawichost and Warsaw Port Praski gauging stations. Model performance was estimated using both water level and discharge observations at gauging stations situated along the river reach.

E. Karamuz (✉) · M. Osuch · R.J. Romanowicz
Institute of Geophysics Polish Academy of Sciences, Warszawa, Poland
e-mail: karamuz@igf.edu.pl

M. Osuch
e-mail: marz@igf.edu.pl

R.J. Romanowicz
e-mail: romanowicz@igf.edu.pl

P. Rowiński and A. Marion (eds.), *Hydrodynamic and Mass Transport at Freshwater Aquatic Interfaces*, GeoPlanet: Earth and Planetary Sciences,
DOI 10.1007/978-3-319-27750-9_13

1 Introduction

Flow routing models play a very important role in real-time flow forecasting and are commonly used in flood forecasting and flood inundation mapping. From a practical point of view of a decision-maker, they should be 'as precise as possible' to predict and asses correctly flood risk (Pappenberger et al. 2006).

In our previous study (Kochanek et al. 2015) within the project "Stochastic flood forecasting system (The River Vistula reach from Zawichost to Warsaw)" a step-by-step procedure of distributed modelling of river flow was presented. In that study a description of the MIKE11 calibration procedure for the studied River Vistula reach was presented. Our objective was to build a model for flood forecasting; therefore, the best possible model fit was important. At the stage of model calibration, the problems appeared with fitting the simulated discharges and water levels to the observations at the gauging stations starting from Gusin, downstream to Warsaw Port Praski. The quality of the MIKE11 results for the Warsaw reach of the River Vistula is of particular importance from the point of view of the flood risk management. To improve the results of hydraulic modelling we decided to take into account uncertainty of downstream boundary condition (RC uncertainty) in model calibration. Two research questions are considered in this study. The first one is the assessment of the extent of the influence of RC on the model simulations upstream. The second question is the assessment of possible improvement of the model results in the Warsaw part of the reach.

In the hydrological practice, water levels are measured in continuous time-frame with relatively high accuracy (Boiten 2008) but discharge measurements are performed only several times a year. On the basis of the measured water levels and discharges, a functional relationship, so-called rating curve, is developed. Due to geomorphological processes, including sediment transport which can significantly change the geometry of the cross-sections, the RC changes in time. The application of a 1D hydrodynamic model MIKE11 requires time series of discharge and/or water levels. In our case the discharge records used as an input for flow routing (upstream boundary condition) are derived from a rating-curve. Reference discharge data used in optimization procedure are obtained in the same manner. As discussed, e.g., by Le Coz et al. (2014) the stage-discharge relationship determined on the basis of field measurements is strongly biased in the highest and lowest discharge ranges (about 5–20 %). Additionally, RC parametrization inaccuracy introduces errors, which are crucial especially in the highest discharges when extrapolation of measurements takes place. In some sections of the river reach high variability of geomorphological conditions creates problems with a clear definition of the RC relationship. Magnuszewski (2015) demonstrates a variability of RC relationship in the period 1919–2010 for Warsaw Port Praski station. From this point of view, taking into account the uncertainty of RC at the calibration stage can bring benefits in the form of a better fit to observations.

In a summary, the variability of RC relationship may results from: (i) shifts of channel geometry (e.g. after flood); (ii) seasonal changes of vegetation growth;

(iii) variation of downstream boundary condition; (iv) hysteresis due to transient flow effects, and (v) ice jam conditions. Sometimes different rating curves for different time periods are required due the non-stationarity in the stage-discharge relationship. To cope with variability of reference regimes, more complex approaches are used, including multi-segment (or piecewise) power functions, hysteresis and over bank flow in rivers with floodplains (Le Coz et al. 2014).

There are many studies on RC uncertainty arising at the stage of its construction. Le Coz (2012) provides a thorough review of the literature regarding the methods for estimating the uncertainty associated with stage-discharge relationships. The impact of uncertainty of boundary conditions on hydraulic modelling is still poorly understood (Domeneghetti et al. 2013). This problem was approached by many researchers (Pappenberger et al. 2006; Di Baldassarre and Montanari 2009; Di Baldassarre and Claps 2011; Di Baldassarre et al. 2011; Domeneghetti et al. 2012). The results clearly indicate that inaccuracy of RC has a significant impact on outcomes of hydrodynamic modelling.

In this study, RC was parameterised using a power law in order to analyze its impact on model results. The solution of the first of the research questions is sought by the application of sensitivity analysis of RC parameters using Morris method (Morris 1991). The second research problem is solved through the uncertainty analysis of the MIKE11 model with and without RC uncertainty taken into account.

It should be emphasized that for the purposes of this study we considered uncertainty of a stage-discharge relationship based on discharge records obtained from the operational monitoring (Institute of Meteorology and Water Management PIB—IMGW). We do not use raw discharge data.

2 Study Area

The study was carried out on a 255 km river reach (Zawichost-Warszawa) of the River Vistula, shown in Fig. 1. The upper part of modelled channel is relatively straight and, to some extent, regulated, with large meanders at the downstream part (Zieliński 1999; Sarnacka 1987). The hydro-morphology of the floodplain remains rich in oxbow lakes and creeks. Existing dikes are irregularly located in the main channel. After the World War II flood protection strategy required the construction of embankments. The flood-protecting levees were built along almost the whole modelled reach on both banks of the river. The first dikes were built in the 19th century (Łajczak et al. 2006). The construction of embankments resulted in narrowing the valley to 730–2000 m (Kowalska 2010).

Nevertheless, the nature of the River Vistula remains semi-natural, which is unique in Europe for such a big river. In the studied river reach there are no large dams or other hydro-technical facilities. The analysis of land use in the middle River Vistula catchment using CORINE LAND COVER data in the period 1990–2012, presented by Gutry-Korycka et al. (2015), indicated small changes, including a decrease (6.4 %) of the agricultural areas, complemented by an insignificant

Fig. 1 Scheme of the modelled reach of the River Vistula

increase of the forested areas (3.3 %). Recently the intense anthropopression towards river floodplain is observed from the industrial, cultural and environmental development of cities and towns. That results in an urgent need for a reliable flood protection strategy.

3 Experimental Design

We use the popular 1D hydraulic model MIKE 11 (DHI 2004) for flow routing. The model was set up with the flow hydrograph as an upstream boundary condition and a rating curve for the downstream boundary condition. Calculations were performed with 30-min time step. The distance between cross-sections varied from 1 to 3 km. In the model the spatial step was chosen taking into account the adequate Courant number that guarantees the accuracy of the numerical scheme. The choice of the stage-discharge relationship as a downstream boundary condition, as opposed to using the observed water level was made due to the model purposes (to enable forecasting capabilities of model).

The applied model requires estimation of roughness coefficients for all 112 cross-sections describing river geometry (Kochanek et al. 2015; Kiczko et al. 2011, 2013). In addition, the description of variability of roughness values across cross-section is needed. In this study we assumed that one value of Manning coefficient represents the cross-section, thus neglecting the differences between the main channel and floodplains.

Water levels and discharges from seven gauging stations (Zawichost, Annopol, Puławy, Dęblin, Gusin, Warsaw-Nadwilanówka, Warsaw-Port Praski) were used simultaneously in the evaluation of the model performance with the Nash-Sutcliffe coefficient (Nash and Sutcliffe 1970) as a criterion. It was assumed that Manning roughness coefficients, specified at the cross-sections nearest to each gauging station, are linearly interpolated in the reaches located in-between. This approach was necessary to fit both flood wave time to peak and water levels at gauging stations along the river reach. Model calibration was carried out using the Simplex Nealder-Mead algorithm (Press et al. 2002).

The estimation of model parameters consists of the minimisation of a chosen objective function (here, Nash-Sutcliffe NS coefficient) calculated using simulated and observed water levels and derived discharges at seven gauged cross-sections. In order to illustrate the influence of the uncertainty of downstream boundary condition on modelling results, we perform two different automatic optimization scenarios using the sum of NS coefficients for water levels and discharges at seven cross-sections:

- only model parameters (roughness coefficients) are optimized using rating curve parameters obtained from fitting the observed water levels and discharges at the downstream cross-section for the calibration period,
- simultaneous optimization of model and rating curve parameters is performed.

The influence of downstream boundary condition on the analysed model output was also assessed using Morris sensitivity method.

4 Implementation of RC Uncertainty

In this study we derived the rating curve relationship at the model's downstream boundary from the observed water levels at Warsaw-Port Praski gauging station and discharges at Warsaw-Nadwilanówka, situated 30 km upstream, available from the operational data of IMGW. Therefore, the obtained rating curve is an approximation of real conditions at this gauging station.

Literature presents a number of mathematical expressions for relating water levels to discharge rates in a given cross-section (Ackers et al. 1978; Petersen-Øverleir 2004; Franchini and Ravagnani 2007). To asses impact of downstream boundary condition on model results we use a power-law function due to its

parsimony and hydraulic justification (Fenton 2001; Petersen-Øverleir 2005). For this study a single segment power function (Eq. 1) was chosen:

$$Q = a(H - H_0)^b, \tag{1}$$

where a and b are optimized function parameters and H_0 is the water level corresponding to zero discharge, Q denotes discharge (m^3/s) and H the water level (a.s.l. m).

We parametrized the rating curve for the historical data of water levels and discharges for calibration period (1.01.2001–31.12.2001) (Fig. 2). For this purpose, we applied a curve fitting toolbox from Matlab which provides the goodness of fit statistics together with parameter estimates. The results of estimated confidence limits at 0.05 confidence levels were applied in further analysis as ranges of uniform distribution for RC parameters during the model calibration, sensitivity and uncertainty analysis.

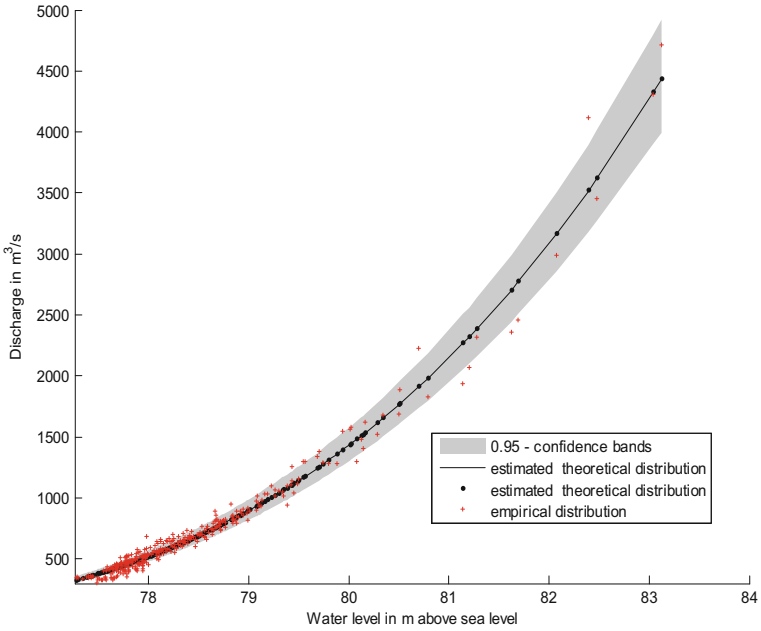

Fig. 2 Semi-empirical rating curve at Warsaw-Port Praski obtained from the available water level and discharge information for the year 2001; *black dots* and *continuous line* denote estimated theoretical distribution, *red crosses* denote empirical distribution and *shaded area* denotes 0.95 confidence limits

5 Results

5.1 Sensitivity Analysis

In this work, sensitivity analysis by the Morris method (Morris 1991) was applied for the estimation of influence of RC on modelled water levels. Detailed description of this method is presented in Campolongo et al. (2007, 2011), Osuch (2015). The results of the Morris method are presented in the form of two measures: μ^* and σ. The first measure, μ^*, represents the overall influence of factor (in our case model parameter) whilst the second measure estimates influence of nonlinearity effect and interactions with other parameters.

In this study we assumed that the model outputs (NS coefficients at seven cross-sections) are influenced by two rating curve parameters (a and b) at the model's downstream boundary and also by seven Manning coefficients, one at the nearest cross-section to each gauging station. In this study the following parameters for the Morris method were chosen: number of parameters = 9, number of sensitivity-related levels = 10, total number of trajectories = 1000, and optimal number of trajectories = 15. The selected nine parameters were drawn from uniform distributions. The lower and upper limits for two parameters of RC were chosen following the estimates of their uncertainty. For other cases the Manning roughness coefficients at gauged cross-sections were changing in the range [0.01, 0.2].

The results of sensitivity analysis in the form of estimates of influence of analysed factor on the model output (NS estimated for water levels) are presented in Fig. 3 for the gauging stations at Dęblin, Gusin, Warsaw-Nadwilanówka and Warsaw-Port Praski. The influence of RC in Warsaw-Port Praski is negligible in all gauged cross-sections upstream of Gusin. Only in the case of Gusin, Warsaw-Nadwilanówka and Warsaw-Port Praski gauging station the estimates of μ^* are higher than 0.01, indicating small influence on model output. The estimated values of second measure, σ, confirm these findings. The sensitivity analysis indicates that the downstream boundary condition influences mainly the Warsaw-Port Praski results.

Similar results were obtained for the analysis of influence of nine factors (parameters of the MIKE 11 and two parameters of the RC) on the NS values calculated for the simulated and observed discharges. The influence of two parameters of RC is negligible in the first four gauged cross-sections comparing to the influence of the MIKE 11 parameters.

5.2 Model Calibration and Validation

The calibration of the model parameters for the studied reach of the River Vistula was performed using two scenarios which allows the influence of the uncertainty of the RC in Warsaw-Port Praski on the simulated water level and discharges at seven

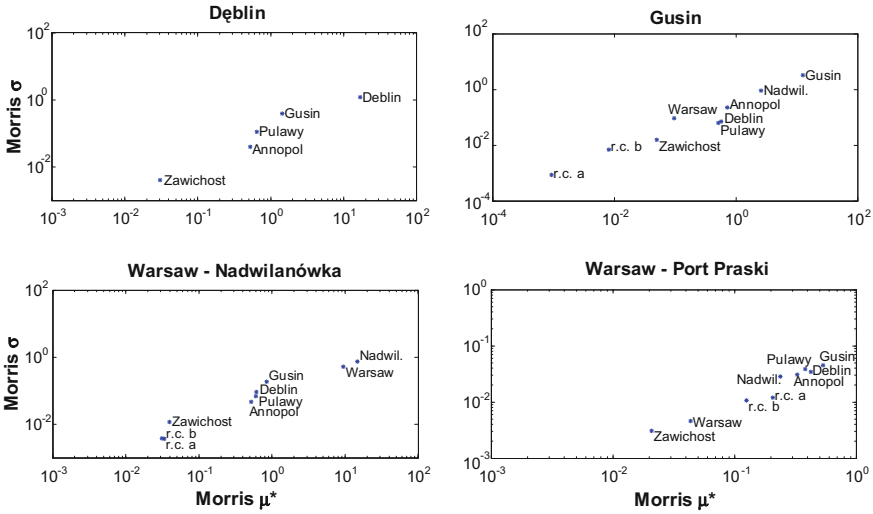

Fig. 3 The results of sensitivity analysis by Morris method. The analysis of influence of nine factors: values of Manning coefficients at seven controller cross-sections and two parameters of the rating curve in Warsaw-Port Praski on the Nash and Sutcliffe (1970) values estimated for water levels in seven gauging stations

controlled cross-sections to be assessed. In the first scenario, it was assumed that only parameters of the MIKE 11 model have an influence on the model output. In this scenario, the downstream boundary condition was specified using the optimised deterministic parameters of the RC in Warsaw-Port Praski for the calibration period.

In the second scenario, the model is characterized by nine parameters which are Manning roughness coefficients at seven gauged cross-sections and two parameters of the rating curve in Warsaw-Port Praski.

For each scenario, the optimisation was done automatically using the observed time series (water levels and discharges) from 1.01.2001 to 31.12.2001. Model calibration was carried out using Simplex Nealder-Mead algorithm (Press et al. 2002) within selected feasible parameter ranges of Manning coefficient [0.01, 0.2] and for the RC parameters ranges: a [1.913, 2.204] and b [3.213, 3.283] following from the estimated by the MATLAB curve-fitting toolbox parametric uncertainty. Model performance was evaluated by the NS criterion for water levels and discharges for seven gauging stations: Zawichost, Annopol, Puławy, Dęblin, Gusin, Warsaw-Nadwilanówka and Warsaw-Port Praski. Since the measurements of discharges in Warsaw-Port Praski are not available, for this gauge the objective function is based on water levels only. As an objective function we applied the sum

of NS values for all analysed gauging stations estimated for water levels and discharges multiplied by −1. In the ideal case the minimum value of the applied objective function should be −13.

We applied multiple starting points of the algorithm to achieve a global solution using local method of optimisation such as Simplex Nealder-Mead algorithm. Five starting points were tested of which the best achieved value of objective function was −11.12 for the first scenario (starting point no. 1) and −11.30 for the second scenario (starting point no. 5). The results of parameter optimisation in the form of optimal parameter values and values of objective function are presented in Table 1. The optimal values of the Manning's roughness coefficient n match the weedy, deep pools (Chow 1959), which is close to reality, since within its modelled reach the River Vistula is mostly an unregulated weedy and relatively deep channel. We also notice that different sets of parameters lead to similar values of the objective function.

The comparison of the estimated values of the objective function between two scenarios shows that results of optimization are slightly better in the second case when nine parameters are optimized (Table 1). The improvement of the value of the objective function results from an increase of goodness of fit in case of water level for Warsaw-Port Praski (Table 2).

In the next step, the best models (with lowest values of the objective function) from each of tested scenarios were validated using the period 1.01.2007–30.10.2010. The results of validation in the form of calculated NS coefficients for seven gauged cross-sections analysed are presented in Table 2. An increase of NS values for Warsaw–Port Praski gauging station for water levels is clearly visible. In the case of Warsaw-Nadwilanówka gauging station, a slight decrease of the NS for water levels is obtained.

The Generalised Likelihood Uncertainty Estimation (GLUE) technique (Beven and Binley 1992) was used for the estimation of parametric uncertainty. This technique is based on multiple Monte Carlo runs of a deterministic model with parameters randomly chosen from an a priori specified distribution. The posterior distribution of the model predictions is obtained using a likelihood measure conditioned on observations. The choice of the likelihood measure should reflect the purpose of the study. As the likelihood measure we use the NS coefficient of determination. The model parameters were sampled 10,000 times from log-normal distribution with mean value for the optimal parameters (starting point 5 for second scenario Table 1). The results of water levels uncertainty for the calibrating period are shown in Fig. 4.

Table 1 The results of identification of Manning's coefficients for two scenarios and 5 starting points of the optimisation algorithm

Starting point no.		Optimal Manning's n							Optimal rating curve parameters		Objective function
		Zawichost	Annopol	Pulawy	Deblin	Gusin	W.-Nadwilanowka	W.-Port Praski	a	b	
First scenario	**1**	**0.0537**	**0.0446**	**0.0389**	**0.0463**	**0.0770**	**0.0568**	**0.0101**	–	–	**−11.1296**
	2	0.0546	0.0447	0.0395	0.0463	0.0789	0.0417	0.0516	–	–	−11.1154
	3	0.0540	0.0437	0.0394	0.0462	0.0781	0.0508	0.0321	–	–	−11.1250
	4	0.0538	0.0443	0.0390	0.0468	0.0778	0.0557	0.0169	–	–	−11.1293
	5	0.0535	0.0446	0.0389	0.0462	0.0778	0.0548	0.0204	–	–	−11.1288
Second scenario	1	0.0521	0.0446	0.0387	0.0455	0.0832	0.0115	0.1045	2.1754	3.2443	−10.9581
	2	0.0558	0.0449	0.0392	0.0454	0.0793	0.0392	0.0579	1.9619	3.2193	−11.2479
	3	0.0552	0.0444	0.0394	0.0452	0.0781	0.0491	0.0357	2.2003	3.2321	−11.0370
	4	0.0538	0.0443	0.0388	0.0462	0.0781	0.0478	0.0379	1.9189	3.2820	−11.1517
	5	**0.0546**	**0.0448**	**0.0388**	**0.0473**	**0.0771**	**0.0518**	**0.0275**	**1.9130**	**3.2130**	**−11.3006**

The highlighted values denote optimum model parameters and the optimum values of the objective function

Table 2 A comparison of the calibration and validation results (NS values) at seven gauged cross-sections for two scenarios

Nash-Sutcliffe function values for								
	Calibration				Validation			
	First scenario		Second scenario		First scenario		Second scenario	
Reference gauge	Water level	Discharge	Water level	Discharge	Water level	Discharge	Water level	Discharge
Zawichost	0.9701	0.9994	0.9705	0.9994	0.9358	0.9999	0.9325	0.9999
Annopol	0.9152	0.9929	0.9184	0.9929	0.9050	0.9770	0.9073	0.9770
Pulawy	0.8474	0.9850	0.8484	0.9849	0.9120	0.9858	0.9126	0.9857
Dęblin	0.7572	0.9443	0.7639	0.9439	0.8846	0.9561	0.8836	0.9559
Gusin	0.7304	0.8536	0.7274	0.8514	0.7450	0.8579	0.7440	0.8562
Warsaw–Nadwilanowka	0.8581	0.7491	0.8420	0.7494	0.8423	0.8097	0.8299	0.8102
Warsaw–Port Praski	0.5268	–	0.7082	–	0.5012	–	0.6628	–

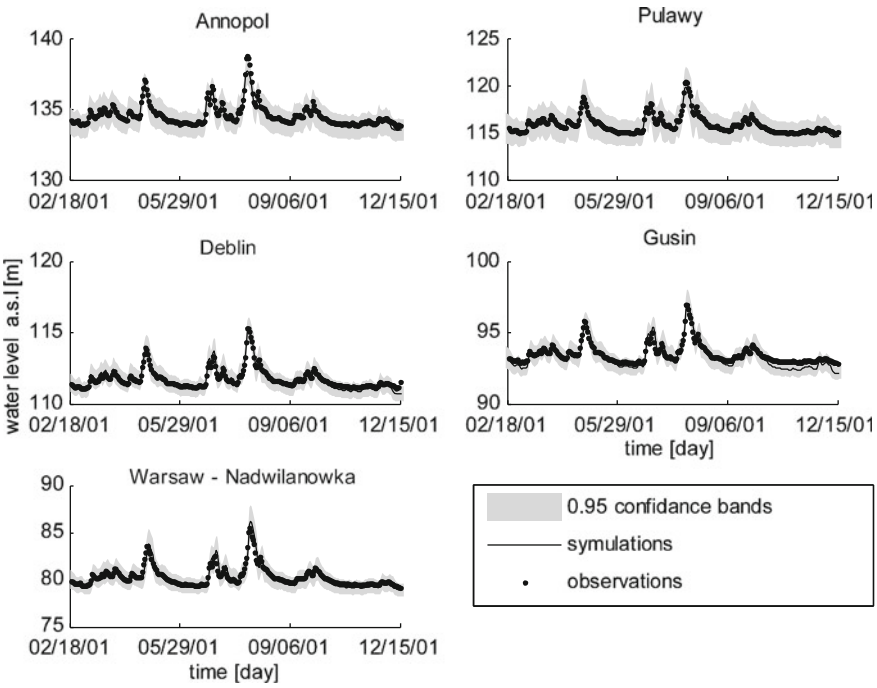

Fig. 4 The results of the MIKE 11 model calibration for water levels at five gauging station; *dots* denote observed water levels, *continuous line* denotes estimated water levels and *shaded area* denotes 0.95 confidence limits

6 Conclusion

The aim of this study was to investigate how the downstream boundary condition affects the results of flow routing model. We applied two scenarios, both including optimization and sensitivity analysis based on Morris method to analyse that problem. In the first scenario, only model parameters were varied with rating curve parameters kept constant and equal to empirical values for the year 2001. In the second scenario, rating curve parameters were varied together with the model roughness coefficients.

The results of sensitivity analysis indicated that the influence of two parameters of RC in Warsaw-Port Praski is negligible for all gauged cross-sections upstream of Gusin. Only in the case of Gusin, Warsaw-Nadwilanówka and Warsaw-Port Praski gauging stations the estimates of μ^* are higher than 0.01 indicating small influence of RC parameters on the model output. This gives an answer to our first research question, regarding the extent of the influence of the downstream boundary condition.

As could be expected, increasing the number of parameters improved model performance. The largest improvement resulted from better fit of water levels in

Warsaw-Port Praski gauging station. Therefore, the second aim of the study, i.e., improvement of the model predictions at the Warsaw reach was fulfilled.

Acknowledgments This work was financed by the project "Stochastic flood forecasting system (The River Vistula reach from Zawichost to Warsaw)" carried out by the IGF PAN for the National Science Centre (contract no. 2011/01/B/ST10/06866). The hydrological data were provided by the Institute of Meteorology and Water Management (IMGW), Poland.

References

Ackers P, White WR, Perkins JA, Harrison JM (1978) Weirs and flumes for flow measurement. Wiley, Chichester

Beven K, Binley A (1992) The future of distributed models: model calibration and uncertainty prediction. Hydrol Process 6:279–298. doi:10.1002/hyp.3360060305

Boiten W (2008) Hydrometry: a comprehensive introduction to the measurement of flow in open channels. CRC Press/ Balkema, Rotterdam

Campolongo F, Cariboni J, Saltelli A (2007) An effective screening design for sensitivity analysis of large models. Environ Model Softw 22:1509–1518. doi:10.1016/j.envsoft.2006.10.004

Campolongo F, Saltelli A, Cariboni J (2011) From screening to quantitative sensitivity analysis. A unified approach. Comput Phys Commun 182:978–988

Chow VT (1959) Open-channel hydraulics. McGraw-Hill, New York 680 p

Danish Hydraulic Institute (DHI) (2004) MIKE 11 GIS reference and user manual. Horsholm, Denmark

Di Baldassarre G, Claps P (2011) A hydraulic study on the applicability of flood rating curves. Hydrol Res 42(1):10–19. doi:10.2166/nh.2010.098

Di Baldassarre G, Montanari A (2009) Uncertainty in river discharge observations: a quantitative analysis. Hydrol Earth Syst Sci 13:913–921. doi:10.5194/hess-13-913-2009

Di Baldassarre G, Laio F, Montanari A (2011) Effect of observation errors on the uncertainty of design floods. Phys Chem Earth Parts A/B/C 42–44:85–90. doi:10.1016/j.pce.2011.05.001

Domeneghetti A, Castellarin A, Brath A (2012) Assessing rating curve uncertainty and its effects on hydraulic model calibration. Hydrol Earth Syst Sci 16:1191–1202. doi:10.5194/hess-16-1191-2012

Domeneghetti A, Vorogushyn S, Castellarin A, Merz B, Brath A (2013) Probabilistic flood hazard mapping: effects of uncertain boundary conditions. Hydrol Earth Syst Sci 17:3127–3140. doi:10.5194/hess-17-3127-2013

Fenton JD (2001) Rating curves: part 2—representation and approximation. In: Proceedings of the conference on hydraulics in civil engineering. Institute of Engineer Australia: Hobart; 28–30 Nov 2001, pp 319–328

Franchini M, Ravagnani F (2007) Costruzione della scala di deflusso in una sezione con sole misure di livello utilizzando le portate registrate a monte ed un modello diffusivo-convettivo. L'Acqua, n. 5, Associazione Idrotecnica Italiana, Roma, 9–20

Gutry-Korycka M, Mirończuk A, Hościło A (2015) Changes of land-use in the middle River Vistula catchment. In: Romanowicz RJ, Osuch M (eds) Stochastic flood forecasting system: the middle vistula case study. GeoPlanet: earth and planetary sciences. Springer

Kiczko A, Romanowicz RJ, Osuch M (2011) Impact of water management policy on flow conditions in wetland areas. Phys Chem Earth Parts A/B/C 36(13):638–645. doi:10.1016/j.pce.2011.07.004

Kiczko A, Romanowicz RJ, Osuch M, Karamuz E (2013) Maximising the usefulness of flood risk assessment for the River Vistula in Warsaw. Nat Hazards Earth Syst Sci 13:3443–3455. doi:10.5194/nhess-13-3443-2013

Kochanek K, Karamuz E, Osuch M (2015) Distributed modelling of flow in the middle reach of the River Vistula. In: Romanowicz RJ, Osuch M (eds) Stochastic flood forecasting system: the middle Vistula case study. GeoPlanet: earth and planetary sciences. Springer

Kowalska A (2010) Wpływ obwałowań na zróżnicowanie roślinności równiny zalewowej w dolinie środkowej Wisły, Nizina Mazowiecka. (Embankments influence on diversity of floodplain vegetation in the Middle Vistula River Valley, Mazovian Plain). Prace Komisji Krajobrazu Kulturowego no 13

Łajczak A, Plit J, Soja R, Starkel L, Warowna J (2006) Changes of the Vistula River channel and floodplain in the last 200 years. Geographia Polonica 79(2):65–87

Le Coz J (2012) A literature review of methods for estimating the uncertainty associated with stage-discharge relations, WMO report, P06a, 21 pp. http://www.wmo.int/pages/prog/hwrp/Flow/flow_tech/documents/WMO_PO6a_RC_uncertainty.pdf

Le Coz J, Renard B, Bonnifait L, Branger F, Le Boursicaud R (2014) Combining hydraulic knowledge and uncertainty gaugings in the estimation of hydrometric rating curves: a Bayesian approach. J Hydrol 509:573–587. doi:10.1016/j.jhydrol.2013.11.016

Magnuszewski A (2015) Influence of channel processes and vegetation in the Vistula river valley in Warsaw on flood safety. In: Romanowicz RJ, Osuch M (eds) Stochastic flood forecasting system: the middle Vistula case study. GeoPlanet: earth and planetary sciences. Springer

Morris MD (1991) Factorial sampling plans for preliminary computational experiments. Technometrics 33(2):161–174

Nash JE, Sutcliffe JV (1970) River flow forecasting through conceptual models. Part I—A discussion of principles. J Hydrol 10(3):282–290. doi:10.1016/0022-1694(70)90255-6

Osuch M (2015) Sensitivity analysis of the flow routing model—multimethod approach. In: Romanowicz RJ, Osuch M (eds) Stochastic flood forecasting system: the middle Vistula case study. GeoPlanet: earth and planetary sciences. Springer

Pappenberger F, Matgen P, Beven KJ, Henry JB, Pfister L, Fraipont de P (2006) Influence of uncertain boundary conditions and model structure on flood inundation predictions. Adv Water Resour 29(10):1430–1449. doi:10.1016/j.advwatres.2005.11.012

Petersen-Øverleir A (2004) Accounting for heteroscedasticity in rating curve estimates. J Hydrol 292(1–4):173–181. doi:10.1016/j.jhydrol.2003.12.024

Petersen-Øverleir A (2005) A hydraulics perspective on the power-law stage–discharge rating Curve. Norwegian Water Resources and Energy Directorate, Oslo, Norway, NVE report 05–05

Press WH, Teukolsky SA, Vetterling WT, Flannery BP (2002) Numerical recipes in C++. Cambridge University Press, Cambridge

Sarnacka Z (1987) Evolution of the Vistula Valley between the outlets of Radomka and Świder in the Late Glacial and Holocene. In: Starkel L (ed) Evolution of the Vistula River Valley during the last 15000 years part II Prace Geograficzne. Special issue no 4

Zieliński J (1999) Wisła Środkowa po przeprowadzeniu prac regulacyjnych (Middle Vistula after regulation). In: Kucharczyk M (ed) Problemy ochrony i renaturalizacji dolin dużych rzek Europy (Problems of protection and renaturalisation of big European rivers). UMCS Publishing House, Lublin, pp 195–200 (in Polish)

Morphological Changes of a Restored Reach: The Case of the Spree River, Cottbus, Germany

Michael Nones and Christoph Gerstgraser

Abstract The main goals of the European Water Framework Directive (WFD) are the improvement of the ecological status of all water bodies by 2027 and continuous monitoring to prevent future degradations. When applied to rivers, the WFD considers hydromorphological elements only as supporting elements for watercourses at good or lower status, while biological elements are considered as fundamental. Nonetheless, various scientific studies have demonstrated that rivers need to be considered in a more holistic way, involving all their characteristics, principally water, sediment and biota. The aim of the present study is to demonstrate the importance of considering sediments during the WFD implementation cycles. To give a practical example, the case study of a restored reach of the Spree River near the city of Cottbus, Brandenburg, Germany, was chosen. The analysis proposed here utilized aerial images, DGMs and cross-section profiles for the pre- and post-project periods, giving information about the morphological changes due to the restoration works. Preliminary results show that the river morphology is affected by fine sand, transported in particular during high flow conditions. This study illustrates that if only biological parameters had been monitored as recommended by WFD, then potential issues would not have been identified for the effective river management.

1 Introduction

Most European rivers have been altered by human activities in the last century, such as the construction of dams that influence flow conditions and the longitudinal migration of organisms, river channelization that has reduced habitat heterogeneity, and many floodplains influenced by agriculture, land drainage and urbanization,

M. Nones (✉) · C. Gerstgraser
gerstgraser - Ingenieurbüro für Renaturierung, An der Pastoa 13,
03042 Cottbus, Germany, Germany
e-mail: nones@gerstgraser.de

P. Rowiński and A. Marion (eds.), *Hydrodynamic and Mass Transport at Freshwater Aquatic Interfaces*, GeoPlanet: Earth and Planetary Sciences,
DOI 10.1007/978-3-319-27750-9_14

have lost their connectivity (Pedersen et al. 2014). Consequently, national authorities and the European Union have developed new policies to safeguard water bodies and aquatic environments, such as the Urban Waste Water Treatment Directive and the Nitrates Directive (both adopted in 1991), the Habitat and Species Directive (approved in 1992), a Directive for Integrated Pollution and Prevention Control (namely, IPPC Directive, become into force in 1996) and a new Drinking Water Directive (adopted in 1998).

In the mid 1990s, the Council and the European Parliament created a Commission to involve all interested parties, with the aim to write a unique proposal for a new water policy. In 1996, the Commission presented a draft of the European Water Framework Directive (hereafter called WFD). The WFD 2000/60/EC (EU 2000) came into force in the year 2000 and sets out new concepts for water management, such as a catchment-based approach for the implementation of water policies (Art. 3), the "polluters-pays" principle, the development of cost-benefit analyses (Art. 9 and Annex III), and public participation during the decision-making processes (Art. 14). The main aim of this Directive, however, is the improvement of the overall ecological status of water bodies, recognizing the present and future value of freshwater ecosystems (Art. 4). Annex V specifies the requirements of an ecological classification for each water body, establishing specific reference conditions, giving more importance to the biological quality elements and introducing hydromorphological quality elements. This approach demonstrates an awareness by the European Commission of the impacts that have resulted from alterations of flow regime and river morphology. Besides this holistic approach, there are some potential areas of weakness, such as derogations and extensions that Member States can apply. As highlighted by the periodical EU reports about the WFD implementation across Europe, many States have applied exemptions, following Arts. 4.4, 4.5, 4.6 and 4.7, to a large part of their water bodies due to disproportionate costs, technical feasibility or natural conditions. These exemptions can regard deadlines extension, less stringent objectives, temporary deterioration due to natural causes, new modifications and new sustainable human development activities (WFD CIS 2009). Another weakness is represented by the classification system used for the biological status, where the integration of the hydromorphological quality elements result insufficient, as explained below (Nardini et al. 2008).

Different studies (Gurnell et al. 2012; Nones 2013; Marion et al. 2014) and projects (e.g., Hyporheisches Netzwerk, www.hyporheisches-netzwerk.de) highlight that aquatic ecosystems are composed of water, sediments and biota, with strong interrelationships. For this reason, the protection of freshwater environments requires an in-depth knowledge of the relationship between physical and biological processes (Marion et al. 2014), fully taking into account all their components. Different approaches at a wide variety of scales have been taken by Member States in order to deal with sediment issues by the redaction of the River Basin Management Plans (RBMPs). In 2009, an analysis performed by SedNet regarding the first implementation cycle of some available RBMPs demonstrates that a range of important relationships between sediments and water management exists, and

highlights the potential benefits associated with achieving better integration of sediment issues into a holistic approach to practical river management (SedNet 2009). Despite the recognition of the relationship between water and sediments, the most important result of the SedNet analysis of the present RBMPs is that the sediments and their contribution are not considered as a priority in the WFD implementation process, due to their complex interactions with water and vegetation and to the lack of clear target values or specific EU guidelines. This "blind" approach could create problems during the application of the Directive, with consequent failure of some river restoration projects, which are not able to fulfill the WFD requirements of Good Ecological Status (GES) due to the inadequate consideration of sediment issues. As reported in other studies about restoration projects (Pedersen et al. 2014), it is difficult to evaluate the morphological adjustments of a river after restoration measures because of the limited information provided by water authorities on physical habitat, water quality and biota. Partially, the lack of clear results can be attributable to inadequate pre- and post-project monitoring programmes, often neglected by water authorities due to their costs and technical feasibility, and partly to the focus of most projects only on the reach scale, without considerations at watershed scale, in contrast with the recommendations reported into the WFD.

To evaluate the present status of WFD implementation and propose some recommendations to Member States for a sustainable development of water bodies, many European projects were funded during past years, such as REFORM (www.reformrivers.eu), REFRESH (www.refresh.ucl.ac.uk) and RESTORE (www.ecrr.org). As part of another FP7 project, HYTECH (hytech.dii.unipd.it), an analysis of the importance of morphological changes in restored rivers and its relationship with the WFD, implementation in three European States has been made (Germany, Italy and the UK). In Germany, a reach of the Spree River near the city of Cottbus, Brandenburg, was chosen as a case study. This river was chosen due to the presence of a recently restored reach, planned, realized and monitored by the local SME gerstgraser - Ingenieurbüro für Renaturierung (gIR 2014), and continuously monitored and studied.

This paper presents the morphological changes that result from the monitoring programme of a restored reach of the Spree River. After a description of the study site and the restoration project, the results of the monitoring are presented by comparing: (i) aerial images spanning the period 2006–2014; (ii) different cross-section profiles taken along the river reach, derived from bathymetric surveys and Digital Ground Models (DGMs) spanning the period 2003–2014.

2 Case Study

The Spree River rises in the Lusatian Mountains at the Czech/Germany border and flows for 380 km to its confluence with the Havel River, a tributary of the Elbe River, in the city of Berlin (Fig. 1a). Important tributaries of this watercourse in

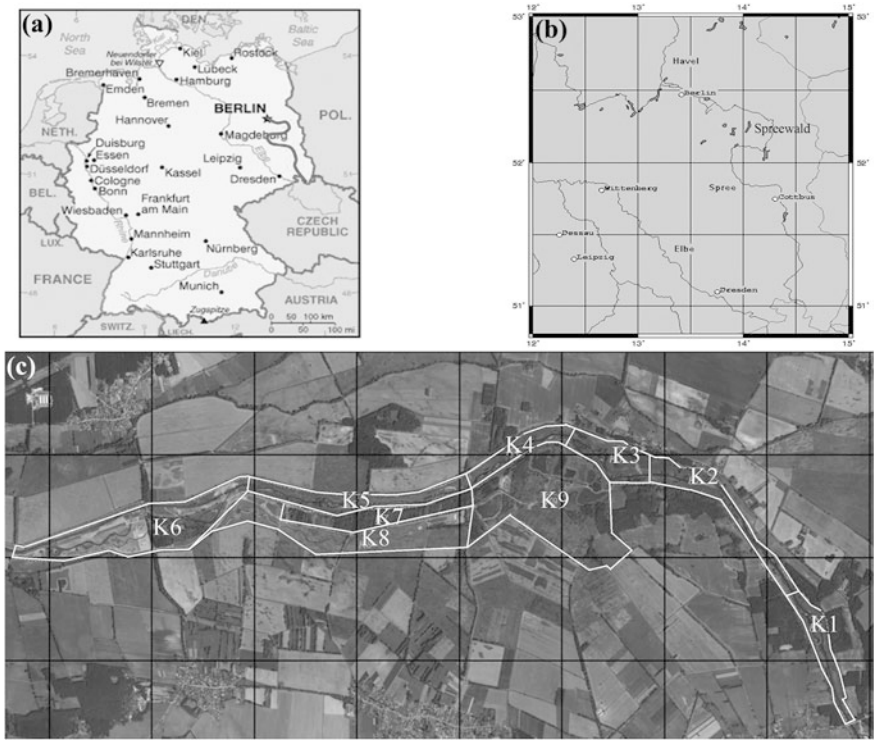

Fig. 1 **a** Map of Germany, with the path of the Spree River; **b** the watercourse in Saxony and Brandenburg; **c** restored river reach, with indication of the various sub-reaches *K1–K9*

Brandenburg are the Dahme, the Löcknitz and the Großes Fließ. The Spree water system is strongly influenced by human intervention, including agriculture and more than one century of coal mining (Hilt et al. 2008). Nevertheless, it is possible to find throughout the course a plurality of closely-spaced braided parts and semi-natural habitats, such as the Spreewald, located downstream of the city of Cottbus (Fig. 1b).

The study site (Fig. 1c) is located approximately 10 km north (downstream) of Cottbus, near coal mining activities. The basin drained by this lowland stream is around 62 km^2. Here, the river is characterized by a low longitudinal gradient around 0.07 %, a mean discharge of 7.5 m^3/s and a bankfull discharge of 35 m^3/s (gIR 2009). The water discharge and the sediment transport are significantly influenced by the retention capacity of the reservoirs of Quitzdorf and Bautzen (Saxony) and Spremberg (Brandenburg). The bed material is composed of fine sand, ranging from 0.06 to 6 mm, with a median diameter of 0.66 mm (gIR 2008).

The restoration project, started at the end of 2006 and completed in 2014, aimed to compensate the destruction of the Natura 2000 site (Gerstgraser and Zank 2012) called “Lakomaer Teiche”, located in the southeast of the Federal State of

Brandenburg. The restored area was divided into nine sub-reaches, called from K1 to K9 (Fig. 1c): the watercourse flows into the K1–K6 sub-reaches, while the remaining three sub-reaches are used to locate floodplains and ponds.

A series of interventions were done, such as reconnection of oxbow lakes, opening of new secondary channels, creation of islands and sand bars by means of groynes (submerged and emerged), increase in bed grain size composition, creation of backwater zones and ponds (gIR 2008). These engineering works were made to increase the flow variability along the river, and to reconnect the floodplains. A higher flow variability, closer to the Spree pristine conditions (Hilt et al. 2008), creates a better environment for macrophytes and local fauna, with different ecotones and zones suitable for spawning (Arscott et al. 2002; Gray and Harding 2007), and contributes to increase the ecological status of the river, fulfilling the WFD requirements.

3 Evolution of the River Reach

In order to evaluate the preliminary results of the restoration project and its contribution to the fulfilment of the WFD goals, a brief analysis of the morphological changes along the restored reach was made, covering the pre- and post-project periods (2006–2014). The study was performed at different scales: at the reach scale by means of aerial images; and at the cross-section scale by comparing various profiles derived from DGMs and bathymetric surveys.

3.1 Comparison of Aerial Images

A series of aerial images taken during the summer period, provided by the Vattenfall Europe Mining AG and spanning the period between 2006 and 2014, were analysed to compare the situation of the river banks before (2006 state) and after the restoration project and to evaluate the planimetric changes of this reach. The resolution of the images is 25 cm, and the discharges associated with the images are quite comparable, close to the mean discharge of the river (7.5 m^3/s). The images relating to the summer of 2013 were discarded, due to flood conditions (gIR 2014) making it impossible to view the bank profiles. The comparison was made by means of the open source software QGis: for each image the banks were identified, 100-m equally-spaced segments were traced on the maps and the lengths of the most important parameters were estimated (Eqs. 1–4), following the approach proposed by Amsler et al. (2005). With these parameters, it was possible to compute the thalweg sinuosity P_t, the braiding index BI and the total sinuosity S for each segment (Eqs. 1–3), and then average these values for each sub-reach Ki (i = 1, 6) of the river.

$$P_t = L_t / L_r \tag{1}$$

$$BI = \Sigma L_i / L_t \tag{2}$$

$$S = \Sigma L_i / L_r \tag{3}$$

$$L_i = L_t + \sum L_s \tag{4}$$

where L_r and L_t are the characteristic lengths of the main channel: L_r represents the length of the right river bank, while L_t is the length of the thalweg path. To describe the secondary channels, only the length of its thalweg L_s was taken into account. For the computation of BI and S, the length L_t was included into the sum of the L_i values (Eq. 4) (Fig. 2).

This analysis provided a preliminary estimate of the effects of the restoration project in terms of planimetric variations, but also highlighted the importance of sediment transport, and in particular its contribution to channel migration and to the definition of the primary flow path. The inspection of consecutive aerial images (Fig. 3) showed that transport of fine sand due to high flow conditions caused the cutoff of secondary channels, the deposition along floodplains and ponds, the decreasing of braiding index and sinuosity, threatening the growth of the macrophytes and fish spawning, all with consequences for the ecological status of the river and its WFD classification. A clear example is visible in sub-reach K5 between 2012 and 2014 (Fig. 3c, d): the huge flood occurred during the summer 2013 had transported a lot of sand and closed some secondary channels and backwater zones along this sub-reach.

In Table 1 the values of the thalweg sinuosity along the studied reach are reported. These values were computed by averaging over the sub-reaches the thalweg sinuosity measured for each segment. All thalweg sinuosity values are less than one, reflecting that the thalweg path is shorter than the right bank, and the river has a meandering planform (as visible in Fig. 1c).

Following Eq. 1, a general slight decrease in the thalweg sinuosity was observed for the entire reach, due to the increase of the right bank length, while the thalweg length remained constant during the study period. A variation was measured, in particular, for the central part of the study reach (namely, sub-reaches K3, K4 and K5). Importantly, analysis of the thalweg sinuosity does not give information about the construction of secondary channels during the restoration process: indeed, thalweg and right bank lengths are characteristics only of the main channel. For this reason, the thalweg sinuosity is not considered as an important index to evaluate the reliability of this restoration project, which rather had the aim to improve the overall river status by means of the reconnection of secondary channels and floodplains despite of the displacement of the main channel thalweg.

To take into account the contribution of secondary channels, it is necessary to evaluate the braiding index of the river (Eq. 2). Values larger than one indicate the

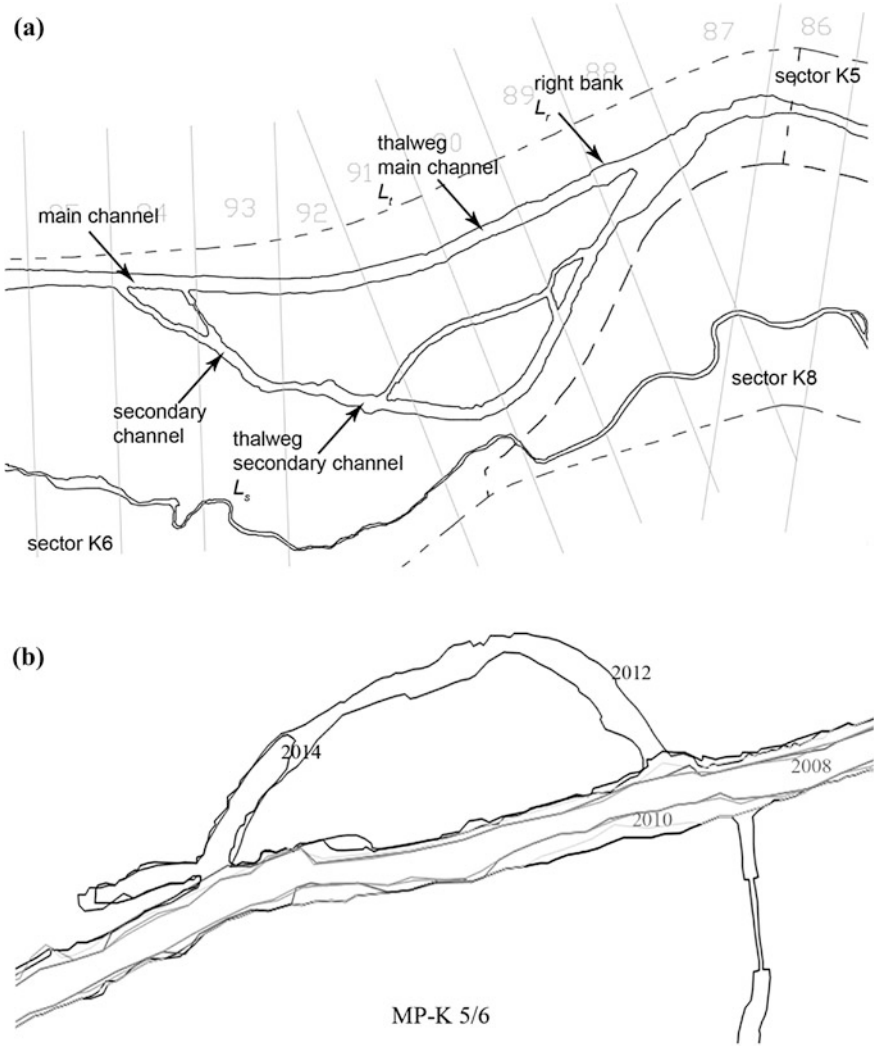

Fig. 2 Planimetric path of the river reach: **a** outline of the 100-m equally-spaced segments and the characteristic lengths; **b** example of the path changes between *2008* and *2014* in a part of the sub-reach *K5*

presence of secondary channels in the analysed reach. In Table 2 the average values of the braiding index for each sub-reach are summarized.

Before the restoration project, this reach of the Spree River was essentially a single thread channel with very few secondary channels, located only in sub-reaches K3 and K6. The increase of the braiding index in some sub-reaches is a result of the restoration works. In this manner, it is possible to take back the reach to a state that is closer to the pristine conditions of the Spree River, typical of around

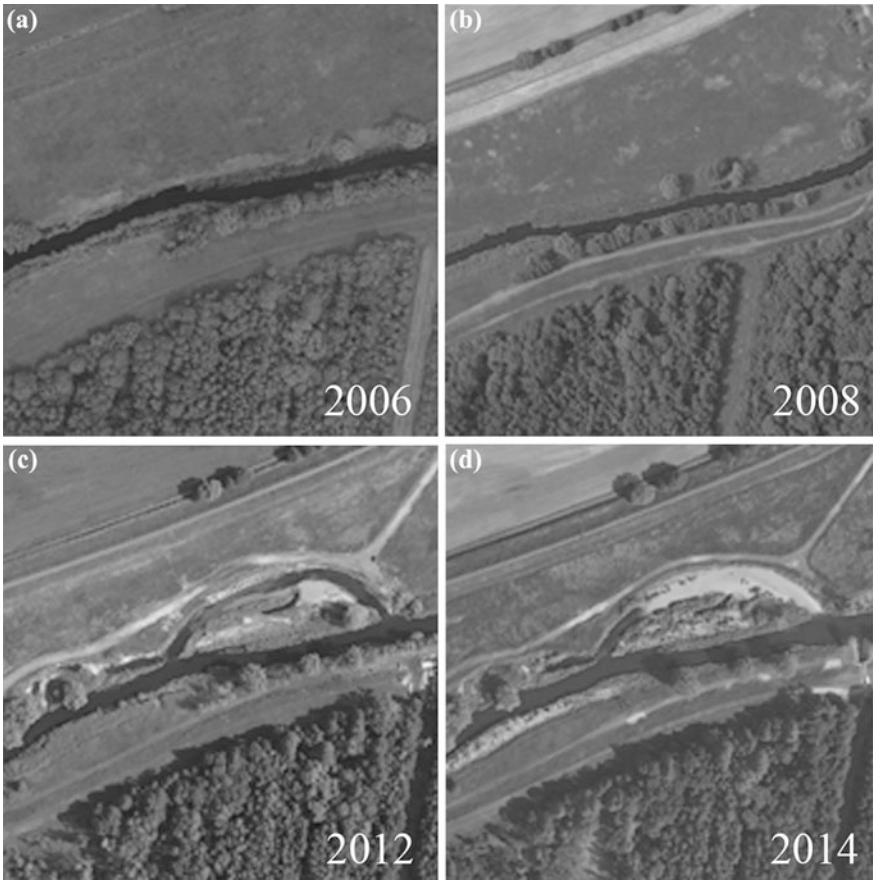

Fig. 3 Comparison of the reach K5 at different periods: straight configuration in *2006* and *2008*, before the restoration measures, re-meandered configuration after the project (*2012*) and cutoff of some secondary channels (*2014*) due to sediment deposition after the flooding event of 2013

Table 1 Averaged values of the thalweg sinuosity P_t for the sub-reaches

	2006	2007	2008	2009	2010	2011	2012	2014
K1	0.97	0.97	0.97	0.97	0.95	0.94	0.91	0.94
K2	0.96	0.96	0.94	0.93	0.90	0.93	0.89	0.88
K3	0.97	0.97	0.96	0.91	0.92	0.94	0.85	0.85
K4	0.94	0.95	0.93	0.94	0.90	0.92	0.81	0.79
K5	0.98	0.98	0.97	0.96	0.93	0.93	0.84	0.80
K6	0.96	0.97	0.98	0.97	0.92	0.95	0.94	0.93

Table 2 Averaged values of the braiding index *BI* for the sub-reaches

	2006	2007	2008	2009	2010	2011	2012	2014
K1	1.00	1.00	1.00	1.09	1.34	1.30	1.26	1.37
K2	1.00	1.00	1.02	1.11	1.24	1.19	1.17	1.23
K3	1.18	1.15	1.37	1.62	1.62	1.35	1.56	1.55
K4	1.00	1.00	1.29	1.32	1.40	1.04	1.45	1.44
K5	1.00	1.00	1.00	1.00	1.03	1.16	1.52	2.78
K6	1.01	1.00	1.01	1.00	1.01	1.01	1.01	2.91

1000 years ago (Hilt et al. 2008). The increase of the braiding index is delayed along the reach, in relation to the progress of the project. Downstream sub-reaches showed a higher increase of the braiding index, but delayed with respect to the upstream sub-reaches (Table 2). Notwithstanding the preliminary indications reported above, a long-term analysis of the braiding index variation is necessary to evaluate the morphological changes and the river recovery in terms of deposition and erosion phenomena along secondary channels and floodplains, especially in the downstream sub-reaches K5 and K6.

With respect to narrower and straighter rivers, previous studies (Arscott et al. 2002; Gray and Harding 2007) suggest that braided rivers constitute a better environment for macrophytes and local fauna, creating different ecotones and zones suitable for spawning. Hydrological connectivity has profound implications in meandering and braided rivers: it regulates the functional and structural attributes of habitat patches and ecotones, giving rise to a diversity of lentic (standing or slow-moving water), lotic (flowing water) and semi-aquatic habitat types. The heterogeneity in habitat conditions in braided river floodplains is one of the major contributing factors to the high biodiversity levels (Gray and Harding 2007) and the consequent high status WFD classification of these rivers.

Changes in total sinuosity (Table 3) provide an overview of the planimetric evolution of the study reach due to the restoration works. Average values for each sub-reach are reported and the data summarize the length of the main and secondary channels with respect to the length of the right bank (Eq. 3). If no secondary channels are present in a sub-reach, the value of the total sinuosity equals the thalweg sinuosity. Data reported in Table 3 give an estimation of the ratio between

Table 3 Averaged values of the total sinuosity *S* for the sub-reaches

	2006	2007	2008	2009	2010	2011	2012	2014
K1	0.97	0.97	0.97	1.06	1.26	1.28	1.12	1.27
K2	0.96	0.96	0.96	1.03	1.11	1.10	1.04	1.05
K3	1.14	1.12	1.32	1.48	1.49	1.23	1.28	1.26
K4	0.94	0.95	1.19	1.24	1.26	0.96	1.15	1.11
K5	0.98	0.98	0.97	0.96	0.96	1.08	1.26	2.25
K6	0.97	0.97	0.98	0.97	0.93	0.96	0.94	2.73

the length of the main channel and the length of the flow path: the higher the total length of secondary channels, the higher the value of the total sinuosity.

When considering the temporal changes in total sinuosity, the most important variations are visible for the downstream part of the studied reach (sub-reaches K5 and K6) during the last two years, similar to the braiding index analysis. This is related to the ending of the restoration works for this part of watercourse (2014). For sub-reaches K1 to K4, an increase of the total sinuosity is observed during the period 2008–2010, corresponding to restoration works. After these restoration measures, the sinuosity decreased slightly, in particular along sub-reaches K2 and K3, as a consequence of the deposition of fine sand along some secondary channels (Fig. 4).

3.2 Cross-Section Profiles

An analysis of the post restoration recovery of the river was also undertaken by observing changes in some cross-section profiles from 2003 to 2014, by means of bathymetric surveys and Digital Ground Models (DGMs). The DGMs refer to the 2005 and 2014 situations, while the bathymetric surveys cover the entire study period, but they are not equally distributed along the reach. Through these comparisons, it was possible to estimate the eroded and deposited volumes, and use these as a basis for forecasting the future evolution of the river.

As an example, Fig. 5 shows the changes for a cross-section located in sub-reach K6 derived from bathymetric surveys. This sub-reach has a relatively stable bed, characterized by slight variations in bed elevation and moderately steep banks, stabilized by vegetation. In 2014, the left floodplain was approximately 0.5 m lower with respect to the 2003 profile, and bed degradation was evident. However, no changes in the main channel width or the elevation of the right bank floodplain were observed during the 2003–2014 period. Similar behaviour has measured for the other sub-reaches, as reported in the following.

Figure 6 reports variations of the riverbed elevation during the period 2005–2014 along the sub-reaches from K1 to K5 as a result of the comparison of the two available DGMs. The analysis of the morphological changes (as for sub-reach K6) is work in progress and is not presented here. The bed elevation variations for the sub-reaches K1–K5 were computed comparing the 50 available cross sections by means of the software AutoCAD and measuring the erosion and deposition areas between the available profiles.

As shown in Fig. 6, the restored river reach is subjected to a diffuse erosional phenomenon, with reach values of about 1 m during the period 2005–2014. Comparing the two DGMs, the mean erosion measured along the reach is of about 0.5 m. This value is consistent with the results derived from the bathymetric surveys. A thorough analysis of the bathymetric surveys, including the missing sub-reaches, will be completed during 2015, and presented in future reports.

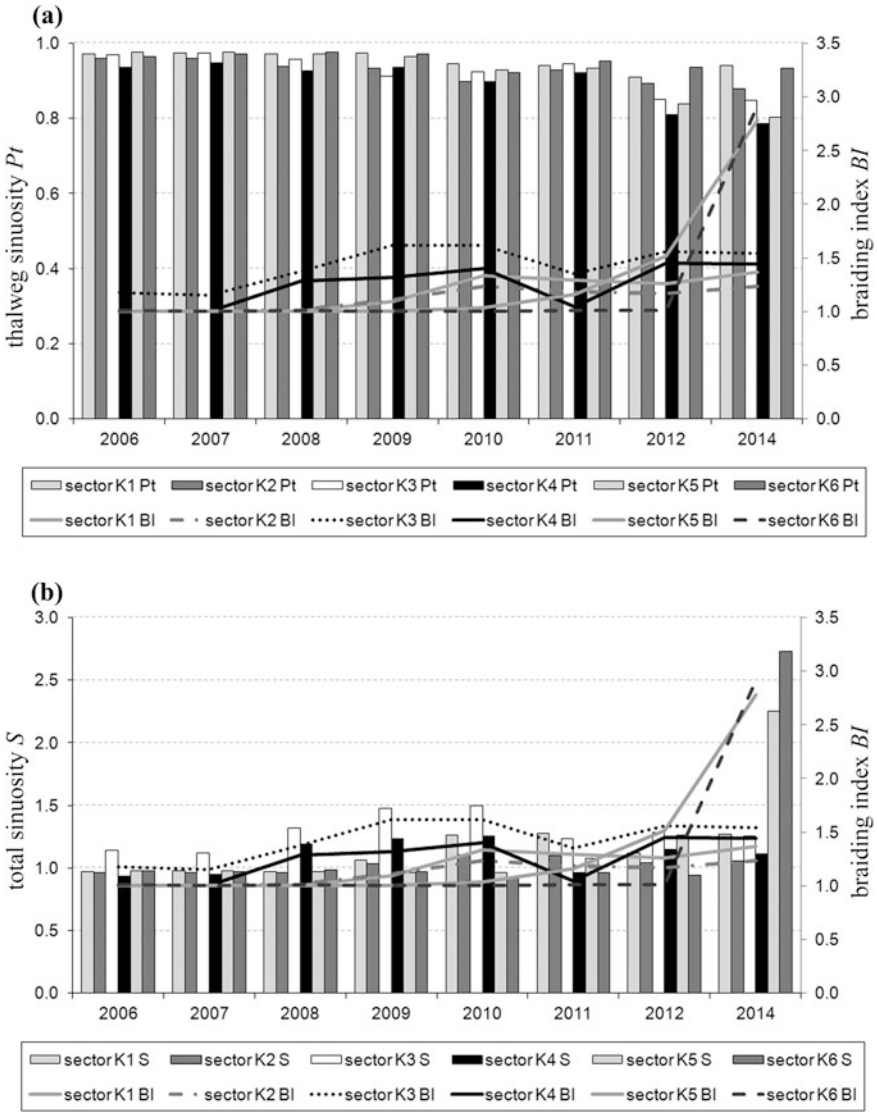

Fig. 4 Variation of the planimetric indices during the study period: **a** thalweg sinuosity and braiding index along the main channel; **b** total sinuosity of primary and secondary channels and braiding index of the main channel

The aim of the present study is to analyse the impact of sediments on a restored river reach, in terms of morphological changes. For this reason, no detailed descriptions of each cross-section profile variations are given here. Under a general point of view, as visible in Fig. 7, the fine sand transported by the flow deposits along the floodplain and in the new-made ponds, while erosion is evident along the

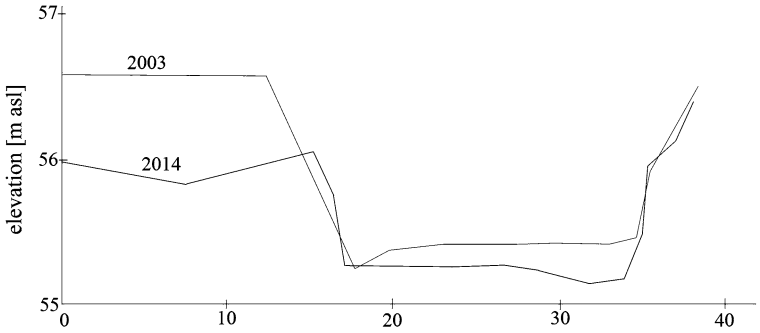

Fig. 5 Example of cross-section profile evolution along the studied reach: comparison between the *2003* measurements and the *2014* profile in sub-reach K6

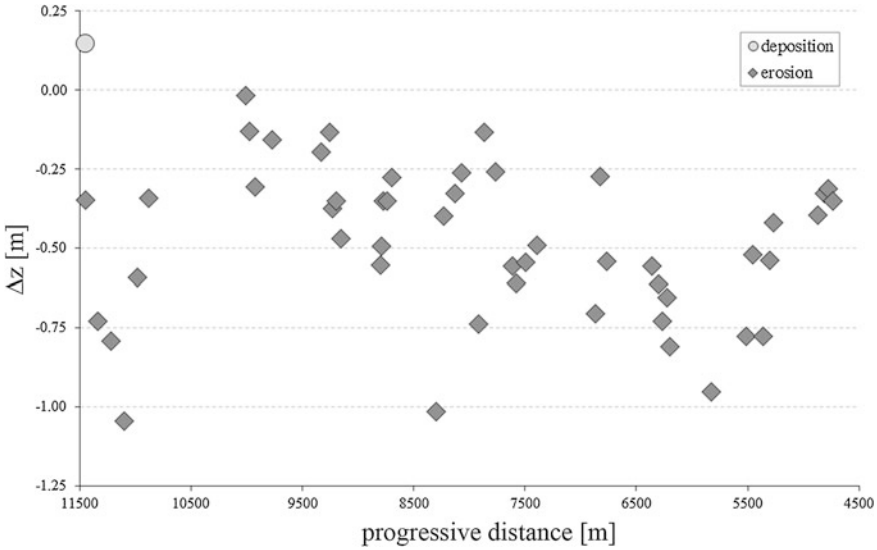

Fig. 6 Changes in bed level elevation between 2005 and 2014 as derived from the DGMs. The *point* indicates a cross section in deposition, while the *squares* indicate cross-sections subjected to erosion

riverbed. The mean erosion along the sub-reaches K1, K5 and K6 is about 0.7 m, while the sub-reach K9 presents the maximum deposits (about 0.75 m).

Generally, it is possible to notice that the goals of the project were fulfilled, fostering an increase of the river total sinuosity and braiding index, coupled with an increase of the river width associated with median discharge, with an enlargement of the active cross section, necessary to increase the flow velocity heterogeneity, creating lentic zones and improving the ecotones, fulfilling the WFD requirements.

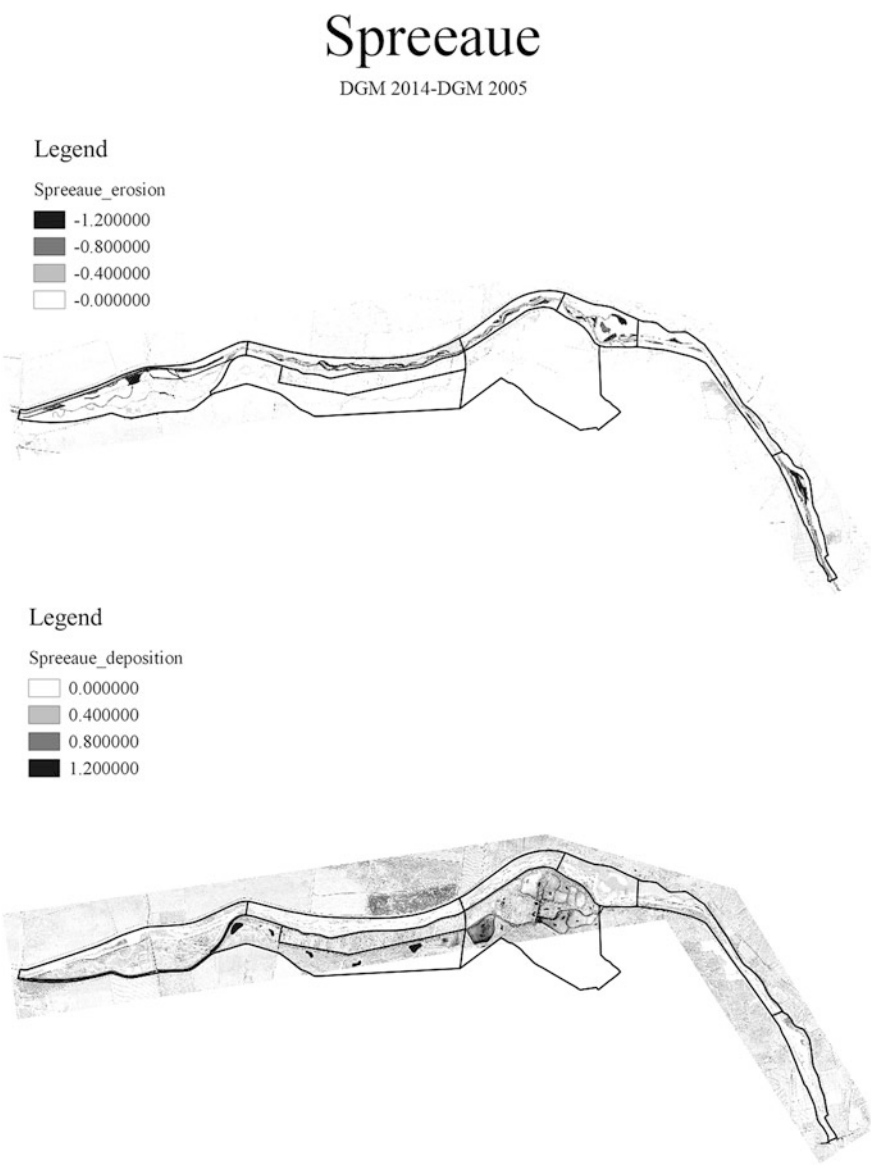

Fig. 7 Comparison of *2005* and *2014 DGMs*: the *upper figure* shows the erosion along the riverbed (sub-reaches K1–K6), while the *lower figure* reports the deposition on floodplains and ponds (sub-reaches K7–K9)

4 Discussion

The impact of sediments and hydromorphological alterations on freshwater habitats were studied along a restored reach of the Spree River in Germany. Due to the lack of direct measurements of the sediment transport, only indirect computational methods were applied. The effects of the restoration measures were analysed at a sub-reaches scale, by means of aerial images and cross-section profiles related to the period pre- and post-restoration. These preliminary results indicate that the objectives of the project are, in large part, fulfilled, but the restoration goals are threatened by the transport of fine sand, especially during high flow events as occurred during the summer of 2013. Comparing the aerial images taken during the period 2006–2014, it is possible to notice that some secondary channels are affected by the depositional phenomena of fine sand, with possible negative consequences on macrophytes and macroinvertebrates. The sand accumulates also along floodplains and ponds, potentially altering the entire aquatic environment and affecting the biological WFD classification, based on aquatic flora and fauna (EU 2000). Additional results will be available during 2015, after a thorough analysis of the monitoring data of fish and macrophytes taken during the summer of 2014. Alterations of the restored cross-section profiles are recognizable also by the analysis of the measured profiles, although it is quite difficult due to the lack of detailed data.

5 Conclusions

Some key points can be drawn from this preliminary work. First, river restoration along the study reach did not restore the fluvial environment to natural/pristine conditions. Habitat diversity and morphological heterogeneity are related to variability of flow conditions and substrate composition, but the increase in the number of channels, the redesign of their form and the addition of coarser sand are not sufficient to improve the river status. Second, the lack of studies about the long-term impact of fine sand transport along the Spree River can threat the restoration project goals.

More monitoring data and detailed field measurements, combined with additional information of reference conditions typical of this riverine environment, are necessary to analyse the complete hydro-morphological changes and adjustments of this restored reach. Additional studies are also required to evaluate and forecast the impact of fine sand transport on macrophyte habitats and macroinvertebrate communities, especially at longer time scale of decades or even centuries, and the impact of sediments during the WFD classification.

Within the monitoring programme of the Spree River performed by the SME gerstgraser - Ingenieurbüro für Renaturierung and the Vattenfall Europe Mining AG, new data about fish and macrophytes were recorded during the summer

of 2014, thus detailed analyses of the impact of sediment transport on the riverine habitat will be reported in future studies.

Acknowledgments This paper was supported by the Research Executive Agency, through the 7th Framework Programme of the European Union, Support for Training and Career Development of Researchers (Marie Curie—FP7-PEOPLE-2012-ITN), which funded the Initial Training Network (ITN) HYTECH "Hydrodynamic Transport in Ecologically Critical Heterogeneous Interfaces", N. 316546. The restoration project and its monitoring are made in collaboration with Vattenfall Europe Mining AG. The insightful comments and suggestions of Geraldene Wharton have been gratefully incorporated in the final version.

References

Amsler ML, Ramonell CG, Toniolo HA (2005) Morphological changes in the Parana River channel (Argentina) in the light of the climate variability during the 20th century. Geomorphology 70:257–278. doi:10.1016/j.geomorph.2005.02.008

Arscott DB, Tockner K, van der Nat D, Ward JV (2002) Aquatic habitat dynamics along a Braided Alpine River ecosystem (Tagliamento River, Northeast Italy). Ecosystems 5:802–814. doi:10.1007/s10021-002-0192-7

EU—European Commission (2000) Directive of the European parliament and of the council 2000/60/EC establishing a framework for community action in the field of water policy. Official Journal C513, 23.10.2000

Gerstgraser C, Zank H (2012) Kompensation der Beseitigung eines FHH-Gebiets. Nul 44 (10):293–299 (in German)

gIR (2008) Monitoringbericht zur Strukturveränderung der Spree in den Kompensationsbereichen K2–K4; Berichtsjahr 2008. gerstgraser Ingenieurbüro für Renaturierung, Cottbus, Germany. Internal report (in German)

gIR (2009) Monitoringbericht zur Strukturveränderung der Spree in den Kompensationsbereichen K1–K4; Berichtsjahr 2009. gerstgraser Ingenieurbüro für Renaturierung, Cottbus, Germany. Internal report (in German)

gIR (2014) Monitoring Strukturveränderung Spree nach dem Hochwasser Juni 2013. gerstgraser Ingenieurbüro für Renaturierung, Cottbus, Germany. Internal report (in German)

Gray D, Harding JS (2007) Braided river ecology. A literature review of physical habitats and aquatic invertebrate communities. Science for conservation, vol 279. Eds. New Zealand Department of Conservation. ISBN 978–0–478–14340–9

Gurnell AM, Bertoldi W, Corenblit D (2012) Changing river channels: the roles of hydrological processes, plants and pioneer fluvial landforms in humid temperate, mixed load, gravel bed rivers. Earth Sci Rev 11:129–141

Hilt S, Schönfelder I, Rudnicka A, Carls R, Nikolaevich N, Sukhodolov A, Engelhardt C (2008) Reconstruction of pristine morphology, flow, nutrient conditions and submerged vegetation of lowland river Spree (Germany) from palaeomeanders. River Res Appl 24:310–329. doi:10.1002/rra.1023

Marion A, Nikora V, Puijalon S, Bouma T, Koll K, Ballio F, Tait S, Zaramella M, Sukhodolov A, O'Hare M, Wharton G, Aberle J, Tregnaghi M, Davies P, Nepf H, Parker G, Statzner B (2014) Aquatic interfaces: a hydrodynamic and ecological perspective. J Hydraul Res 52(6):644–758. doi:10.1080/00221686.2014.968887

Nardini A, Sansoni G, Schipani I, Conte G, Goltara A, Boz B, Bizzi S, Polazzo A, Monaci M (2008) The water framework directive: a soap bubble? An integrative proposal: FLEA (Fluvial Ecosystem Assessment). Centro Italiano per la Riqualificazione Fluviale

Nones M (2013) Riverine dynamics at watershed scale: hydro-morpho-biodynamics in rivers. LAP Lambert Academic Publishing, p 140. ISBN-13: 978-3659367854

Pedersen ML, Kristensen KK, Friberg N (2014) Re-meandering of lowland streams: will disobeying the laws of geomorphology have ecological consequences? PLoS ONE 9(9): e108558. doi:10.1371/journal.pone.0108558

SedNet (2009) Integration of sediment in river basin management. Report on the 2nd SedNet round table discussion. Hamburg

WFD CIS no. 20 (2009) Common implementation strategy for the water framework directive (2000/60/EC). Guidance document on exemptions to the environmental objectives

Impact of River Restoration on Hydromorphological Processes: The River Flinta as a Case Study

Tomasz Kałuża, Krzysztof Szoszkiewicz, Artur Radecki-Pawlik, Natalia Walczak and Karol Plesiński

Abstract This paper deals with problems related to the improvement of the hydromorphological conditions of the river Flinta in its sections located in the Natura 2000 area. Based on a comprehensive study of the hydromorphological status of the river, four sections have been selected, where restoration measures can efficiently improve the river habitat conditions. For each of these sections we propose a set of technical and biological measures. One of the proposed solutions, investigated as a pilot project, was to construct plant barriers (sediment traps—vegetative baskets). Systematic measurements were carried out during one and a half year. These measurements provided information on the possible consequences of such actions in terms of hydromorphological changes.

1 Introduction

The restoration of natural fluvial conditions in river ecosystems is one of the key issues in river engineering. These actions are carried out for environmental purposes, but also because of their significant economic importance. The natural aspect is concerned with the creation of favourable conditions for life and development of ecological communities and an overall increase in biodiversity. Already an average

T. Kałuża (✉) · N. Walczak
Department of Water and Sanitary Engineering, Poznan University of Life Sciences,
ul. Piątkowska 94A, 60-649 Poznań, Poland
e-mail: tomasz.kaluza99@gmail.com

K. Szoszkiewicz
Department of Ecology and Environmental Protection, Poznan University of Life Sciences,
ul. Piątkowska 94C, 60-649 Poznań, Poland

A. Radecki-Pawlik · K. Plesiński
Department of Hydraulic Engineering and Geotechnique, University of Agriculture,
al. Mickiewicza 24/28, 30-059 Kraków, Poland

P. Rowiński and A. Marion (eds.), *Hydrodynamic and Mass Transport at Freshwater Aquatic Interfaces*, GeoPlanet: Earth and Planetary Sciences,
DOI 10.1007/978-3-319-27750-9_15

intensity of river bed transformation maintains the basic properties of the fluvial ecosystem and may lead to the restoration of the natural processes by themselves.

Those watercourses which are the most anthropogenically transformed are unable to independently reproduce natural processes. Their restoration requires various revitalization activities to be implemented. The process of running water restoration currently plays an important role in water environment protection and applies especially to those regions of river valleys which have been heavily technically trained in the past (Gordon et al. 2004). Biological and anthropogenic actions aimed at improving the ecological status of rivers often cause drastic hydromorphological changes (Church 1996). The assessment of these changes and their dynamics is crucial for proper planning and verification of restoration activities (Graf 1998).

Our paper presents the concept of improving the hydromorphological conditions of the river Flinta in its sections located in the Natura 2000 area. Based on a comprehensive study of the hydromorphological status of the river, four sections have been selected, the modification of which will help to improve the status of the aquatic environment. For each section we propose a set of technical and biological activities, with a potential to significantly improve the status of abiotic habitat of the river. One of the proposed solutions was to construct a plant barrier (sediment traps—vegetative baskets). This solution has been investigated as a pilot project. Vegetative filters or sediment traps are used to produce hydromorphological changes in rivers (Jarrett 1991). While there has been a significant amount of research performed on plot-scale (Tollner et al. 1982) and on laboratory-scale (Hämmerling et al. 2014) using either real or simulated vegetation, very little is known on water flow and sediment transport within field-scale Vegetative Filters, VF (Daniels and Gilliam 1996; Schmitt et al. 1999; Sheridan et al. 1999).

On a selected section of the river Flinta near the village of Rożnowo three plant barriers (sediment traps) were put in the river bed. Systematic measurements were taken over a period of one and a half year. The research focused on velocity distributions, changes in the river bed morphology and variations of sediment. Results of field work provided information on the possible consequences of such actions with regard to the hydromorphological changes. This allowed us to evaluate the effectiveness of such investments.

2 Study Area

The river Flinta (Fig. 1) is a right tributary of the river Wełna, to which it flows in the village of Rożnowo-Młyn in the commune of Rogoźno. The total length of its catchment is about 27 km and the total catchment area is 345.47 km^2. The hydrological regime of the river is that of the snow-rain fed type. On the river Flinta, the maximum inflow associated with spring thaw usually occurs in March. The low-flow summer period usually lasts from June till the end of the hydrological

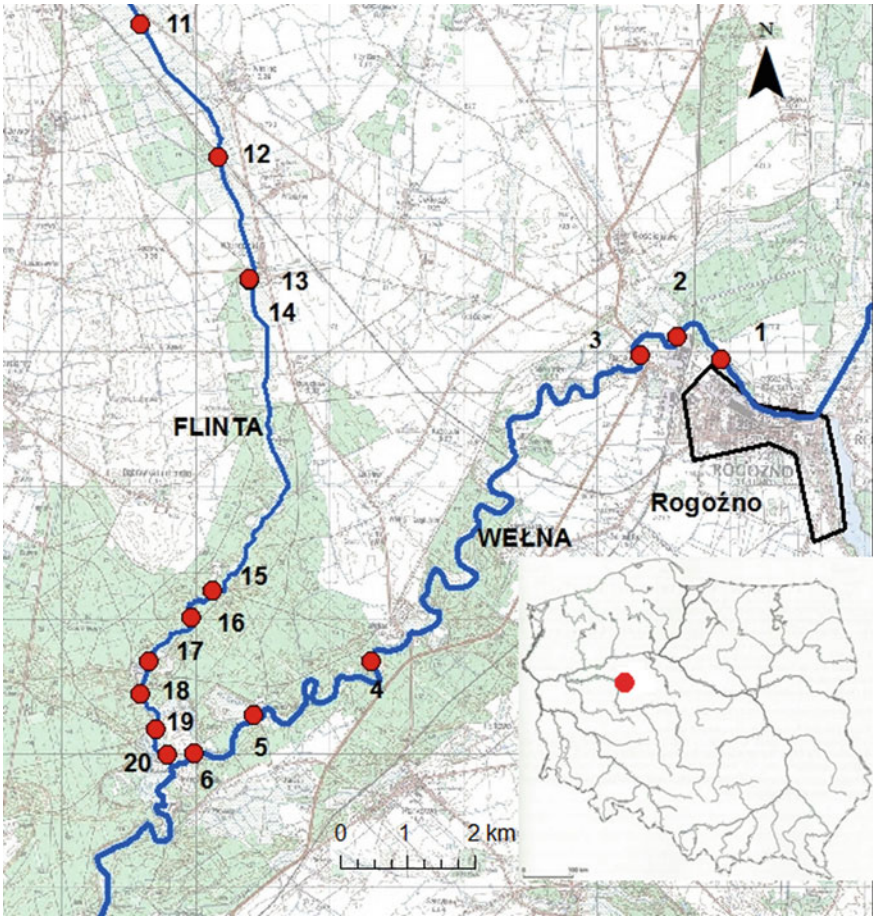

Fig. 1 The region under study: the Flinta catchment area with the location of the measurement points used for the hydromorphological assessment

year with a minimum in July and August. The short-term high water, appearing after exceptionally high rainfalls, may occasionally pose a flood risk.

In the catchment area of the river Flinta, at the confluence with the river Wełna there is a Special Protection Area "Nature 2000" (Puszcza Notecka—PLB300015). Outside the catchment area, along the Wełna and in close proximity to the Flinta, a Special Area of Conservation (SAC)—Dolina Wełny (PLH300043)—is located. There are also other protected areas in the impact area of the catchment, namely the Protected Landscape Area (PLA) Puszcza Notecka, which partly overlaps the SAC Puszcza Notecka and the nature reserve Źródliska Flinty including its buffer zone.

The concept of restoration has been tested on the river Flinta. The Flinta is a relatively strongly meandering lowland watercourse with sandy and stony substrate. As for lowlands, the altitude differences are relatively high and the river flow is

partly fairly rapid. The valuable aquatic vegetation thrives in the river and rich fish fauna typical of fluvial ecosystems is well-developed. Unfortunately, the quality of habitat is spoiled by the advancing eutrophication and the hydromorphological modifications.

3 Methods of Hydromorphological Survey of the River Flinta

In 2013, a hydromorphological survey of the river Flinta was carried out. The hydromorphological evaluation was conducted at the selected sites (Fig. 1) according to the River Habitat Survey (RHS) method (Environment Agency 2003). The RHS data cover a stretch of over 500 m of the river. The RHS survey was performed on 10 profiles (spot-checks) distributed at 50 m intervals. Two numerical metrics based on the RHS protocol were produced:

- the Habitat Modification Score (HMS), based on the extent and type of artificial features and modifications, and
- the Habitat Quality Assessment (HQA), based on the extent and variety of natural features recorded.

High values of HQA indicate an extensive presence of a number of natural river features and a high landscape diversity along the river, while low values imply lack of natural features (Kałuża et al. 2014). A low HMS indicates limited artificial modifications of the watercourse, whereas higher values reveal a considerably high modification of the habitat.

The combination of the two numerical RHS metrics (HMS and HQA) enables one to estimate the hydromorphological status of a river site (Walker et al. 2002) in a five class system, where classes I, II, III, IV and V correspond to a very good, good, moderate, poor and bad hydromorphological status, respectively. The RHS survey was completed for 10 sites of the river Flinta (Fig. 1, Table 1).

The RHS survey showed a large variation in the degree of river hydromorphological degradation both in terms of human-induced degradation and in the form of occurrence of the attributes of a natural fluvial ecosystem (Table 2). On the river Flinta, the natural fluvial environment attributes were the most numerous in Smolarz (65 HQA) and on two sites situated near the Piłka Reservoir (62 and 58 HQA). The level of hydromorphological degradation was determined by using the HMS index. This index indicates the highest degree of river modifications in Ryczywół (45 HMS) and Ninino (13 HMS). The most common form of hydromorphological alteration was bank profiling, which was found in Ryczywół. Moreover, in Ryczywół, Ninino and Wiardunki, channel bed profiling was identified. Several parts of the river banks were reinforced, usually in the form of rip-rap. Among the engineering constructions, several weirs impounding the Piłka Reservoir were detected.

Table 1 Sites on the river Flinta surveyed hydromorphologically

No.	Site name	Section characteristics
11	Ryczywół	Resectioned and deepened channel, resectioned and partly reinforced banks
12	Ninino	Resectioned and deepened channel, resectioned banks
13	Wiardunki 1	Resectioned and deepened channel, resectioned and partly reinforced banks
14	Wiardunki 2	Resectioned and deepened channel, resectioned banks
15	Smolarz 1	Natural section
16	Smolarz 2	Natural section
17	Piłka above weirs	Weirs, impoundments, partly reinforced banks
18	Piłka below weirs	Semi-natural section
19	Rożnowo above mouth	Rececticned banks
20	Rożnowo mouth	Rececticned banks

Table 2 The hydromorphological classification of sites surveyed on the river Flinta based on the HQA and HMS metrics

No.	Site name	HQA	HMS	Hydromorphological status
11	Ryczywół	28	43	V
12	Ninino	39	13	III
13	Wiardunki 1	38	2	II
14	Wiardunki 2	33	9	III
15	Smolarz 1	71	0	I
16	Smolarz 2	73	0	I
17	Piłka above weirs	53	9	III
18	Piłka below weirs	60	0	I
19	Rożnowo above mouth	36	11	IV
20	Rożnowo mouth	27	6	IV

4 The River Flinta Restoration Programme

The restoration concept (Szoszkiewicz et al. 2014) was developed based on the undertaken hydromorphological survey. To improve the hydromorphological status of the river Flinta, we proposed several restoration measures for the most degraded parts. We tried to reduce the number of engineering modifications such as impoundments, channel and bank profiling, concrete and rip-rap reinforcements etc. A full list of proposed restoration measures is given in Table 3.

It was found that a comprehensive restoration requires efforts on a large scale—thirteen various technical and biological measures were proposed to stimulate the fluvial processes and to improve habitat for the development of living aquatic organisms in the river. Analysis (based on the HQA and HMS metrics) of potential

Table 3 The river Flinta restoration programme

No.	Measures	Number of units	Unit
1	Wooden deflector	4	Piece
2	Wood-stone deflector	40	Piece
3	Wooden weir	7	Piece
4	Willow faggots	2	Distance
5	Brushwood mattresses	2	Piece
6	Tree planting	180	Seedling
7	Spawning gravel insert	4	Surface
8	Fish bypass	1	Piece
9	Tree trunk	14	Piece
10	Wooden poles	1	Distance
11	Concrete weir removal	1	Piece
12	Rip-rap on willow mattress	4	Piece
13	Rip-rap on willow mattress	13	Piece

changes and may be obtained by the river Flinta Restoration Programme have shown that in some places the restoration effects can be exceptionally ecologically effective whereas in some other sites only limited benefits are to be expected.

The performed simulations (Szoszkiewicz et al. 2014) show that the proposed measures enable the achievement of various hydromorphological improvements on the river Flinta. We were able to select sites where the restoration would influence significantly the hydromorphological status. Hydraulic measurements proved that the proposed activities would not significantly deteriorate the high water flow and would not increase the flood risk.

A particularly large number of measures were proposed in areas where former profiling was preserved: between Ryczywół and Wiardunki. The Piłka impoundment was proposed for removal, as it disrupts the migration of fish fauna and other organisms, and is the cause of other disturbances to the fluvial processes in the river. Moreover, we have widely proposed the replacement of artificial building materials with local and natural materials such as wood, local cobbles and gravel. Deflectors were proposed on the realigned river sections to initiate meandering and other fluvial processes.

The introduction of tree vegetation on banks has also been proposed. Trees significantly enrich the river habitat by providing organic matter in the form of leaves and branches, which are utilized by many aquatic organisms. In addition, diversified shading caused by planted trees adds variety to the riverbed conditions, which stimulates river biodiversity.

5 The Pilot Project—Plant Basket Hydraulic Structures (PBHS)

Most of the proposed technical and biological restoration measures aimed at the improvement of the ecological status of the river Flinta remain untested in Poland or at least not on a large scale. It is recommended to assess and validate them through experimental field research. One of the proposed solutions was to construct structures within the river channel in the form of plant barriers working as sediment traps—such structures are called plant basket hydraulic structures (PBHS). The PBHS—submerged plant trays—have been examined as a pilot project. In the experiment, the submerged plant trays were introduced in the cross section at km 0 + 100 near the village Rożnowo (Fig. 2b). All the plastic trays (measuring 70 × 40 × 30 cm) were filled with loose river sand and concrete blocks. In each tray,

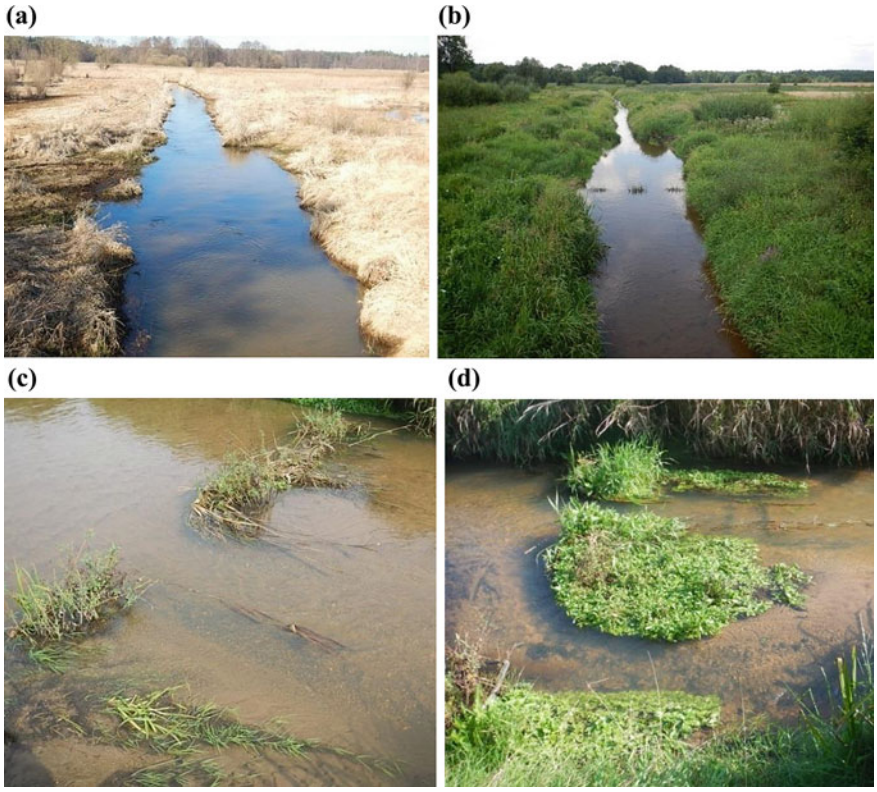

Fig. 2 The investigated plant barrier (sediment traps)—pilot project: **a** location of the study site on the river Flinta near Rożnowo, **b** the river bed and the sediment traps on 25.09.2013, **c** the sediment traps with plant debris on 25.09.2013, **d** the sediment traps with plant debris and plants growing on it on 2.10.2014

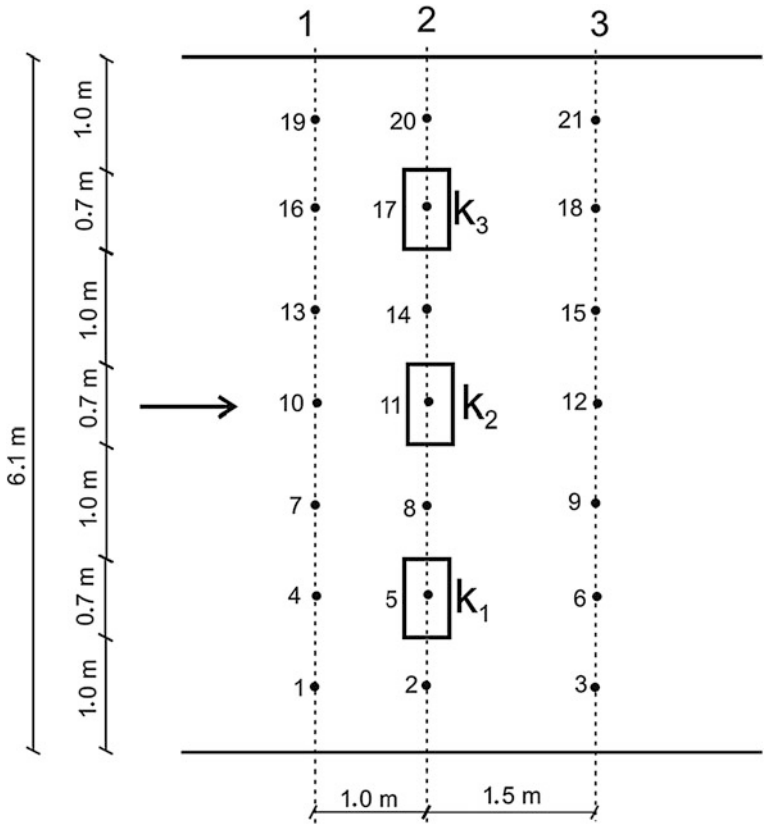

Fig. 3 Investigated vegetative baskets and the measuring points along the Flinta in the case study research reach

willow cuttings were placed (approx. 30 pieces per basket). The trays with cuttings were submerged in the river bed. They were placed in one cross-section at a distance of 1 m between each other (Fig. 3).

Before the experiment began (cross-section without trays—Fig. 2a), the hydrometric measurements were taken. The cross-sectional geometry was defined as well as the slope of the surface and the distribution of velocities. After the installation of trays, the hydrometric measurements were recorded systematically over a period of one and a half year of usage (the tests were performed during five measurement sessions: 2.08.2013, 25.09.2013, 10.11.2013, 14.05.2014 and 2.10.2014). Changes of sediment grain size were analysed. Additionally, the amount and size of plant debris caught in the plant barrier (plant formation) was studied (Fig. 2c, d). The hydromorphological changes and the development of natural plant succession were estimated as well (Fig. 2d).

6 The Study of Flow Conditions

In each series, the hydrometric measurements of water flowing in an open channel, excluding the flow within a gravel river bed (Radecki-Pawlik 2014; Carling et al. 2006), were conducted with a velocitimeter, the OTT Nautilus 2000, and an electromagnetic flow sensor, the FLAT Model 801 from Valeport. These devices allow the measurement of water flow velocity in the range from 0.001 to 10 m s^{-1}. They also measure the velocities of water just above the river and stream bed, which is important not only for the movement of sediment (Radecki-Pawlik et al. 2014) but also in the case when one takes into consideration the presence of invertebrates (Wyżga et al. 2012a, b, 2013; Radecki-Pawlik and Skalski 2008; Skalski et al. 2012). Their operation is based on the measurement of electromagnetic induction in the flowing liquid. By using these devices, a few measurement divisions were determined in the field, which consisted of the following parameters:

- a set of several instantaneous velocities measured just above the river bed, V (m s^{-1}),
- average velocity, V_{av} (m s^{-1}), which was determined depending on the of the water depth (Czetwertyński and Szuster 1978):
  - h < 0.20 m:

$$V_{av} = V_{0.4h}\ (\mathrm{m\,s^{-1}}) \tag{1}$$

  - 0.20 m ≤ h ≤ 0.60 m:

$$V_{av} = \frac{V_{0.2h} + 2V_{0.4h} + V_{0.8h}}{4}\ (\mathrm{m\,s^{-1}}) \tag{2}$$

  - h > 0.60 m:

$$V_{av} = \frac{V_d + 2V_{0.2h} + 3V_{0.4h} + 3V_{0.8h} + V_p}{10}\ (\mathrm{m\,s^{-1}}) \tag{3}$$

If the velocity profile is measured near a surface and it plots approximately as a straight line on a linear-log plot then the shear stress can be calculated from the slope of the profile using the equation:

$$\tau = \rho \cdot (V_*)^2 (\mathrm{N\,m^{-2}}) \tag{4}$$

where:

ρ = 1000 kg m^{-3} is the water density,

V_* is the shear velocity (m s^{-1}).

Shear velocity V_* is obtained along hydraulically rough stream bed and can be expressed as (Gordon et al. 2004):

$$V_* = \frac{a}{5.75}(\mathrm{m\,s^{-1}}) \tag{5}$$

where a is the slope of the logarithmic velocity profile (velocity vs. log(depth)).

Next, the average Reynolds numbers was (Chow 1959):

$$Re = \frac{V_{av} \cdot h}{V}(-) \tag{6}$$

The measurements can be carried out either continuously or as an averaged measurement over a predetermined time interval. Some of the measurements were carried out before the construction of the sediment traps and the remaining ones were taken after the installation of the traps. The measuring points (1–21) are shown in Fig. 3. The results are gathered into a group of measurement points from the period when the river course was undisturbed, with no sediment traps (2 August 2013), and from the period after the installation of the sediment traps (25 September 2013 and all of the measurements in 2014). The results of the calculation of some chosen basic hydraulic parameters, like V_{av}, Re and τ, were the analysed hydraulics of the river Flinta in the measuring sections (Figs. 4, 5 and 6).

The analyses performed based on the measurement results showed a considerable increase in the variability of flow conditions below the installed PBHS. Based on the velocity measurements carried out, the coefficient of velocity variability s was determined (the coefficient is defined as the ratio of the average standard deviation to the average velocity). Results show that its value almost doubled

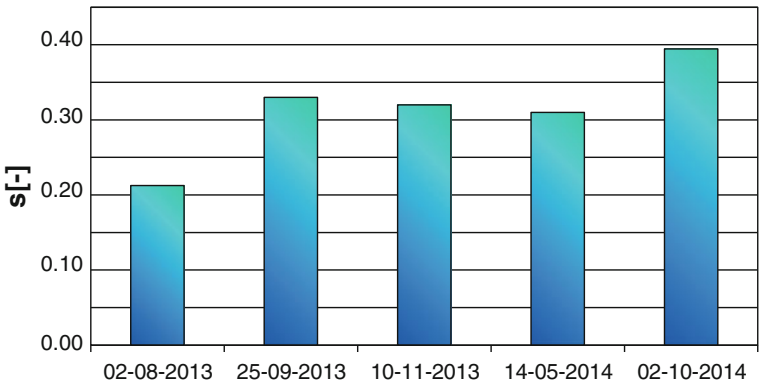

Fig. 4 The increase in the coefficient of velocity variability at the cross-section below the PBHS over the time under study

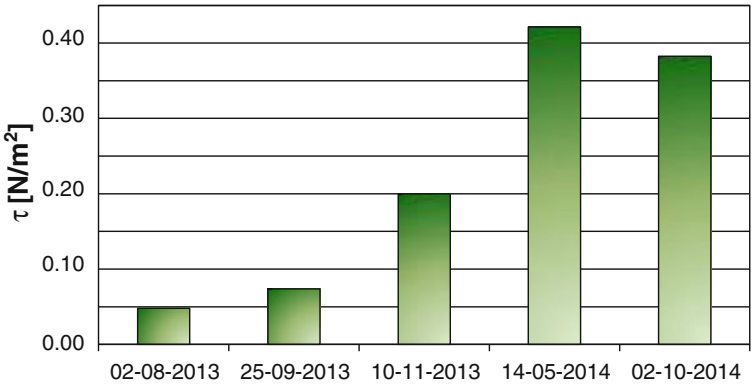

Fig. 5 Average shear stress before and after the installation of PBHS over the time under study

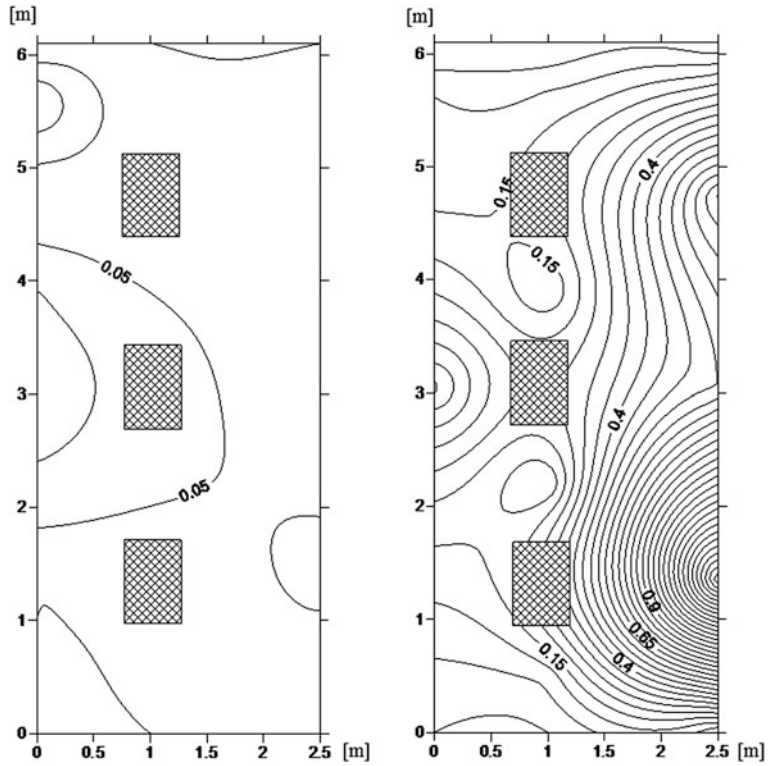

Fig. 6 Distribution of shear stress over the reach with installed PBHS shortly after the installation of baskets—25.09.2013 (**a**) and 1 year into the research—2.10.2014 (**b**). Geometrical dimensions in m and shear stress in N m^{-2}

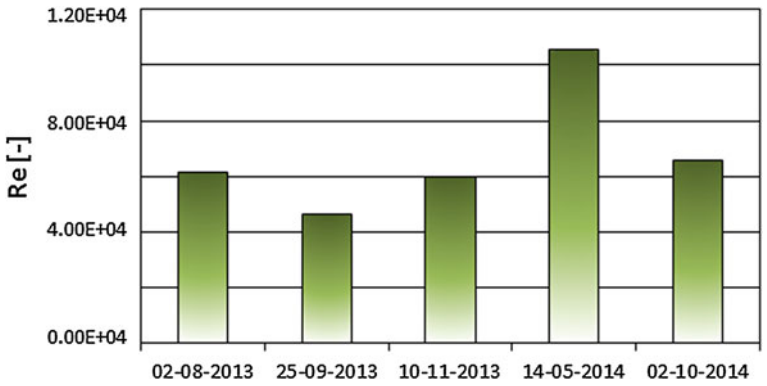

Fig. 7 Average values of Reynolds number before and after the installation of PBHS over the time under study

(Fig. 4), rising from 0.21 (before the installation of baskets) to 0.39 (the last measurement after the installation).

Considerable changes also involved the values of shear stress τ. After the installation of the PBHS these values increased significantly (Fig. 5). The average shear stress before the installation of baskets was $\tau = 0.048$ N m^{-2}. After the installation (and after one year in operation), this value rose maximally to $\tau = 0.42$ N m^{-2}. Figure 6 shows the distribution of stress over the reach with installed PBHS shortly before the installation of baskets—on 25.09.2013 (Fig. 6a) and 1 year into the research—2.10.2014 (Fig. 6b). Interestingly, no influence of the installation of PBHS was observed on the Reynolds number (Fig. 7). Its average value was about 68 thousand (–).

7 Discussion and Conclusions

Based on the River Habitat Survey evaluation, the most hydromorphologically-degraded parts of the river Flinta were identified. To improve the hydromorphological status, several restoration measures were proposed to reduce the level of degradation and to stimulate development of the fluvial forms of the river ecosystem.

The performed simulations show that the proposed measures enable the achievement of various hydromorphological improvements on the river Flinta. We were able to select sites where the restoration would have a significant influence on the hydromorphological status. Moreover, we have widely proposed the replacement of artificial building materials with local and natural materials such as wood, local cobbles and gravel. Deflectors and sediment traps were proposed on the realigned river sections to initiate meandering and other fluvial processes.

The study of vegetative sediment traps confirms their usefulness in activation and initiation of the hydromorphological processes. Thus, the following conclusions have been drawn from the analysis of hydraulic and sediment results within the traps of the investigated area:

1. Vegetative baskets change the hydrodynamic conditions and lead to sediment accumulation and formation of river backwaters before and after the obstacle.
2. The introduced vegetative baskets cause plant debris accumulation, which influences the hydrodynamic flow conditions.
3. The installation of vegetative baskets on the river bed alters the flow conditions. Shear stress is an example of an affected hydraulic parameter—its value before the vegetative sediment traps increased significantly from $\tau = 0.027$ N m^{-2} (2.08.2013) to $\tau = 0.465$ N m^{-2} (2.10.2014).
4. The highest shear stress was observed after 1 year of study (on October 2, 2014) upstream of the vegetative sediment traps PBHS K1: $\tau = 1.699$ N m^{-2}. In contrast, the smallest shear stress was measured between basket K1 and the right riverbank: $\tau = 0.067$ N m^{-2}.

Acknowledgements Work funded by the National Science Centre grant awarded based on the decision no DEC-2011/01/B/ST10/06959.

References

Carling P, Whitcombe L, Benson I, Hankin B, Radecki-Pawlik A (2006) A new method to determine interstitial flow patterns in flume studies of sub-aqueous gravel bedforms such as fish nests. River Res Appl 22(6):691–701

Chow VT (1959) Open-channel hydraulics. McGraw-Hill, New York, p 680

Church M (1996) Channel morphology and typology. In: Red G, Petts P (eds) Carlow River flows and channel forms. Blackwell Science Oxford

Czetwertyński E, Szuster A (1978) Hydrology and hydraulics (in Polish). Hydrologia i hydraulika. WSiP. Warszawa, p 360

Environment Agency (2003) River habitat survey in Britain and Ireland—field survey guidance manual: 2003 version. Environment Agency, Warrington

Daniels RB, Gilliam JW (1996) Sediment and chemical load reduction by grass and riparian filters. SSSA J 60(1):246–251

Gordon ND, McMahon TA, Finlayson BL, Gippel CJ, Nathan RJ (2004) Stream hydrology. An introduction for ecologists. Wiley, London

Graf WH (1998) Fluvial hydraulics: Flow and transport processes in channels of simple geometry. In collaboration with MS Altinakar, John Wiley and Sons, England, p 681

Hämmerling M, Walczak N, Zawadzki P, Kałuża T (2014) Delay in the flow of plant debris on floodplains overgrown with shrub. Acta Scientiarum Polonorum, Formatio Circumiectus 13(4):95–108

Jarrett R (1991) Wading measurements of velocity profiles. Geomorphology 4:243–247

Kałuża T, Pietruczuk K, Szkoszkiewicz K, Tymiński T (2014) Bewertung und Klassifizierung der Oberflächengewässer in Polen gemäβ den WRRL-Anforderungen. WasserWirtschaft 12:24–29

Radecki-Pawlik A (2014) Hydromorphology of rivers and streams—In Polish. Agricultural University Publishing House. Wydawnictwo UR w Krakowie. Kraków, Hydromorfologia rzek i potoków górskich, p 308

Radecki-Pawlik A, Skalski T (2008) Bankfull discharge determination using the new invertebrate bankfull assessment method. J Water Land Dev 12:145–153. ISSN (Online) 2083-4535, ISSN (Print) 1429-7426. doi:10.2478/v10025-009-0011-z, February 2009

Radecki-Pawlik A, Bucała A, Plesiński K, Oglęcki P (2014) Ecohydrological conditions in two catchments in the Gorce Mountains: Jaszcze and Jamne streams—Western Polish Carpathians. Sour Doc Ecohydrol Hydrobiol 14(3):229–242

Schmitt TJ, DosskeyM G, HoaglandK D (1999) Filter strip performance and processes for different vegetation, widths, and contaminants. J Environ Qual 28(5):1479–1489

Sheridan JM, Lowrance R, Bosch DD (1999) Management effects on runoff and sediment transport in riparian forest buffers. Trans ASAE 42(1):55–64

Skalski T, Kedzior R, Radecki-Pawlik A (2012) Riverine ground beetles as indicators of inundation frequency of mountain stream: a case study of the Ochotnica stream, southern Poland. Sour Doc Baltic J Coleopterol 12(2):117–126

Szkoszkiewicz K, Pietruczuk K, Kałuża T, Strzeliński P (2014) Opportunities and assumptions of restoration the Wełna and Flintariver. In Polish. Możliwości i założenia renaturyzacji rzek. Monografia pod redakcją Jarosława Batora, Macieja Gąbki, Emilii Jakubas pt. Koncepcja lasu modelowego w zarządzaniu i ochronie różnorodności biologicznej rzek Wełny i Flinty (Wielkopolska). Bogucki Wydawnictwo Naukowe Poznań, pp 127–139

Tollner EW, Barfield BJ, Hayes JC (1982) Sedimentology of erect vegetal filters. J Hydraul Div ASCE 108(12):1518–1531

Walker J, Diamond M, Naura M (2002) The development of physical habitat objectives. Aquat Conserv Mar Freshw Ecosyst 12:381–390

Wyżga B, Oglęcki P, Radecki-Pawlik A, Skalski T, Zawiejska J (2012a) Hydromorphological complexity as a driver of the diversity of benthic invertebrate communities in the Czarny Dunajec River, Polish Carpathians. Hydrobiologia 696:29–46

Wyżga B, Zawiejska J, Radecki-Pawlik A, Hajdukiewicz H (2012b) Environmental change, hydromorphological reference conditions and the restoration of Polish Carpathian rivers. Earth Surf Process Landforms 37:1213–1226

Wyżga B, Oglęcki P, Hajdukiewicz H, Zawiejska J, Radecki-Pawlik A, Skalski T, Mikuś P (2013) Interpretation of the invertebrate-based BMWP-PL index in a gravel-bed river: sight from the Polish Carpathians. Hydrobiologia 712:71–88

River-Bed Morphology Changes During the Winter Season in the Regulated Channel of the Wilga River, Poland

Joanna Sziło and Robert J. Bialik

Abstract Field investigations of the river bed morphology in the regulated channel of the Wilga River in Poland are presented. All data were collected with the use of an echo sounding system mounted on the ADCP (acoustic Doppler current profiler), which was also used to obtain the water flow velocities, discharges and river bathymetry during the days of measurements. It is shown that the analysed channel consists mostly of regular sand waves, which change their length and height during the winter season. The dependence of the shape of bedforms and channel bed morphology on the existence of a vegetation patch, which is directly associated with decreasing water temperature, is discussed briefly. The paper confirms changes in bed profiles with the increase in the water discharge. Moreover, a 3-dimensional digital elevation model of the channel obtained with the use of the ArcGIS software is introduced. In addition, the single-sided spectra of bed-elevation are analyzed. The results suggest that in the case of vegetation existing in the channel, the spectra are characterized by a scaling region with the exponent "−2", which tends to be "−3" when the plants disappear.

1 Introduction

Fluvial bedforms have been investigated for more than half a century and many studies have been devoted to the analysis of the dynamics and geometry of such forms (i.e. Kennedy 1963; Nikora et al. 1997; Ashley 1990; Parsons et al. 2013;

J. Sziło (✉)
Centre for Polar Studies, Institute of Geophysics, Polish Academy of Sciences, Księcia Janusza 64, 01-452 Warsaw, Poland
e-mail: jszilo@igf.edu.pl

R.J. Bialik
Institute of Geophysics, Polish Academy of Sciences, Księcia Janusza 64, 01-452 Warsaw, Poland
e-mail: rbialik@igf.edu.pl

P. Rowiński and A. Marion (eds.), *Hydrodynamic and Mass Transport at Freshwater Aquatic Interfaces*, GeoPlanet: Earth and Planetary Sciences,
DOI 10.1007/978-3-319-27750-9_16

Radecki-Pawlik et al. 2010; Aberle et al. 2010) to mention just a few of them and to the proper description of the flow over bedforms (i.e. McLean and Smith 1986; McLean et al. 1994; Parsons et al. 2013; Sukhodolov et al. 2006; or Bialik et al. 2014a). However, in spite of the attention paid to these problems many questions still need investigation.

Several interesting issues have been presented in the lecture "River Ice Effects on Fluvial Morphology and Ecology: Unanswered Questions" given by Professor Robert Ettema, during his visit to the Institute of Geophysics PAS on 6 November 2014, due to the inauguration ceremony of the Interdisciplinary Polar Studies, which strongly encouraged the authors to conduct this research. It has been clearly indicated that only several works address the phenomenon of sediment transport under ice cover and at low water temperature being around freezing point (Sayre and Song 1979; Hong et al. 1984; Lau and Krishnappan 1985; Tsai and Ettema 1994; Ettema et al. 2000; Knack and Shen 2015). Most of this research observed the increase in depth of ice-covered flows. However, as noted by Smith and Ettema (1995), the investigation of dunes geometry and the sediment transport due to the movement of the dunes at low water temperature have been limited in the previous studies, at least until 1995.

Other interesting aspects subject to ongoing research include sediment transport and channel morphodynamics in vegetated rivers. It is well known that these processes differ in both intensity and nature compared to those characterizing bar bed rivers. For example, Cavedon (2012), based on laboratory experiments, claimed that for a sufficiently high density of stems, the length of vegetation on bedforms is not influenced by vegetation density, but only by the distance between the plants. In contrast, while the height of the forms seems again not to depend on vegetation density, it is more probably related to the characteristics of the flow field and sediment properties. However, she stated that this statement requires further analysis, particularly in natural field conditions.

The current study is the continuation of the previous investigation carried out in the same part of the regulated channel of the Wilga River conducted by Bialik et al. (2014a). In contrast to the previous work, the current measurements have been conducted more accurately and with higher frequency (more campaign days were considered). The most important aspect is that this research has been performed during the whole winter season, beginning from the late autumn, and finished in the early spring. Thus, this work may provide valuable information on changes in river-bed morphology caused by the formation of ice on shores, the appearance of frazil ice, and loss of vegetation at the bottom of the trough and its shores.

The main goal of this study is to document changes of the river channel morphology during the winter season (October 2014–March 2015) in the regulated channel of the Wilga River. Great attention is also paid to the loss of vegetation and its influence on the sediment transport in the form of the river-bed forms. It should be noted that all the measurement campaigns were done at low water temperature, being mostly below 5 °C and during 2 days of measurement almost around freezing point. For the purpose of the investigation of the flow structure and the river bathymetry an acoustic Doppler current profiler (ADCP) was used.

2 Study Site

The field measurements were carried out in the regulated part of the Wilga River (Fig. 1), which is a lowland and sandy bed river being the right tributary of the Vistula River, located 55 km south of Warsaw. In order to achieve the goals of the paper, a regulated channel of 820 m in length, which ends by the water step and which was explored in a previous study by Bialik et al. (2014a), was selected to carry out the measurements. The chosen channel has a trapezoidal shape and its mean width ranged from 8.80 to 13.80 m. In addition, the final part of the channel of 220 m in length was covered by seasonal plants, which were observed, from August to December. Moreover, ice on the riverbanks appeared on 7 January 2015 (Fig. 1). The hydraulic characteristics of the Wilga River are presented in Table 1.

The bathymetry, discharge and water velocity fields were obtained using the acoustic Doppler current profiler (ADCP RiverSurveyor S5, manufactured by a SonTek). This device is equipped with an echo-sounding system, working at the

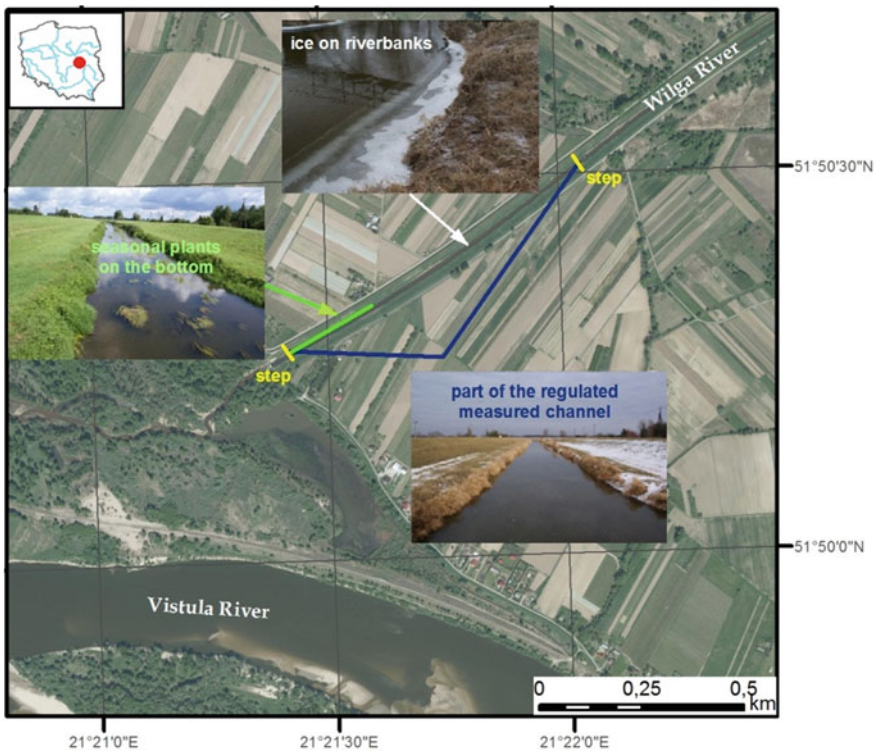

Fig. 1 Location of the study site

Table 1 Basic hydraulic characteristics

	H (m)	Q (m^3 s^{-1})	T (°C)	U (m s^{-1})	Re	Fr
29.10.2014	0.45	1.07	4.83	0.21	6.19×10^4	0.10
19.11.2014	0.47	1.24	5.71	0.25	7.90×10^4	0.12
24.11.2014	0.44	1.02	5.13	0.24	6.99×10^4	0.12
04.12.2014	0.46	0.98	2.32	0.21	5.81×10^4	0.10
18.12.2014	0.52	1.44	4.62	0.29	9.81×10^4	0.13
29.12.2014	0.85	5.25	0.59	0.45	21.78×10^4	0.16
07.01.2015	0.60	2.17	0.22	0.36	12.15×10^4	0.15
09.03.2015	0.61	2.91	7.19	0.38	16.28×10^4	0.16
26.03.2015	0.53	1.90	10.38	0.31	12.71×10^4	0.14

H Longitudinal mean flow depth, *U* longitudinal depth averaged flow velocity, *Q* discharge, *Re* = UH/v—Reynolds number, *Fr* = $U(Hg)^{-0.5}$—Froude number

frequency of 1 MHz and with an accuracy of 1 % for flow velocity (for details see, for example, Bialik et al. 2014a, b). Obtained data ware processed in MATLAB and ArcGIS software. In order to conduct bathymetry analysis of the channel, at least 5000 points of the bed elevation were collected on each day of measurement. An important part of the measurements was to evenly cover the channel by points. Thus, the measurements were made downstream, along the three survey lines, the first in the mainstream and two close (50 cm) to the right and the left bank, as well. Moreover, several cross-sections were made along the reach on each day of measurements, which give additional points for the bed elevation analysis and which were used to calculate the discharge. It should be noted that on 26 March 2015 more than 100 cross-section profiles at a distance of 800 metres along the channel were obtained, which allows us to present a reliable digital model of the channel. The details are presented in Sect. 3.

In order to compare the current granulometric distribution curve with the results of the previous study by Bialik et al. (2014a) conducted in the same location, the sediment samples were collected. They were taken from both the main channel and close to the riverbank, as well. Data obtained on 29 October 2014 suggest that the dunes in the channel consisted mostly of medium sand with D_{16} = 0.37 mm, D_{50} = 0.65 mm and D_{84} = 0.91 mm showing very small changes in the granulometry of the sediment in comparison to the curve obtained on 26 March 2014 when D_{16} = 0.34 mm, D_{50} = 0.62 mm and D_{84} = 0.91 mm. Moreover, the inclusive phi (φ) standard deviation was below 0.35, suggesting that the material was very well sorted. Figure 2 presents the granulometric distribution curves for measurements on both days, 26.03.2014 and 29.10.2014.

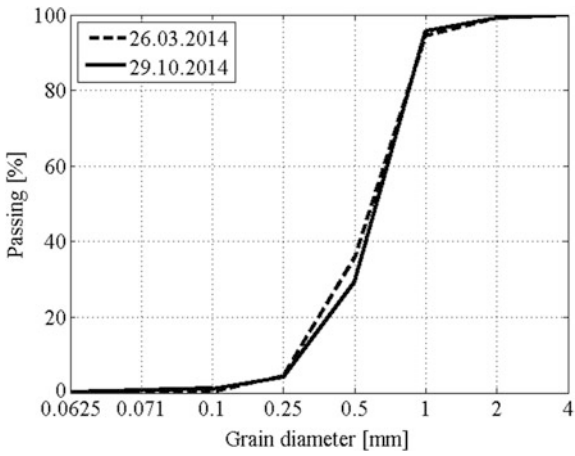

Fig. 2 Granulometric distribution curves of bed sediment

3 Results

3.1 Morphology of the Channel

Figure 3 shows flow velocities across the characteristic channel section measured using the ADCP on 9 March 2015. It is seen that the flow velocity has the classic distribution with the highest values in the mainstream. However, it should be noted that during the vegetation period, plants slow down the velocity in the region of their existence, which strictly influences the changes in the morphology.

Figure 4 shows a comparison of the river-bed elevation profiles for all considered days. As has already been observed in a previous study on the Wilga River (i.e. Nikora et al. 1997; Bialik et al. 2014a), large dunes are covered by smaller dunes and ripples. Furthermore, the movement of the bedforms is also clearly visible. From 29.10.2014 to 4.12.2014 we can identify only minor changes in the bed profiles, which were collected during periods of low discharge, Q $\sim$ 1.0 $m^3\ s^{-1}$. Furthermore, it can be seen that with the decrease of vegetation on 18.12.2014 also

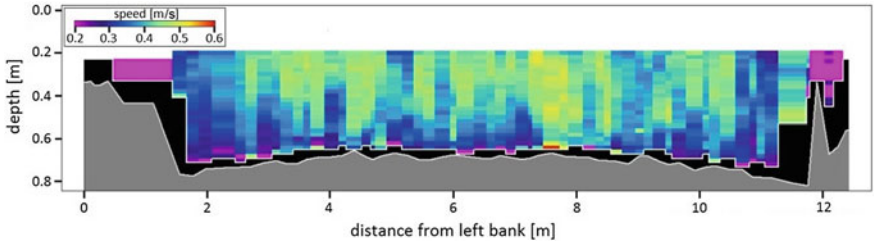

Fig. 3 Velocity spatial distribution on a characteristic channel section measured using an acoustic Doppler current profiler on 9 March 2015

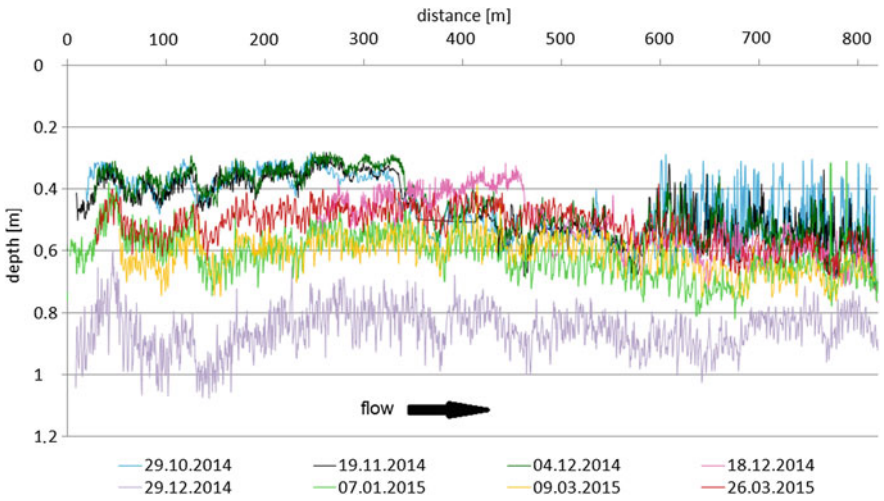

Fig. 4 Longitudinal profiles measured in the main channel of bed elevations for each day

the beginning of the higher discharges with the extreme observed on 29.12.2014 was indicated. These two phenomena significantly altered the shape of the profiles. Plants on the bottom were observed in the last 220 m length of the channel. Just before the existence of vegetation, around 200 m of the channel was eroded. It could be explained as a result of the occurrence of plants, which create a barrier for flowing water. After the vegetation season, the elevation of the river bed was more aligned (from 29.12.2014 to 26.03.2015).

As presented in Fig. 4, the river bottom has greatly changed during the whole measurement period. For instance, sections of maximal depth on 29 October 2014 were covered with sediment during the next 5 months, whereas the other parts of the channel, with the highest elevation, became the deepest place in the channel. Moreover, as given by the first three profiles the transport at the low discharge was very slow. In order to compare the changes in the river-bed morphology the digital elevation models (DEM) of the channel obtained with use of the ArcGIS software are presented for 2 days (Figs. 5 and 6). The deepest places in the channel are located near the river banks, alternately on the left and right side. It is well known that such depth distribution is characteristic for non-regulated rivers that seek to form meanders. Moreover, these models confirm that the shape and dimensions of the bedforms have also been changed. It can also be seen that the dunes in the channel are 3-dimensional, which contradicts some previous works, as it is usually assumed that the dunes in the regulated channels should be 2-dimensional, as was done, for example, by Bialik et al. (2014a).

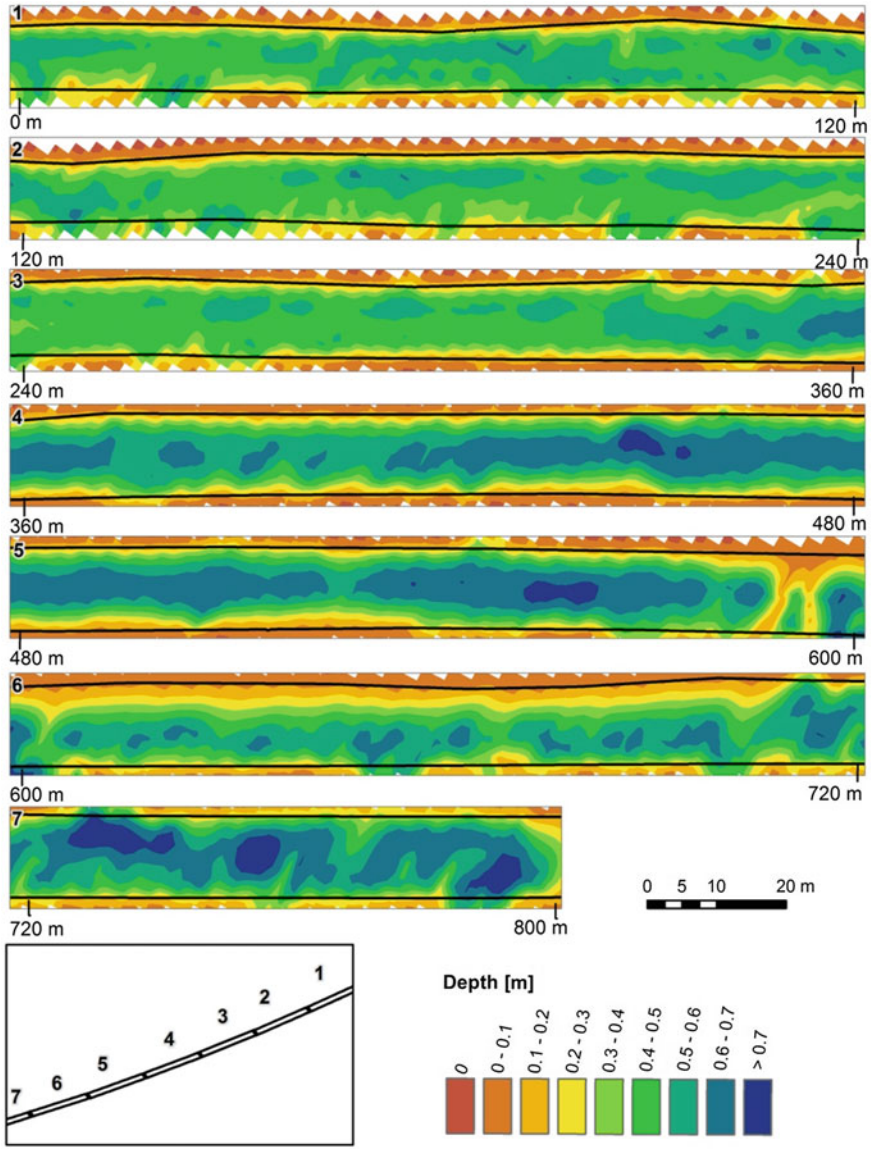

Fig. 5 River bathymetry on 29.10.2014

3.2 Main Processes in the Channel

Figure 7 shows a spatial analysis of the main fluvial processes, which play a key role in formation of the channel structure. The analysis was prepared with ArcGIS software based on the channel bathymetry. The input bathymetry layers were taken

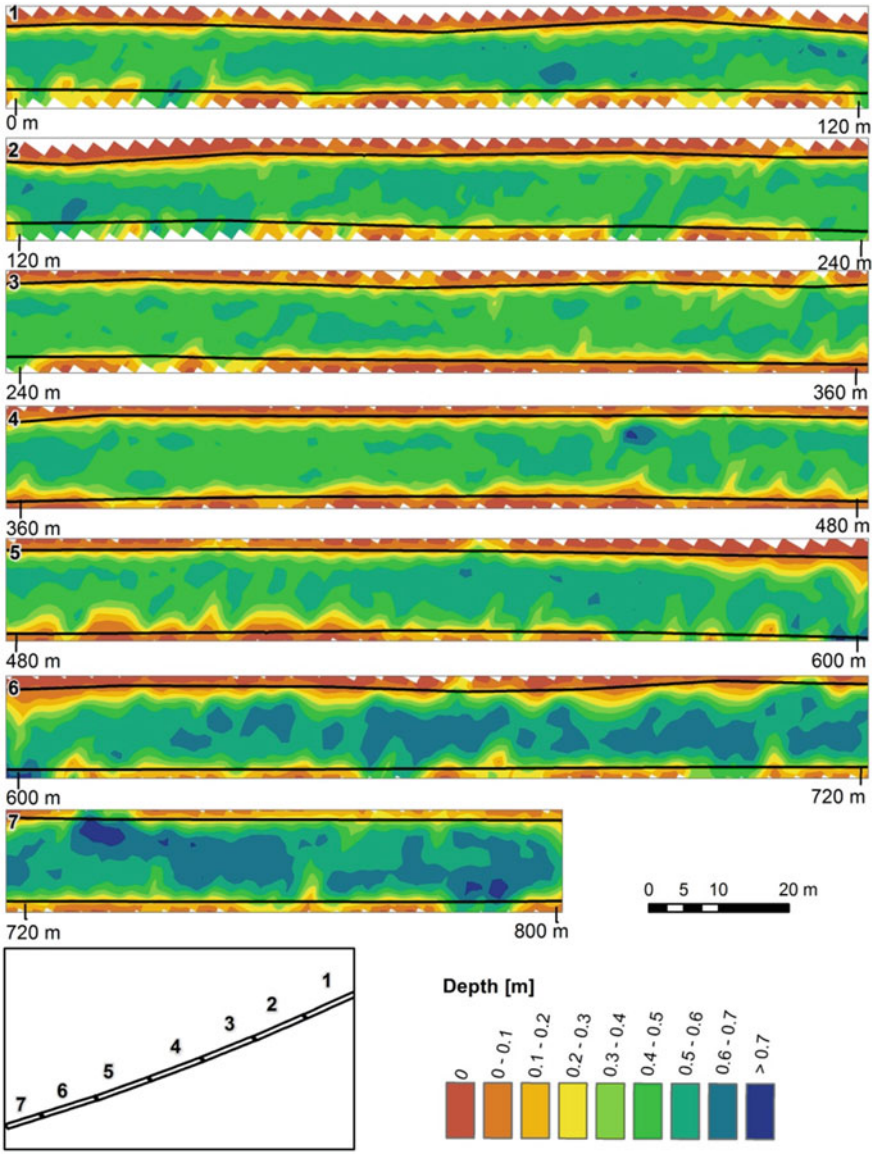

Fig. 6 River bathymetry on 26.03.2015

from 26 March 2015 and 29 October 2014. The phenomenon could occur with varying direction and intensity during this time period. Therefore, the analysis indicates only general tendencies of the channel evolution.

The main morphodynamics process analysis shows that a significant role in the formation of the channel structure is played by sediment transport. The main

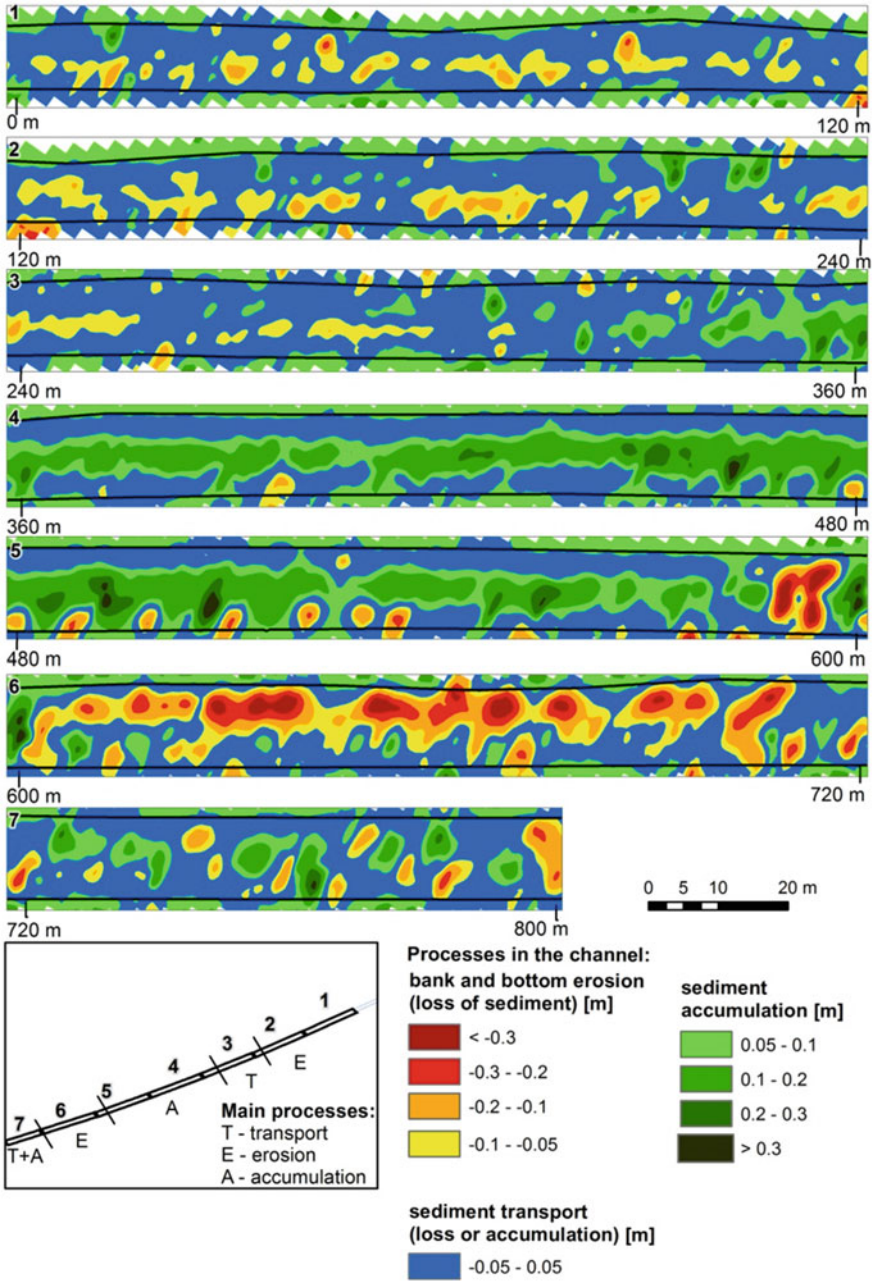

Fig. 7 Main morphodynamic processes in the channel

process behind the water step was river-bed erosion to 180 m. Next, sediment transport stretched to 300 m. Accumulation processes were the highest from 360 to 580 m, where maximal accumulation of sediment reached 0.2–0.3 m. After that, bottom and bank erosion was the highest at the distance from 600 to 720 m. This situation could be associated with the loss of vegetation on the bottom of the channel. Moreover, the sequence of the main processes (erosion, accumulation and transport), occurring in the regulated channel is the same as in the natural non-regulated river channel. It means that the bottom is eroded and then sediment is transported and accumulated (Fig. 7). The studies of this kind can contribute to the assessment of evolutionary state of the entire regulated river channel.

3.3 *Spectral Analysis*

Finally, for all the profiles from the main channel the single-sided power spectra of bed elevations were calculated. It should be noted that the spectral analysis belongs to quite commonly used methods of the bedform investigations. One of the findings of the previous studies associated with spectral analysis was to firstly propose (Hino 1968; Jain and Kennedy 1974) and further confirm (i.e. Nikora et al. 1997; Aberle et al. 2010; Bialik et al. 2014a) the existence of two scaling regions in the longitudinal wavenumber spectrum, the first one with "−3" and the second one with "−2" scaling exponents. However, it is not clear which ranges of frequency correspond to which regions. Nikora et al. (1997) showed that the region with scaling exponent "−3" exists for small frequencies, which was in contradiction with the proposition given by Hino (1968). Figure 8 shows the single-side wavenumber

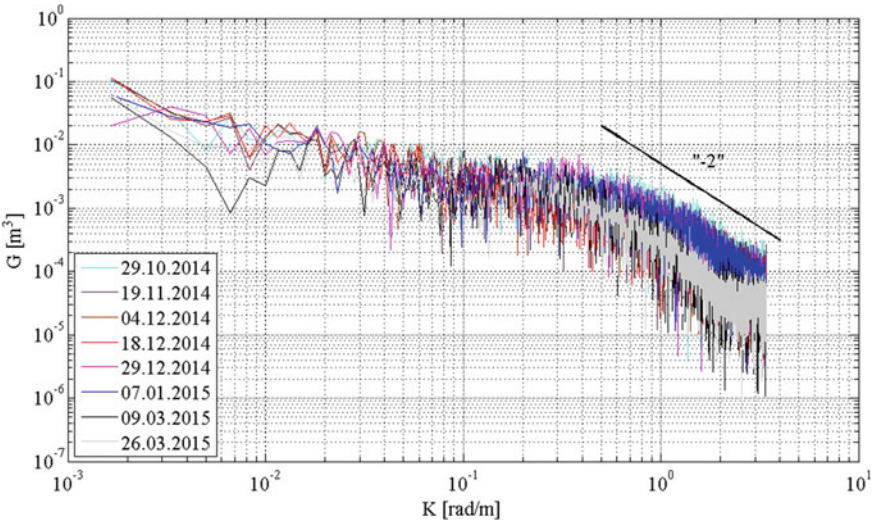

Fig. 8 Single-sided spectra of bed elevation for all measurements

spectra of bed-elevation for all considered longitudinal profiles, where K is the wavenumber ($K = 2\pi/L$, L is the wavelength). One can see that the spectra of bed-elevation profiles with existing vegetation are characterized by the scaling region with the exponent "−2", which tends to be "−3" with the disappearance of the vegetation, which may explain some differences found in the previous works. We hypothesized that an additional drag due to the vegetation existence is causing erosion at the patch edge and affects the shape of the spectra. However, this finding needs future analysis.

4 Conclusions

The analysis of the river-bed morphology changes during the winter season at the regulated channel of the Wilga showed that there is a significant dependence between bathymetry and vegetation patch on the river bed. It is associated with a decrease in the water temperature, for a longer period below 5 °C. However, the direct effect of temperature on the bedform shape has not been observed. Moreover, the obtained results show that the assumption of 2-dimensional bedforms is too strong and that in similar studies the 3-dimensionality of bedforms should be taken into consideration. It has been confirmed that although the channel is regulated, the location of the main processes leads to the finding that non-regulated rivers are seeking to form meanders. In addition, the sequences of the main processes (erosion, transport, deposition) are the same as in the non-regulated channel. The power of the ArcGIS software in such analysis is presented allowing the use of the spatial analysis in GIS for this type of tasks. Finally, the calculated single-sided spectra of bed elevation suggest that in the case of vegetation existing in the channel it is characterized by the scaling region with the exponent "−2", which tends to be "−3" with the disappearance of the plants.

Acknowledgments The study was supported by the Polish National Science Centre project "Field experimental investigation of hydrodynamics of water flow-vegetation-sediment interactions at the scale of individual aquatic plant" No. UMO-2014/13/D/ST10/01123 and within the project for Young Scientists No. 500-10-16 provided by the Institute of Geophysics, Polish Academy of Sciences. Joanna Sziło gratefully acknowledges the financial support from the Interdisciplinary Polar Studies. Finally, the authors are very grateful to colleagues from the Institute of Geophysics: Mikołaj Karpiński, Bartłomiej Luks, Michał Pętlicki, Joanna Ćwiąkała and Magda Ścibor for their help in conducting the fieldwork.

References

Aberle J, Nikora V, Henning M, Ettmer B, Hentschel B (2010) Statistical characterization of bed roughness due to bedforms: a field study in Elbe River at Aken, Germany. Water Resour Res 46(W03521)

Ashley GM (1990) Classification of large-scale subaqueous bedforms: a new look at an old problem. J Sediment Petrol 60(1):160–172

Bialik RJ, Karpiński M, Rajwa A, Luks B, Rowiński PM (2014a) Bedform characteristics in natural and regulated channel: a comparative field study on the Wilga River, Poland. Acta Geophys 62(6):1413–1434

Bialik RJ, Karpiński M, Rajwa A (2014b) Discharge measurements in lowland rivers: field comparison between an electromagnetic open channel flow meter (EOCFM) and an acoustic Doppler current profiler (ADCP). In: Bialik, Majdański, Moskalik (eds) GeoPlanet: earth and planetary sciences, achievements, history and challenges in geophysics, pp 213–222. doi:10.1007/978-3-319-07599-0_12

Cavedon V (2012) Effects of rigid stems on sediment transport. PhD thesis, Universita Degli Studi Di Tranto, pp 1–217

Ettema R, Braileanu F, Muste M (2000) Method for estimating sediment transport in ice-covered channels. J Cold Reg Eng 14(3):130–144

Hino M (1968) Equilibrium-range spectra of sand waves formed by flowing water. J Fluid Mech 34(3):565–573

Hong RJ, Karim MF, Kennedy JF (1984) Low-temperature effects on flow in sand-bed stream. J Hydraul Eng 110(2):109–125

Jain SC, Kennedy JF (1974) The spectral evolution of sedimentary bedforms. J Fluid Mech 63 (2):301–314

Kennedy JF (1963) The mechanics of dunes and antidunes in erodible-bed channels. J Fluid Mech 16(4):521–546

Knack I, Shen HT (2015) Sediment transport in ice-covered channels. Int J Sediment Res 30 (1):63–67

Lau YL, Krishnappan BG (1985) Sediment transport under ice cover. J Hydraul Eng 111(6):934–950

McLean SR, Smith JD (1986) A model for flow over two-dimensional bed forms. J Hydraul Eng 112:300–317

McLean SR, Nelson JM, Wolfe SR (1994) Turbulence structure over two-dimensional bed forms: Implications for sediment transport. J Geophys Res 99(C6):12, 729-12, 747

Nikora VI, Sukhodolov AN, Rowiński PM (1997) Statistical sand wave dynamics in one-directional water flows. J Fluid Mech 351:17–30

Parsons DR, Jackson PR, Czuba JA, Engel FL, Rhoads BL, Oberg KA, Best JL, Mueller DS, Johnson KK, Riley JD (2013) Velocity mapping toolbox (VMT): a processing and visualization suite for moving-vessel ADCP measurements. Earth Surf Proc Land 38:1244–1260

Radecki-Pawlik A, Carling P, Książek L (2010) Sand-gravel subaquatic bed forms system in the Raba River—the morphology and granulometrics. In: 12th river morphological colloquium "fluvial systems in space and time", Bundesanstalt für Gewässerkunde BfG Koblenz, Germany, pp 47–58

Sayre WW, Song GB (1979) Effects of ice covers on alluvial channel flow and sediment transport processes. IIHR Report No 2018. Iowa City, Iowa Institute of Hydraulic Research, University of Iowa

Smith BR, Ettema R (1995) Ice-cover influence on flow and bedload transport in dune-bed channels. IIHR Report No. 374. Iowa City, Iowa Institute of Hydraulic Research, University of Iowa

Sukhodolov AN, Fedele JJ, Rhoads BL (2006) Structure of flow over alluvial bedforms: an experiment on linking field and laboratory methods. Earth Surf Proc Land 31:1292–1310

Tsai WF, Ettema R (1994) Ice cover influence on transverse bed slopes in a curved alluvial channel. J Hydraul Res 32(4):561–581

Optimizing Multi-purpose Reservoir Operation Using Particle Swarm Intelligence

Mohammed Abdallah and Jürgen Stamm

Abstract Developing an efficient multi-objective reservoir operation policy is one of the most challenging water resources tasks due to a big number of involved parameters, in addition to the question of proper system representation. Therefore, the aim of the paper is to apply Particle Swarm Optimization (PSO) technique to optimal operation of the Atbara River basin reservoir system. An objective function is defined to minimize the squared difference between targeted and generated hydropower as well as irrigation demands to be solved using a set of tuned (PSO), and then applied in Girba multi-purpose reservoir. The results showed a tangible improvement in power production, up to 15 % increase, satisfying at the same time the irrigation demands. Three performance measures of reliability, resilience, and vulnerability have been applied based on model outputs and required release values that satisfy the system's demands. All measures indicated an improvement of the system's performance, exhibiting the reliability increase to 97 %, instead of current 86 %.

1 Introduction

Optimizing reservoir management and operation is a very complex procedure as it involves various operational objectives such as hydropower, flood control, and irrigation with different conflicting and priority degrees. This leads to increased complexity of decision-making process as many variables and system's constraints

M. Abdallah (✉)
Experienced Researcher, HYTECH-GHT PHOTONICS, via Istria 55, 35135 Padua, Italy
e-mail: mabdallah@t-online.de

J. Stamm
Professor of Hydraulic Engineering, Head of Hydraulic Engineering and Technical Hydro Mechanics Institute (IWD), Dresden University of Technology, George-Bähr-Strasse1, D-01062 Dresden, Germany

P. Rowiński and A. Marion (eds.), *Hydrodynamic and Mass Transport at Freshwater Aquatic Interfaces*, GeoPlanet: Earth and Planetary Sciences,
DOI 10.1007/978-3-319-27750-9_17

should be taken into account and integrated carefully to the system with the associated uncertainty, particularly of the inflow and demand.

During last decades, several simulation models have been developed (Rani and Moreira 2009) to generate different release policies of reservoir systems through testing different operational scenarios. However, this strategy can answer only the "what if" question, which means that an additional tool aiming at determining the best alternative among the suggested diverse scenarios is required.

Due to the complex dynamic, nonlinear and nonconvex reservoir optimization problems (Labadie 2004), several linear, nonlinear, and dynamic optimization models have been developed, as reported in many state-of-the-art reviews (Lund and Gutzman 1999). In this context, the literature review shows a clear tendency to develop new optimization techniques that can overcome the shortcomings of the above-mentioned techniques (Rani and Moreira 2009).

Accordingly, applying swarm intelligence to find the optimum solution of these problems has attracted attention of many researchers in different disciplines during the last decades; it includes the use of the capability of population search, which can help in avoiding the drawbacks of traditional techniques. These applications have been extended successfully to the field of reservoir operation, and some researchers applied particle swarm optimization (PSO) in reservoir operation problem (Reddy 2006). However, these applications are still limited to certain case studies, in addition to adopting many simplifications, which are either aimed at decreasing the complexity of uncertainty, or linearizing the problem.

In this study, (PSO) model has been developed and verified at Girba reservoir based on outputs of different inflows and demand scenarios, updated system's state, and Parameterization-Simulation-Optimization Reservoir Hedging Model (PSO-HDG), where different parameter selection and calibration procedures used to adjust the model have been applied.

To check the performance of optimization model, some indices of reliability, resilience, and vulnerability have been calculated based on optimized release and compared with current operation policy, based on nonlinear optimization; the comparison reflects a real improvement of hydropower generation and fulfilment of other demands when applying the PSO-HDG model.

2 Particle Swarm Optimization (PSO) Model

Particle Swarm Optimization is a population-based search algorithm originally proposed by Eberhart and Kennedy (1995). It depends on information exchange between individuals of the population (swarm) flown through hyper-dimensional search space, where particles learn from each other within the swarm and use this knowledge to be more similar to the "better" neighbours.

Each i-th particle of the swarm in a search space can be a potential solution, and moves through this space where the position of each particle changes according to its own experience and that of neighbors. Thus, the position of each particle can be

represented by D-dimensional vector, $X_i = (x_{i1}, x_{i2}, \ldots, x_{iD})^T$, particle velocity (changing particle position) can be represented by another D-dimensional vector $V_i = (v_{i1}, v_{i2}, \ldots, v_{iD})^T$, the best previous particle position $P_i = (p_{i1}, p_{i2}, \ldots, p_{iD})^T$. Therefore, the position of P_i is changed according to the following equations:

$$v_{id}^{n+1} = \chi(w v_{id}^{n} + c_1 r_{1,i,d}^{n}(P_{id}^{n} - x_{id}^{n}) + c_2 r_{2,i,d}^{n}(P_{gd}^{n} - x_{id}^{n}) \quad (1)$$

$$x_{id}^{n+1} = x_{id}^{n} + v_{id}^{n+1} \quad (2)$$

where: d = 1, 2, …, D; i = 1, 2, …, N; N = swarm size; n = iteration number; χ = constriction coefficient; w = inertia weight; c_1, c_2 = acceleration coefficients; r_1, r_2 = random numbers; $X_{d,max}$, $X_{d,min}$ = upper and lower bounds of the search space.

The above parameters need to be adjusted and set properly in order to converge to the best solution; therefore, benchmark testing function will be used as demonstrated in the next section. So, fine-tuning of (c_1, c_2) in Eq. (1) as a positive constant may result in faster convergence of the algorithm (Reddy 2006). Clerc (2006) stated that the small c_1 value can induce a premature convergence, while the large value may slow the convergence down; for that reason, the authors recommend a value of 0.7 or 0.8 for the first swarm particle.

The other acceleration coefficient, c_2, should not be too large either, and it is recommended to take a value between 1.5 and 1.7; however, there is no direct justification for this number so far, and it is fully empirical (Clerc 2006).

The constriction factor (χ) is taken as 1 in the first particle swarm algorithm, but later researches show if particle's velocity is allowed to move without boundaries; this will lead swarm's set to scatter over the search space and never converge to the optimum solution. Therefore, to control the velocity changes, the constriction factor (χ) was introduced firstly by Clerc (1999) to force the swarm particles to achieve better convergence through the use of Eqs. (1) and (2), and then it was kept updated regularly in iteration process. Furthermore, the main role of inertial weight (w) is to provide the balance between exploration and exploitation process through determining the contribution rate of a particle's previous velocity to its velocity at the current time step (Bansal et al. 2011).

3 PSO-HDG Reservoir Optimization Model

The objective function of this study is designed to minimize the sum of squared deficits for annual demands and hydropower generation in a monthly scale; this function can be written as follows:

$$f\min = \sum_{i=1}^{12} (D_t - R_t) + \sum_{i=1}^{12} (Tp_t - PP_t) \quad (3)$$

where D_t, R_t, Tp_t, PP_t are system's demand, system's release in Mm^3, targeted power, and produced power in GWh, respectively. This equation is subject to the following constraints:

- Parameterized mass balance equation:

$$\begin{aligned} R_t &= a_t * I_t + b_t * S_t + m_t \quad \forall t = 1, 2, \ldots, 12 \\ S_{t+1} &= I_t + S_t - R_t \end{aligned} \tag{4}$$

  where a and b, are the rules coefficients for the interval time t and m is a constant
- Hydropower generation equation:

$$\begin{aligned} PP_t &= k_t * TR_t * H_t \quad \forall t = 1, 2, \ldots, 12 \\ H_t &= x_t * S_t^{y_t} \end{aligned} \tag{5}$$

  $k_t = \rho \cdot g \cdot C_p$ where k_t, TR_t, and H_t are power coefficient, turbine release, and reservoir head level (m), respectively. x_t and y_t are constants extracted from Yevdjevich (1965) equation.
- Storage constraints:

$$S_{\min} \le S_t \le S_{\max} \quad \forall t = 1, 2, \ldots, 12 \tag{6}$$

  where S_{min} and S_{max} are the minimum and maximum storage in Mm^3, respectively.
- Parameter constraints:

$$\begin{aligned} a_{\min} \le a_t \le a_{\max} \quad \forall t = 1, 2, \ldots, 12 \\ b_{\min} \le b_t \le b_{\max} \quad \forall t = 1, 2, \ldots, 12 \\ m_{\min} \le m_t \le m_{\max} \quad \forall t = 1, 2, \ldots, 12 \end{aligned} \tag{7}$$

- Demand constraints:

$$D_{\min} \le D_t \le D_{\max} \quad \forall t = 1, 2, \ldots, 12 \tag{8}$$

- Release constraints:

$$\begin{aligned} R_{\min} \le R_t \le R_{\max} \quad \forall t = 1, 2, \ldots, 12 \\ R_t \ge TR_t \quad \forall t = 1, 2, \ldots, 12 \end{aligned} \tag{9}$$

- Hydropower constraints:

$$TP_t \geq PP_t \quad \forall t = 1, 2, \ldots, 12 \tag{10}$$

In order to distribute the shortage evenly in case of occurrence; the squared deficit has been normalized. The final reservoir optimization fitness function can be written as follows:

$$F = wt_1 \sum_{t=1}^{12} \left[\frac{D_t - (a_t * I_t + b_t * S_t + m)}{D_t} \right]^2 + wt_2 \sum_{t=1}^{12} \left[\frac{Tp_t - (k_t * TR_t * x_t * S_t^{y_t})}{Tp_t} \right]^2$$
$$\forall t = 1, 2, \ldots, 12 \tag{11}$$

where wt_1 and wt_2 are constant weights to determine the priority of each objective function based on reservoir operation priority, e.g., values of (1, 1) are typical when satisfying other demands has the same priority as the hydropower generation.

4 Study Area and System Description

The Atbara River basin, where Girba reservoir is located within the Sudan border, lays in Ethiopia, Eritrea, and Sudan. The river is characterized by highly seasonal pattern: the flood peak, with an average of 2000 m^3/s, occurs in August and almost dry period, with an average annual flow of around 12,000 Mm^3, occurs during summer months (April–May).

The reservoir has been launched in 1964 with design storage capacity of 1300 Mm^3 to ensure supplying of around 200,000 hectares as a major purpose. A set of seven deep sluices, each of them with a discharge capacity of 1100 m^3/s, and five spillways, each passing 200 m^3/s, have been constructed by operation range of 12 m between 473 m raised to be 474.5 m as a maximum and 462 m as a minimum operation level, while the tail water downstream varies between 432 and 448 m.

Two turbines, three turbine pump stations, and four compensating pumps are installed to generate 17.8 MW of hydropower and raised reservoir level to the main irrigation canal level during low flow seasons. The Atbara River carries big sediment load during the flood season in July–September, estimated by an average of 20 million ton per year; hence, the reservoir is exposed to catch part of this quantity. According to Abdallah and Stamm (2012), Girba reservoir has experienced a severe sediment accumulation during its operation period due to either natural river morphological processes as a major cause or some other operational reasons which leads to a decrease in reservoir's capability to meet its design purposes efficiently; therefore, by 2010, Girba reservoir lost over 50 % of design capacity.

The operation procedures of Girba reservoir divided the hydrological year into the four main periods:

1. 1–31 July—rising period;
2. 1–20 August—period just before peak;
3. 21 August–30 September—peak period;
4. 1 October–30 June—recession and low flow periods.

The reservoir operated during the first period in a minimum operation level of 462 m to decrease sediment deposition; hence, the generated power is very low and irrigation demands abstraction depends mainly on pumps. This minimum operation level policy continues till the second week of August or when the river flow reaches more than 200 million m^3/day, then the reservoir flushing started for 3–5 days; afterwards, the policy is resumed. When the high flood peak starts to recess and most of heavy sediment load is washed out, the reservoir starts filling procedures gradually to reach the maximum operation level by October and keeps it until the river flow becomes less than water requirements; then, the withdrawing from the reservoir starts and continues till the end of the period.

5 Analysis and Results

The particle swarm optimization model, described in the previous sections, has been applied to Girba reservoir in order to meet two objectives: (1) finding the optimal or near optimal solution to the reservoir operation problem in terms of increasing hydropower production, which would satisfy the irrigation and other demands; and (2) comparing the model outputs with current system operation policy applying the nonlinear optimization model results.

PSO-HDG reservoir optimization model's Eq. (11) has first been tested and calibrated with respect to many optimization benchmark functions, and then applied to Girba reservoir system inputs and constraints to obtain the optimum release that would correspond to the optimum storage values.

Based on the PSO model calibration process and sensitivity analysis, the PSO parameters N, n, χ, w, c_1, c_2, r_1, and r_2 have been adjusted to take the values of 30, 100, 0.79, 0.8, 1.62, 0.7, 0.8 and 0.79, respectively, while the upper and lower bounds, $X_{d,max}$ and $X_{d,min}$, take the reservoir's maximum and minimum storage values.

Based on available data; A monthly operation time interval has been adopted in the same way like the real applied policy; however, due to annual sediment accumulation which decreases the storage capacity, carefully selected years have been simulated based on the availability of updated bathymetric survey data. To ensure accurate storage estimation, a frame time of 6 years (72 months), where the years of available survey data are included in-between, have been designed accordingly, as shown in Table 1.

Table 1 Girba reservoir simulation periods

	Months
1st simulation period	(January 1975–December 1980)
2nd simulation period	(January 1982–December 1987)
3rd simulation period	(January 1990–December 1995)
4th simulation period	(January 2005–July 2010)
Total no. of months	283

To handle the optimization equation constraints, the fuzzy model outputs of Abdallah and Stamm (2012) are used. These are based on "IF-THEN" principle, where "IF" represents the vector of fuzzy explanatory variable (inflow, storage), and "THEN" the fuzzy consequences (release). This approach has been used to define the storage, release, and demand bounds at each simulation period based on an applied operation policy, besides Abdallah and Stamm's (2014) parameterization approach to define the *(a, b, m)* parameters of PSO-HDG model.

5.1 Reservoir Storage Model's Results

Since the PSO model applied the same operation policy and the same input data as the real case study, a comparison between measured and simulated reservoir storage has been made; the PSO-HDG model results show a tendency of keeping more storage for a long period, as shown in Fig. 1, while emptying reservoir to the minimum allowable operation level during July and August. This behavior can be observed till the third simulation period, where the storage capacities have not yet been affected by sediment accumulation. However, the model is still reflecting the same tendency, but the seasonality nature of inflow and deteriorated capacity reduce this additional volume; nevertheless, the model is still showing a better performance than the actual operation policy described in Sect. 4.

This tendency of keeping the storage volume for a longer time and emptying reservoirs totally by July has two advantages: (1) increases the hydropower generation due to increased available reservoir head level, and (2) decreases sediment accumulation by passing the whole sediment peak in July and August through keeping the reservoir at the minimum operation level.

5.2 Hydropower Generation

To analyze hydropower production of Girba reservoir, the PSO-HDG model outputs of storage and release have been applied to calculate the projected hydropower production, as shown in Fig. 2. This figure shows the total annual produced power in case of using the measured data and optimization of PSO-HDG model with increasing or decreasing percentage.

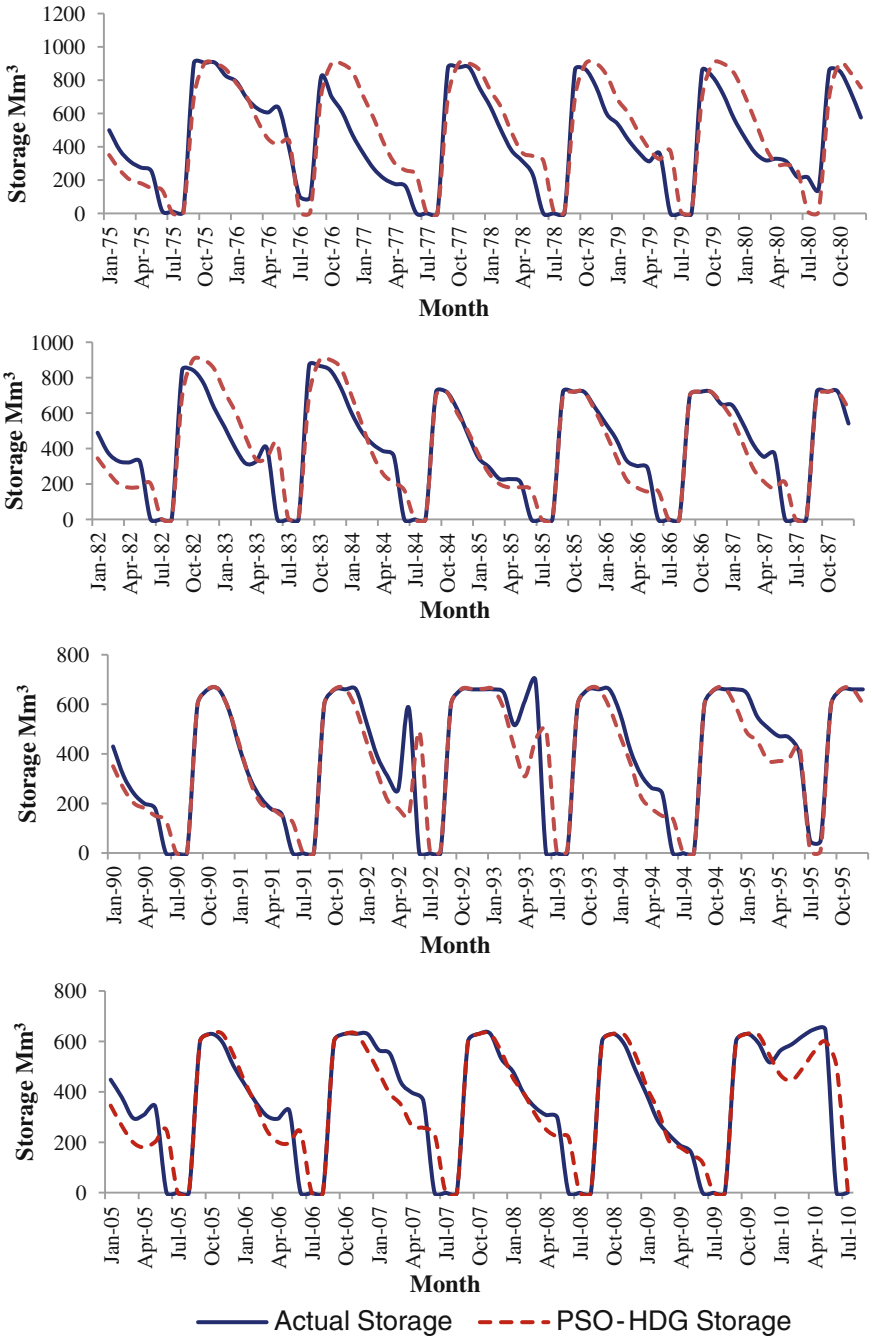

Fig. 1 Actual and optimized storage of the girba reservoir

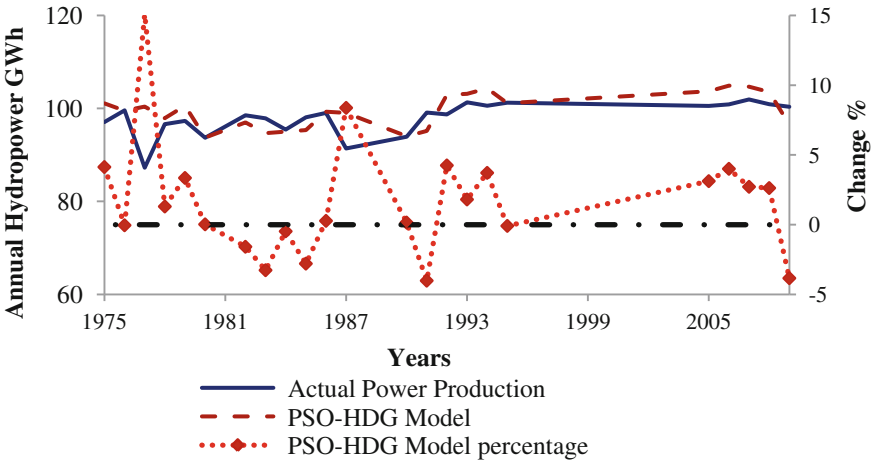

Fig. 2 Actual and optimized annual power production

It can be noticed from this graph that a real improvement, up to 15 % increase in power production, can be reached comparing to the applied operation policy that adopted the same objective function even with low turbines capacity besides using the compensating pumps to raise reservoir's level during dry season. However, a reduction between 1 and 4 % is expected during summer normally, because of the PSO-HDG model's tendency of giving more priority to satisfy irrigation demands at the cost of hydropower production during summer months.

Based on these results, more hydropower can be produced by applying PSO-HDG model; nevertheless, two things have to be considered here: (1) determining the priority purpose to orient the model for getting the best results; and (2) in case of irrigation priority, some decrease in power production during November–January is expected in case of PSO-HDG, as the model tends to release water later in order to distribute water deficit through the whole operation year.

5.3 PSO Model Performance Measures

Reliability, resiliency, and vulnerability tests have been applied to check the PSO-HDG performance based on model outputs and required release values that satisfied the system's demands.

These measures can be mathematically expressed as follows:

$$\text{Reliability} = 1 - \frac{Average\ Annual\ \ Water\ Deficit}{Total\ Annual\ Demands} \tag{12}$$

$$\text{Average Annual Water Deficit} = \frac{1}{T}\sum_{i=1}^{T}\frac{\sqrt{(Deficit)^2}}{Demand} \tag{13}$$

From above two equations, the system's reliability can be estimated to determine the percentage of both, satisfaction and failure, while resilience can be used here according to Loucks and Beek (2005) as a probability of having a satisfactory value in the time period ($t + 1$), given an unsatisfactory value in any time period t. In reservoir operation, this definition can be formulated as:

$$\text{Resilience} = \frac{\sum SP_{sh}}{\sum SP_t} \tag{14}$$

where SP_{sh} and SP_t refer to satisfactory value that follows a shortage period, and total shortage period, respectively. Both reliability and resilience are a positive measure in percentage: the higher the values, the better the system's performance.

Defining the worst and critical operation scenarios is a crucial factor in reservoir operation; thus, vulnerability is used here as a probabilistic measure to know the extent of differences between the threshold value and unsatisfactory values during operation period (Loucks and Beek 2005). Accordingly, this can be written as:

$$\text{Vulnerability } C_v = \max\left\{\sum_{t\in i} C - X_t, \quad i = 1\ldots N\right\}. \tag{15}$$

$$\text{Relative Vulnerability} = \frac{C_v}{\sum\limits_{t\in J_n} D_t} \tag{16}$$

C *and* J_n refer here to the condition where demand has not been satisfied, while D_t is the demand at time step t. According to Hashimoto et al. (1982), vulnerability shows the worst system performance scenario during the period where demands cannot be fully satisfied and considers a negative measure, for which the smaller values are better than the highest ones, as shown in Table 2.

From this table, the competence of PSO-HDG model in terms of achieving higher overall annual reliability and resilience through all simulation periods can clearly be observed, although some deficit can occur during dry season, when a trade-of has to be made between satisfying the irrigation and hydropower demands of the upcoming months.

Table 2 PSO-HDG average annual performance measures

	Reliability	Resilience	Vulnerability (Mm^3)	Relative vulnerability
Actual	0.86	0.47	214.2	0.34
PSO-HDG	0.97	0.59	108.6	0.28

To estimate the extent of worst scenario during monthly operation period, the calculated relative vulnerability shows the good performance of PSO-HDG model in reducing the system vulnerability efficiently, even in cases of relatively low reliability or resilience values comparing to the measured ones.

As a conclusion, these results mean, regardless how reliable the system is, if the shortage occur, the consequence will not be worse than applying the current operation policy, due to the low vulnerability value of particle swarm optimization model.

6 Conclusion

A new particle swarm intelligence optimization model to improve reservoir operation has been developed and formulated in this paper to avoid the shortcomings of traditional optimization techniques in solving such complicated nonlinear problems.

The developed model has been firstly verified to two benchmark optimization testing functions to calibrate and validate model parameters; afterwards, the model has been extended to be applied in Girba multipurpose reservoir. The main objective function of optimization model is to maximize hydropower production while keep satisfying irrigation demands at the highest possible rate. Accordingly, a fitness function of reservoir parameterization PSO-HDG model has been formulated using the study area conditions and constraints.

To check the efficiency of PSO-HDG model, performance analysis has been conducted, considering its reliability, resilience, and vulnerability. The PSO-HDG model shows a real improvement in terms of increasing hydropower generation, besides satisfying other demands in most cases.

These results clearly show the competence of particle swarm optimization model in obtaining better results with minimum computational effort and time comparing to the applied operation.

References

Abdallah M, Stamm J (2012) Developing an optimum multipurpose reservoir operation policy under uncertain conditions. Nile Watersci Eng J 10:232

Abdallah M, Stamm J (2014) Parameterization of reservoir operating rules based on fuzzy model. 37 Dresdner Wasserbaukolloquium "simulation techniques and models for hydraulic engineering and water management", Heft 50, Germany

Bansal JC, Singh PK, Mukesh S, Abhishek V, Shimpi SJ, Ajith A (2011) Inertia weight strategies in particle swarm optimization. IEEE 978-1-4577-1123-7/11

Clerc M (1999) The swarm and the queen: towards a deterministic and adaptive particle swarm optimization. In: Proceedings of the 1999 ICEC, Washington, DC, pp 1951–1957

Clerc M (2006) Particle swarm optimization. ISTE Ltd

Eberhart R, Kennedy J (1995) A new optimizer using particle swarm theory. In: Proceedings of the sixth international symposium on micro machine and human science (Nagoya, Japan). IEEE Service Center, Piscataway, NJ

Hashimoto T, Stedinger JR, Loucks DP (1982) Reliability, resiliency and vulnerability criteria for water resource system performance evaluation. Water Resour Res 18(1):14–20

Labadie JW (2004) Optimal operation of multireservoir systems: State-of-the-art review. J Water Resour Plann Manage 130(2):93–111

Loucks DP, Beek EV (2005) Water resources systems planning and management. UNESCO publishing, Delft hydraulics, Netherlands

Lund JR, Guzman J (1999) Derived operating rules for reservoirs in series or in parallel. J Water Resour Plann Manage ASCE 125(3):143–153

Rani D, Moreira M (2009) Simulation-optimization modeling: a survey and potential application in reservoir system operation. Water Resour Manage 24:1107–1138

Reddy MJ (2006) Swarm intelligence and evolutionary computation for single and multiobjective optimization in water resource systems. PhD Thesis, Indian Institute of Science-Bangalore, India

Yevdjevich VM (1965) Stochastic problems in design of reservoirs. Paper presented at the seminar in water resources research at Colorado State University, USA

Flume Experiments on Gravel Bed Load Transport in Unsteady Flow—Preliminary Results

Magdalena M. Mrokowska, Paweł Rowiński, Leszek Książek, Andrzej Strużyński, Maciej Wyrębek and Artur Radecki-Pawlik

Abstract This chapter presents settings and results of laboratory experiments on bed load transport. Experiments were performed for unsteady hydrographs and for steady flow conditions. Continuous measurements of transported mass and flow rate reveal a clockwise hysteresis of bed load rate versus flow rate. A comparison between bed load rate in unsteady and steady flow shows that it depends to a large extent on sediment supply. The results are discussed in the light of variable sediment supply, and suggestions for procedure of further experiments are presented.

1 Introduction

Unsteady flow may trigger serious morphological changes at the water-ground interface in a relatively short time, compared to steady flow conditions. Better understanding and description of unsteady flow in recent years (Ghimire and Deng 2013; Mrokowska et al. 2015; Rowiński et al. 2000; Shen and Diplas 2010) has caused rising interest in sediment transport in such flow conditions (Tabarestani and Zarrati 2015). The abundance of processes that may occur in the unsteady flow makes the problem of sediment transport very complex and difficult to describe in general laws. Beside variable flow parameters, there is a lot of aspects referring to the sediment itself, such as armoring, winnowing, downstream fining, and sediment supply. It has been observed so far that bed load transport is variable during a hydrograph, and this variability depends on the spatial arrangement of sediment grains (Mao 2012), sediment supply from upstream (Parker et al. 2003), and

M.M. Mrokowska (✉) · P. Rowiński
Institute of Geophysics, Polish Academy of Sciences, Ks. Janusza 64,
01-452 Warsaw, Poland
e-mail: m.mrokowska@igf.edu.pl

L. Książek · A. Strużyński · M. Wyrębek · A. Radecki-Pawlik
Department of Hydraulic Engineering and Geotechnics, Agriculture University in Krakow,
Al. Mickiewicza 21, Kraków, Poland

P. Rowiński and A. Marion (eds.), *Hydrodynamic and Mass Transport at Freshwater Aquatic Interfaces*, GeoPlanet: Earth and Planetary Sciences,
DOI 10.1007/978-3-319-27750-9_18

variable shear stress (Guney et al. 2013; Qu 2002). However, the problem is still open for systematic research.

Sediment supply plays significant role in bed load transport. The following laboratory settings to study gravel or bimodal (gravel-sand) sediments have been considered so far: no sediment feeding (Bombar et al. 2011; Wang et al. 2014; Guney et al. 2013), manual sediment feeding to prevent bed erosion (Qu 2002), designed sediment supply (Parker et al. 2003), pulse sediment supply (Humphires et al. 2012), and sediment recirculation conditions (Mao 2012).

In this chapter, we present the settings and preliminary results of experiments on gravel bed load transport in unsteady flow in comparison with steady flow conditions. Data analysis has revealed that bed load transport is sensitive to sediment supply to large extent. This observation is a motivation to analyze experimental data from this point of view. Objectives of this study are to (1) analyze to what extent total sediment supply affects bed load transport in unsteady flow, (2) examine variability of bed load rate during the passage of an unsteady hydrograph in comparison with bed load rate in steady flow, (3) analyze changes in grain size distribution and bed elevation after the passage of a hydrograph. It is the first phase of our research on bed load transport. We present preliminary results with the discussion of problematic aspects and recommendations for further studies.

2 Materials and Methods

2.1 Facilities and Experimental Set-up

The experiments were performed in a 12 m-long, 0.485 m-wide and 0.60 m-deep flume (Książek 2000) with locked recirculating water system (Fig. 1a) in the laboratory of Faculty of Environmental Engineering and Land Surveying, Agricultural University of Krakow. The flume was adjusted to bed slope of 0.0083, and equipped with an ultrasonic flow meter on inlet pipe, five resistive water level sensors, a bed load trap with the system to measure cumulative submerged mass of sediment in the outlet of the flume, and a point gauge.

Measurements of flow were performed using ultrasonic flow meter Portaflow 330 with an accuracy of ±0.02 % of measured value. Measurements were taken within the range of 0.010–56 $m^3\ h^{-1}$. The water temperature during the experiments varied from 19.4 to 21.4 °C.

Water surface level was measured with resistive sensors in five points located on right-hand wall of cross-sections denoted in Fig. 1 as L1, L2, L3, L4 and L5. The accuracy of measurements was ±1 mm.

Cumulative submerged mass of sediment was measured with a frequency of 1 Hz using a specially designed system connected with the bed load trap. The dimensions of trap inlet were 0.20 m × 0.42 m. Two inlet guide piers directed the whole transported sediment into the trap. Inside the trap, a movable box was

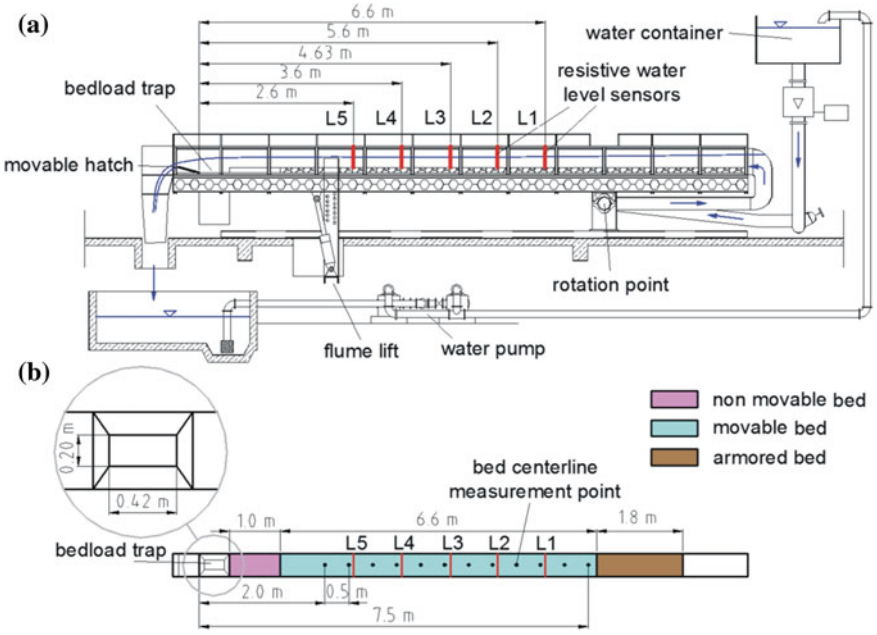

Fig. 1 Scheme of hydraulic tilting flume and experimental settings: **a** side view, **b** plan view

installed with possibility to remove it from the trap, and put on the weighing scales to measure the total mass of sediment collected during an experiment.

As indicated in Fig. 1b, the initial section of about 1.8 m was armored by coarse gravel of gradually decreasing diameter to prevent scouring and to reduce the intensity of turbulence over the rough bed. Next 6.6 m-long test section, a movable bed section, was filled with the studied sediment, well-mixed and screeded to the 0.12 m-thick layer. Last 1.0 m-long section was non-movable bed made of a smooth panel.

In the centerline of the movable bed section, twelve measurement points of bed elevation were chosen every 0.5 m. Moreover, in every cross-section (L1, …, L5) bed elevation was measured in 22 points with spatial resolution of 0.02 m. Measurements of bed elevation were taken by a point gauge with the accuracy of ±0.5 mm.

Composition of the sediment was determined by sieve analysis. Sediment used for the experiment, denoted throughout the chapter as the initial sediment, consisted mostly of gravel and sand (Fig. 2). According to standards PN-EN ISO 14688-1 and 14688-2 it is classified as fine gravel. The characteristic dimensions of grains are mean grain size d_m = 4.93 mm, maximum grain size d_{max} = 18 mm. Following the value of granulometric grain size diversity coefficient C_u ($1 \leq C_u \leq 5$), the initial sediment could be classified as uniformly graded.

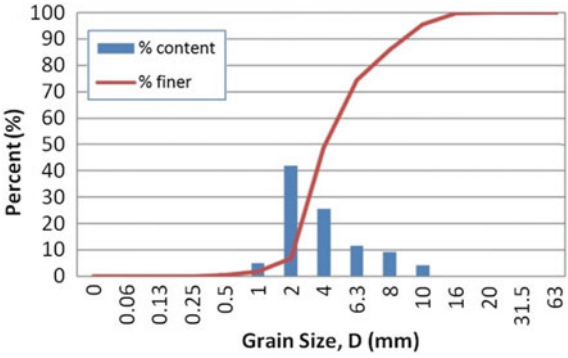

Fig. 2 Grain size curve of initial sediment

2.2 *Experimental Procedure*

Experiments on sediment transport in steady and unsteady flow were performed. Before each run, the movable bed section was prepared according to procedure presented in the previous section. Next, the initial bed elevation was measured in the centerline points of the movable bed section.

Steady flow experiments were initialized by wetting the bed, next the flow rate was increased gradually until the target value was achieved. Duration of experiments was long enough to achieve equilibrium conditions. During the flow, the initial sediment was supplied upstream manually in a rate assessed using procedures worked out previously for the flume. Finally, flow rate was gradually decreased, and pump was switched off.

During unsteady flow experiments, after wetting the bed, flow rate was increased to the level below initial motion of sediment. Next, a triangular hydrograph was initiated. The flow was increased by designed steps until the peak flow was reached, and next the flow rate was gradually decreased in the same manner. During the passage of the hydrograph, initial sediment was supplied upstream in amount assessed manually to prevent erosion of bed (procedure similar to that described in Qu 2002). During each experiment, the downstream tailgate was kept at one level.

Synchronous measurements of flow rate, water level in five cross-sections and the cumulative mass of transported sediment were taken. Once a run was completed, bed elevation was measured in the centerline points of the movable bed in the same locations as before the run. Additionally, transverse bed elevation profiles were taken in five cross-sections, the same as water surface level measurements (L1, …, L5), with transverse spatial resolution of 0.02 m. Moreover, surface sample of sediment of d_{max} thickness and area of 0.3 m × 0.5 m was taken at the location between 4.3 and 4.8 m (Fig. 1). This sample is denoted as the final sediment throughout the chapter.

2.3 Flow Conditions

Two triangular hydrographs were designed with flow rate ranging between 4.5 and 156.6 $m^3\ h^{-1}$. The hydrographs are distinct from one another by the steepness of their limbs. The first hydrograph is denoted by Hyd1, and the second by Hyd2 throughout the text. They were generated by manual regulation of a valve on the inlet pipe. Lack of automatic control of the flow rate was a drawback; however, satisfactory repeatability of hydrographs presented in the paper was achieved. Three experimental runs of Hyd1 and two runs of Hyd2 are presented herein. The characteristics of each run are demonstrated in Table 1, and hydrographs are depicted in Fig. 3.

Four steady flow experiments were carried out for the following values of the flow rate: 70, 95, 120, and 145 $m^3\ h^{-1}$, denoted as St1, St2, St3, and St4, respectively. Table 2 presents flow conditions during these experiments, and Fig. 3 demonstrates steady flow hydrographs. Flow rate Q was obtained directly form measurements, water depth h was computed as a difference between average water level measured in cross-sections L1, …, L5, and average bed level assessed from

Table 1 Hydraulic parameters of unsteady flow experiments

Parameter	Hyd1_1	Hyd1_2	Hyd1_3	Hyd2_1	Hyd2_2
Q_{max} ($m^3\ s^{-1}$)	0.0414	0.0435	0.0435	0.0405	0.0430
Q_{max} ($m^3\ h^{-1}$)	149.04	156.6	156.7	145.8	154.8
Q_{min} ($m^3\ s^{-1}$)	0.0013	0.0021	0.0021	0.0030	0.0035
Q_{min} ($m^3\ h^{-1}$)	4.7	7.6	7.6	10.8	12.6
h_{max} (m)	0.096	0.102	0.096	0.096	0.103
h_{min} (m)	0.015	0.019	0.019	0.019	0.024
Rising limb duration (s)	409	411	408	256	256

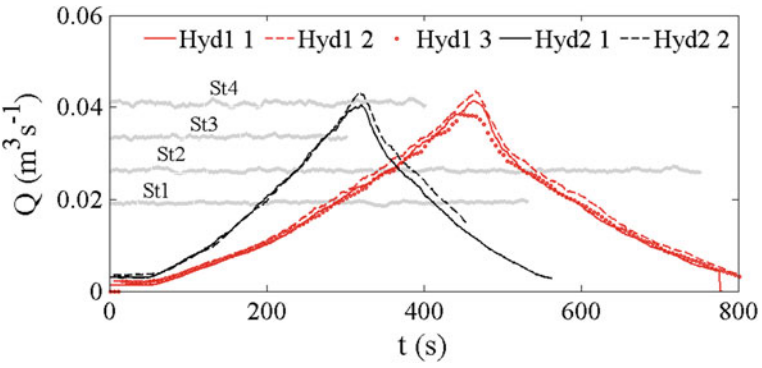

Fig. 3 Hydrographs for steady and unsteady flow experiments

Table 2 Hydraulic parameters of steady flow experiments

Parameter	St1	St2	St3	St4
Q (m^3 s^{-1})	0.0194	0.0263	0.0333	0.0403
Q (m^3 h^{-1})	70	95	120	145
h (m)	No data	0.078	0.085	0.097
Duration (s)	511	751	301	401

bathymetric measurements, mean velocity U was evaluated based on Q and h. Data of h and U are missing for St1, as bathymetric measurements were not taken. Duration of experiments varied between 500 and 1700 s, and duration indicated in the Table 2 refers to the period for which equilibrium conditions were attained.

2.4 *Evaluation of Bed Load Rate and Water Surface Slope*

Bed load rate is computed from cumulative mass data for both steady and unsteady flow tests. For steady flow tests, straight lines are fitted to cumulative mass data, and bed load rate is computed as their first derivatives.

For unsteady flow tests, two approaches are applied. Figure 4 presents results for Hyd1_1. In the first approach a five-point difference quotient is applied to cumulative mass data (q_{fp}). As results are noisy, which is usually the case in such studies (Lee et al. 2004; Qu 2002), next FFT (Fast Fourier Transform) is applied to filter the data (q_{FFT}). Frequency cutoff threshold is set to 0.02 Hz. In the other approach, a Savitzky-Golay filter (Press et al. 2007; Savitzky and Golay 1964) is applied to raw cumulative transport data (q_{SG}). This method uses moving window to average data by a polynomial. In this analysis, a quadratic polynomial in a window of length equal to 41 is applied. Both approaches have been implemented in Matlab. Comparison between the results of FFT and Savitzky-Golay filter shows that the results are compatible. The advantage of Savitzky-Golay filter here is the lack of oscillations present in FFT results.

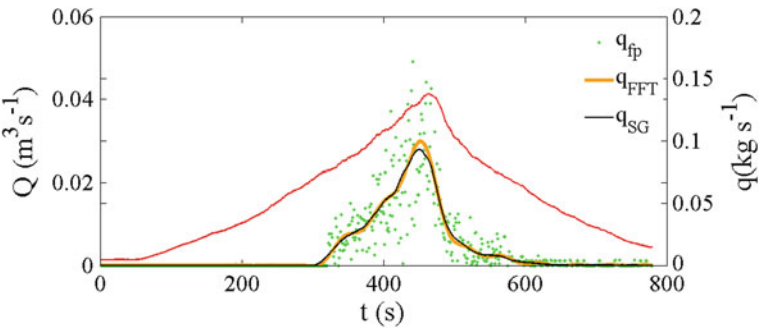

Fig. 4 Comparison between two methods of bed load rate evaluation for Hyd1_1

Water surface slope is a critical parameter that reflects non-uniformity of flow, and is used to compute friction slope (Ghimire and Deng 2013; Rowiński et al. 2000; Mrokowska et al. 2015). Water level measurements were taken in 5 cross-sections to evaluate water surface slope by five-point difference quotient:

$$S_w \approx \frac{-H(x+2\Delta x)+8H(x+\Delta x)-8H(x-\Delta x)+H(x-2\Delta x)}{12\Delta x}, \quad (1)$$

where Δx = spatial step (m), here 1 m. Measurements were designed so as to collect data necessary to apply formula on friction velocity:

$$u* = (gRS_w)^{0.5}, \quad (2)$$

where u_* is the friction velocity [ms^{-1}], R the hydraulic radius [m], and S_w the water surface slope [−].

3 Preliminary Results

3.1 *Sediment Transport with Variable Total Supply—Cumulative Transported Mass*

Cumulative transported mass in steady flow conditions reveals linear pattern, and in unsteady flow S-shape pattern (Fig. 5), as expected. In unsteady flow, total mass of supplied sediment (W_{sup}) is variable between experiments (Table 3), which results in different total mass of sediment collected during runs of the same hydrograph (W_t). For both hydrographs, the bigger mass of sediment is supplied the bigger mass is transported. However, this pattern applies until some particular threshold is achieved. For Hyd1 it is observed that hydrographs Hyd1_1 and Hyd1_3 transport

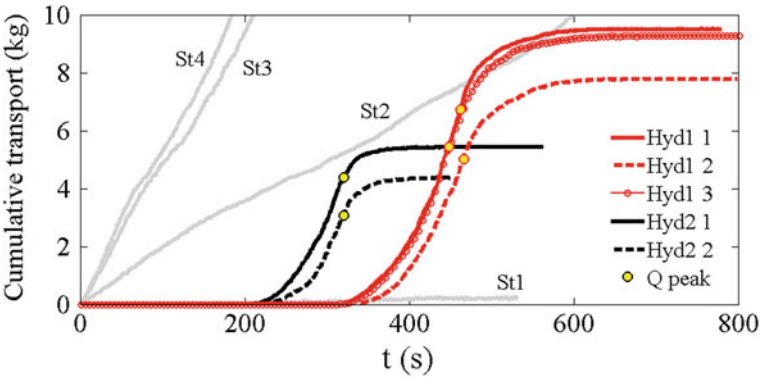

Fig. 5 Time variation of cumulative mass in steady and unsteady flow experiments

Table 3 Data on sediment supply and total mass of sediment transported by hydrographs

Parameter	Hyd1_1	Hyd1_2	Hyd1_3	Hyd2_1	Hyd2_2
W_{sup} (kg)	13.46	11.59	18.19	10.60	8.33
W_t (kg)	9.505	7.787	9.280	5.444	4.383
WQ_{max} (kg)	6.719	5.020	5.451	4.390	3.070
WQ_{max}/W_t	0.707	0.644	0.587	0.807	0.701

almost the same mass of sediment (with difference of 0.23 kg) despite significant difference in W_{sup} (4.73 kg). From this result we infer that such value of W_{sup} exists that maximum W_t is achieved. For Hyd1 this value is around W_{sup} = 13.46 kg, for Hyd2 it cannot be assessed, as there is no evidence that threshold value of W_t is achieved.

Data of cumulative transport show that the majority (over 50 %) of total mass is transported until the flow peak is achieved. Hence, transport processes are more intensive along a rising limb of a hydrograph.

3.2 *Hysteresis and Time Lag—Impact of Flow Unsteadiness on Bed Load Rate*

The results of bed load rate q in steady flow are as follows: 0.0006 kg s^{-1} for St1; 0.0173 kg s^{-1} for St2; 0.049 kg s^{-1} for St3; and 0.0718 kg s^{-1} for St4. When they are plotted against flow rate Q, the linear character of $Q(q)$ relationship may be inferred, which is shown in Fig. 6 (dotted blue line represents fitted linear function).

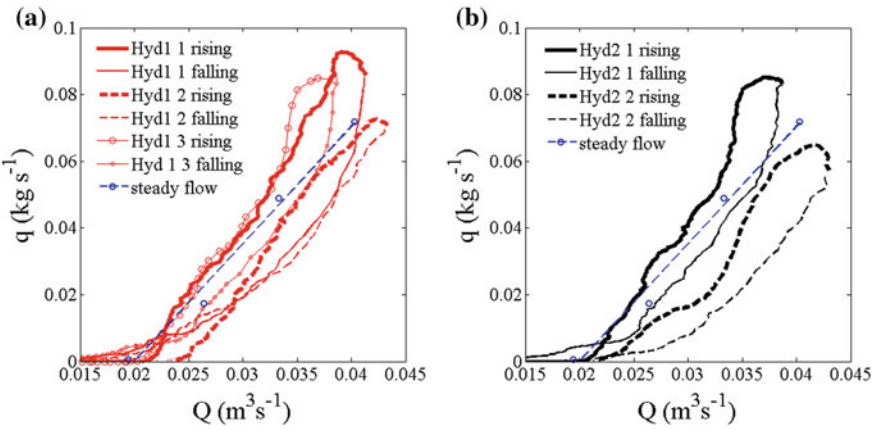

Fig. 6 Relationship between bed load rate q versus flow rate Q in steady and unsteady flow tests **a** Hyd1, **b** Hyd2

For unsteady flow, bed load rate is variable in time, and a clockwise hysteresis is observed, which reflects the fact that more intensive transport occurs during a rising limb. It is seen form Fig. 6 that the maximum bed load rate occurs in a rising limb of hydrographs. Time lag between the peak of flow rate and the peak of bed load rate is as follows: 12 s for Hyd1_1; 8 s for Hyd1_2; 6 s for Hyd1_3; 4 s for Hyd2_1; and 9 s for Hyd2_2 s.

Comparison between unsteady and steady flow experiments reveals that bed load rates during Hyd1_2 and Hyd 2_2 are below bed load rate for the same flow rate in steady flow. This may be explained by smaller amount of supplied sediment in these unsteady flow tests. On the other hand, for other three hydrographs: Hyd1_1, Hyd1_3 and Hyd2_1 with larger W_{sup}, transport is more intensive along a rising limb than for the same flow rate during steady flow.

Bed load rate depends on flow parameters which set sediment grains into motion. Figure 7 presents bed load rate for two hydrographs along with friction velocity and water surface slope data. As could be seen from the figure, maximum bed load rate, as well as maximum friction velocity occur before the maximum flow rate. It is indicative of dominant transport process along the rising limb of a hydrograph near the peak where shearing forces acting on bed are stronger.

In unsteady flow, the water surface slope S_w is a significant factor affecting friction force and friction velocity (Eq. 2), and variability of S_w is presented in the lower part of Fig. 7. Results of water surface slope show that it was difficult to obtain pattern expected during wave propagation. Results are compatible with theoretical pattern along rising limbs of the hydrographs, but they deviate along falling limbs (especially in Fig. 7b)—the peak after Q_{max} is unexpected. It is caused by difficulties with controlling water surface slope in the flume. Similar problems have been reported by Qu (2002).

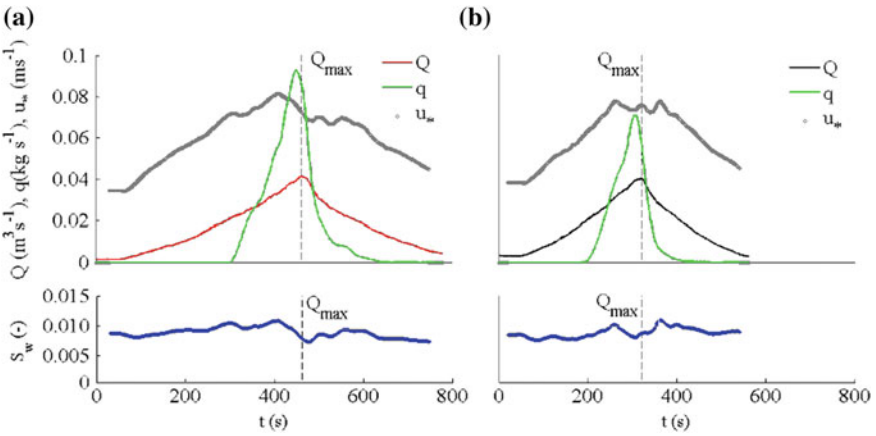

Fig. 7 Bed load rate and flow parameters Q, u^*, and S_w for **a** Hyd1_1 and **b** Hyd2_1

3.3 Changes in Grain Size Distribution and Bed Elevation

Changes in bed composition after the passage of hydrographs compared to the initial bed are analyzed. Characteristics of initial and final bed composition are presented in Fig. 8 and in Table 4. From Fig. 8 it could be seen that the percent finer for each grain size decreases after each experiment compared to initial bed conditions, except for Hyd1_3. When it comes to the mean grain size d_m, it increases after the passage of hydrographs Hyd1_1, Hys1_2, Hyd2_1, and Hyd2_2 (Table 4). These changes are probably due to washing out of sand fraction whose content at the end of these four experiments decreases about 1.5–3.7 %. On the other hand, for Hyd1_3 mean grain size d_m decreases. Reverse trend in the final composition of bed material for Hyd 1_3 may be related to the fact that during this experiment the highest mass of sediment was supplied (Table 3), and consequently the flow was not able to wash out so much fine sediment as in other experiments.

The average level of initial bed is assessed to analyze changes of bed elevation after the passage of a hydrograph. More experimental data sets not presented herein are used to evaluate the average level of initial bed, 12 experiments in total. Next, changes in bed elevation relative to this level are assessed. Bed elevation changes are analyzed in twelve centerline points and in five cross-sections L1, …, L5. Data

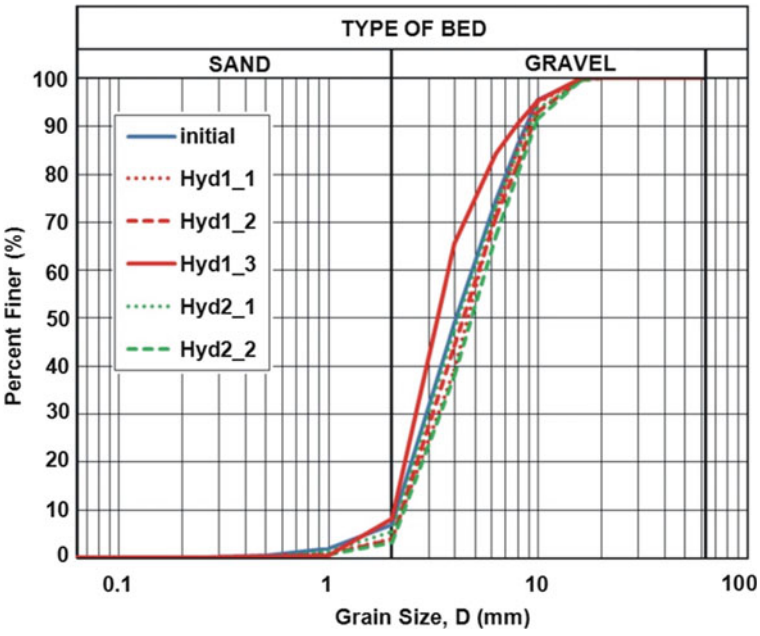

Fig. 8 Grain size distribution curves of initial sediment and final sediment for unsteady flow experiments

Table 4 Initial and final grain size composition of bed material for unsteady flow experiments

Parameter	Initial	Final				
		Hyd1_1	Hyd1_2	Hyd1_3	Hyd2_1	Hyd2_2
d_m (mm)	4.93	5.29	5.35	4.29	5.15	5.66
Sand fraction (%)	6.89	3.90	3.78	8.06	5.40	3.20
Gravel fraction (%)	93.08	96.07	96.21	91.90	94.58	96.78

Table 5 Changes of bed elevation after passage of unsteady hydrograph

Parameter	Hyd1_1	Hyd1_2	Hyd1_3	Hyd2_1	Hyd2_2
In centerline points					
Average bed change (mm) ± 0.5 mm					
	−2.6	−1.3	−2.7	−1.5	−0.1
No. of eroded/accumulated/stable points					
	9/2/1	9/2/1	10/1/1	7/2/3	5/5/2
In cross-sections L1, …, L5					
Average bed change (mm) ± 0.5 mm					
	−2.5	−2.3	−3.1	−3.0	−2.2
No. of eroded/accumulated/stable cross-sections					
	4/0/1	5/0/0	4/0/1	5/0/0	3/0/2

notation: (+) accumulation, (–) erosion

from each cross-Sect. (22 points) are averaged. Results presented in Table 5 show that erosion is prevalent in each experiment.

Please note that location of accumulation and erosion areas was variable in space and time during the experiments. The average bed level change in the centerline points and cross-sections is of similar magnitude (Table 5), up to −2.7 and −3.1 mm, respectively. Erosion is not higher than d_m in average, and may be considered as irrelevant. Minimum average bed elevation change in both the centerline points and cross-sections are obtained for hydrographs Hyd1_2 and Hyd2_2. It is noteworthy that for these hydrographs bed load rates are below bed load rate for the same flow rate in steady flow (Fig. 6).

4 Recapitulation

In this chapter, we have presented preliminary results of experiments on bed load transport in unsteady flow in comparison with steady flow conditions. For the settings applied in the experiments, the bed load rate is variable during an unsteady hydrograph, and the maximum bed load transport occurs in a rising limb, as expected for unarmored bed conditions (Guney et al. 2013; Qu 2002).

Curtail aspect of the experiments is sediment supply. During the experiments, sediment was added manually to prevent excessive bed erosion. The analysis of changes of bed elevation has shown that after the passage of a hydrograph, bed was eroded in a majority of measurement points; however, the erosion is of insignificant magnitude. The amount of supplied sediment varied between the experiments. Although the difference in supply seems to be irrelevant compared to the dimensions of the flume, it affects the amount of transported sediment, as well as bed load rate. It has been observed that a threshold value of the supply exists which results in the maximum total sediment mass transported during a hydrograph. The analyses have revealed that the relation between bed load rate in unsteady flow and bed load rate in steady flow equilibrium conditions depends to large extent on sediment supply. These observations may be a starting point for further systematic research.

In nature, wide spectrum of sediment availability occurs. In experiments aiming to find general laws it seems sound to study in a first row limiting conditions, such as no feed (Bombar et al. 2011; Guney et al. 2013) or pulsed supply (Humphires et al. 2012). We propose another case which is more complex to execute: maximum sediment feed without excessive deposition, which is initiated in this study. To design such experiment, several tests have to be performed to assess the threshold value of supplied sediment and the rate of sediment feed. Such experiment may provide unique data to find relations between bed load transport in unsteady and steady flow, and to account for flow capacity to transport sediment when it is not limited. Such relations have been so far designed for no feed conditions (Bombar et al. 2011).

There are two problematic aspects of presented experiments which should be carefully considered in similar studies. The first one is high sensitivity of bed load transport on sediment supply. This makes it impossible to provide a comparison of sediment transport dynamics between two studied hydrographs: Hyd1 and Hyd2, and consequently to analyze the impact of unsteadiness on sediment transport. Such analysis requires comparable sediment supply conditions, which is not attained in this study.

Another problematic aspect stems from difficulties to control the pattern of water surface slope during the passage of a hydrograph in laboratory, which was also pointed in Qu (2002). In the majority of experiments presented herein, the water surface slope is against its expected pattern along the falling limb of a hydrograph. We recommend to pay special attention to control water surface slope in future studies. It is crucial for attaining repeatability of tests and reliable evaluation of resistance parameters such as friction velocity.

Conclusions reached herein will be taken into consideration while designing further experimental tests that will provide systematic data to study bed load transport in unsteady flow.

Acknowledgments This study has been financed by National Science Centre. Grant No. DEC-2011/01/N/ST10/07395.

The authors would like to thank Wojciech Bartnik and Alicja Michalik for organizing hydraulic flume and lab in the Faculty of Environmental Engineering and Land Surveying, Agricultural University of Krakow. Also we are thankful Jacek Florek, Fryderyk Skalicz, Agnieszka Woś and Wiktoria Czech for their help during the experiment.

References

Bombar G, Elçi S, Tayfur G, Güne M, Bor A (2011) Experimental and numerical investigation of bed-load transport under unsteady flows. J Hydraul Eng 137(10):1276–1282

Ghimire B, Deng Z (2013) Event flow hydrograph-based method for modeling sediment transport. J Hydrol Eng 18(8):919–928

Guney M, Bombar G, Aksoy A (2013) Experimental study of the coarse surface development effect on the bimodal bed-load transport under unsteady flow conditions. J Hydraul Eng 139 (1):12–21

Humphries R, Venditti JG, Sklar LS, Wooster JK (2012) Experimental evidence for the effect of hydrographs on sediment pulse dynamics in gravel-bedded rivers. Water Resour Res 48: W01533

Książek L (2000) Morphological changes of the river bed and its relationship with drag force for individual grains, Doctoral Thesis, Agriculture University in Krakow, Manuscript (in Polish)

Lee KT, Liu YL, Cheng KH (2004) Experimental investigation of bedload transport processes under unsteady flow conditions. Hydrol Process 18(13):2439–2454

Mao L (2012) The effect on bed load transport and bed sediment spatial arrangement. J Geophys Res 117:FO3024

Mrokowska MM, Rowiński PM, Kalinowska MB (2015) A methodological approach of estimating resistance to flow under unsteady flow conditions. Hydrol Earth Syst Sci 19: 4041–4053

Parker G, Toro-Escobar CM, Ramey M, Beck S (2003) Effect of floodwater extraction on mountain stream morphology. J Hydraul Eng 129(11):885–895

Press WH, Flannery B, Teukolsky SA, Vetterling W (2007) Savitzky-golay smoothing filters. In: Numerical recipes in C. the art of scientific computing. Cambridge University Press, pp 650–655

Qu Z (2002) Unsteady open-channel flow over a mobile bed. Ph.D. thesis, No. 2688, École Polytechnique Fédérale de Lausanne, Lausanne, Switzerland

Rowiński PM, Czernuszenko W, Pretre JM (2000) Time dependent shear velocities in channel routing. Hydrol Sci J 45(6):881–895

Savitzky A, Golay M (1964) Smoothing and differentiation of data by simplified least squares procedures. Anal Chem 36(8):1627–1639

Shen Y, Diplas P (2010) Modeling unsteady flow characteristics for hydropeaking operations and their implications on fish habitat. J Hydraul Eng 136(12):1053–1066

Tabarestani MK, Zarrati AR (2015) Sediment transport during flood event: a review. Int J Environ Sci Technol 12(2):775–788

Wang L, Cuthbertson A, Pender G, Cao Z (2014) The response of bed-load sediment transport and bed evolution under unsteady hydrograph flows river flow 2014. In: Schleiss et al (eds) Taylor & Francis Group, London, pp 1619–1627. ISBN 978-1-138-02674-2

Experimental Investigation of Hydraulically Different Surface Roughnesses

Paride Nardone and Katinka Koll

Abstract Surface roughnesses present hydraulic differences that can be characterised investigating time averaged velocity profiles, turbulence, Reynolds and form induced stresses. The latter, unlike the other flow characteristics, have not been considered in detail in previous studies. An experimental study of the turbulent flow over five different surface roughnesses is presented. They have been constructed with natural and artificial materials, and with different geometries. The experiments were carried out in a laboratory flume and the 3D flow field has been measured with a Nortek Vectrino Profiler. The double averaged Navier-Stokes equations methodology has been applied to study the spatial heterogeneity of the time averaged flow. The results confirm the studies made in previous works with different surface roughnesses and the form induced stresses reveal the hydraulic differences and similarities for the different investigated roughnesses.

1 Introduction

The influence of rough surfaces on the flow has been the topic of many research activities since the last century and nowadays it is the base for many applications, e.g., the study of biophysical critical interfaces in the management of natural and constructed water systems (Marion et al. 2014). Different kinds of surface roughnesses made of artificial and natural material were used to study the influence of the rough elements characteristics on the turbulent flow field.

The velocity distribution and the resistance law over rough walls at different Reynolds numbers were systematically investigated by Nikuradse (1933), who used

P. Nardone (✉) · K. Koll
Leichtweiß-Institut Für Wasserbau, TU Braunschweig,
Braunschweig, Germany
e-mail: p.nardone@tu-bs.de

K. Koll
e-mail: katinka.koll@tu-bs.de

P. Rowiński and A. Marion (eds.), *Hydrodynamic and Mass Transport at Freshwater Aquatic Interfaces*, GeoPlanet: Earth and Planetary Sciences,
DOI 10.1007/978-3-319-27750-9_19

roughnesses made of sand with different grain sizes glued as densely as possible on pipes of various diameters. Other kinds of surface roughness made of artificial and natural material, with different sizes, shapes and spacing, were used by Schlichting (1936) with the aim to specify a characteristic number to predict the resistance for the same type of roughness at varying Reynolds number and relative roughness ratios k/R, where k is the geometrical roughness height, and R is the hydraulic radius. One of the main findings was that the maximum flow resistance does not occur at the greatest density of the roughness elements. This was confirmed in following works made by, e.g., Morris (1955), Raupach et al. (1980), Jiménez (2004). Another important result from Schlichting (1936) was the influence of the roughness shape; the absolute roughness was less for the regular roughness (spheres and spherical segments) than for the irregular sand grains.

Based on the spacing of the roughness elements, Morris (1955) defined three kinds of flow: quasi-smooth (dense elements), isolated obstacles (wide spacing), and wake-interference (intermediate condition). In the case of isolated and quasi smooth obstacles, Perry et al. (1969) defined two types of roughness: k-type, where the effective roughness is proportional to the height of the roughness elements, and d-type, where the turbulence of the flow field is determined by the water depth and independent of the roughness height (see also Raupach et al. 1991).

The double averaged Navier-Stokes equations are a suitable methodology to investigate flows over rough beds. This methodology was introduced by atmospheric scientists (Wilson and Shaw 1977; Raupach and Shaw 1982; Finnigan 1985). The theoretical background and applications to open channel flows are presented in Nikora et al. (2001, 2007a, b). In the averaging procedure, time averaged variables are decomposed into spatially averaged and spatial fluctuation parts according to $\bar{\theta}_i = \langle \bar{\theta}_i \rangle + \tilde{\theta}_i$, where the angle brackets denote spatial averaging, the overbar denotes temporal averaging, and the tilde denotes spatial fluctuation. For two-dimensional, steady, uniform flow conditions over a fixed rough bed and a flat water surface, the longitudinal component of the double averaged momentum equation can be written as (Nikora et al. 2007a),

$$\rho g S_b + \frac{1}{\phi}\frac{\partial \phi \tau}{\partial z} - f_p - f_v = 0, \tag{1}$$

where ρ = the fluid density, g = gravity acceleration, S_b = bed slope, ϕ = roughness geometry function, τ = total fluid stress, z = vertical coordinate, and f_b and f_v form and viscous drag per unit fluid volume, respectively. The total shear stress τ is defined as

$$\tau = \rho\left[-\langle \overline{u'w'} \rangle - \langle \tilde{u}\tilde{w} \rangle + \frac{\nu}{\phi}\frac{d\phi\langle \bar{u} \rangle}{dz}\right], \tag{2}$$

where $\langle \bar{u} \rangle$ = double averaged longitudinal velocity component, u' and w' = longitudinal and vertical temporal fluctuation velocity components, $\tilde{u}$ and

$\tilde{w}$ = longitudinal and vertical spatial fluctuation velocity components, and ν = kinematic viscosity.

In the flow region closer to and below the roughness crests, the form induced stresses $\langle \tilde{u}\tilde{w} \rangle$ can contribute significantly to the total fluid stress and may be used to characterize hydraulic differences of roughnesses (e.g., Nikora et al. 2007b; Aberle et al. 2008; Pokrajac et al. 2008).

The aim of this paper is to apply the DAM to different surface roughnesses, made of artificial and natural material, focusing on the form induced stresses as a tool to distinguish different types of roughness. For this purpose, data from laboratory experiments are used to analyse the vertical distribution of the double averaged horizontal velocity component, Reynolds and form induced stresses.

2 Experimental Apparatus and Methodology

The experiments were carried out in a 6 m long, 0.30 m wide, and 0.30 m deep laboratory flume, and with a fixed slope of 0.001 (Fig. 1). A water depth of 0.10 m was kept constant and the discharge was adapted for the different surface roughnesses in order to have steady uniform flow conditions (Table 1). A Vectrino Profiler was installed on an automatic traverse system and used for flow velocity point measurements (Fig. 1).

Five surface roughnesses were used which are shown in Fig. 2: fine gravel glued on a plastic board, a rubber carpet with pyramidal elements, a plastic sheet with smooth edged cones, and two rough surfaces made of sharp edged plastic bars glued on a wooden board with different spacing of the bars. The spacing between the bars was designed considering previous experiments reported in literature that studied densely and widely distributed bars roughnesses (Perry et al. 1969; Bandyopadhyay 1986; Jiménez 2004; Leonardi et al. 2007; Pokrajac et al. 2008; Jin

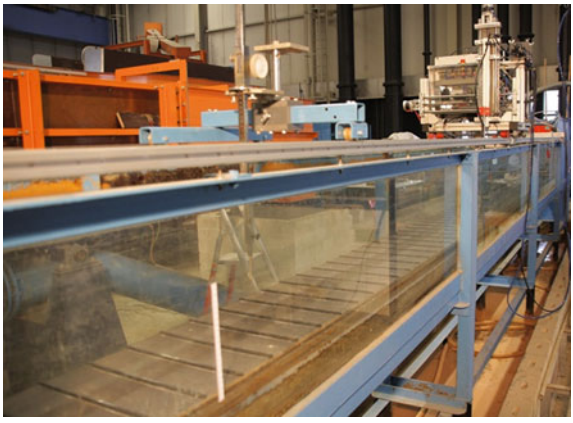

Fig. 1 Laboratory flume

Table 1 Discharge and mean flow velocity for the performed experiments

Surface roughness	Gravel bed	Pyramid	Cones	Dense bars	Wide bars
Discharge Q (l/s)	10.0	12.7	10.5	11.5	8.5
Bulk velocity u_m (m/s)	0.33	0.42	0.35	0.38	0.28

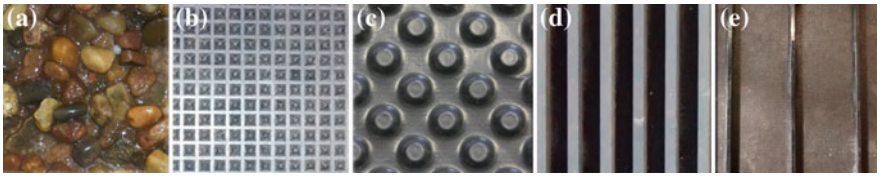

Fig. 2 Surface roughnesses: **a** gravel bed; **b** pyramid; **c** cones; **d** dense bars; and **e** wide bars

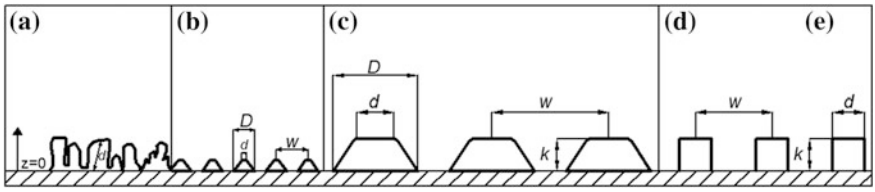

Fig. 3 Geometrical characteristics of the surface roughnesses: **a** gravel bed; **b** pyramid; **c** cones; **d** dense bars; **e** wide bars

Table 2 Geometrical characteristics of the surface roughnesses

Surface roughness	k (mm)	d (mm)	D (mm)	w (mm)
Gravel bed		3–6	–	–
Pyramid	2	1	4	6
Cones	6	8	16	25
Dense bars	6	6	–	18
Wide bars	6	6	–	90

and Herwig 2013). The geometrical height, k, the diameter, d, and the spacing, w, are shown in Fig. 3 and reported in Table 2.

Nine velocity profiles were measured in each run. In the case of wide bars, due to the wide space between the roughness elements, the number of profiles was increased to fifteen. The measuring section started 2.5 m downstream of the inlet to ensure fully developed uniform flow.

Longitudinal, Δx, and lateral, Δy, spacing between the velocity profiles was set to 2 cm (see Fig. 4). The point measurements were spaced 2 mm along the vertical coordinate z and, based on preliminary experiments, recorded at a sampling frequency of 100 Hz for a sampling period of 1 min.

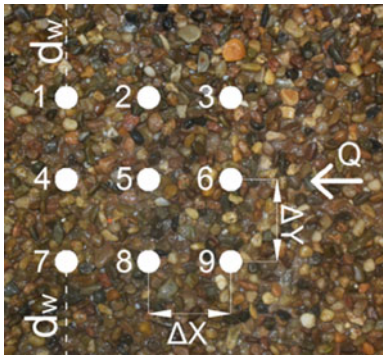

Fig. 4 Measuring points, Dx = 2 cm, Dy = 2 cm, d_w (distance to the walls) = 13 cm

The measurements started at z = 2 mm in case of the pyramids and at z = 4 mm in the other cases, due to signal interferences. The sampling volume size was set to 1 mm up to a distance of 8 mm above the roughness top, and to 3 mm up to 6 cm below the water surface, in order to ensure a correlation factor larger than 80 % and a signal to noise ratio larger than 20 dB.

The data were filtered with a MATLAB script based on a despiking method, with spikes replacement, as reported in Goring and Nikora (2002).

Double averaged velocity profiles, turbulence intensities, Reynolds and form induced stresses were analysed.

3 Results

In Fig. 5 the double averaged velocity profiles are plotted. According to the discharge which had to be adjusted to reach the constant water depth (Table 1), the wide bars represented the largest roughness resulting in the lowest velocity followed by the cones and the dense bars. The spacing of the bars was chosen to represent flow over a quasi-smooth bed (dense bars) and isolated objects (wide bars). Thus, the cones presented the intermediate case of wake-interference flow. The velocity over the pyramids was highest due to the smaller height of the elements.

It could have been expected that the velocity over the gravel bed is comparable to the velocity of the cones, because the adjusted discharge was quite similar. However, Fig. 5a shows that the velocity profile of the gravel bed was close to the dense bars. When scaled with the bulk velocity, as shown in Fig. 5b, the velocity profile of the gravel bed even fits to the pyramids.

Reynolds stresses are plotted in Fig. 6. The profiles of the variance (Fig. 6a) linearly increased towards the bed and were grouped together until a distance of 1.0 cm above the bed. At this height the variance of the gravel bed separated from the others showing a distinct maximum just above the roughness tops. The main difference between the gravel bed and the other roughnesses is the irregularity of the

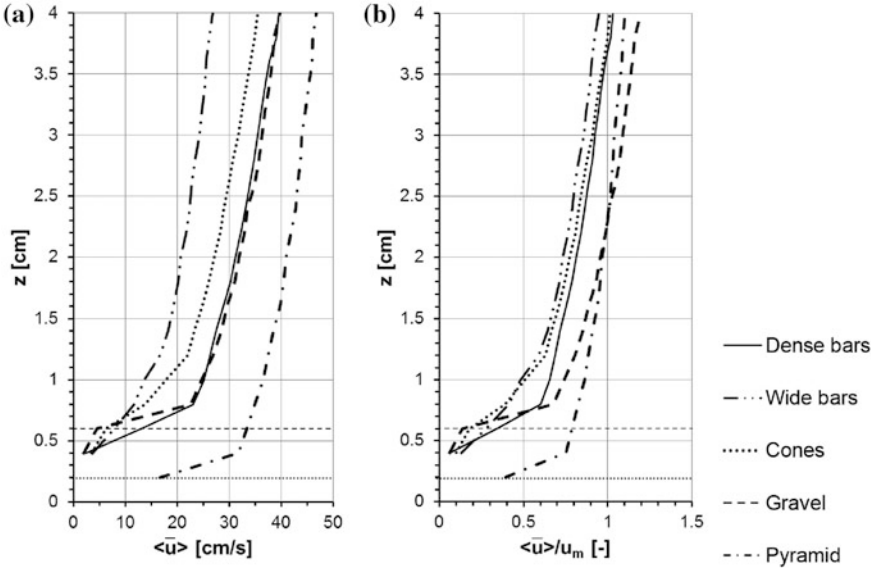

Fig. 5 Vertical profiles of the double averaged horizontal velocity component. The *horizontal round dot* and *dashed lines* represent the top of the pyramid and the top of the other roughnesses, respectively (Note that the water level is at $z = 10$ cm)

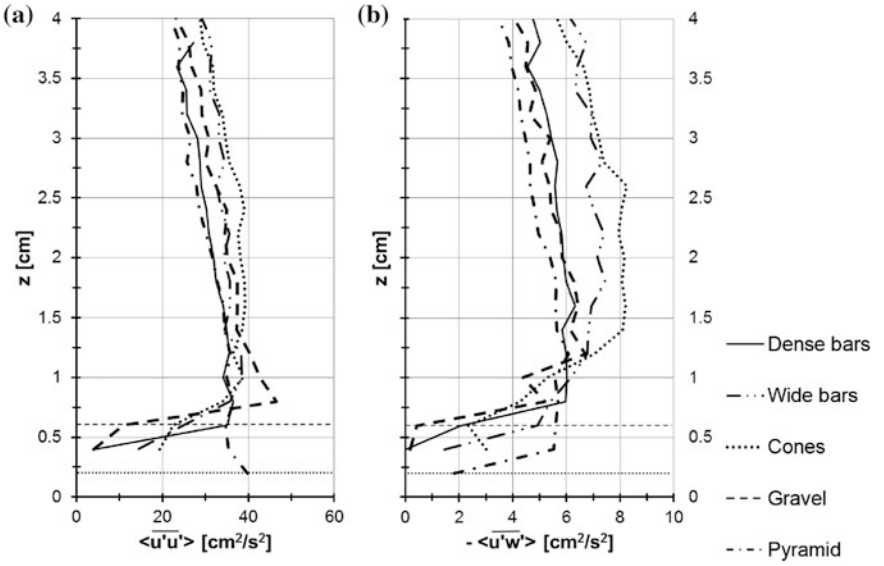

Fig. 6 Reynolds stresses: **a** variance, **b** covariance

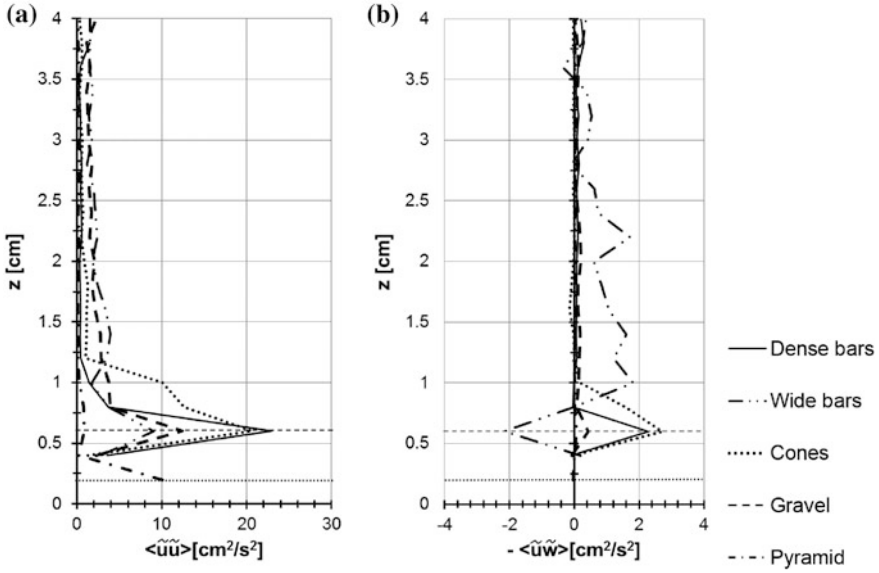

Fig. 7 Form induced stresses: **a** variance, **b** covariance

height of the elements. The grain diameter varied between 3 and 6 mm whereas the artificial elements had constant heights of 6 and 2 mm, respectively.

The shape of the vertical profiles of the covariance (Fig. 6b) changed between $z = 1.2$ cm and $z = 0.8$ cm, except for the cones. Above that, height two groups can be distinguished. The Reynolds stresses of the gravel bed, dense bars, and pyramid roughness revealed the influence of secondary currents caused by the walls of the flume which were negligible in case of the cones and wide bars. This effect is attributed to the lower hydraulic roughness of the first three roughnesses which have a higher density of elements, with the spacing, *w,* three times the geometrical roughness height, *k,* for pyramid and dense bars, and less for the gravel bed. In the case of cones and wide bars *w* is equal to 4 and 15 k, respectively.

In Fig. 7 the form induced stresses are compared. Figure 7a shows the spatial heterogeneity of the longitudinal velocity component. As expected, the form induced stresses were small at larger distances to the roughness tops. The profiles deviated from the constant trend at about two times the roughness height *k* and reached their maximum values on the roughness crests at $z/k = 1$.

Also the profiles of the form induced covariance (Fig. 7b) presented the maximum value on the roughness tops and the deviation from the constant profile just above it. As for the variance, the maximum values occurred for the cones and the dense bars. The gravel bed had much lower form induced stresses related to the spacing of the roughness elements.

The main difference can be observed in the case of wide bars. The form induced stresses were not zero far from the roughness crests and the maximum values were

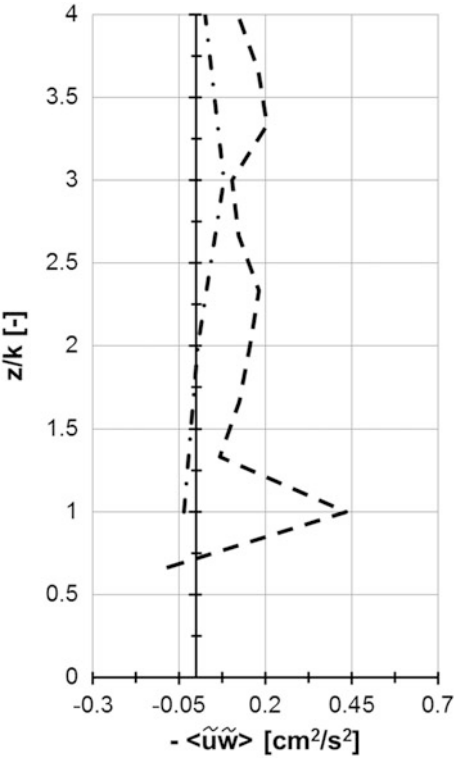

Fig. 8 Form induced stresses of pyramid (*dash-dot*) and gravel (*dash*) roughnesses

negative, showing a form induced momentum transfer in the upward direction above the bars and in the downward direction within the gaps.

As reported in Pokrajac et al. (2008), this is a consequence of the wide space between the bars that leaves space for the re-attached flow to align with the bed.

Furthermore, applying the quadrant analysis, Pokrajac et al. (2007) show that the negative form induced stress result from a very strong section of momentum transferred upwards located above the bars.

The form induced stresses for gravel and pyramid roughnesses were very small and therefore are plotted again in Fig. 8. The form induced stresses of the flow above the gravel bed increased towards the bed and peaked at the roughness crests. For the pyramids the form induced stresses are negligible even at the roughness tops.

4 Summary and Conclusions

Five surface roughnesses with differences in geometry and material were analysed. The difference in the double averaged velocity profiles was mainly related to the different roughness geometrical heights, with the maximum velocity in the case of pyramid roughness. Wide and dense bars had similar profiles, with different velocity magnitudes related to the elements density. Wide bars exerted a higher resistance on the flow than the dense bars, that behaved like a quasi-smooth flow.

In the case of variance components of Reynolds stresses, the values decreased close to the bed and were mainly grouped. In the covariance case the cones and wide bars grouped together, with higher values compared to the other three roughnesses. At greater distances from the bed the Reynolds stresses were larger for the wide bars than for the dense bars. This was mainly related to the eddies that in the first case were shed into the flow increasing the turbulence effect. Similarities are shown in the profiles for pyramid and gravel roughnesses, despite the different materials, but with a comparable elements' distribution.

The form induced stresses were close to zero far from the roughness top and reached the maximum values on the crests. Cones and dense bars presented almost the same maximum value. This can be related to the differences in the elements spacing and shape. The main difference between wide and dense bars is shown in the covariance term, where the wide bars have a negative form induced stress. This is related to the wide spacing between the bars and to the strong upward momentum (Pokrajac et al. 2008), denoting an isolated obstacle behaviour.

The cones profile was similar to the one for dense bars, but the form induced stresses started to increase at a larger distance from the roughness crests compared to the wide bars. This can be related to different distribution of the roughness elements, with a high three-dimensionality for the cones.

Gravels and pyramid roughnesses presented differences in the magnitude of the values but similar trends, despite the different roughness materials.

The results show how the double averaged methodology and in particular the form induced stresses can be used to characterize different surface roughnesses. The impact on the flow related to the different material and geometries has been shown. Further experiments are required to investigate the flow close to the surface roughness and experiments with different roughnesses and the same approaching velocity have to be performed.

Acknowledgments This work was supported by the Research Executive Agency, through the 7th Framework Programme of the European Union, Support for Training and Career Development of Researchers (Marie Curie-FP7-PEOPLE-2012-ITN), which funded the Initial Training Network (ITN) HYTECH 'Hydrodynamic Transport in Ecologically Critical Heterogeneous Interfaces', No. 316546.

References

Aberle J, Koll K, Dittrich A (2008) Form induced stresses over rough gravel-beds. Acta Geophys 56(3):584–600

Bandyopadhyay PR (1986) Drag reducing outer-layer devices in rough wall turbulent boundary layers. Exp Fluids 4:247–256

Finnigan JJ (1985) Turbulent transport in flexible plant canopies. In: Hutchinson BA, Hicks BB (eds) The forest-atmosphere interaction. D. Reidel Publishing Co, Dordrecht, pp 443–480

Goring DG, Nikora V (2002) Despiking acoustic doppler velocimiter data. J Hydraul Eng 128 (1):117–126

Jiménez J (2004) Turbulent flows over rough walls. Annu Rev Fluid Mech 36:173–196

Jin Y, Herwig H (2013) From single obstacle to wall roughness: some fundamental investigations based on DNS results for turbulent channel flow. Z Angew Math Phys 64:1337–1351

Leonardi S, Orlandi P, Antonia RA (2007) Properties of d- and k-type roughness in a turbulent channel flow. Phys Fluids 19:125101-1–125101-6

Marion A, Nikora V, Puijalon S, Bouma T, Koll K, Ballio F, Tait S, Zaramella M, Sukhodolov A, O'Hare M, Wharton G, Aberle J, Tregnaghi M, Davies P, Nepf H, Parker G, Statzner B (2014) Aquatic interfaces: a hydrodynamic and ecological perspective. J Hydraul Res 52(6):744–758

Morris HM (1955) Flow in rough conduits. Am Soc Civ Eng Trans 2745:373–410

Nikora V, Goring D, McEwan I, Griffiths G (2001) Spatially averaged open channel flow over rough bed. J Hydraul Eng 127(2):123–133

Nikora V, McEwan I, McLean S, Coleman S, Pokrajac D, Walters R (2007a) Double averaging concept for rough-bed open-channel and overland flows: theoretical background. J Hydraul Eng 133(8):873–883

Nikora V, McLean S, Coleman S, Pokrajac D, McEwan I, Campbell L, Aberle J, Clunie D, Koll K (2007b) Double averaging concept for rough-bed open-channel and overland flows: applications. J Hydraul Eng 133(8):884–895

Nikuradse J (1933) Laws of flow in rough pipes. NACA Tech Memo 1292:1950

Perry AE, Schofield WH, Joubert PN (1969) Rough wall turbulent boundary layers. J Fluid Mech 37(2):383–413

Pokrajac D, Campbell LJ, Nikora V, Manes C, McEwan I (2007) Spatially-averaged flow over artificial roughness: a new application of quadrant analysis. Exp Fluids 42:413–423

Pokrajac D, McEwan I, Nikora V (2008) Spatially averaged turbulent stress and its partitioning. Exp Fluids 45(1):73–83

Raupach MR, Shaw RH (1982) Averaging procedures for flow within vegetation canopies. Bound Layer Meteor 22:79–90

Raupach MR, Thom AS, Edwards I (1980) A wind tunnel study of turbulent flow close to regularly arrayed rough surfaces. Bound Layer Meteor 18:373–397

Raupach MR, Antonia RA, Rajagopalan S (1991) Rough-wall turbulent boundary layers. Appl Mech Rev 44(1):1–25

Schlichting H (1936) Experimental investigation of the problem of surface roughness. NACA Tech Memo 823:1–34

Wilson NR, Shaw RH (1977) A higher order closure model for canopy flow. J Appl Meteorol 16:1197–1205

Sensitivity of the Flow to the Inclination of a Single Submerged Groyne in a Curved Flume

Bahaeldeen A. Zaid and Katinka Koll

Abstract In order to investigate the effect on the flow field due to small changes in the inclination of a single submerged groyne, laboratory tests have been conducted. A double curved S-flume with a length of 26 m, width of 2.4 m and depth of 0.4 m was used. The investigations were done at a reference inclination of 60° for a single submerged groyne. The inclination was then varied by ±5° and ±10°. The groyne width and height as well as the hydraulic conditions (discharge of 130.6 l/s and water depth of 10 cm) were kept constant to ensure that the effect is only due to the change in the inclination. The groyne was installed in the first cross-section of the first curve. The 3D flow field was measured using a Nortek Vectrino Plus in nine cross-sections with seven vertical profiles each. The total flow measurement points were 325 in each run. The results of the experiments have shown no significant changes in the flow field due to the change of inclination up to ±10° given that the projected length and the hydraulic boundary conditions were kept constant. However, localized effects at cross-section no 1 are evident and the inclination of 60° showed the lowest stream-wise velocity. Comparison of the flow field with and without groyne revealed decreasing velocities at the outer bank and increasing velocities at the inner bank supporting the purpose of the structure which is bank protection.

1 Introduction

The responsibility of hydraulic engineers in ecologically-appropriate management of rivers is generally acknowledged nowadays. However, the anthropogenic environment has to be protected against flooding and uncontrolled erosion of a river course as well. The latter task often resulted in heavily modified rivers with banks even fixed with brick or concrete walls. These banks as a habitat as well as the

B.A. Zaid (✉) · K. Koll
Leichtweiß-Institut für Wasserbau, TU Braunschweig, Braunschweig, Germany
e-mail: b.zaid@tu-braunschweig.de

P. Rowiński and A. Marion (eds.), *Hydrodynamic and Mass Transport at Freshwater Aquatic Interfaces*, GeoPlanet: Earth and Planetary Sciences,
DOI 10.1007/978-3-319-27750-9_20

transition areas between water and land are lost. Thus, the re-opening of heavily protected banks and replacing the walls by locally limited protection measures is a highly promising approach in nature-oriented hydraulic engineering.

During the last decades, several variations of in-stream structures such as groynes, barbs, vanes and bendway weirs were developed and studied regarding their potential to protect river banks. The structures are typically anchored to the river bank, and project into the stream. Due to their inclination, the flow is directed into the center of the channel. This reduces the flow velocities at the outer bank. Moreover, the structures provide habitat improvement as they create flow heterogeneities and pool habitats, shelter, and thereby increase biodiversity (Shields et al. 1995). The advantage of the flow redirection structures over the traditional revetments regarding the habitat improvements has made them increasingly popular (Scurlock et al. 2014).

The sustainable design of ecologically-appropriate measures, however, requires a fundamental understanding of the interactions between water, sediment, and biota (Marion et al. 2014). This paper cannot fulfill this challenging task, but aims on the hydraulic design.

The design of in-stream structures is, yet, based on primary experimental studies, experience, and engineering judgment (Copeland 1983) or on the analog method (Radspinner et al. 2010), which infers transferring experience from one river to another, comparable river. Information on the effect of specific geometric parameters of the structure on the flow field are limited (Scurlock et al. 2014).

The geometric parameters affecting the design of the structures are: width, length, height, inclination, crest inclination and the projected length (perpendicular distance from the structure tip to the outer bank).

Several laboratory studies were conducted on a group of these structural parameters. Matsuura and Townsend (2004) studied different inclinations of a group of stream barbs as well as the number of barbs within a group to evaluate the effectiveness for providing bank protection in a curved channel. Also, Hemmati et al. (2012) investigated the effect of the angle of inclination of bendway weirs, combined with varying lengths of the weirs on the scour and deposition in a bend. Among other geometric parameters Bhuiyan et al. (2010) examined the inclination of vanes. Jamieson et al. (2013) studied the inclination of a barb system on the flow field, on scour and on deposition. Considering the aforementioned studies, different structures were employed (barbs, bendway weirs and vanes), and a group of parameters was studied (angle, length, projected length and number of structures).

The study presented in the following focuses on the evaluation of the sensitivity of the flow field to the inclination of a submerged groyne. This kind of in-stream structure differs from the previously investigated structures as (a) it is submerged throughout its length, i.e. the crest inclination is zero, and (b) constitutes a very shallow structure which is submerged even at low flow conditions. To eliminate the effects induced by the change of other parameters, a single submerged groyne was employed. The projected length was kept constant, whilst the inclination was varied. The experiments form part of a larger research project on submerged groynes, which aims to understand the hydraulic effect of each single geometric

parameter, before moving on to combinations of different parameters. These studies constitute a fundamental component of a design guide line for submerged groynes currently under development.

2 Laboratory Experiments

The laboratory experiments were carried out in the hydraulic laboratory of the Leichtweiß-Institute. A large double curved flume was designed for the experiments. The S-flume has a length of 26 m, a width of 2.4 m and a depth of 0.4 m (see Figs. 1 and 2b). The flume is made of concrete and has a rectangular cross-section. The longitudinal slope is fixed to 0.001 and the lateral slope is zero. A flap gate at the outlet allows adjusting the water level. The flume is equipped with an automatic traverse.

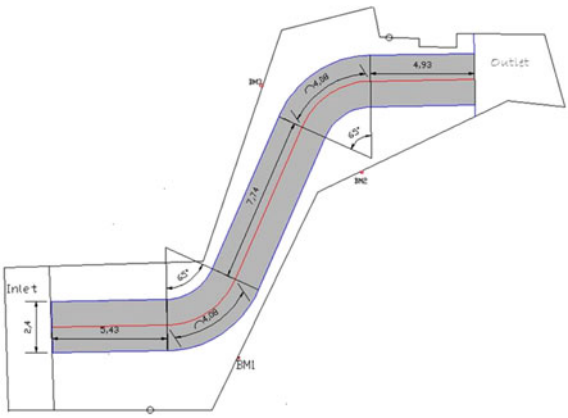

Fig. 1 S-Flume layout

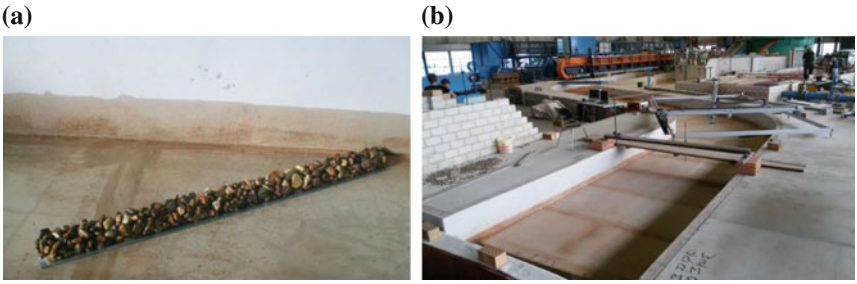

Fig. 2 Photos of **a** the groyne and **b** the S-flume

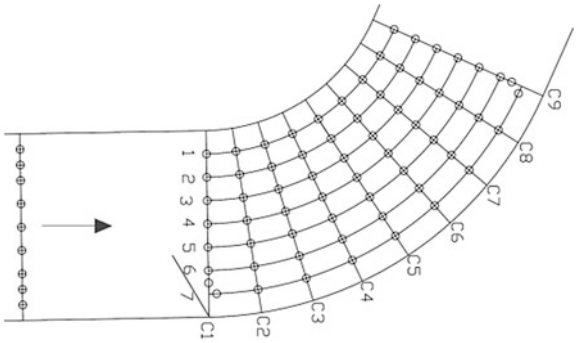

Fig. 3 Measuring grid

The groyne was constructed from glued gravel of size 12–16 mm to consider the irregular surface of natural groynes (Fig. 2a). The height of the groyne was 2.5 cm and the width was 6 cm. The projected length of the groyne was kept constant to one third of the total width of the flume, i.e. 80 cm. For all runs the groyne was installed at the first cross-section of the first curve and attached to the outer bank (see Fig. 3).

Measurements of the three dimensional flow field were done in the first curve of the flume. The measurement grid is plotted in Fig. 3. It consisted of nine cross-sections with cross-section C1 at the beginning of the curve and C9 at its end 4.08 m downstream. Each cross-section contained seven verticals. The distance between the verticals as well as the distance between the outer verticals and the walls was 0.3 m. In each vertical there were five measurement points at 1, 2, 3, 4 and 5 cm above the bottom. In cross-sections C1 and C9 the verticals next to the right bank (L7) had to be shifted because of the frame of the traverse. The replacing verticals are shifted by 10 cm in longitudinal and transversal direction, respectively. In total the velocity was measured in 325 points.

The flow boundary conditions were kept constant throughout the experiments. The discharge was 130.6 l/s resulting in a water depth of 10 cm (adjusted without the groyne). Point gauges were used to measure the water depth. The inlet of the flume was designed to ensure a straight flow field upstream of the first curve. The approaching flow was checked in a cross-section 2.4 m upstream of C1 using a micro propeller.

The 3D flow field was measured with a Vectrino Plus from NORTEK. The sampling rate was set to 100 Hz and the sampling duration was, in general, 60 s. The sampling duration was extended to 90 s if the average correlation was below 70 %. The Vectrino data was processed using WinAdv software. To ensure high quality data, the data was filtered with minimum correlation of 70 %. For removing the spikes from the data the phase-space threshold despiking method from Goring and Nikora (2002), as modified in Wahl (2002), was used. The software was also used to calculate the stream-wise velocity u parallel to the curve tangent, the transverse velocity v perpendicular to u (positive towards the left bank) and the

Table 1 Experimental groyne setup

Run no.	Inclination (°)	Projected length (cm)	Groyne length (cm)
E0	–	–	–
E1.1	60°	80	92.4
E1.2	55°	80	88.3
E1.3	65°	80	85.1
E1.4	50°	80	97.7
E1.5	70°	80	100.04

vertical velocity w (positive towards the water surface). Using a down-looking probe the measurements were possible up to 50 % of the water depth.

Six experiments were carried out. The first experiment E0 was performed without a groyne. The following five experiments were carried out with a single groyne positioned in cross-section C1 with varying angle of inclination. An angle of 60° was chosen as reference inclination. In order to keep the projected length constant, the groyne length had to be adapted. Table 1 summarizes the parameters of the experiments.

3 Results

Comparing the results of run E0 without groyne and run E1.1 with the groyne inclined by 60°, the redirection of the flow from the outer bank towards the inner bank becomes obvious. The longitudinal profile L7 (30 cm from the right bank) of the stream-wise velocity u 3 cm above the bed (0.5 cm above the groyne) is plotted in Fig. 4. It shows a maximum decrease in u by about 44 % at cross-section C1. Note that the positions of the verticals in L7 at C1 and C9 had to be shifted (see Fig. 3). The reduction of the stream-wise velocity remained until the end of the curve but decreased to almost 15 % at C9.

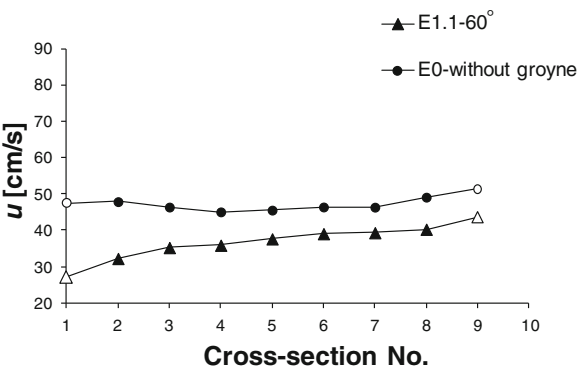

Fig. 4 Longitudinal profile L7 of the stream-wise velocity u 3 cm above the bed (*white filled symbols* indicate longitudinally shifted positions)

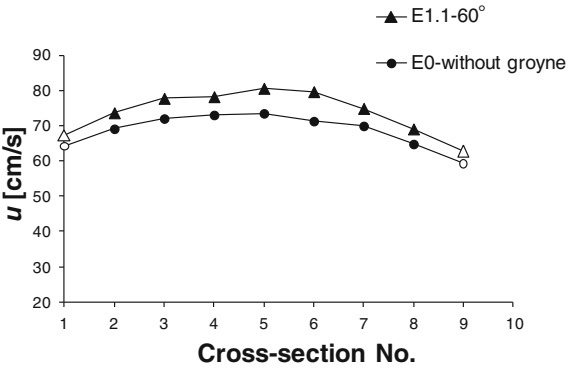

Fig. 5 Longitudinal profile L1 of the stream-wise velocity u 3 cm above the bed

On the other hand, the stream-wise velocity u increased towards the inner bank, as presented in Fig. 5 for the longitudinal profile L1 (30 cm from the left bank). The velocity increased by 5–11 % due to the presence of the groyne.

The redirection of the flow due to the groyne can be further seen in the top view of the flow field presented in Fig. 6. The velocities were highest at the inner bank even in run E0 (Fig. 6a) which is attributed to the rectangular cross-sectional shape. The change of the velocities concentrated on the regions close to the banks with a decrease at the right bank, almost unchanged velocities in the center and an increase at the left bank. The vectors show that the flow was parallel to the banks throughout the curve because the stream-wise velocity was much higher than the transversal component (see also Fig. 8). Due to the groyne, the flow direction was affected only in cross-sections C2 and C3 (Fig. 6b).

The distribution of the velocity over the depth and width is presented in Fig. 7 for cross-section C2. Besides the continuous increase of the stream-wise velocity component towards the inner bank (indicated by the colors), the circulation due to the curve is indicated by the vectors of transversal and vertical components in

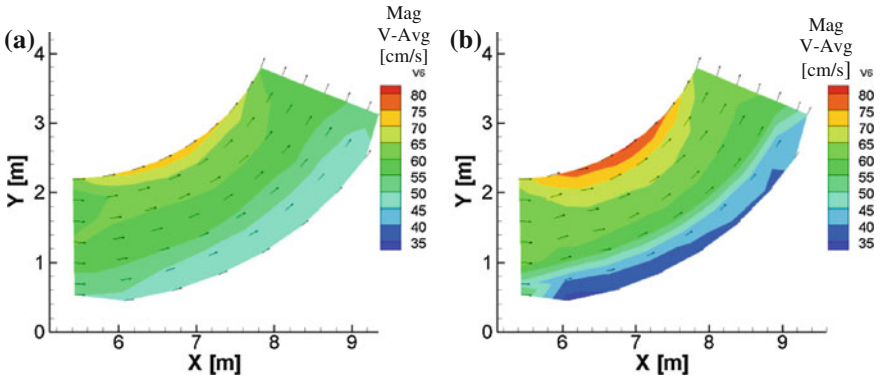

Fig. 6 Top view of the velocity field 3 cm above the bed for **a** run E0 without groyne and **b** run E1.1 with groyne at 60°

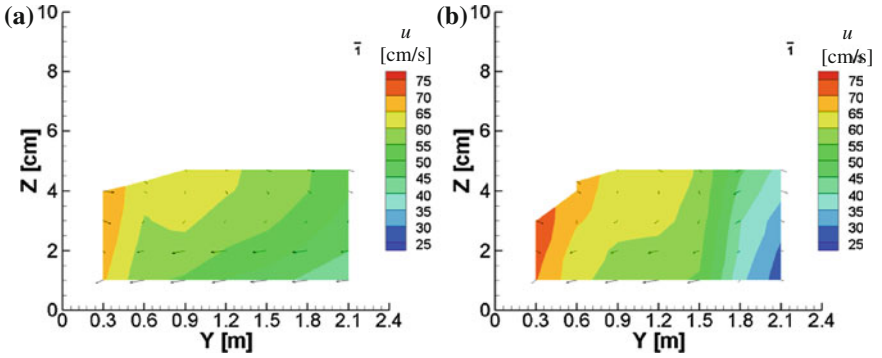

Fig. 7 Cross-sectional velocity field at C2 for **a** run E0 without groyne and **b** run E1.1 with groyne at 60°

Fig. 7a for the experiment without groyne. Figure 7b shows that in the cross-section about 70 cm downstream of the groyne the circulation was almost unaffected by the groyne. This indicates a local effect of the groyne for vertical and transversal velocities in contrast to the effect throughout the curve for the stream-wise velocity (see Fig. 6b).

The sensitivity of the velocity to the inclination of the groyne is shown in Fig. 8. The three velocity components at a height of 3 cm above the bed are plotted

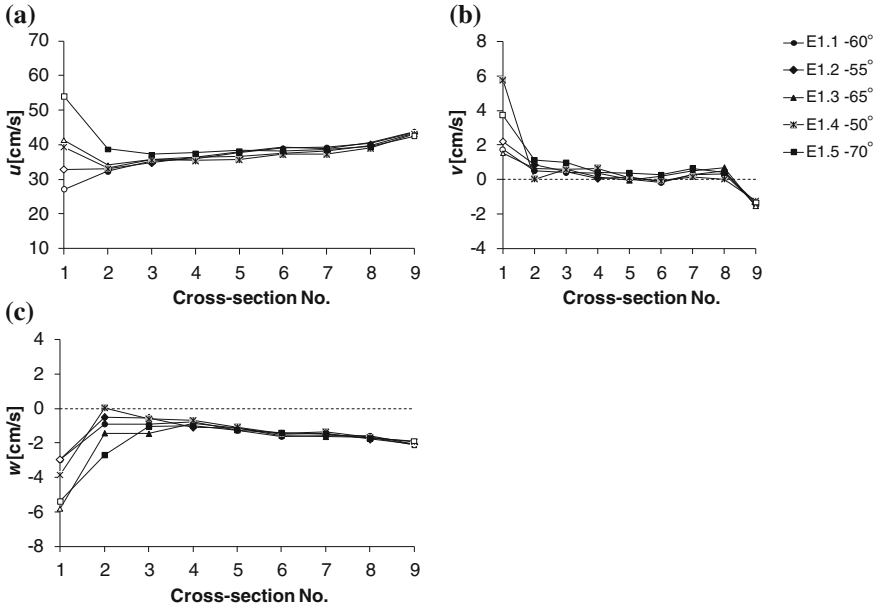

Fig. 8 Longitudinal profile L7 3 cm above the bed of **a** stream-wise velocity *u*, **b** transversal velocity *v*, and **c** vertical velocity *w* (*white filled symbols* indicate longitudinally shifted positions)

exemplarily for the longitudinal profile L7. Localized effect of the inclination on flow can be seen at C1 at which the groyne was installed (see Fig. 8a). The inclination of 60° was found to have the lowest stream-wise velocity at C1 (see Fig. 9). This local effect can be attributed to the distance between groyne and measuring points in C1. The higher the angle the closer located was the groyne to the measuring points and vice versa. It has to be noted that run E1.1 did not fit in this order which cannot be explained yet. Starting from C2 down to C9, the effect of the inclination becomes insignificant except for the test run with 70° inclination where the effect extended down to C3.

The change of the transversal component (Fig. 8b) cannot be related to the angle of inclination. A measuring grid designed to investigate the flow field in the vicinity of the groyne is necessary to study the transversal component. Along the curve v was in general directed towards the outer bank until cross-section C8. In the last cross-section the velocity was distinctly negative presenting the effect of the end of the curve and the following straight reach.

Also the vertical component (Fig. 8c) was not sorted according to the angle of inclination which again is attributed to local effects. However, in C2 the vertical component decreased with increasing inclination, indicating a stronger flow directed towards the bed if the groyne was closer to the measuring points. Along the curve w was negative as is expected for the flow along the outer bank in a curve.

In transversal direction the influence on the flow field was limited to longitudinal profile L7 and L6 which were directly affected by the blockage of the groyne. In L5 the changes of the velocities already vanished. The distance of L5 to the right wall was 90 cm and thus larger than the projected length of the groyne which was kept constant to 80 cm.

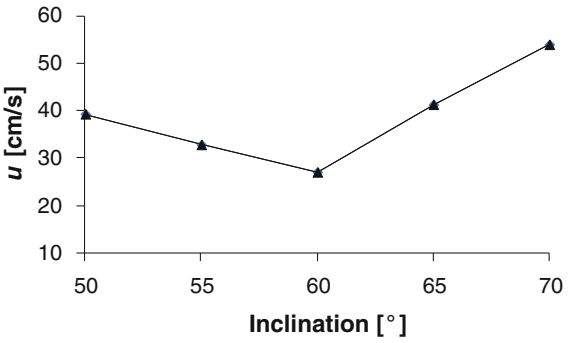

Fig. 9 Stream-wise velocity at C1 for different groyne inclinations

4 Conclusions

The effect of a single submerged groyne on the flow field in a curve as well as the effect of the inclination of the groyne has been experimentally investigated. Compared to the flow field without groyne it could be shown that the velocity at the outer bank decreased and increased at the inner bank along the curve. The result supports the applicability of this in-stream structure for bank protection purposes.

The evaluation of the inclination was done for a groyne with a reference inclination of 60°. The range of the variation of the angle was ±5° and ±10°. In this range and taking into account that the projected length was kept constant, the results showed no significant effect on the flow field from C2 to C9. At C1, where the groyne was installed, the effect of the inclination can be observed and the inclination of 60° showed the lowest stream-wise velocity. Further investigations varying systematically, first, single parameters of the groyne and later on parameter combinations will follow.

Acknowledgments This work was supported by the Research Executive Agency, through the 7th Framework Programme of the European Union, Support for Training and Career Development of Researchers (Marie Curie—FP7-PEOPLE-2012-ITN), which funded the Initial Training Network (ITN) HYTECH 'Hydrodynamic Transport in Ecologically Critical Heterogeneous Interfaces', N.316546.

References

Bhuiyan F, Hey RD, Wormleaton PR (2010) Bank-attached vanes for bank erosion control and restoration of river meanders. J Hydraul Eng 136(9):583–596

Copeland RR (1983) Bank protection technique using spur dyke. Final report U. S. Army Engineer Waterways

Goring DG, Nikora VI (2002) Despiking acoustic Doppler velocimeter data. J Hydraul Eng 128 (1):117–126

Hemmati M, Ghomeshi M, Kashefipour SM, Shafai-Bejestan M, Lanzoni S (2012) Experimental investigation of the effects of angle and length of bendway weirs on scouring and sedimentation in a meander river. J Amer Sci 8(9):912–917

Jamieson EC, Rennie CD, Townsend RD (2013) 3D flow and sediment dynamics in a laboratory channel bend with and without stream barbs. J Hydraul Eng 139(2):154–166

Marion A, Nikora V, Puijalon S, Bouma T, Ka Koll, Ballio F, Tait S, Zaramella M, Sukhodolov A, O'Hare M, Wharton G, Aberle J, Tregnaghi M, Davies P, Nepf H, Parker G, Statzner B (2014) Aquatic interfaces: a hydrodynamic and eco-logical perspective. J Hydraul Res 52(6):744–758

Matsuura T, Townsend RD (2004) Stream-barb installations for narrow channel bends—a laboratory study. Can J Civ Eng 13(3):478–786

Radspinner RR, Diplas P, Lightbody AF, Sotoropoulis F (2010) River training and ecologic enhancement potential using instream structures. J Hydraul Eng 136(12):967–980

Scurlock SM, Thornton CI, Drew CB, Abt SR (2014) Quantification of transverse in-stream structure hydraulics. J Hydraul Eng 1–9. doi:10.1061/(ASCE)HY.1943-7900.0000952

Shields FD Jr, Cooper CM, Knight SS (1995) Experiment in stream restoration. J Hydraul Eng 121 (6):494–502

Wahl TL (2002) Discussion of 'despiking acoustic Doppler velocimeter data' by Derek G Goring and Vladimir I Nikora. J Hydraul Eng 129(6):484–486

PIV-PTV Measurements of a Tailings Dam-Break Flow

Rui Aleixo, Yavuz Ozeren and Mustafa Altinakar

Abstract To experimentally study transient flows such as dam-break flows, imaging techniques are often used due to the constraints imposed by the highly transient nature of such phenomena. In this paper an experimental laboratory study of tailings dams made with a combined PIV + PTV algorithm is presented. In this algorithm the PIV technique is first applied to determine an estimator for the sediment layer velocity field. The obtained estimator is then used to compute a displacement estimator for the PTV approach. In this method the first step (PIV) provides a global estimation of the sediments velocity field and in the second step (PTV) a particle-by-particle analysis is obtained leading to an increased spatial resolution of the measurements. The obtained algorithm is applied to a laboratory tailings dam-break flow to obtain relevant information about the behavior of the tailings. This paper is a summary of the research presented in other papers by the authors.

R. Aleixo (✉)
CERIS Civil Engineering Research and Innovation for Sustainability Instituto Superior Técnico, Universidade de Lisboa, Lisbon, Portugal
e-mail: rui.aleixo@tecnico.ulisboa.pt

R. Aleixo
GHT Photonics, Padua, Italy

Y. Ozeren · M. Altinakar
National Center for Computational Hydroscience and Engineering, University of Mississippi Oxford, Mississippi, USA
e-mail: yozeren@ncche.olemiss.edu

M. Altinakar
e-mail: altinakar@ncche.olemiss.edu

P. Rowiński and A. Marion (eds.), *Hydrodynamic and Mass Transport at Freshwater Aquatic Interfaces*, GeoPlanet: Earth and Planetary Sciences,
DOI 10.1007/978-3-319-27750-9_21

1 Introduction

1.1 Tailings Dam-Break Flow

Tailings dam-break flows can be seen as a particular case of a severe transient debris flows. Debris flows are a type of gravity driven flows that occur when a mixture of poorly sorted sediments with water flows down a slope. In this type of flow the liquid and solid phases play a determinant role and make this flow different from, for example, a rock avalanche or a water flood. The importance associated to the study of tailings dams-break flows lies in their catastrophic consequences for human activities and environment. Failure of tailings dams may release a mixture of fine sediments and water to the environment. The outflowing mixture generally behaves as a non-Newtonian fluid and may travel long distances destroying and harming built and natural environment on its path. Due to their construction methods tailings dams are more prone to collapse. A list of tailings dam accidents can be found in Rico et al. (2007).

Current shallow water models of dam-break flow based on various rheological models, expressed in terms of global flow parameters, fail to accurately predict the behavior of tailing dam failures flows. One of the reasons for this is the lack of understanding of the non-Newtonian behavior of the tailings and water mixture. For a better comprehension of the physics of the tailings dam break flows, a set of laboratory scale experiments is undertaken. These experiments focus in the micro-scale details such as the local velocity field, to investigate other local features like the shear driven sediment flow and water-sediments interaction.

Figure 1a–c illustrates the time evolution of a laboratorial tailings dam-break flow (present study). Due to their whole-field measurement capability and time resolution, imaging techniques are the natural option to address measurements in dam-break Aleixo et al. (2011) and in particular tailings dams flows (Aleixo et al. 2014). In the present paper the main goal will be the measurement of velocity fields in the sediment layer using imaging techniques. The complexity of the flow and the need for data that can be used to validate numerical models justifies the present experimental study as well.

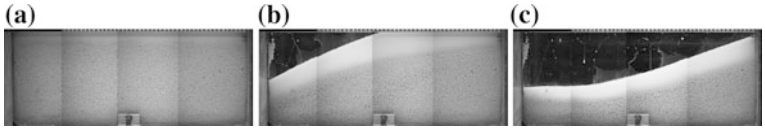

Fig. 1 Three different times of the tailings dam-break flow: **a** $t = 0$ s, **b** $t = 1.25$ s and **c** $t = 2.5$ s. The water is white due to the addition of TiO_2 , used to make the water opaque for the wave front tracking

2 Velocity Measurement Techniques

2.1 PIV: Particle Image Velocimetry

Particle Image Velocimetry is an Eulerian method of measuring velocity. Currently PIV can be considered an established and mature measurement technique. The core of modern PIV is the image cross-correlation operation, first introduced by Keane and Adrian (1992). In this technique, two consecutive flow images are divided into smaller areas, referred hereafter as interrogation windows, and the cross-correlation is made between corresponding interrogation windows. The correlation peak associated with each pair of interrogation windows is a measure of the most probable displacement and its position can be determined up to sub-pixel resolution (Raffel et al. 2007). Modern PIV algorithms use interrogation window distortion in order to improve the cross-correlation, as proposed by Scarano and Riethmuller (2000). In the present paper, a Matlab based PIV algorithm, MATPIV v1.6.1, developed by Sveen (2004) was used. An application of this algorithm to dam-break flows was presented in Oertel and Bung (2012).

PIV has many advantages: its robustness and accuracy make it an adequate tool to study the whole fluid flow. Using a high speed camera it is also possible to measure instantaneous velocities. In the present case, where the analysis is focused on the velocity field of the tailings, the seeding particles used will be the tailings particles themselves. In this case PIV is also referred as Granular PIV (Lueptowand et al. 2000). Dry granular flows were analyzed by Pudasani et al. (2005) by means of PIV.

When studying granular flows, often it is also desirable to determine the trajectories, speeds and final destinations of individual particles. This type of information cannot be obtained from PIV. Another approach, known as Particle Tracking Velocimetry, should be used.

2.2 PTV: Particle Tracking Velocimetry

Contrary to PIV that tracks patterns of particles, PTV relies on the identification and matching of individual particles between consecutive frames. The need to detect, match and track particles makes PTV a quite expensive method in terms of computational resources when compared, for instance, with PIV. This is particularly important when large seeding concentrations are present, such as in the case of tailings dams. Furthermore, large seeding concentrations raise two other concerns: (a) the collisions between particles that may lead to local significant gradients and out of plane motions; (b) finding the matching particle in a dense area of similar particles. To overcome these last two concerns the PTV algorithm chosen is the Voronoï Tracking algorithm first proposed by Capart et al. (2002) and extended to 3D by Spinewine et al. (2003). This algorithm is based on the Voronoï tessellation

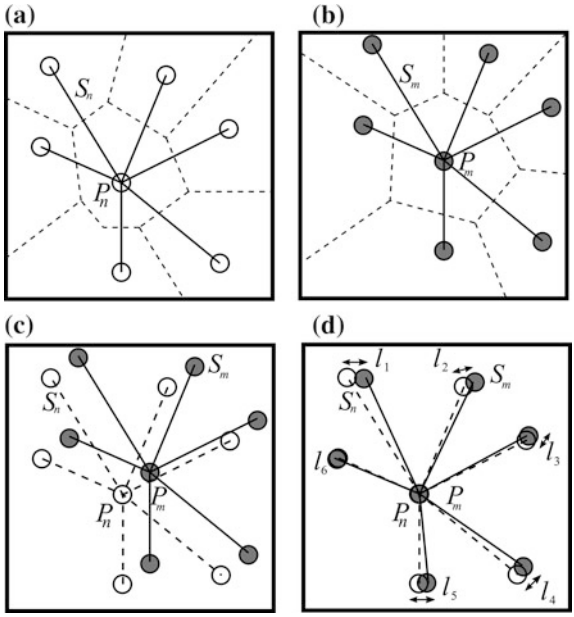

Fig. 2 Illustration of the Voronoï PTV tracking scheme. **a** Images at time t with Voronoï polygon and Voronoï star; **b** image at time $t + dt$ with respective Voronoï polygon and Voronoï star; **c** displacement of the Voronoï star; **d** overlapping of the corresponding stars for displacement determination

of space. Centers of detected particles become the centers of Voronoï polygons, as depicted in Fig. 2a, b. The star formed by the union of the immediate neighbors, as depicted in Fig. 2, is referred as Voronoï star and can be used as a matching pattern. Star displacement between the two frames is depicted in Fig. 2c.

The star-distance is a measurement of the degree of discrepancy between the patterns formed by the two stars. As illustrated in Fig. 2d, the star distance between two particles is defined as the median of the distances between the star extremities, $l_1, l_2, \ldots$, once these two particles have been made to coincide. Two stars match if the following condition holds:

$$\text{match}\,(P_{n,m}) = \min(\text{dist}_S(S_{n,1}, S_{m,2})) \tag{1}$$

where $P_{n,i}$ is the pair of particles (n, i) to be matched and $S_{n,1}$ denotes the Voronoï star in frame 1 centered in the particle n and $S_{m,2}$ is the Voronoï star centered in particle m in frame 2.

Two of the advantages of this method are the stability of the Voronoï star and diagram and the ability to cope with gradients. More detailed information can be found in Capart et al. (2002).

Since the particle distribution is random, the velocity field will also be randomly distributed throughout the image plane. A procedure to structure the velocity field, that is, to present the velocity field in a regular grid must be put forward. In this paper a binning method is used. This method consists of: (a) dividing the obtained velocity field into a regular grid of bins; and (b) then calculating the averages of velocity of the vectors in each bin. Binning method was used in Aleixo et al. (2011)

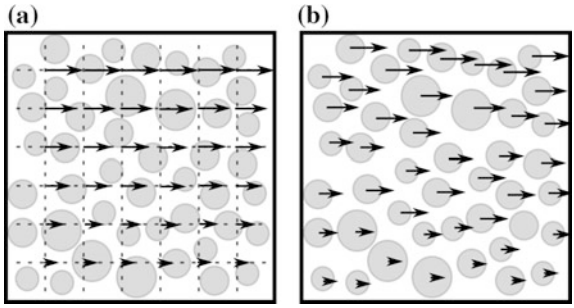

Fig. 3 Illustration of the combined PIV-PTV approach. **a** Random particle distribution and the obtained PIV velocity field; **b** interpolation of the PIV field to each particle location

and Cowen and Monismith (1997). The latter applies also the Voronoï tracking algorithm to dam-break flows.

2.3 A Combined PIV-PTV Tool

The difficulties in using PTV to process batches of flow images involving large time velocity gradients together with the capacity of the PIV to track them suggested the combination of both techniques. PTV can be optimized if an estimation of the velocity is provided to the tracking algorithm. With this velocity estimation it is possible to determine the expected displacement of each individual particle:

$$\mathbf{d}_i = \mathbf{v}_i dt \tag{2}$$

where $\mathbf{d}_i$ stands for displacement vector estimator for particle i, $\mathbf{v}_i$ is the velocity vector estimator for particle i and dt is the time interval between consecutive frames.

A similar approach was used by Stitou and Riethmuller (2001) in order to increase PIV spatial resolution and was referred as Super-Resolution PIV. Figure 3 illustrates the principle of combining PIV and PTV in a granular flow (Aleixo et al. 2014a, b)

3 Experimental Setup

3.1 The Dam-Break Platform

The experiments were carried out at the experimental dam-break setup of NCCHE located at the USDA-ARS, National Sedimentation Laboratory in Oxford, Mississippi, USA. The setup consisted of a 3.66 m wide and 7.6 m long tilting

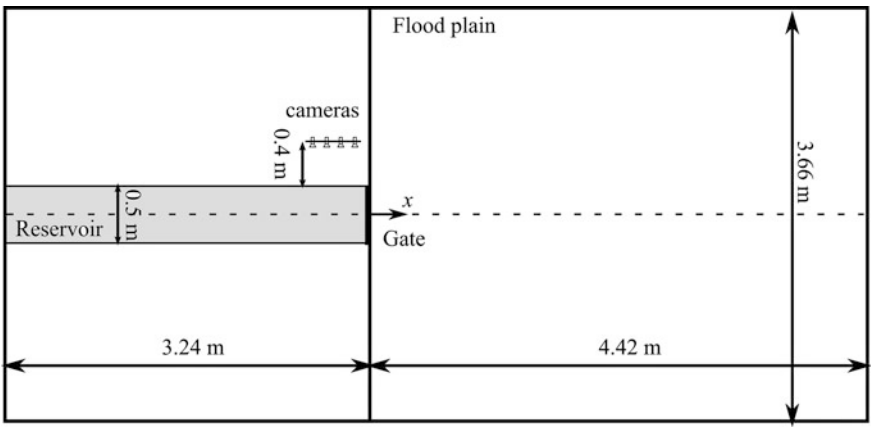

Fig. 4 Scheme of the flume where the experiments were made

platform, 3.24 m long portion of which was surrounded by 0.61 m high sidewalls to serve as a reservoir. The downstream 4.42 m-long portion represented the floodplain. To simulate dam failure a sliding gate was located at the center of the wall separating the reservoir from the floodplain. A weight drop mechanism allowed pulling the gate upwards at speeds up to 8 m/s. The reservoir bed was made of painted aluminum while the floodplain bed was made out of smooth PVC. A sump located under the test flume was used as a sump to storage the water. For the experiments the upstream reservoir was channelized by two clear acrylic walls on both sides of the gate. In this configuration, the upstream reservoir was 0.50 m wide, 0.63 m high and 3.24 m long, as depicted in Fig. 4. The drop height was set as 2 m for all the experiments which provided a gate removal speed of about 8 m/s. Initial conditions were set by adjusting the water and sediment heights in the upstream reservoir. A description of this flume can be found in Ozeren et al. (2013).

3.2 Sediments

To simulate the tailings PVC white pellets were used. These PVC pellets have an elliptical cylinder shape and the physical properties are listed in Table 1. The sediments were placed in the upstream channel, compacted with a vibrator following a predefined procedure and then leveled with a moving paddle. The paddle height was adjusted to the required sediment elevation. The water was fed into the

Table 1 Physical properties of the sediments

Property	d_{50} (mm)	ρ (kgm^{-3})	Shape factor	Porosity	Angle of repose
Value	2.87	1420	0.83	0.4	30°

channel's upstream extremity by means of a hose equipped with a diffuser to minimize the bed deformation. The tested flow condition consisted in an initial sediment level of 0.20 m and above the channel bed and a water level of 0.4 m above the channel bed. For visualization and water tracking purposes the water was seeded with a solution of TiO_2 in order to make it opaque.

3.3 Instrumentation

To measure the flow, 4 high speed cameras were used. They were placed side by side in a rigid aluminum support. The optical axes of the cameras were perpendicular to the side wall (Fig. 4). Each camera was equipped with 35 mm, f1.4 C-mount lenses covering an area about 0.5 m × 0.2 m at a distance of 0.4 m from the wall. Cameras' maximum acquisition frequency is of 1 kHz at maximum resolution (1 Mpix). The acquisition frequency of each camera was set at 400 Hz and the respective resolution was 1024 × 720 pixels. The cameras were synchronized with the gate and triggered by a computer.

4 Results

4.1 Evaluation of the Combined PIV-PTV Approach

To evaluate the velocity field at each particle's location, two interpolation schemes were used: linear and cubic. Using the obtained flow images, the capacity to track particles between 5 consecutive frames centered in t = 0.5, 1.0, 1.5, 2.0, 2.5 and 3.0 s was evaluated and the results are presented in Fig. 5a. As it can be seen the combination of PIV with PTV allows to track more particles, in particular when considering a linear interpolation of the PIV velocity field. This is put into evidence in Fig. 5b where the velocity fields obtained with each method are depicted. It is possible to see that only PTV fails to track particles in the upper layer of the sediment layer, whereas the combined approach provides a better description of the flow.

4.2 Velocity Fields Results

The velocity fields obtained for the sediment bed are depicted in Fig. 6 for selected times. It was seen that the sediment motion is initially limited to a thin sediment layer at the interface between the sediment and water free-surface layer. The velocities in the sediment layer are negligibly small except near the gate (Fig. 6a).

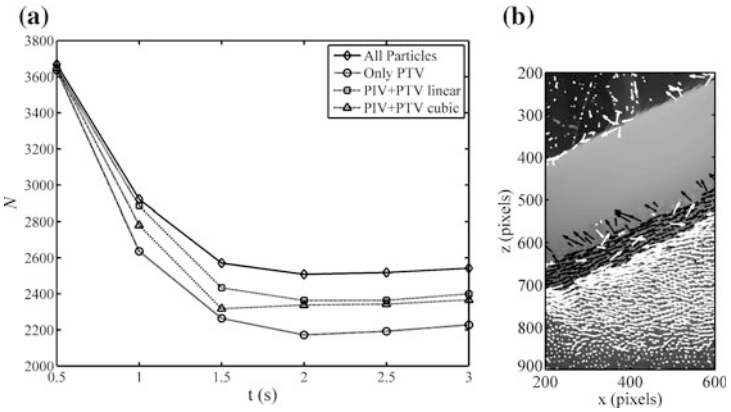

Fig. 5 **a** Number of particles tracked in each instant using: only PTV, PIV + PTV with a linear scheme of interpolation and PIV + PTV with a cubic scheme of interpolation. **b** Velocity fields determined using only PTV and with the combined approach PIV + PTV at t = 1.19 s. *White arrows* only PTV; *Black arrows* PIV + PTV

From 0.5 to 1 s after the gate opening (Fig. 6b, c), the thickness of the moving surface layer has increased slightly (darker area in Fig. 6b, c). The velocities in the sediment layer have also increased. At about 1.1 s after the gate opening, a failure plane appears and sediments above the failure plane slide downstream as a mass failure. This mass failure and the failure surface are visible in light gray in Fig. 6d.

4.2.1 Identification of the Mass Failure Region

The three flow regions described in the previous section can be visualized by plotting the vorticity of the velocity field, which reveals the shear regions between the layers, as shown in Fig. 7a–c. In those figures the mass failure region clearly appears as a low vorticity region between two shear layers that evolve with time. The mass failure region appears at approximately $t = 1.08$ s (Fig. 7a). At $t = 1.25$ s (Fig. 7b) the mass failure layer is clearly delineated by the shear layers above and below. In the following time (Fig. 7c), the mass failure layer deforms, becomes smaller and will disappear at a later time.

4.2.2 Velocity Profiles Analysis

In Fig. 8 the dimensionless velocity profiles at $x = -0.1991$ m are plotted at different times ($t \leq 1.1250$ s). The velocities are scaled with the maximum velocity, u_{max}, measured at the top of the sediment layer and the height where this maximum velocity occurs, z_{max}, is used to scale the elevation from the bed. One can see that in the range $0.3 < z/z_{max} < 0.8$ the velocity is almost constant. This can be considered

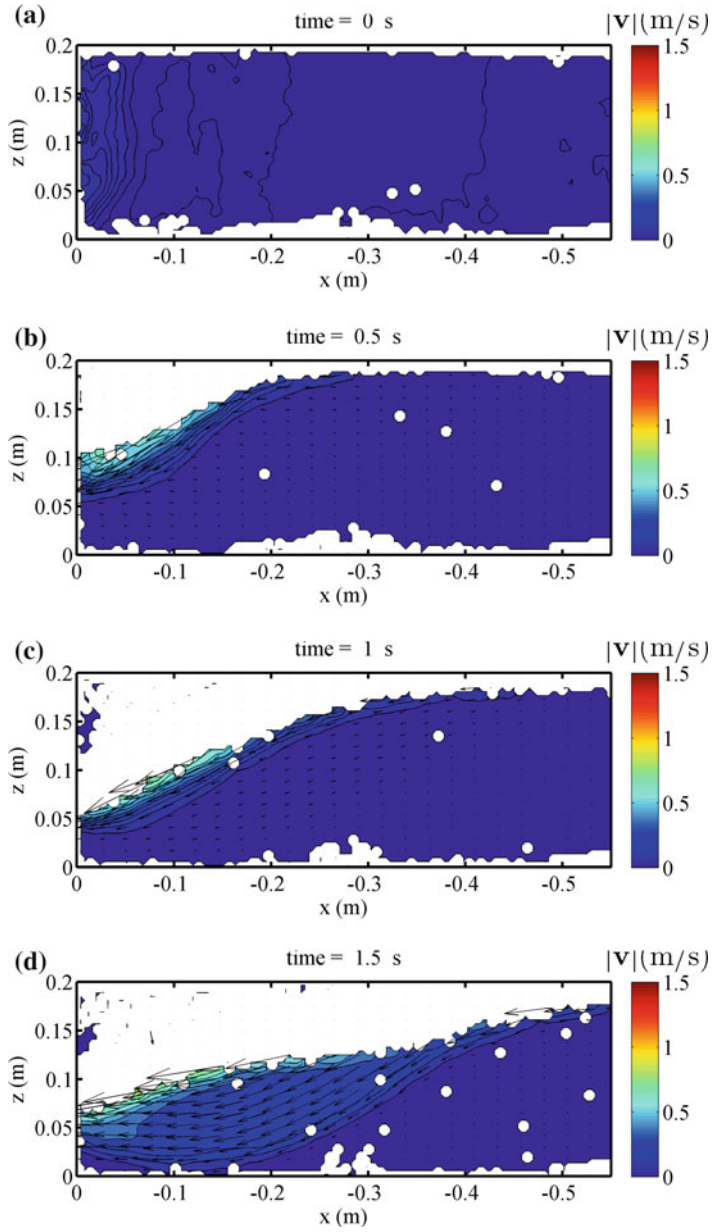

Fig. 6 Velocity fields determined using the combined PIV-PTV approach for different times. (Only 1-out-of-6 vectors is depicted in the horizontal direction and only 1-out-of-3 vectors is depicted in the vertical direction)

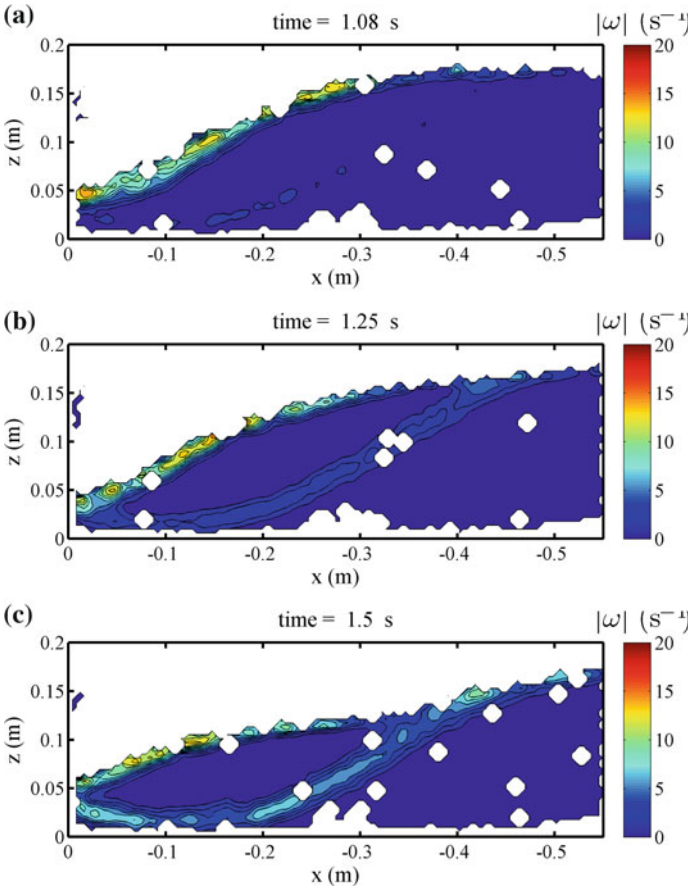

Fig. 7 Vorticity contours for different times illustrating the evolution of the plug flow. Two shear layers are clearly seen (*gray areas*) and between them the plug flow

as a plug flow. Up to $t = 1.0625$ s, the constant velocity profile increases slowly. The last profile at $t = 1.1250$ s, however, shows a sudden increase due to the mass failure at $t = 1.08$ s. In the region $z/z_{max} < 0.3$, the velocity increases sharply from zero at the bed to match the velocity of the sediment layer above. In the region $z/z_{max} > 0.8$, the shear stress induced by the free-surface flow controls the movement of sediments as sheet flow. The velocity in the sheet flow layer increases linearly to match the velocity of the free surface flow near the sediment-water interface.

With the velocity field information obtained from Fig. 6 and from the shear layers identified in Fig. 7 three regions can be identified from the bottom of the

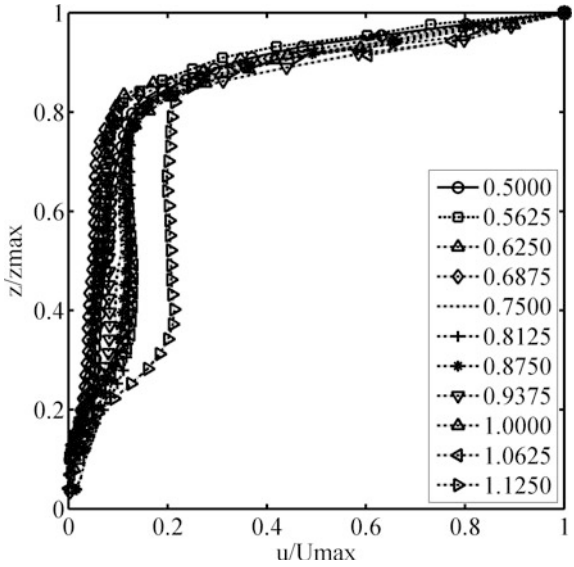

Fig. 8 Non-dimensional velocity profiles for different times at reservoir section $x = -0.1991$ m. Legend indicates times in seconds

channel to the top of the sediment layer: a shear layer near the channel bottom, a middle layer, and a top shear layer. It was observed that in the shear layer near the bottom the velocity increases linearly to reach a maximum value of U_o. The thickness of this shear layer, which is the vertical distance from the bed where the maximum velocity is observed, is here denoted by z_o. The evolution of U_o and z_o is shown in Fig. 9a. It is possible to observe that the thickness of the bottom shear layer, z_o, remains constant while the maximum velocity, U_o, increases with time. Until the initiation of the mass failure at $t = 1.08$ s the maximum velocity is increasing slowly; however, the mass failure causes a sudden acceleration and the maximum velocity increases linearly until $t = 1.5625$ s. The middle layer corresponds to the mass failure layer. In this layer, the velocity can be assumed as approximately constant, although it slightly decreases with elevation from the bed. The topmost layer represents the sheet flow layer driven by free-surface flow induced shear. In this layer the velocity increases linearly with the height. The bottom shear layer parameters: maximum velocity, U_o, and thickness, z_o, were used to scale the obtained velocity profiles for times $1.1250\text{ s} \leq t \leq 1.7500\text{ s}$. The results are depicted in Fig. 9b. As it can be seen, the obtained profiles collapse to a single curve, indicating that these are convenient scale parameters.

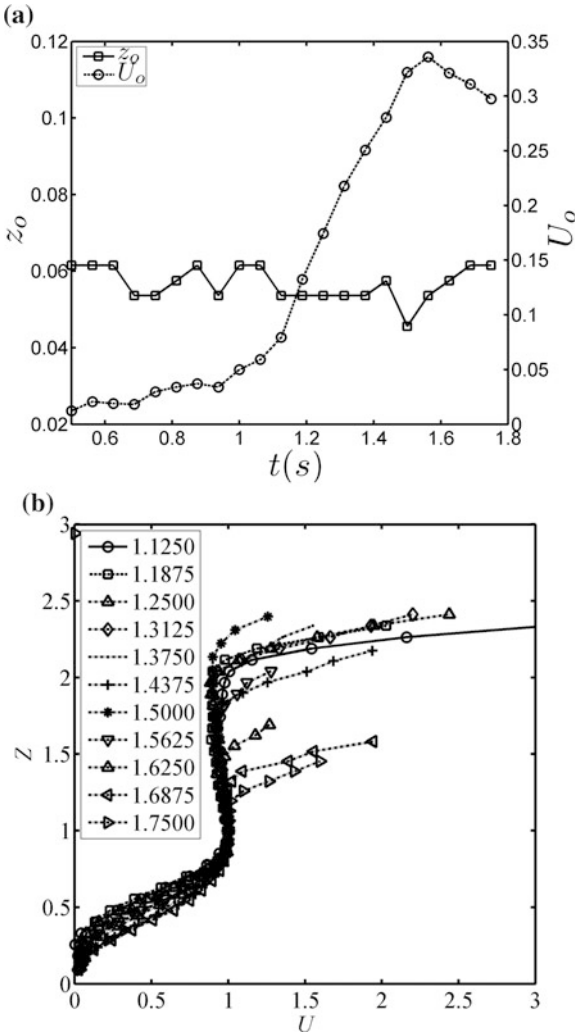

Fig. 9 **a** Evolution of z_o and U_o with time at reservoir section $x = -0.1991$ m. **b** Non-dimensional velocity profiles for different times at reservoir section $x = -0.1991$ m. Legend indicates times in seconds

5 Conclusions

This paper presented a study of tailings dam-break flows by means of an analysis tool obtained from the combination of PIV with PTV. The combined approach has shown to be capable of detecting and track particles in the different velocity scales of the tailing dam-break flow.

Detailed measurements on a tailings dam break flow were performed using a combined PIV + PTV approach. Using the proposed combined approach it was observed that it was possible to successfully track more particles than by using just PTV. It was also verified that a linear interpolation scheme allowed for more particles successfully tracked than the other tested scheme (cubic interpolation).

In the presented study of the tailings dam flow it was possible to identify and quantify different features of the flow. In the first instants, after the gate removal, the sediment flows is processed in two ways: (a) as sheet flow (upper sediment layer); (b) as a low velocity plug flow (sediment bed). As time evolves, the water flow-bed interaction will cause the appearance of a mass failure. In this condition three flow layers were identified: (a) immediately close to the bottom a shear layer with constant thickness was observed. The maximum velocity of this layer increased almost linearly with time; (b) above this layer a plug flow region with a constant velocity was observed. This constant flow velocity profile increases with time until the plug flow region collapses; (c) an upper sheet flow layer in the interface between the water flow and the sediment layer. The identification of the different layers was made possible through the determination of the flow vorticity. Pertinent scaling variables for the upper transport layer and the mass failure region were determined.

Acknowledgments This work was supported by the US Department of Homeland Security sponsored Southeast Region Research Initiative (SERRI) at the US Department of Energy Oak Ridge National Laboratory, and to the USDA Agriculture Research Service under the Specific Research Agreement No. 58-6408-1-609 monitored by the USDA-ARS National Sedimentation Laboratory (NSL) and The University of Mississippi (UM). The authors also thank the technical support provided by J. Ferguson, A. Gebrehana and T. Gannaway during the experimental campaign.

First author is now supported by the Research Executive Agency, through the 7th Framework Programme of the European Union, Support for Training and Career Development of Researchers (Marie Curie FP7PEOPLE2012ITN), which funded the Initial Training Network (ITN) HYTECH: Hydrodynamic Transport in Ecologically Critical Heterogeneous Interfaces, No. 316546.

References

Aleixo R, Soares-Frazão S, Zech Y (2011) Velocity-field measurements in a dam-break flow using a PTV Voronoï imaging technique. Exp Fluids 50(6):1633

Aleixo R, Ozeren Y, Altinakar M, Wren D (2014a) Velocity field measurements in tailings dam failure experiments using a combined PIV-PTV approach. In: Proceedings of the 3rd IAHR Europe conference. Porto, Portugal

Aleixo R, Ozeren Y, Altinakar M (2014b) Tailings dam-break flow analysis by means of a combined PIV-PTV tool. In: Proceedings of the river flow 2014 conference, Lausanne, Switzerland

Capart H, Young D, Zech Y (2002) Voronoï imaging methods for the measurement of granular flows. Exp Fluids 32:121

Cowen E, Monismith S (1997) An hybrid digital particle tracking velocimetry technique. Exp Fluids 22:199

Keane R, Adrian R (1992) Theory of cross-correlation analysis of PIV images. Appl Sci Res 49:191

Lueptowand RM, Akonu A, Shinbrot T (2000) PIV for granular flows. Exp Fluids 28(2):183

Oertel M, Bung D (2012) Initial stage of two-dimensional dam-break waves: laboratory versus VOF. J Hydraul Res 50(1):89

Ozeren Y, Altinakar M, Wren D (2013) Experimental measurements of dam-break flow. In: 6th international perspective on water resources and the environment conference (IPWE 2013), Izmir, Turkey, 7–9 Jan 2013

Pudasani S, Hsiau SS, Wang Y, Hutter K (2005) Velocity measurements in dry granular avalanches using particle image velocimetry technique and comparison with theoretical predictions. Phys Fluids 17(9):093301

Raffel M, Willert C, Werely S, Kompenhans J (2007) Particle image velocimetry—a practical guide. Springer, Heidelberg

Rico M, Benito G, Salgueiro A, Diez-Herrero A, Pereira H (2007) Reported tailings dam failures: a review of the european incidents in the worldwide context. Elsevier, Netherlands

Scarano F, Riethmuller M (2000) Advances in iterative multigrid PIV image processing. Exp Fluids 29:S051–S060

Spinewine B, Capart H, Larcher M, Zech Y (2003) Three-dimensional Voronoï imaging methods for the measurement of near-wall particulate flows. Exp Fluids 34(2):227

Stitou A, Riethmuller M (2001) Extension of PIV to super resolution using PTV. Meas Sci Technol 12:1398

Sveen K (2004) An introduction to MatPIV v. 1.6.1, no 2 ISSN 2:0809–4403

On Evaluating Flow Resistance of Rigid Vegetation Using Classic Hydraulic Roughness at High Submergence Levels: An Experimental Work

Vittorio Pasquino, Paola Gualtieri and Guelfo Pulci Doria

Abstract Vegetation resistance is generally evaluated using drag coefficient C_D related to friction factor f; however, some authors examined a possibility of employing classic hydraulic roughness coefficients (i.e., Nikuradse's or Strickler's) to calculate vegetation resistance in case of high submergence ($h/k > 5$, in which h is flow height and k represents vegetation height). In order to compare conventional roughness at high submergence levels, an experimental methodology was developed, focused, in particular, on fully submerged and rigid vegetation, for different hydraulic conditions and varying non-dimensional vegetation density.

1 Introduction

In the last 20 years, river rehabilitation has assumed an important role in all world environmental policies; therefore, preserving riparian vegetation (trees, macrophytes, etc.) has become fundamental in order to well manage river basins. Furthermore, concerning hydraulic aspects, vegetation causes an increase in water levels, decrease in flow velocity, captures sediments, could decrease ground erosion, and improves water quality; it is nowadays clear in hydraulic engineering that it is necessary to deepen the knowledge on vegetation flow interactions, including resistance aspects.

V. Pasquino (✉)
CUGRI Consorzio Inter-Universitario Per La Previsione E Prevenzione Dei Grandi Rischi, Via Giovanni Paolo II, 132-84084-Campus Di Fisciano, Fisciano (SA), Italy
e-mail: vittorio.pasquino@unina.it

V. Pasquino · P. Gualtieri · G.P. Doria
Civil Construction and Environmental Engineering Department, University of Naples Federico II, Via Claudio 21, 80125 Naples, Italy
e-mail: pgualtie@unina.it

P. Rowiński and A. Marion (eds.), *Hydrodynamic and Mass Transport at Freshwater Aquatic Interfaces*, GeoPlanet: Earth and Planetary Sciences,
DOI 10.1007/978-3-319-27750-9_22

In the literature, plant settings are classified as rigid or flexible and submerged (flow depth h bigger than vegetation height k: $h > k$) or emergent. In this work we evaluate flow resistance due to fully submerged rigid vegetation, focusing on the case of submergence values greater than 5 (i.e., $h/k > 5$) and using classic hydraulic roughness coefficients, Nikuradse's k_N or Strickler's k_S. We compare different trends by developing a methodology applied to ten sets of experimental data collected for this study.

2 Classic Hydraulic Roughness Applied to Vegetation Resistance

In the literature, the actual trend is to consider friction factor f to be more appropriate for evaluating flow resistance in open channel flows rather than classic roughness coefficients (Nikuradse's or Strickler's). Beecham et al. (2005) showed that Keulegan equation underestimated their experimental studies; Ferguson (2010), and Mrokowska et al. (2015) made some experimental comparisons about suitability of Manning roughness n for different hydraulic conditions and finally suggest to use a friction factor f considering it more stable. Powell (2014) founded a dimensionless hydraulic geometry equation that performs better than the logarithmic flow law (Nikuradse's) and then the variable power flow law (Strickler's).

Vegetation resistance is largely computed using friction factor f directly related to the drag coefficient C_D that, in turn, is directly linked with the shape of the object crossed by the flow. It is well known that in case of low submergence, classic roughness cannot be used by definition; nevertheless, recent literature has considered the possibility of using classic hydraulic roughness for open channel flows. Lopez and Garcia (2001) showed that vegetation resistance measured with Manning coefficient n (well-known to be directly linked to ks) exhibits an almost constant value up to a specific threshold of vegetation density. Augustijn et al. (2008) examined the use of conventional flow resistance equations for vegetated flows finding that for the submergence ($h/k > 5$), the Manning roughness represents the best correlation with the experimental data. Huthoff (2012) assumed a two-layer model considering surface layer flowing on a wall created by vegetation layer and evaluating flow resistance using the Manning equation. Konings et al. (2012) presented a model to derive Manning roughness height n as a function of flow and vegetation properties relating shear stress to the mean velocity profile by considering Gioia and Bombardelli's (2002) approach. Nepf (2012) asserted that in case of submerged vegetation filling completely the channel width, hydraulic resistance depends only by submergence ratio: the Authors, in fact, found that Manning roughness n assumes a constant trend for increasing h/k ratio. This aspect confirm the work of Augustijn et al. (2008) that showed how in condition of high

submergence, the Manning coefficient decreases with increasing submergence ratio and eventually levels off ($h/k > 5$). We use this last consideration as a key aspect of our research. In the next section we try to answer the following questions: if it is possible to use classic roughness height (Nikuradse's, Strickler's, Chèzty's) for high discharge and consequently high submergence levels, which roughness coefficient could be considered as more stable to evaluate flow resistance and why?

We consider Nikuradse's and Strickler's roughness heights, k_N and k_S, in the same dimension (m); to do this, we will use literature results for open channel flows. In fact, concerning Darcy-Weisbach formula and its use in open channel flows, Yen (2002) combined it with Colebrook-White equation neglecting viscosity effects and Reynolds number, obtaining:

$$V = -K_1\sqrt{8g}\log\left(\frac{k_N}{K_2 R}\right)\sqrt{RS} \tag{1}$$

in which $K_1 = 2$ and K_2 depends on the shape of the channel, g is the gravity acceleration, R is the hydraulic radius (for a wide rectangular channels it is equal to the flow height, h) k_N (m) is Nikuradse roughness coefficient, and S is channel slope. This equation is equivalent to the Keulegan formula.

On the other hand, as concerns Manning's equation, thanks to Chow (1988), following Gioia and Bombardelli analysis (2002), we can write:

$$V = \frac{R^{2/3}S^{1/2}}{K_n \phi_S k_s^{1/6}} \tag{2}$$

in which K_n ($L^{1/2}T^{-1}$) is a conversion factor in Manning's equation and Φ_s ($m^{-1/2}$ s) = 0.04 is a coefficient used to relate the Manning roughness n (s $m^{-1/3}$) and the Strickler roughness height k_S (m). Definitely, k_S represents an average grain size.

As it is possible to compare k_N (m) and k_S (m), we show the results of our experimental work in order to evaluate different roughness trends for different hydraulic conditions (different flow depths h, channel flows S, and flow discharges Q). Moreover, we consider only the vegetation non-dimensional density λ (defined as the product of m (number of cylinders per m^2), D (diameter of cylinder), k (cylinder height))as a key parameter.

3 Experimental Methodology

Experimental measurements were performed in the laboratory of the Department of Civil, Construction and Environmental Engineering of the University of Naples Federico II. The channel, with a variable slope, was 8 m long and had a cross-section of 0.40 × 0.40 m^2 (see Fig. 1).

Fig. 1 Experimental channel

Vegetation was simulated using rigid cylinders of height k = 1.5 cm and diameter D = 0.4 cm, set in two arrangements (aligned and staggered) with three non-dimensional densities λ (0.024, 0.048 and 0.096) (Fig. 2).

Experimental measurements were performed in a channel of rectangular cross-section with a uniform flow by varying the flow rate, the channel slope and the hydraulic radius. The quantities h, S and V were measured in each proof.

Ten runs were performed, each with 5–10 flow depths. Non-dimensional vegetation density, λ, assumed values from 0.096 to 0.024, whilst the maximum submergence values h/k ranged from 5 to 8.78. Details are shown in Table 1.

In Table 1 "Arr." represents Arrangement (aligned or staggered), k the vegetation height, D the vegetation diameter, m the number of cylinder per unit area, λ the non-dimensional vegetation density, $(h/k)_{max}$ the maximum submergence ratio value.

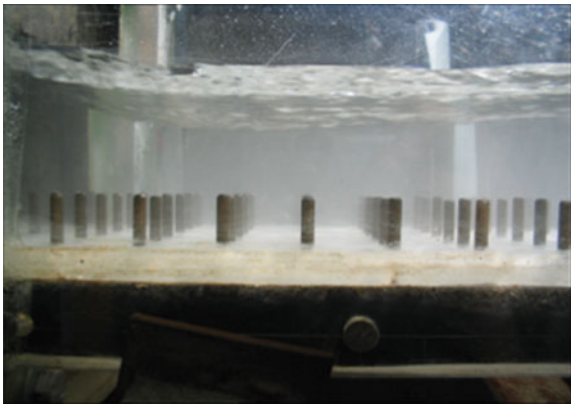

Fig. 2 Vegetation simulated as rigid cylinders. Vegetation height k = 1.5 cm

Table 1 Experimental setup

Run	Arr.	K (m)	D (m)	M (m^{-2})	λ(−)	Flow depths	$(h/k)_{max}$
1	Al.	0.015	0.004	1600	0.096	9	8.78
2	Al.	0.015	0.004	1600	0.096	6	6.50
3	St.	0.015	0.004	800	0.048	10	5.72
4	Al.	0.015	0.004	800	0.048	7	8.27
5	St.	0.015	0.004	800	0.048	7	5.31
6	St.	0.015	0.004	800	0.048	9	6.88
7	Al.	0.015	0.004	400	0.024	10	5.40
8	St.	0.015	0.004	400	0.024	6	5.63
9	Al.	0.015	0.004	400	0.024	7	6.79
10	St.	0.015	0.004	400	0.024	5	5.55

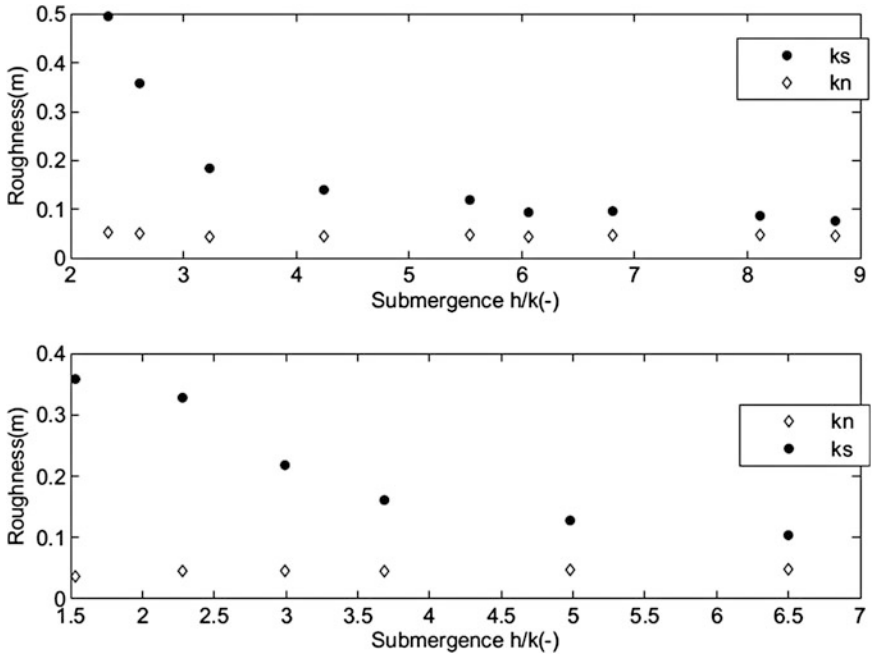

Fig. 3 Run 1–2. Horizontal axis: submergence ratio (h/k). Vertical axis: roughness coefficients. *Squares* represent Strickler's roughness; *diamonds* Nikuradse's roughness

Now, in Figs. 3, 4, 5, 6 and 7 we report results of our experiments. In each diagram, the submergence ratios, $h/k(-)$, are plotted on the horizontal axis, and roughness coefficients values (m), k_N and k_s, are plotted on the vertical axis.

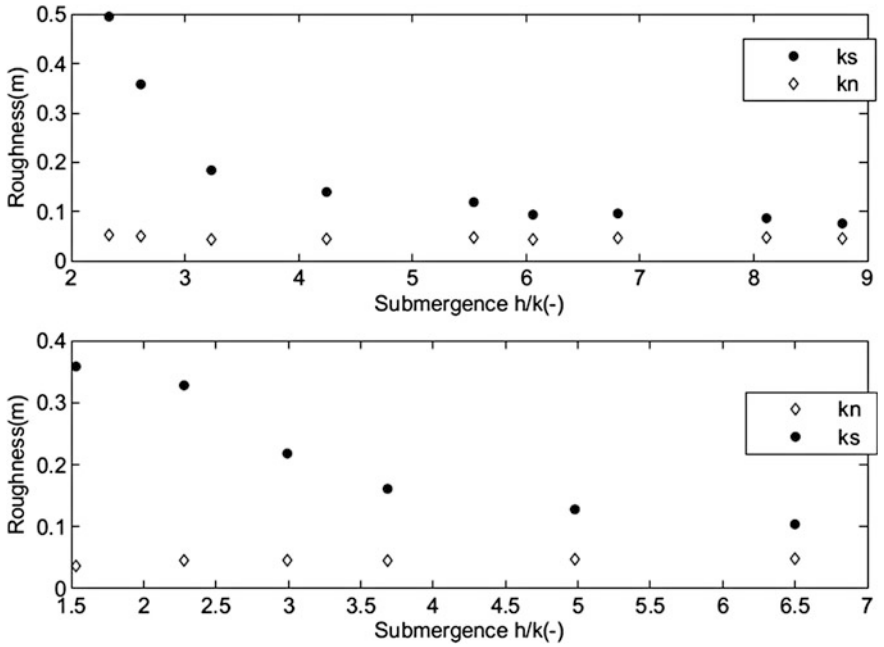

Fig. 4 Run 3–4. Horizontal axis: submergence ratio (h/k). Vertical axis: roughness coefficients. *Squares* represent Strickler's roughness; *diamonds* Nikuradse's roughness

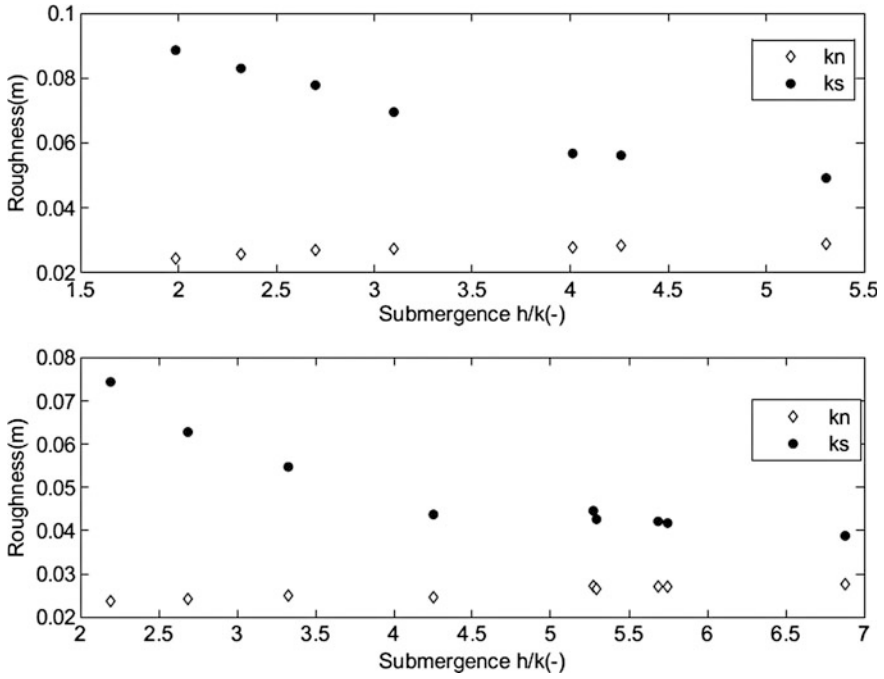

Fig. 5 Run 5–6 Horizontal axis: submergence ratio (h/k). Vertical axis: roughness coefficients. *Squares* represent Strickler's roughness; *diamonds* Nikuradse's roughness

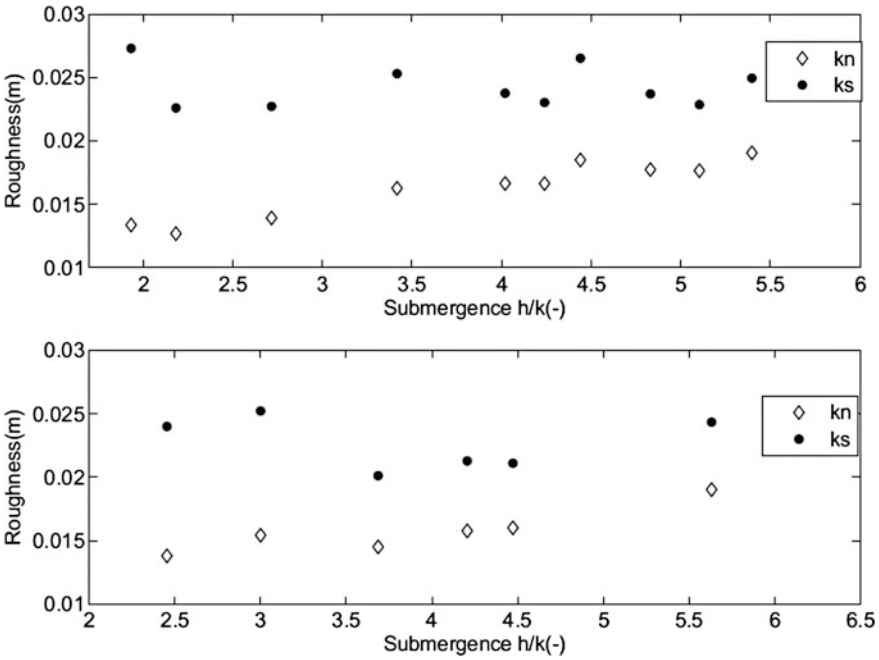

Fig. 6 Run 7–8. Horizontal axis: submergence ratio (h/k). Vertical axis: roughness coefficients. *Squares* represent Strickler's roughness; *diamonds* Nikuradse's roughness

4 Discussion

In the experimental work we collected a total of 76 points for different hydraulic conditions by varying flow discharge Q, channel slope S, flow depth h (and consequently hydraulic radius R too) and vegetation dimensionless density λ in ten different runs.

As expected, trends for coefficients k_N and k_S are different but it is noteworthy that each curve exhibits a horizontal trend for increasing submergence ratio; according to Augustijn et al. (2008), conventional resistance equations seem to work better at higher levels of submergence (h/k equal to 5 or more) but, in spite of a general idea, at the first sight, the Nikuradse roughness height k_N seems to have a trend more horizontal than Strickler roughness height k_S also for a submergence value less than 5. In future research it is necessary to deepen our knowledge about this trend, trying to evaluate roughness height behavior with further experimental studies as a function of hydraulic parameters and finally identify the best resistance formula that must be used.

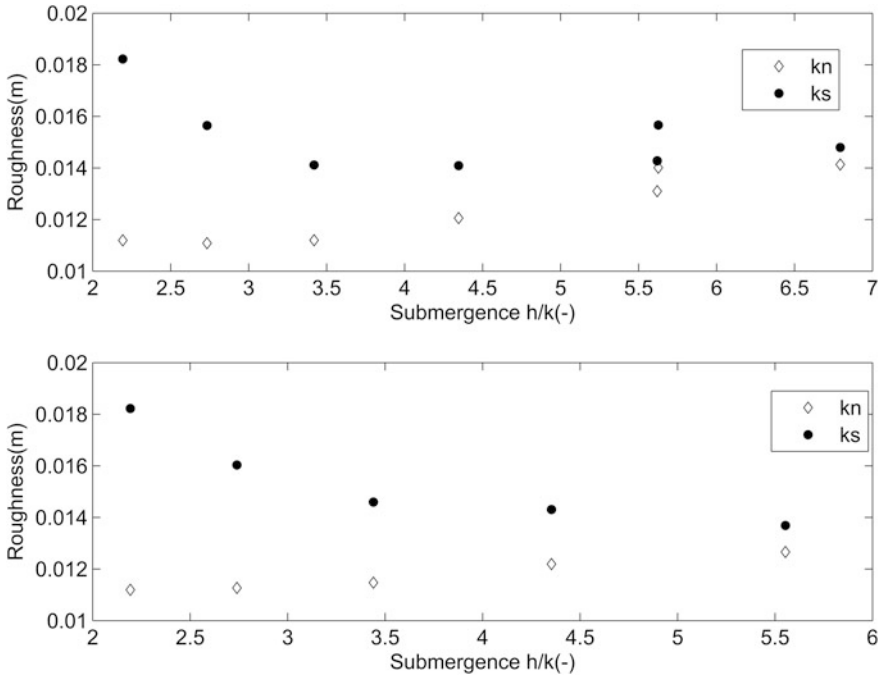

Fig. 7 Run 9–10. Horizontal axis: submergence ratio (h/k). Vertical axis: roughness coefficients. *Squares* represent Strickler's roughness; *diamonds* Nikuradse's roughness

5 Conclusions

At present, the vegetation resistance is evaluated using friction factors depending on hydraulic parameters such as Froude number F, Reynolds number Re, cross-sectional shape η, etc.; however, lots of authors (Lopez and Garcia 2001; Huthoff et al. 2007; Augustijn et al. 2008; Nepf 2012; Konings et al. 2012; Huthoff et al. 2013; Mrokowska et al. 2014) examined the use of conventional flow resistance equations and, hence, using classic roughness height for vegetated flows in which submergence ratio was more than 5, i.e. $h/k > 5$. Thanks to this, in our experimental work we collected 10 runs for different hydraulic conditions, finding effectively that Nikuradse and Strickler roughness heights, k_N and k_S, assume constant value for high submergence. However, at the first sight, the Nikuradse roughness height seems to the authors to assume more stable values than k_S, meaning that maybe it could be considered more suitable to evaluate vegetation resistance in case of high submergence, also if this would have to be studied in depth with statistical methods. However, this result could be considered significant as Strickler's (or Manning's) roughness height is largely used in lots of hydrodynamic models for vegetated floodplains.

Clearly this has to be investigated and deepened in future research, in which the authors will try to develop a new hydraulic model directly linked with vegetation density λ and vegetation height *k*.

Acknowledgments Vittorio Pasquino wants to acknowledge his Ph.D. Supervisor, Professor Guelfo Pulci Doria (1942–2014) for his unforgettable teachings and advices.

References

Augustijn DCM, Huthoff F, van Velzen EH (2008). Comparison of vegetation roughness descriptions. In: Proceedings River Flow 2008 International Conference, Izmir, Turkey, 343–350

Beecham S, Khiadani MH, Kandasamy J (2005) Friction factors for spatially varied flows with increasing discharge. J Hydraul Eng-ASCE 131:792–799

Chow VT (1988) Open Channel Hydraulics. Mc-Graw Hill, New York, NY, USA

Ferguson R (2010) Time to abandon the manning equation? Earth Surf Process Landforms 35:1873–1876

Gioia G, Bombardelli FA (2002) Scaling and similarity in rough channel flows. Phys Rev Lett 88 (1):14501–14504

Huthoff F (2012) Theory for flow resistance caused by submerged roughness elements. J Hydraul Res 50(1):10–17

Huthoff F, Augustijn DCM, Hulscher SJMH (2007) Analytical solution of the depth averaged flow velocity in case of submerged rigid cylindrical vegetation. Water Resour Res 43:W06413. doi:10.1029/2006WR005625

Huthoff F, Straatsma WM, Augustijn DCM, Hulscher SJMH (2013) Evaluation of a simple Hydraulic resistance model using flow measurements collected in vegetated waterways. *Open J Mod Hydrol* 3: 28–37. http://dx.doi.org/10.4236/ojmh.2013.31005

Konings AG, Katul GG, Thompson SE (2012) A phenomenological model for the flow resistance over submerged vegetation. Water Resour Res 48:W02522. doi:10.1029/2011WR011000

Lopez F, Garcia M (2001) Mean flow and turbulence structure of open-channel flow through nonemergent vegetation. J Hydraul Eng 127(5):392–402

Mrokowska MM, Rowiński PM, Kalinowska MB (2014) Notes on the estimation of resistance to flow during flood wave propagation. Hydrol Earth Syst Sci Discuss 11:13311–13352

Mrokowska MM, Rowiński PM, Kalinowska MB (2015) A methodological approach of estimating resistance to flow under unsteady flow conditions. Hydrol Earth Syst Sci 19:4041–4053. doi:10.5194/hess-19-4041-2015

Nepf HM (2012) Hydrodynamics of vegetated channels. J Hydraul Res 50(3):262–279

Powell M (2014) Flow resistance in gravel-bed rivers: progress in research. Earth-Sci Rev 136:301–338

Yen BC (2002) Open channel flow resistance. J Hydraul Eng 128(1):20–39

Effective Method for Continuous Measurement of Bedload Transport Rates by Means of River Bedload Trap (RBT) in a Small Glacial High Arctic Gravel-Bed River

Waldemar Kociuba

Abstract The determination of the threshold values and parameters of bedload transport in river beds is necessary for undertaking effective hydrotechnical works, including anti-flood, retention, energy engineering measures, etc. This paper presents a new device for the continuous measurement of movable bed-surface particles, namely the "River Bedload Trap—RBT" *[European patent No. EP 2333161]*. The article discusses the methodological difficulties in the effective estimation of bedload transport rate. It presents an innovative measurement strategy and device with the potential to satisfy the stringent requirements set by fluvial geomorphology and hydrotechnical analyses. The applied technical solution based on direct continuous measurement and anchored RBT sets is analysed in detail and compared to the existing measurement systems. The study confirmed the high effectiveness of the implemented measurement strategy and technical solution for quantitative bedload transport rates and flux. The application of RBT for continuous monitoring of bedload flux in the conditions of High Arctic gravel-bed rivers was evidenced to permit obtaining high efficiency and credible results.

1 Introduction

Fluvial transport, and particularly its rate and texture, is a good indicator of the condition of the natural environment in various climatic zones (Beylich and Warburton 2007). The analysis of fluvial transport components permits precise specification of the rate and direction of transformations of geoecosystems of any significance. The estimation of bedload flux is an important indicator of changes in the regime of river systems. The amount of movable bedload particles, constituting

W. Kociuba (✉)
Faculty of Earth Sciences and Spatial Management,
Maria Curie-Skłodowska University, Lublin, Poland
e-mail: waldemar.kociuba@umcs.pl

P. Rowiński and A. Marion (eds.), *Hydrodynamic and Mass Transport at Freshwater Aquatic Interfaces*, GeoPlanet: Earth and Planetary Sciences,
DOI 10.1007/978-3-319-27750-9_23

a resultant of the geomorphic processes in the river basins, is one of the elements of identification of the mechanisms of fluvial transport (Reid et al. 1980; Ergenzinger and Schmidt 1994; Powell et al. 1998; Bogen and Møen 2003; Bogen et al. 2003; Laronne et al. 2003; Hassan et al. 2005; Rickenmann and McArdell 2007; Vatne et al. 2008; Raven et al. 2010; Turowski et al. 2010, 2011; Rickenmann et al. 2012; Beylich and Laute 2014; Kociuba and Janicki 2014; Kociuba et al. 2014). The determination of the bedload flux provides an important indicator of the origin, routes of distribution, and conditions of bedload transport and deposition (Kociuba and Janicki 2014; Beylich and Laute 2014). In the cold-climate environment, bedload flux shows high temporal and spatial variability (Kociuba et al. 2010, 2014; Beylich and Laute 2014; Kociuba and Janicki 2013, 2014). It is primarily determined by climate-driving factors, i.e. temperature, precipitation, and rate of ablation (Østrem et al. 1967; Ashworth and Ferguson 1986; Gurnell and Clark 1987; Warburton 1990; Kociuba and Janicki 2014).

The basic feature distinguishing bedload flux in the Arctic morphoclimatic zone is the local character of bedload supply to fluvial waters (Hammer and Smith 1983), and predominance (70–90 %) of loads transported during flood flows (Orwin et al. 2010). The determination of the velocity and volume of transported bedload, sources and tracks of sediment delivery, and the assessment of conditions of its transport and deposition are very important for the accurate assessment of the present mechanisms of adaptation of the channel systems to the high-rate of changes in environmental conditions (Kociuba et al. 2010, 2014; Kociuba and Janicki 2014).

The determination of the threshold values and parameters of bedload transported in river beds is necessary for undertaking effective hydrotechnical works, including anti-flood, retention, energy engineering measures, etc.

The objective of the paper is to present the River Bedload Trap (RBT) as a new device for continuous measurement of movable bed-surface particles, and to determine the complex character of bedload transport processes in the context of methodological difficulties in the effective estimation of bedload transport rate.

2 Method

The effective determination of the amount of transported bedload is of high importance for research on fluvial geomorphology, as well as for hydrotechnical works (e.g., Rickenmann and McArdell 2007; Raven et al. 2010; Turowski et al. 2011; Rickenmann et al. 2012, Beylich and Laute 2014, Kociuba and Janicki 2014). This particularly concerns regions distinguished by considerable volumes of bedload transported by rivers (e.g. montane or Arctic regions). Their severe climate and orographic conditions determine the applied methodology and devices (e.g., Reid et al. 1980; Ergenzinger and Schmidt 1994; Powell et al. 2001; Bogen and Møen 2003; Froehlich 2003; Bogen et al. 2003; Laronne et al. 2003; Hassan et al. 2005;

Rickenmann and McArdell 2007; Bunte et al. 2008; Vatne et al. 2008; Raven et al. 2010; Turowski et al. 2010, 2011; Kociuba et al. 2010, 2014; Rickenmann et al. 2012; Beylich and Laute 2014; Kociuba and Janicki 2014).

2.1 Comparison of RBT with Other Bedload Measurement Systems

Devices continuously collecting bedload material in the channel bed (e.g. Milhous 1973; Hayward and Sutherland 1974; Tacconi and Billi 1987; Reid et al. 1980, 2002; Zwoliński 1989, 1993; Lewis 1991; Powell et al. 1998; Garcia et al. 2000; Sear et al. 2000; Rickenmann et al. 2012) are considered the most effective (e.g. Milhous 1973; Hayward and Sutherland 1974; Tacconi and Billi 1987; Reid et al. 1980, 2002; Zwoliński 1989, 1993; Lewis 1991; Powell et al. 1998; Garcia et al. 2000; Sear et al. 2000; Rickenmann et al. 2012) among other numerous direct methods. Techniques employing such devices are described as "mobile particles collection". Permafrost conditions (Arctic region) usually do not permit digging and permanent embedding of such devices. Systems of continuous bedload monitoring, such as Vortex or Birkbeck (Table 1), as well as modern measurement methods, e.g., luminescent, magnetic, radio-emitter, radioisotope, or acoustic method (Bogen and Møen 2003; Froehlich 2003; Bogen et al. 2003; Rickenmann et al. 2013; Beylich and Laute 2014), require electricity supply. This makes their application in the high-energy conditions of mountain or polar rivers difficult.

Good effects are obtained by the application of direct samplers permitting immediate measurement of bedload transport rate and obtaining material for GSD analyses. The application of portable bedload samplers of the Helley-Smith type (Helley and Smith 1971; Emmett1980; Bunte et al. 2008; Beylich and Laute 2014), however, is restricted due to the low representativeness (spot measurement in a short term) and a decrease in efficiency in the case of medium- and coarse-grained (>16 mm) gravels. Due to the small opening (7.6–10 cm), only transport of grains not exceeding 64 mm can be measured efficiently. The measurement technique requires significant interference of the operator in the sampling process.

Much better effects are obtained using a device anchored in the river bed during the measurement (Table 1). Results obtained by means of CSU/FS bedload traps (Bunte and Abt 2009) show high efficiency of sampling. This permits accurate description of the relations between the hydrological conditions of the stream and bedload flux.

The group of "anchored samplers" also includes a new device for measurement of bedload transport rate in river beds, namely the "River Bedload Trap—RBT". It is a portable sampler designed for trapping material transported in the river channel as a result of dragging, and directly above the bed—in saltation and suspension (Fig. 1). The device has obtained a patent in Poland [*No. 210267*] and Europe [*EP 2333161*].

Table 1 Usefulness of the devices for the measurement of bedload transport rate

	Continuous measurement, restricted time			Point measurement, short term			Anchored samplers[a] continuous measurement, flexible term	
Sampler features	Vortex sampler	Birkbeck sampler	Unweigh-able pit traps	Basket sampler	H-S pressure-difference sampler	Large pressure-difference sampler	CSU/FS bedload trap Net-frame sampler	RBT
Facility of operation	±	+	±	±	+	–	–	+
Portability	–	–	+	±	+	+	±	±
Anchorage in the river bed	+	+	+	–	–	–	±	+
Manner of anchoring in the river bed[b]	–	–	–	±	+	±	±	+
Width of the input opening	+	+	+	+	–	±	+	+
Restriction of measurement term	+	+	+	±	–	–	+	+
Possibility of sampling for GSD analysis	+	–	±	+	+	+	+	+

[a]continuous measurement possible; [b][—] interference in the shape of the river bed. *Source* Bunte et al.2004 [*amended by the author*]

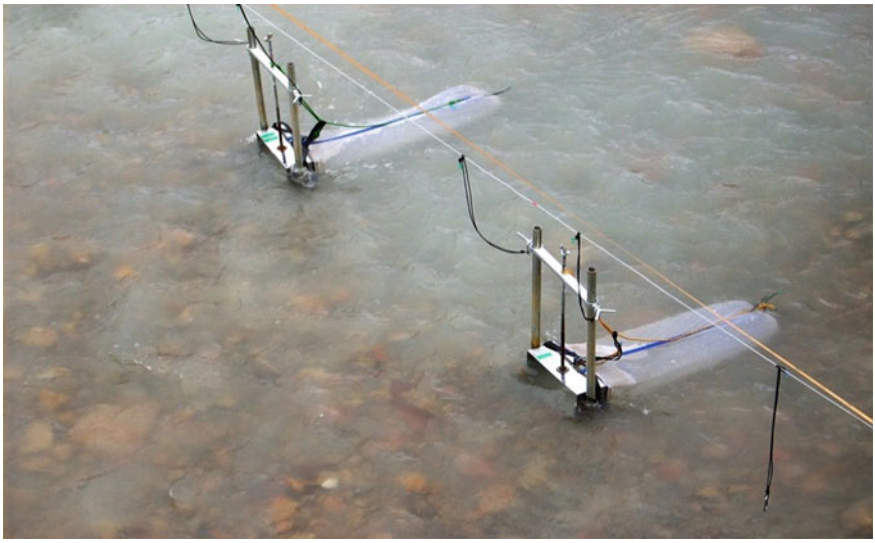

Fig. 1 An example of RBT devices (2 modules) in the Scott River

The proposed direct samplers including a set of anchored RBT modules were applied in the measurements in the Scott River catchment.

2.2 Basic Parameters and Advantages of the RBT Sampler

The RBT sampler is applicable in gravel-bed rivers in the presence of a coarse surface layer composed of clean gravel and cobble. The sampler is equipped in a securing system anchored in the bed and banks of the river channel, as well as an 8-point horizontal and vertical stabilisation system ensuring perfect contact of the sampler with the channel bottom, and permitting maintaining a constant position during the measurement with no necessity for the operator's interference (Fig. 2). The high capacity of the container permits flexible selection of the measurement term from several minutes (Rachlewicz and Zwoliński 2012) up to 24 h (Kociuba et al. 2010), adjusted to the transported fractions and hydraulic conditions of the river channel. The size of grains possible to sample in case of net-containers for cobble and gravel fractions (maximum mesh 2 mm) ranges from 2 to 256 mm.

The modular structure, facility of use, and short term of emptying/arming (from 2 to 5 min at each measurement site) permit maintaining measurement continuity. The high quality of materials used ensures the device's long working life with no need for repairs.

Fig. 2 Example measurement profile comprising RBT devices (5 modules) with the securing system

2.3 Advantages of RBT

- *Assembly*: easy; independent; at the measurement site; modular construction;
- *Operation*: easy; one-man operation in conditions permitting operation (preferred depth enabling entering the river by operator—up to 1.3 m—or operation from a boat or bridge);
- *Manner of measurement*: direct, continuous;
- *Measurement term*: flexible measurement term adjusted to the hydraulic and morphological conditions of the river; possibility for conducting continuous measurement in assumed time intervals, e.g. 3, 6, 12, 24 h;
- *Manner of assembly*: sampler anchored in the channel bed, 8 points of horizontal and vertical stabilisation; proportional distribution in the channel cross-profile, permitting the estimation of the spatial differentiation of the process;
- *Location of measurement*: always at the same measurement sites;
- *Contact with the channel bed*: regulated pressure on the bed, does not change the shape of the cross profile, does not require digging in the bed or assembly of a base;
- *Time of operation of a measurement site*: 2–5 min;
- *Time of operation of the entire measurement profile*: 10–20 min;
- *Manner of operation*: directly by the operator, operation entirely above the water surface;
- *Material*: sampler made of thin stainless sheetmetal (the highest efficiency mentioned in the literature on the subject, e.g. Ryan and Porth (1999))
- *Maximum sample volume*: 45–50 kg;

- *Optimum sample volume (up to 40 % of container/sample bag capacity)*: 18–20 kg;
- *Maximum sampler width*: from 0.4 m (version for sand and fine gravel fractions) to 0.25 m (version for gravel and coble fractions); universal width of 0.3 m; size and proportions of the body ensuring free trapping of grains of up to 128 mm;
- *Maximum RBT sampler length*: 0.9 m (minimum container length: 0.75 m);
- *Maximum RBT sampler capacity*: approximately 0.5 m^3;
- *Size of grains possible to trap*: 0.25–256 mm; depending on the mesh size, possible application of nets for gravel fractions (maximum mesh 2 mm), or for sand fractions (maximum mesh 0.25 mm);
- *Method of measurement of bedload transport rate*: based on weight or volume;
- *Measurement efficiency*: efficiency of particle trapping, relatively low hydraulic resistance of the body and container;
- *Security during operation*: system securing the device against damage (collision with floating matter, e.g. logs, ice floats, etc.);
- *Infrastructure*: does not require electricity supply;
- *Possibility for performing GSD analysis of material sampled*: yes.

Anchored RBT devices, proportionally distributed in the channel cross-profile, combine the advantages of portable H-S samplers (facility of use, immediate result, one-man operation), CSU/FS bedload traps (high efficiency, stability—anchorage in the channel bed), and continuous measurement systems (permanent measurement sites, continuous measurement) with simultaneous lack of restrictions in the measurement series duration.

2.4 Measurement Strategy and Bedload Transport Rate Estimation

The measurement of bedload transport volume and rate at the monitoring sites involving the application of RBT (Fig. 2) in the scope of the author's own programme commenced in 2009 (Kociuba et al. 2010). The even distribution of RBTs (every 1.5–2 m) in the channel cross-profiles permitted the determination of both the temporal and spatial variability of bedload transport. Bedload collected by each of the traps was drained and weighed for the purpose of calculating bedload transport rate and flux. The measurement was performed in a daily cycle (every 24 h) at constant times.

Bedload transport rate [q_b (in kg m^{-1} d^{-1})] in the measurement profiles was calculated based on the weight of the collected bedload [G_s (in kg)].

$$q_b = \frac{G_s}{S_w T} \text{ (kg m}^{-1}\text{d}^{-1}\text{)}$$

where

G_s is the sample weight (in kg),

S_w is the sampler width (in m), and

T is total sampling time (in 24 h).

Total bedload flux (Q_b) was calculated as the quotient of the mean cross-section transport rate q_a and channel width [w_c (in m)].

3 Results of Application of RBT for Bedload Transport Measurement

The effectiveness of operation of RBT devices was confirmed in a monitoring study (2009–2013) conducted by the Maria Curie-Skłodowska University, Lublin, in the Scott River catchment on SW Spitsbergen (Kociuba et al. 2010, 2012, 2014; Kociuba and Janicki 2014), and by the University of Adam Mickiewicz, Poznań, in the Dynamisk Bekken catchment on Central Spitsbergen (Rachlewicz and Zwoliński 2012). Both of the experimental field studies were carried out in gravel-bed streams (Scott River with a glacial alimentation regime—NW part of the Wedel-Jarlsberg Land, and non-glaciated Dynamisk Bekken catchment—Central Spitsbergen) are incorporated to test areas I.A.G./A.I.G. Working Groups: 'SEDIBUD' (Sediment Budgets in Cold Environments).

3.1 Experimental Field Study with the Application of RBT

The RBT sampler was designed by the author for the purposes of a research project of the Deputy Rector of the Maria Curie-Skłodowska University for Scientific Studies and International Cooperation, entitled: "The functioning of the channel and slope system of the sub-polar zone in the conditions of global climate changes", implemented in the Scott River catchment in 2009. Bedload transport rates measured by means of a set of original RBT sets constructed by the author were analysed over five consecutive melt seasons (2009–2013) in two cross-sections located in the lower course of the gravel-bed proglacial Scott River. The first series of continuous measurements (2009) obtained in one cross profile over two months (59 measurement days; 227 samples taken) was the first successful attempt of the quantitative estimation of bedload transport dynamics in the rivers of the Wedel-Jarlsberg Land (Spitsbergen) (Kociuba et al. 2010, 2014). During five consecutive melt seasons, a total of 1224 samples of transported bedload were collected over 220 measurement days. Approximately 21 tons of moving bedload particles was discharged by the river through the cross-profile closing the catchment above the alluvial fan. The mean daily bedload flux Q_b in particular measurement profiles varied from 88 to 128 kg day^{-1}. It showed high variability in particular seasons, from 46 (2012) to 242 kg day^{-1} (2011).

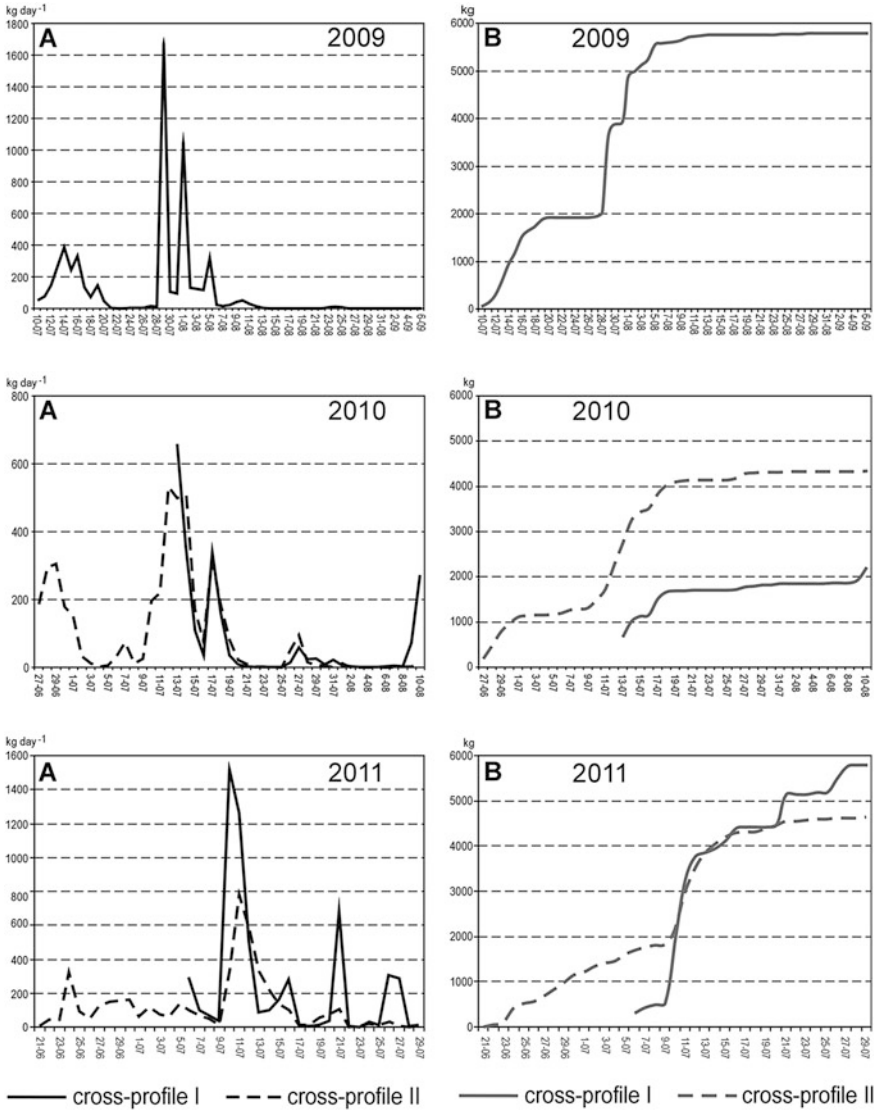

Fig. 3 Diagram of spatial and temporal variability of bedload transport. Course of daily bedload flux in analysed cross-profiles during consecutive measurement periods (**a**). Cumulative diagram of the bedload flux discharged over each of the cross-profiles (**b**)

The variability of the amount of transported bedload during melt seasons 2009–2011 is presented in Fig. 3. The visible disproportion of consecutive measurement periods (between particular cross-profiles) was dependent on the moment of disappearance of the ice cover.

The obtained results suggest high variability of daily and seasonal values of bedload flux. The maximum daily bedload flux reached 1670 kg day^{-1} (2009), 660 kg day^{-1} (2010), and 1518 kg day^{-1} (2011). The max. volume of bedload discharged over each of the measurement periods through cross-profiles was estimated at 5784 kg (59 days), 4345 kg, and 5814 kg, respectively.

The analysis of the distribution of daily values of bedload flux also suggests high variability of bedload transport in the analysed channel cross-profiles. The highest disproportion was recorded during melt season 2011, where in spite of a 40 % longer measurement period in the second cross-profile, the volume of bedload discharged by the Scott River was lower by 20 % (Fig. 3). This suggests the tendency for aggradation and deposition of bedload particles within the alluvial fan separating both of the cross-profiles.

The course of bedload flux shows the fluctuating character of bedload movement. Periods of intensive bedload movement are alternated with periods of low activity, or even stagnation (Fig. 3). Intensive transport results from the occurrence of flood flows, and occurs several times (usually from 2 to 3 times) over a snowmelt season. First, it occurs in the period of melting of the snow cover at the end of June. The next ones, usually occurring around mid-July and in the second half of August, are distinguished by considerable bedload flux values. They play the dominant role in the total volume of discharged bedload.

The measurements confirmed the dominance of bedload transport during floods. The volume and rate of bedload flux were determined by the frequency of occurrence of flood discharges. The highest daily values recorded in consecutive seasons constituted from 12 to 73 % of total bedload flux during each melt-season. The multi-seasonal analysis revealed high temporal and spatial variability of bedload transport rate, resulting in changes in the morphology of the channel, and during floods, also the valley floor (Kociuba et al. 2012; Kociuba and Janicki 2014). From 2010, all collected samples were subject to GSD analyses (Kociuba and Janicki 2015).

Szpikowski et al. (2014) points out the important role of bedload transport via traction and saltation as a significant portion of denudational material discharged from the Dynamisk Bekken catchment. The field study in the catchment involving the application of RBT, performed in August 2012, confirmed the important role of precipitation floods for a total sediment yield. Measurements of water discharge and bedload by the RBT sampler (Kociuba et al. 2010) were conducted at three sites: in the central part of the watercourse (at the end of the valley near the Wordiekammen Massive in the upper part of the alluvial fan), in the central part of the alluvial fan, and in the lower part of the alluvial fan (Szpikowski et al. 2014). Monitoring of bedload transport was conducted in selected straight stream sections with a very gentle slope (the mean slope of the longitudinal profile of the brook within the alluvial fan is 74 ‰), where water flows in a single channel. RBT samplers were in operation for 5–10 min at each location. The volume of bed material collected over this short term varied from 25 to 29 kg (Rachlewicz and Zwolinski 2012). This preliminary study in the Dynamisk Bekken catchment suggests a high proportion of bedload in the overall amount of sediment discharged from the catchment. The

observations suggest that bedload transport concerns various fractions of medium- and coarse-grained sand as well as cobbles. The author also highlights that in periods of low discharge, the proportion of bedload material decreases considerably. The author concludes that an increase in this form of sediment discharge occurs at the beginning of the ablation season, i.e. in June. This confirms the results obtained by Kociuba and Janicki (2014, 2015) in the Scott River catchment, although has not yet been subject to field research in Dynamisk Bekken.

4 Conclusion

- The innovative measurement strategy and equipment (RBT device) applied in this study has the potential to satisfy the stringent requirements set by fluvial geomorphology and hydrotechnical analyses.
- In comparison to the existing measurement systems, the applied technical solution based on direct and continuous measurement and anchored RBT set proved to be highly effective in the case of determination of quantitative bedload transport rates and flux. The application of RBT for continuous monitoring of bedload flux in the conditions of High Arctic gravel-bed rivers was evidenced to permit obtaining high efficiency and credible results.
- The implementation of the original research strategy and technique of bedload transport measurement by means of RBT devices will permit measurement standardisation and development of a unified research strategy, postulated by a number of scholars (among others Warburton 1990; Beylich and Warburton 2007; Zwoliński 2007).
- Due to the considerable values of the innovative equipment (RBT), i.e. high measurement efficiency and facility of operation, it can be applicable in the calibration of electro-acoustic devices, so far performed by means of less efficient methods (e.g. Bogen and Møen 2003 or Beylich and Laute 2014).
- The research shows high temporal and spatial variability of the volume of transported bedload and its "episodic" character. The determined effect of flood flows on bedload transport was also confirmed. The highest daily values recorded in consecutive seasons constituted 73 % of total bedload flux.
- Spatial variability manifested in the disproportion of bedload flux in the analysed cross-profiles was evidenced. Lower bedload flux values recorded in the analogical measurement periods in the measurement profile closing the catchment below the alluvial fan show the predominance of aggradation tendencies.

Acknowledgements The study was supported by grant of the National Science Centre No. 2011/01/B/ST10/06996 and project POIG.01.03.02-00-082/10, EU in the scope of the Operational Programme Innovative Economy, 2007–2013, Priority 1. 'Research and development of modern technologies'. I am particularly grateful to all of the colleagues included in the team of the Maria Curie-Skłodowska University Polar Expeditions for their collaboration in the field and at other stages of the research.

References

Ashworth PJ, Ferguson RI (1986) Interrelationships of channel processes, changes and sediments in a proglacial braided river. Geogr Ann 68A:361–371

Beylich AA, Warburton J (eds) (2007) Analysis of source-to-sink fluxes and sediment budgets in changing high-latitude and high-altitude cold environments. SEDIFLUX Manual, 1st edn. Norwegian Geological Survey Report, 158 pp

Beylich AA, Laute K (2014) Combining impact sensor field and laboratory flume measurements with other techniques for studying fluvial bedload transport in steep mountain streams. Geomorphology 218:72–87

Bogen J, Moen K (2003) Bed load measurements with a new passive acoustic sensor. In: Bogen J, Fergus T, Walling DE (eds) Erosion and sediment transport measure-ment in rivers: technological and methodological advances, vol 283. IAHS, Wallingford, pp 181–192

Bogen J, Fergus T, Walling DE (eds) (2003) Erosion and sediment transport in rivers: technological and methodological advances, vol 283. IAHS, Wallingford, 238 pp

Bunte K, Abt SR (2009) Transport relationships between bedload traps and a 3-inch Helley-Smith sampler in coarse gravel-bed streams and development of adjustment functions. Report submitted to the Federal Interagency Sedimentation Project, Vicksburg, MS, 138 pp

Bunte K, Abt SR, Potyondy JP, Swingle KW (2008) A comparison of coarse bedload transport measured with bedload traps and Helley-Smith samplers. Geodin Acta 21(1/2):53–66. http://www.treesearch.fs.fed.us/pubs/30814

Bunte K, Abt SR, Potyondy JP, Ryan SE (2004) Measurement of coarse gravel and cobble transport using a portable bedload trap. J Hydraul Eng 130:879–893

Emmett WW (1980) A field calibration of the sediment-trapping characteristics of the Helley–Smith bed load sampler. US Geological Survey Professional Paper 1139, 44 pp

Ergenzinger P, Schmidt K-H (eds) (1994) Dynamics and geomorphology of mountain rivers. lecture notes in earth sciences,vol 52. Springer, Berlin, Heidelberg, 326 pp

Froehlich W (2003) Monitoring bed load transport using acoustic and magnetic devices. In: Bogen J, Fergus T, Walling DE (eds) Erosion and sediment transport measurement in rivers. Technological and methodological advances. IAHS Publication 283:201–210

Garcia C, Laronne JB, Sala M (2000) Continuous monitoring of bedload flux in a mountain gravel-bed river. Geomorphology 34:23–31

Gurnell AM, Clark MJ (eds) (1987) Glacio-fluvial sediment transfer: an alpine perspective. Wiley, Chichester, 524 pp

Hammer KM, Smith ND (1983) Sediment production and transport in proglacial stream: Hilda Glacier, Alberta, Canada. Boreas 12:91–106

Hassan MA, Church M, Lisle TE, Brardinoni F, Benda L, Grant GE (2005) Sed-iment transport and channel morphology of small, forested streams. J Am Water Res Assoc 41:853–876

Hayward JA, Sutherland AJ (1974) The Torlesse stream vortex-tube sediment trap. J Hydrol (New Zeland) 13:41–53

Helley EJ, Smith W (1971) Development and calibration of a pressure-difference bedload sampler. US Geological Survey Open-File, Report 18 pp

Kociuba W, Janicki G, Siwek K (2010) Dynamics of changes the bed load outflow from a small glacial catchment (West Spitsbergen). In: de Wrachien D, Brebbia CA (eds) Monitoring, Simulation, Prevention and Remediation of Dense Debris Flow III. WITPress, Southampton, Boston, pp 261–270

Kociuba W, Janicki G, Siwek K, Gluza A (2012) Bedload transport as an indicator of contemporary transformations of arctic fluvial systems. In: de Wrachien D, Brebbia CA, Mambretti S (eds) Monitoring, Simulation, Prevention and Remediation of Dense and Debris Flows IV. WIT Press Southampton, Boston, pp 125–135

Kociuba W, Janicki G (2013). Fluvial processes. In: Zagórski P. Harasimiuk M. Rodzik J.(eds) The geographical environment of NW part of Wedel Jarlsberg land (Spitsbergen, Svalbard), Wydawnictwo UMCS, Lublin, pp 192–211

Kociuba W, Janicki G (2014) Continuous measurements of bedload transport rates in a small glacial river catchment in the summer season (Spitsbergen). Geomorphology 212:58–71

Kociuba W, Janicki G, Siwek K (2014) Variability of sediment transport in the Scott River catchment (Svalbard) during the hydrologically active season of 2009. Quaestiones Geographicae 33(1):39–49

Kociuba W, Janicki G (2015) Changeability of movable bed-surface particles in natural, gravel-bed channels and its relation to bedload grain size distribution (Scott River, Sval-bard). Geogr Ann 97A:507–521

Laronne JB, Alexandrov Y, Bergman N, Cohen H, Garcia C, Habersack H, Powell DM, Reid I (2003) The continuous monitoring of bed load flux in various fluvial environments. IAHS Publication 283:134–145

Lewis J (1991) An improved bedload sampler. In: Proceedings of the 5th Federal Inter-agency Sedimentation Conference, Las Vegas, Nevada, Subcommittee of the Interagency Advisory Committee on Water Data, pp 61–68

Milhous R (1973). Sediment transport in a gravel-bottomed stream. PhD thesis, Oregon State University, Corvallis, USA, 232 pp

Orwin JF, Lamoureux SF, Warburton J, Beylich AA (2010). A framework for char-acterizing fluvial sediment fluxes from source to sink in cold environments. Geogr Ann 92A:155–176

Østrem G, Bridge CW, Rannie WF (1967) Glacio-hydrology, discharge and sediment transport in the Decade Glacier area, Baffin Island, N.W.T. Geogr Ann 49A:268–282

Powell DM, Reid I, Laronne JB, Frostick LE (1998) Cross stream variability of bed-load flux in narrow and wide ephemeral channels during desert flash floods. In: Klingeman PC, Beschta RL, Komar PD, Bradley JB (eds) Gravel-Bed Rivers in the Environment. Water Resources Publications LLC, Highlands Ranch, Colorado, pp 177–196

Powell DM, Reid I, Laronne JB (2001) Evolution of bed load grain size distribution with increasing flow strength and the effect of flow duration on the caliber of bed load sediment yield in ephemeral gravel bed rivers. Water Resources Research 37(5):1463–1474

Rachlewicz G, Zwoliński Z (2012) Wykorzystanie urządzenia RBT w pomiarach materiału wleczonego. Efektywność urządzenia RBT na tle innych bezpośrednich metod pomiaru [Use the device RBT in measurements of bed material. The effectiveness of the device RBT to other direct methods of measurement]. MS: 22 pp. (in Polish)

Raven E, Lane SN, Ferguson R (2010) Using sediment impact sensors to improve the morphological sediment budget approach for estimating bedload transport rates. Geomorphology 119:125–134

Reid I, Layman JT, Frostick LE (1980) The continuous measurement of bedload discharge. J Hydraul Res 18:243–249

Reid I, Laronne JB, Powell M (2002) The Nahal Yatir bedload database: sediment dynamics in a gravel-bed ephemeral stream. Earth Surf Proc Land 20:845–857

Rickenmann D, McArdell BW (2007) Continuous measurement of sediment transport in the Erlenbach stream using piezoelectric bedload impact sensors. Earth Surf Proc Land 32:1362–1378

Rickenmann D, Turowski JM, Fritschi B, Klaiber A, Ludwig A (2012) Bedload transport measurements at the Erlenbach stream with geophones and automated basket samplers. Earth Surf Process Landforms 37:1000–1011

Rickenmann D, Laronne JB, Turowski JM, Vericat D (eds) (2013). International workshop of acoustic and seismic monitoring of bedload and mass movements. Birmensdorf, Switzerland, 109 pp

Ryan SE, Porth LS (1999) A field comparison of three pressure-difference bedload samplers. Geomorphology 30:307–322

Sear DA, Damon W, Booker DJ, Anderson DG (2000) A load cell based continuous recording bedload trap. Earth Surf Proc Land 25:672–689

Szpikowski J, Szpikowska G, Zwoliński Z, Kostrzewski A (2014) Magnitude of Fluvial Transport and Rate of Denudation in A Non-Glacierised Catchment in A Polar Zone, Central Spitsbergen. Geogr Ann 96A:447–464

Tacconi P, Billi P (1987) Bed load transport measurement by a vortex-tube trap on Vir-ginio Creek, Italy. In: Thorne CR, Bathurst JC, Hey RD (eds) Sediment Transport in Gravel-Bed Rivers. Wiley, Chichester, pp 583–615

Turowski JM, Rickenmann D, Dadson SJ (2010) The partitioning of the total sediment load of a river into suspended load and bedload: a review of empirical data. Sedimentology 57:1126–1146

Turowski JM, Badoux A, Rickenmann D (2011) Start and end of bedload transport in gravel-bed streams. Geophys Res Lett 38:L04401. doi:10.1029/2010GL046558

Vatne G, Naas ØT, Skarholen T, Beylich AA, Berthling I (2008) Bed load transport in a steep snowmelt-dominated mountain stream as inferred from impact sensors. Norw. J Geogr NorGeogr Tidsskr 62:66–74

Warburton J (1990) An alpinie proglacial fluvial sediment budget. Geogr Ann 72A:261–272

Zwoliński Z (1989) Geomorficzne dostosowywanie się koryta Parsęty do aktualnego reżimu rzecznego. Dokum Geogr 3(4):1–144 (in Polish)

Zwoliński Z (1993). Dynamics of bed load transport in the Parsęta River channel, Poland. In: Marzo M, Puigdefábregas C.(eds) Alluvial Sedimentation Special Publications of the International Association of Sedimentologists 17: 77–87

Zwoliński Z (2007) Hydrological polar monitoring—methodical proposition. Monit Nat Environ 8:29–39 (in Polish)

Step Length Influence in Modelling Advection and Diffusion of Bed-Load Particles

Martina Cecchetto, Simon Tait and Andrea Marion

Abstract A bed-load transport model has been derived in order to attain a better prediction of particle motion along river beds. Scientific studies have now moved towards a particle based approach in order to physically address the actual motion characteristics of the bed grains, such as the distance between entrainment and deposition, i.e. the step length. Step length clearly accounts for the heterogeneity faced by a grain along its path, such as bed roughness, flow intensity, river morphology. In this study, particles' step lengths are regarded as a stochastic variable denoted by a lognormal distribution, whose statistics account for the effect of both bed arrangement and the near bed shearing flow. The 1D Exner equation is then reformulated to account for tracing particles by considering the deposition term as a function of the upstream entrainment events and the displacements computed by a particle before stopping. The implemented numerical method enables the computation of the concentration of bed-load tracers in time and space. As revealed by the model results, the step length distribution acts as a source of diffusion for particle motion along the river bed. The extent of advection and diffusion is not only controlled by the statistics of the step length, but it is also strongly influenced by the level of bed roughness. The thickness of the exchange layer also plays a role in the transport behaviour, as it delays particles temporarily stored in the active layer.

M. Cecchetto (✉) · S. Tait
Department of Civil & Structural Engineering, The University of Sheffield, Sir Frederick Mappin Building, Mappin Street, Sheffield, UK
e-mail: m.cecchetto@sheffield.ac.uk

A. Marion
Department of Industrial Engineering, University of Padua, Via Marzolo 9, 35131 Padova, Italy

P. Rowiński and A. Marion (eds.), *Hydrodynamic and Mass Transport at Freshwater Aquatic Interfaces*, GeoPlanet: Earth and Planetary Sciences,
DOI 10.1007/978-3-319-27750-9_24

1 Introduction

Studies of sediment transport have aimed to investigate river morphology and calculate total or fractional bed-load discharge. Nowadays this process is not completely defined and, as environmental risks are more exposed, scientists tried to formulate physical and mathematical models for bed-load transport. The supply of new sediment or the erosion of deposited sediment can alter a river's ecosystem and its physical-chemical processes. Besides, some pollutants tend to bind to the sediment particles and travel with them. In case of contamination, the sediment acts as a way of transport for potentially damaging chemical compounds. Understanding its motion characteristics, such as travelling time and distances as well as periods of rest, should help develop more appropriate remediation and protection strategies.

Early work on sediment transport prediction was characterized by an empirical approach aiming to quantify the total bed-load discharge. Several empirical calibrated relationships were derived based on bulk, aggregated parameters, such as time and spatially averaged bed shear stress rather than the mechanics of grain movement (Meyer-Peter and Muller 1948; van Rijn 1984). With time, efforts were started to explore the actual motion of particles, considering a particle based approach more appropriate for understanding transport mechanisms (Drake et al. 1987; Einstein 1950). Travelling distance and motion characteristics were then evaluated as functions of hydraulic parameters and/or size distributions (Hassan et al. 1992; McEwan et al. 1948; Wilcock and Kenworthy 2002). Despite the great variability of conditions, mean values for particles motion features were reckoned to be a good compromise for overcoming all the possible realizations. The use of tracers has helped to develop particle-based tracking techniques under the assumption that a subgroup of grains behaves similar to the entire population. Many techniques have been employed when operating with tracers. The most widely used method consists of painted grains, which are followed in subsequent images of the bed acquired at regular time steps (Campagnol et al. 2013; Drake et al. 1987; Hassan et al. 2013; Wong et al. 2007); isotopic tracers were used to estimate sediment budgets in floodplains (Viparelli et al. 2013); magnetically tagged particles were also employed to reconstruct their trajectory over time (Ferguson and Wathen 1998); passive radio tracers allowed to detect particles position without disturbing the bed and guaranteeing high recovery percentages (Bradley and Tucker 2012; Liébault et al. 2011). Experiments of grain motion have encouraged researchers toward a stochastic approach of bed-load transport (Furbish et al. 2012; Ganti et al. 2010; Hassan and Church 2000; Lajeunesse et al. 2010; Wong et al. 2007). Introducing the distribution of particle trajectories into new models of bedload transport is equivalent to simulating the heterogeneity that a grain encounters along its path. Step lengths are then better described by a probability density function influenced by flow characteristics (Hassan et al. 1992; McEwan et al. 2004; Wong et al.2007), along with the bed roughness originated by graded material and particle arrangement (Hassan and Church 2000; Nikora 2001; Pelosi and Parker 2014; Wilcock and Kenworthy 2002). The variety of formulations

proposed in literature consists of exponential distribution (Einstein 1950; Ganti et al. 2010; Sayre and Hubbell 1965), gamma density function (Yang and Sayre 1971), and power laws (Liébault et al. 2011). The distributions of grain step length derived from experiments could be incomplete because of the uncertainty in the evaluation of the longest steps. Nevertheless, what emerges from experiments with tracers is a picture of the character of bed-load particle motion: grains are not only advected downstream but they also diffuse. Turbulent fluctuations along with bed irregularities are believed to be the source of diffusion by Drake et al. (1987). Nikora et al. (2002), Ganti et al. (2010), and Pelosi and Parker (2014) consider bed roughness, especially in well mixed material, as the driving factor of diffusion.

In this study, step length is assumed stochastically distributed and its statistics accounts for the heterogeneity in river channel. Once its stochasticity is included in the 1D Exner's equation, the advective and diffusive behavior of bed-load particles emerges. The influence of bed characteristics is then investigated to show their significance on bed load transport. This work, embedded in the wider study of aquatic interfaces started by HYTECH. HYTECH Project, aims to understand the interaction between water, biota and sediment with a new multidisciplinary approach. Within this framework, the investigation of sediment motion should shed light of processes occurring at the water-sediment interface (Marion et al. 2014).

2 Model Formulation

Changes in local and instantaneous bed elevation depend on the movement of particles within the stream bed. Entrainment and deposition along with the different position occupied by a particle during its motion cause the bed elevation to fluctuate over its averaged value. The Exner equation expressed in entrainment terms describes this process (Ganti et al. 2010; Parker et al. 2000):

$$\left(1-\lambda_p\right)\frac{\partial \eta(x,t)}{\partial t} = D(x,t) - E(x,t) \tag{1}$$

where λ_p, x and t denote, respectively, the bed porosity, the streamwise coordinate and the time. Equation (1) expresses the variation in bed elevation η as a function of the entrainment and deposition rate, namely $E(x,t)$ and $D(x,t)$. When a particle is entrained, it will travel a distance r before it is trapped again in the bed where it will rest at a waiting position before, potentially, being picked up again. The deposition of a particle at a given position x can then be regarded as a function of the entrainment event that has occurred beforehand at an upstream location equal to the particle's travel distance r. With r we define the streamwise particle's step length from the initiation of motion to position of complete rest. As grains experience different bed arrangement and flow intensity along the heterogeneous rivers bed,

step length should be described in stochastic terms via a probability density function $f_S(r)$. Deposition rate is then expressed as:

$$D(x,t) = \int_0^\infty E\left(x - r, t - r/v_p\right) f_S(r) dr \tag{2}$$

with v_p the particle's travelling velocity, and r/v_p the particle's travelling time. Deposition rate, as expressed in Eq. (2), accounts for the likelihood that an entrained tracing particle has travelled for a distance r before being stopped in x. Experiments aiming to study bed-load particle motion tend to use a tracer. Letting f_T (x,t) denote the concentration of tracers, entrainment and deposition rate of tracing particles can thus be formulated as a function of the total entrainment and deposition:

$$E_T(x,t) = E(x,t) f_T(x,t) \tag{3}$$

$$D_T(x,t) = \int_0^\infty E\left(x - r, t - r/v_p\right) f_T\left(x - r, t - r/v_p\right) f_S(r) dr \tag{4}$$

Consider the case of a bed in equilibrium, where neither aggradation nor degradation occurs on average. Under this assumption, the entrainment and deposition rate is constant in x and t, and the only part of the bed deposit exchanging sediment with the bed-load transport is the active layer. This surficial region acts as both source and storage for transported sediment, and it is characterized by thickness L_a (Hirano 1971; Parker et al. 2000).

Equation (1) can then be reformulated in order to obtain the mass conservation for tracers in the active layer assuming a bed in equilibrium:

$$\left(1 - \lambda_p\right) L_a \frac{\partial f_T(x,t)}{\partial t} = D_T(x,t) - E_T(x,t) \tag{5}$$

By combining Eqs. (3) and (4) into Eq. (5), we get:

$$\left(1 - \lambda_p\right) \frac{L_a}{E} \frac{\partial f_T(x,t)}{\partial t} = \int_0^\infty f_T\left(x - r, t - r/v_p\right) f_S(r) dr - f_T(x,t) \tag{6}$$

Equation (6) reveals the importance of particle's step length in addressing bed-load transport. As mentioned earlier, a probabilistic description of step length is essential when dealing with the variability of stream environments.

3 Step Length Distribution

The distance covered by a bed load particle between its entrainment to the position of stop is denoted as the step length. Step length has been widely investigated via experiments. Tracking particles in either laboratory flumes or actual rivers bed has helped to clarify the modes of movement (Drake et al. 1987) and to measure particles' trajectories. In field experiments, where environmental conditions limit the monitoring capability, the distance measured between two consecutive observations is actually the sum of several particle step lengths, resulting in the so-called global trajectory (Nikora et al. 2002) or travel distance. On the other hand, when particles are tracked in laboratory tests, the areal extent of the detected window reduces the number of trajectories observed for describing step length statistics. In other words, particles with step lengths greater than the size of the investigation area cannot be accounted for, as nothing can be assessed about the extent of their trajectory. Experimental evidence and a new approach to sediment transport have revealed the stochastic nature of particles' step length. A grain travelling on the bed experiences a great variety of obstacles (local bed arrangements, bed forms, and channel morphologies), disturbances (aquatic vegetation and animals, human structures), and flow regimes. A description of step length in probabilistic terms should help to include all the encountered heterogeneity. Step length probability distribution should then account for both the flow conditions acting on particles (Hassan et al. 1992; McEwan et al. 2004; Wong et al. 2007) and the roughness produced by different arrangements of bed grains, which greatly affects particle's stability (Hassan and Church 2000; Nikora 2001; Nikora et al. 2002; Wilcock and Kenworthy 2002).

To incorporate these two aspects into the distribution statistics, data collected by Lajeunesse et al. (2010) has been studied. They performed three series of experiments tracking dyed grains' motion in steady uniform flow. The calculated probability density functions $f_s(r)$ allowed them to express the most probable step length, i.e. r in correspondence of the distribution peak, as a function of the excess in shear velocity, u^*-u^*_{critic}, and the particle settling velocity, V_s.

Discarding the shear velocity threshold, their re-analysed data can be fitted by a second order law (Fig. 1) and provides the following most probable step length value for a given grain size d of moving particles:

$$\overline{\mu_r} = d\left[107.8\left(\frac{u^*}{V_s}\right)^2\right] \tag{7}$$

The value obtained with Eq. (7) refers to bed with a nearly uniform grain size distribution, leaving aside the influence of roughness elements on particles motion. Nonetheless, the bed surface topography plays a fundamental role in governing grains displacement and stability in graded bed material (Nikora et al. 2002; Wilcock and Kenworthy 2002). A grain, whose size is greater than the surrounding particles, is more likely to travel for longer distances compared to a grain of smaller

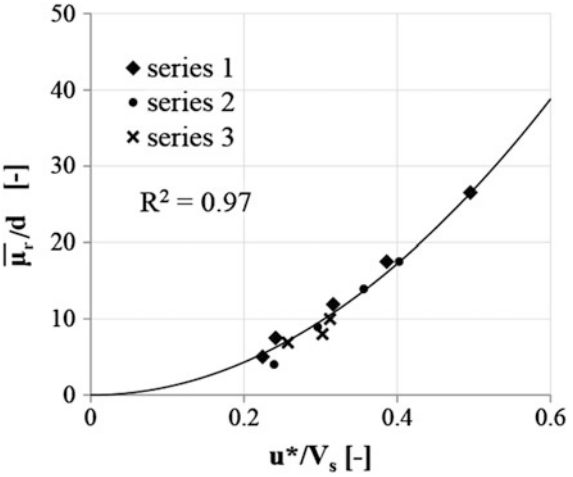

Fig. 1 Most probable step length as a function of shear (u^*) and settling velocities (V_s). Rhombuses, circles and crosses represent values from three experiments with increasing particles size. The continuous line denotes the fitted trendline (after Lajeunesse et al. (2010))

size, which can be easily trapped and stopped by bigger protruding bed elements. To include this effect, Eq. (7) has been adjusted by multiplying the mean step length for the square ratio of the moving particle size over the standard deviation of bed elevation, $(d/\sigma_b)^2$.

The standard deviation of bed elevation can be either obtained from direct experimental measurements or from formulas reported in literature. For instance, in natural gravel beds Nikora et al. (1998, 2001) expressed σ_b as a function of d_{50}, the 50th percentile of particle size distribution of the surficial bed deposit, i.e. 4 σ_b = 1.5 d_{50}. The effect of bed roughness is either to increase the mean travel distance for bigger particles or to reduce it for particles smaller in size than the surrounding "obstacles". On a bed characterized by d_{50}, a grain with doubled size, $2d_{50}$, will undergo a mean step length 30 times greater than the one it would have experienced on a bed of similar material, $2d_{50}$. On the contrary, smaller grains, e.g. of size $0.5d_{50}$, travelling over the same bed, d_{50}, will only double their most probable step length, as their size slightly overcomes the standard deviation of bed level elevation. The square relationship between d and σ_b presented in this study certainly needs confirmation.

It is here assumed that the deviation in step length can be considered proportional to the mean value, that is, $\sigma_r = k\mu_r$, although further investigations are recommended in order to support this hypothesis.

4 Model Parameters

Equation (6) has been numerically solved with a finite difference method in order to obtain the evolution of tracers' concentration in the active layer. The fraction of bed-load tracing particles has been reconstructed along 20 m in the longitudinal

direction for a total duration of 12 min. The numerical grid consists of spatial steps size of 4 mm and time intervals of 1 s. This scheme represents a good compromise between the required computational time and the simulation of particle's travel time and trajectory. The accuracy and the sensitivity of the numerical solution to these spatial and temporal steps should be the subject of further study.

The model, and its parameters, refer to a series of experiments performed by Marion to study the longitudinal and vertical sorting in graded bed deposit (Marion 1995). The simulation depicts the case of coarse sand tracers of uniform size $d_T = 0.8$ mm travelling over a bed consisting of a mixture of both gravel and sand. The bed material is characterized by $d_{16} = 0.13$ mm, $d_{84} = 4.8$ mm and sorting coefficient 1.9 mm. The presented case replicates a typical laboratory experiment, where tracers are injected within the bed and tracked in time and space. The initial fraction of tracing particles is assumed constant along a 3 m long section upstream, and equal to 0.2, which corresponds to the volumetric proportion of material of size 0.8 mm within the bed. In order to increase the mobility of tracers the ratio between shear velocity and tracers critical value was $u^*/u^*_c = 2.15$, which corresponds to Shields parameter far beyond the threshold of incipient motion of sand particles with size $d_T = 0.8$ mm.

According to experimental data (Lajeunesse et al. 2010) step length has been reasonably assumed to be lognormally distributed and in the present simulation the calculated mean value is about $140d_T$ since it accounts for both the flow intensity and the bed roughness. As a first attempt, the standard deviation of step length is considered proportional to the mean value, $\sigma_r = k\mu_r$, with k = 0.4.

The active layer thickness, despite its great variability, is assumed constant in the model. Values of average active layer thickness can be derived either proportional to the mean grain size of the bed deposit mixture, $L_A = 0.5 \div 0.6d_{50}$ (Nikora et al. 1998), or to the standard deviation of bed level elevation, $L_A = 1.62\sigma_b$ (Wong et al. 2007). Both formulations lead to equivalent active layer thicknesses when σ_b is expressed as a function of d_{50} for natural gravel beds, i.e. $4\sigma_b = 1.5d_{50}$.

The entrainment rate E can be measured along the experiments. However, in this study it is calculated by means of Wilcock's formulation for beds deposits consisting of a mixture of sand and gravel (Wilcock and Kenworthy 2002). This formulation is reckoned to better account for the texture structure of the bed on the derivation of entrainment rates.

Particles' travelling velocity v_p is an important parameter for estimating the deposition contribution in x following an upstream entrainment event (Eq. 4). As measurements are not provided, particles' velocity is assumed equal to the mean near bed flow velocity calculated in correspondence to half a tracer's diameter above the bed, i.e. $z = 0.5d_T$. Velocity for different types of rough-bed flows could be derived via the layers subdivision formulation of Nikora et al. (2001).

With the aforementioned set of parameters (named "*original*" in Table 1), a typical solution to Eq. (6) is presented in Fig. 2. It shows that bed-load particles, while being advected downstream, tend to diffuse too. The first and the second moment of the tracers cloud coordinates allowed to quantify respectively the extents

Table 1 Parameters used for the simulations: mean bed material size d_{50}, tracers size d_T, shear velocity over critical shear velocity calculated for tracers u^*/u^*_c, entrainment rate E, tracers' velocity v_p, deviation factor k for step length statistics

	d_{50} (mm)	d_T (mm)	u^*/u^*_c (−)	E (m^3/m^2s)	v_p (m/s)	k (−)	U_A/u^* (−)	E_D/u^*d_{50} (−)
Original (Fig. 2)	1	0.8	2.15	3×10^{-5}	0.17	0.4	0.17	75
k case (Fig. 3a)	1	0.8	2.15	3×10^{-5}	0.17	0.8	0.17	110
u* case (Fig. 3b)	1	0.8	2.40	4.5×10^{-5}	0.19	0.4	0.22	119

The dimensionless advection and diffusion coefficients, U_A/u^* and E_D/u^*d_{50}, respectively, are also presented

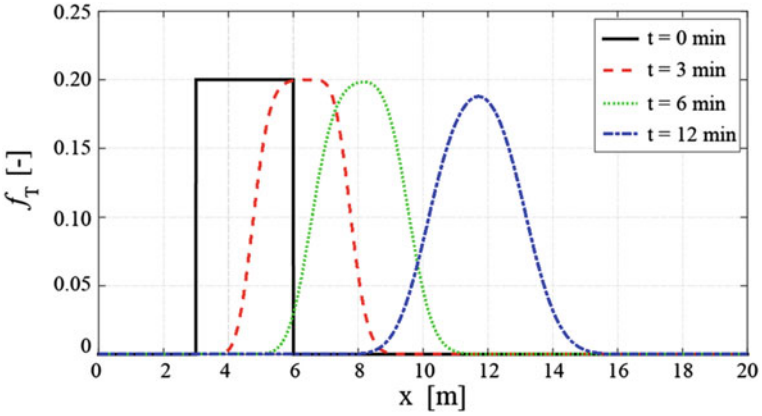

Fig. 2 Solution of Eq. (6), referring to the simulation "*original*" (Table 1). Curves of tracer concentration in the active layer are derived at 3, 6 and 12 min from the initial plateau injection

of the advection and diffusion, later on denoted as advective velocity U_A and diffusion coefficient E_D. The stochastic nature of the step length acts here as a source of diffusion in bed-load transport.

5 Results and Discussion

Since input parameters are either assumed or derived in the previously simulated case (Fig. 2), the model has been tested to obtain the sensitivity of tracers' concentrations in response to changes of flow intensity and step length statistics. Afterwards, the sensitivity of the results to the bed mixture, with regards to the standard deviation of bed level elevation and the thickness of the exchange layer, has also been part of the investigation.

5.1 *Influence of Particle's Trajectory and Flow Intensity*

The standard deviation of particles' step length has an observable uncertainty. In this study, σ_r is assumed positively correlated to the mean step length. The proportional coefficient k has been varied to assess its influence. Figure 3a compares the model solutions when only k changes ("k case" in Table 1). The comparison shows that the coefficient k affects the diffusion leaving advection invariant. A greater diffusion is caused by a broader spectrum of possible particle's steps; this stretches the concentration curves as individual grains can travel for greater or lesser distances.

On the other hand, flow intensity, expressed in the model in terms of shear velocity, affects not only the statistics of the step length distribution but also the entrainment rate. As reported in Table 1 "u* case", an increase of only 10 % in

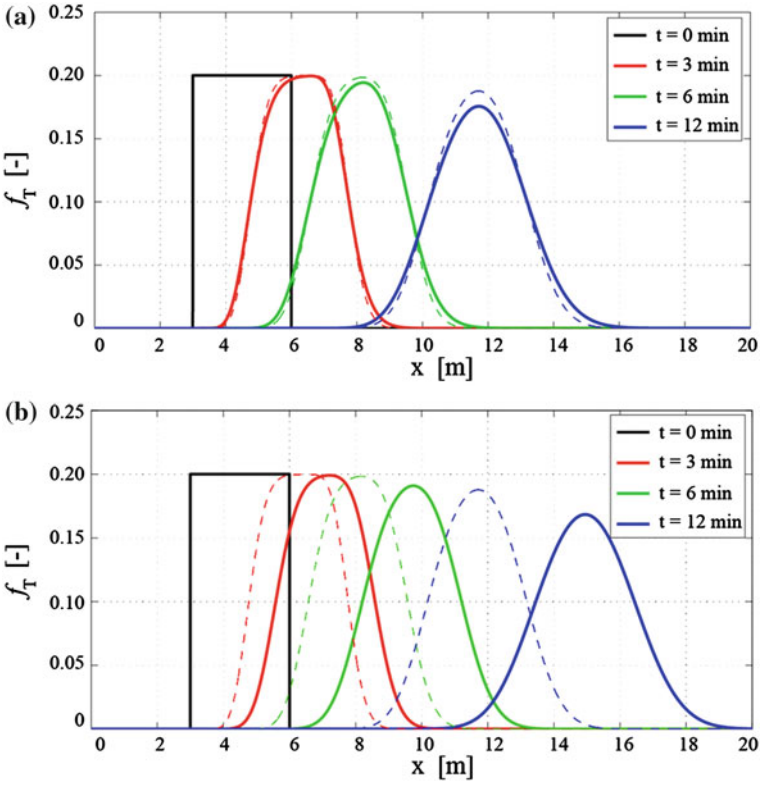

Fig. 3 Model results when k (panel **a**) and u*(panel **b**) vary. *Dashed lines* represent the original solution as reported in Fig. 2. Model parameters are presented in Table 1

shear velocity causes an entrainment rate 50 % greater. This is reflected by an enhanced mobility of tracers, resulting in greater advection velocity and diffusion coefficient (Fig. 3b).

Table 1 reports the parameters used in the simulations along with the dimensionless advection and diffusion coefficients.

5.2 *Influence of the Bed Configuration*

It is interesting to notice how sensitive the model is to the bed configuration and roughness. The standard deviation of bed level elevations and the thickness of the active layer have been previously considered proportional to the mean size of bed material mixture, namely $\sigma_b = k_1 d_{50}$ and $L_A = k_2 d_{50}$. The original values of k_1 and k_2, namely 0.37 and 0.60, respectively, have been varied in order to study their effect on the advection velocity, U_A, and on the diffusion coefficient, E_D. Curves in Fig. 4 are derived for different ratios of tracer size over the mean bed composition diameter, i.e. d_T/d_{50} = 0.4, 0.8, 1.2 and 2.5. This enables the investigation of the behavior of particles of different size when moving over the same bed, as the relative roughness level changes along with the entrainment rate experienced by particles. A rougher bed characterized by higher values of σ_b slows down bed-load particles as they encounter more obstacles along their motion. Advection rate decreases and, consequently, diffusion takes place to a smaller extent (Fig. 4a, b).

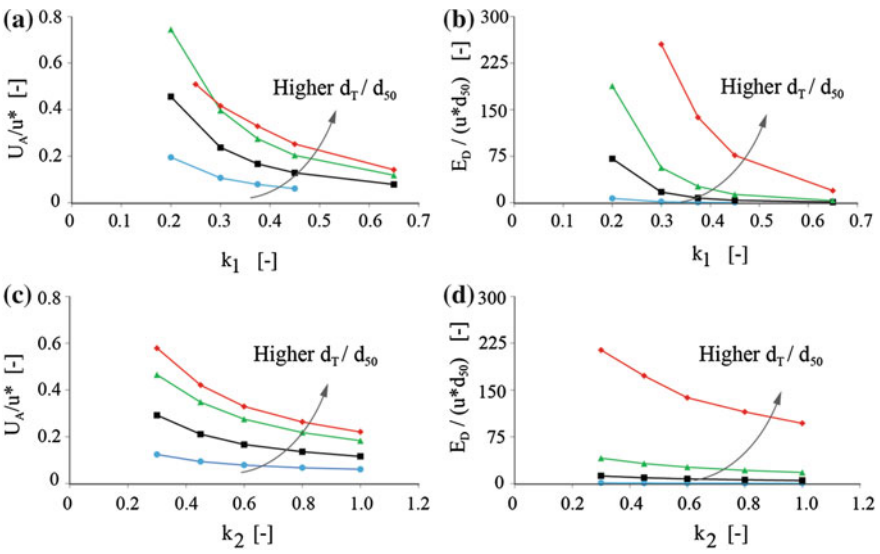

Fig. 4 Dimensionless advection and diffusion rate when varying k_1 (**a** and **b**), and k_2 (**c** and **d**). Plots show the variation for different ratios of d_T/d_{50}, i.e. 0.4, 0.8, 1.2 and 2.5

Likewise, an increase of active layer thickness reduces the advective flux: the thicker the active layer, the more likely the grains get trapped in the bed instead of simply moving downstream (Fig. 4c). A similar trend is observed when dealing with the diffusion coefficient (Fig. 4d). Increasing the active layer thickness does not encourage the diffusion, as particles get trapped in deeper regions of the bed where they are unlikely to be exposed again in the time frame in which the tracers' concentrations are measured. These trends are observed for all the d_T/d_{50} ratios. However, for greater ratios, i.e. tracers comparable or bigger than the bed roughness, the decrease of advection and diffusion rate is more significant, and curves are shifted towards higher values as the size of tracers greatly affects the step length statistics and consequently the motion behavior. Surely the role played by the bed roughness appears more important than the one operated by the active layer, particularly in the variation of the diffusion coefficient. Overall, larger particles experience smaller entrainment rates (about one order of magnitude lower) but this is counterbalanced by the increase in mobility resulting from greater values of step length mean and standard deviation.

The type of diffusion that emerges from the solution of Eq. (6) is anomalous, as the second moments of particle coordinates grow in time with exponent $\gamma = 0.75$, typical of super diffusive regimes (Nikora et al. 2002). The assumption of normal diffusion is no longer sensible when considering the heterogeneity of the particle step length.

One of the key parameters in modeling bed load transport appears to be the bed roughness, since it governs the rate bed load grains move downstream and the thickness of the exchange layer. The storage operated by the active layer greatly affects the motion, suggesting a likely vertical diffusion process for longer time scales. This, together with step length statistics, requires further investigation in order to confirm the model's assumptions.

6 Conclusions

The Exner's equation has been reformulated in order to derive the concentration of bed-load tracing particles in the active layer over time and space for a bed in equilibrium. The implemented numerical model clearly shows the influence river's heterogeneity has on particles motion. Considering grains travel distance as a stochastic quantity brings into the Exner equation the variability of situations a particle can meet, leading to describe its motion as both advective and diffusive. Bed roughness, represented as standard deviation of bed elevation, and flow intensity are the main driving parameters in the step length derivation. In this regard, the role of roughness elements, along with the size of the exchange active layer, has been investigated to show the influence of rivers bed on the motion of particles of different sizes. Step length extent, as well as advection and diffusion rate, is negatively correlated with the bed roughness. Despite the model results, more research is needed in achieving a consistent formulation of the bed roughness

and active layer roles on particle's step length and resting time, since they have been reported merely proportional to the mean bed particle size. Besides, the assumed statistics for step length distribution should be confirmed, particularly the expression of the standard deviation of tracers' travelling distance. This could possibly be achieved via experiments denoted by greater spatial and temporal scales.

Acknowledgments This work was supported by the Research Executive Agency, through the 7th Framework Programme of the European Union, Support for Training and Career Development of Researchers (Marie Curie—FP7-PEOPLE-2012-ITN), which funded the Initial Training Network (ITN) HYTECH 'Hydrodynamic Transport in Ecologically Critical Heterogeneous Interfaces', No. 316546.

References

Bradley DN, Tucker GE (2012) Measuring gravel transport and dispersion in a mountain river using passive radio tracers. Earth Surf Process. Landforms 37:1034–1045

Campagnol J, Radice A, Nokes R, Bulankina V, Lescova A, Ballio F (2013) Lagrangian analysis of bed-load sediment motion: database contribution. J Hydralics Res 51(5):589–596. doi:10.1080/00221686.2013.812152

Drake TG, Shreve RL, Dietrich WE, Whiting PJ, Leopold LB (1987) Bed load transport of fine gravel observed by motion-picture photography. J Fluid Mech 192:193–217

Einstein H A (1950) The bed-load function for sediment transportation in open channel flows. Technical bulletin number 1026, United States Department of Agriculture, Soil Conservation Service, Washington, DC 78 pp

Ferguson RI, Wathen SJ (1998) Tracer-pebble movement along a concave river profile: virtual velocity in relation to grain size and shear stress. Water Resour Res 34(8):2031–2038

Furbish DJ, Haff PK, Roseberry JC, Schmeeckle MW (2012) A probabilistic description of the bed load sediment flux: 1. Theory. J Geophys Res 117:F03031. doi:10.1029/2012JF002352

Ganti V, Meerschaert MM, Foufoula-Georgiou E, Viparelli E, Parker G (2010) Normal and anomalous diffusion of gravel tracer particles in rivers. J Geophys Res 115: F00A12. doi:10.1029/2008JF001222

Hassan MA, Church M, Ashworth PJ (1992) Virtual rate and mean distance of travel of individual clasts in gravel-bed channels. Earth Surf Proc Land 17:327–617

Hassan MA, Church M (2000) Experiments on surface structure and partial sediment transport on a gravel bed. Water Resour Res 36(7):1885–1895

Hassan MA, Voepel H, Schumer R, Parker G, Fraccarollo L (2013) Displacement characteristics of coarse fluvial bed sediment. J Geophys Res Earth Surf 118:155–165. doi:10.1029/2012JF002374

Hirano M (1971) On riverbed variation with armouring. Proc Jpn Soc Civ Eng 195:55–65

Lajeunesse E, Malverti L, Charru F(2010) Bed load transport in turbulent flow at the grain scale: experiments and modeling. J Geophys Res 115:F04001. doi:10.1029/2009JF001628

Liébault F, Bellot H, Chapuis M, Klotz S, Deschatres M (2011) Bedload tracing in a high-sediment-load mountain stream. Earth Surf Process Land. doi:10.1002/esp.2245

Marion A (1995) Analisi sperimentale della dinamica verticale dei sedimenti negli alvei fluviali, Ph.D. thesis, University of Padua, Padua, Italy

Marion A, Nikora V, Puijalon S, Bouma T, Koll K, Ballio F, Tait S, Zaramella M, Sukhodolov A, O'Hare M, Wharton G, Aberle J, Tregnaghi M, Davies P, Nepf H, Parker G, Statzner B (2014)

Aquatic Interfaces: a hydrodynamic and ecological perspective. J Hydraul Eng doi:10.1080/00221686.2014.968887
McEwan I, Sorensen M, Heald J, Tait S, Cunningham G, Goring D, Willetts B (2004) Probabilistic modelling of bed-load composition. J Hydraul Eng. doi:10.1061/(ASCE)0733-9429(2004)130:2(129)
Meyer-Peter E, Muller R (1948) Formulas for bedload transport. International Association for Hydraulic Structures Research, Report of the second meeting, Stockholm, pp. 39–64
Nikora IV, Goring DG, Biggs BJF (1998) On gravel-bed roughness characterization. Water Resour Res 34(3):517–527
Nikora V, Goring D, McEwan I, Griffiths G (2001) Spatially averaged open-channel flow over rough bed. J Hydraul Eng 127(2)
Nikora V, Habersack H, Huber T, McEwan I (2002) On bed particle diffusion in gravel bed flows under weak bed load transport. Water Resour Res 38(6). doi:10.1029/2001WR000513
Parker G, Paola C, Leclair S (2000) Probabilistic Exner sediment continuity equation for mixtures with no active layer. J Hydraul Eng
Pelosi A, Parker G (2014) Morphodynamics of river bed variation with variable bedload step length. Earth Surf Dynam 2:243–253
Sayre W, Hubbell D (1965) Transport and dispersion of labeled bed material, North Loup River, Nebraska, US Geological Survey Professional Paper, 433-C, 48 pp
van Rijn LC (1984) Sediment pick-up function. J Hydraul Eng 110(10)
Viparelli E, Lauer JW, Belmont P, Parker G (2013) A numerical model to develop long-term sediment budgets using isotopic sediment fingerprints. Comput Geosci 53:114–122
Wilcock PR, Kenworthy ST (2002) A two-fraction model for the transport of sand/gravel mixtures. Water Resour Res 38(10):1194. doi:10.1029/2001WR000684
Wong M, Parker G, DeVries P, Brown TM, Burges SJ (2007) Experiments on dispersion of tracer stones under lower-regime plane-bed equilibrium bed load transport. Water Resour Res 43:W03440. doi:10.1029/2006WR005172
Yang C, Sayre W (1971) Stochastic model for sand dispersion. J Hydraul Div 97:265–288

An Evolution Volume Balance Approach to Determine Relevant Discharge Threshold for Bed Load Transport

Najibullah Sadid, Felix Beckers, Markus Noack, Stefan Haun and Silke Wieprecht

Abstract The aim of this study is to investigate discharge rates at which a flow hydrograph becomes relevant for bed load transport on the example of the Alpine river Saalach. Two characteristic flow hydrographs of the river Saalach are selected and reduced to discharges above pre-specified values. With each set of reduced hydrographs, a 2D morphological simulation is conducted. Two important morphological parameters, namely total river bed evolution (i) and sorting effects of the active layer (ii) are analyzed and evaluated. Moreover, an additional simulation is conducted with a linearly increasing flow hydrograph as boundary condition to analyze the initiation of bed load transport as a function of discharge (iii). The results are analyzed and evaluated with respect to the total sediment output at the downstream boundary of the model and at some inner control sections to validate the findings for (i) and (ii). The model results show: (i) For regions with fine bed materials, discharge thresholds between 100 and 130 m^3/s and for regions with mainly coarse bed materials discharge thresholds in the range between 150 and 180 m^3/s can be identified as relevant discharges for bed load transport and may be used for reducing hydrographs without affecting the accuracy of the model results; (ii) The active layer shows no obvious changes in the mean diameter of sediments for all tested hydrographs. (iii) The investigations with a linearly increasing flow hydrograph show that the sediment output from the investigated river reaches increase significantly for discharges exceeding 150 m^3/s.

N. Sadid (✉) · F. Beckers · M. Noack · S. Haun · S. Wieprecht
Institute for Modelling Hydraulic and Environmental Systems, University of Stuttgart, Pfaffenwaldring 61, 70569 Stuttgart, Germany
e-mail: Najibullah.sadid@iws.uni-stuttgart.de

P. Rowiński and A. Marion (eds.), *Hydrodynamic and Mass Transport at Freshwater Aquatic Interfaces*, GeoPlanet: Earth and Planetary Sciences,
DOI 10.1007/978-3-319-27750-9_25

1 Introduction

Morphological models of rivers are increasingly used to predict long term behavior and response of rivers to natural and man-made changes. A challenging task in morphological modelling is still to shorten the simulation time. A possible strategy to reduce the computation time for morphological modelling is to determine which base flows can be eliminated from a hydrograph due to their marginal effect on bed load transport and on river geometry.

Bed load transport is a complex process and several parameters such as geometry, flow regime, sediment grain size distribution and river bed surface characteristics have an influence. From channel design, restoration and maintenance point of view there are several terms defined for the discharge which controls the channel form. Occasionally in literature the term channel-forming discharge is used (e.g. Powell et al. 2005; Biedenharn et al. 2000). In some other studies the term bankfull discharge and effective discharge are used alternatively (e.g. Andrews 1980). The effective discharge is defined as the increment of discharge that transports the largest sediment load in the long term. Wolman and Miller (1960) made an analysis of flow magnitude and recurrence frequency to determine the effective discharge. The bankfull discharge is defined as the maximum discharge a channel can convey without overflowing onto the floodplains (Copeland et al. 2001; Shields et al. 2003). Inglis (1941) proposed that in natural rivers a single steady flow, he named as dominant discharge, could be determined that would form the same bankfull geometry as the natural flow events. Biedenharn et al. (2000) called this discharge a channel forming discharge and proposed a procedure for determining the channel forming discharge based on flow-frequency distribution and a bed load rating curve. The reviewed former studies indicate that not all naturally occurring discharges in a river are involved in bed load transport and in channel morphology development; rather, there is a threshold for the discharge at which bed load starts to move significantly.

Most of the previously presented studies that deal with the determination of a single steady discharge, that would produce the same basic channel form as a natural flow hydrograph over a long period, attach an important condition to their studies. This condition was that all rivers were in regime (morphologically in equilibrium). However, this pre-requisite is hardly met for the river Saalach selected in this study due to excessive erosion in the past as a result of heavy modifications that have pushed the river into a morphologically unstable condition.

Different from previously conducted studies which have a focus on flow magnitude, its and recurrence frequency and sediment transport quantity, in this study an evolution volume (sedimentation and erosion volume) balance validated by bed load transport analysis and sorting of river bed sediment is presented. Associating these morphological calibration and validation parameters for the determination of threshold discharge are important, since the model should reproduce these parameters also with the reduced hydrographs (eliminated base flows).

Therefore, in this study the focus is on the determination of a threshold discharge by employing an evolution volume analysis approach. If the evolution volume from a simulation result does not change as a result of using a natural hydrograph or a reduced hydrograph over a certain discharge threshold, this implies that the withdrawn base flows from the natural hydrograph have no influence on bed load transport and hence can be eliminated. The threshold discharge used for the elimination of the base flows could in addition be further increased until the evolution volume change becomes significant.

The second important parameter which is analyzed, is the bed load transport rate. Bed load transport rate can provide information if the evolution of river bed occurs locally within the model domain or if a significant amount of sediments is transported through the outflow boundary. If at a certain discharge rate no significant bed load transport is detectable, this should also be reflected in the evolution volume change and vice versa.

Additionally, the sorting effect of the active layer is analyzed. This is necessary because the eliminated smaller discharges or base flows may affect the sediment sorting of the active river bed. The aim of this parameter analysis is to quantify the impact of the hydrograph reduction on coarsening and fining of active river bed sediments as a result of the base flow eliminations from the natural hydrograph by the application of the herein described method. If most of the base flows are eliminated from natural hydrographs and only peak flows are present in a reduced hydrograph, this may lead to an alteration in grain size distribution of the active river bed sediments. Therefore, the bed sorting parameter is used as a controlling parameter to validate and support the introduced evolution volume balance approach to determine relevant discharge thresholds for bed load transport.

2 Methods

2.1 Study Area

The river Saalach is located in the southern part of the German/Austrian Danube catchment. It is characterized by an Alpine river regime with low flows in the winter and high flows in the summer (the annual average daily discharge is equal to 38.9 m^3/s, and the discharge during a hundred year flood is equal to 917 m^3/s) (Bayerisches Landesamt für Umwelt 2015). Furthermore, the river Saalach is the largest tributary of the river Salzach with respect to water and sediment input, which finally mouths into the river Inn.

The river Saalach flows through a diverse geology, consisting of alluvial sand and gravel at the chainage of 20.0–11.8 km, followed by clay, silt and sandstone lenses at the chainage of 11.8–7.4 km. The zone between the chainage of 7.4–5.06 km contains even finer materials (clay and silt with (d_{95}) < 0.5 mm) which are very vulnerable to extensive erosion (Braunstingl and Grebmayer 2000).

Further downstream, at the chainage of 5.06–0.8 km, the materials include weak to strong silty sand.

Many man-made river modifications have altered the natural regime of the river and limited as a consequence the consistency of sediments along the river course. Restricted river dynamics, due to the straightening of the river, has led to increased flow velocities and thus to increased bed shear stresses. The Kibling dam, which was built in 1913 at the chainage of 20.69 km, is one of several barriers that traps sediments and hinders sediment input into the downstream part of the river Saalach. As a result, the river morphology is not in an equilibrium condition.

In 1985 sediment feeding has started downstream of the Kibling reservoir as a mitigating measure. During the years 1985–1999, a total amount of 21,195 m^3 of sediment was taken from the Saalach lake and fed back downstream of the Kibling reservoir. The sediment feeding intensified since 1999 and yearly about 50,000 m^3 of sediments are dumped downstream of the Kibling reservoir. In addition, several transverse structures such as ramps and weirs were built in the river to reduce the erosion process and to stabilize the river bed. The majority of these structures were already built passable for sediments or adapted over time.

2.2 Hydrograph Reduction (Elimination of Base Flows)

Two hydrographs of the years 2005 and 2007, both consisting of base flows during winter and peak discharges during summer, are used as input data for this study. The hydrograph of the year 2005 represents a year with a single high flood event whereas the hydrograph of the year 2007 represents a year with several medium flood events during the summer months. The reason of selecting different hydrographs is to find out the significance of base flows compared to seasonal peak events as it happened in 2007 (maximum discharge of 290 m^3/s) and in 2005 (maximum discharge of 530 m^3/s). The hydrograph of the year 2005 is reduced by eliminating all discharges below a pre-defined threshold values of 30, 50, 70, 100, 130, 150, 180, 200 and 250 m^3/s. The hydrograph of the year 2007 is reduced using threshold discharges of 100, 130, 150, 180, 200 and 250 m^3/s. Threshold discharges smaller than 100 m^3/s are not used for the second hydrograph (2007) because it was noted from the simulations with reduced hydrographs of the year 2005 that threshold discharges less than 100 m^3/s have no effect on the set criteria (relevance for bed load transport). The complete hydrograph as well as six of the eight sets of reduced hydrographs of the year 2005 are shown in Fig. 1a–f.

2.3 2D Hydro-Morphological Modelling

The 2D morphological model Hydro_FT-2D is used to calculate bed load transport and bed evolution. The model is based on the two-dimensional hydrodynamic

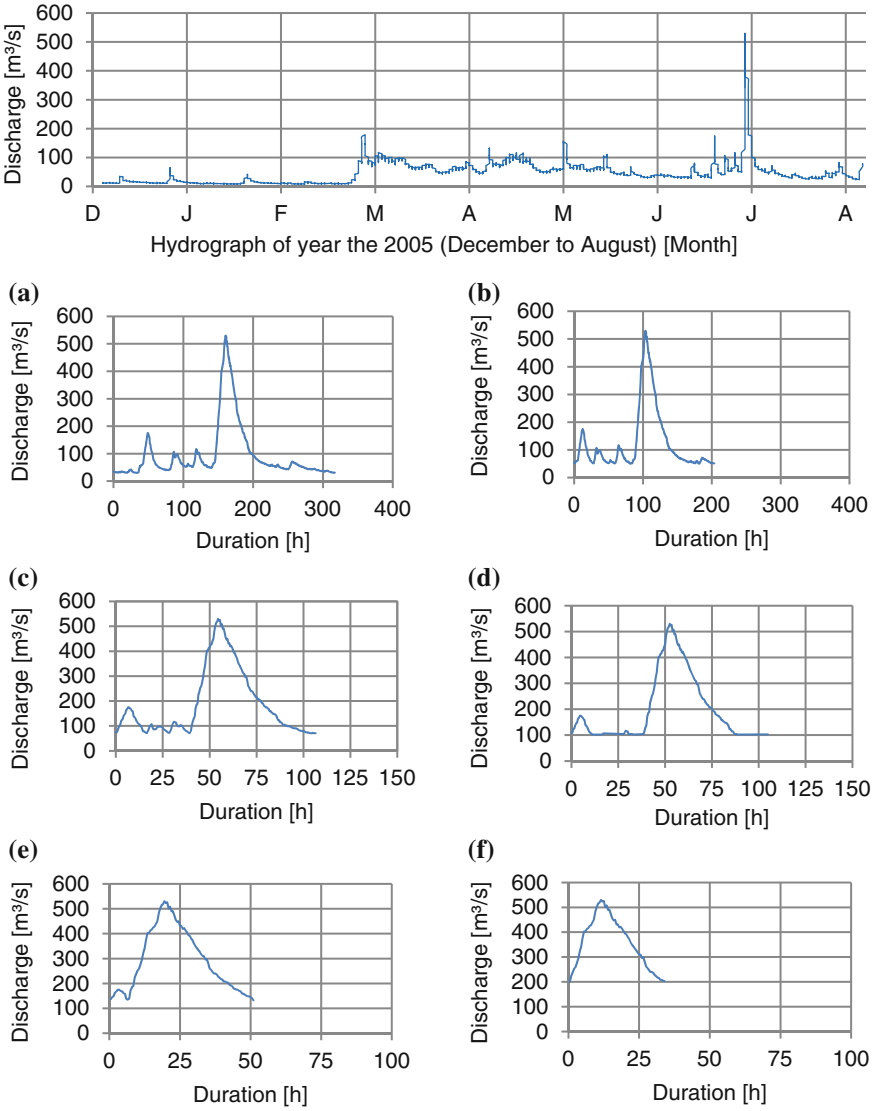

Fig. 1 Hydrograph from the year 2005 and six of the eight sets of reduced hydrographs with discharges above the pre-defined threshold discharges: **a** 30 m^3/s; **b** 50 m^3/s; **c** 70 m^3/s; **d** 100 m^3/s; **e** 130 m^3/s and **f** 200 m^3/s

model Hydro_AS-2D to simulate sediment transport processes. It solves the Mayer-Peter-Mueller, Engelund-Hansen or Ackers-White equation for bed load transport and the Exner equation for river bed evolution. The layering approach implemented into this model is based on the multi-layer concept of Hirano (1971) and can simulate up to 12 sediment grain size classes (Nujic 2015). In this

Table 1 Main model parameters for all simulations

Parameters	Value
Critical Shields parameter	0.047
Pre-factor of Meyer-Peter Müller formula	5.8
Active layer thickness	$1.0*d_{max}$
Sediment friction angle	37°
Sediment density	2,650 kg/m^3

investigation, the river bed consists of an active layer followed by a second layer. The sediment grain size distribution is defined in eight grain classes. To simulate the morphodynamic response to each set of the reduced hydrographs as hydraulic inflow boundary condition, the Mayer-Peter-Mueller equation is applied. The morphological parameters are kept identical for all runs and are listed in Table 1.

At the end of each model run, three parameters, namely total evolution volume (erosion and deposition), discharge to bed load transport rate relation and the active bed sediment sorting effect, are evaluated. It is observed that not all parts of the main channel are active with respect to the river bed evolution. Hence only the active area of the main channel is selected for the river bed evolution analysis. The active areas are further divided into three sections, as shown in Fig. 2, to precisely evaluate the differences in results coming from a different river geometry and bed sediment sizes. The active section A ranges from the chainage 18.4 to 17.2 km. The active section B ranges from the chainage 16.4 to 15.2 km and the active section C ranges from the chainage 8.0 to 4.8 km. Within each section, total sedimentation and erosion volume are computed and evaluated for each simulation run.

The second parameter is the mean diameter of sediments in the active layer (d_m), which is used to analyze the sorting effect, namely the fining or coarsening within the active layer. The mean diameter of the active layer sediment is extracted from the model output files and evaluated for each of the three earlier mentioned active sections.

The third parameter which is analyzed is the discharge-bed load transport rate relation. The hydraulic input however differs here from the previous model setup. Due to the complexity and unsteadiness of the hydrographs, a linearly increasing flow hydrograph is used instead of the reduced hydrographs to clearly track the incipient motion or start of bed load transport as a function of the flow discharge. To extract the bed load transport as a function of discharge, control sections are placed at important stations along the river such as model outflow, zones of fine and coarse bed material as well as at zones upstream and downstream of weirs and ramps. These control sections record flow and bed load transport rates at each time step of the simulation.

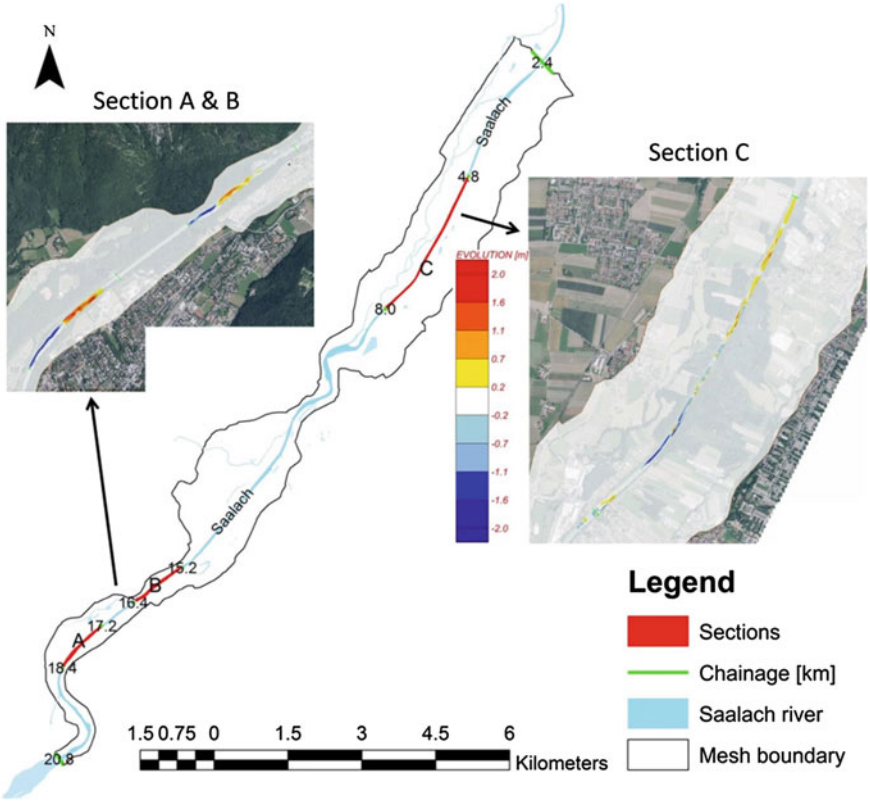

Fig. 2 Active *sections A*, *B* and *C* of the river Saalach. *Section A* is located in the upstream area and ranges from the chainage 18.4–17.2 km. *Section B* ranges from the chainage 16.4–15.2 km and the active *section C* is located downstream and ranges from the chainage 8.0–4.8 km

3 Results and Discussion

3.1 River Bed Evolution Volume Analysis

Total river bed evolution volume from the simulation results and the difference between them, for all three active sections, A, B and C, of the river Saalach are plotted in Fig. 3. The notations a, b and c describe the results from the hydrograph of 2007 and the notations a1, b1 and c1 describe the results from the hydrograph of 2005. In the upstream section, shown in Fig. 3a, a1, the evolution volume remains almost constant until a threshold discharge of 180 m^3/s is reached. It can be indicated that the evolution volume starts to decrease drastically along with an increasing threshold discharge to 250 m^3/s. This change in evolution volume, as shown in (a) and (a1), represents an approximately 15 and 5 cm simulated change in the river bed, respectively. For section B, the significant change in the evolution

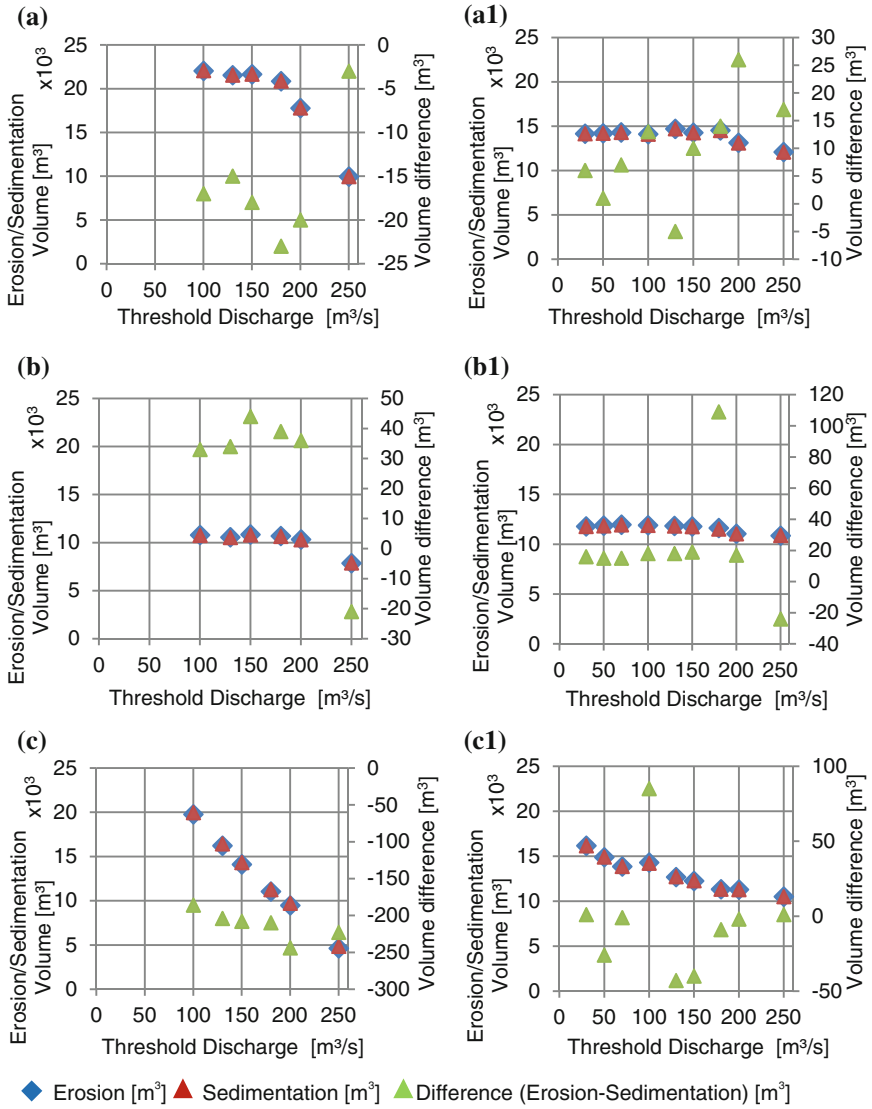

Fig. 3 Evolution volume as a function of threshold discharges for the hydrographs of 2007 for section A (**a**), section B (**b**) and section C (**c**); and for the hydrographs of 2005 for section A (**a1**), section B (**b1**) and for section C (**c1**)

volume starts at a similar threshold discharge in the range of 150 and 180 m^3/s, as shown in Fig. 3b, b1, respectively. However, the corresponding change in evolution volume is rather small in comparison to the section A and shows only a simulated bed change of approximately 5 cm for (b) and 1.5 cm for (b1). As expected for the section C, where the bed material contains very fine sediments, the change in

evolution volume is obvious even for a threshold discharge of 100 m^3/s, as shown in Fig. 3c, c1. The change in evolution volume is almost linearly decreasing along with an increasing threshold discharge. It can be noted that the difference in erosion and sedimentation volume are not considerably noticeable, especially for section A and B. However, the erosion volume for the section C tends to be higher than the sedimentation volume due to the fact that the active layer consists of finer materials compared to sections A and B.

3.2 Sorting of Active Bed Layer Sediment

The morphological model results for the mean diameter of active bed layer sediment shows similar results for each pair of reduced hydrographs of the years 2005 and 2007. Therefore, it is assumed sufficient to present the reduced sets of hydrographs of the year 2005 (see Fig. 4).

In general, in active regions there is a strong fining of bed sediments from initial assigned sediments, as it can be seen in Fig. 4 for section A(a), B(b) and C(c). The mean diameter of the active layer sediment (d_m) decreases due to this process, for instance, for the sections A and B from approximately 130 and 100 mm (measured) to an average of 50 and 60 mm (simulated), respectively (see Fig. 4a, b). This general fining is due to the mixing with the second layer sediments which consist of finer materials compared to the active surface layer. However, a conducted comparison of the model results from all sets of simulations shows no visible trend of either coarsening or fining. The important point that needs to be considered is the difference in the development of the respective erosion and sedimentation zone, in particular, when the hydrograph is reduced at a discharge threshold of 200 m^3/s. The active river bed sediment fining region is, for instance, in Fig. 4a for a hydrograph reduced to discharges over 250 m^3/s much shorter compared to the other simulation results and ranges from chainage 18.05–17.4 km. This means the evolution area is 350 m less developed in the direction of flow, which reflects directly a sharp decrease in evolution, as also presented in Fig. 3 in Sect. 3.1. In the zone containing fine material, the evolution distance becomes even shorter for each simulation with a differently reduced input hydrograph, as shown in Fig. 4c.

3.3 Discharge—Bed Load Transport Rate Relation

The results of the simulation with a linearly increasing flow hydrograph as an inflow boundary condition is shown in Fig. 5a–e. This simulation aims to investigate the start of bed load transport as a function of the flow discharge. The bed

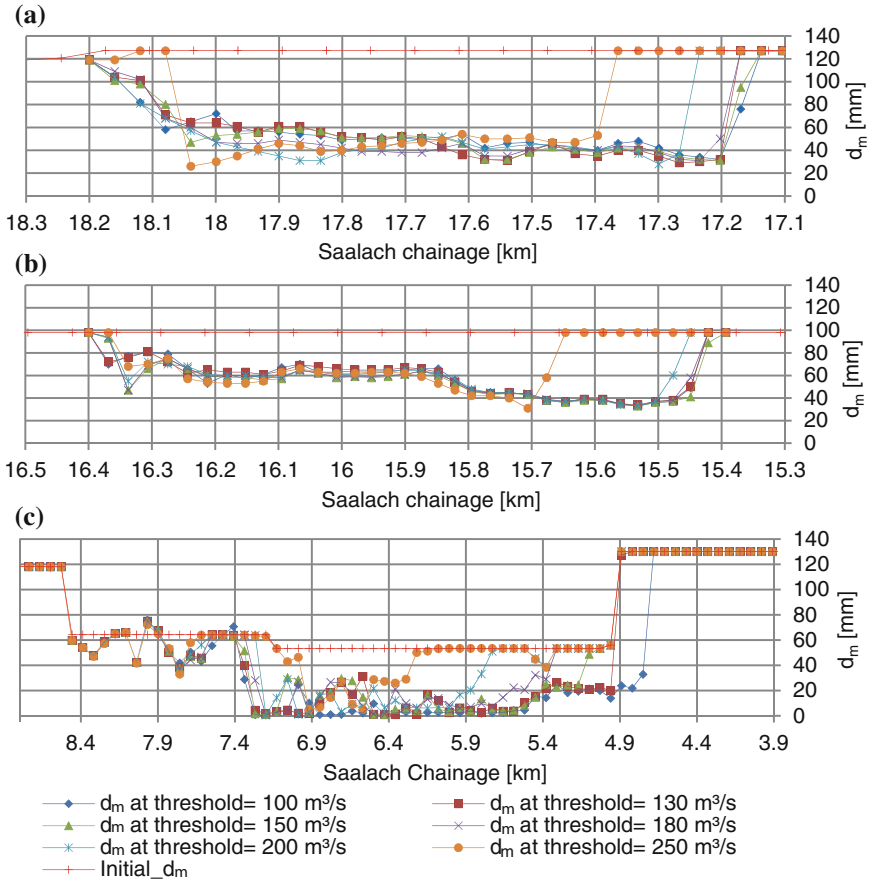

Fig. 4 Mean diameter of active bed sediment (d_m) at section A (**a**); section B (**b**); section C (**c**)

load transport starts at the model outflow and at most of other control sections at a discharge rate of about 150 m^3/s. Significant variations in the initiation of the bed load transport, for example, are observed between Fig. 5c, e. In Fig. 5c the bed load transport rate starts to increase for discharges larger than 275 m^3/s. The reason could be coarse bed material or a changing river geometry inducing minor shear stresses at similar discharges compared to other regions. In Fig. 5e the detected bed load transport rate at the chainage of 7.1 km is more critical. It can be noted that an increase of bed load transport starts already at discharges between 75 and 100 m^3/s. Therefore, this region tends to an earlier begining in bed load transport at lower discharges, which is decisive in the final selection of the threshold discharge for eliminating the base flows.

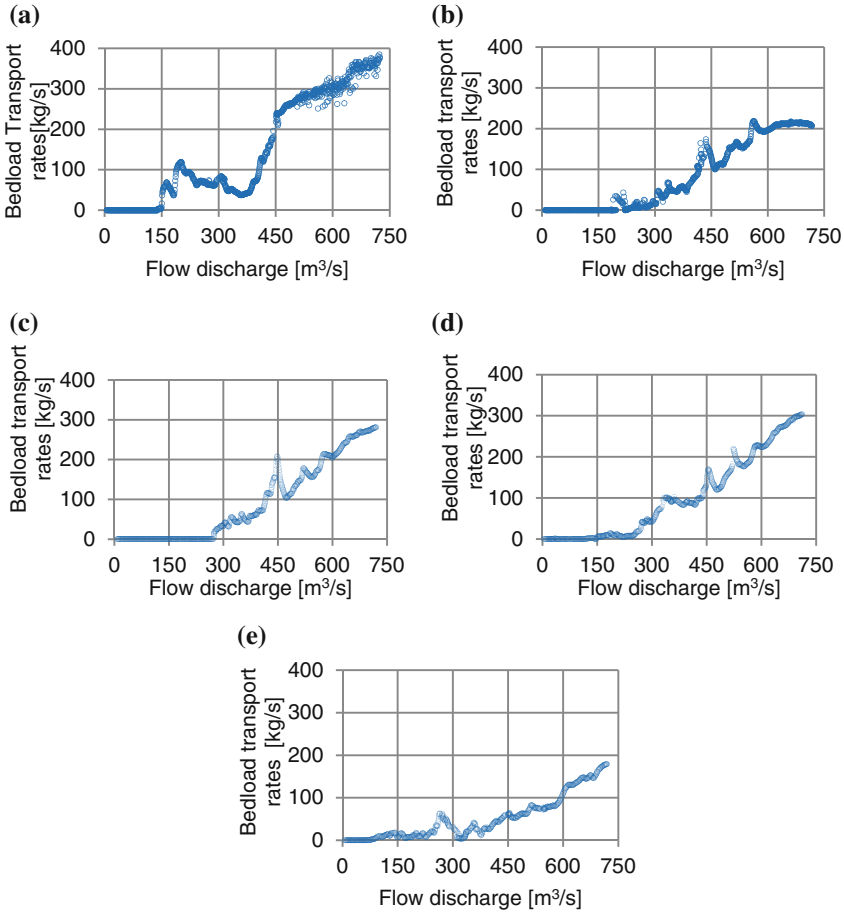

Fig. 5 Bed load transport rate as a function of flow discharge at **a** model outflow; **b** chainage 18.3 km; **c** chainage 17.25 km; **d** chainage 16.25 km; **e** chainage 7.1 km

4 Conclusions

The evolution volume analysis for the three active sections, A, B and C, of the river Saalach shows that a threshold discharge for eliminating the base flows from the natural hydrograph can be determined to be in the range of 100–130 m^3/s. If the zone that consists of fine materials is excluded from the analysis, a threshold discharge can even be determined to be in the range of 150–180 m^3/s. The evolution volume starts to change significantly when the threshold discharge is increased to discharges over 180 m^3/s. The threshold discharge is additionally validated by the bed load transport rate at the outflow of the model and at some significant inner sections of the river. With this method very local effects can be

detected, compared to the previously performed evolution volume analysis. The results indicate that bed load transport starts at a discharge of 150 m^3/s in most river regions. However, in zones with fine bed material, the bed load transport already starts between discharges of 75 and 100 m^3/s. The chosen threshold discharges are further evaluated with respect to the active river bed sediment sorting. The model results show no specific trend of fining or coarsening in the active river bed for all tested hydrographs. Therefore, it can be concluded that the findings from the river bed evolution volume analysis and the discharge–bed load transport rate relation are decisive for the determination of a threshold discharge for the river Saalach.

The determined threshold discharges, by means of the applied method, result in a total hydrograph time reduction by 95 % for the chosen hydrographs. This allows performing long simulations in considerably less time with an adequate accuracy of the model results. This method for reducing the hydrographs is found to be comprehensive in terms of morphological parameters analysis and considered as reasonably applicable for a long term morphological investigation of the river Saalach and hence can be transferred to similar tasks in other rivers.

References

Andrews ED (1980) Effective and bankfull discharge of streams in the Yampa basin, western Wyoming. J Hydrol 46:311–330

Bayerisches Landesamt für Umwelt (2015) Pegel im Donaugebiet, Siezenheim/Saalach. http://www.hnd.bayern.de/pegel/abfluss/pegel_abfluss.php?pgnr=18643505&standalone. Accessed 30 Jan 2015

Biedenharn DS, Copeland RR, Thorne CR, Soar PJ, Hey RD, Watson CC (2000) Effective discharge calculation: a practical guide. ERDC/CHL TR-00-15. U.S. Army Corps of Engineers, Coastal and Hydraulics Laboratory, Vicksburg

Braunstingl R, Grebmayer Th (2000). Geologischer Schlußbericht zum Bohrprogramm 1997/98. Amt der Salzburger Landesregierung und Bayern Landesamt für Wasserwirtschaft, Salzburg/München, 1–21. (Internal report, in German)

Copeland RR, McComas DN, Thorne CR, Soar PJ, Jonas MM, Fripp JB (2001) Hydraulic design of stream restoration projects. Technical Report No. ERDC/CHL TR-01-28. U.S. Army Engineer Research and Development Center, Vicksburg

Hirano M (1971) River bed degradation with armouring. Trans JSCE 3(2)

Inglis CC (1941) Meanders of rivers, vol 24. Central board of irrigation (India) Publication, Gurgaon, pp 98–99

Nujic M (2015) Hydro_FT-2D Erweiterung zu Hydro_AS-2D zur Simulation des Stofftransports. (Manual, in German)

Powell GE, Mecklenburg D, and Ward A (2005) Evaluating channel-forming discharges: a study of large rivers in Ohio, Soil & water division of ASABE, vol 49, pp 35–46

Shields FD, Copeland RR, Klingeman PC, Doyle MW, Simon A (2003) Design for stream restoration. J Hydraul Eng 129(8):575–584

Wolman MG, Miller JP (1960) Magnitude and frequency of forces in geomorphic processes. J Geol 68:54–74

Significance of the Sediment Properties and Aquatic Environmental Conditions on the Erodibility of Deposited Beds

Irene Seco, Manuel Gómez-Valentín, Simon Tait and Andrea Marion

Abstract The reliability of the prediction of sediment transport loads in aquatic environments is significantly dependent on the sediment bed behaviour regarding erosion. Besides the ambient environmental conditions, the residence or consolidation period may generate changes in the nature and structure of the sediment deposits. This review highlights the importance of the sediment properties in the assessment of their re-suspension and mobilization. Unconsolidated cohesive beds of sediments often display lower critical shear stress values at the solid-water interface than those observed for the same sediment type but in consolidated beds. When dealing with cohesive sediments, the time dependent physical and biochemical processes are among the main aspects that influence the observed higher resistance to erosion. A prior characterization of the local material accumulated in the studied environment is crucial in enhancing transport prediction performance.

I. Seco (✉) · A. Marion
Department of Industrial Engineering, University of Padua, Via Marzolo 9, 35131 Padua, Italy
e-mail: irene.seco@unipd.it

A. Marion
e-mail: andrea.marion@unipd.it

M. Gómez-Valentín
Department of Hydraulic, Maritime and Environmental Engineering Technical University of Catalonia, Jordi Girona 1-3, 08034 Barcelona, Spain
e-mail: manuel.gomez@upc.edu

S. Tait
Department of Civil and Structural Engineering, University of Sheffield, Mappin Street, Sheffield S1 3JD, UK
e-mail: s.tait@sheffield.ac.uk

P. Rowiński and A. Marion (eds.), *Hydrodynamic and Mass Transport at Freshwater Aquatic Interfaces*, GeoPlanet: Earth and Planetary Sciences,
DOI 10.1007/978-3-319-27750-9_26

1 Introduction

The terms "sediments" or "particles", when transport of solids in water flows is addressed, indicate a wide range of particulate matter. Sediment particles found in aquatic environments (natural streams, estuaries, wetlands, canals, etc.) can vary widely in character as they often come from a variety of sources. Sediment deposits might be complex mixtures of inorganic and organic material, non-homogeneous in composition and in particle size distribution. Additionally, different environments' conditions may lead to physical, chemical and biological transformation processes within the deposited beds.

Enhancement of the prediction of sediment transport is necessary for a more sustainable management of pollution and anthropogenic impacts on the natural environment because most pollutants are attached to solids (Mehta et al. 1989). Pollutants such as heavy metals, hydrocarbons, organic matter and nutrients are often associated with the finest size fractions (Bertrand-Krajewski et al. 1993; Gasperi et al. 2010; Verbanck et al. 1994). The assessment of sediment transport under the action of moving water constitutes a significant and complex problem for hydraulic engineering in general. The wide range of the mechanisms involved provides significant complexity to the sediment movement issue.

Deposition, release and re-suspension, and subsequent transport, are affected by the hydraulic conditions and dynamics of water flows, but also by mechanical and biochemical interaction between particles within the sediment deposits. Additional complexity is incorporated to the process due to particle nature, characteristics and composition. The temporal and spatial variability of the sediments deposited in some aquatic environments enlarge the difficulties in the reliable assessment of sediment transport loads in response to changing hydraulic conditions. In this context, the knowledge of the sediment characteristics and behaviour under different environments is important when sediment mobilization is being evaluated.

This review forms part of the work carried out within the ongoing HYTECH project "Hydrodynamic Transport in Ecologically Critical Interfaces", for developing management strategies in the field of hydrodynamic, biological and ecological flow-biota and flow-sediment interactions in aquatic interfaces (Marion et al. 2014). Better understanding of the sediment erosion and transport mechanisms is essential in enhancing the prediction of pollution and vulnerability of the natural environments regarding anthropogenic emissions.

2 Cohesive and Non-cohesive Sediments

From a practical point of view, in many environments a threshold between coarse cohesionless and cohesive sediment deposits is established at a particle size of 63 μm diameter (Land et al. 2012; Mehta et al. 1989; Mitchener and Torfs 1996). Particles finer than this value often form deposits that are considered cohesive while

deposits composed of coarser particles are usually denoted as non-cohesive. However, often this size limit is rather general and the distinction between cohesive and cohesiveless sediment is not so clearly defined and depends also on the nature of the sediments present in the deposit (Mehta et al. 1989).

Sediment mixtures with a fine fraction composed of organic matter and/or with varying clay/silt content can form beds with different degrees of cohesiveness (Banasiak et al. 2005; Mitchener and Torfs 1996) even though they contain some proportion of coarser granular sediment.

Regarding sediment nature and properties, there are substantial differences between granular and cohesive particles, and therefore their behaviour. The cohesive sediment bed structures might display complex chemical and biological composition and distinctive physical characteristics when comparing against purely non-cohesive sediments from rivers. Differences can be also significant regarding the sediment particles size distribution in the bed structure.

In particular, cohesive features in sediments have a significant effect on the initiation of motion.

3 Sediment Entrainment and Transport

While the entrainment, re-suspension and transport mechanisms acting on granular sediments are in general well understood (and widely modelled), the behaviour of coarse granular sediments within cohesive deposits is not so clear.

Most of the research in the field of sediment transport was developed for the hydrodynamic conditions of rivers and open channels. The validity of the results obtained in computing non-cohesive sediment transport capacity using physically based models, has driven their later application in systems with cohesive sediments, under the assumption of similarity of the sediment transport processes. While physical processes involved in the movement of sediment particles are essentially the same (fluid drag and particle self-weight driven process), the processes involved in the initiation of particle motion differ.

Most of the classical sediment transport equations (Meyer-Peter and Müller (1948) and derivatives, and Van Rijn (1984) among others) consider in general homogeneous coarse sediment deposits, although, in many environments, sediments are often heterogeneous mixtures of particles (in size distribution and in biochemical composition) and this must be considered in evaluating the erosion mechanisms. The application of sediment transport equation proposed for uniformly sized coarse particles in such environments where sediment mixtures or cohesive deposits exist might therefore be inappropriate.

The erosion of non-cohesive sediments is strongly dependent on physical factors such as the size of the particles and their density, and to a lesser extent their shape—reflecting their self-weight and the applied fluid drag and lift forces. Meanwhile, for cohesive sediments and sand-mud mixtures, the influence of the surface interaction between particles becomes much more relevant (Grabowski et al. 2011; Mitchener

and Torfs 1996). In analysing cohesive sediment movement, it is necessary to take into consideration extra factors, such as organic composition and deposit pore water pressure, as well as environmental conditions during consolidation periods, all potentially playing a role in changing the resistance to erosion under the action of turbulent flows.

Sediment erosion and transport is usually evaluated by an excess shear stress concept. One of the most widely used expressions for the quantification of the erosion rate (E) in the field of cohesive consolidated sediment beds is the formulation showed at Eq. (1) (Parchure and Mehta 1985), first proposed by Partheraides (1965). The erosion rate (mass of sediment eroded per unit bed area per unit time) is a function of the applied bed shear stress (τ_b), the critical shear stress at the sediment-water interface (τ_c) and the erosion coefficient M. This expression allows the quantification of the rate of erosion from a uniform-size cohesive deposit with uniform strength with respect to depth (Skipworth et al. 1999).

$$E = M\left(\frac{\tau_b - \tau_c}{\tau_c}\right) \tag{1}$$

The shear stress expresses an influence of the flow over the sediment deposit. The Shield's criterion, defined for granular sediment, establishes the equilibrium condition for the case when the average bed-shear stress (τ_b) is equal to the critical bed-shear stress value (τ_c) (see Eq. 2). The mobilization will occur when the bed-shear stress becomes greater than the critical value. The instant at which a particle with determined characteristics is released from the deposit and mobilized by the water flow is named: *threshold of motion* or *incipient motion*. It is therefore a relevant factor in erosion process modelling.

$$\begin{aligned} \text{Equilibrium condition} \quad & \tau_b = \tau_c \\ \text{Particle movement condition} \quad & \tau_b > \tau_c \end{aligned} \tag{2}$$

As water flows throughout the overlay sediment deposits, the hydrodynamic forces (lift and drag) are exerted on the particles. The erosion resistance depends on the excess between the hydrodynamic (destabilizing) forces acting over the sediment bed and the resisting forces due to gravity (e.g. weight, and inter-particle friction) and internal forces (e.g. pore-water suction or surface forces). The internal resistive forces might be linked with biochemical forces between particles.

Cohesion and adhesion are internal particles attractive forces, mainly dependent on the sediment biochemical properties, which create inter-grain bonds. The cohesive forces are associated with electromagnetic attraction between contiguous particles influenced by chemical mechanisms, while adhesive forces are mainly related to a biological binding linkage (Grabowski et al. 2011; Righetti and Lucarelli 2007). Adhesion mechanisms refer to bonding forces developed between particles in the presence of an inter-particle additional substance such as the extracellular polymeric substances (EPS) (Black et al. 2002; Righetti and Lucarelli 2007, 2010), which act as a binding agent. The presence of organic matter and fine

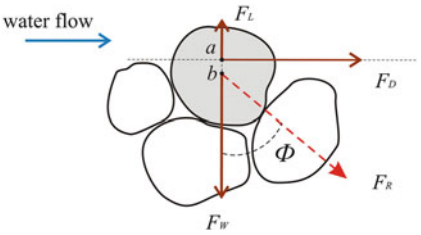

Fig. 1 Forces acting on a prominent granular particle in a non-cohesive bed-deposit subject to steady water flow [after Metha et al. (1997) and Mehta and Letter (2013)]

size particles has the greatest influence on the development of these mechanisms due to their chemical composition and their high surface-area-to-volume ratios.

Under a steady flow, a prominent particle on the bed will experience a force in the streamwise direction, proportional to the exposed area, due to pressure differences around the particle, named the drag force (F_D). The other hydrodynamic force called the lift force (F_L) will oppose the submerged weight of the grain (F_W) (Mehta et al. 1997). A scheme of the forces acting on a particle subjected to hydrodynamic forces is shown in Fig. 1.

The equilibrium condition is established when the resultant of forces mentioned above form an angle smaller than the repose angle Φ, with respect to the normal direction. Ignoring the small moment due to the couple arm ab, at the threshold of motion the repose angle is given by Eq. (3). This assumes that the drag, lift and weight forces all act through the same point b (centre of mass of the grain) and at entrainment the grain rotates about a single position. The entrainment occurs once the ratio between the mobilising force and the restoring force exceeds this equilibrium condition.

$$\tan \phi = \frac{F_D}{F_W - F_L} \tag{3}$$

For coarse sediments this repose angle is directly related to the grain size (Mehta et al. 1997; Mehta and Letter 2013). However, for cohesive sediments, the equilibrium in the mass of particles is affected by cohesion and adhesion processes which can effectively increase the resistive forces (Gerbersdorf et al. 2005; Mehta et al. 1997). Nevertheless, their point and lines of action are difficult to determine. Thus, using the concept of Φ and determining its value is complex as it no longer has a direct link with the physical properties of the particle.

A schematic representation of the cohesive force (F_C) acting on a granular particle in a cohesive bed can be seen in Fig. 2. The cohesive force will act on a point of intergranular contact o rotation point c, and is here considered in normal direction. In this situation, the repose angle is defined as shown in Eq. (4) after Mehta et al. (1997). The cohesive force is then considered in the equilibrium condition by adding an extra weight to the particle. This can be considered an

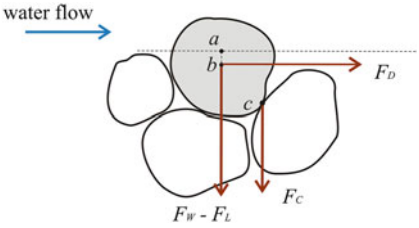

Fig. 2 Forces acting on a prominent granular particle in a cohesive bed-deposit subject to steady water flow (Mehta et al. 1997)

attempt of improvement in the evaluation of the condition of incipient motion despite this ratio between forces does not take the line of action into account.

$$\tan \phi = \frac{F_D}{F_W - F_L + F_C} \tag{4}$$

Due to continuous variations in the water flow conditions on the fluid-sediment interface, there are permanent variations in the mobilizing forces. Additionally, in cohesive beds, biochemical reactions under different environmental conditions lead to variation of the binding forces between particles and hence generate changes in the restoring forces. Thus, in these conditions, it is difficult to establish the ratio of the forces acting on the particle (or floc) at the point of entrainment. The threshold of motion is even more complicated to establish if dealing with non-uniform particles sizes, heterogeneous in composition, or with varying cohesiveness degree. Research effort was intensified in the last decades in understanding the mechanisms involved when cohesive and adhesive forces interact with the lift and drag forces (Black et al. 2002; Fang et al. 2014; Grabowski et al. 2011; Righetti and Lucarelli 2010).

Experiences in the field of sewer cohesive sediments conclude that the predictive formulations are highly sensitive to the input variables that characterize the sediment properties, particularly the specific gravity and the critical shear stress (Ashley et al. 2003). In addition, critical shear stress (τ_c) will depend on the cohesive mechanisms that have developed within a deposit.

Experimental results on erosion of cohesive sediment deposits (Nalluri and Alvarez 1992) conclude that after a consolidation period, the critical shear stress is higher than the values found for equivalent non-cohesive deposits (with similar size distribution). Shear stress values determined in this study using synthetic cohesive sediment were in the order of about 2.5 N/m^2 (superficial layers) to 7 N/m^2 (consolidated deposits) (Butler et al. 2003; Nalluri and Alvarez 1992). The resistance to erosion of cohesive sediment might be several levels of magnitude greater to the threshold of motion shear stress calculated for granular-non-cohesive sediment (Butler et al. 2003) due to the cohesion mechanisms generated under certain environmental conditions.

Addressing the hydrodynamic aspects of sediment erosion and transport, the knowledge of properties and behaviour of the sediments and sediment deposits are relevant. Physical characteristics, biochemical properties and biological aspects are the major issues that influence the threshold of motion over cohesive sediment deposits, as Grabowski et al. (2011) summarized. Previous deposition and consolidation of the sediments in a bed structure is also dependent on the sediment nature and characteristics.

The prediction of erosion rates through the application of classical transport equations requires the knowledge of at least sediment physical characteristics (when dealing with coarse sediments). The following sections will overview these relevant properties and processes.

4 Physical Properties Affecting Erodibility

When considering a potential of re-suspension from bed deposits, variations in the physical properties values are relevant. The most significant properties influencing the erodibility and transport are the particle size and its grain size distribution, the particle and deposit density, and deposit porosity (Grabowski et al. 2011; De Sutter et al. 2003).

4.1 Particle Size

The particle size is a commonly used parameter involved in the assessment of deposition and transport. In the sediment transport equations, the size of sediment particles is usually considered through a "mean particle size" (ds). Aside from the mean particle size, the structure of a sediment deposit also influences the resistance to erosion of the deposited layer of sediments.

Inter-particles forces are enhanced in fine sediment beds (Gerbersdorf et al. 2005). A lower mean particle size is also observed in sediment beds with significant organic content (Grabowski et al. 2011). Thus, the relative proportion of each size fraction might have an effect on the sediment bed erodibility. It is then convenient to consider the distribution of the particle sizes by ranges.

Furthermore, because of the development of attractive forces, cohesive and fine particles in suspension tend to flocculate and agglomerate. Flocculation might alter not only the size of particles (flocs) susceptible to be transported, but also their density and porosity (Droppo 2004). Thus, the overall mean size and the particle size distribution are influenced by the cohesive nature of the sediments. An apparent sediment floc diameter may then become relevant when assessing sediment transport and the typical d_{50} used in most of the transport formulas may not be an appropriate parameter. Hence, when dealing with the transport of cohesive

sediments that aggregate in clusters, an "effective particle size" can be a more adequate parameter to be considered (Droppo 2004).

4.2 Porosity and Water Content

An important consideration in sediment transport is the combined volume occupied by the particles and the interparticle voids. The ratio of the voids volume to the total volume of the deposit is represented by the dimensionless parameter p named porosity.

Observations have indicated that a high degree of porosity is directly related with high erodibility of the sediment deposits.

As new particles or flocs settle on the bed, the expulsion of the water contained in the pores occurs by self-weight consolidation (Been and Sills 1981; Mehta et al. 1989). This process (independent of the particles nature) leads over time to a continuous reduction of space between grains, which translate in a densification of the bed (and reduction of porosity).

A reduction in porosity can also be linked with biological mechanisms occurring during long consolidation periods (Grabowski et al. 2011). Results from laboratory and field studies with cohesive sediments from estuarine and riverine muds show that water content is inversely correlated with erodibility (Grabowski et al. 2011).

4.3 Bulk Density

The parameter termed as bulk density or dry density (ρ_b) can be found in the definition of some sediment transport formulations. It is referred to the dried mass per unit volume of a sediment bed. This parameter considers therefore the porosity of the deposit and has units of mass/volume. The bulk density, together with the water content and porosity, provides an idea of the proportion between solids and liquid in the sediment deposit, which indicates a level of consolidation of the sediment structure and therefore is an indicator directly correlated with the resistance to erosion (Grabowski et al. 2011).

Sediment deposits density (ρ_s) is also strongly influenced by the heterogeneity of sediments caused by the wide diversity of sources. In general, sediment deposits characterized by significant organic composition have lower average density than the sediment beds with highest inorganic content. The average density in sediment deposits with high organic composition could reach values as low as the water density, and they can even float. Because of their nature, the existence of organic compounds in a sediment bed leads to lesser values of bulk density (Grabowski et al. 2011).

5 Biochemical Transformations Affecting Erodibility

In natural aquatic environments, the water-sediment interface constitutes the most biologically-active region (Black et al. 2002; Marion et al. 2014), where a continuous interaction between sediments, organic matter and inhabitant organisms occur. Hydrodynamics and biological processes will have significant influence on the entrainment and mobilization of sediments at this interface by the time of high circulating flows (Black et al. 2002; Marion et al. 2014). So it is relevant to consider the biological activity and processes as well as the behavior of organic particles interacting under these environments, and how this affects the sediment bed stability.

During deposition and storage of sediments in the course of the low-flow-period, sediments are exposed to complex and age-dependent transformation processes (termed maturation). Biological and chemical degradation of the organic matter and the microorganisms growth are strongly influenced by the water environmental conditions: residence time length (Hoeft et al. 2011; Raunkjær et al. 1994), temperature and oxygen availability (Rudelle et al. 2011; Schellart et al. 2005; Seco et al. 2014). The deposit structure may be strengthened or weakened under different environment influence.

Chemical or organic cohesion together with microbiological activity in sediments can develop strong bonding forces between particles, influencing the structure of the bed (Banasiak et al. 2005; Mehta et al. 1997). Microorganisms' activity might produce EPS that promote flocculation and generate biological adhesion between particles, leading to stronger structures in the sediment matrix (Black et al. 2002; Righetti and Lucarelli 2007). Microbial biofilm growth also contributes to the sediment stability at the surface of the bed (Black et al. 2002; Fang et al. 2014). The microorganism activity can thus affect the erodibility of a deposit by transforming the sediment properties during their living cycle.

Beds formed by the deposition of soft sediment with significant organic content might initially result in low density and high porosity layers that can be easily be eroded. Over time, the biological transformations act creating intra-particle bonding forces that strengthen the deposited sediments regarding erosion (bioconsolidation) or disaggregating particles and generating changes in the sediment chemistry weakening the beds (bioturbation) (Black et al. 2002; Droppo and Stone 1994; Land et al. 2012; Marion et al. 2014; Righetti and Lucarelli 2007; Seco et al. 2014).

6 Consolidated Cohesive Sediment Bed Structure

The formation of a bed with cohesive structure is often a complex process that involves consolidation, dehydration, chemical interactions between the particles, biological degradation or decomposition of the organic matter over time. Rheological changes were studied in sewer sediments (Ristenpart 1995). The results

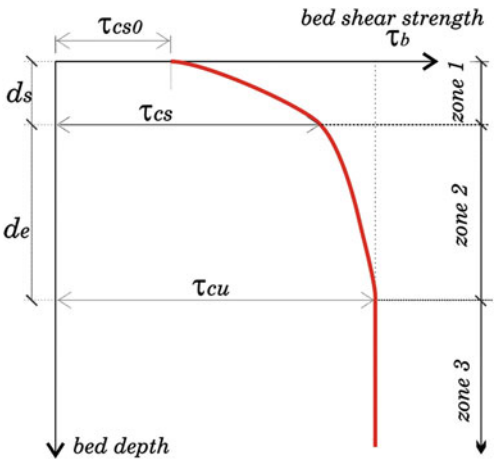

Fig. 3 Schematic representation of the three zones in a critical bed-shear stress profile in depth [after Parchure and Mehta (1985)]

obtained indicate the existence of an increase in density and a reduction in the organic matter over time. Additionally it was found that the longer the consolidation period, the higher the probability of the generation of a top layer in the solid deposit with a greater erosion resistance (Nalluri and Alvarez 1992).

Cohesive sediments with organic composition will also experience self-weight physical consolidation, linked to time dependent physical mechanisms of the intra-grain pore water. Both processes, bio and physical consolidation, might act at different times, and can generate vertically stratified sediment beds regarding erosional strength (Mehta et al. 1989; Parchure and Mehta 1985; Seco 2014).

In studies of estuaries' environments, Parchure and Mehta (1985) and Mehta et al. (1989) proposed a structure of the sediment bed with increasing strength in the resistance to erosion with depth, as shown in Fig. 3. The upper layer of sediment located just under the water interface exhibits a critical bed-shear stress that goes from a low value of strength (τ_{cs0}) and rapidly increases with depth until a τ_{cs} value. In the second zone there is also an increase of the resistance strength but evidenced much more slowly than in the upper zone. The equilibrium is reached once arrived to the third zone, after which the shear stress is kept almost constant (τ_{cu}) in depth.

The lower resistance to erosion of the bed surface (τ_{cs0}) is possibly related with the low density of the sediments in this layer that are continuously flocculating, but also with gas or oxygen bubbles trapped in superficial biofilms that pulls the particles away (Black et al. 2002).

The occurrence of stratification of the sediment bed regarding strength was also verified in different water environments, such as sewer systems (Schellart et al. 2005; Seco 2014; Skipworth et al. 1999). The vertical increment of resistance to erosion of the bed in these laboratory studies was due to a combination of physical and biochemical consolidation processes occurring during storage time.

Analysis of the influence of the length of the consolidation time on the deposit erodibility shows different effects. Results from laboratory studies carried out with

organic sediments from sewer systems suggested that as the residence time lengthens this leads to increasing strengths of the deposits (Seco 2014; Seco et al. 2014). However, the above-mentioned initial strengthening effect that can be related to a physical consolidation, may be reversed when biological transformation process continued along prolonged periods under certain environmental conditions, weakening the deposits (Banasiak et al. 2005; Tait et al. 2003). It has been suggested that under oxygen-rich conditions, the aerobic microbial activity generated gas bubbles close to the sediment surface within the sediment deposit, reducing the initial resistance to erosion.

Fine sediments suspended in a water column are continuously interacting and flocculating. During this process, superficial fine-grained lamina (SFGL) (Droppo and Stone 1994) might be formed as the upper sediment structure as a result of the accumulation of soft sediment with small fall velocity. For the period of low flow conditions, the SFGL layer shows a time-dependent cohesive behaviour, strengthening its resistance to erosion (Fang et al. 2014). Because of the increase of strength in this layer, it is usually termed in the literature as "armour" or "crust". The "armouring" effect might also be linked with a microbial biofilm formation in sediment beds with organic compounds or under the nutrient-rich water environments.

The increase of resistance linked to a surface "armouring" effect could be responsible for differences in the incipient motion in sediments with cohesive behaviour compared with the coarse sediments. Research carried out with mixtures of cohesive and non-cohesive sediments (Nalluri and Alvarez 1992) suggests that the influence of the cohesion is relevant just until the strength to break the bonds between particles of the consolidated structure is exceeded. Once the critical shear stress is exceeded, there occurs a sudden collapse of the structure of the upper layer of the consolidated deposit (Butler et al. 2003; Delleur 2001; Nalluri and Alvarez 1992). Since the initiation of motion, the particles are re-suspended and transported in a similar way as if they were non-cohesive (Nalluri and Alvarez 1992), until reaching the next layer of stratified bed with highest erosion resistance.

7 Conclusions

Sediment particles can vary widely in character and composition in aquatic systems. Wide variations in the properties of natural sediments have led to wide variability in the anticipated erosional resistance of sediment deposits. Difficulties in the prediction of the threshold of entrainment lead to high uncertainty in predicting transport loads because of this high variability in time and space of the sediments characteristics and the environmental influence.

Traditional conceptual models of grain entrainment include a force balance of just the particle weight and simple parameterisations of the fluid drag and lift forces. This type of model has been modified using simple empirical factors to represent the effect of granular grain size variation (sheltering and exposure). Observations of

deposits containing high proportions of fine inorganic and organic material have clearly shown that the traditional force balance approach does not work. This is not surprising as this traditional approach does not take into account: cohesive surface forces and forces caused by the change in pore water pressure and the internal grain re-arrangement as the pore water pressure dissipates. These time dependent forces are not accounted for but are clearly reflected in experiments in which the erosion threshold of sediment deposits, containing fine grained organic or inorganic sediment. Therefore, it is not unexpected that the currently used force balance computational methods are often unsuccessful for a widespread application that might involve sediments of non-uniform composition (e.g. organic and inorganic) subjected to different environmental conditions (e.g. water temperature, oxygen level, etc.)

The quantitative evaluation of the critical shear stress of cohesive sediments and sediment mixtures is complex, strongly time dependent, and often site specific. Cohesive and organic unconsolidated sediment deposits might display lower shear strength against erosion with respect to the boundary shear stresses displayed by inorganic deposits (equivalent in sediment size). However, the erodibility of cohesive sediments deposits is affected by the interaction of several transformation processes (physical, chemical and biological processes) and these mechanisms might lead to generate stronger or weaker sediment beds.

It is clear that a significantly improved conceptual model of particle entrainment is needed. It must be able to take into account the development and the point and line of application of all time invariant and time dependent forces. In this way the time varying behaviour of cohesive deposits can be quantified reliably.

The dependence of the erodibility on the sediment properties is difficult to analyse due to the complex interactions between the sediments under different environmental conditions. Nevertheless, as it was highlight in this review, the cohesive nature of sediments is relevant, and the biological reactions should be considered since it clearly has a strong influence on the erosional behaviour and thus on the amount of sediment transported.

Acknowledgments The research leading to these results has received funding from the European Community's Seventh Framework Programme FP7-PEOPLE-2012-ITN under grant agreement no 316546. The corresponding author wishes to thanks for the financial support given by the AGAUR (Generalitat de Catalunya) FI-DGR (IUE/2644/2010).

References

Ashley RM, Crabtree RW, Fraser A, Hvitved-Jacobsen T (2003) European research into sewer sediments and associated pollutants and processes. J Hydraul Eng 129:267

Banasiak R, Verhoeven R, De Sutter R, Tait SJ (2005) The erosion behaviour of biologically active sewer sediment deposits: observations from a laboratory study. Water Res 39:5221–5231

Been K, Sills GC (1981) Self-weight consolidation of soft soils: an experimental and theoretical study. Géotechnique 31:519–535. doi:10.1680/geot.1981.31.4.519
Bertrand-Krajewski J-L, Briat P, Scrivener O (1993) Sewer sediment production and transport modelling: a literature review. J Hydraul Res 31:435–460. doi:10.1080/00221689309498869
Black KS, Tolhurst TJ, Paterson DM, Hagerthey SE (2002) Working with natural cohesive sediments. J Hydraul Eng 128:2–8. doi:10.1061/(ASCE)0733-9429(2002)128:1(2)
Butler D, May RWP, Ackers J (2003) Self-cleansing sewer design based on sediment transport principles. J Hydraul Eng 129:276–282. doi:10.1061/(ASCE)0733-9429(2003)129:4(276)
Delleur JW (2001) Sediment movment in drainage systems. In: Mays LW (ed) Stormwater collect system design handbook. McGraw-Hill, pp 14.1–14.25
De Sutter R, Rushforth PJ, Tait SJ, Huygens M, Verhoeven R, Saul AJ (2003) Validation of existing bed load transport formulas using In-Sewer sediment. J Hydraul Eng 129:325–333
Droppo IG (2004) Structural controls on floc strength and transport. Can J Civ Eng 31:569–578. doi:10.1139/l04-015
Droppo IG, Stone M (1994) In-channel surficial fine-grained sediment laminae. Part I: Physical characteristics and formational processes. Hydrol Process 8:101–111
Fang H, Shang Q, Chen M, He G (2014) Changes in the critical erosion velocity for sediment colonized by biofilm. Sedimentology 61:648–659. doi:10.1111/sed.12065
Gasperi J, Gromaire-Mertz MC, Kafi-Benyahia M, Moilleron R, Chebbo G (2010) Contributions of wastewater, runoff and sewer deposit erosion to wet weather pollutant loads in combined sewer systems. Water Res 44:5875–5886. doi:10.1016/j.watres.2010.07.008
Gerbersdorf SU, Jancke T, Westrich B (2005) Physico-chemical and biological sediment properties determining erosion resistance of contaminated riverine sediments—Temporal and vertical pattern at the Lauffen reservoir/River Neckar, Germany. Limnol - Ecol Manag Inl Waters 35:132–144. doi:10.1016/j.limno.2005.05.001
Grabowski RC, Droppo IG, Wharton G (2011) Erodibility of cohesive sediment: the importance of sediment properties. Earth Sci Rev 105:101–120. doi:10.1016/j.earscirev.2011.01.008
Hoeft S, Wellmann S, Tränckner J, Krebs P (2011) Experiments on evolution of particle size in raw wastewater. In: 12th international conference on urban drain
Land LE, Kolker AS, Gambrell RP (2012) Biotic and abiotic controls on sediment aggregation and consolidation: implications for geochemical fluxes and coastal restoration. Mar Environ Res 79:100–110. doi:10.1016/j.marenvres.2012.05.012
Marion A, Nikora V, Puijalon S, Bouma T, Koll K, Ballio F, Tait SJ, Zaramella M, Sukhodolov A, O'Hare M, Wharton G, Aberle J, Tregnaghi M, Davies P, Nepf H, Parker G, Statzner B (2014) Aquatic interfaces: a hydrodynamic and ecological perspective. J Hydraul Res 1–15
Mehta AJ, Hayter EJ, Parker WR, Krone RB, Teeter AM (1989) Cohesive sediment transport. I: process description. J Hydraul Eng 115:1076–1093
Mehta AJ, Kirby R, Stuck JD, Jiang J, Parchure TM (1997) Erodibility of organic-rich sediments: a Florida perspective. Report UFL/COEL/MP-97/01. Coastal Oceanographic Engineering Department; University of Florida
Mehta AJ, Letter JV (2013) Comments on the transition between cohesive and cohesionless sediment bed exchange. Estuar Coast Shelf Sci 131:319–324. doi:10.1016/j.ecss.2013.07.001
Meyer-Peter E, Müller R (1948) Formulas for bed-load transport. In: IAHR, 2nd Meet. International association hydraulic structures research. Stockholm, Sweden, pp 39–64
Mitchener H, Torfs H (1996) Erosion of mud/sand mixtures. Coast Eng 29:1–25. doi:10.1016/S0378-3839(96)00002-6
Nalluri C, Alvarez EM (1992) The influence of cohesion on sediment behaviour. Water Sci Technol 25:151–164
Parchure TM, Mehta AJ (1985) Erosion of soft cohesive sediment deposit. J Hydraul Eng 111:1308–1326. doi:10.1061/(ASCE)0733-9429(1985)111:10(1308)
Partheniades E (1965) Erosion and deposition of cohesive soils. J Hydraul Div 91:105–139
Raunkjær K, Hvitved-Jacobsen T, Nielsen PH (1994) Measurement of pools of protein, carbohydrate and lipid in domestic wastewater. Water Res 28:251–262

Righetti M, Lucarelli C (2007) May the shields theory be extended to cohesive and adhesive benthic sediments? J Geophys Res Ocean 112:C05039. doi:10.1029/2006JC003669

Righetti M, Lucarelli C (2010) Resuspension phenomena of benthic sediments: the role of cohesion and biological adhesion. River Res Appl 26:404–413. doi:10.1002/rra.1296

Ristenpart E (1995) Sediment properties and their changes in a sewer. Water Sci Technol 31:77–83

Rudelle E, Vollertsen J, Hvitved-Jacobsen T, Nielsen AH (2011) Anaerobic transformations of organic matter in collection systems. Water Environ Res 83:532–540. doi:10.2175/106143010X12681059116699

Schellart ANA, Veldkamp RG, Klootwijk M, Clemens F, Tait SJ, Ashley RM, Howes C (2005) Detailed observation and measurement of sewer sediment erosion under aerobic and anaerobic conditions. Water Sci Technol 52:137–146

Seco I (2014) In-sewer organic sediment transport : study of the release of sediments during wet-weather from combined sewer systems in the Mediterranean region in Spain. PhD Thesis. Universitat Politècnica de Catalunya

Seco I, Gómez-Valentín M, Schellart ANA, Tait SJ (2014) Erosion resistance and behaviour of highly organic in-sewer sediment. Water Sci Technol 69:672–679. doi:10.2166/wst.2013.761

Skipworth PJ, Tait SJ, Saul AJ (1999) Erosion of sediment beds in sewers: model development. J Environ Eng 125:566–573. doi:10.1061/(ASCE)0733-9372(1999)125:6(566)

Tait SJ, Ashley RM, Verhoeven R, Clemens F, Aanen L (2003) Sewer sediment transport studies using an environmentally controlled annular flume. Water Sci Technol 47:51–60

Van Rijn LC (1984) Sediment transport, Part I: bed load transport. J Hydraul Eng 110:1431–1456. doi:10.1061/(ASCE)0733-9429(1984)110:10(1431)

Verbanck MA, Ashley RM, Bachoc A (1994) International workshop on origin, occurrence and behaviour of sediments in sewer systems: summary of conclusions. Water Res 28:187–194

An Analysis of Entrainment and Deposition Rate Fluctuations in Weak Bed Load Transport

Seyed Abbas Hosseini-Sadabadi, Alessio Radice and Francesco Ballio

Abstract The kinematics of particles moving over a fixed rough bed was experimentally investigated. Motion of sediment particles was recorded from the top of a pressurized duct using a CCD camera, and the then image processing was applied in order to track each particle. Particle tracking provides quantitative information about the time evolution of particle position and velocity. However, in this paper, the attention is focused onto the entrainment and deposition of particles. The entrainment rate may be used to quantify the solid discharge (through, for example, some pick-up function); the deposition rate is the counterpart of the former, that has however received comparatively less attention in previous studies of sediment transport. Temporal signals of the entrainment and deposition rates were investigated for different spatial and temporal scales, demonstrating how the intermittency of the transport process affects the fluctuation patterns. Consequently, the (spatial or temporal) scale dependency of the statistical moments of these rates was explored. An expected result was found, with scale-independent average values of the entrainment and deposition rates and a strong dependence on the support scale for the standard deviation values.

S.A. Hosseini-Sadabadi (✉) · A. Radice · F. Ballio
Department of Civil and Environmental Engineering, Politecnico Di Milano, Piazza L. Da Vinci 32, 20133 Milan, Italy
e-mail: seyedabbas.hosseini@polimi.it

A. Radice
e-mail: alessio.radice@polimi.it

F. Ballio
e-mail: francesco.ballio@polimi.it

P. Rowiński and A. Marion (eds.), *Hydrodynamic and Mass Transport at Freshwater Aquatic Interfaces*, GeoPlanet: Earth and Planetary Sciences,
DOI 10.1007/978-3-319-27750-9_27

1 Introduction

Investigation of sediment transport processes throughout the visual observation of particle motion has been a key topic for a number of studies during the past decades (from the pioneering works of Francis 1973; Fernandez Luque and Van Beek 1976; Drake et al. 1988, to the most recent ones of, for example, Lajeunesse et al. 2010; Ramesh et al. 2011; Roseberry et al. 2012; Julien and Bounvilay 2013; Heays et al. 2014).

The investigation of sediment kinematics may be approached from a Lagrangian (e.g., Nikora et al. 2002; Bialik et al. 2012; Campagnol et al. 2013) or Eulerian (e.g., Radice et al. 2009, 2010) point of view. The former is related with analysis at particle scale and requires tracking individual particles to provide particle-related information, whilst the second accounts for a finite control volume comprehending several or many particles and studies the transport properties within this volume.

The present study is focused on the temporal patterns of entrainment and deposition rates in weak bed-load transport. These rates are, on the one hand, related with suitably chosen control volumes and are therefore Eulerian quantities (appropriate definitions are given below). On the other hand, they are related with particle start and stop; therefore, rate values could be computed only provided that each grain was individually tracked. Measurements were thus conducted in a Lagrangian way, but data on single particle motion were averaged using appropriate spatial and temporal support scales to obtain values for the Eulerian quantities of interest. The manuscript is structured as follows: first, the experimental facilities and a benchmark experiment are presented; then, a definition framework is given for the considered variables; third, results are presented accounting for the temporal evolution of entrainment and deposition rates and for the scaling properties of their statistical moments; finally, the major conclusions of the work are outlined.

2 Experimental Run

The experiments described here were performed in a flume (Fig. 1) at the Hydraulics Laboratory of the Politecnico di Milano, Italy. The channel length is 5.8 m, while the rectangular cross-section is 0.4 m wide and 0.11 m high.

Sediment used for the experiments was made of uniform quasi-spherical PBT grains with equivalent dimension $d = 3$ mm and density $\rho_g = 1.27 \times 10^3$ kg/m^3. A fixed rough bed was employed by gluing two layers of sediment particles onto steel plates. For easier visualization, the bed was entirely painted in black, while the bed-load grains released into the channel were white. To feed the channel with particles, an impulsive automatic sediment feeder was used. The sediment transport capacity for this flume and particles was estimated by Campagnol et al. (2012a) and formulated as:

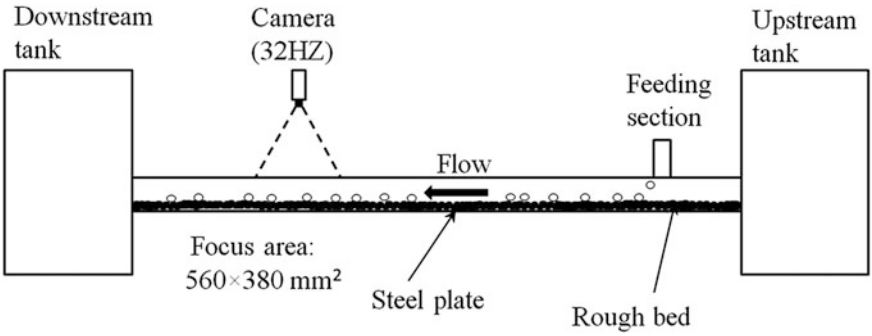

Fig. 1 Sketch of the experimental facility

$$q^* = 0.008\left[\left(\frac{Q}{Q_c}\right)^2 - 1\right]^{1.3} \tag{1}$$

where q^* is the dimensionless sediment transport rate per unit width, Q is the flow discharge and Q_c = 10.0 l/s is the threshold discharge for sediment motion.

A package of two Ultrasonic Velocity Profilers (UVP) was used to measure the time-averaged stream-wise velocity profile and the shear velocity (u^*) was consequently calculated from the profile using the following equation:

$$u(z) = \frac{u^*}{\kappa}\ln\frac{z}{z_0} \tag{2}$$

where $u(z)$ is the time-averaged stream-wise velocity at elevation z, κ = 0.4 is the Karman constant and z_0 is a hydrodynamic roughness length.

The experiment used in this study was performed with a discharge of 14.1 l/s; other characteristics of the experiment were: bulk flow velocity U = 320 mm/s; u^* = 15.6 mm/s; Reynolds number $Re = 3.5 \times 10^4$; particle Reynolds number $Re^* = 47$; $q^* = 0.008$.

A CCD camera placed above the channel recorded the motion of particles while passing through its observation field (Fig. 1), which corresponded to a focus area of 650 × 380 mm^2. In order to avoid picture distortion due to the presence of a free surface, a transparent lid was present at the top of the channel resulting in a fully pressurized system. Several earlier studies (e.g., Ettema 2008; Radice 2009) showed that the mechanics of sediment transport in covered flows is not significantly different from that in free-surface flows.

Bed-load particles were tracked along their motion using the Streams software (Nokes 2012), that was successfully used for previous experiments run with similar configurations to that described here (Campagnol et al. 2013, 2014). The output results from tracking consist of the stream-wise (x) and transverse (y) coordinates of particles at each frame (i.e., at each time instant) together with the corresponding

particle velocities. Although the main scope of the present paper is the investigation of entrainment and deposition rates, a statistical analysis was preliminary performed for intermediate trajectories. The latter were defined by Nikora et al. (2002) as particle motions between two successive periods of rest, and could be recognized within the paths tracked for each particle. Thanks to this, length and time duration of intermediate trajectories could be estimated, as well as mean grain velocity components. Mean trajectory lengths in x and y directions were $L_x = 26.5$ mm and $L_y = 1.09$ mm, respectively; the corresponding mean sediment velocity components were $V_x = 39.7$ mm/s and $V_y = 2.8$ mm/s; the mean particle travel time was $T = 0.6$ s.

3 Definitions

Differently from fluid flows, particle motion is characterized by motion and stillness terms alternating with each other. Results from particle tracking were first used to determine if a grain was moving or still at a certain instant. The algorithm introduced by Campagnol et al. (2013) was used also here. A particle was considered at motion if its x position was smaller than all those occupied in following instants, otherwise it was considered still (see the illustrative sketch in Fig. 2). Moving and still particles were assigned labels of 1 and 0, respectively.

Each particle motion event is bounded by entrainment and deposition (e.g., Drake et al. 1988). After labeling particle motion, instants of entrainment and deposition were determined (obviously, with a temporal resolution depending on the frame rate of the camera) as in Fig. 2. In the depicted examples, two transitions from label 0 to 1 and two transitions from 1 to 0 identify two particle entrainment events and two deposition events, respectively. Sometimes very short groups of zeros or ones were found in the temporal evolution of the assigned label. Therefore, validation criteria were introduced for entrainment and deposition events. An entrainment event was validated if, after it, a particle travelled a distance of at least

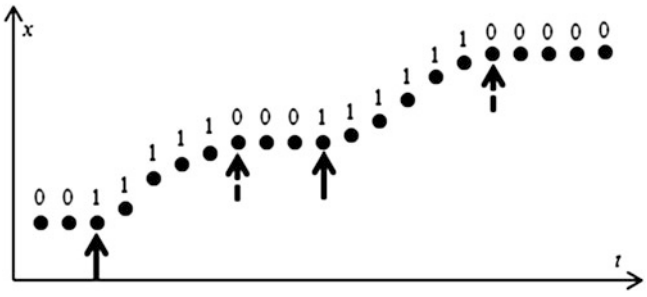

Fig. 2 Definition sketch for particle motion (labels 0/1), entrainment events (*continuous arrows*) and deposition events (*dashed arrows*)

one grain size (following Drake et al. 1988). Similarly, a deposition event was validated if, after it, the particle was at rest for a time larger than d/V_{mean}, with V_{mean} as the mean velocity of the grain before deposition.

The above sketch clarified definitions of particle entrainment and deposition events accounting for just one grain. In the experiment considered here, many particles were present and thus events were distributed in time and in space. Entrainment and deposition rates (E and D) were quantified introducing spatial and temporal reference scales (A and Δt, respectively, identifying an area of the bed and a sampling temporal interval):

$$E = \frac{N_E W_g}{A\Delta t}; \quad D = \frac{N_D W_g}{A\Delta t} \tag{3}$$

where N_E and N_D are the numbers of entrainment and deposition events detected within A and Δt, and W_g is the volume of one particle.

4 Results

The time evolution of the entrainment and deposition rates is depicted in Fig. 3 considering $A = 200 \times 200$ mm^2 and different values of Δt. The shorter time scale used (0.05 s) was only slightly larger than the camera frame (1/32 s) and resulted in very low values of N_E and N_D: for example, the E value computed with (3) for just one entrained particle was equal to 0.007. The larger temporal scale, which is larger than the mean duration of intermediate trajectories introduced above, obviously enabled more entrainment and deposition events to occur in a single time interval; a value of E equal to 0.005 would in this case correspond to 10 entrained particles. Decreasing the temporal scale of sampling introduces less averaging of the fluctuation pattern: the signal for the lower time scale is characterized by noticeable intermittency (defined as the presence of zero values in the time series for E and D) and higher spikes. Similar considerations were made, for example, by Campagnol et al. (2012b) considering time series of sediment transport rate.

In addition to the temporal scale, the spatial one also affects the fluctuation pattern of entrainment and deposition rates. This is illustrated by Fig. 4, which is the counterpart of Fig. 3: a fixed temporal scale of 0.4 s was used with two different spatial scales. The latter had the same width of 200 mm and lengths of 50 mm (twice the average length of intermediate trajectories) and 200 mm. The low peaks at 0.003 for E and D correspond to just one particle for the smaller area; for the larger one, values of 0.005 would correspond to 6 entrained or deposited particles. Evidently, as for times, a larger spatial scale produces more averaging of fluctuations and reduces the intermittency of the entrainment or deposition process. Also in this case, the behavior of E and D reflects similar ones of other key quantities depicting sediment transport: for example, Radice et al. (2009) and Campagnol

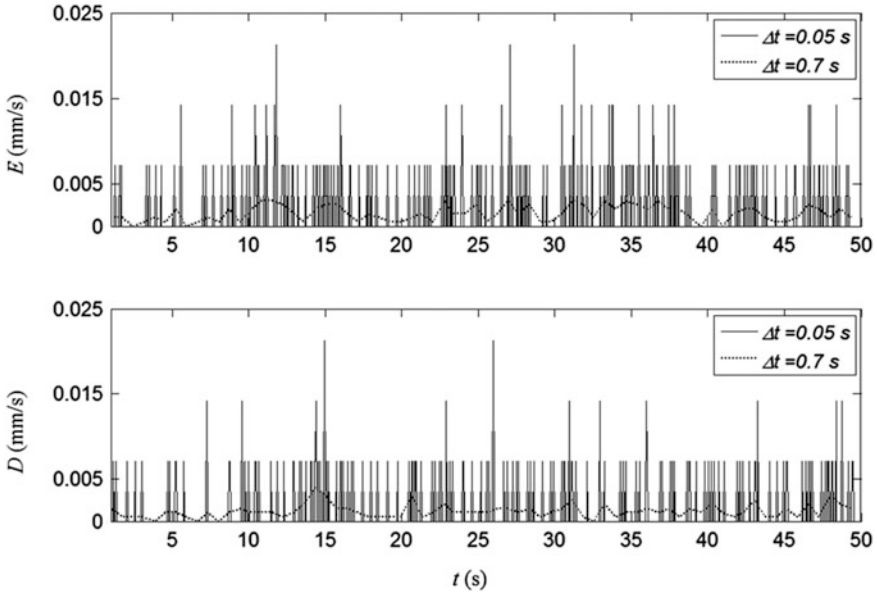

Fig. 3 Temporal variation of E and D for fixed spatial scale and changing time scale

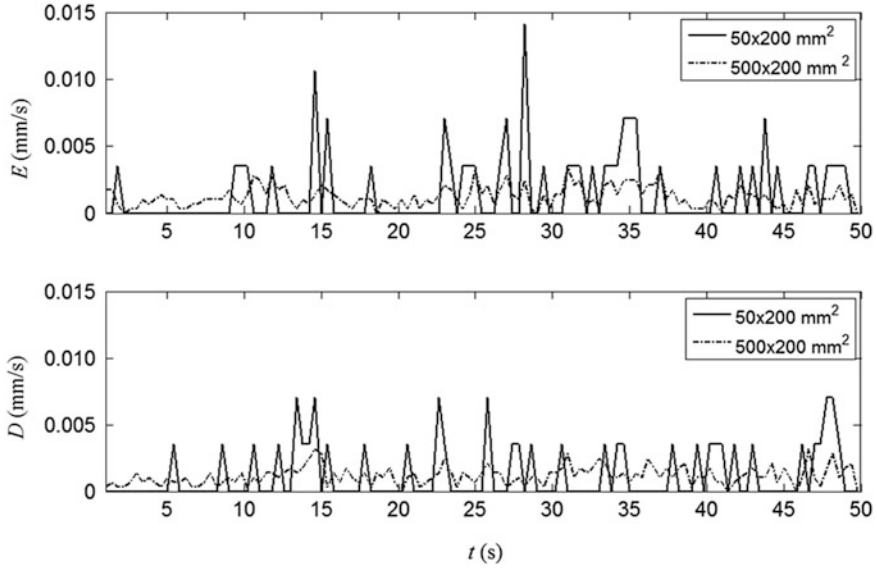

Fig. 4 Temporal variation of E and D for fixed temporal scale and changing the spatial scale

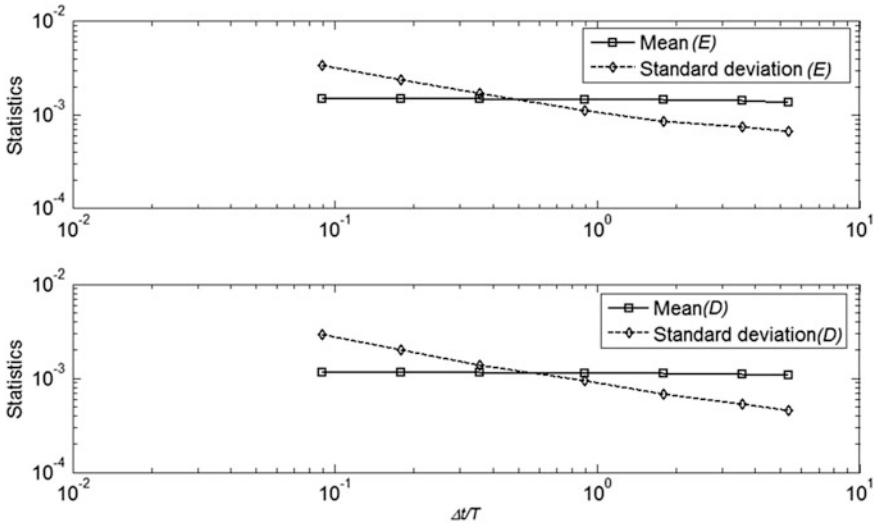

Fig. 5 Statistics (mean and standard deviation) of E and D for different temporal scales and fixed spatial scale

et al. (2012b) gave analogous arguments for bed-load sediment concentration and solid discharge, respectively.

The first- and second-order statistical moments (mean and standard deviation) of E and D were systematically analyzed for a range of temporal and spatial scales. The dependency of moments on the temporal scale was investigated using the following Δt s: 0.05, 0.1, 0.2, 0.5, 1, 2, and 3 s; these time intervals were made dimensionless using the average duration of intermediate trajectories. The spatial averaging scale for the analysis was maintained constant and equal to 200×200 mm^2. For the spatial scale analysis, a constant $\Delta t = 0.4$ s was used and the following areas were selected: 5×200, 10×200, 20×200, 50×200, 200×200, and 500×200 mm^2. All these areas had the same width of 200 mm while the scale was enlarged by increasing the length in the stream-wise direction (L) that was normalized by the average length of intermediate trajectories. Results are depicted in Figs. 5 and 6. The mean values of E and D resulted scale-independent, meaning that numbers of entrained and deposited particles increase linearly with the spatial and temporal scale used for sampling. By contrast, the standard deviation of the quantities decreases for increasing scale, reflecting the fact that averaging N_E and N_D over larger samples results in lower fluctuations. In all plots of Figs. 5 and 6, a power law with exponent close to –0.5 was obtained for the scaling behavior of standard deviations. Such result is consistent with the already mentioned findings of Radice et al. (2009) and Campagnol et al. (2012b) for bed-load sediment concentration and solid discharge. In the referenced works, a mathematical derivation was proposed to support the exponent of –0.5, also providing arguments on deviations from this trend being due to self-correlation of

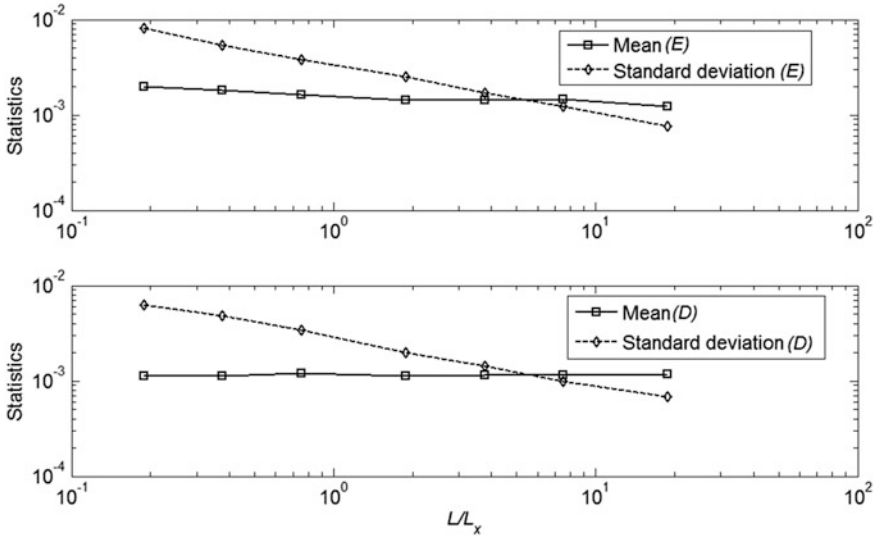

Fig. 6 Statistics (mean and standard deviation) of E and D for different spatial scales and fixed temporal scale

quantities. Results show that the E and D fields are not significantly auto-correlated within the ranges of scales explored here. Entrainment and deposition rates indicating analogous behavior to the solid discharge q_s and concentration C is a reasonable outcome, as both C and E are linearly correlated with q_s (frequently mentioned equations are $q_s = C \times V_x$ and $q_s = E \times L_x$, e.g., Seminara et al. 2002; Parker et al. 2003; Radice et al. 2006) and D is an obvious counterpart of E in transport processes at dynamic equilibrium.

5 Conclusions

Motion of bed-load particles over a fixed rough bed was experimentally studied. An image-based, particle tracking technique was used to obtain quantitative information about the instantaneous position and velocity of individual particles. Starts and stops of particle movements were recognized from the tracking data, and temporal series of the entrainment and deposition rates were obtained for a range of spatial support scales and sampling time intervals. The scale dependency of statistical moments of the samples for entrainment and deposition rates was investigated. Proof-of-concept, preliminary results were derived from one experiment under weak bed-load condition. As the results presented in this paper were obtained from a single experiment, the findings shall be further validated considering several tests (analysis is currently in progress). The main conclusions drawn from the study are summarized as follows:

1. The time series for E and D show that quantities are highly fluctuating for small support scales, for which the intermittency of the sediment transport process clearly emerges and high spikes are detected. For increasing support scales, the fluctuation pattern becomes 'smoother' due to averaging over larger numbers of entrained and deposited grains.
2. The mean values of both E and D are scale independent, whereas a strong scale dependency was found for the standard deviation of these parameters, in agreement with the previous conclusion.
3. The trend of variation of the standard deviation of E and D with a support scale was well approximated by a power law with exponent of –0.5, suggesting that the two rates be self-uncorrelated, at least in the ranges of scales explored in this work. These findings are consistent with those obtained in earlier works for other key quantities of sediment transport (solid discharge, sediment concentration).

References

Bialik RJ, Nikora VI, Rowiński PM (2012) 3D Lagrangian modelling of saltating particles diffusion in turbulent water flow. Acta Geophys 60(6):1639–1660

Campagnol J, Ballio F, Hosseini Sadabadi SA, Sazadul H (2014) Particle motion of bed-load sediment moving over a smooth bed. In: Proceedings of river flow 2014, VII international conference on fluvial hydraulics, Lausanne, Switzerland

Campagnol J, Radice A, Nokes R, Bulankina V, Lescova A, Ballio F (2013) Lagrangian analysis of bed-load sediment motion: database contribution. J Hydraul Res 51(5):589–596

Campagnol J, Radice A, Ballio F (2012a) Insight on how bed configuration affects properties of bed load motion. In: Proceedings of ICSE 2012, VI international conference on scour and erosion, Paris, France

Campagnol J, Radice A, Ballio F (2012b) Scale-based statistical analysis of sediment fluxes. Acta Geophys 60(6):1744–1777

Drake TG, Shreve RL, Dietrich WE, Whiting PJ, Leopold LB (1988) Bedload transport of fine gravel observed by motion-picture photography. J Fluid Mech 192:193–217

Ettema R (2008) Ice effects on sediment transport in rivers. In: Garcìa MH (ed) Sedimentation engineering, ASCE manual report on engineering practice. vol 110, 613–648

Fernandez Luque R, Van Beek R (1976) Erosion and transport of bed-load sediment. J Hydraul Res 14(2):127–144

Francis JRD (1973) Experiments on the motion of solitary grains along the bed of a water-stream. Proc R Soc Lond A 332:443–471

Heays KG, Friedrich H, Melville BW, Nokes R (2014) Quantifying the dynamic evolution of graded gravel beds using particle tracking velocimetry. J Hydraul Eng 140:04014027

Julien PY, Bounvilay B (2013) Velocity of rolling bed load particles. J Hydraul Eng 139(2):177–186

Lajeunesse E, Malverti L, Charru F (2010) Bed load transport in turbulent flow at the grain scale: experiments and modeling. J Geophys Res 115:F04001

Nikora V, Habersack H, Huber T, McEwan I (2002) On bed particle diffusion in gravel bed flows under weak bed load transport. Water Resour Res 38(6):17

Nokes R (2012) Streams v. 2.00. System theory and design. University of Canterbury, Christchurch

Parker G, Seminara G, Solari L (2003) Bed load at low Shields stress on arbitrarily sloping beds: alternative entrainment formulation. Water Resour Res 39(7):1183

Radice A (2009) Use of the Lorenz curve to quantify statistical nonuniformity of sediment transport rate. J Hydraul Eng 135(4):320–326

Radice A, Ballio F, Nikora V (2010) Statistics and characteristic scales for bed load in a channel flow with sidewall effects. Acta Geophys 58(6):1072–1093

Radice A, Ballio F, Nikora V (2009) On statistical properties of bed load sediment concentration. Water Resour Res 45:W06501

Radice A, Malavasi S, Ballio F (2006) Solid transport measurements through image processing. Exp Fluids 41:721–734

Ramesh B, Kothyari UC, Murugesan K (2011) Near-bed particle motion over transitionally-rough bed. J Hydraul Res 49(6):757–765

Roseberry JC, Schmeeckle MW, Furbish DJ (2012) A probabilistic description of the bed load sediment flux: 2. particle activity and motions. J Geophys Res 117(F3):F03032

Seminara G, Solari L, Parker G (2002) Bed load at low shields stress on arbitrarily sloping beds: failure of the Bagnold hypothesis. Water Resour Res 38(11):1249

Erratum to: Hydrodynamic and Mass Transport at Freshwater Aquatic Interfaces

Paweł Rowiński and Andrea Marion

Erratum to:
P. Rowiński and A. Marion (eds.), *Hydrodynamic and Mass Transportat Freshwater Aquatic Interfaces*, GeoPlanet: Earth and Planetary Sciences,
DOI 10.1007/978-3-319-27750-9

The book was inadvertently published with an incorrect initial of M. Paweł Rowiński. The correct name is Paweł Rowiński rather than M. Paweł Rowiński.

The updated original online version for this book can be found at DOI 10.1007/978-3-319-27750-9

P. Rowiński (✉)
Polish Academy of Sciences, Institute of Geophysics, Warsaw, Poland

A. Marion
Department of Industrial Engineering, University of Padua, Padua, Italy

P. Rowiński and A. Marion (eds.), *Hydrodynamic and Mass Transport at Freshwater Aquatic Interfaces*, GeoPlanet: Earth and Planetary Sciences,
DOI 10.1007/978-3-319-27750-9_28